Fatigue and Fracture Mechanics

30th Volume

Kenneth L. Jerina and
Paul C. Paris, editors

ASTM

STP 1360

STP 1360

Fatigue and Fracture Mechanics: 30th Volume

Kenneth L. Jerina and Paul C. Paris, editors

ASTM Stock Number: STP1360

ASTM
100 Barr Harbor Drive
West Conshohocken, PA 19428-2959
Printed in the U.S.A.

ISBN: 0-8031-2617-4
ISSN: 1040-3094

Photocopy Rights

Peer Review Policy

Each paper published in this volume was evaluated by two peer reviewers and at least one editor. The authors addressed all of the reviewers' comments to the satisfaction of both the technical editor(s) and the ASTM Committee on Publications.

The quality of the papers in this publication reflects not only the obvious efforts of the authors and the technical editor(s), but also the work of the peer reviewers. In keeping with long-standing publication practices, ASTM maintains the anonymity of the peer reviewers. The ASTM Committee on Publications acknowledges with appreciation their dedication and contribution of time and effort on behalf of ASTM.

Printed in Baltimore,MD
January 2000

Dedication

This volume of proceedings of the 30th National Symposium is dedicated to Edward T. Wessel for his long-standing support of the Symposium series and for his leadership associated with ASTM committee activities.

Mr. Wessel began his activities with the E-8 Committee through its predecessor E-24 when it was an ASTM special committee investigating fracture problems associated with the Polaris rocket motor cases in the late 1950s. During that time and to the present, he and the group he led at Westinghouse Research Laboratories made many monumental contributions to fracture mechanics. Scores of outstanding research papers from individuals in his research group have been published in the National Symposium volumes. The hallmark of his leadership was a spirited team effort to understand and advance many aspects of fracture mechanics. Therefore, this dedication is a well-deserved "thank you" to Edward T. Wessel and is enthusiastically endorsed by all associated with the National Symposium series.

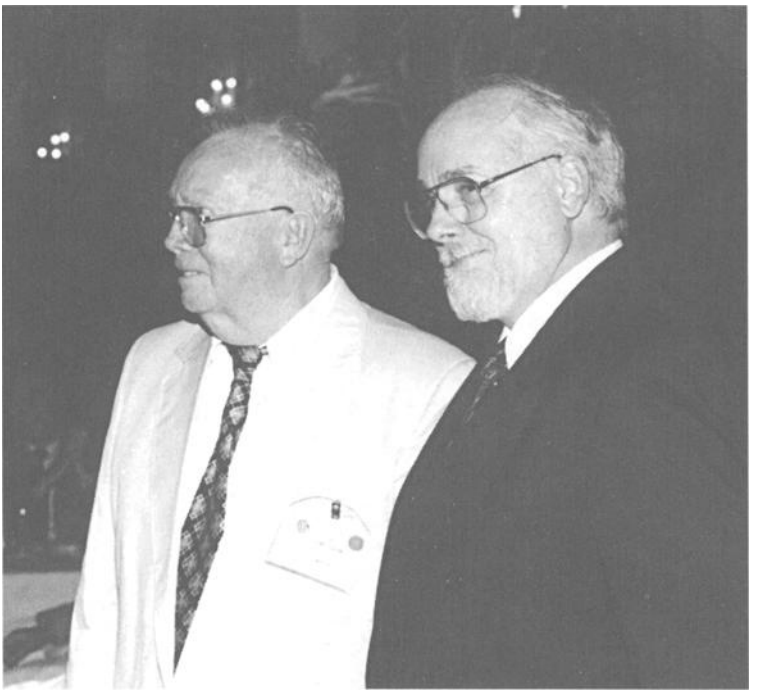

Edward Wessel (left) with E-8 Chairman Stephen W. Hopkins at the 30th National Symposium banquet.

Contents

Foreword ix

JERRY L. SWEDLOW MEMORIAL LECTURE

Elastic-Plastic Fracture Mechanics: Where Has It Been? Where Is It Going?—J. D. LANDES 3

SESSION I

Technical Basis for the Master Curve Concept of Fracture Toughness Evaluations in the Transition Range—D. E. MCCABE, J. G. MERKLE, AND K. WALLIN 21

A Unifying Principle for Evaluating Fracture Toughness in the Elastic and Plastic Regimes with Planar Fracture Specimens—J. R. DONOSO AND J. D. LANDES 34

A Micromechanical Evaluation of the Master Curve—M. E. NATISHAN AND M. T. KIRK 51

Method for Predicting *J-R* Curves from Charpy Impact Energy—P. C. GIOIELLI, J. D. LANDES, P. C. PARIS, H. TADA, AND L. LOUSHIN 61

Fracture Toughness Testing with Notched Round Bars—C. D. WILSON AND J. D. LANDES 69

SESSION II

3-D Finite Element Modeling of Ductile Crack Growth in Thin Aluminum Materials—A. S. GULLERUD, R. H. DODDS, JR., R. W. HAMPTON, AND D. S. DAWICKE 85

***J-Q-M* Approach for Failure Assessment of Fusion Line Cracks: Two-Material and Three-Material Modes**—C. THAULOW, Z. ZHANG, Ø. RANESTAD, AND M. HAUGE 102

Fracture Mechanics Validity Limits and Physical Evidence of Constraint in Fracture—D. M. LAMBERT AND H. A. ERNST 115

The Role of Cohesive Strength and Separation Energy for Modeling of Ductile Fracture—T. SIEGMUND AND W. BROCKS 139

Modeling the Ductile to Cleavage Transition in Steels and Structures—I. C. HOWARD, Z. H. LI, M. A. SHEIKH, AND SIRIUS 152

A Computational Fracture Mechanics Approach for the Analysis of Facesheet-from-Core Disbond of Honeycomb Core Sandwich Panels—S. C. TERMAATH, A. R. INGRAFFEA, AND P. A. WAWRZYNEK 169

SESSION III

Crack Wake Influence Theory and Elastic Crack Closure Measurement—J. K. DONALD, G. M. CONNELLY, P. C. PARIS, AND H. TADA 185

Fatigue Crack Propagation and Load Interaction Effects in a Titanium Alloy—M. LANG AND J. M. LARSEN 201

Fatigue Analysis of Multiple Site Damage in Lap Joint Specimens—H.-L. WANG AND A. F. GRANDT, JR. 214

A Combined Experimental and Finite Element Study of Crack Closure Effects in Modified 1070 Steel—J. D. DOUGHERTY, T. S. SRIVATSAN, AND J. PADOVAN 227

Subsurface Fatigue Crack Initiation and Propagation Behavior of Induction-Hardened Shafts under the Effect of Residual and Applied Bending Stresses—H.-Y. ZHANG, R. I. STEPHENS, AND G. GLINKA 240

SESSION IV

Estimation Procedure for Determination of Fatigue Crack Propagation in Metal Alloys—R. W. HERTZBERG 263

The Fracture and Fatigue Crack Growth Behavior of Forged Damage-Tolerant Niobium Aluminide Intermetallics—F. YE, C. MERCER, D. FARKAS, AND W. O. SOBOYEJO 278

The Effect of Biaxial Strain Ratio and Periodic Compressive Overstrains on Fatigue Crack Growth Mode and Crack Growth Rate—A. VARVANI-FARAHANI AND T. H. TOPPER 299

Determination of C_t-Parameter Considering Effects of Accumulated Creep Deformation During Loading Period—J. H. LEE, Y. J. KIM, AND K. B. YOON 313

A New Multiparameter Model for the Prediction of Fatigue Crack Growth in Structural Metallic Materials—A. B. O. SOBOYEJO, M. A. FOSTER, C. MERCER, J. C. PAPRITAN, AND W. O. SOBOYEJO 327

SESSION V

Fracture Mechanics: Forgotten German and Austrian Pioneers of the Turn of the 20th Century—HANS P. ROSSMANITH 347

Development of Consistent Size Criteria for ASTM Combined Fracture Mechanics Standards—J. A. JOYCE AND R. L. TREGONING 357

Use of the Instrumented Bolt and Constant Displacement Bold-Loaded Specimen to Measure In-Situ Hydrogen Crack Growth in High-Strength Steels—G. N. VIGILANTE, J. H. UNDERWOOD, AND D. CRAYON 377

Prediction of S-N Fatigue Curves Using Various Long-Crack-Derived ΔK_{eff} Fatigue Crack Growth Curves and a Small Crack Life Prediction Model—J. R. BROCKENBROUGH AND G. H. BRAY 388

Stress and Fracture Analyses of Semi-Elliptical Surface Cracks—J. C. NEWMAN, JR., W. G. REUTER, AND C. R. AVELINE, JR. 403

SESSION VI

Early Stage Fatigue Damage Characterization in Aluminum Alloys and Stainless Steels with Meandering Winding Magnetometer Technology—V. WEISS, N. GOLDFINE, AND M. NATISHAN 427

Finite-Element Fracture Analyses of Welded Beam-Column Connections—W.-M. CHI, G. G. DEIERLEIN, AND A. R. INGRAFFEA 439

A Plate Element-Based Model for Mixed-Mode Debonding of Composite Stitched Stiffened Panels—E. H. GLAESSGEN, I. S. RAJU, AND C. C. POE, JR. 456

Indexes 473

Foreword

The 30th National Symposium on Fatigue and Fracture Mechanics was held at Washington University in St. Louis 23–25 June 1998. The technical session presentations were in the "Moot Court Room" of the Anheuser-Busch Hall, and the conference banquet was held in Holmes Lounge, a recently renovated room in Ridgley Hall that dates back to the 1904 World's Fair. Professors Kenneth L. Jerina and Paul C. Paris hosted and co-chaired the festivities (Fig. 1).

It is of special interest to note that Dr. George R. Irwin, a founder of this symposium series and 91-years-old attended these sessions. His arrival at the technical sessions was greeted with a standing ovation. Whereupon he proceeded to a front row seat and participated in discussions of the technical presentations. Sadly, a few months later, in October 1998, Dr. Irwin passed away. Figure 2 shows him at the banquet surrounded by many friends.

The banquet for the 30th National Symposium took on a "belle epoch" theme from the 1904 World's Fair Holmes Lounge venue, the classic cuisine provided by Cafe de France and the entertainment provided by the Ragtimers, a ragtime musical group associated with Washington University. In addition, the banquet provided an elegant forum for Stephen W. Hopkins, Chairman of the ASTM E-8 sponsoring committee, to present several awards and honors. The first was to announce and congratulate Edward T. Wessel for being chosen for a special award of ASTM for his many years of leadership within E-8. Next, Professor John D. Landes was honored with a plaque acknowledging his presentation of The Swedlow Memorial Lecture at this symposium, as depicted in Fig. 3.

Mr. Hopkins also surprised Professor Paris by presenting him with the ASTM Dudley Medal for co-founding the symposium series and his contributions to these symposia. Professor Paris was also

FIG. 1—*Co-chairmen Professors Jerina (left) and Paris.*

FIG. 2—*Dr. George R. Irwin (center) and friends.*

designated as the National Symposium subcommittee "honorary chairman" and keeper of the "symposium bell" by E-8 Chairman Hopkins. Figure 4 shows this presentation.

Another award associated with this symposium was that for the best presentation of a paper. This award was presented to Professor Richard W. Hertzberg at the November 1998 meeting of ASTM Committee E-8 by Chairman Hopkins. This presentation is shown in Fig. 5.

FIG. 3—*Professor John D. Landes (left) receiving his award from E-8 Chairman Hopkins.*

FIG. 4—*Professor Paris receiving the ASTM Dudley Medal.*

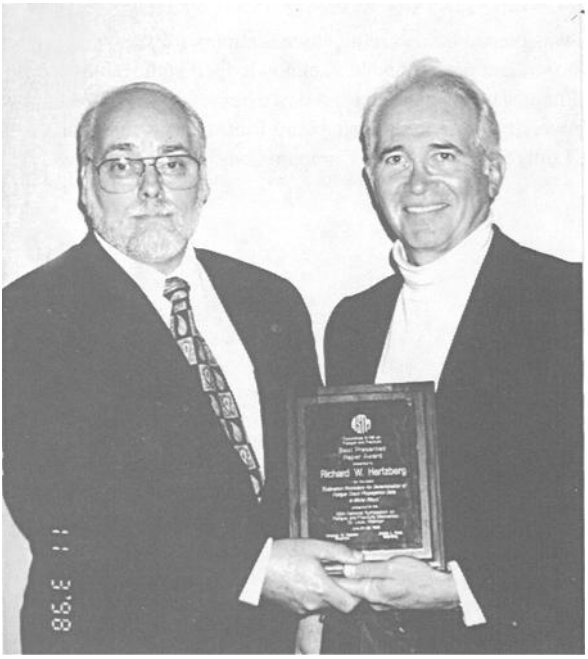

FIG. 5—*Professor Hertzberg receiving the best presentation award.*

FIG. 6—*Ms. S. TerMaath cited for the best student presentation by Mr. J. Schiele.*

Special emphasis was placed on receiving student papers for this symposium, of which nine were presented. Each of the student presenters was acknowledged at the banquet with a certificate for their meritorious efforts. Plaques were awarded for the two best papers. Figure 6 shows Ms. Stephanie Ter-Maath of Cornell University receiving a cash award for the best student presentation from Mr. James Schiele, CEO of St. Louis Screw and Bolt Company, who donated the award.

Kenneth L. Jerina
Materials Research Laboratory
Washington University,
St. Louis, MO

Paul C. Paris
Mechanical Engineering
Washington University
St. Louis, MO

Jerry L. Swedlow Memorial Lecture

John D. Landes[1]

Elastic-Plastic Fracture Mechanics: Where Has It Been? Where Is It Going?

REFERENCE: Landes, J. D., **"Elastic-Plastic Fracture Mechanics: Where Has It Been? Where Is It Going?"** *Fatigue and Fracture Mechanics: 30th Volume, ASTM STP 1360,* P. C. Paris and K. L. Jerina, Eds., American Society for Testing and Materials, West Conshohocken, PA, 2000, pp. 3–18.

ABSTRACT: Elastic-plastic fracture mechanics (EPFM) is the name given to a body of fracture technology that includes parameters, test methods, and analysis techniques. EPFM began in the 1960s, soon after it was recognized that the linear elastic approach to fracture mechanics was too limited to cover many engineering applications. It began in response to real engineering problems and continues to develop in the same application-driven mode. The development of EPFM spans more than three decades. It involved many people and a multitude of good ideas. Some of the people have gone on to other pursuits, and many of the ideas have been set aside or discarded in the never-ending debate about which is the best approach. The development of EPFM is not complete, nor is the controversy ended. It is important to look back at the factors that influenced such a vast development of technology before trying to forge ahead.

This paper takes a look at the area of fracture mechanics called EPFM. It considers the development of a technology that involved people, places, and a seemingly inexhaustible supply of technical ideas. It considers what happened in the past, what is going on in the present, and speculates about what will happen for the future. Its purpose is to stop for a moment and consider for EPFM: Where has it been? Where is it going?

KEYWORDS: elastic-plastic, fracture mechanics, history, people, events, technology, future

It is an honor to be chosen as the 9th Jerry Swedlow Memorial lecturer. Jerry Swedlow was a friend and colleague in the field of fracture mechanics research. He was a long-time national chair of this Symposium series. He was also a contributor to the subject whose history will be recounted in this lecture. His life and contributions to the field of fracture mechanics are still remembered by many of us.

Introduction

The history of the development of fracture mechanics involves more than the body of technical literature that evolved. That alone is voluminous; much of it is lost or forgotten. A thorough recounting of all of the literature could provide one type of history, one that is technically complete and factual but hopelessly boring. Rather, the more interesting part of this development involves events, places, and mainly people. This part of the history exists in peoples' memories; it will soon be forgotten and lost forever unless it is documented in writing. The lecture that forms the basis of this paper is scheduled for 35 minutes, not for the entire three days of the symposium; even that would not be enough. Therefore, the scope of this history has to be limited. The subject that I want to address is a little of the history of the development of the part of fracture mechanics called elastic-plastic fracture mechanics (EPFM). This will not be a comprehensive and definitive treatise on the subject. Neither will the claim be made that it is the whole truth or nothing but the truth. Rather it is limited to the facts,

[1] University of Tennessee, 310 Perkins Hall, Knoxville, TN 37996-2030.

tempered by time, that remain in my memory, what I saw and what appeared to me to make an impact on this subject. The part of the history that I present would not be the same one that another person might write. Therefore, events, places, and people that were undoubtedly important to another person might be missing, not because they do not belong, but because they do not form the part of my memory that I am recording here.

Beginnings at Lehigh

The beginning of the fracture mechanics story for me was at Lehigh University. I went there in 1960 as a prospective freshman, complete with brown and white dink (some kind of freshman hat) and loads of anxiety. The first person I met in what was to become my decade at Lehigh was my dormitory counselor, a Lehigh junior named James Rice; he was a member of the upperclassmen counselors group called Gryphons. Of course, there was no way to know at the time that I was meeting someone who was to become a legend in the fracture mechanics field as well as the entire field of applied mechanics, the very person who would start me on the path to a career in fracture mechanics. He was just a friendly face, someone who tried to help new freshmen recover from homesickness. Jim Rice in those days soon gained a reputation for his ability to help with those conceptual problems with physics and mathematics that all new university students have. "What does it mean in the limit as Δx goes to zero; why not let it be zero to start with and avoid this confusion." Every evening when study time began, a line would form at his door; these were freshmen with seemingly unsolvable technical problems that Jim could solve or explain in a minute or so. First the lineup was small, containing students from our section of about 25 students, those who had Jim as their counselor, but soon the lineup became bigger and bigger, as the entire freshmen class found that here was someone who knew the answers to all of the technical problems ever posed to freshmen. I still did not understand his special ability; I thought that all upperclassmen could do that. Upon meeting another upperclassmen counselor, I asked, "Why don't you help your students like Jim Rice does for us; then they wouldn't have to bother him every night." "You don't understand," he replied, "Jim has an understanding that is levels above ours; we can't do what he does." The world of fracture mechanics would soon learn this.

As a relief from the nightly lineup, Jim that year got involved in student politics. Along with that were the meetings and sessions of liquid refreshment that followed. Often he would not return to his room until after midnight. The line was always there waiting. He always took the time to help, no matter how he felt. In spite of his many talents, what he could not do for himself was wake up in the morning. The various members of his section had wake up duty, assigned on a rotating basis. That required going into his room at the appointed time (his door was never locked), pulling him out of his bed, and standing him up to make sure he was awake. For the person who did not take his assignment seriously enough, this process was completely reversible.

Jim Rice told all of the freshmen who were engineering students about a new department and major, Engineering Mechanics, led by Ferd Beer, later famous for his undergraduate engineering textbooks. This new major was Jim's choice and his recommendation for everyone not set on a specific engineering discipline. On hearing about the basic and theoretical nature of the curriculum, I asked, "What advantage does this have over basic curricula like physics and mathematics." "In those," Jim said, "you need a Ph.D. before you are seriously considered as a contributor to new technology. In mechanics, you can become a contributor at a much earlier stage in your career." Jim was an early contributor. He also mentioned a previous undergraduate, named John Hutchinson, who had completed this program and then gone on to Harvard to become a superstar. Jim finished a B.S. degree in 1962. He stayed at Lehigh for graduate work, finishing an M.S. degree in 1963 and a Ph.D. in 1964. He could take five graduate classes per semester for credit while teaching undergraduate classes and work on his dissertation at the same time. Then, in his spare time, he worked on topics that were not part of his dissertation research and wrote papers that have become all-time classics in the field of fracture mechanics. On a recommendation form for a fellowship, one professor had to answer the

question, "Is this person creative?" He answered, "Jim Rice is the most creative person on campus; that includes all students and faculty."

Anyway, about one third of Jim's section, including me, signed up for that new major, Engineering Mechanics. That was a critical decision that began my career in fracture mechanics. During my third year as an undergraduate, a new honors program was introduced to us. Thanks to the efforts of Jim Rice, our class was the biggest in the history of that major and ready for an honors program. In that program, I was introduced to two young professors, Paul Paris and George Sih. They told us about their research area called fracture mechanics, a new research field started only a few years before by George Irwin. The objective of the honors program was to begin a summer project that would carry to the fourth and senior year. I chose to work with Paul Paris on a fatigue crack growth project, for no good reason other than Professor Paris told a good story about his work. About six students were involved. All of the others chose different professors. The projects involved simple mechanics concepts that undergraduates could understand. They required intuitive reasoning and a simple experimental setup. When it came to simplifying a problem and designing experimental setups, only Paul Paris seemed to have the intuitive skills and experimental know how to make the projects work. By mid-summer, Paul Paris was advising all of the honors students, not only me.

The young professor, Paul Paris, was committed to helping students developing rudimentary skills in fracture mechanics. Also, he was extremely busy, traveling nearly every week. Paul was difficult to find when you wanted a conference, but when you finally did find him, he would give you the rest of the day if needed. He never once said, "Come back some other time, I am too busy right now." Knowing what I do now about being a professor, he was probably always too busy; he simply chose to let the students' needs come first.

My first formal instruction in fracture mechanics came from a course that Paris and Sih were offering, what I believe was the first fracture mechanics course on a university campus. I took this course in the spring of 1964. At that time it was already a seasoned course, although the bulk of what we know as fracture mechanics technology had yet to be discovered. In that course I sometimes pondered the problems of fracture mechanics with a graduate student named Dick Hertzberg, now known among other accomplishments for his textbook on deformation and fracture. That course, as well as the interaction with Paul Paris in the honors program, guided me into the discipline known as fracture mechanics; I decided to stay at Lehigh for graduate work; it was the biggest university center for fracture mechanics work at that time, I would guess perhaps of all time.

A theoretical M.S. thesis in fracture advised by Fazil Erdogan convinced me that I would prefer the experimental approach. The help with the experimental approach came from an expert in experimental fracture mechanics work named Bob Wei, who joined the faculty in 1966. He was my Ph.D. advisor. A year later George Irwin joined the Lehigh faculty. During my Ph.D. years at Lehigh, Paul Paris felt that fracture mechanics was ready for its own symposium. With help from George Irwin, the National Symposium on Fracture Mechanics was initiated and held at Lehigh in 1967. Still being part of the group that was headed by Paul Paris, I was asked to be one of the projectionists. So my first offering to this Symposium series that has now reached its thirtieth meeting was as a projectionist. This role continued for the second and third Symposia, 1968 and 1969. I got to meet all of the speakers; I had to load their slides. One of the speakers that I met in 1967 was Ed Wessel. He as well as the others were enthusiastic about this new field called fracture mechanics. After my Ph.D. experience at Lehigh, my desire to pursue a career in fracture mechanics was certain.

Early Westinghouse Years

My decision to go to work at Westinghouse after finishing a decade at Lehigh was not just an accident. My professors at Lehigh said that a group headed by Ed Wessel at Westinghouse was doing the best work in the field of experimental fracture mechanics, my main interest at the time. I was fortunate enough to be hired. I moved to Pittsburgh in January of 1970. Two of the first things that Ed

did after I began working was to describe the major task that he wanted to address and to introduce me to Jim Begley. I already knew Jim from Lehigh, but I was a mechanics student and he was a metallurgy student. At Lehigh our paths crossed only occasionally; at Westinghouse we were to become a team formed to attack a new and important problem.

Jim Begley in those years was extremely creative; he always seemed to be working on a new idea. His head was so full of research plans that he sometimes forgot the smaller details of life like where did he park his car, or when is that meeting scheduled, likely yesterday. I can remember times when there was a project review upcoming, something often feared by many researchers and sometimes requiring at least a week of preparation and worry. Jim had a different approach. Several times on the morning of such a review, when asked, "Jim are you ready for the project review today," he would answer, "Is that thing today? I forgot all about it." Then with only a piece of chalk and a blackboard he could lay out the project goals, progress, and reasons why this project was better than most in previous history, in such a way that the sponsor was completely sold on the work we were doing. Although Jim and I only worked together about five years, that work had a marked influence on our careers.

Ed Wessel during the decade of the 1970s went on to develop perhaps the most recognized group ever assembled to do fracture mechanics research. He had a definite philosophy for attacking problems, which he would express with sayings like; "I pick good people and let them alone to do the work; I take care of all the administrative horse potatoes so that the workers do not get bogged down with that." Also, "when we work, we work hard; when we play, we play hard." He led the way in both categories. Perhaps the thing that best illustrates his success as a manager is the final demise of the group. Westinghouse thought that the group was doing so well that anyone could manage it. In the early 1980s they decided to replace Ed with another manager. The group soon dispersed and the researchers left for other organizations, going to universities, national laboratories, and other companies.

The task that Ed Wessel described to Jim Begley and me seemed difficult. "After more than ten years of fracture mechanics, we can still handle only predominantly linear-elastic behavior. The materials that we use in the structures that Westinghouse builds do not experience fracture under linear-elastic loading. We have to extend the current approach of fracture mechanics to cover the cases of interest to Westinghouse." Then he showed us what is now called the million dollar fracture toughness curve, a series of K_{Ic} test results from an A533B steel plate on specimen sizes going from 1T (1 inch thick) to 12T (twelve inches thick). Even with 12 inches thick there was no valid K_{Ic} past a very limited temperature value, far below operating temperature of the nuclear reactor pressure vessels that used this material. "The design of the nuclear reactor pressure vessel is so critical that we have to develop a way to measure fracture toughness, all the way to operating temperature," Ed said. Jim Begley and I were assigned to begin to work on this problem.

It is interesting to me to note that at the time we began this work there was adequate funding to do the job. Also, nobody asked for a detailed write-up of what we planned to find with this funding and exactly when we planned to find it. We did not have a lot of milestones, monthly deliverables, strategic plans. We had a problem to solve, funding to go ahead, but none of the modern controls that impede technical progress in the guise of fiscal responsibility or safeguarding the taxpayers' money. I sometimes wonder whether starting 20 years later, in this modern funding climate, the elastic-plastic fracture mechanics work that was conducted at Westinghouse in the 1970s could have been accomplished today.

The work that Jim Begley and I began at Westinghouse led to the proposal of the J integral [*1*] as a parameter to characterize fracture toughness when linear-elastic conditions no longer prevail. The decision to try J was not so straightforward as I now like to present. "Since K is the single parameter that gives the magnitude of the dominant term of the crack tip stresses under linear-elastic conditions, etc., and a crack tip stress equation can be written for nonlinear elastic conditions with J, etc., then J is the logical extension of K for elastic-plastic conditions." It was not that straightforward in the be-

ginning. We began working on an experimental procedure that considered non-linear energies of loading. The approach was essentially an experimental scheme; the idea of a path-independent integral had not come up yet. At the same time the experimental approach was being considered, we were reading papers by Rice, Hutchinson, and McClintock [*2–5*]. One day Jim Begley said, "You know this testing method we are trying is just the physical energy rate definition that Jim Rice has attached to his J integral." From there on ideas began to take shape; what we measured by our experimental approach was J; the path independence related the boundary loading stresses to the crack tip field stresses. Finally, the crack tip stress equations which contained J as the scaling coefficient of the crack tip stress and strain fields made the choice sound logical. From a field theory point of view it was just an extension of the K approach that Irwin had proposed more than a decade before [*6*].

Jim Begley and I, having convinced ourselves that we were on to something that could be important in solving the problem that Ed Wessel posed, convinced him that we were making progress. Jim once said, "I can see this idea being so important that we could publish more than one paper from it, maybe even three or four." Ed Wessel did not like to keep ideas hidden for long. He was always in favor of going to the experts with the idea to see what they thought. The experts at the time, at least relating to this idea, were the two people who had led me into the field of fracture mechanics in the first place, Jim Rice and Paul Paris. We invited them separately to Westinghouse to discuss the idea. Neither liked it very well at first. Jim gave a list of reasons why J probably could not work as a fracture toughness parameter. Paul expressed the opinion that this was a good start and if we keep working we might get to the correct approach before long. Jim Begley and I were not that easily discouraged. We went on with experiments, and they were encouraging.

An important step in the development of the J approach was the convening of an experts meeting on April 13, 1971. The attendance list is Attachment 1 to this paper. All of the people interested in the subject were present, including Jerry Swedlow, the person who is remembered by this lecture series. Ed Wessel opened the meeting with an introduction to what the meeting was about; he was always supportive of the work we did. Jim Rice gave the lead lecture, recounting what was known about J and the non-linear characterization of crack tip stress fields. The series of presentations continued, with most of the major researchers giving some viewpoint on elastic-plastic fracture. George Irwin even talked about COD. During the meeting there was a lot of disagreement and controversy until I presented the experimental results that Jim Begley and I had developed to date. The controversy slowed down considerably. Paul Paris summarized the results of the meeting. His lead statement was "we have more agreement at this point than we have disagreement." In fact, a major hurdle was passed at this meeting in the development of a new approach to fracture mechanics. You can notice the name for the meeting is "Elastic-Fully Plastic Fracture Criteria Meeting"; this was apparently the forerunner to elastic-plastic fracture mechanics.

An interesting footnote to this meeting that I found in notes from the meeting is that Jim Rice proposed the form of the equation for calculating J, basically work of loading divided by the uncracked ligament area, that was to become the Rice, Paris, Merkle approach [*7*] of a few years later. His analysis was based on perfect plasticity and was not taken seriously by the group at the time since they feared that hardening might alter the form of the expression. Also, when asked by Herb Corten what to do about high temperature, Jim replied, "I have another integral for that." That is the integral that was later to become the C^* integral used to correlate creep crack growth data.

The first set of papers on J as a fracture criterion was presented at the Fifth National Symposium on Fracture Mechanics, held at the University of Illinois, in September 1971. Two papers were presented, and the first proposed the J integral as a fracture criterion with theoretical justification [*8*]; the term HRR to describe the nonlinear crack tip stress field first appears in that paper. The second paper showed data to confirm that J gave an independent fracture toughness measurement for initiation of ductile fracture on two geometries, a compact specimen, and a center-cracked tension geometry [*9*]. An interesting fact is that there were two compensating errors in the second paper. Without these errors made as they were, J might not have looked so good and might have been abandoned. Later a

Attachment 1

ATTENDANCE LIST

Elastic-Fully Plastic Fracture Criteria Meeting

John Landes	W R&D
Ed Wessel	"
J. Begley	"
P. Toolin	"
W. G. Clark	"
W. A. Logsdon	"
W. O. Shabbits	"
W. K. Wilson	"
W. VanBuren	"
S. K. Chan	"
P. C. Riccardella	W NES
Herb Corten	Univ. of Illinois
P. Paris	Del Research
B. Gross	NASA
E. Roberts, Jr.	"
J. E. Srawley	"
F. A. McClintock	MIT
J. Swedlow	Carnegie-Mellon Univ.
J. W. Hutchinson	Harvard Univ.
G. R. Irwin	Lehigh Univ.
J. R. Rice	Brown

paper was written to point out these two errors and the benefit of having made them in that way [*10*]. The first two papers were received with a lot of enthusiasm, and the encouragement to go forward was given.

Later the work was presented at the Theoretical and Applied Mechanics Conference in Moscow in 1972. This was the first large exposure to the international audience. When the applied mechanics people, who like to pick at new work, asked me difficult and embarrassing questions, it was Frank McClintock, also part of my session, who came to my rescue. During the same trip, I had the opportunity to visit The Welding Institute in England and present the J approach. I met people like Michael Dawes and John Harrison. Since they favored the COD [*11*] approach, they were not so convinced that the J approach had merit.

Ed Wessel, who was always looking for the practical application of the research, soon suggested that the idea of writing a standard test method for J be taken to ASTM Committee E24 on Fracture. The idea was presented at the spring 1972 meeting of Committee E24, then held in March, and accepted. The statement was made that the K_{Ic} test method, ASTM E 399 [*12*], took nearly ten years to develop and ballot into a standard; gaining from that experience we should go much faster. We apparently did not learn from E 399; the first J standard was accepted in 1981, nearly ten years later [*13*]. It was decided to form a task group, ASTM E24.01.09, and hold an organizational meeting at Westinghouse. This was done on May 31, 1972. The attendance list and first page of the minutes are Attachment 2 to this paper. By this time the J integral approach to elastic-plastic fracture was well known. It is interesting to note that this meeting was held separately from the regular E24 committee week, a practice that is still continued by working groups that have serious business to complete. The EPFM Task Group was later given the status of a full subcommittee, E24.08. Ed Wessel was the first chairman of the Subcommittee. He served as that chair for more than 20 years.

Other Approaches

The decade of the 1970s was a time for the development of nonlinear or elastic-plastic fracture approaches. Clearly J was not the choice of everyone. In fact it was not the first proposed method. The crack opening displacement, COD, approach suggested by Alan Wells [*11*] preceded the J proposal by ten years. This had been fairly well accepted by the British fracture mechanics community. A COD test method and design curve were being developed so that the technology involving COD was much advanced compared to the new work on J. The COD, later named crack-tip opening displacement, CTOD, was one of the major surviving approaches from that decade; the other, of course, is the J approach. Perhaps the work that showed that the two are related so that they are really a similar parameter, both characterizing a crack tip stress field, gave them the support to endure for these last three decades [*14*].

COD was not the only alternative approach suggested. Equivalent energy [*15*], nonlinear energy [*16*], and δ_5 [*17*] were all proposed and supported. I never completely understood what made one idea endure while another was discarded. We would like to think that technical merit was the key ingredient, but I am not convinced of that. Certainly marketing and technical politics plays a role in shaping technology.

During the 1970s none of the approaches were universally accepted around the world. Many symposia and technical meetings would involve discussions about the various proposed criteria. Many papers presenting J-based fracture toughness data would get the question, "Why did you do it that way, J is not the correct parameter to use, you should use this other one." Always the problems of path independence and the irreversible nature of plasticity were stated. The comment was often made, "Why continue with the J approach when it has all of these limitations." I would answer, "If J has these limitations based on problems with plasticity methods, so do the other approaches, nobody has bothered to look." I remember an international meeting in 1982, held in Paris, France. The meeting proceeded with several days of presentations, mainly involving testing approaches and data. There

Attachment 2

Research and Development Center

Beulah Road
Pittsburgh Pennsylvania 15235

August 3, 1972

MINUTES OF THE ORGANIZATIONAL MEETING FOR TASK GROUP TG-E24.01.09, J INTEGRAL

May 31, 1972
Westinghouse R&D Center
Pittsburgh, Pennsylvania

Working document for committee use only. Not for publication except as expressly approved by the chairman of the committee or the executive secretary of the Society.

Attendance: The attendance for this meeting is listed alphabetically in Attachment 1 to these minutes.

The meeting of Task Group E24.01.09 was called to order at 9:00 a.m.

Attachment 2
(cont'd)

ATTENDANCE LIST

J. M. Barsom	U. S. Steel Research Labs
J. A. Begley	Westinghouse Research Labs
S. K. Chan	Westinghouse Research Labs
H. Corten	University of Illinois
J. P. Gallagher	Wright-Patterson Air Force Base
C. Griffis	NRL
A. Hattangadi	Westinghouse STD
J. G. Kaufman	Alcoa Research Laboratories
J. D. Landes	Westinghouse Research Labs
W. A. Logsdon	Westinghouse Research Labs
F. J. Loss	NRL
J. Merkle	ORNL
S. Novak	U. S. Steel Research Labs
P. C. Paris	Del Research
P. Riccardella	Westinghouse NES
Sailors	University of Illinois
W. O. Shabbits	Westinghouse Research Labs
J. E. Srawley	NASA Lewis
L. Swedlow	Carnegie-Mellon
E. T. Wessel	Westinghouse Research Labs
W. K. Wilson	Westinghouse Research Labs
H. Wygonik	Alcoa Research Laboratories

was something strange about the conduct of the meeting that I just could not identify. Later, I realized that the data were all presented based on J as the characterizing parameter, and nobody ever questioned whether that was the correct parameter. The whole international community at that meeting just accepted that it was.

Middle Westinghouse Years

The task group to develop a J-based test criterion was formed. It had a second meeting in September 1972 at Harvard. The list of attendees is Attachment 3. You can see the distinguished list of participants. By then many of the famous names in applied mechanics, who took an interest in fracture, were at least interested in what was happening with J, if not a supporter. Included in the list are the three famous mechanics professors of the Division of Applied Sciences at Harvard: Rice, Hutchinson, and Budiansky. Those three, along with Paul Paris for us at Westinghouse, formed the final authority on whether any new idea we had was worth pursuing. We often made a trip to Harvard to spend a day discussing new ideas with those four. They were always gracious and frank. I am often thankful that the great authorities of our times on questions of applied mechanics were people that were not only approachable for those of us "working in the trenches," but were people we could call friends. In hearing some of the historical incidents in the theoretical and applied mechanics field of warring rival factions, having leaders in the field who can be called friends cannot be taken for granted. I once heard a person remark about his experience with one of the Harvard group. He said, "I was at a meeting last week and had a chance to go to dinner with Jim Rice. You know what, he was just like a normal person."

To develop a standard test method, a lot of collaborating work would be needed. The work on J-based fracture got a lot of support from other investigators. People like Griffis and Yoder [*18*] and Turner and students [*20*] showed evidence that the J-based fracture toughness test was feasible. On the analytical side, Rice, Paris, Merkle [*7*], Merkle and Corten [*21*], and McMeeking and Parks [*22*] developed approaches that made the calculation of J easier. There were those who developed the techniques to enhance the experimental measurement of the *J-R* curve. The elastic unloading compliance method was introduced by Paris and coworkers [*23*] and made computer interactive by Joyce and Gudas [*24*].

During these middle years at Westinghouse, Jim Begley was soon to leave for a university position. Other people in Ed Wessel's group helped to carry on the work of elastic-plastic fracture mechanics. Among them, Bill Wilson, Bill Logsdon, Norm Dowling, Bill Brose, Garth Clarke, Don McCabe, Ashok Saxena, and Hugo Ernst made important contributions that added to the development of EPFM. Some of the key work on EPFM other than fracture toughness measurement was begun. Work on using J for a fatigue crack growth correlation parameter when the loading was nonlinear was introduced by Dowling [*25*]. The parameter C^* for creep crack growth was introduced [*26*]. This work was later greatly extended by Saxena.

One of the things that helped to make the J approach become more universally accepted started as a disappointment for us at Westinghouse. In the middle 1970s a request for a proposal for a large program to be sponsored by the Electric Power Research Institute, EPRI, was announced. We submitted a proposal and hoped for a part of the contract because we felt that we were leaders in the field. The contract was awarded to Battelle Memorial Institute and General Electric with Mel Kanninen and Fong Shih, respectively, as project leaders. The feeling was that the Westinghouse approach was too parochial, focusing only on J, and the sponsors were looking for a broader scope of investigation. The loss of that contract was a big disappointment for us; however, when the end of the contract came, the conclusion was that, of all of the approaches to elastic-plastic fracture, the J approach was best. This project also developed the Handbook of J solutions for power-hardening stress-strain laws [*27*], the EPFM version of the famous Tada et al. "K Handbook" [*28*]. The completion of this work did much to allow J to gain acceptance. As it turned out, the fact that J was recommended by organizations other than Westinghouse was a key to its acceptance.

One of the problems with the J approach was that it was used only to measure fracture toughness, *J-R* curves, and J_{Ic}. It was little more than a small specimen test that could be used to get a converted K_{Ic} for which a linear elastic application of the toughness value was made. Once I was asked, "When you at Westinghouse measure J toughness values, what do you do with them?" Somewhat stumped

Attachment 3

Attendance

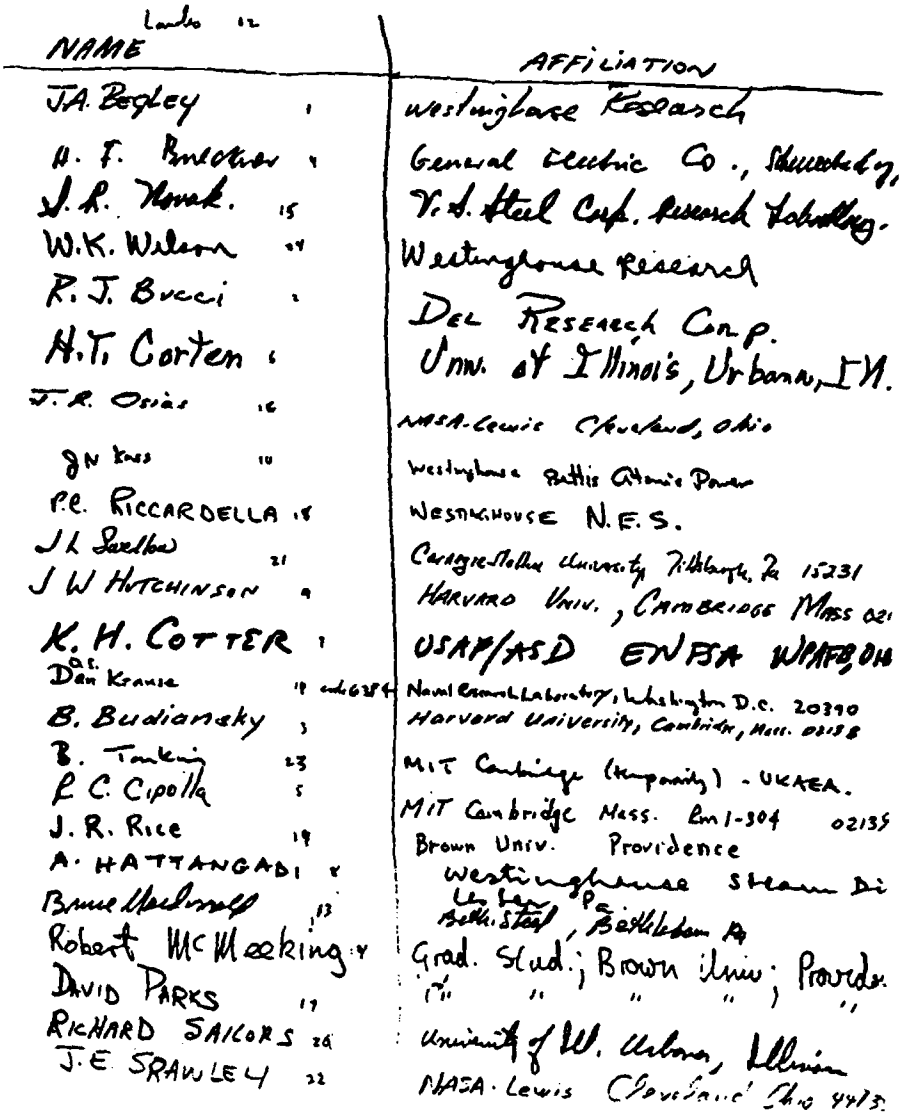

NAME	AFFILIATION
J.A. Begley	Westinghouse Research
A. F. Emerton	General Electric Co., Schenectady,
J. R. Novak.	U.S. Steel Corp. Research Laboratory.
W.K. Wilson	Westinghouse Research
R. J. Bucci	Del Research Corp.
H.T. Corten	Univ. of Illinois, Urbana, Ill.
T. R. Osias	NASA-Lewis Cleveland, Ohio
J N Kass	Westinghouse Bettis Atomic Power
P.C. RICCARDELLA	WESTINGHOUSE N.E.S.
J L Swedlow	Carnegie-Mellon University Pittsburgh, Pa 15231
J W HUTCHINSON	HARVARD Univ., CAMBRIDGE Mass 02
K. H. COTTER	USAF/ASD ENFSA WPAFB, OH
Dan Kraus	Naval Research Laboratory, Washington D.C. 20390
B. Budiansky	Harvard University, Cambridge, Mass. 02138
B. Tanken	MIT Cambridge (Company) - UKAEA.
F. C. Cipolla	MIT Cambridge Mass. Rm 1-304 02139
J. R. Rice	Brown Univ. Providence
A. HATTANGADI	Westinghouse Steam Di
Bruce Macdonald	Lehigh Univ. Bethlehem Pa
Robert McMeeking	Bethlehem Steel, Bethlehem Pa
DAVID PARKS	Grad. Stud.; Brown Univ; Provide
RICHARD SAILORS	" " " " " "
J.E. SRAWLEY	University of Ill. Urbana, Illinois
	NASA-Lewis Cleveland Ohio 4413

by this, I answered, "At Westinghouse we usually write a paper about it." The truth was that an application scheme for J was needed. What solved this was the work of Paris and students at Washington University that introduced the tearing modulus, T, [29] and the *GE-EPRI Handbook* that allowed the J to be calculated for structural components [27]. With the tearing modulus and later the J-T dia-

gram [*30*], the question of what do you do with J was answered. Questions were still being asked about the applicability of J for growing cracks. Work of Hutchinson and Paris answered this [*31*].

The work on EPFM during that middle 1970s was so focused that it seemed a good idea to organize a symposium devoted to that subject. The first ASTM Symposium on Elastic-Plastic Fracture was held in Atlanta in 1977. The resulting STP that came from that Symposium, *ASTM STP 668*, although only a volume of 33 papers, contains many of the classical papers of that time [*32*]. The work from the EPRI contract, Paris and coworkers, as well as some of the latest on the CTOD and its relationship to J were documented there. When the Second in the series was held in Philadelphia in 1981, the number of papers more than doubled to 74 [*33,34*]. That period in the history of EPFM marks the greatest interest in that as a special topic. When the third and last of the series was held in Knoxville in 1986, the interest was already dropping. New but related subjects like creep cracking and fatigue crack growth under nonlinear loading were a major part of the new topics included under EPFM and related topics.

Modern Work on EPFM

After the intense interest in EPFM during the 1970s and early 1980s, the interest seemed to drop in level. In fact, part of the reason was that the interest in purely linear elastic approaches to fracture mechanics was also dropping, and EPFM was becoming the normal approach to fracture mechanics; it was no long a special or separate topic. Sometimes the LEFM approach is now looked at as the case where only the linear part of J, or CTOD, applies. Therefore, the distinction or need to study EPFM separately from LEFM nearly vanished. Also, the controversy over whether J or CTOD is the correct parameter to use has nearly vanished. J and CTOD are just two different parameters that can be used. The measurement is similar, and the application is often similar. Work is still continuing as much as ever. During the past 15 years several new areas have emerged.

One area of concentration was on the development of test standards. The work to make the testing procedure better has been a constant topic of interest and is still continuing. Five different ASTM test standards were written relating to fracture toughness testing with J and CTOD [*35–39*]. The latest method, E 1820, combines all of the test methods for the past and is often labeled the "common method."

Another area that has received attention in the past decade is the question of how to predict the size and geometry dependence of the J-R curve. Numerical work with porous material has illustrated that such a geometry dependence is real and can be predicted at least in trend [*40*]. This suggests that the J approach can still be used and the geometry dependence predicted. Other approaches have suggested alternate parameters. For example, the use of a crack opening angle, CTOA, suggested by Newman and Dawicke [*41*] and the energy dissipation rate suggested by Turner and coworkers [*42*] are candidate methods for eliminating the geometry dependence in the characterization of the R curve for EPFM.

Other new areas for EPFM include the development of application schemes. Failure analysis diagrams, FADs [*43,44*], are the most popular, but others application methods have been proposed [*45,46*].

The past ten years have shown tremendous progress on the handling of constraint. The holding of two special ASTM symposia for that subject has shown the intense in the topic [*47,48*]. The development of the two-parameter fracture mechanics approaches, K and T [*49*] or J and Q [*50,51*], has helped tremendously in the understanding of the constraint issue. Also, the fracture process for a condition of low constraint can be transferred to the equivalent for high constraint using a small-scale yielding definition of J [*52*]. Part of the constraint issue is involved with how to handle shallow cracks [*53*], a topic that has received much attention lately.

The progress on understanding constraint has lead the way to the handling of the transition fracture toughness problem for steels, a problem that has been pondered for several decades. Transition

fracture characterization required both the handling of the constraint problem and statistical problems. The development of the master curve approach has led the way to the standardization of the testing and analysis of the transition fracture toughness data [*54,55*].

The list of names involved in the research has changed; some old names remain, and many new ones have emerged. The team of Dodds and Anderson has become prominent. Joyce and Gudas is now usually Joyce and Link. Schwalbe and coworkers and Wallin have made their presence felt from Europe. All of these and many more have continued the work once called EPFM.

Future of EPFM

The title of this talk asks, "Where is EPFM going?" I wish I knew; well, maybe I do not. The events that forged my career and led me to the field of fracture mechanics seem from this vantage point as fortuitous and completely unpredictable. But this is the story of nearly every career. The one thing that is predictable about the future of the technology is that nobody can accurately forecast the course of events. What is in the future for EPFM will be directed by an unforeseen set of events.

Certainly there are pet problems that I would like to put before this audience. The problem of finding a way to transfer the ductile fracture toughness R curves from one geometry to another, be it with J, CTOD, or another parameter remains to be completely solved. The problem of handling multiple and non-proportional loading in the nonlinear regime has not been addressed. The problem of making our through crack characterization tell us what to do for the part-through crack is still being studied. These and others are important problems to work on in the future.

The important thing for those planning to continue EPFM is to let the application needs guide the future. Work hard to solve those problems that arise, but do not spend much time trying to predict them. Strategic planning and five-year goals are management tools. They give the managers something to show their own bosses as progress in the making. However, they have little input to technical progress, and they do little to help us forecast or solve the critical problems of the future.

One thing that seems to me to be a threat to future progress is the current trends in research funding. The present emphasis, at least in academia, is to develop programs with large dollar values. The goal of research becomes more one of obtaining money than of solving problems that produce technical benefits. Often there is more time spent on writing proposals and looking for funding in the technical community than there is in doing the actual research to solve the technical problems. In the past the technical problems were solved because the technical community consisted mainly of workers, not beggars. If there is no change in this trend, EPFM might go nowhere.

Summary

EPFM as a discipline in fracture mechanics is reaching the end of its third decade. It has had a wonderful past, full of exciting discoveries and interesting people. The key part of its history, for me, involves more than the key technical accomplishments; it is really the interaction of the people, their personalities, ideas, and individual brilliance that are most remembered. I am happy that I had the opportunity to stand so close to the action during these past thirty years, to know the people, to see how they behaved and some of their accomplishments. I believe that the history of the development of fracture mechanics needs to be documented. I encourage others to follow with their stories.

References

[*1*] Rice, J. R., "A Path Independent Integral and the Approximate Analysis of Strain Concentrations by Notches and Cracks," *Journal of Applied Mechanics,* Vol. 35, 1968, pp. 379–386.

[*2*] Rice, J. R. and Rosengren, G. F., "Plane Strain Deformation Near a Crack Tip in a Power Hardening Material," *Journal of the Mechanics and Physics of Solids,* Vol. 16, 1968, pp. 1–12.

[*3*] Hutchinson, G. W., "Singular Behavior near the End of a Tensile Crack Tip in a Hardening Material," *Journal of the Mechanics and Physics of Solids,* Vol. 16, 1968, pp. 13–31.

[4] McClintock, F. A., "Plasticity Aspects of Fracture," *Fracture,* H. Liebowitz, Ed., Vol. 3, Academic Press, New York, 1971, pp. 47–225.

[5] Rice, J. R., "Mathematical Analysis in the Mechanics of Fracture, *Fracture,* H. Liebowitz, Ed., Vol. 2, Academic Press, New York, 1971, pp. 191–311.

[6] Irwin, G. R. "Analysis of Stresses and Strains Near the End of a Crack Traversing a Plate," *Journal of Applied Mechanics, Transactions of ASME,* Vol. 24, 1957, pp. 361–364.

[7] Rice, J. R., Paris, P. C., and Merkle, J. G., "Some Further Results of the J-Integral Analysis," *Progress in Flaw Growth and Fracture Toughness Testing, ASTM STP 536,* American Society for Testing and Materials, 1973, pp. 231–245.

[8] Begley, J. A. and Landes, J. D., "The J-Integral as a Fracture Criterion," *Fracture Toughness, Proceedings of the 1971 National Symposium on Fracture Mechanics Part II, ASTM STP 514,* American Society for Testing and Materials, 1972, pp. 1–26.

[9] Landes, J. D. and Begley, J. A., "The Effect of Specimen Geometry on J_{Ic}," *Fracture Toughness, Proceedings of the 1971 National Symposium on Fracture Mechanics, ASTM STP 514,* American Society for Testing and Materials, 1972, pp. 24–39.

[10] Begley, J. A. and Landes, J. D., "Serendipity and the J Integral," *International Journal of Fracture,* Vol. 12, Noordhoff International Publishing, 1976, pp. 764–766.

[11] Wells, A. A., "Unstable Crack Propagation in Metals: Cleavage and Fast Fracture," *Proceedings of the Crack Propagation Symposium,* Vol. 1, Paper 84, Cranfield, UK, 1961.

[12] ASTM E 399, "Test Method for Plane-Strain Fracture Toughness of Metallic Materials," *ASTM, Annual Book of Standards,* Vol. 03.01.

[13] Test Method for J_{Ic}, a Measure of Fracture Toughness, ASTM E 813–81, *ASTM Annual Book of Standards,* Vol. 03.01.

[14] Dawes, M. G., "Elastic-Plastic Fracture Toughness Based on CTOD and J-Contour Integral Concepts," *Elastic-Plastic Fracture, ASTM STP 668,* J. D. Landes, J. A. Begley, and G. A. Clarke, Eds., American Society for Testing and Materials, 1979, pp. 307–333.

[15] Witt, F. W., "Fracture Behavior of Reactor Pressure Vessel Steel in the Frangible, Transitional and Tough Regimes," *Nuclear Engineering and Design,* Vol. 20, 1972, pp. 237–249.

[16] Liebowitz, H. and Eftis, J. "On Nonlinear Effects in Fracture Mechanics," *Engineering Fracture Mechanics,* Vol. 3, 1971, p. 267.

[17] Hellman, D. and Schwalbe, K.-H., "Geometry and Size Effects on J-R and δ-R Curves Under Plane Stress Conditions," *Fracture Mechanics: Fifteenth Symposium, ASTM STP 833,* R. J. Sanford, Ed., American Society for Testing and Materials, 1984, pp. 577–605.

[18] Griffis, C. A. and Yoder, G. R., "Initial Crack Extension in Two Intermediate Strength Aluminum Alloys," *Journal of Engineering Materials and Technology, Transactions,* American Society of Mechanical Engineers, Series H, Vol. 98, No. 2, April 1976, pp. 152–158.

[19] Yoder, G. R. and Griffis, C. A., "Application of the J-Integral to the initiation of Crack Extension in a Titanium 6AL-4v Alloy," *Mechanics of Crack Growth, ASTM STP 590,* American Society for Testing and Materials, 1976, pp. 61–81.

[20] Sumpter, J. G. D. and Turner, C. E., "Method for Laboratory Determination of J_c," *Cracks and Fracture, ASTM STP 601,* American Society for Testing and Materials, 1976, pp. 3–18.

[21] Merkle, J. G. and Corten, H. T. "A J Integral Analysis for the Compact Specimen, Considering Axial Force as Well as Bending Effects," *Journal of Pressure Vessel Technology,* ASME, Vol. 96, Series J, No. 4, November 1974, pp. 286–292.

[22] McMeeking, R. M. and Parks, D. M., "On Criteria for J-Dominance of Crack Tip Fields in Large-Scale Yielding," *Elastic-Plastic Fracture, ASTM STP 668,* J. D. Landes, J. A. Begley, and G. A. Clarke, Eds., American Society for Testing and Materials, 1979, pp. 175–194.

[23] Clarke, G. A., Andrews, W. R., Paris, P, C., and Schmidt, D. W., "Single Specimen Tests for J_{Ic} Determination," *Mechanics of Crack Growth, ASTM STP 590,* American Society for Testing and Materials, 1976, pp. 24–42.

[24] Joyce, J. A. and Gudas, J. P. "Computer Interactive J_{Ic} Testing of Navy Alloys," *Elastic-Plastic Fracture, ASTM STP 668,* J. D. Landes, J. A. Begley, and G. A. Clarke, Eds., American Society for Testing and Materials, 1979, pp. 451–468.

[25] Dowling, N. E. and Begley, J. A., "Fatigue Crack Growth During Gross Plasticity" *Mechanics of Crack Growth, ASTM STP 590,* American Society for Testing and Materials, 1976, pp. 82–103.

[26] Landes, J. D. and Begley, J. A., "A Fracture Mechanics Approach to Creep Crack Growth," *Mechanics of Crack Growth, ASTM STP 590,* American Society for Testing and Materials, 1976, pp. 128–148.

[27] Kumar, V., German, M. D., and Shih, C. F., "An Engineering Approach for Elastic-Plastic Fracture Analysis," NP 1931, EPRI Project 1237-1, July 1981.

[28] Tada, H., Paris, P. C., and Irwin, G. R., "*The Stress Analysis of Cracks Handbook,*" Paris Productions Inc., St. Louis, MO, 1985.

[29] Paris, P. C., Tada, H., Zahoor, A., and Ernst, H. A., "The Theory of Instability of the Tearing Mode of Elastic-Plastic Crack Growth," *Elastic Plastic Fracture, ASTM STP 668,* J. D. Landes, J. A. Begley, and G. A. Clarke, Eds., American Society for Testing and Materials, 1979, pp. 5–36.

[30] Paris, P. C. and Johnson, R. E., "A Method of Application of Elastic-Plastic Fracture Mechanics to Nuclear Vessel Analysis," *Elastic-Plastic Fracture: Second Symposium, Volume II—Fracture Resistance Curves and Engineering Applications, ASTM STP 803,* C. F. Shih and J. P. Gudas, Eds., American Society for Testing and Materials, 1983, pp. II-5–II-40.

[31] Hutchinson, J. W. and Paris, P. C., "Stability Analysis of J-Controlled Crack Growth," *Elastic-Plastic Fracture, ASTM STP 668,* J. D. Landes, J. A Begley, and G. A. Clarke, Eds., American Society for Testing and Materials, 1979, pp. 37–64.

[32] *Elastic Plastic Fracture, ASTM STP 668,* J. D. Landes, J. A. Begley, and G. A. Clarke, Eds., American Society for Testing and Materials, 1979.

[33] *Elastic-Plastic Fracture: Second Symposium, Vol. I—Inelastic Crack Analysis, ASTM STP 803,* C. F. Shih and J. P. Gudas, Eds., American Society for Testing and Materials, 1983.

[34] *Elastic-Plastic Fracture: Second Symposium, Vol. II—Fracture Resistance Curves and Engineering Applications, ASTM STP 803,* C. F. Shih and J. P. Gudas, Eds., American Society for Testing and Materials, 1983.

[35] "Standard Test Method for J_{Ic}, a Measure of Fracture Toughness," ASTM E 813–88, *ASTM Annual Book of Standards,* Vol. 03.01.

[36] "Standard Test Method for Determining J-R Curves," ASTM E 1152–87, *ASTM Annual Book of Standards,* Vol. 03.01.

[37] "Standard Test Method for Crack-Tip Opening Displacement (CTOD) Fracture Toughness Measurement," ASTM E 1290-89, *ASTM Annual Book of Standards,* Vol. 03.01.

[38] "Standard Method for J-Integral Characterization of Fracture Toughness," ASTM E 1737-96, *ASTM, Annual Book of Standards,* Vol. 03.01.

[39] "Standard Method for Measurement of Fracture Toughness," ASTM E 1820-96, *Annual Book of Standards,* Vol. 03.01.

[40] Xia, L. and Shih, C. F. "Ductile Crack Growth—I. A Numerical Study Using Computational Cells with Microstructurally Based Length Scales," presented at the NRC Workshop on Constraint Effects in Fracture No. 2, 20 April 1994, Annapolis, MD.

[41] Dawicke, D. S., Sutton, M. A., Newman, J. C. Jr., and Bigelow, C. A., "Measurement and Analysis of Critical CTOA for an Aluminum Alloy Sheet," *Fracture Mechanics: 25th Volume, ASTM STP 1220,* F. Erdogan, Ed, American Society for Testing and Materials, 1995, pp. 358–379.

[42] Turner, C. E. and Kolednik, O., "Application of Energy Dissipation Rate Arguments to Stable Crack Growth," *Fatigue and Fracture of Engineering Materials and Structures,* Vol. 17, No. 10, October 1993, pp. 1109–1127.

[43] Milne, I., Ainsworth, R. A., Dowling, A. R., and Stewart, A. T., "Assessment of the Integrity of Structures Containing Defects," Central Electricity Generating Board Report R/H/R6-Rev-3, May 1986.

[44] Bloom, J. M., "Validation of a Deformation Plasticity Failure Assessment Diagram Approach to Flaw Evaluation," *Elastic-Plastic Fracture: Second Symposium, Volume II—Fracture Resistance Curves and Engineering Applications, ASTM STP 803,* C. F. Shih and J. P. Gudas, Eds., American Society for Testing and Materials, 1983, pp. II-206–II-238.

[45] Landes, J. D., Zhou, Z., and Brown, K. H., "An Application Methodology for Ductile Fracture Mechanics," *Fracture Mechanics: Twenty-Third Symposium, ASTM STP 1189,* Ravinder Chona, Ed., American Society for Testing and Materials, 1993, pp. 229–264.

[46] Schwalbe, K.-H. and Cornec, A., "The Engineering Treatment Model (ETM) and Its Practical Application," *Fatigue and Fracture of Engineering Materials and Structures,* Vol. 14, No. 4, 1991, pp. 405–412.

[47] *Constraint Effects in Fracture, ASTM STP 1171,* E. M. Hackett, K-H. Schwalbe, and R. H. Dodds, Eds., American Society for Testing and Materials, 1993.

[48] *Constraint Effects in Fracture: Theory and Applications, ASTM STP 1244,* Mark Kirk and Ad Bakker, Eds., American Society for Testing and Materials, 1994.

[49] Hancock, J. W., Reuter, W. G., and Parks, D. M., "Constraint and Toughness Parameterized by T," *Constraint Effects in Fracture, ASTM STP 1171,* E. M. Hackett et. al., Eds., American Society for Testing and Materials, 1993, pp. 21–40.

[50] O'Dowd, N. P. and Shih, C. F., "Family of Crack-Tip Fields Characterized by a Triaxiality Parameter: Part I—Structure of Fields," *Journal of the Mechanics and Physics of Solids,* Vol. 39, 1991, pp. 989–1015.

[51] O'Dowd, N. P. and Shih, C. F., "Family of Crack-Tip Fields Characterized by a Triaxiality Parameter: Part II—Fracture Applications," *Journal of the Mechanics and Physics of Solids,* Vol. 40, 1992, pp. 939–963.

[52] Anderson, T. L. and Dodds, R. H., "Specimen Size Requirements for Fracture Testing in the Transition Region," *Journal of Testing and Evaluation, JTEVA,* American Society for Testing and Materials, Vol. 19, 1991, pp. 123–134.

[53] *Proceedings, Shallow Crack Fracture Mechanics, Toughness Tests and Applications,* M. G. Dawes, Technical Director, TWI Conference, September 1992.

[54] Wallin, K., "Statistical Modeling of Fracture in the Ductile to Brittle Transition Region," *Defect Assessment in Components—Fundamentals and Applications,* J. G. Blauel and K. H. Schwalbe, Eds., ESIS/EGF9, 1991, pp. 1–31.

[55] Wallin, K., "Fracture Toughness Transition Curve Shape for Ferritic Structural Steels," *Proceedings of the Joint FEFG/ICF International Conference on Fracture of Engineering Materials,* Singapore, 6–8 August 1991, pp. 83–88.

Session I

Donald E. McCabe,[1] *John G. Merkle,*[2] *and Kim Wallin*[3]

Technical Basis for the Master Curve Concept of Fracture Toughness Evaluations in the Transition Range

REFERENCE: McCabe, D. E., Merkle, J. G., and Wallin, K., **"Technical Basis for the Master Curve Concept of Fracture Toughness Evaluations in the Transition Range,"** *Fatigue and Fracture Mechanics: 30th Volume, ASTM STP 1360,* P. C. Paris and K. L. Jerina, Eds., American Society for Testing and Materials, West Conshohocken, PA, 2000, pp. 21–33.

ABSTRACT: An American Society for Testing and Materials (ASTM) standard method (E 1921–97) has been developed that exclusively uses fracture mechanics test practices and advanced statistical methods to establish the ductile-to-brittle transition range of fracture toughness for structural steels. The development of suitably accurate analyses had been slowed in the past due to an incomplete understanding of the operational mechanisms that control the fracture toughness behavior of structural steels. New perspectives taken are (1) that dominant linear-elastic conditions need not be rigidly enforced in specimens and (2) that the effect of specimen size on fracture toughness performance is mostly controlled by a weakest-link mechanism instead of being completely controlled by crack tip constraint conditions. The weakest-link behavior is defined from local cleavage crack initiators such as precipitates, inclusions, and grain boundary embrittlement, namely, all microstructural features in steel. Statistical models can be built upon such mechanisms that result in defined fracture probability levels and, when coupled to a master curve concept, can more accurately define the true location of the ductile-to-brittle transition temperature.

An integral part of the ASTM test standard development work has been the production of a supporting technical basis document. This document presents substantial background data and supporting theoretical aspects that have been used to justify the method development. The paper will include some of the salient features presented.

KEYWORDS: T_0, master curve, ASTM Standard E 1921, transition range, toughness, Weibull, pressure vessel steels

The fracture toughness property that is of most relevance to structural steel applications is the location of the ductile-to-brittle transition temperature. The empirical test results that have been used for many years to identify this temperature are test-method-specific and are of uncertain relevance to in-service conditions for a sharp crack embedded in a dominant elastic stress field and loaded under semi-static conditions. Only fracture mechanics-based test methods are capable of such simulations. However, to simulate service conditions, linear elastic analyses will suffice, and such conditions are usually associated with the ASTM K_{Ic} test practice E 399 [*1*]. It is also necessary to test within the transition range where K_{Ic} validity conditions can only be satisfied with huge specimens that are beyond routine laboratory practice capabilities [*2*]. A special American Society of Mechanical Engineers (ASME) task group had found a temporary resolution in the early 1970s that has been used on pressure vessel steels [*3*]. Namely, a substantial collection of E 399 valid K_{Ic} data were obtained from a variety of sources and plotted against normalized temperature. All data were referenced to a nil-duc-

[1] Metals and Ceramics Division, Oak Ridge National Laboratory, Oak Ridge, TN 37831-6151.
[2] Engineering Technology Division, Oak Ridge National Laboratory, Oak Ridge, TN 37831-8049.
[3] Technical Research Centre of Finland, P.O. Box 1700, Kemistinte 3, Espoo, FIN-02044, Finland.

tility temperature (RT_{NDT}) (based on empirical test results) and then plotted, perhaps expecting all of the data to lie on a generic lower-bound curve. The result was considerable data scatter, so, instead, an approximate statistical method applied was to draw a lower-bound curve to the data scatter and postulate that this curve will never be appreciably violated by data for past or future production of pressure vessel steels. From this standpoint, the lower-bound K_{Ic} curve has been regarded as a universal curve and, surprisingly, it has remained in use despite its limitations for more than 25 years. Most prominent among these weaknesses is the uncertainty associated with empirically derived test temperatures, RT_{NDT}. Hence, the uncertainty in fracture analyses due to not knowing the correct transition temperature had not been eliminated.

This paper describes a new fracture-mechanics-based methodology for transition range toughness definition [*4*]. The technology incorporates advanced statistical methods to model generic data scatter characteristics of steels. Elastic-plastic fracture toughness evaluation methods are used, and the linear elastic-based constraint requirements are abandoned in favor of a weakest-link model to define the specimen size effects that have been observed experimentally [*5*]. The concept that fracture mechanics data tend to follow a universal curve shape is retained except that, in this case, the concept of a universal curve is fully justified both theoretically and experimentally. ASTM test method E 1921–97 [*6*] uses these new concepts, and the background information developed in support of the standard has been prepared in a U.S. Nuclear Regulatory Commission NUREG report, *Technical Basis for an ASTM Standard on Determining the Reference Temperature, T_0, for Ferritic Steels in the Transition Range.* Temperature, T_0, is used as a reference temperature in a similar way as RT_{NDT} has been used, except that it is developed entirely from fracture mechanics data, and it is based upon median toughness instead of a lower-bound curve, as has been the case for the ASME K_{Ic} curve.

Managing Data Scatter

The new viewpoint is that the scatter of fracture-mechanics-type data is recognized as being an omnipresent characteristic of structural steels. The concept to be presented in the following sections acknowledges that data scatter results from randomly distributed cleavage-triggering sources such as carbide cracking, multiple cleavage crack clustering, and dislocation pile-ups. The theoretical basis for data distributions uses weakest-link theory coupled to a Poisson distribution assumption for cleavage crack triggering as follows:

$$P_f = 1 - \exp(-\rho V) \tag{1}$$

The exponential term in Eq 1 is the probability of finding no critical cleavage sources in volume V when there are ρ critical particles per unit volume. P_f represents the cumulative probability of failure.

In the present case, attention is given to volume elements that are local to the crack tip where the highest stresses are concentrated. The active volume for cleavage crack sources scales according to $(B/B_0)\,K_1^4$ [*7*]. B is a crack front length, and B_0 is an arbitrarily definable dimension. Other elements that define the critical volume are recognized as being fixed values. Hence, the fundamental result from applying weakest-link theory is:

$$P_f = 1 - \exp\left[-\frac{B}{B_0}\left(\frac{K_1}{K_0}\right)^4\right] \tag{2}$$

Two deficiencies of Eq 2 that do not model the true characteristics of steel are (1) that there can be some fraction of cleavage trigger sources that have weak crack drive energy that will arrest, and (2) steels do not approach zero fracture toughness as suggested by the equation. Hence, the statistical model was modified via introduction of the hazard function that resolves both deficiencies men-

tioned. The model that emerges from these analyses as the most practical is:

$$P_f = 1 - \exp\left[-\left(\frac{B}{B_0}\right)\left(\frac{K_{Jc} - K_{min}}{K_0 - K_{min}}\right)^4\right] \tag{3}$$

K_{min} is the toughness level below which cleavage cracks cannot propagate. K_0 is a scale parameter identified at a point where $K_{Jc} = K_0$ and $P_f = 0.632$. Equation 3 can be utilized to set up a convenient-size effect relationship. By setting P_f equal for two specimen sizes, where $B = B_1$ or $B = B_2$, the following relationship results:

$$K_{Jc(2)} = (K_{Jc(1)} - K_{min})\left(\frac{B_1}{B_2}\right)^{1/4} + K_{min} \tag{4}$$

Equation 4 suggests that specimen size has a rather subtle effect on fracture toughness distributions, and this appears quite apparent from the experimental evidence that has been obtained [*5*]. Hence, size effects can only be demonstrated with ample replications at each size level. On the other hand, the various constraint-based models that have been suggested usually indicate more pronounced size effects that are generally not well supported experimentally [*5*]. The important benefit from the abandonment of absolute constraint control theories is the recognition that elastic-plastic methods can be utilized to the extent that specimens of reasonable sizes can be applied to the development of plant-specific fracture mechanics data. Fracture toughness at the point of crack instability can be calculated in units of *J*-integral, J_c, and these values are then converted into their equivalence in units of stress intensity factor, K_{Jc}, given by:

$$K_{Jc} = \sqrt{J_c E} \tag{5}$$

Small Sample Statistics

Equation 3 is the statistical model that has been found to be the most suitable for fitting fracture-mechanics-based data. At first, all three parameters, namely, Weibull slope, *b*, scale parameter, K_0, and lower bound, K_{min}, were best fitted to individual data sets [*8*]. Data replication needs for accurate characterization of data distributions were unappreciated at that time. Also, in the early stages, an application of this methodology for the establishment of a fracture-mechanics-based transition curve using fracture-mechanics-based reference temperatures had not been considered. The tools needed to apply the statistical approach were developed later [*9*] and have since served as a justification for the development of an ASTM standard method. The concept was made practical for general use after it was found through a sensitivity study using Monte Carlo techniques that K_{Jc} data populations for a variety of steels tend to have a common Weibull slope of approximately 4 when lower-bound K_{min} values are set to 20 MPa$\sqrt{m}$. These results compared favorably with available experimental data found in the literature (Fig. 1). This study also made it abundantly clear that extremely large data samplings, on the order of 50 or more specimens, must be used to develop sufficient measurement accuracy on slope, *b*, and minimum toughness, K_{min}, in the Weibull model, Eq 3. As has been previously discussed, the rationale for this characteristic of K_{Jc} data distributions has since been justified in theory.

Experimental evidence for the ASTM test method justification has been found in the form of data taken from a Materials Properties Council/Japan Society for the Promotion of Science (MPC/JSPS) round-robin activity [*1*] (see Table 1, Part I(a)). Eighteen participating laboratories had tested about 150 specimens divided between three test temperatures, −50, −75, and −100°C. The test material was A 508 class 3 pressure vessel steel, and 1T compact specimens had been taken from the ¼ and ¾ through-thickness locations in the plate. Sample size (replication) for each participant was five

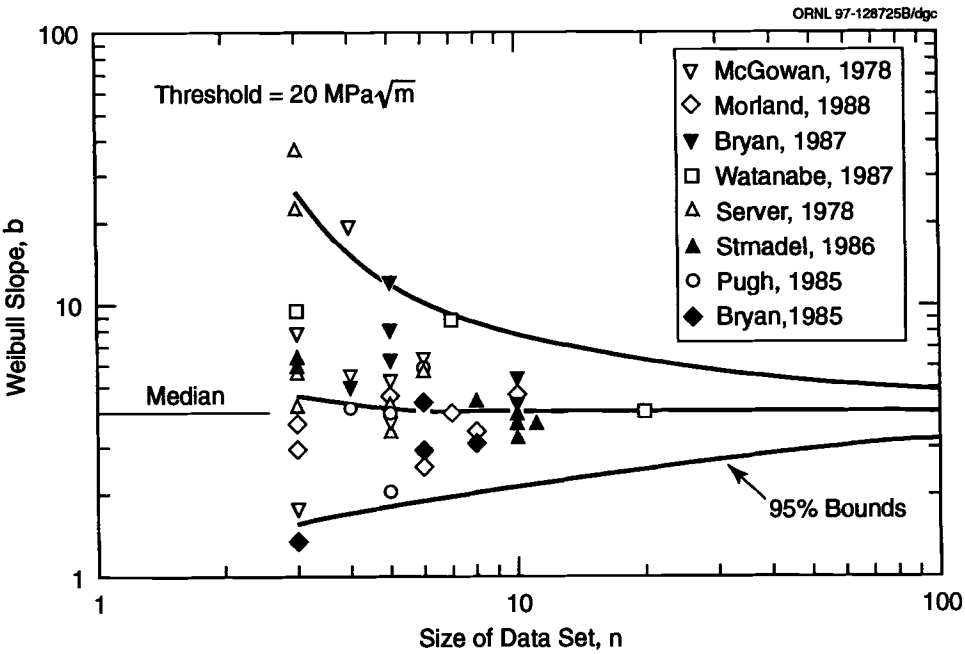

FIG. 1—*Comparison of the distribution of Weibull slopes calculated from small data sets with Monte Carlo predicted confidence limits when* K_{min} *is set at 20 MPa*$\sqrt{m}$.

specimens. Figure 1 suggests that for a sample size of 5, Weibull slopes, *b*, obtained by least-squares fitting have a 95% probability of being between 2 and 12. Only 2 of 28 experimental slope determinations was outside of these bounds. These same data, after combining into three test temperature groups to develop sample sizes of about 50 specimens, were analyzed for slopes (see the "Total" rows). All three groups tend to converge to a slope of four. Since two of the three Weibull parameters are declared to be deterministic parameters of the model, only the number of specimens needed to determine K_0 remained to be determined from experimental data. Monte Carlo methods were again employed to settle upon sample size requirements. Data populations (nominal groups of 50) were represented by data from the MPC/JSPS round-robin activity. Sample sizes ranged from 3 to 20 in the simulation, as is indicated in the first column of Table 2. Each sampling was repeated 100 times, and standard deviation on $K_{Jc(med)}$ values are also presented. Clearly, sample sizes on the order of 20 specimens provide the optimum accuracy, but, at the same time, this is obviously not a practical number to recommend for general use. Standard deviation among repeated tests always seemed to plateau between six and eight replications. Such numbers represent a more practical recommendation for standardization purposes. However, it is accepted that error potential accompanies such replication. For a six- to eight-specimen sampling, there is about 10% probability that there will be more than 10°C error in true transition temperature identification [*1*]. To compensate, a recommendation is made to apply margin adjustments to T_0 temperature determinations when the acknowledged error potential is not acceptable in a specific application. It should be noted at this point that there is a fixed relationship between K_0 and $K_{Jc(med)}$ so that the required sample size is the same for either parameter.

$$K_{Jc(med)} - 20 = (K_0 - 20)[\ln 2]^{1/4}\ \text{MPa}\sqrt{\text{m}} \tag{6}$$

TABLE 1—*Analysis of MPC/JSPS round-robin data.*

I(a)		I(b)	
Laboratory	Best slope[a]	K_o [b] (MPa√m)	T_o (°C)
Test temperature, -50°C			
B	3.0	294	-115
C	4.1	284	-113
E	2.6	241	-103
H	4.3	277	-111
J	12.6	177	-83
O	1.8	205	-93
P	6.0	187	-87
Q	3.5	262	-108
R	3.8	233	-101
Combined data	3.75	250	-105
Test temperature, -75°C			
A	2.8	184	-111
C	3.7	168	-105
D	8.8	161	-103
H	5.8	156	-101
J	5.5	148	-97
K	7.1	177	-109
N	3.9	163	-104
Q	5.1	192	-114
R	6.5	150	-98
Combined data	5.8	166	-105
Test temperature, -100°C			
A	5.0	118	-107
C	3.0	127	-112
E	4.0	132	-114
F	5.4	120	-108
G	5.6	109	-101
H	5.1	114	-104
L	11.3	143	-120
M	3.4	101	-95
Q	3.9	139	-118
R	2.8	114	-104
Combined data	4.3	123	-109

[a]By linear regression.
[b]Maximum likelihood with K_{min} = 20 MPa√m.

TABLE 2—*Monte Carlo simulation (100 trials; population, 50 1T C(T) A 508 class 3 specimens; −75°C test temperature).*

Sample Size	Population Size	Number of Trials	$K_{Jc(med)}$, MPa$\sqrt{m}$	Standard Deviation, MPa$\sqrt{m}$	Total Population
3	50	100	154.2	16.5	$K_{Jc(med)}$ = 153 MPa$\sqrt{m}$
4	50	100	154.4	15.0	T_0 = −104°C
5	50	100	154.5	12.5	
6	50	100	153.4	11.8	
7	50	100	151.9	11.6	
8	50	100	152.2	11.1	
9	50	100	153.7	9.1	
10	50	100	153.4	8.5	
20	50	100	153.1	6.1	

Concept of the Master Curve

The title of E 1921-97 suggests that the main objective is to determine a reference temperature, T_0. This temperature is used to set up a master curve, and here is where advanced statistical methods can be used to an advantage. Improved definition of transition range curve shape is the principal benefit.

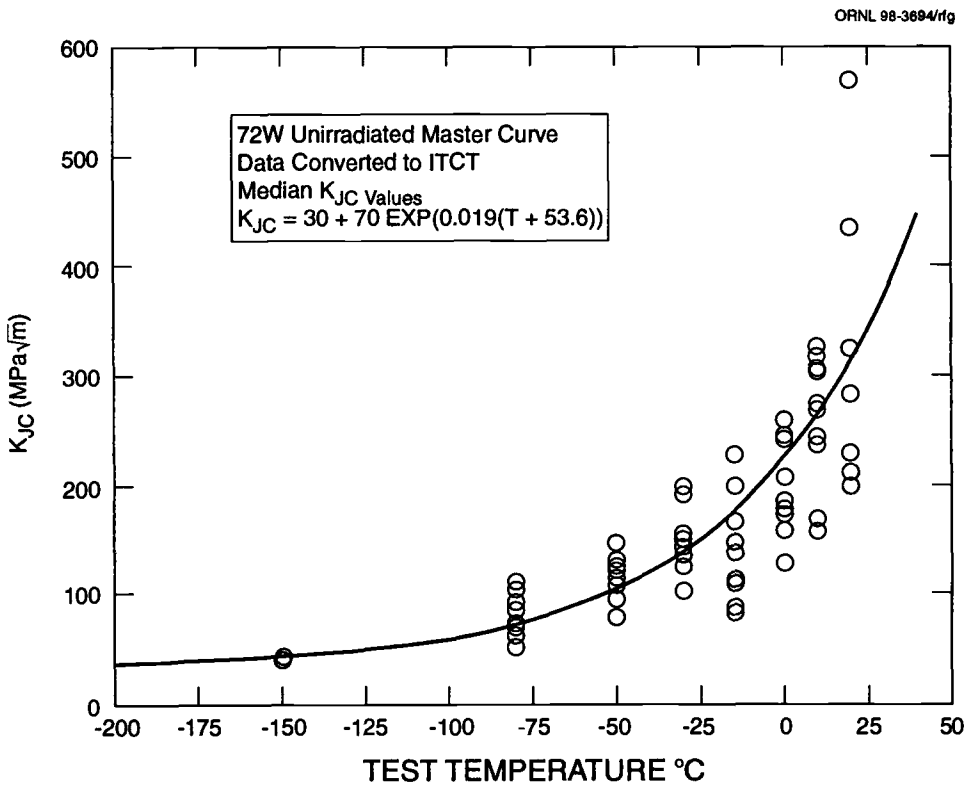

FIG. 2—*Example of master curve and Weld 72W data from the HSSI Fifth Irradiation Series.*

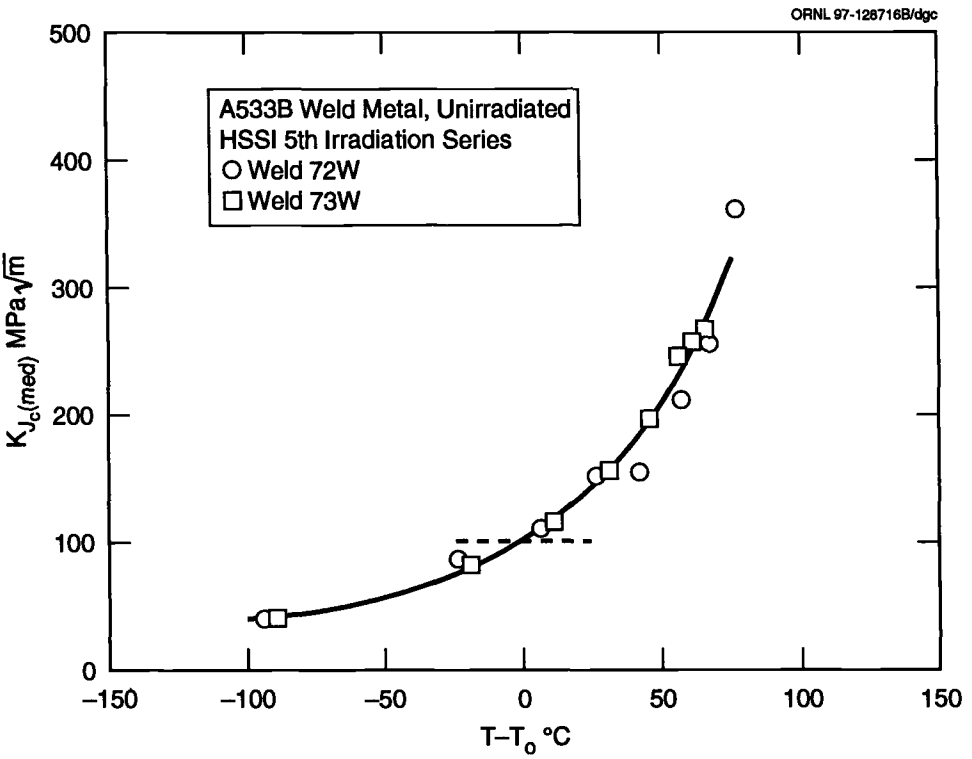

FIG. 3—*Median* K_{Jc} *values plotted against master curve for two weld metals (72W and 73W) in the unirradiated condition.*

The following master curve equation applies to median toughness obtained from 1T specimens or for K_{Jc} data from specimens of other sizes converted to 1T equivalence (1T size means that specimen thickness B = 1 in.).

$$K_{Jc(med)} = 30 + 70 \exp[0\,019(T - T_0)]\text{MPa}\sqrt{\text{m}} \tag{7}$$

Equation 7 expresses the median K_{Jc} as a function of temperature for data scatter modeled by Eq 3. Figure 2 shows an example of data sampling taken at eight test temperatures. The experiment used two weld metals identified as 72W and 73W, and two material conditions were evaluated. These were as-received and irradiated to a fluence of 1.5×10^{19} n/cm^2 (>1 MeV). Figure 3 shows only the unirradiated data reduced to median values. All data clearly followed the shape of the master curve. This master curve model has been tested on at least 14 different groups of data consisting mostly of pressure vessel steels [*4*].

Determination of Reference Temperature, T_0

There are two options available to fit experimental data to the three-parameter Weibull model. The method that was first recommended in early drafts of E 1921–97 is known as a "rank method," where K_{Jc} data are ranked according to increased values, and then each value is assigned a rank cumulative

failure probability value obtained from the following expression [*6*]:

$$(P_f)_i = (i - 0.3)/(N + 0.4) \tag{8}$$

These data are then plotted in Weibull x-y coordinates, as shown in Fig. 4. Then a line with a fixed slope of 4 is least-squares fitted to the data.

The rank method mentioned above has been replaced (in the more recent versions of the standard) in favor of the maximum likelihood method of data fitting. The weakness of the rank method is that values of P_f obtained from Eq 8 also have a probability distribution that can contribute some to the uncertainty of K_0 determinations. In fact, Eq 8 is simply one of several available estimator expressions for P_f. Figure 5 illustrates estimating uncertainties by showing the 95% confidence limits on P_f as a function of K_{Jc} for different sample sizes. As indicated, the accuracy of P_f estimation by Eq 8 is a function of sample size. There apparently is no satisfactory alternative since Eq 8 is known to be the most accurate among the several available estimator equations [*4*].

The maximum likelihood method minimizes the error due to the P_f estimate contribution. The point of maximum likelihood on the P_f density function is solved in terms of likelihood slope, $\delta L/\delta K_0$, the derivation of which is covered in Ref *4*. The result is that K_0 is determined without the necessity of ranking data and least-squares fitting to the Weibull slope of 4. The solution for K_0 takes the following form:

$$K_0 = \left[\sum_{i=1}^{N} \frac{(K_{Jc} - K_{min})^4}{(N - \zeta)}\right]^{1/4} + K_{min}\text{MPa}\sqrt{\text{m}} \tag{9}$$

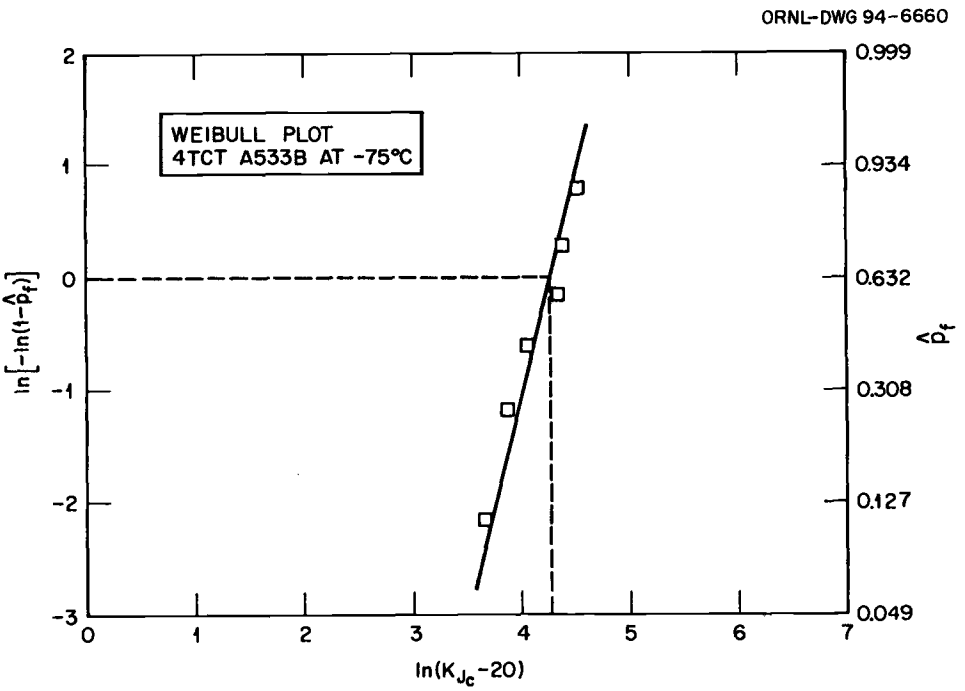

FIG. 4—*Example* K_{Jc} *data plotted in Weibull coordinates along with a least-squares fitted line with a slope of 4.*

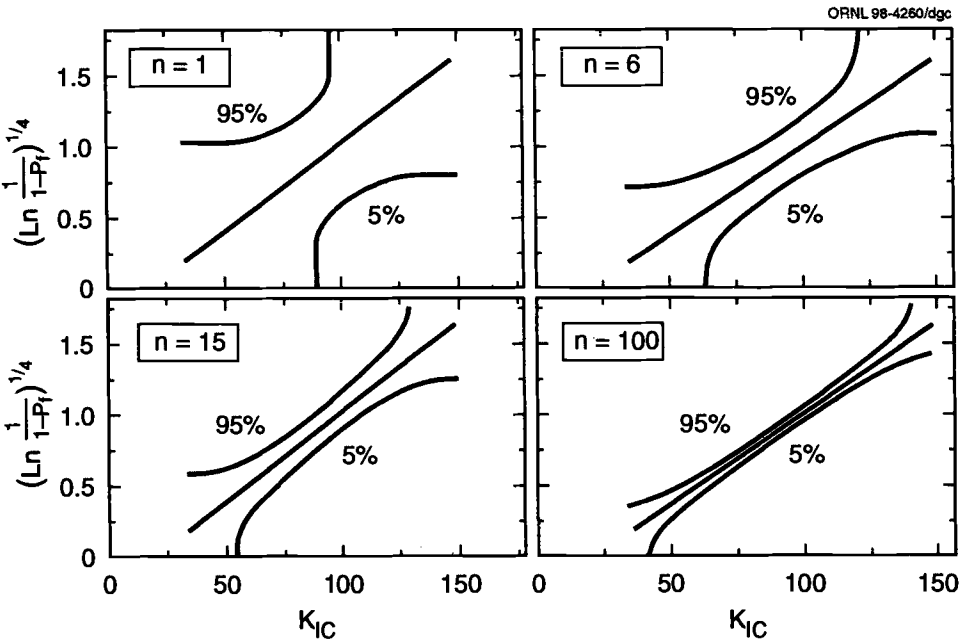

FIG. 5—*Reliability of small sample data sets of size* n, *when expressed in cumulative probability coordinates.*

The term ζ in the denominator of Eq 9 is a bias adjustment factor, nominally equal to [1 − ln(2)]. Bias correction for all intents and purposes becomes insignificant when the number of replicates, N, is six or more. Table 1, Part I(b), presents the use of Eq 9 on the MPC/JSPS round-robin data.

Data censoring is readily incorporated into Eq 9 by replacing N with r, where r represents the number of valid data. When data are censored, it is because they are deemed to be ineligible members of the data population, the existence of which can be credited as information, but under restrictions. For example, if a K_{Jc} value has been determined on a specimen that failed a constraint control limit, that datum is censored from the data population and a constraint-limit-based K_{Jc} value obtained in the following Eq 10 is used in its place:

$$K_{Jc(limit)} = (Eb_0\sigma_{ys}/30)^{1/2} \tag{10}$$

The term b_0 is the initial remaining ligament length, and σ_{ys} is the material yield strength. It is required that when data censoring is used in the determination of K_0, K_{Jc} data input should be for only one specimen size. Having determined K_0 at the known test temperature, T, Eqs 6 and 7 can be used to determine reference temperature, T_0 (see also Table 1, Part I(b)).

Establishment of Tolerance Bounds

Since slope is used as a deterministic parameter in the Weibull model, standard deviation on $K_{Jc(med)}$ can be calculated without any need for additional supporting data. The statistical method uses gamma functions that are calculated from the known Weibull slope. Reference *4* shows how this de-

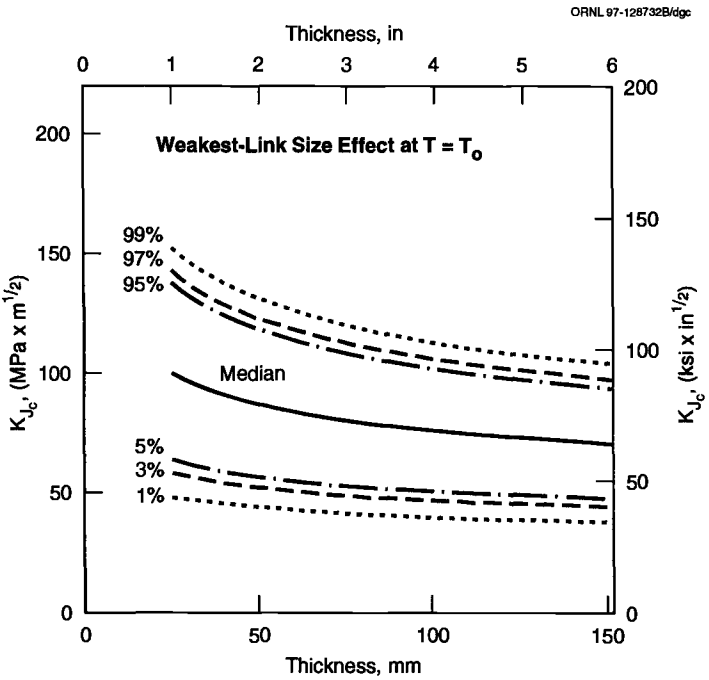

FIG. 6—*Effect of specimen size on median* K_{Jc} *and tolerance bound trends as predicted by the weakest-link model, established at test temperature equal to* T_0.

termination is made. The result is:

$$\sigma = 0.28\, K_{\mathrm{Jc(med)}} \left[1 - \frac{K_{\min}}{K_{\mathrm{Jc(med)}}} \right] \tag{11}$$

Given known standard deviations that are a function of $K_{\mathrm{Jc(med)}}$, tolerance bound curves on data scatter can be calculated by combining Eqs 7 and 11 and tabulated standard normal deviates, z, from mathematical tables given for cumulative probabilities. The general form for equations of upper or lower tolerance bound curves is as follows:

$$K_{\mathrm{TB}} = (30 + 28z) + (70 + 19.6z) \exp[0\,019(T - T_0)]\mathrm{MPa}\sqrt{\mathrm{m}} \tag{12}$$

An interesting outcome from Eq 12 is that lower tolerance bound curves tend to be almost insensitive to specimen-size effects (Fig. 6) [*12*]. Therefore, tolerance bounds drawn on the master curve with 1T specimen size assumption also tend to cover non-size-adjusted K_{Jc} data from tests on large specimens.

Some Verification of the Universal Curve Concept

Originally, twelve data sets had been used to recognize that K_{Jc} data distributions tend to follow a common curve shape (Fig. 7). In this case, scale parameter, K_0, was used. Currently, $K_{\mathrm{Jc(med)}}$ is used,

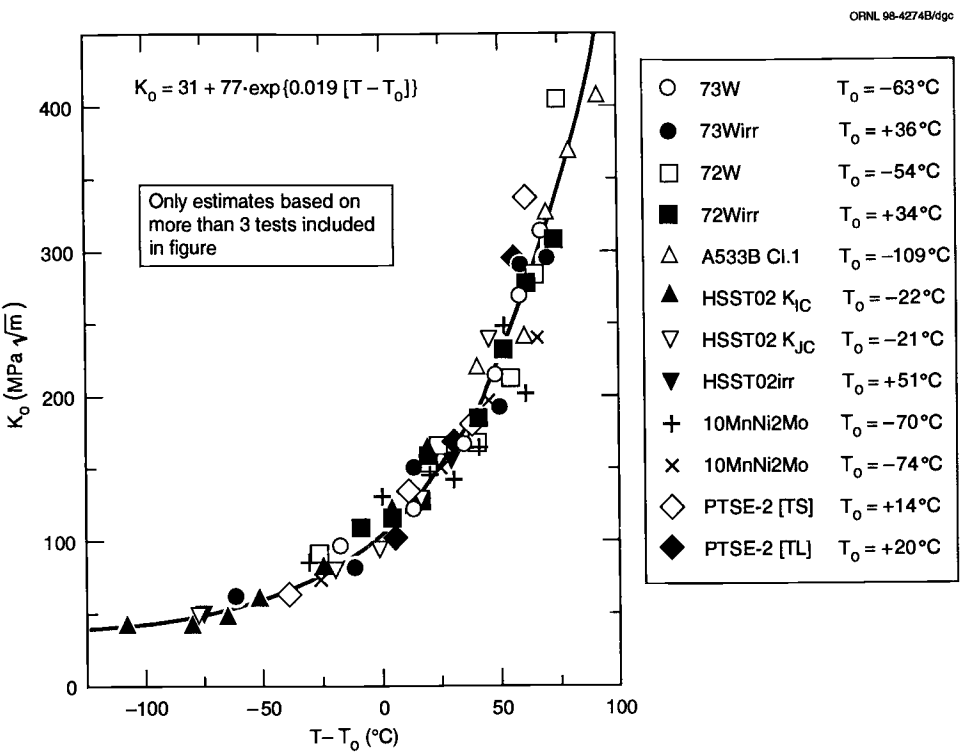

FIG. 7—*Original data used to develop the master curve equation shown.*

differing by the proportionality indicated in Eq 6. Many other materials have since been added to the original observation, covering different grades of ferritic steels, hence broadening the applicability of the universal curve concept. At the same time, there have been concerns that the rationale for such behavior is not immediately evident. Among these, the retention of master curve shape after irradiation hardening seems to have violated the hypothesis of a consistent relationship between material yield strength and fracture toughness for a given material [*12*]. Several theoretical models that explain transition range fracture toughness have been based on such an assumed relationship. However, Fig. 8 shows the seemingly typical retention of master curve shape after strengthening from irradiation exposure.

It has been shown that material yield strength appears to consist of thermal and athermal components [*4*]. The athermal part is connected to certain dislocation slip-constricting effects local to precipitates and grain boundaries. On the other hand, the matrix material in grains will retain unaltered thermally sensitive characteristics and it is this part of the microstructure that controls the transition range fracture toughness trend. Figure 9 shows how the material strength versus temperature relationship is maintained when an athermal component of yield strength is removed. Hence, the lack of material-strengthening mechanisms influencing master curve toughness trend can be explained. Other areas of concern such as strain rate effects, temper embrittlement, low upper-shelf materials, etc., are currently being evaluated.

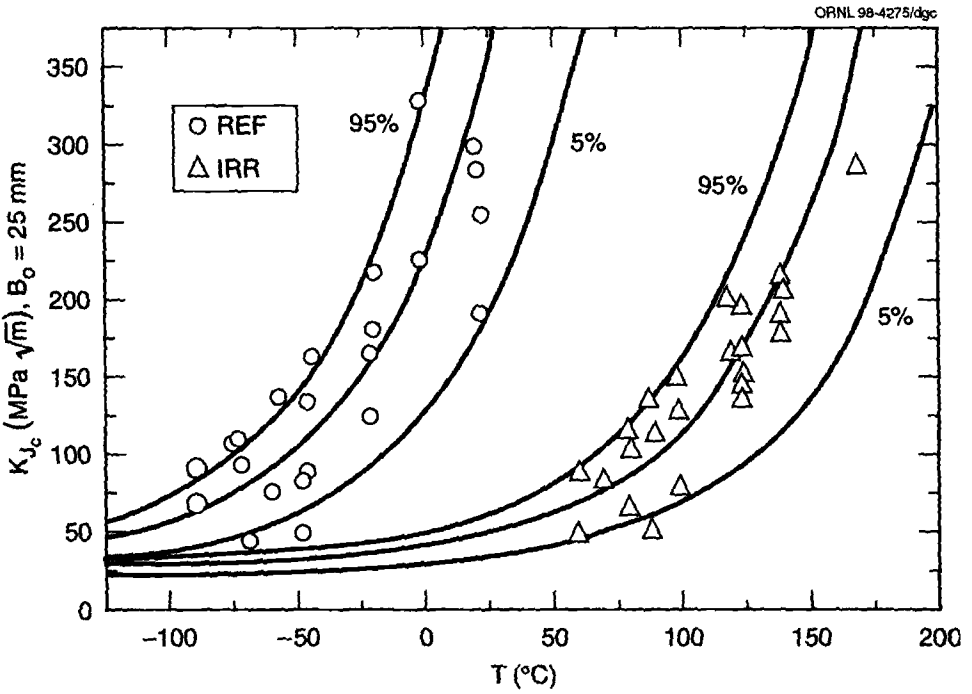

FIG. 8—*Relation between fracture toughness and temperature for unirradiated and irradiated steel.*

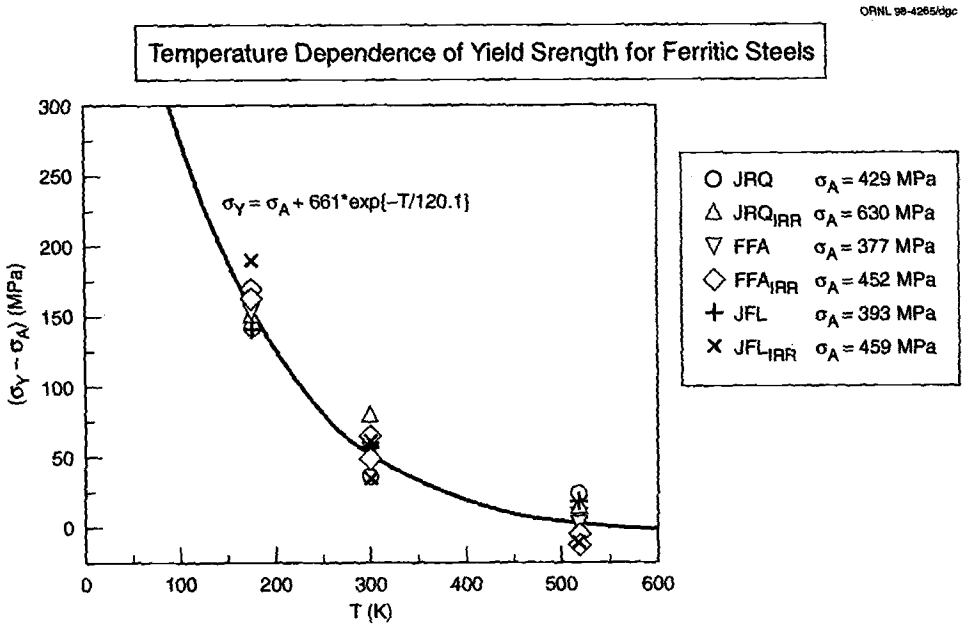

FIG. 9—*Thermal part of material yield strength after the separation of "athermal" part of yield strength.*

Conclusions

The accuracy of defining the true transition range behavior of structural steels has been improved by the introduction of a new statistically supported methodology. Fracture mechanics test methods are used to establish the true location of the transition curve. The cause of extreme data scatter and the reason for specimen size effects on data are explained by weakest-link theory. Data scatter is modeled, and tolerance bounds on data scatter are defined in terms of cumulative probabilities for occurrence. A universal transition curve is defined, the shape of which has been justified by repeated confirmatory experimental evidence. The universal curve concept appears to be undisturbed by material hardening mechanisms, and the reason for this insensitivity to material-hardening mechanisms can be rationalized.

Acknowledgments

This research is sponsored by the Division of Engineering Technology, Office of Nuclear Regulatory Research, U.S. Nuclear Regulatory Commission, under Interagency Agreement DOE 1886-N011-9B with the U.S. Department of Energy under Contract DE-AC05-96OR22464 with Lockheed Martin Energy Research Corporation.

References

[1] ASTM Standard Test Method E 399-90, "Plane-Strain Fracture Toughness of Metallic Materials," *Annual Book of ASTM Standards,* Vol. 03.01, 1996.

[2] "PVRC Recommendations on Toughness Requirements for Ferritic Materials," *Welding Research Council Bulletin 175,* Welding Research Council, New York, August 1972.

[3] *White Paper on Reactor Vessel Integrity Requirements for Level A and B Conditions,* EPRI TR-100241, Electric Power Research Institute, Palo Alto, CA, January 1993.

[4] Merkle, J. G., Wallin, K., and McCabe, D. E., *Technical Basis for an ASTM Standard on Determining the Reference Temperature,* T_o *for Ferritic Steels in the Transition Range,* Draft NUREG, to be published.

[5] McCabe, D. E., Zerbst, U., and Heerens, J., *Development of Test Practice Requirements for a Standard Method on Fracture Toughness Testing in the Transition Range,* GKSS Report 93/E/81, GKSS-Forschungszentrum, Geesthacht GmbH, Germany, 1993.

[6] ASTM Standard Test Method E 1921–97, "Determination of Reference Temperature, T_o, for Ferritic Steels in the Transition Range," *Annual Book of ASTM Standards,* Vol. 03.01, 1998.

[7] Stienstra, D. I. A., *Stochastic Micromechanical Modeling of Cleavage Fracture in the Ductile-Brittle Transition Region,* MM-6013-90-11, Texas A & M University, College Station, Texas, 1990.

[8] Landes, J. D. and McCabe, D. E., "Effect of Section Size on Transition Temperature Behavior of Structural Steels," *Fracture Mechanics: Fifteenth Symposium, ASTM STP 833,* R. J. Sanford, Ed., American Society for Testing and Materials, Philadelphia, 1984, pp. 378–382.

[9] Wallin, K., "The Scatter in K_{Ic} Results," *Engineering Fracture Mechanics,* Vol. 19, No. 6, 1984, pp. 1083–1093.

[10] Van Der Sluys, W. A. and Miglin, M. T., "Results of MPC/JSPS Cooperative Testing Program in the Brittle-to-Ductile Transition Region," *Fracture Mechanics: Twenty-Fourth Volume, ASTM STP 1207,* American Society for Testing and Materials, 1994, pp. 308–324.

[11] Miranda, C. A. J. and Landes, J. D., "Influence of the Number of Specimens in the Reference Temperature Determination: The Monte Carlo Approach," Paper 1401, IPEN/CNEN/SP, 1997, to be published.

[12] Neville, D. J. and Knott, J. F., "Statistical Distributions of Toughness and Fracture Stress for Homogeneous and Inhomogeneous Materials," *Journal of The Mechanics and Physics of Solids,* Vol. 34, No. 3, 1986, pp. 243–291.

J. R. Donoso[1] *and J. D. Landes*[2]

A Unifying Principle for Evaluating Fracture Toughness in the Elastic and Plastic Regimes with Planar Fracture Specimens

REFERENCE: Donoso, J. R. and Landes, J. D., **"A Unifying Principle for Evaluating Fracture Toughness in the Elastic and Plastic Regimes with Planar Fracture Specimens,"** *Fatigue and Fracture Mechanics: 30th Volume, ASTM STP 1360,* P. C. Paris and K. L. Jerina, Eds., American Society for Testing and Materials, West Conshohocken, PA, 2000, pp. 34–50.

ABSTRACT: Recently, Donoso and Landes proposed the existence of a common format equation (CFE) for developing calibration functions for two-dimensional fracture specimens. In the CFE approach, the relation between load, plastic displacement, and uncracked ligament size is expressed as the product of three terms: (1) a constraint factor, (2) a geometry and crack length-dependent function (G), and (3) a hardening function (H). The history-dependent component of the calibration functions, namely H, has been explored by the same authors, using two different hardening functions: a power law and a three-parameter function, designated as the LMN function. For the geometry function G, on the other hand, a power-law dependence on normalized ligament length, i.e., $G \propto (b/W)^m$ (where W is the specimen width), is used for all of the classical two-dimensional fracture specimens. This type of behavior for G has been derived from the GE EPRI Handbook equations and has also been observed experimentally. From such a relationship, a crack-length independent value of eta plastic, η_{pl}, is obtained that is equal to the exponent m.

The application of a ductile fracture methodology requires, in addition to the calibration functions, the fracture toughness of the material, usually given by the J-R curve. The computation of J, according to standard procedures, needs both its elastic and plastic contributions. The elastic component is normally evaluated in terms of K, the stress-intensity factor for the geometry and test conditions. The plastic component of J, on the other hand, is equal to the area under the load-plastic displacement curve per unit net section area of specimen, multiplied by the plastic eta factor, η_{pl}. The purpose of this work is to extend the use of the CFE approach to the elastic region of the load-displacement curve of standard fracture specimens, focusing on both their elastic compliances and their elastic eta factors, η_{el}. The elastic compliances and the G functions of the predominantly bend-type geometries, i.e., SE(B), C(T), and SE(T) specimens, are compared, showing that the elastic and the plastic eta factors are practically equal. This allows one to evaluate J in these geometries in terms of total displacement. The same does not apply, however, to the tensile M(T) and DE(T) geometries. In addition, K factors will be derived for the bend-type geometries based on the dependence of the elastic compliance with ligament size.

KEYWORDS: fracture, elastic, plastic, unifying load, separation

Calibration functions for two-dimensional fracture specimens, representing the relation between load, P, plastic component of the displacement, v_{pl}, and crack length, a, have been obtained either by analytical, empirical, or numerical means. Recently, Donoso and Landes [*1*] proposed the existence of a common format equation (CFE) for developing such functions based on elastic-plastic numerical solutions obtained from the GE-EPRI Handbook [*2*]. In the CFE approach [*1*], the behavior of the fracture specimen is expressed as the product of three terms to describe the load, P, as a function of both plastic displacement, v_{pl}, and crack length a (or, as shall be used throughout

[1] Materials Science Department, Universidad Tecnica Federico Santa Maria, Valparaiso, Chile.
[2] Engineering Science and Mechanics Department, University of Tennessee, Knoxville, TN 37996-2030.

this work, ligament b):

(1) a constraint factor, Ω/κ;
(2) a geometry and crack length-dependent function, G, and
(3) a hardening function, H, that represents the stress-strain behavior of the material.

The history-dependent component of the calibration functions, namely H, has been explored by the same authors, using two different stress-strain relations: a power law and a three-parameter function, designated as the LMN function. Further, it was shown that normalized load and normalized displacement for planar, two-dimensional fracture specimens, may be separately obtained from cylindrical specimen stress and strain data, respectively, by making use of an appropriate model [*3*]. The evaluation of the size constraint factor, on the other hand, may be done by comparison of actual data to the model equation for the calibration function, using either a power law type of relation [*4*] or the LMN function [*3*].

As for the geometry function G, before the advent of the CFE, only equations for the SE(B) and C(T) specimens were available. Sharobeam and Landes [*5*], working on experimentally obtained data, proposed a power law dependence on the normalized ligament, i.e., $G \propto (b/W)^m$ (where W is the specimen width), for other test geometries including C(T), M(T), SE(T), and DE(T). In the CFE, this same type of behavior was developed for all of the classical two-dimensional fracture specimens, deriving it from the *GE EPRI Handbook* numerical solutions. The values of m were the same as those proposed earlier in Ref *5*.

The application of a ductile fracture methodology requires, in addition to the calibration functions, the fracture toughness of the material, usually given by the *J-R* curve. The computation of J, according to standard procedures, ASTM Standard Test Method for Determining *J-R* Curves (E 1152-87), needs both its elastic and plastic contributions. The elastic component is normally evaluated in terms of K, the stress-intensity factor for the geometry and test conditions. The plastic component of J, on the other hand, is equal to the area under the load-plastic displacement curve per unit net section area of specimen multiplied by the plastic eta factor, η_{pl}.

In what follows, the use of the CFE approach will be extended to the elastic region of the load-displacement curve of the standard fracture SE(B), C(T), M(T), DE(T), and SE(T) specimens, evaluating their elastic compliances in terms of the quantity b/W. Based on the dependence of the elastic compliance with ligament size, the stress intensity factors, K, will be evaluated for these geometries, as well as the elastic eta factors, η_{el}, required for the computation of J_{el}.

The Elastic Compliance

The CFE approach for the relation between load, plastic displacement, and uncracked ligament has the following generic form [*1*]:

$$P = \{\Omega/\kappa\} \cdot G \cdot H \tag{1}$$

in which Ω/κ is a size constraint factor, G is a geometry-related function, and H is a hardening, material-dependent function. Being that these two functions, G and H, are independent of one another, load separation is feasible. In the original CFE paper [*1*], G was shown to depend on normalized ligament, b/W, according to the power law relation:

$$G = B\,W\,C\,(b/W)^m \tag{2}$$

where B is the specimen thickness. This expression was derived from the GE EPRI solutions [*2*] and agrees very well with experimentally obtained values [*5*]. In Eq 2, m is an exponent that is indepen-

dent of crack length [*1*] and fairly independent of both the plastic displacement and the material [*6*]. Values for C and m are tabulated in Ref *1* for the five common fracture test geometries: SE(B), C(T), SE(T), DE(T), and M(T).

The single specimen form for the J integral can be written as

$$J = \frac{\eta}{Bb} \int P dv \tag{3}$$

in which b is the uncracked ligament, B is the specimen thickness, η is a factor, and the integral term represents the area under the load-displacement record. The various ASTM standards that deal with J (see, for example, E 1152-87), require its evaluation as the sum of an elastic and a plastic contribution:

$$J = J_{el} + J_{pl} \tag{4}$$

where

$$J_{el} = \frac{K^2}{E}(1 - \nu^2) \tag{5}$$

for plane strain conditions, and J_{pl} is of the form

$$J_{pl} = \frac{\eta_{pl}}{Bb} \int P dv_{pl} \tag{6}$$

In Eq 6, the plastic eta factor, η_{pl}, may be computed from Eq 2. In fact, by definition, eta plastic is equal to [*5*]:

$$\eta_{pl} = \left(\frac{b}{W}\right)\frac{G'}{G} \tag{7}$$

so it may be easily shown that $\eta_{pl} = m$.

The elastic compliances for the various fracture geometries may be found in Tada's handbook of elastic solutions [*7*] and in various ASTM standards for fracture testing. The relations between load line displacement, v, or crack mouth opening displacement (*cmod*), δ, and crack length are given either in tabular form or as analytical solutions valid for a certain range of a/W values. These latter forms were chosen to analyze their behavior in terms of the normalized ligament, b/W, and will be described separately by geometry starting with the C(T) specimen.

1. The C(T) *Specimen*

A generic relation for the compliance, common to both *cmod* and v, is of the form (E 1152-87):

$$BE'c = Y^2\{A_0 + A_1(a/W) + A_2(a/W)^2 + A_3(a/W)^3 + A_4(a/W)^4 + A_5(a/W)^5\} \tag{8}$$

in which $E' = E$, for plane stress, $E' = E/(1 - \nu^2)$ for plane strain conditions, and c is compliance. The term Y is a function of a/W and has the form

$$Y = \left[\frac{W + a}{W - a}\right] \tag{9}$$

TABLE 1—*C(T) elastic compliance polynomial coefficient* A_i.

	A_0	A_1	A_2	A_3	A_4	A_5
v	2.163	12.219	−20.065	−0.9925	20.609	−9.9314
δ	1.614	12.68	−14.23	−16.61	35.05	−14.49

for v, whereas for δ is equal to

$$Y = \left[\frac{W + a}{W - a}\right]\left[1 + \frac{0.25}{a/W}\right]^{1/2} \tag{10}$$

The A_i coefficients are listed in Table 1, as obtained from E 1152-87.

The dependence of the functions $BE'c(v)$ and $BE'c(\delta)$ (Eq 8) on b/W is shown in Fig. 1, on a log-log plot. With the exception of very large ligament sizes ($b/W > 0.6$), the behavior is linear in the range $0.90 > a/W > 0.40$, with slopes of −2.283 and −2.167 for load line displacement and *cmod,* respectively, and correlation coefficients >0.999. The relations resulting from the linear regression are:

$$\log BE'c(v) = 0.88113 - 2.28313 \log (b/W) \tag{11}$$

and

$$\log BE'c(\delta) = 1.08466 - 2.16706 \log (b/W) \tag{12}$$

This may be written as

$$c(x) = (A/BE')\,(b/W)^{-\mu} \tag{13}$$

where $A = 7.6055$ and $\mu = 2.283$ for $x = v$, and $A = 12.1523$ and $\mu = 2.167$ for $x = cmod$. Since the compliance relates displacement to load, one can write

$$x = c(x)\,P \tag{14}$$

Solving for P:

$$P = x\,c^{-1}(x) = x\,(BE'/A)\,(b/W)^{\mu} \tag{15}$$

Normalizing the displacement x by W, and rearranging, leads to:

$$P = \Omega^*\,B\,W\,C^*\,\{(b/W)^{\mu}\}\{E\,(x/W)\} \tag{16}$$

One can compare Eq 15 with Eq 1, the CFE, and recognize the following relations:

$$G_{el} = B\,W\,C^*\,\{(b/W)^{\mu}\} \tag{17}$$

$$H_{el} = \{E\,(x/W)\} \tag{18}$$

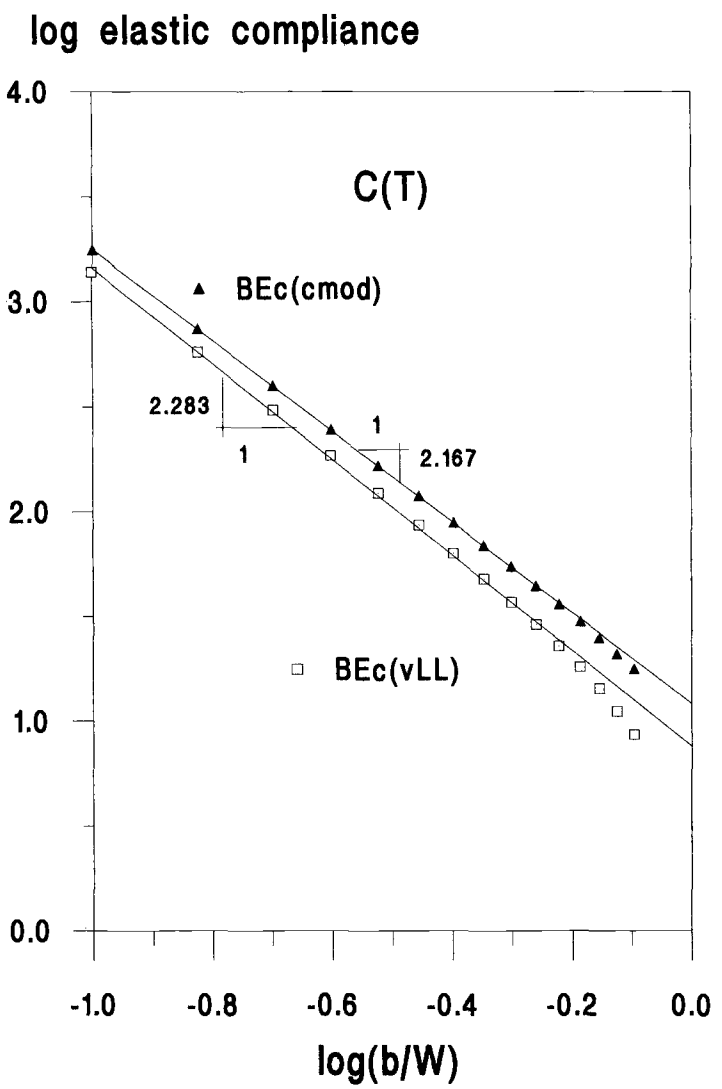

FIG. 1—*Log-log plots of elastic compliance for load line displacement,* v (v_{LL})*, and* cmod*, as a function of* b/W*, C(T) specimen.*

and Ω^*, the constraint term, as being equal to 1 for plane stress, and to $1/(1 - \nu^2)$ for plane strain. The coefficient C^* is equal to $1/A$; Table 2 summarizes the values of μ and C^*. This way, the calibration functions for the plastic range have their counterparts in the above elastic relations. The elastic G function is also a power law on the normalized ligament b/W, whereas the elastic H is simply the product of Young's modulus times the normalized displacement x/W. Further, the principal characteristic of the calibration function, i.e., the ligament-independent normalized load, P_N, may be written as

$$P_N = P/G = \Omega^* E (x/W) \tag{19}$$

TABLE 2—*Elastic and plastic G function parameters for the C(T) specimen.*

	C^*	μ	C	m	μ/m
v	0.1315	2.283	1.553	2.236	1.021
δ	0.0823	2.167	1.489	2.174	0.997

The form of Eq 19 is worth analyzing: normalized load, P_N, has units of stress, whereas the term (x/W) has units of strain. In this context, Eq 19 is a restatement of the stress-strain relation in the elastic region for a given specimen geometry [*3*].

2. The SE(B) Specimen

The generic form for the load line compliance is of the form [E 1152-87,7]

$$BE'c(v) = Y^2 \{A_0 + A_1(a/W) + A_2(a/W)^2 + A_3(a/W)^3 + A_4(a/W)^4\} \tag{20}$$

whereas that for the *cmod* compliance is:

$$BE'c(\delta) = Z \{A_0 + A_1(a/W) + A_2(a/W)^2 + A_3(a/W)^3 + A_4/(1 - a/W)^2\} \tag{21}$$

In Eqs 20 and 21, Y and Z have the following forms:

$$Y = 4W/(W - a) \tag{22}$$

$$Z = 24(a/W) \tag{23}$$

for the standard specimen dimensions.

Table 3 shows the values of the various A_i for the SE(B) specimen.

The dependence on b/W of the elastic compliance functions of Eqs 20 and 21 is shown in Fig. 2 for SE(B). In this case, the behavior is also linear in the range $0.90 > a/W > 0.40$, but the slopes are different: -2.047 and -2.351 for load line displacement and *cmod,* the correlation coefficients being >0.9999 and 0.997, respectively. The relations resulting from the linear regressions are:

$$\log [BE'c(v)/16] = -0.07053 - 2.04673 \log (b/W) \tag{24}$$

$$\log [BE'c(\delta)/24] = -0.52991 - 2.35136 \log (b/W) \tag{25}$$

from which the generic Eq 12 for the compliances as a function of b/W will have the following parameters: $A = 13.60$ and $\mu = 2.047$ for $x = v$, and $A = 81.305$ and $\mu = 2.351$ for $x = cmod$.

TABLE 3—*SE(B) elastic compliance polynomial coefficients,* A_i.

	A_0	A_1	A_2	A_3	A_4
v	1.193	−1.980	4.478	−4.433	1.739
δ	0.76	22.28	3.87	−2.04	0.66

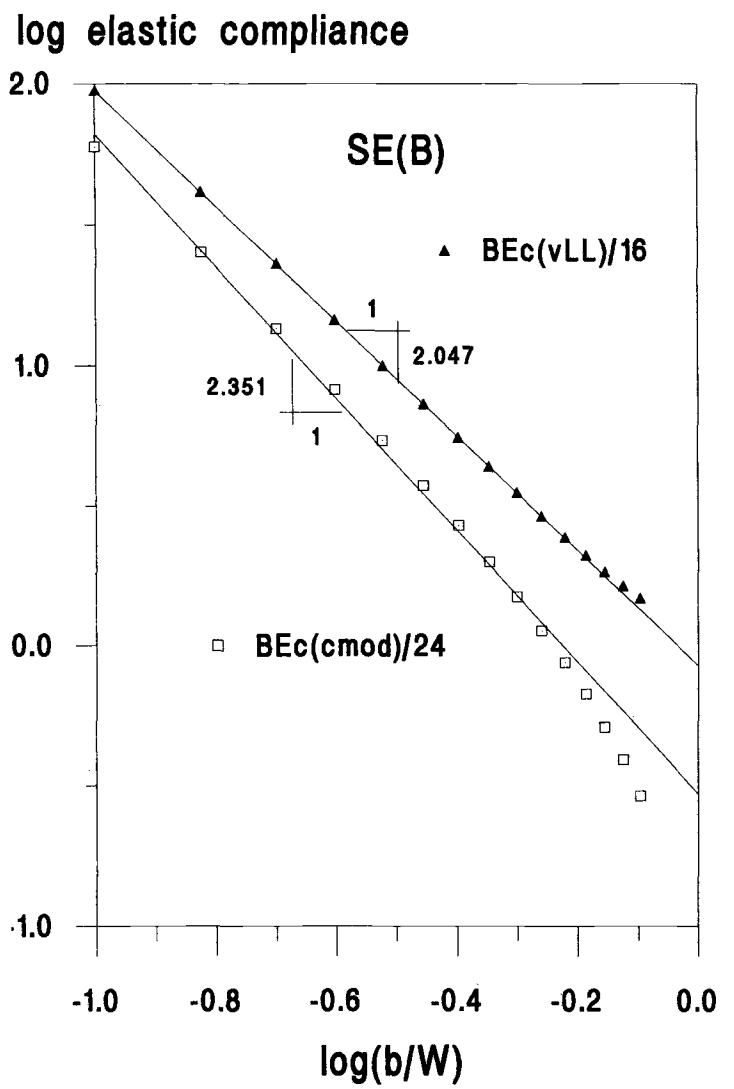

FIG. 2—*Log-log plots of elastic compliance for load line displacement,* v (v_{LL})*, and* cmod*, as a function of* b/W*, SE(B) specimen.*

The values of the respective parameters for both G functions are shown in Table 4.

3. The SE(T) Specimen

The expression for the load line compliance is [7]:

$$E'Bc(v) = \frac{4(a/W)^2}{(1 - a/W)^2}\left[0.99 - \frac{a}{W}\left(1 - \frac{a}{W}\right)\left\{1.3 - 1.2\left(\frac{a}{W}\right) + 0.7\left(\frac{a}{W}\right)^2\right\}\right] \quad (26)$$

TABLE 4—*Elastic and plastic* G *function parameters for the SE(B) specimen.*

	C^*	μ	C	m	μ/m
v	0.0735	2.047	1	2	1.024
δ	0.0123	2.351	1.072	1.982	1.186

whereas that for the *cmod* compliance is:

$$E'Bc(\delta) = \frac{4(a/W)\left\{1.46 + 3.42\left(1 - \cos\frac{\pi a}{2W}\right)\right\}}{\left(\cos\frac{\pi a}{2W}\right)^2} \tag{27}$$

The dependence of the elastic compliance functions of Eqs 26 and 27, in the form $\log(BE'c/4)$ in terms of $\log(b/W)$ for the SE(T) specimen, is shown in Fig. 3. In this case, the behavior is not lin-

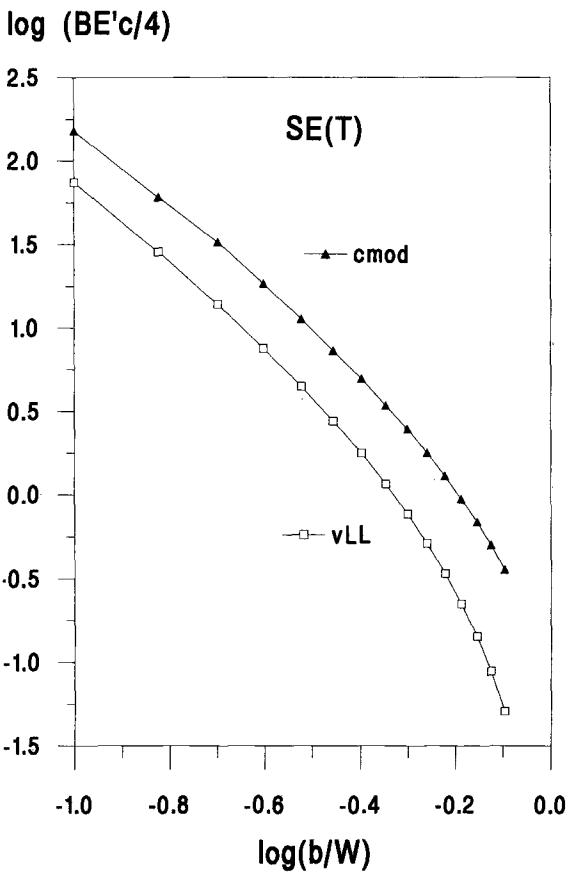

FIG. 3—*Log-log plots of elastic compliance for load line displacement,* v (v_{LL}), *and* cmod, *as a function of* b/W, *SE(T) specimen.*

ear, but the two curves follow a similar trend. However, if one compares the inverse function $(4/BE'c)$ with $\beta(b/W)(h_3a/W)^{1/10}$, which is the fundamental function used to develop the CFE (plastic behavior) parameters [*1*], then there is a similarity between the elastic and plastic curves for the range $0.90 > a/W > 0.70$. This behavior is shown in Fig. 4; the SE(T) CFE function has a slope of 2.364. If one considers a value of $h/W = 2$ for the ratio of height h over width W for the SE(T) specimen, then the best line passing through points in the range $0.90 > a/W > 0.50$ (Fig. 5) has a slope of 2.366, which is almost identical to the CFE m for the SE(T) specimen. The inclusion of the size of the specimen implies the use of the total displacement compliance in lieu of the displacement due to the crack alone. In Fig. 5, the elastic *cmod* compliance is also shown, with a similar slope, 2.343, valid in the range $0.90 > a/W > 0.70$. The summary of parameters for the SE(T) specimen is shown in Table 5.

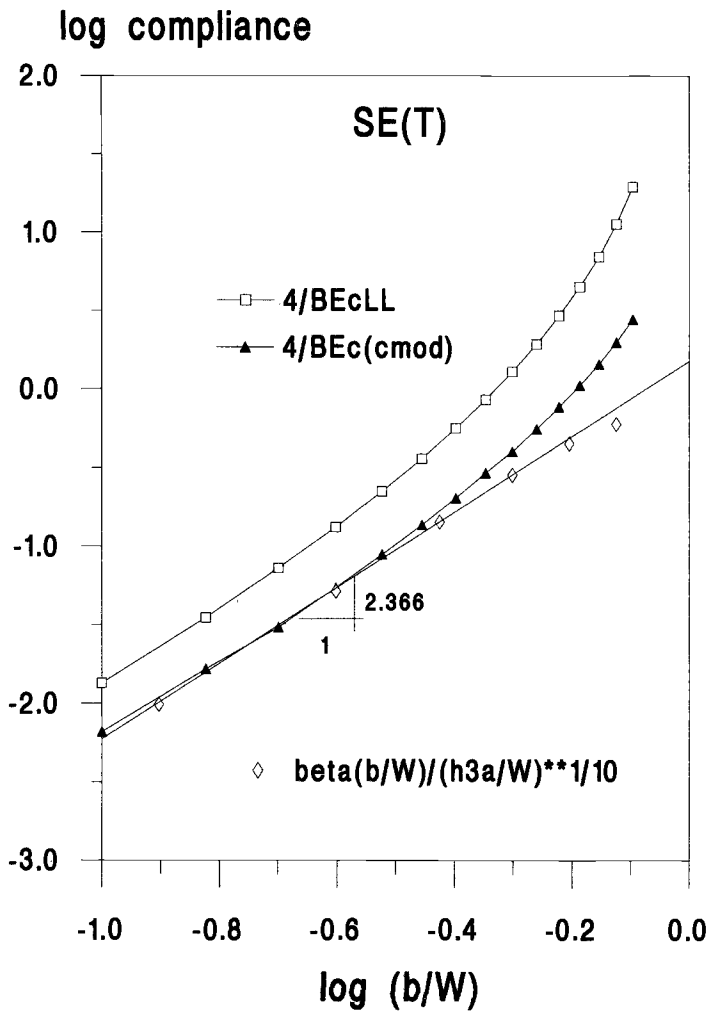

FIG. 4—*Comparison between CFE (plastic) slopes and elastic slopes, SE(T) specimen.*

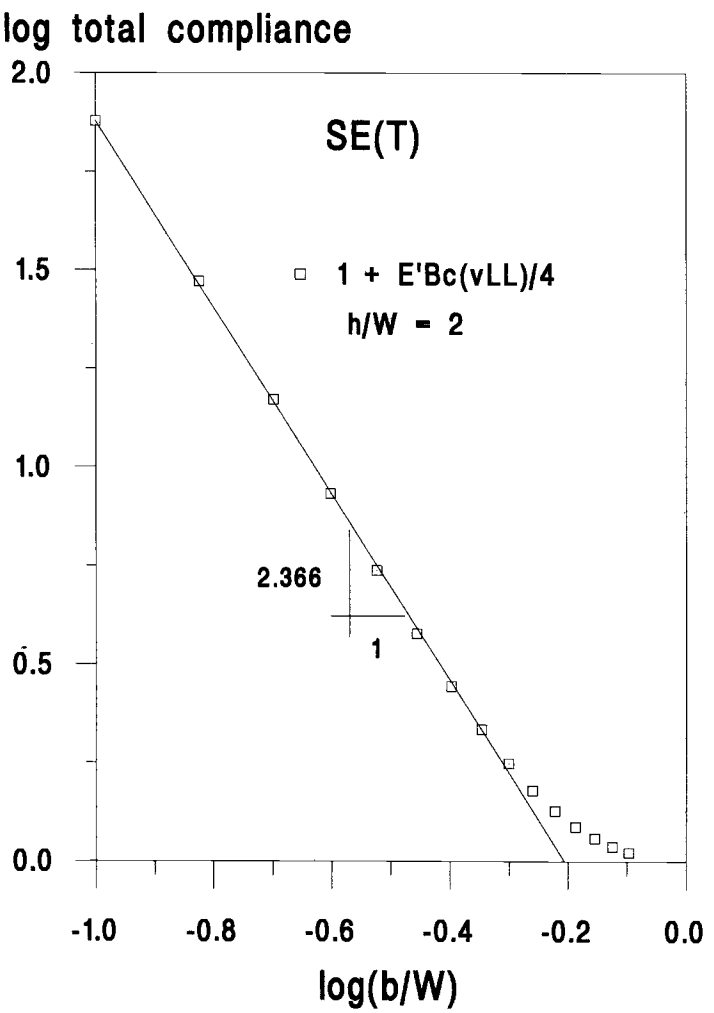

FIG. 5—*Total compliance of the load line displacement, SE(T) specimen.*

TABLE 5—*Elastic and plastic* G *function parameters for the SE(T) specimen.*

	C^*	μ	C	m	μ/m
v	0.7683	2.366	4.27	2.364	1.000
δ	0.3525	2.343	4.58	2.345	0.999

4. The DE(T) Specimen

The generic form for the compliance of the DE(T) specimen (also common to the M(T) specimen) is:

$$x = \frac{4\sigma a}{E'} V_i(a/W) \tag{28}$$

where for $x = cmod$, $i = 1$, and for $x = v$ (displacement due to the crack), $i = 2$. In Eq 28, σ is the nominal tensile stress acting on the plate of width $2W$, $2a$ is the total crack length, and V_i is the function that depends on a/W, to be analyzed.

The function V_1, for *cmod*, is:

$$V_1 = \frac{1}{\left(\frac{\pi a}{2W}\right)}\left\{0.459\left(\sin\frac{\pi a}{2W}\right) - 0.065\left(\sin\frac{\pi a}{2W}\right)^3 - 0.007\left(\sin\frac{\pi a}{2W}\right)^5 + \cosh^{-1}\left(\sec\frac{\pi a}{2W}\right)\right\} \tag{29}$$

whereas V_2, for v, is:

$$V_2 = \frac{1}{\left(\frac{\pi a}{2W}\right)}\left\{0.0629 - 0.0610\left(\cos\frac{\pi a}{2W}\right)^4 - 0.0019\left(\cos\frac{\pi a}{2W}\right)^8 + \ln\left(\sec\frac{\pi a}{2W}\right)\right\} \tag{30}$$

Figure 6 shows the plots of $BE'c/2$ for both v and *cmod*. A reasonable linear behavior is found for the range $0.85 > a/W > 0.60$, with slopes (μ's) of roughly 0.5 for *cmod* and 0.96 for v. The comparative results with the CFE parameters (plane stress) are shown in Table 6.

5. The M(T) Specimen

The analysis of the M(T) case is similar to that for the DE(T) specimen. The functions to be analyzed are:

$$V_1 = -0.071 - 0.535(a/W) + 0.169(a/W)^2 + 0.020(a/W)^3 - \frac{1.071}{(a/W)}\ln(1 - a/W) \tag{31}$$

and

$$V_2 = -1.071 + 0.250(a/W) - 0.357(a/W)^2 + 0.121 \times (a/W)^3 - 0.047\,(a/W)^4 + 0.008(a/W)^5 - \frac{1.071}{(a/W)}\ln(1 - a/W) \tag{32}$$

for *cmod* and v, respectively.

Figure 7 shows the plots of $BE'c/2$, again for v and *cmod*. A reasonable linear behavior is found only for the range $0.85 > a/W > 0.60$, with slopes (μ's) of the order of 1.046 for *cmod* and 1.070 for v. The comparative results with the CFE parameters (plane stress) are shown in Table 7.

A summary of all elastic compliance and plastic G function parameters obtained thus far may be seen in Table 8.

From the results shown in Table 8, several interesting conclusions may be inferred in relation with the μ values, and the μ/m ratios:

(a) μ is very similar to m (within $\pm 3\%$) for a number of cases that may be ascribed as being the primarily "bend" type specimens. These are the C(T), SE(B), and SE(T) specimens.

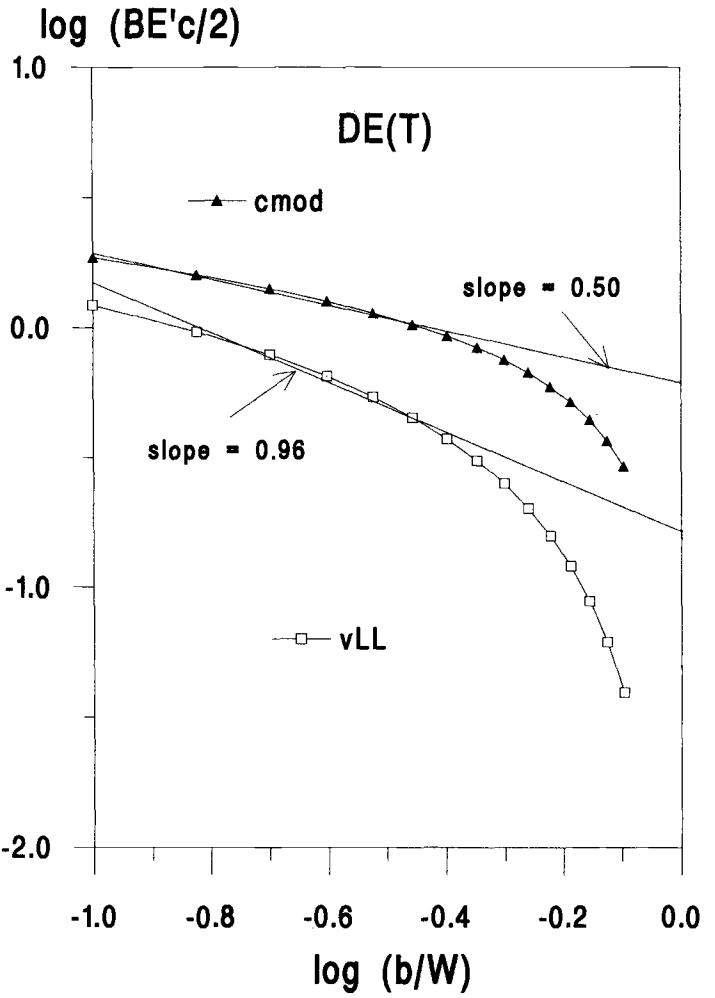

FIG. 6—*Log-log plots of elastic compliance for load line displacement,* v (v_{LL})*, and* cmod*, as a function of* b/W*, DE(T) specimen.*

(b) The similarity between μ and m is given primarily for v rather than for δ. In fact, the ratios μ/m for v for these three geometries are practically equal to one.

(c) The same similarity between the exponents μ and m is found for δ only in the C(T) and SE(T) cases; the SE(B) geometry shows a large deviation between the two parameters.

TABLE 6—*Elastic and plastic* G *function parameters for the DE(T) specimen.*

	C^*	μ	C	m	μ/m
v	3.043	0.96	4.308	1	0.960
δ	0.8131	0.50	3.744	0.82	0.610

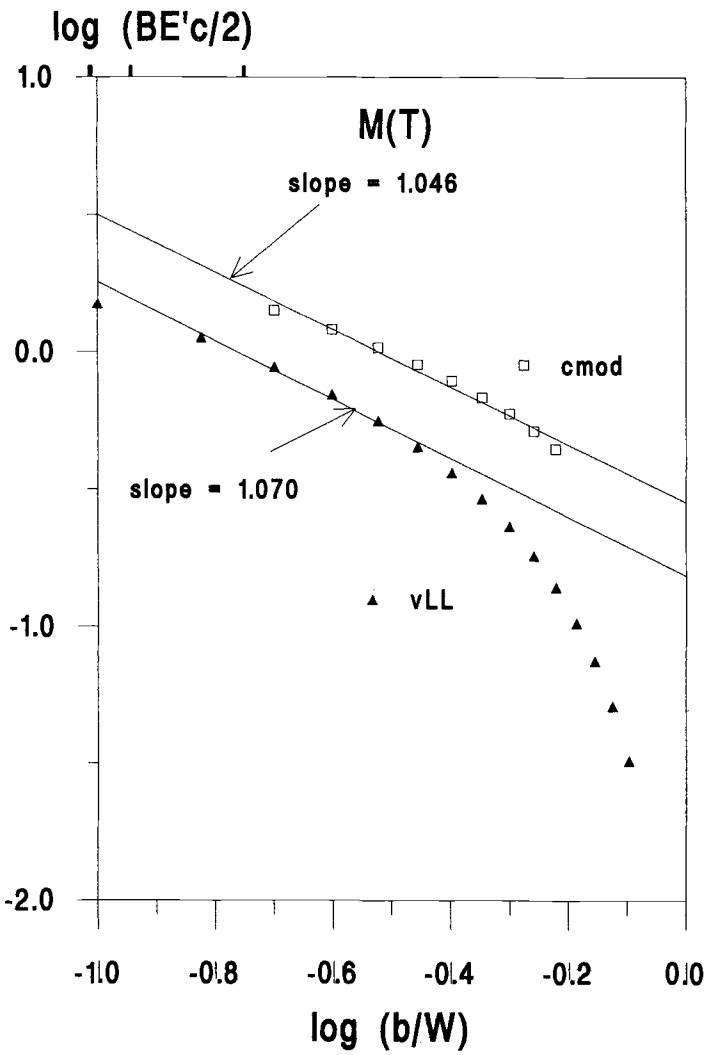

FIG. 7—*Log-log plots of elastic compliance for load line displacement,* v (v_{LL})*, and* cmod*, as a function of* b/W*, M(T) specimen.*

TABLE 7—*Elastic and plastic* G *function parameters for the M(T) specimen.*

	C^*	μ	C	m	μ/m
M(T), v	3.259	1.070	3.731	1	1.070
M(T), δ	1.756	1.046	2.020	0.889	1.177

TABLE 8—*Elastic and plastic* G *function parameters for all specimens.*

	C^*	μ	C	m	μ/m
C(T), v	0.1315	2.283	1.553	2.236	1.021
C(T), δ	0.0823	2.167	1.489	2.174	0.997
SE(B), v	0.0735	2.047	1	2	1.024
SE(B), δ	0.0123	2.351	1.072	1.982	1.186
SE(T), v	0.7683	2.366	4.27	2.364	1.000
SE(T), δ	0.3525	2.343	4.58	2.345	0.999
DE(T), v	3.043	0.96	4.308	1	0.960
DE(T), δ	0.8131	0.50	3.744	0.82	0.610
M(T), v	3.259	1.070	3.731	1	1.070
M(T), δ	1.756	0.046	2.020	0.889	1.177

If one is willing to accept a larger margin of difference between μ and m for v, then the DE(T) and M(T) geometries may be included for a given crack length range, with absolute differences of 4 and 7%, respectively. Table 9 shows a list of the situations for which m and μ may be considered as "practically equal," together with the range of a/W for which this assertion seems justified. The additional inclusion of a column with the ratio $\mu/2C^*$ will be justified presently.

Compact Form for K

The conventional definition of K from the elastic compliance variation with crack length is [7]:

$$K^2 = \left[E' \frac{P^2}{2B}\frac{dc}{da}\right] = \frac{1}{2}\left(\frac{P}{BW}\right)^2 W \frac{d(E'Bc)}{d(a/W)} \tag{33}$$

From Eq 15 and $\Omega * E = E'$, we can write

$$\frac{P}{BW} = C^*(b/W)^{\mu}E'(x/W) \tag{34}$$

and, since from Eq 12,

$$BE'c = A(b/W)^{-\mu} \tag{35}$$

TABLE 9—*Elastic and plastic* G *function parameters for specimens with* $\mu/m \approx 1$.

Geometry	a/W	C^*	μ	$\mu/2C^*$	C	m	μ/m
C(T), v	0.45/0.90	0.1315	2.283	8.68	1.553	2.236	1.021
C(T), δ	0.45/0.90	0.0823	2.167	13.165	1.489	2.174	0.997
SE(B), v	0.20/0.90	0.0735	2.047	13.925	1	2	1.024
SE(T), v	0.50/0.90	0.7683	2.366	1.54	4.27	2.364	1.000
SE(T), δ	0.50/0.90	0.3525	2.343	3.325	4.58	2.345	0.999
DE(T), v	0.65/0.85	3.043	0.96	0.158	4.308	1	0.960
M(T), v	0.50/0.85	3.259	1.070	0.164	3.731	1	1.070

one can obtain

$$\frac{d(E'Bc)}{d(a/W)} = -\frac{d(E'Bc)}{d(b/W)} = \mu A(b/W)^{-\mu-1} \tag{36}$$

Substituting Eqs 34, 35, and 36 into Eq 33, one can show that

$$\frac{K^2}{E'} = \frac{1}{2}\mu\frac{Px}{Bb} \tag{37}$$

which, stated as an integral form, using $x = v_{el}$, becomes

$$\frac{K^2}{E'} = \frac{\mu}{Bb}\int_0^v P dv_{el} \tag{38}$$

One can recognize the left-hand side of Eq 38 as Eq 5, so that

$$J_{el} = \frac{K^2}{E'} = \frac{\mu}{Bb}\int_0^v P dv_{el} \tag{39}$$

and $\mu = \eta_{el}$. Thus, Eq 4 for total J, becomes

$$J = \frac{\eta_{el}}{Bb}\int P dv_{el} + \frac{\eta_{pl}}{Bb}\int P dv_{pl} \tag{40}$$

51

If $\eta_{el} = \eta_{pl}$, as is the case for the geometries and a/W limits listed in Table 9, then Eq 40 may be written as one single integral:

$$J = \frac{\eta}{Bb}\int P dv \tag{41}$$

where $\eta = \eta_{el} = \eta_{pl} = \mu = m$, and v is the total displacement, or the sum of the elastic and the plastic components. Therefore, if $\mu = m$, the total J of Eq 4 could be evaluated as the total area under the $P - v$ curve.

On the other hand, from Eqs 34 and 37 the compact form proposed for K in this work, using either load-line displacement, v, or *cmod*, may be shown to be:

$$K = \frac{P}{B\sqrt{W}}\sqrt{\frac{\mu}{2C^*}(b/W)^{-\mu-1}} \tag{42}$$

Using the standard, abbreviated form for K as:

$$K[BW^{1/2}]/P = Y \tag{43}$$

wherefrom Y may be written in the form:

$$Y = \sqrt{\frac{\mu}{2C^*}}(b/W)^{(-\mu-1)/2} \tag{44}$$

On looking at Eq 44, the reason for inserting the column $\mu/2C^*$ in Table 9 becomes now apparent: the square root of this term will be the coefficient of $(b/W)^{(-\mu-1)/2}$ that allows one to obtain the

function Y. The K functions in Tada's handbook of elastic solutions [7] are written in terms of polynomial functions of a/W, and compact functions similar to that of Eq 44 can also be developed in the format

$$Y = Y_0(b/W)^{-Z} \tag{45}$$

Table 10 lists the values of coefficient Y_0 and exponent z of the format given by Eq 45, both for the compact form developed here, using only the load-point displacement, and for that obtained from Tada's polynomial solutions, only for the three "bend" type specimens. Included in Table 10 are the a/W range of validity, the error band produced when using the "compliance" compact K form as compared to Tada's K calibration, and Y_0 and z for both K equations.

Thus, within the normal range of usage of specimen crack length, a compact form for K may be used that may be derived either from the elastic handbook [7], or from the compliance formulas, also included in Tada's handbook.

The advantages of this compact form for K are at least two: one has already been discussed and relates J to the total area under the load versus load-point displacement. The second advantage of this compact format has to do with fatigue crack-growth calculations starting from Paris's Law, i.e.,

$$da/dN = C(\Delta K)^m \tag{46}$$

where C and m are Paris' Law coefficient and exponent, respectively. The classical solutions that lead to N_f, the number of cycles to failure under fatigue crack growth, must go through an iteration process to integrate the term

$$N_f = \int_{a_0}^{af} \frac{da}{C(\Delta K)^m} \tag{47}$$

since ΔK contains the polynomial functions already mentioned in the form

$$\Delta K = \Delta\sigma\sqrt{(\pi a)} \cdot f(a/W) \tag{48}$$

Clearly, direct, analytical integration of Eq 46 with a complex function in the integrand is rather cumbersome and might have to be carried out by other means, i.e., numerical integration. If ΔK is written in the compact form as:

$$\Delta K = \frac{P}{B\sqrt{W}} Y_0(b/W)^{-z} \tag{49}$$

TABLE 10—*Values of* Y_0 *and* z *for the* K *compact equation.*

		Compliance K		Tada's Solution		
Geometry	a/W	Y_0	z	Y_0	z	Error
C(T)	0.50/0.85	2.9462	1.6415	3.1816	1.5787	±3.5%
SE(B)	0.35/0.90	3.7316	1.5235	3.6278	1.5389	−3.5%/+0%
SE(T)	0.65/0.90	1.2410	1.6830	1.1198	1.7387	−2.5%/+1.7%

Equation 47 becomes a much simpler form to integrate:

$$N_f = \frac{1}{C}\left[\frac{B\sqrt{W}}{\Delta P\, Y_0}\right]^m \int_{b_f}^{b_0} (b/W)^{mz}\, db = \frac{W}{C(mz+1)}\left[\frac{B\sqrt{W}}{\Delta P\, Y_0}\right]^m [(b_0/W)^{mz+1} - (b_f/W)^{mz+1}] \quad (50)$$

with the calculation of b_f done in the usual way using the value of K_{Ic}. Other applications of the compact form for K may be found in other fracture-related disciplines, like creep, stress-corrosion, and so on.

Conclusions

1. The elastic compliance relations for the various planar fracture specimens, $c(x)$, where x stands for v or *cmod,* have been revised and stated in a format similar to that of the common format equation, with a clear separation between the geometry (G) component and the hardening, material-related (H) term.
2. In the elastic range, the G function is of the form $G_{el} = C^* B W (b/W)^{\mu}$, with a striking similarity to its counterpart in the plastic range. On the other hand, the elastic H function is of the form $H_{el} = E (x/W)$, where x stands for v or *cmod.*
3. For the "bend" type specimens, μ is approximately equal to m for most of the cases analyzed. In particular, the C(T), SE(B), and SE(T) geometries, for which cases $x = v$, have $\mu = m$ within 2.4% error or less.
4. The fact that $\mu = m$ implies that $\eta_{el} = \eta_{pl}$. This allows one to write J as the area under the load versus total displacement curve without the need to separate the elastic from the plastic contribution.
5. On the other hand, the fact that the elastic compliance equations may now be expressed in a simpler, compact form allows one to write K also in a compact form in terms of a single power law expression on b/W, using the parameters C^* and μ derived for the elastic compliance.
6. The compact format for K may be used in a number of applications for which until now a complex, polynomial function has been employed. One such application is the evaluation of N_f, the number of cycles to failure in fatigue crack growth. In this case, the integration to get N_f, a cumbersome process when using the functions based upon a/W, becomes a straightforward exercise when using the compact form based on the power law expression on b/W.

Acknowledgments

This work has been supported by FONDECYT-CHILE, Project No. 1980169.

References

[1] Donoso, J. R. and Landes, J. D., "Common Format for Developing Calibration Curves in Elastic-Plastic Fracture Mechanics," *Engineering Fracture Mechanics,* Vol. 47, No. 5, 1994, pp. 619–628.

[2] Kumar, V., German, M. D., and Shih, C. F., "An Engineering Approach for Elastic-Plastic Fracture Analysis," NP 1931, EPRI Project 1237–1 (July 1981).

[3] Donoso, J. R. and Landes, J. D., "The Common Format Equation Approach for Developing Calibration Functions for Two-Dimensional Fracture Specimens From Tensile Data," *Engineering Fracture Mechanics,* Vol. 54, No. 4, 1996, pp. 499–512.

[4] Donoso, J. R. and Landes, J. D., "The Role of Constraint on the Calibration Functions for the Prediction of Ductile Fracture Behavior in Structural Components," *International Journal of Fracture,* Vol. 63, 1993, pp. 275–285.

[5] Sharobeam, M. W. and Landes, J. D., "The Load Separation Criterion and Methodology in Ductile Fracture Mechanics," *International Journal of Fracture,* Vol. 37, 1991, pp. 81–104.

[6] Donoso, J., Labbe, F., and Mora, C., "Evaluation of Plastic Eta Factors in Weld Metal Fracture Specimens: A Comparison Between Limit Load and Common Format Solutions," *Engineering Fracture Mechanics,* Vol. 44, No. 4, 1993, pp. 515–520.

[7] Tada, H., Paris, P. C., and Irwin, G. R., *The Stress Analysis of Cracks Handbook,* Del Research Corporation, Hellertown, PA, 1973.

MarjorieAnn E. Natishan[1] *and Mark T. Kirk*[2]

A Micromechanical Evaluation of the Master Curve

REFERENCE: Natishan, M. E. and Kirk, M. T., **"A Micromechanical Evaluation of the Master Curve,"** *Fatigue and Fracture Mechanics: 30th Volume, ASTM STP 1360,* P. C. Paris and K. L. Jerina, Eds., American Society for Testing and Materials, West Conshohocken, PA, 2000, pp. 51–60.

ABSTRACT: The cleavage fracture model of Wallin et al. [*1*] suggests that the variation of median and bounding values of fracture toughness with temperature is predictable on a micro-mechanical basis. ASTM has recently adopted a standard [ASTM Standard Test Method for the Determination of Reference Temperature, T_o, for Ferritic Steels in the Transition Range (E 1921-98)] for characterizing the variation of the fracture toughness of ferritic steels in the transition temperature range that draws heavily on the work of Wallin et al. and on subsequent developments [*1–5*]. The new standard expresses the median toughness transition for a 1T specimen as:

$$K_{Jc}|_{median} = 30 + 70 \cdot \exp[0.019(T - T_o)]$$

where temperature is measured in degrees Celsius and K_{Jc} is measured in MPa$\sqrt{m}$. Similar equations express the variation of bounding toughness values (e.g., 95% lower bound) with temperature. The numeric coefficients in all of these equations do not depend on the type of steel tested. This invariance suggests that chemistry, heat treatment, and other metallurgical variables are *not* thought to influence the exponential increase with temperature of the plastic work necessary for crack propagation, the dominance of carbides as the particles that initiate cleavage fracture, or the distribution of carbide particles.

The ASTM E 1921 Master Curve represents existing fracture toughness data well for nuclear pressure vessel steels and their weldments [*6*]. This empirical evidence suggests that the material invariance attributed to the Master Curve coefficients in ASTM E 1921 is at least approximately correct for this class of steel. But the microstructural bounds of applicability for the Master Curve are not clear.

In this paper we examine the physical basis for the Wallin et al. Master Curve with the aim of distinguishing the classes of steels to which the methodology applies from those to which it does not. We use this physical understanding to calculate the temperature dependence of the plastic work for ferritic steels to demonstrate theoretical validity of a single "master curve."

KEYWORDS: Master Curve, fracture toughness transition behavior, T_o, steel

To maintain their operating licenses, nuclear plant operators must demonstrate that the effects of irradiation embrittlement do not compromise the safe operation of their reactor pressure vessel (RPV) [*7*]. The variation of the RPV steel's fracture toughness with temperature provides a key input to these analyses. Currently, the ASME K_{Ic} curve provides this toughness characterization:

$$K = 36.5 + 3.086 \cdot \exp[0.011 \cdot (T - RT_{NDT} + 55.56)] \quad (1)$$

where K is in MPa$\sqrt{m}$, T is the temperature of interest (in °C), and RT_{NDT} is an index temperature (in °C). RT_{NDT} is determined by testing specimens as per ASTM Standard Test Method for Conducting Drop-Weight Test to Determine Nil-Ductility Transition Temperature of Ferritic Steels (E 208-

[1] Professor of mechanical engineering, University of Maryland, College Park, MD.
[2] Senior mechanical engineer, Westinghouse Electric Company, Pittsburgh, PA 15235.

95a) to determine the nil-ductility temperature (T_{NDT}), and by testing Charpy-V notch (CVN) specimens as per ASTM Standard Test Methods for Notched Bar Impact Testing of Metallic Materials (E 23-96) to determine the 1.016-mm (40-mil) lateral expansion transition temperature (T_{40}). RT_{NDT} is then defined as follows:

$$RT_{NDT} = \text{MAX}\{T_{NDT}, T_{40} - 33.33\} \tag{2}$$

A two-step process established the appropriate RT_{NDT} for an irradiated material, and thus the appropriate K_{Ic} curve for use in a RPV assessment. The first RT_{NDT} is determined in the unirradiated condition for the limiting material in the RPV (i.e., the part of the RPV having the lowest toughness). Throughout the operational life of the vessel, tests of CVN specimens removed from surveillance capsules determine the shift of the 41-J (30 ft-lb) CVN transition temperature produced by irradiation. This shift is added, along with margins to account for uncertainties, to the RT_{NDT} for the unirradiated material to estimate the RT_{NDT} of the irradiated material.

This approach to estimating the fracture toughness of an irradiated RPV steel does not rely on the measurement of any fracture toughness values, but rather on correlations to fracture toughness. It was necessitated by the large specimen size required for "valid" linear-elastic fracture toughness values. The approach typically underpredicts fracture toughness, sometimes to a considerable degree. This perception of low toughness can lead to premature plant closure because of regulatory limits on pressurized thermal shock. Furthermore, low toughness limits the permissible pressure-temperature envelope for routine heat-up and cool-down operations. This may cause these operations to be performed in a manner that increases overall plant risk due to the increased probability for pump trips and due to the increased time spent in transient (versus steady state) conditions. Such restrictions can currently be addressed only by annealing the RPV. Annealing is an expensive and risky process that no domestic nuclear operator has yet to undertake.

An alternative to annealing for remediation of low toughness is to update the technology used to estimate toughness from that represented by Eq 1, which was developed over 25 years ago. Technological advancements made during this time facilitate this alternative. These developments are as follows:

Mathematical Description of Fracture—Current ASME code relies on linear elastic fracture mechanics (LEFM) for both its toughness characterization and its structural assessment methodology. While LEFM provides an adequate description of the driving force to fracture in a thick-section RPV, its requirement for contained plasticity at fracture confounds efforts to measure toughness using the small specimens contained in RPV surveillance capsules. Advancements in elastic plastic fracture mechanics (EPFM) enable the testing of smaller fracture toughness specimens while still ensuring the applicability of these results to the assessment of much larger structures.

Physical Understanding of Fracture—Advances in the understanding of the micro-mechanisms responsible for cleavage fracture enable definition of the lower transition curve based on limited replicate fracture tests conducted at a single temperature. The theoretical background for these advances follow from the work of many investigators [*8–11*]. Wallin et al. [*1*] have led in combining these advances into a predictive tool, a technique commonly referred to as the Master Curve.

Previous studies have focused on empirical validation of the Master Curve [*4,6,12,13*]. While useful demonstrations for well-characterized alloys such as nuclear RPV steels, these studies cannot be used to predict the classes of alloys and product forms to which the Master Curve applies. In this paper we will provide a physical rationale for why one transition curve shape (i.e., the variation of critical-*J* with temperature) should apply to all ferritic steels. We begin by describing a new ASTM standard that uses the Master Curve to determine a transition curve index temperature

called T_o. The premises necessary for this standard to work are then discussed. This discussion motivates examination of theoretical constitutive models. These constitutive models are used to describe how the temperature dependence of fracture toughness enters the Master Curve and what controls this temperature dependence. We conclude with an example calculation that illustrates how this temperature dependence can be calculated from a theoretical basis common to all ferritic steels.

The ASTM Master Curve Standard, E 1921-98

The recently adopted ASTM Standard Test Method for the Determination of Reference Temperature, T_o, for Ferritic Steels in the Transition Range (E 1921-98) draws heavily on the work of Wallin et al. and on subsequent developments [*1–5*]. The new standard expresses the median transition curve for a 25.4-mm-thick specimen as follows:

$$K_{Jc(med)} = 30 + 70 \cdot \exp[0.019(T - T_o)] \tag{3}$$

where temperature (T) is in °C and K_{Jc} is in MPa$\sqrt{m}$. Analogous to the K_{Ic} curve (Eq 1), T is the temperature of interest while T_o is an index temperature. T_o is defined as the temperature at which the median fracture toughness of a 1T (i.e., a 25.4-mm-thick) fracture mechanics specimen is 100 MPa$\sqrt{m}$. Both the reference size (25.4 mm) and the reference toughness (100 MPa$\sqrt{m}$) are selected purely for convenience.

E 1921 provides the following protocol for estimating T_o:

- Replicate experiments are conducted using one size specimen tested at a single temperature in lower transition. Between six and ten replicates are required, with the exact quantity depending on the median fracture toughness of the data set. Tests are considered valid provided three requirements are satisfied:

$$K_{Jc(med)} > 50 \text{ MPa}\sqrt{m} \tag{4}$$

and

$$\text{MIN}(b,a,B) \geq \frac{30 \cdot K_{Jc}^2}{\sigma_{ys} \cdot E} \tag{5}$$

where b is the specimen ligament, a is the crack length, B is the specimen thickness, σ_{ys} is the yield strength, and E is the elastic modulus. Also, the amount of ductile crack growth that precedes cleavage fracture may not exceed 5% of the specimen ligament, i.e.:

$$\Delta a_{max} = 0.05 \cdot b \tag{6}$$

- T_o is estimated as follows from a data set having the minimum number of valid replicates:
Step 1: If 1T specimens were not tested, measured K_{Jc} values are converted to equivalent 1T values using the following formula, which is derived from a weakest link failure model [*3*]:

$$K_{Jc}|_1T = 20 + (K_{Jc}|_{Measured} - 20) \cdot \left[\frac{B}{25.4}\right]^{1/4} \tag{7}$$

Step 2: The 1T equivalent K_{Jc} values are used to estimate the median fracture toughness ($K_{Jc(med)}$).

Step 3: The index temperature T_o is calculated from the test temperature and $K_{Jc(med)}$. The relationship between T_o and $K_{Jc(med)}$ is fixed because the Master Curve shape (Eq 3) is presumed to apply to all ferritic steels.

$$T_o = T_{Test} - \frac{1}{0.019} \cdot \ln\left[\frac{K_{Jc(med)} - 30}{70}\right] \tag{8}$$

This size requirement of Eq 5 permits determination of K_{Jc} values using fracture specimens as small as CVN size for most RPV steels. Currently, CVN specimens are removed from surveillance capsules and tested to estimate RT_{NDT} by Eq 2, a value then related to fracture toughness using the K_{Ic} curve (Eq 1). The Master Curve provides the alternative of testing these CVN samples as small fracture toughness specimens to quantify directly the effects of irradiation using the Master Curve temperature index T_o. This alternative promises a more accurate representation of the RPV steel toughness than possible using the K_{Ic} curve simply because toughness is measured directly for the RPV steel of interest, rather than inferred through relationships with RT_{NDT} and CVN transition temperatures. However, for the Master Curve alternative to work the assumptions that underlie Eqs 3 through 8 must hold.

Premises of the Master Curve Approach

Equations 3 through 8 provide a means to illustrate the following premises, which underlie the Master Curve as introduced by Wallin et al. [*1*] and as implemented by ASTM E 1921.

One Transition Curve Shape—Within the transition range, plastic deformation occurs by dislocation glide only. Other deformation mechanisms, such as twinning on the lower shelf and ductile hole growth in the upper transition/upper shelf, produce fracture toughness versus temperature relationships different from that of Eq 3. The Master Curve does not account for these deformation mechanisms, so they are eliminated from consideration by the validity requirements of E 1921. Specifically, Eq 4 excludes the lower shelf, while Eqs 5 and 6 together eliminate upper transition/upper shelf. Within these limits, one transition curve shape (Eq 3) applies to all ferritic steels. This permits estimation of T_o using tests conducted at temperatures other than T_o itself (Eq 8).

Fracture is Controlled by a Weakest Link Process—In transition, fracture is controlled by carbide cracking, wherein failure of a single carbide is the necessary event for failure of the specimen. The observation that the distribution of carbide sizes takes the same form for all ferritic steels [*1*], and the assumption that the fraction of carbides involved in fracture is independent of temperature [*1*], leads to the notion that a Weibull distribution having a slope of 4 and a minimum of 20 MPa$\sqrt{\text{m}}$ describes the distribution of toughness at a fixed temperature equally well for all ferritic steels [*2*]. These observations permit the quantification of size effects, so that experiments conducted on different size specimens can be interpreted on a common basis (Eq 7). Furthermore, they enable calculation of statistical tolerance bounds based on the limited replication required by E 1921.

In their 1984 paper, Wallin et al. illustrate how these two premises lead to a Master Curve [*1*]. They characterize the stress distribution in the vicinity of a crack tip using *J*. Loading to a particular *J* produces a particular crack-tip stress field (σ_{yy}). This σ_{yy} value is used with a Griffith failure criteria [*8*] to determine the particle radius needed to cause fracture, i.e.:

$$r_{CRIT} = \frac{\pi(\gamma_s + w_p)E}{2(1 - \nu^2)\sigma_{yy}^2} \tag{9}$$

The critical event for fracture of ferritic steels in transition is failure of a carbide. Wallin et al. there-

fore describe the material by a carbide distribution:

$$\Pr\{r \geq r_{crit}\} = P \cdot \exp[-Q \cdot r] \tag{10}$$

where P and Q are constants. The probability of encountering a carbide of radius exceeding r_{crit} is therefore the failure probability associated with a particular J value. Repetition of this process for progressively higher levels of J produces a relationship between fracture toughness and the probability of failure at a fixed temperature.

The dependence of fracture toughness on temperature enters the Wallin et al. model *only* through the plastic work term (w_p) in Eq 9. Wallin et al. assume a form for w_p that includes both athermal and thermal terms:

$$w_p = w_0 + [w_p(0) - w_0] \cdot \exp[m \cdot T] \tag{11}$$

Plastic work per unit volume is the area under the true stress versus true strain curve integrated to the point of material failure. Consequently, w_p depends on the variation of stress with strain (i.e., on the constitutive equation) and on the strain at failure determined under constraint conditions appropriate for crack tip loading. Thus, the temperature dependence of the flow curve and the plastic strain at fracture control the temperature dependence of the Master Curve. We examine these factors in the following section.

Zerilli and Armstrong Constitutive Equation

To understand the physical basis for a single "Master Curve" for all ferritic steels we need to connect the Master Curve equation back through the equation for plastic work dependence on temperature to the constitutive equations that have been developed to describe the plastic deformation behavior of metals. Considerable work has been accomplished in modeling flow curve behavior, both from an empirical basis [*14*] and from a physical basis [*15,16*]. The most commonly accepted, physically based, flow curve equation is that derived by Zerilli and Armstrong [*17*] (known as the *Z-A* equation) given below for BCC metals:

$$\sigma_{Flow} = \Delta\sigma'_G + \frac{k}{\sqrt{l}} + C_5\varepsilon^n + C_1 \cdot \exp[-C_3T + C_4T \cdot \ln(\dot{\varepsilon})] \tag{12}$$

where temperature (T) is in °K, $\Delta\sigma'_G$ is the contribution to the stress required for dislocation motion due to solute atoms in the lattice, k is the stress intensification at the grain boundary, l is the grain diameter, ε is the true strain, n is the strain-hardening exponent, $\dot{\varepsilon}$ is the strain rate, and C_1, C_3, C_4, and C_5 are material constants. For our purposes the exponential strain rate term is considered to be constant.

The derivation of Eq 12 was based on the assumption of dislocation-controlled plastic deformation in BCC metals. The combination of thermal and athermal terms accounts for the contribution of the various microstructural features to the stress required for dislocation motion. The last component of Eq 12 is the thermal term; it describes the change in flow curve behavior with temperature. This term is derived based on the effects of temperature on the Peierls-Nabarro stresses within the crystal lattice that resist dislocation motion. This contribution to flow stress decreases exponentially with temperature, in apparent contradiction to the exponential increase of both plastic work and fracture toughness with temperature proposed in the Master Curve method.

The thermal component of the Z-A equation was derived to describe the effects of temperature on the stress required for dislocations to move between equilibrium positions within the lattice. Dislocation motion through the crystal occurs by atoms changing position relative to each other, or "jump-

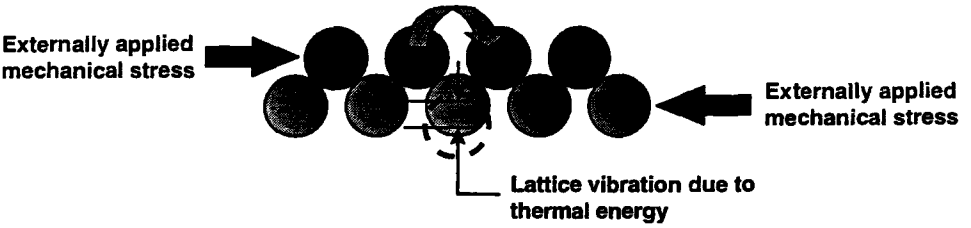

FIG. 1—*Illustration of the combined effects of mechanical stress and thermal energy on the ability of atoms to jump between equilibrium lattice sites.*

ing" between equilibrium lattice sites as shown in Fig. 1. This motion is opposed by a friction (named Peierls-Nabarro) stress due to the presence of other lattice atoms. For dislocation "jumping" to occur there must be enough energy supplied to the system, either via an externally applied mechanical stress or via thermal energy, to enable dislocations to overcome these short-range barriers and change position. This process results in plastic flow of the material. The amount of energy required for dislocation motion through these short-range barriers in the lattice depends on atom spacing within the lattice and on the amplitude of atom vibration about their lattice positions. At temperatures above absolute zero, atoms tend to vibrate about their lattice positions due to the thermal energy in the system. As temperature is increased, the amplitude of atom vibration increases, resulting in an increased probability that an atom at any particular lattice site will be "out of position" at any given point in time. As atoms move out of position the activation energy for dislocation motion around them is reduced. This reduced activation energy reduces the applied shear stress required for dislocation motion and, thus, for plastic deformation. Since the basic response of a metal to increased temperature is increased lattice or atom vibration, the only effect of temperature on the flow curve behavior is to change the ease with which dislocations move through the lattice. The coefficient for this thermal term should therefore only vary with lattice parameter and remain unaffected by other microstructural parameters. This thermal term accounts for the downward shift of the flow curve with increasing temperature.

The effects of other aspects of the microstructure on flow curve behavior are accounted for in the three athermal terms in the *Z-A* equation. The first term ($\Delta\sigma'_G$) describes the effects of solute atoms on the flow curve accounting for the effects of substitutional and interstitial atoms on dislocation motion. The second term ($k/\sqrt{l}$) accounts for the effects of grain boundaries and is known as the Hall-Petch relationship. The third term ($C_5\varepsilon^n$) accounts for strain hardening or increasing dislocation density on flow behavior and describes parabolic hardening. The effect of these microstructural parameters on dislocation motion controls the shape of the flow curve, but the parameters do not vary with temperature in BCC materials.

The athermal terms in the *Z-A* equation will therefore affect only the temperature at which the fracture toughness transition occurs. Because the thermal term in the *Z-A* equation describes the variation of flow behavior with temperature for a BCC material, it is this term that is expected to account for the shape of the fracture toughness transition. However, the thermal term describes a decrease in flow stress with increasing temperature. This results in a predicted decrease in the area under the true stress versus true strain curve, and, consequently, a decrease of plastic work with increasing temperature. This trend is counter to the Wallin et al. model [*1*] and suggests that an additional parameter must be considered.

So far we have examined the shift in the flow curve predicted with temperature from the *Z-A* equation. Integration of this equation gives us plastic work per unit volume but we must also consider the variation of the total strain to fracture with temperature to provide the limits of integration to truly

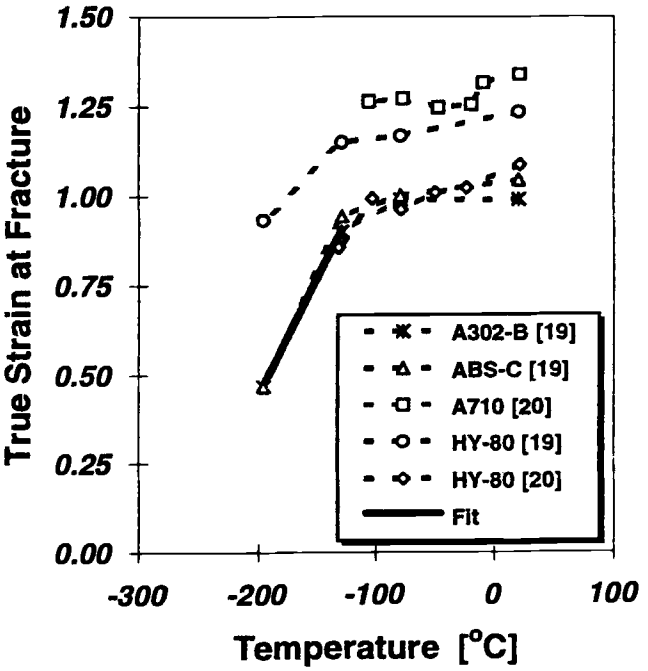

FIG. 2—*Variation of strain to fracture with temperature determined by uniaxial tension testing.*

capture the variation of plastic work with temperature. Figure 2 shows data obtained from several studies on the variation of strain to fracture in uniaxial tensile tests with temperature. As can be seen from this figure strain to fracture increases with test temperature for a wide range of steels in much the same manner. Using these data to truncate the true stress, true strain curves and integrating gives us a value of plastic work that increases with increasing temperature, similar to the trend used by Wallin et al [*1*]. Details of this calculation are described in the following section.

Calculation of a Master Curve

In Eq 9 we showed that the variation of critical-*J* values with temperature depends only on the variation of plastic work with temperature. In this section we calculate the variation of plastic work with temperature and compare the form of this variation with the Wallin Master Curve.

The plastic work per unit volume to cause fracture is the area under the stress-strain curve. This area depends on the flow curve (i.e., on the variation of stress with strain) and on the strain the material can withstand prior to fracture. The variation with temperature of these two variables therefore determines the variation with temperature of plastic work.

In general, plastic work can be expressed as follows:

$$w_p(T) = \int_0^{\varepsilon_{fail}(T)} \sigma(\varepsilon,T)d\varepsilon \tag{13}$$

where $\sigma(\varepsilon,T)$ represents the flow curve and $\varepsilon_{fail}(T)$ represents the plastic strain to fracture. As discussed previously, Eq 12 proposed by Zerilli and Armstrong [*17*] describes completely the flow

curve for BCC materials, with a thermal term determined only by the lattice parameter. Thus, we adopt Eq 12 for $\sigma(\varepsilon,T)$ in Eq 13 and use the thermal coefficients obtained by Zerilli and Armstrong for Armco Iron [*17*]. C_1, C_3, and C_4 should apply equally well to all ferritic steels. Conversely, the athermal terms and coefficients ($\Delta\sigma_G' + k/\sqrt{l} + C_5\varepsilon^n$) are expected to depend on the microstructure of the particular steel considered. To account for this material dependence, we adopt the value of 400 MPa reported by McCabe et al. [*18*] as the total of the athermal terms for unirradiated A533B (on average). Furthermore, we held strain rate fixed at 1×10^{-4}/s. Figure 3 presents the variation with temperature of both the thermal component of the flow stress (the exponential term in Eq 12) and the total flow stress based on these assumptions.

While Zerilli and Armstrong provide a rigorous theoretical basis for the flow curve, an empirical approach is currently necessary to determine the variation of the strain at fracture ($\varepsilon_{fail}(T)$) with temperature. To perform the integration of Eq 13 properly, the strain at fracture should be determined for a stress state characteristic of crack-tip loading. Such data are difficult to obtain experimentally. Here we use true-strain to fracture data determined from tensile testing and focus attention on the form of the variation of plastic work with temperature, rather than on the values predicted. To this end, true-strain to fracture data are collected from the literature for various ferritic and tempered martensitic steels (see Fig. 2) [*19,20*]. These data suggest that the strain at fracture varies with temperature in a consistent manner for a number of different steels. Figure 2 also shows a least-squares fit to three of these data sets in the transition temperature region (<-120°C). This fit was used to set the integration limit in Eq 13 and is as follows:

$$\varepsilon_{fail} = 1.75 + \frac{T(°C)}{152} \tag{14}$$

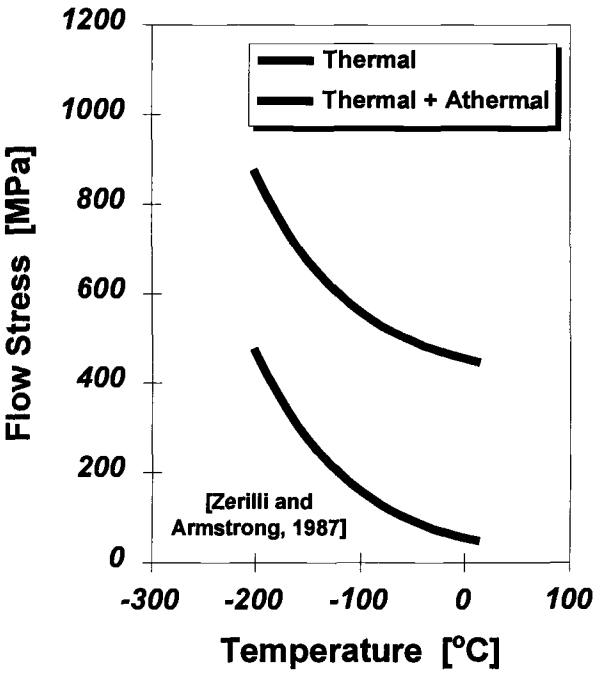

FIG. 3—*Variation of the thermal and total flow stress with temperature as predicted by the Zerilli/Armstrong equation.*

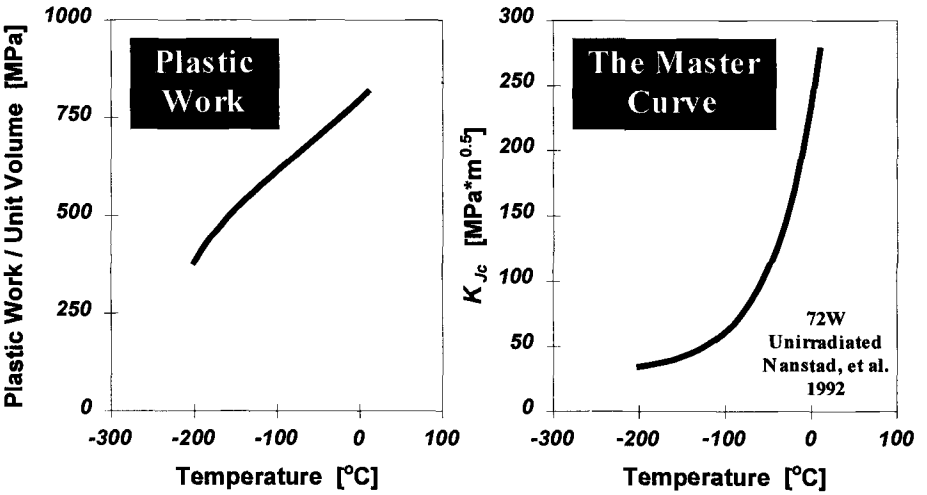

FIG. 4—*Temperature dependence of plastic work per unit volume (left) contrasted with the temperature dependence of the Master Curve.*

Using Eqs 12 and 14 as input to Eq 13 predicts an increasing plastic work term with temperature illustrated in Fig. 4 (here we plot w_p beyond the fit range of Eq 14 for purposes of illustration). Figure 4 also shows the median 1*T* Master Curve for weld 72W reported by Nanstad et al. [*21*]. While the predicted temperature dependence of the plastic work term does not match exactly the temperature dependence of the Master Curve, Fig. 4 demonstrates an increase of plastic work per unit volume with increasing temperature. This calculation provides an initial validation of the curve shape basis described by the Wallin et al. model [*1*] using the physics-derived constitutive equation of Zerilli and Armstrong.

Two refinements to this calculation are expected to improve substantially the theoretical justification for a single Master Curve shape. In this paper we used the total strain to fracture from a uniaxial tensile test to set the integration limit of Eq 13 only because such information is readily available in the literature. The total strain to fracture for a uniaxial specimen clearly does not provide an adequate representation of strain to fracture for crack-tip stress states. Use of the uniform strain to fracture should provide greater accuracy, but further work is needed to quantify the combined effects of stress state and temperature on strain to fracture. Secondly, the plastic work values obtained by integrating the *Z-A* equation are work per unit volume of material. These values must be multiplied by the volume of material that participates in fracture (e.g., the plastic zone size, the process zone size, two grain diameters) to obtain a value of plastic work in better agreement with other values reported in the literature [*10,11*].

Summary and Conclusions

The information presented herein provides a physical basis for a single "master" toughness transition curve that applies with equal accuracy to all ferritic steels. The temperature dependence of the flow curve is controlled only by the lattice structure. Other factors that can vary with steel composition and heat treatment, such as the grain size and the work-hardening rate, influence only the athermal term of the flow curve. Consequently, these factors influence the position of the transition curve on the temperature axis (i.e., T_o as determined by ASTM E 1921-98), but *not* its shape. This understanding suggests that the breadth of applicability of Wallin's Master Curve to other microstructures is predictable based on the physics of the fracture process.

In an example calculation, we demonstrate that the plastic work to fracture, which gives the Master Curve its temperature dependence, can be expected to increase with increasing temperature. The temperature dependence of the plastic work to fracture depends on the temperature dependence of two variables: the flow curve and the strain to fracture. The temperature dependence of the flow curve is physically derived by Zerilli and Armstrong and has a sound theoretical basis for ferritic steels. By comparison, the physical basis for the variation with temperature of the strain to fracture requires further attention. Available data from the literature suggest that the temperature dependence may be similar for a variety of steels. Use of literature data in an example calculation predicts the expected increase of plastic work with increasing temperature. Further investigation is, however, needed to establish an appropriate physical basis for the variation of the plastic strain to fracture with temperature and the effect of stress state on this property.

References

[1] Wallin, K., Saario, and Törrönen, "Statistical Model for Carbide Induced Brittle Fracture in Steel," *Metal Science,* Vol. 18, 1984, pp. 13–16.

[2] Wallin, K., "The Scatter in K_{1c} Results," *Engineering Fracture Mechanics,* Vol. 19, No. 6, 1984, pp. 1085–1093.

[3] Wallin, K., "The Size Effect in K_{1c} Results," *Engineering Fracture Mechanics,* Vol. 22, 1985, pp. 149–163.

[4] Wallin, K., "Irradiation Damage Effects on the Fracture Toughness Transition Curve Shape for Reactor Vessel Steels," *International Journal of Pressure Vessels and Piping,* Vol. 55, 1993, pp. 61–79.

[5] Wallin, K., "Re-Evaluation of the TSE Results Based on the Statistical Size Effect," VTT Manufacturing Technology, Report VALB97, 1995.

[6] Kirk, M., Lott, R., Kim, C., and Server, W., "Empirical Validation of the Master Curve for Irradiated and Unirradiated Reactor Pressure Vessel Steels," presented at the 1998 ASME/JSME Pressure Vessel and Piping Symposium, 26–30 July 1998—San Diego, CA.

[7] Nuclear Regulatory Commission 10 CFR Part 50, "Fracture Toughness Requirements for Light Water Reactor Pressure Vessels."

[8] Griffith, "The Phenomena of Rupture and Flow in Solids," *Philosophical Transactions,* Series A, Vol. 221, 1920, pp. 163–198.

[9] Ritchie, Knott, and Rice, "On the Relationship Between Critical Tensile Stress and Fracture Stress in Mild Steels," *Journal of the Mechanics and Physics of Solids,* Vol. 21, 1973, pp. 395–410.

[10] Curry and Knott, *Metal Science,* Vol. 12, 1978, pp. 511–514.

[11] Curry and Knott, *Metal Science,* Vol. 13, 1979, pp. 341–345.

[12] Sokolov, M. A., Wallin, K., and McCabe, D. E., "Application of Small Specimens to Fracture Mechanics Characterization of Irradiated Pressure Vessel Steels," *Fatigue and Fracture Mechanics: 28th Volume, ASTM STP 1321,* J. H. Underwood, B. D. MacDonald, and M. R. Mitchell, Eds., American Society for Testing and Materials, 1997, pp. 263–279.

[13] Sokolov, M. A., "Statistical Analysis of the ASME K_{1c} Database," *Journal of Pressure Vessel Technology,* Vol. 120, February 1998, pp. 24–28.

[14] Johnson, G. R. and Cook, W. H., *Proceedings, 7th International Symposium on Ballistics,* Am. Def. Prep. Org. (ADPA), The Netherlands, 1983, p. 541.

[15] Klopp, R. W., Clifton, R. J., and Shawki, T. G., *Mechanical Materials,* Vol. 4, 1985, p. 385.

[16] Clifton, R. J., "Dynamic Plasticity," *Journal of Applied Mechanics,* Vol. 50, US N4B, December 1983, pp. 941–948.

[17] Zerilli, F. J. and Armstrong, R. W., "Dislocation-Mechanics-Based Constitutive Relations for Material Dynamics Calculations," *Journal of Applied Physics,* Vol. 61, No. 5, 1 March 1987, pp. 1816–1825.

[18] McCabe, D. E., Wallin, K., and Merkle, J. G., "Technical Basis for an ASTM Standard on Determining the Characterization Transition Temperature, T_0, for Ferritic Steels in the Transition Range," NUREG/CR-5504, 1998.

[19] Clausing, D. P., "Tensile Properties of Eight Constructional Steels Between 70 and -320°F," *Journal of Materials,* JMLSA, Vol. 4, No. 2, July 1969, pp. 473–492.

[20] Gudas, J. P., "Micromechanisms of Crack Arrest in Two High Strength Steels," David Taylor Naval Ship Research and Development Center, DTNSRDC/SME-87-20, December 1987.

[21] Nanstad, R. K. et al, "Irradiation Effects on Fracture Toughness of Two High-Copper Submerged-Arc Welds," HSSI Series 5, NUREG/CR-5913, U.S. Nuclear Regulatory Commission, 1992.

Paulo C. Gioielli,[1] *John D. Landes,*[1] *Paul C. Paris,*[2] *Hiroshi Tada,*[2] *and Les Loushin*[3]

Method for Predicting J-R Curves from Charpy Impact Energy

REFERENCE: Gioielli, P. C., Landes, J. D., Paris, P. C., Tada, H., and Loushin, L., **"Method for Predicting J-R Curves from Charpy Impact Energy,"** *Fatigue and Fracture Mechanics: 30th Volume, ASTM STP 1360,* P. C. Paris and K. L. Jerina, Eds., American Society for Testing and Materials, West Conshohocken, PA, 2000, pp. 61–68.

ABSTRACT: In this paper a mechanistic rationale for the fracture process is applied to the CVN impact test so that the *J-R* curve fracture toughness could be estimated for materials that have only a CVN energy value as the fracture toughness characterization. The method assumes that the fit to the *J-R* curve can be given a standard form by assuming that the product of *J* and the tearing modulus, *T,* is a constant. Given this standard fitting form, the CVN energy is used to estimate a point on the *J-R* curve. Using this single point and the constant $J \times T$ product, the *J-R* curve is estimated with the two-parameter power law fit specified in ASTM standards. The procedure is applied to metals that undergo purely ductile fracture, that is, those that have CVN energy that would be characterized as "upper shelf" or 100% shear.

The method requires a calibration between impact energy, which has energy contributions from factors other than the fracture process, and the *J-R* curve point used in the fit. It is calibrated using three steel alloys where both CVN energy on the upper shelf and *J-R* curve fracture toughness data exist. The results show that a consistent calibration factor can be assumed that applies to all of the steels. Using that factor and the standard *J-R* curve fit, the prediction was good for all the steels examined. From these *J-R* curves, the initiation toughness value J_{IC} can also be determined using the J_{IC} construction from ASTM Standard Method E 1820. The resulting determination of J_{IC} shows why the simple process of fitting data sets does not give a universal prediction of toughness. The material tensile strength plays a role in the determination of J_{IC}.

KEYWORDS: *J-R* curve, impact test, steel, Charpy

J-R curves characterize the fracture toughness property for metals that fail by a ductile mode. Although the test method to measure the *J-R* curve has been standardized for many years, it still remains a somewhat difficult test to conduct, one that requires special equipment, and is therefore beyond the capability of many laboratories. For many structural components where design against ductile failure is required, a *J-R* curve fracture toughness characterization would make the design more realistic, often removing unnecessary conservatism; however, these data may not be available for the material of interest.

The Charpy V-notch (CVN) impact test is one that is familiar to many laboratories. Values of CVN energy are often available for materials used in structural applications. Attempts to correlate fracture toughness with Charpy impact energy has often been tried. Barsom and Rolfe [*1–2*], Sailors and Corten [*3*], Berley and Logsdon [*4*], and Marandet and Sanz [*5*] are the better known of these

[1] Ph.D. candidate and professor, respectively, Mechanical and Aerospace Engineering and Engineering Science, University of Tennessee, 310 Perkins Hall, Knoxville, TN 37996-2030.
[2] Mechanical Engineering, Washington University.
[3] ARCO Chemical Company, Newton Square, PA.

correlations, which were basically curve fittings to series of toughness versus CVN energy data without employing a mechanistic rationale. The result is that often the fit applies only to a limited class of materials. Marandet and Sanz [5] found a good correlation between transition temperatures achieved by impact and K_{IC} tests. However, their results were limited to materials with less than 15 to 20% shear.

In this paper a mechanistic rationale for the fracture process is applied to the CVN impact test so that the *J-R* curve fracture toughness could be estimated for materials that have only a CVN energy value as the fracture toughness characterization. The method assumes that the fit to the *J-R* curve can be given a standard form by assuming that the product of J and the tearing modulus, T, is constant. Given this standard fitting form, the CVN energy is used to estimate a point on the *J-R* curve. Using this single point and the constant $J \times T$ product, the *J-R* curve is estimated with the two-parameter power law fit specified in ASTM Standard Test Method for Measurement of Fracture Toughness (E 1820-96). The procedure is applied to metals that undergo purely ductile fracture, that is, have CVN energy that would be characterized as "upper shelf" or 100% shear.

The method requires a calibration between impact energy, which has energy contributions from factors other than the fracture process, and a *J-R* curve point used in the fit. The calibration was made using three steel alloys where both CVN energy on the upper shelf and *J-R* curve fracture toughness data exist. The results show that a consistent calibration factor can be assumed that applies to all of the steels. Using that factor and the standard *J-R* curve fit, the prediction was good for all the steels examined. From these *J-R* curves, the initiation toughness value J_{IC} can also be determined using the J_{IC} construction from the ASTM Standard Test Method E 1820-96. The resulting determination of J_{IC} shows why the process of fitting J_{IC} versus CVN energy data sets does not give a universal prediction of toughness. The material tensile strength plays a role in the determination of J_{IC}.

The Mechanistic Rationale

The Charpy V-notch specimen (Fig. 1) can be considered as a SE(B), single edge bend specimen defined in ASTM Standard Test Method E 1820-96, with $W = 10$ mm, $B = 10$ mm, $a = 2$ mm, and $b = 8$ mm. When the specimen breaks, the Δa will be 8 mm, and J at $\Delta a = 8$ mm, labeled $J_{\Delta a=8mm}$, can be calculated by dividing the Charpy energy, E_{CNV}, by the initial remaining ligament area $S =$

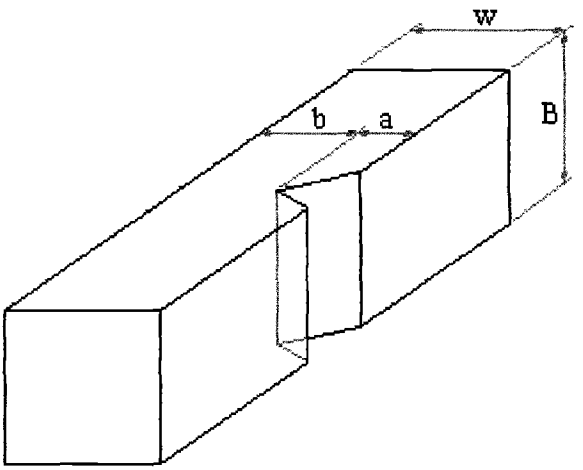

FIG. 1—*Charpy V-notch specimen.*

80 mm^2. However, this value, E_{CNV}/S, has energy contributions from factors other than the fracture process such as a V-notch rather than a sharp fatigue precrack. Therefore E_{CNV} must be divided by an energy calibration factor, F_G, to find the correct value for $J_{\Delta a=8mm}$:

$$J_{\Delta a=8mm} = \frac{E_{CVN}}{F_G \cdot S} \tag{1}$$

Using *J-R* curve data from a standard ASTM E 1820 test, fitted with a two-parameter power law extrapolated to $\Delta a = 8$ mm, and the E_{CVN} from a Charpy V-notch test for the same material, the value of the calibration factor, F_G, can be determinated as follows:

$$F_G = \frac{E_{CVN}(kJ)}{C_1(0.008\ m)^{C_2} \cdot 8 \cdot 10^{-5}\ m^2} = \frac{E_{CVN}\ (in. - lb)}{C_1\ (0.315\ in.)^{C_2}\ 0.124\ in.^2} \tag{2}$$

Where C_1 and C_2 are the fitting parameters of the power law:

$$J = C_1 \Delta a^{C_2},\ J \text{ in kJ/m}^2 \text{ and } \Delta a \text{ in m or } J \text{ in in.-lb/in.}^2 \text{ and } \Delta a \text{ in in.} \tag{3}$$

However, the value $J_{\Delta a=8mm}$ is only a single point on a *J-R* curve. The constants for a two-parameter power law fit cannot be solved. One way to reduce the number of constants is to make an assumption about the shape of the *J-R* curve using the product of J and the tearing modulus, T, as a constant:

$$T = \frac{E}{\sigma_0^2}\frac{dJ}{da} \tag{4}$$

Assuming:

$$J \cdot T = \text{constant} \tag{5}$$

Applying Eq 4 in Eq 5 and integrating we will have:

$$\int J\,dJ = \text{const} \cdot \int da \Rightarrow J^2 = \text{const} \cdot \Delta a \tag{6}$$

$$\therefore J = C_1 \Delta a^{0.5} \tag{7}$$

With this theoretical exponent for the power law, Eq 7 represents now a *J-R* curve fit with only one constant, C_1. Using value $J_{\Delta a=8mm}$ in Eq 7, the constant C_1 can be easily solved (Eq 8) defining the complete *J-R* curve.

$$C_1 = \frac{J}{\Delta a^{0.5}} = \frac{E_{CVN}}{F_G \cdot 8 \cdot 10^5 \sqrt{0.008}} = 139.75\frac{E_{CVN}}{F_G}, \text{ in SI units}$$

$$\text{or} = \frac{E_{CVN}}{F_G \times 0.124\sqrt{0.315}} = 14.37\frac{E_{CVN}}{F_G}, \text{ in I-P units} \tag{8}$$

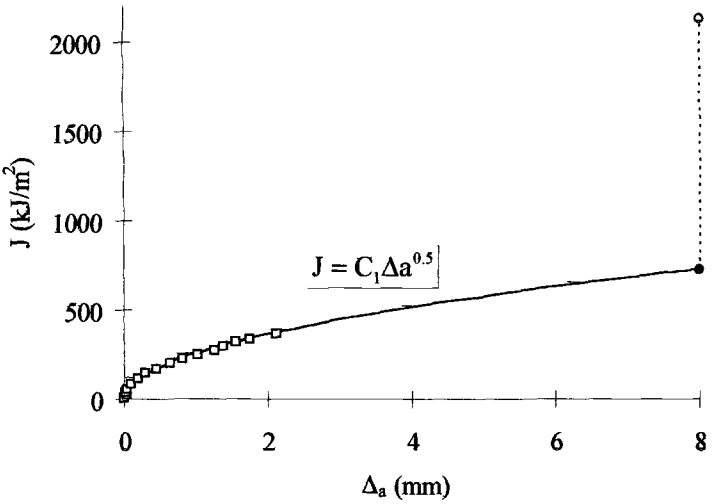

FIG. 2—*Plot showing the mechanistic rationale for the Charpy V-notch and* J-R *curve correlation.*

The entire scheme for predicting the *J-R* curve starting with E_{CVN} is graphically represented in Fig. 2. The data points shown are from a standard ASTM E 1820 test.

From the predicted *J-R* curve (Eq 7), the initiation toughness value J_{IC} can be determined using the J_{IC} construction from ASTM E 1820. J_{IC} is defined as the intersection of the *J-R* curve, from Eq 3, and the blunting line shifted 0.2 mm from the origin along the abscissa:

$$J_{IC} = 2\sigma_Y \, (\Delta a \; 0.2 \text{ mm}) \tag{9}$$

The more general solution of J_{IC} involves combining Eqs 3 and 9. Usually this solution cannot be made in closed form. However with $C_2 = 0.5$, Eqs 7 and 9 form a quadratic equation that can be solved in closed form finding:

$$J_{IC} = C_1 \sqrt{\frac{C_1}{4\sigma_Y}\left[\frac{C_1}{2\sigma_Y} + \sqrt{\left(\frac{C_1}{2\sigma_Y}\right)^2 + 8 \cdot 10^{-4}}\right]} + 2 \cdot 10^{-4}, \text{ for } J_{IC} \text{ in kJ/m}^2$$

$$J_{IC} = C_1 \sqrt{\frac{C_1}{4\sigma_Y}\left[\frac{C_1}{2\sigma_Y} + \sqrt{\left(\frac{C_1}{2\sigma_Y}\right)^2 + 0.032}\right]} + 0.008, \text{ for } J_{IC} \text{ in in.-lbs/in.}^2 \tag{10}$$

The J_{IC} expressions in Eq 10 are complex forms that involve both E_{CVN} and material tensile strength. It is evident that a simple correlation obtained by plotting E_{CVN} and a fracture toughness value like J_{IC} would not work for all materials.

F_G Calibration

Data from modified A302 Grade B and vintage A533 Grade B steels [*6*] and an A508-Class 2A steel [*7*] were analyzed to calibrate F_G. Table 1 shows the data for calibration and all the F_G values. Since there is some scatter in the F_G values, a statistical analysis could be used. A three-parameter

TABLE 1—*Data for calibration and the factor* F_G.

Specimen	Steel	Size	Temperature, °C	E_{CVN}, J	C_1	C_2	σ_Y (Mpa)	F_G
A508-19	A508	2T	204	147	2915	0.31	627	2.82
A508-23	A508	2T	204	138	7041	0.49	434	2.62
A508-24	A508	1T	204	138	2748	0.34	434	3.25
Z2 L-S	A302	2T	204	233	4211	0.34	477	3.47
Z2 L-T	A302	1T	288	218	12124	0.54	497	3.10
Z2 T-L	A302	0.5T	82	171	7730	0.45	493	2.46
Z2 T-L2	A302	0.5T	204	171	6957	0.48	470	3.12
Z2 T-L3	A302	1T	204	171	2988	0.36	470	4.14
Z2 T-L4	A302	1T	288	171	4734	0.43	500	3.62
Z3 L-S	A302	2T	288	173	2162	0.25	517	3.33
Z3 L-T	A302	1T	288	175	3894	0.36	517	3.20
Z3 T-L	A302	1T	288	116	1330	0.27	517	3.98
Z8 L-S	A533	0.5T	204	209	14830	0.54	465	2.39
Z8 T-L	A533	0.5T	204	131	3100	0.34	481	2.65
Z8 T-L2	A533	0.5T	204	131	2851	0.37	481	3.36

Weibull statistical model was used because it fits better when the data have values skewed about the average. A normal distribution may not fit the data because it is always symmetric around its center. The third parameter, subtracting unity from F_G, was chosen as one because when $F_G = 1$ all energy goes into the fracture process.

The F_G values in Table 1 give the following three-parameter Weibull statistical fit:

$$1 - P = \exp\left[-\left(\frac{F_G - 1}{2.33}\right)^{4.44}\right] \tag{11}$$

$$F_G \text{ (med.)} = 3.15 \qquad F_G (5\%) = 2.19 \qquad F_G (95\%) = 3.98$$

Where F_G (med.) is the median or 50% probability point on the fit, and F_G (5%) and F_G (95%) are the upper and lower 5% confidence levels.

J-R Curves Prediction

The C_1 values for a *J-R* curve approximation were calculated using F_G (med.), F_G (5%), and F_G (95%). Since F_G is in the denominator $J = C_1$ (95%), $\Delta a^{0.5}$ is a lower bound of the *J-R*, while $J = C_1$ (5%) $\Delta a^{0.5}$ is a upper bound, and $J = C_1$ (med.) $\Delta a^{0.5}$ is the average *J-R* curve. The plots in Figs. 3 to 5 show how well a *J-R* curve can be predicted using this method. Figure 3 is a example of a good prediction with the correlated and measured *J-R* curves lying almost together. Figures 4 and 5 are examples where the predicted *J-R* curves are not as good but still acceptable compared to the scatter normally found in *J-R* tests. Table 2 shows the predicted C_1 and J_{IC} values from F_G (5%, med, 95%) and ASTM E 1820.

Discussion

For most specimens a relatively good prediction was found in *J-R* curves as well as in J_{IC} values. This is good evidence that the method works. However, for different specimens of the same material (Z2T-L, Z2T-L2, Z2T-L3, Z2T-L4), with the same E_{CVN}, the scatter in the *J-R* curve causes a large error in the prediction.

J_{IC} is in the beginning of *J-R* curve, while the adjusted $J_{\Delta a=8mm}$ is at the end. Any change in the fitting exponent C_2 from 0.5 alters J_{IC}; however, the assumption of constant shape in *J-R* curve was

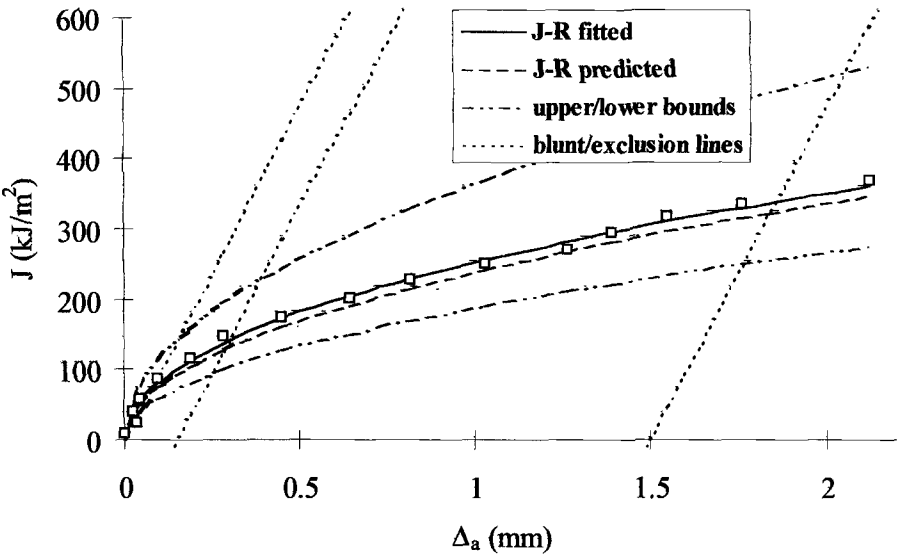

FIG. 3—*Plot showing the predicted and measured* J-R *curves for an ASTM A302 steel.*

proven to be reasonable. Most specimens had C_2 close to 0.5, while the rest might have C_2 closer to this value if more points, beyond the exclusion lines, were included in the *J-R* fitting.

The Weibull statistic worked better than the normal distribution, showing some shifting in the F_G average that would not be detected otherwise. There was no evidence from the results that F_G is a

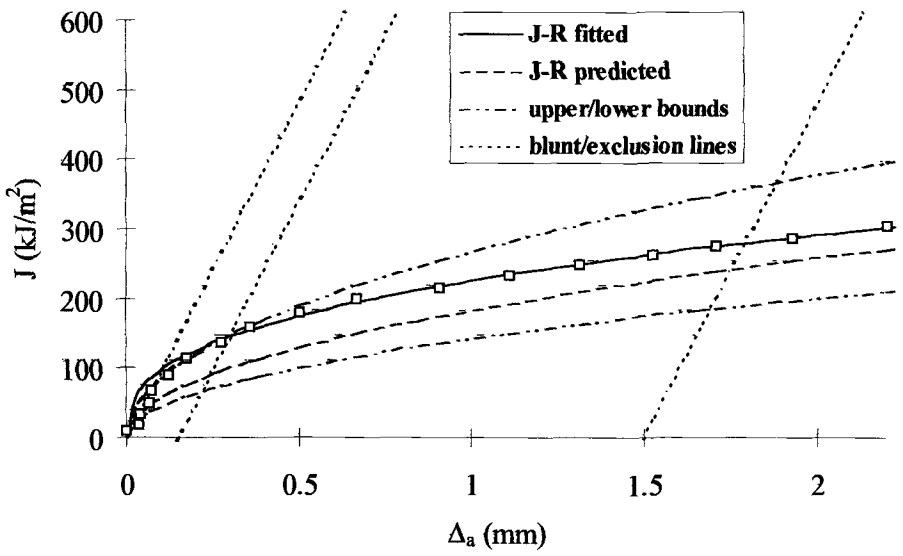

FIG. 4—*Plot showing the predicted and measured* J-R *curves for an ASTM A533 steel.*

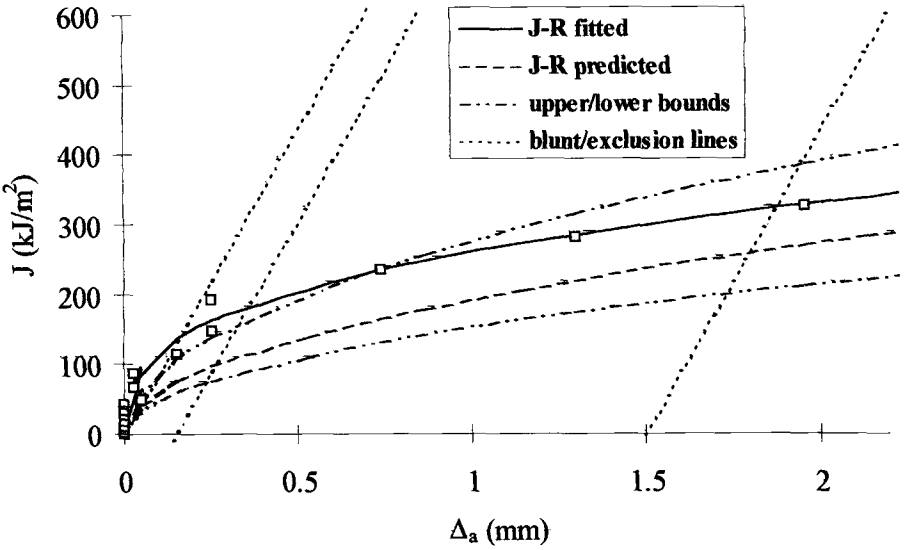

FIG. 5—*Plot showing the predicted and measured* J-R *curves for an ASTM A508 steel.*

function of the materials properties; nevertheless, a bigger range of different steels should be used to confirm that.

The *J-R* curves predicted here could be used with a normalization method [*8*] to predict load versus displacement curves of the specimens. Previous results have shown that variation in *J-R* curves do not strongly influence this result [*9*], so the predicted *J-R* curve might give a good estimate of failure load in this analysis method.

TABLE 2—J_{IC} *according to ASTM E 1820 and the predicted* C_1 *and* J_{IC}.

Specimen	J_{IC} E 1820 (kJ/m²)	C_1 (5%)	C_1 (med.)	C_1 (95%)	J_{IC} (5%) (kJ/m²)	J_{IC} (med.) (kJ/m²)	J_{IC} (95%) (kJ/m²)
A508-19	219.8	9370	6535	5160	172.1	111.0	84.4
A508-23	122.1	8816	6148	4855	177.2	111.4	83.6
A508-24	195.2	8816	6148	4855	177.2	111.4	83.6
Z2 L-S	342.3	14816	10332	8159	353.9	212.3	155.4
Z2 L-T	162.4	13863	9667	7634	315.3	191.6	141.2
Z2 T-L	232.6	10917	7613	6012	226.2	141.0	105.3
Z2 T-L2	160.6	10917	7613	6012	230.3	142.8	106.4
Z2 T-L3	170.0	10917	7613	6012	230.3	142.8	106.4
Z2 T-L4	153.9	10917	7613	6012	225.0	140.5	105.0
Z3 L-S	325.7	11003	7674	6060	224.8	140.7	105.3
Z3 L-T	238.8	11177	7794	6155	229.6	143.4	107.3
Z3 T-L	155.8	7365	5136	4056	133.6	86.5	65.9
Z8 L-S	244.6	13343	9305	7348	307.4	186.2	136.9
Z8 T-L	229.1	8318	5800	4580	159.0	101.4	76.6
Z8 T-L2	155.3	8318	5800	4580	159.0	101.4	76.6

Conclusions

- It is possible to correlate the *J-R* curve and Charpy V-notch Energy using a mechanistic rationale.
- The largest errors found in the prediction could be explained by the scatter in the *J-R* curves for the same material.
- The assumption of constant shape in the *J-R* curve ($C_2 = 0.5$) looks to be reasonable.
- The Weibull statistical model works well in the F_G calibration.
- The median value from the examples used here gave an energy reduction factor F_G of 3.15.

References

[1] Barsom., J. M. and Rolfe, S. T., "Correlations Between K_{IC} and Charpy V-Notch Test Results in the Transition-Temperature Range," *Impact Testing of Metals, ASTM STP 466,* American Society for Testing and Materials, 1970, pp. 281–302.

[2] Barsom, J. M., *International Metallurgical Reviews,* Vol. 19, 1974, pp. 183–198.

[3] Sailors, R. H. and Corten, H. T., *Fracture Toughness, ASTM STP 514,* American Society for Testing and Materials, 1972, pp. 164–191.

[4] Begley, J. A. and Logsdon, W. A., "Correlation of Fracture Toughness and Charpy Properties for Rotor Steels," Westinghouse Scientific Paper 71-1E7-MSLRF-P 1, 1971, p. 16.7.

[5] Marandet, B. and Sanz, G., "Evaluation of the Toughness of Thick Medium Strength Steels by Using Linear-Elastic Fracture Mechanics and Correlations Between K_{IC} and Charpy V-Notch," *Flow Growth and Fracture, ASTM STP 631,* American Society for Testing and Materials, 1977, pp. 72–95.

[6] McCabe, D. E., Manneschimidt, E. T., and Swain, R. L., "Ductile Fracture Toughness of Modified A 302 Grade B Plate Materials," Oak Ridge National Laboratory Report NUREG/CR-6426, Vol 2, 1997.

[7] Landes, J. D., McCabe, D. E., and Ernest, H. A., "Elastic-Plastic Methodology to Establish R-Curves and Instability Criteria," Westinghouse R&D Report 81-2D7-ELASP-R1, 1981.

[8] Landes, J. D., Zhou, Z., Lee, L., and Herrera, R., "Normalization Method for Developing J-R Curves with LMN Function," *Journal of Testing and Evaluation,* JTEVA, Vol. 19, No. 4, July 1991, pp. 305–311.

[9] Landes, J. D., Zhou, Z., and Brown, K. H., "An Application Methodology for Ductile Fracture Mechanics," *Fracture Mechanics: Twenty-Third Symposium, ASTM STP 1189,* R. Chona, Ed., American Society for Testing and Materials, Philadelphia, 1993, pp. 229–264.

Christopher D. Wilson[1] *and John D. Landes*[2]

Fracture Toughness Testing with Notched Round Bars

REFERENCE: Wilson, C. D. and Landes, J. D., **"Fracture Toughness Testing with Notched Round Bars,"** *Fatigue and Fracture Mechanics: 30th Volume, ASTM STP 1360,* P. C. Paris and K. L. Jerine, Eds., American Society for Testing and Materials, West Conshohocken, PA, 2000, pp. 69–82.

ABSTRACT: A method to simplify fracture toughness testing and reduce testing costs is discussed. An alternative specimen geometry, the notched round bar (NRB), has been combined with a simpler testing methodology. A multispecimen technique using notched round bars with finite notch root radii ρ was applied to 2024-T351 and overaged 2024 aluminum alloy. No fatigue precracking was used. A graph of apparent fracture toughness K_ρ versus the square root of notch root radius $\sqrt{\rho}$ was extrapolated to $\rho = 0$, corresponding to a fatigue precracked configuration. The resulting fracture toughness values were the same as those obtained from ASTM E 399 tests. Apparent fracture toughness J_ρ, determined from NRB *J-R* curves for overaged 2024, was graphed versus notch root radius ρ. The extrapolated value of fracture toughness was the same as that obtained from ASTM E 813 and E 1152 tests.

KEYWORDS: apparent fracture toughness, *J*-integral, notched round bar (NRB), finite radii notches

Problems with Fracture Toughness Test Methods

Four problems exist in fracture toughness test methods, such as ASTM E 399 Test Method for Plane-Strain Fracture Toughness of Metallic Materials, ASTM E 813 Test Method for J_{Ic}, A Measure of Fracture Toughness, and ASTM E 1152 Test Method for Determining *J-R* Curves. First, knowing the material response in advance or at least having an educated guess is necessary with current methods. Second, the standard specimens are often analyzed as planar geometries, ignoring the varying stress triaxiality through the thickness. Third, there are many inconsistencies between the practices described in the current tests. Fourth, the current tests are complicated and expensive and tend to get more complicated as new revisions are implemented. Each of these problems is discussed in more detail below.

Knowing Material Response in Advance

Using the three ASTM test methods previously mentioned requires the user to decide a priori which test to apply. If the material does not respond to loading as expected, then the test is invalid, and the specimen and valuable testing time are wasted. This scenario is not uncommon in K_{Ic} testing.

Varying Triaxiality Specimen Geometries

The standard specimens have planar geometries. For thin planar specimens, a plane stress condition exists on the lateral surfaces, and the stress triaxiality is nearly uniform through the thickness. For thick planar specimens, a plane stress condition exists on the lateral surfaces of the specimen and transitions toward a plane strain condition in the middle of the specimen. If the planar specimen is

[1] Assistant professor, Tennessee Technological University, Cookeville, TN.
[2] Professor, The University of Tennessee, Knoxville, TN.

thick enough, a state of plane strain will exist in the middle. Thus, the stress triaxiality will always vary from plane stress to plane strain (or nearly plane strain) in planar specimens.

Inconsistencies Between Fracture Toughness Test Methods

There are several inconsistencies that can be addressed. First, crack front measurements in the K_{Ic} test involve taking two surface measurements and three interior measurements along the crack front; crack front measurements in the J_{Ic} test involve seven interior measurements. Both choices were rather arbitrary. Regardless of the test method, the uneven crack growth that occurs in planar specimens is a problem that cannot be removed from the test. Second, two arbitrary yield strengths are used in the fracture toughness tests: 0.2% offset yield strength (σ_{ys}) and effective yield strength (σ_Y), taken to be the average of the 0.2% offset yield strength and the tensile ultimate strength to account for strain hardening. Third, the m-factor used in relating J and K to CTOD (CTOD = $m\frac{J}{\sigma_Y}$) is inconsistently used. The value of m depends on strain hardening and is not unity for elastic materials. Although m can vary from 1.25 to 2.5 for common structural steels, the blunting line construction used in E 813 and E 1152 assumes $m = 1$.

Complicated and Expensive Procedures

All the current tests are much more complicated and expensive than standard tension testing. These complications may even discourage some industries from performing qualitative fracture toughness testing.

During the past 25 years, the standard fracture toughness testing procedures have relied on specimens that are expensive to fabricate. These specimens must be fatigue precracked, taking both operator and machine time. The standard specimens require expensive instrumentation to record the load-line displacement. These factors make fracture toughness tests much more expensive to perform than tension tests.

Possible Solutions

Common Test Method

One possible solution to simplify fracture toughness testing and reduce testing costs is use of the common test method ASTM E 1820 Test Method for Measurement of Fracture Toughness. In 1996, ASTM approved this common test method, which provides, in a single test method, the procedures and guidelines found in the E 399, E 813, and E 1152 test methods. These three fracture toughness test methods were developed over a 30-year span by engineers and scientists with different backgrounds and different problems. One of the great strengths of ASTM is its diversity; however, 30 years of diversity has led to some unnecessary duplication and inconsistency in the fracture toughness tests. Many of the differences in test procedures do not have a sound theoretical basis. The common test method does not assume the nature of the material's response to loading. Instead, the common test method develops a logical framework for calculating fracture toughness after the material's response to loading is determined. The common test method should alleviate many of the inconsistencies between the current test methods. Unfortunately, the methodology in the common test method is complicated. This is the price of versatility.

Starting Anew

Another possible solution to simplify fracture toughness testing is to start anew. The notched round bar was rejected as a specimen geometry by The Committee on Rapid Inexpensive Tests for Determining Fracture Toughness [*1*] in the 1970s because of high-load-capacity requirements and difficulty in fatigue precracking. The perceived difficulty with high load requirements was unfounded—

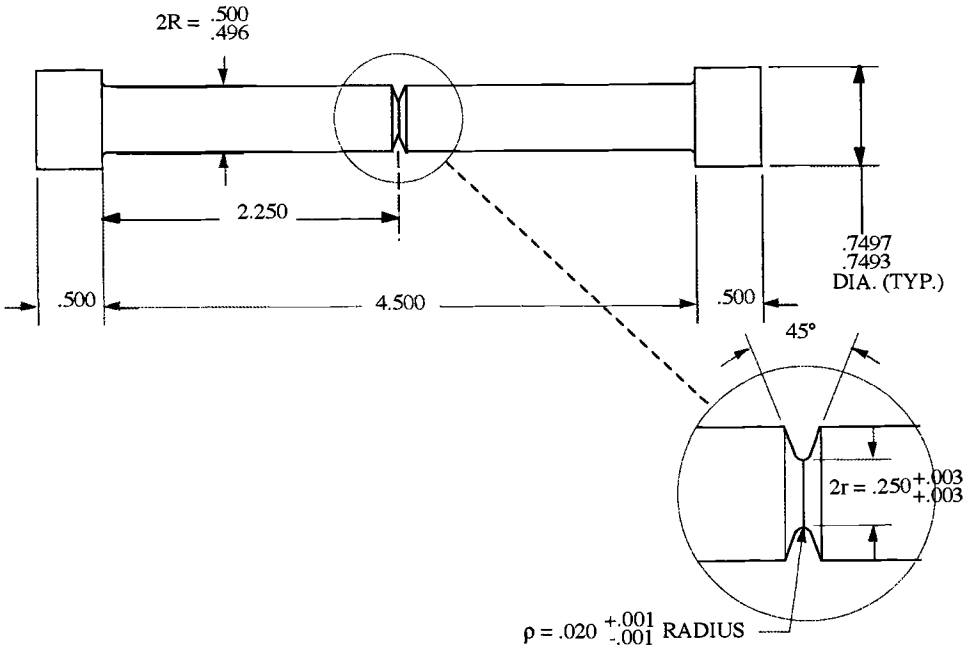

FIG. 1—*Engineering drawing of the notched round bar specimen (1 in. = 25.4 mm).*

conventional wisdom at the time dictated that a round bar with a very large nominal radius, 63 mm, would be necessary to maintain the stress triaxiality level of a 25-mm-thick planar specimen. The difficulty with fatigue precracking was real—asymmetric crack growth occurred when small load misalignments occurred. However, if smaller nominal radius (13 mm or less) specimens are used and if the precracking requirement can be removed, the notched round bar seems likely to be a reasonable alternative to current test geometries.

The notched round bar (NRB), shown in Fig. 1, has three characteristic radii: the nominal radius R, the notch neck radius r, and the notch root radius ρ. There are five possible advantages when using the NRB specimen instead of planar fracture toughness specimens. First, the notched round bar loaded in tension is essentially a two-dimensional (axisymmetric) geometry that develops uniform stress triaxiality along the circumferential notch front. Therefore, the issue of two-dimensional idealizations like plane stress and plane strain versus full three-dimensional analysis can be avoided. Second, the geometry allows equal access to the notch tip, making it ideal for stress corrosion cracking tests. Third, the geometry is ideal for mixed-mode I-III fracture toughness testing. Fourth, the geometry is attractive for dynamic or impact fracture toughness testing. Fifth, notched round bars combined with a simpler test methodology may reduce fracture toughness testing costs.

Previous Work with Notched Round Bars

In 1965, during the early development of fracture toughness testing methodology, many different specimen geometries, including the notched round bar, were critically examined by Brown and Srawley [2]. Tensile and fatigue properties had long been determined using notched round bars, and some of the earliest fracture toughness tests were naturally attempted with this geometry. The major difficulties with using notched round bars were the issue of how sharp a notch must be to simulate fatigue

precrack and the lack of an accurate K calibration. These problems led Brown and Srawley to favor other specimen geometries.

Brown [*3*] noted that only a small amount of K_{Ic} data had been generated by 1975 from fatigue precracked round bars because of the difficulty with maintaining concentric crack growth during fatigue cycling. Precracking was often done in reverse bending on a lathe. A second difficulty came in trying to determine when the crack had grown to the desired length for the toughness test.

In the late 1980s, Stark and Ibrahim [*4–6*] performed fracture toughness tests on small fatigue precracked round bars with a nominal radius R of 4.2 mm and a notch neck radius r of approximately 2 mm so that $r/R \approx 0.5$. Using the maximum load in the test to calculate K_{Ic}, their results were within 3% of 50-mm C(T) data for a high-strength aluminum alloy. Even though the ligament areas of the precracked round bars were significantly smaller than those of the 50-mm C(T)s, they found no significant size effect.

Stark and Ibrahim used finite element analyses to determine two size requirements for a valid K_{Ic} test. First, the fatigue crack must be at least twice the plastic zone size in depth. Second, the average axial stress across the final ligament at fracture must not exceed 2.5 times the yield strength so that general yielding does not precede fracture. Stark and Ibrahim did report that a significant number of their specimens had eccentric final ligaments. They analyzed the specimens in question to determine a bending correction to the stress intensity factor.

In 1995, Giovanola et al. [*7*] used small precracked round bars to measure the fracture toughness of Ti-10V-2Fe-3Al, HY-130 steel, and A508 class 2A steel. These materials were selected because they have a wide range of fracture toughness to yield strength ratios and were previously well characterized. The specimens had an R of 8 mm and an initial r of 4 mm. Precracking was done on a lathe until the ratio of crack size a to R varied from 0.56 to 0.78, where $a = R - r$. Eccentricity increased with increasing crack size, varying from 0.10 to 0.75 mm. In an arrangement similar to a standard tensile test, crack opening was measured using a 25.4-mm gage length. The maximum load was used for calculating fracture toughness based on fractographic evidence and analysis of the load-displacement records.

For the Ti-10V-2Fe-3Al, K_{Ic} values obtained using cracked round bars were about 15% lower than determined using a conventional specimen. For the embrittled HY-130, fractographic analysis revealed that initiation and propagation of the crack were cleavage driven. For the ductile HY-130, fractographic evidence revealed that crack initiation occurred at maximum load, followed by a rapid "quasi-stable" growth for a certain distance before complete instability. For the A508 material, the cracked round bars gave similar toughness values as conventional specimens. Crack eccentricity occurred in specimens of all three materials.

In contrast to using global stress field approaches based on K or J to describe the mechanics of fracture, the French research group F. M. Beremin [*8–11*] developed a local approach to the fracture mechanics of cracked round bars in the 1980s. Their local approach required precise elastic-plastic finite element analyses combined with a damage function to model void growth leading to ductile fracture. They measured ductile crack initiation, stable crack growth, and instability on fatigue precracked round bars. They simulated void growth using a model proposed by Rice and Tracey [*12*] in 1969. The model requires the determination of parameters that locally describe the change in size of a cavity as a function of hydrostatic stress, yield strength, and plastic strain. The local approach assumes that failure occurs when a critical void density is reached in a material. F. M. Beremin concluded that a local criterion can be used in more complex situations than global criteria based on K or J.

Relating Notches to Cracks

In the previous section, the focus was on fracture toughness testing with notched round bars that had been fatigue precracked. Beyond a change in geometry, there is still a need to simplify the test

methodology. To simplify the test methodology by removing the fatigue precracking requirement demands a study of the relationship between finite radii notches and sharp cracks (approaching a zero radius). This relationship must be studied from the perspective of the mechanics of notches and cracks and the material response of notches and cracks.

The mechanical relationship between a notch and a sharp crack was derived by Irwin [*13*]

$$K_\rho = \lim_{\rho \to 0} \frac{\sqrt{\pi}}{2} \sigma_{max} \sqrt{\rho} \tag{1}$$

where ρ is the notch root radius, and σ_{max} is the local stress at the notch tip. It should be noted that σ_{max} is typically a function of ρ and is often written as $k_t \sigma_{nom}$, where k_t is the stress concentration factor and σ_{nom} is the nominal stress at the notch neck. This result provides a connection between the mechanics of a notch and the mechanics of a crack.

The connection between the material responses of a notch and a crack is more difficult to quantify. The apparent fracture toughness, as obtained from a notched specimen, is the critical stress intensity factor calculated by considering the notch to be a sharp crack. The apparent fracture toughness is not a material property because it is dependent on the size of the notch root radius that is used. The modifier "apparent" is used to distinguish the notch-dependent fracture toughness from the fracture toughness obtained using sharp cracks.

In 1964, Irwin [*13*] conducted some fracture toughness tests on double edge tension DE(T) specimens made from H-11 steel with a yield strength of 1600 MPa. His tests were conducted using notched, not cracked, specimens. His results are shown in Fig. 2. Below a certain notch root radius

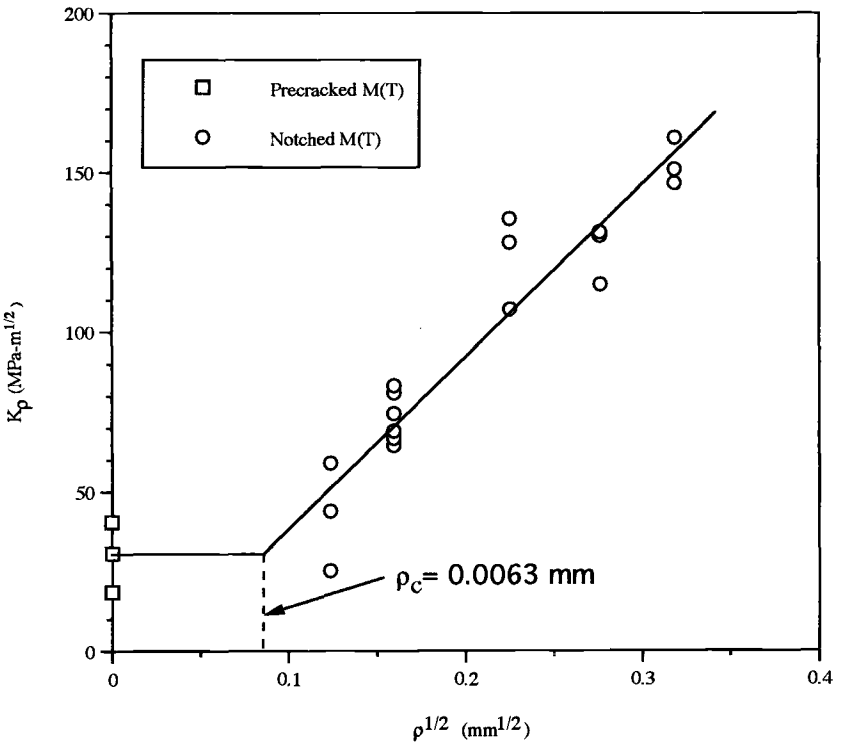

FIG. 2—*Apparent fracture toughness versus square root of notch root radius for H-11 steel* [13].

ρ_C, the apparent fracture toughness K_ρ is approximately constant. Irwin identified the limiting critical radius as $\rho_C = 0.0063$ mm. This plateau value is approximately equal to the fracture toughness value obtained from fatigue-precracked specimens. Above the limiting critical radius, the graph of K_ρ versus $\sqrt{\rho}$ was linear.

In 1968, Wilshaw, Rau, and Tetelman [*14*] conducted fracture toughness tests on single edge bend SE(B) specimens made from a high-nitrogen steel with a yield strength of 830 MPa. A similar relationship between apparent fracture toughness and $\sqrt{\rho}$ was found. The limiting critical radius was $\rho_C = 0.05$ mm.

In 1977, Begley, Logsdon, and Landes [*15*] applied a similar procedure to determine J_{Ic} for ASTM A471 NiCrMoV rotor steel with a yield strength of 760 MPa and 6061-T651 aluminum alloy with a yield strength of 290 MPa using both middle crack tension M(T) specimens and compact tension specimens. In addition, they performed fracture toughness tests using fatigue precracked specimens and found excellent agreement with a linearly extrapolated value of fracture toughness for a zero notch radius (Fig. 3) from the notched (no fatigue precrack) specimens. Note that the abscissa in Fig. 3 is ρ since the elastic component of J is proportional to K^2. No plateau or limiting critical notch root radius was discernible.

More recently in 1996, Reiff and Ernst [*16*] determined that initiation values of CTOD of a structural steel and a pressure vessel steel could be calculated by extrapolating apparent CTOD values from notched Charpy specimens to a zero notch root radius. They used four different sizes of notch root radii and observed a linear increase in CTOD. By extrapolating to a zero notch root radius, they obtained CTOD values that equaled those obtained from fatigue precracked Charpy specimens. Again, no plateau or limiting critical notch root radius was apparent in the tests.

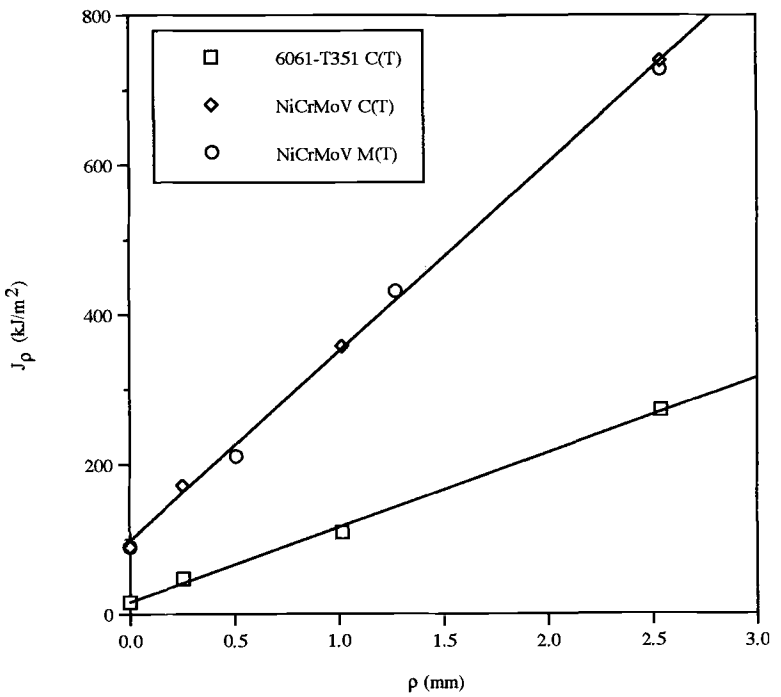

FIG. 3—*Apparent fracture toughness versus notch root radius for 6061-T351 and NiCrMoV [15].*

Research Plan

A combined experimental and analytical research program was implemented to study the suitability of the notched round bar (NRB) for fracture toughness testing. The purpose of the experimental program was to determine fracture toughness of several materials using both conventional fracture toughness specimens and notched round bars. Fracture toughness for the notched round bars was to be determined using a multispecimen approach, i.e., examining a graph of apparent fracture toughness K_ρ (or J_ρ) versus $\sqrt{\rho}$ (or ρ) and extrapolating to $\rho = 0$. The analytical program's purpose was to determine how to calculate K and J for the notched round bar.

Two materials were experimentally tested and analytically modeled: 2024-T351 and overaged 2024 aluminum alloy. All tests were conducted at room temperature. Young's modulus E was determined to be 73 GPa and Poisson's ratio ν was taken as 0.33. Tensile strength tests were conducted for both materials. For 2024-T351, the 0.2% offset yield strength was 390 MPa, the ultimate tensile strength was 480 MPa, and the Ramberg-Osgood hardening exponent was 15. For the overaged 2024, the 0.2% offset yield strength was 180 MPa, the ultimate tensile strength was 315 MPa, and the Ramberg-Osgood hardening exponent was 5.

Experimental Program

The NRB specimen details are shown in Fig. 1. The specimens had a nominal radius R of 6.35 mm (0.25 in.) and a neck radius r of 3.175 mm (0.125 in.), thus $r/R = 0.5$. Three different notch root radii were used: $\rho = 0.127$, 0.254, and 0.508 mm (0.005, 0.010, and 0.020 in.). All specimens had a notch flank angle of 45°. All notch root radii ρ had a tolerance of ± 0.025 mm (± 0.001 in.).

To maintain proper alignment, buttonhead ends were used in place of threaded ends. A mechanical gripping apparatus, typical of low-cycle fatigue testing, was used. Alignment was checked according to ASTM E 602 Test Method for Sharp-Notch Tensile Testing with Cylindrical Specimens. ASTM E 602 allows no more than 10% bending stress for a nominal tensile stress of 205 MPa. Typical bending stresses due to misalignment were no larger than 5% of the nominal tensile stress.

All tests were conducted on screw-driven universal testing machines with uniform crosshead motion. An extensometer with a gage length of 10 mm and a 10% extension range was used in all tests. Load and gage displacement data were recorded with an x-y plotter and digitized afterward.

Two test series were conducted. K_{Ic} testing was performed on the 2024-T351 aluminum alloy with 50-mm C(T) and NRB specimens. J_{Ic} and J-R curve testing was performed on the overaged 2024 aluminum alloy using both 25-mm C(T) and NRB specimens.

The 2024-T351 and overaged 2024 aluminum specimens were machined from a 50-mm-thick plate. For 2024-T351, standard K_{Ic} fracture toughness tests were conducted using fatigue precracked 50-mm C(T) specimens. Nonstandard blunt-notch 50-mm C(T) specimens with notch root radii matching the NRB specimens were also tested. For the overaged 2024, standard J_{Ic} and J-R curve fracture toughness tests were conducted using fatigue precracked 25-mm C(T) specimens. In addition, nonstandard blunt-notch 25-mm C(T) specimens with notch root radii matching the NRB specimens were tested. Duplicate tests were conducted for each combination of specimen type and notch root radius.

Analytical Program

In conjunction with the experimental program, an analytical program was conducted. Although K (and hence elastic J or J_{el}) expressions for the notched round bar are readily available, plastic J or J_{pl} for the notched round bar geometry needed to be determined. The load separation method, developed by Paris, Ernst, and Turner [*17,18*], was used to quantify J_{pl}. An extension to the load separation method, called the normalization method, developed by Landes and Herrera [*19,20*], was used to determine crack growth Δa without requiring unloading compliance data.

The load separation and normalization methods required analytical load-displacement curves to determine J_{pl}. Large strain, nonlinear finite element analyses were used to model the load-displacement response of both aluminum alloys. The nonlinear material response was modeled using isotropic hardening with a von Mises yield criterion, and again with a Drucker-Prager yield criterion (essentially, a generalized von Mises yield function that includes both the von Mises effective stress and a hydrostatic stress term). Further details concerning the finite element analyses and the calculation of J_{pl} and Δa are given by Wilson [*21*].

Results

K_{Ic} *Testing of 2024-T351 Aluminum Alloy*

Representative experimental NRB load-displacement P-v curves for 2024-T351 for each notch root radius ρ are shown in Fig. 4. The P-v records for all three values of ρ follow a common curve with the smallest ρ data failing at a lower load. It was observed that all specimens failed, separating into two pieces, before the load reached an instability point predicted by $dP = 0$. No discontinuities in the P-v records were encountered during the tests. No surface crack growth was observed during the tests.

The methodology in ASTM E 399 was considered invalid for the NRB geometry because of the high level of plasticity attained in the finite radii specimens. Therefore, apparent fracture toughness values from the experimental P-v curves were determined using J calculations as outlined in the E 813 test method. The values of J at final instability, J_c, were converted to K using $J = K^2/E'$, where $E' = E/(1 - \nu^2)$. These results are shown in a graph of apparent fracture toughness K_ρ versus $\sqrt{\rho}$ in Fig. 5.

To determine fracture toughness K_{Jc}, a curve fit was needed to extrapolate down to $\rho = 0$. Based on Irwin's data shown in Fig. 2, a linear extrapolation will probably provide an overly conservative value for fracture toughness. To more realistically model the plateau region for small ρ, an exponential function was used

$$K_\rho = C_0 10^{C_1\sqrt{\rho}} \tag{2}$$

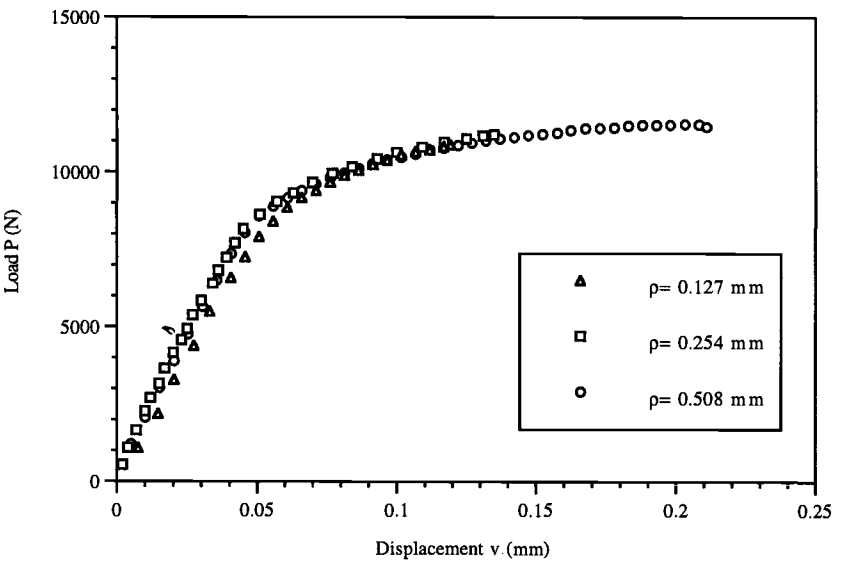

FIG. 4—*NRB load-displacement results for 2024-T351.*

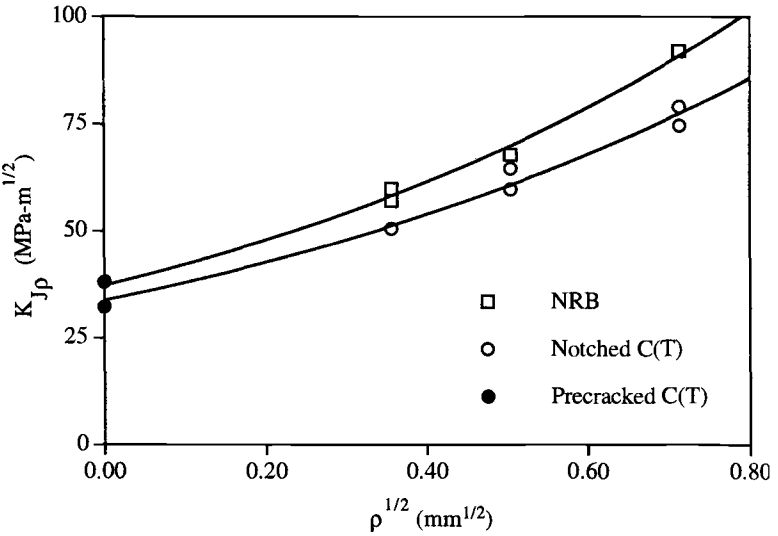

FIG. 5—*Apparent fracture toughness versus square root of notch root radius for 2024-T351.*

where C_0 and C_1 are coefficients to be determined in a least squares method after the exponential function is linearized. The value of C_0 will be the fracture toughness determined by the multispecimen technique. The particular form of the exponential function was chosen solely for convenience and is not based on any mechanical or material considerations.

Using the apparent NRB fracture toughness values from the three finite notch radii, the resulting curve fit gave a value of K_{Jc} = 37 MPa$\sqrt{\text{m}}$ for a zero notch root radius.

In addition to NRB specimens, compact tension C(T) specimens were also tested. Using ASTM E 813, the average value of K_{Jc} for the precracked C(T) specimens was 35 MPa$\sqrt{\text{m}}$. If ASTM E 399 is used to determine fracture toughness, the resulting average K_{Ic} for the precracked C(T) specimens was 38 MPa$\sqrt{\text{m}}$.

Apparent fracture toughness K_ρ values were determined from the blunt-notch C(T) specimens. Extrapolating to a zero notch root radius gave K_{Jc} = 35 MPa$\sqrt{\text{m}}$. Thus, the value of fracture toughness extrapolated from both NRB and blunt notched C(T) specimens was close to the fracture toughness calculated using precracked C(T) specimens.

J_{Ic} *and* J-R *Curve Testing of Overaged 2024 Aluminum Alloy*

Representative experimental notched round bar load-displacement P-v records for the overaged 2024 for each notch root radius ρ are shown in Fig. 6. The P-v curves for all three values of ρ follow a common curve to a point where unloading occurs. Unlike the previously described 2024-T351 results, all the overaged 2024 test records fail beyond a point where the differential load dP is zero. This observation indicates that some ductile crack growth occurred before fracture, although no surface crack growth was observed.

To develop a *J-R* curve, the normalization method was used to determine the apparent change in r/R as ductile crack growth occurred in a specimen. An effective crack length a was defined as

$$a = R - r = R\left(\frac{1 - r}{R}\right) \tag{3}$$

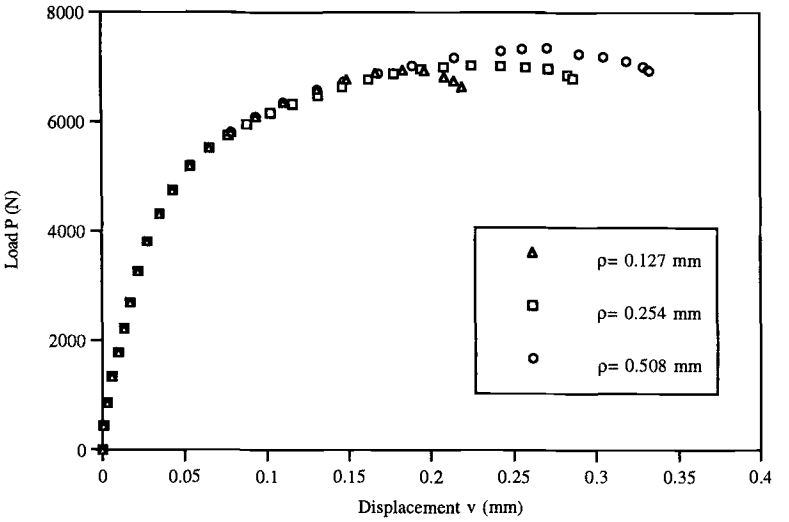

FIG. 6—*NRB load-displacement results for overaged 2024.*

For each P-v data pair, a value of a was calculated. J was calculated in accordance with the E 813 test method. The resulting J-R curves are plotted in Fig. 7.

For comparison, the J-R curves from precracked 25-mm C(T) and notched (without precracking) 25-mm C(T) specimens are plotted in Fig. 8. The maximum crack extension Δa found in any of the NRB test records was 0.4 mm, while the maximum crack extension found in the notched C(T) test records was 2.3 mm. Clearly, the notched round bar geometry did not develop a significant amount of crack extension.

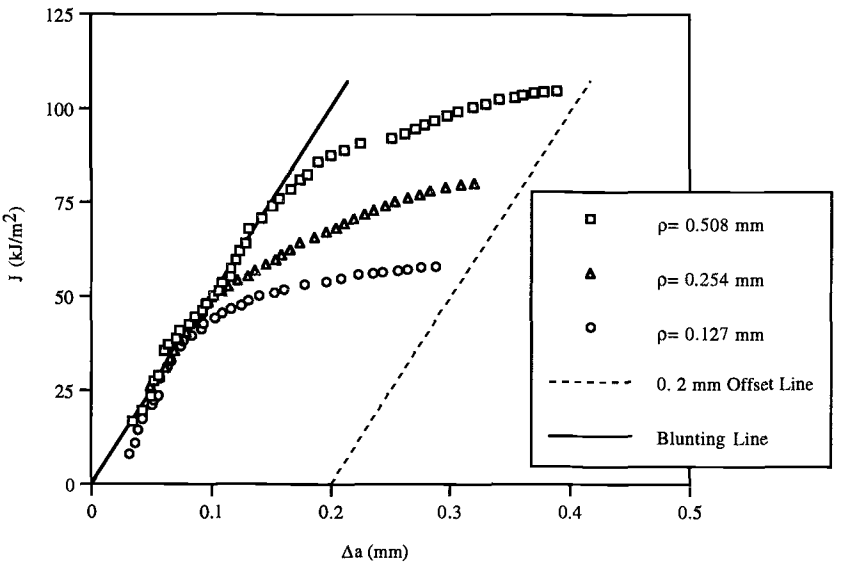

FIG. 7—*NRB* J-R *Curve for overaged 2024.*

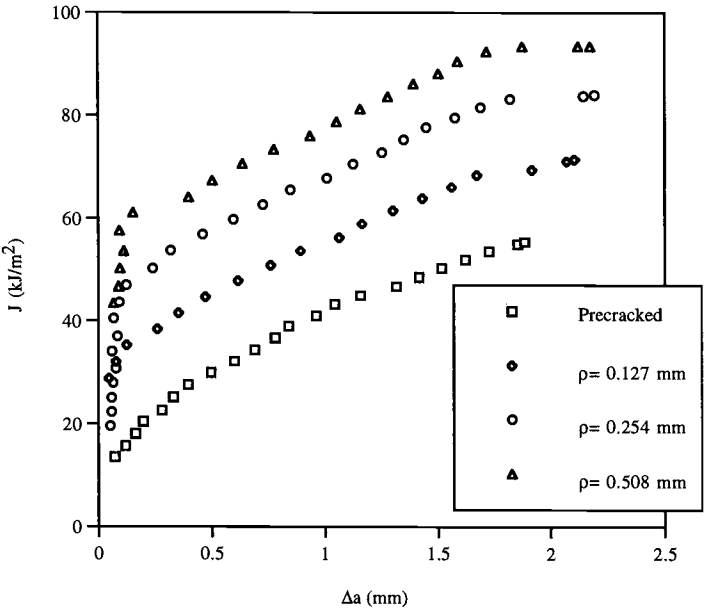

FIG. 8—*25-mm C(T)* J-R *Curve for overaged 2024.*

The blunting line and the 0.2-mm offset lines are also shown in Fig. 7. According to the E 813 test method, the intersection of the fitted *J-R* curve with the 0.2-mm offset line is the fracture toughness J_c. However, none of the NRB *J-R* curves extended to this intersection. Thus, the E 813 methodology was not used to determine J_Q for the notched round bars.

In this research program, J_c was taken as the J value at the intersection of the blunting line and the power law curve fit of the *J-R* curve for data points clearly off the blunting line. For the NRB test records shown in Fig. 7, an exclusion line parallel to the blunting, but offset by a distance of 0.025 mm was used. It is recognized that such a construction for precracked specimens would result in very low values of J_c (J_Q) compared to the E 813 test method. However, the E 813 test method assumes that sharp cracks are used and that blunting occurs only with subsequent loading. This is not the case for the notched round bar, which has a finite notch root radius before monotonic loading. A comparison of J_c values developed in this manner for the NRB specimens and J_Q values developed using the E 813 test method for 25-mm C(T) specimens is shown in Fig. 9.

Extrapolating the apparent J_ρ values for the NRB specimens to $\rho = 0$ mm in Fig. 9 gave $J_c = 20$ kJ/m^2. The value of J_Q from the precracked 25-mm C(T) specimens was also 20 kJ/m^2. It was surprising to note that the apparent J_Q values for the notched 25-mm C(T) specimens did not follow a linear relationship with notch root radius ρ for $\rho = 0.508$ mm. If this notch root radius is excluded from an extrapolation to zero notch root radius, then the predicted J_c value is essentially the same as the precracked results. Re-examining Fig. 8 did not reveal any reason for the anomalous behavior of the larger notch root radius 25-mm C(T) specimens.

Discussion

The notched round bar geometry gave comparable results to traditional fracture toughness specimen geometries, such as the compact tension and single edge bend geometries for 2024-T351 and overaged 2024. For initiation fracture toughness of 2024-T351, the fracture toughness determined us-

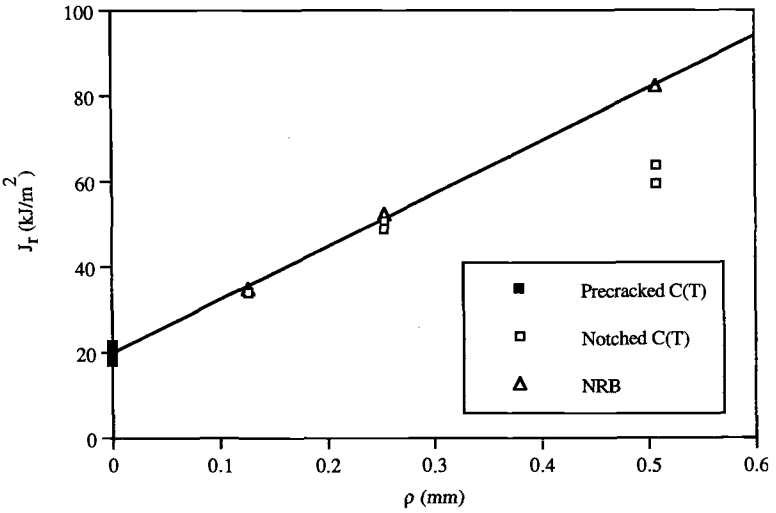

FIG. 9—*Apparent fracture toughness versus notch root radius for overaged 2024.*

ing notched round bars was the same as the fracture toughness obtained using precracked C(T) specimens. The E 399 test methodology was not suitable for the NRB geometry because of the large amount of plasticity found in the load-displacement record. The increased plasticity level was expected because of bluntness of the notch root radius versus a sharp precrack. Therefore, *K*-based analysis was not used on the notched round bars.

A critical value of *J*, J_c was determined for the 2024-T351 using the E 813 test methodology and converted to K_{Jc}. The extrapolation of apparent fracture toughness K_{Jc} to zero notch root radius ρ using a graph of K_ρ versus $\sqrt{\rho}$ worked well for both the NRB geometry and the notched (but not precracked) C(T) geometry. In fact, the apparent fracture toughness values for a given notch root radius for both the C(T) and NRB geometries lie very close together (Fig. 5). Reexamining the results of Begley, Logsdon, and Landes [*15*] in Fig. 3 reveals a similar result for a NiCRMoV steel. Both C(T) and M(T) specimens gave the same extrapolation line to J_c.

There is no mechanical significance in using an exponential function for the curve fitting procedure. Similar results were obtained using a third-order polynomial to extrapolate to a zero notch root radius. Further investigations are underway to develop additional data to add to the sparse set presented in Fig. 5. Additionally, investigations are underway to develop a mechanical model for relating apparent fracture toughness to notch root radius.

For the overaged 2024 aluminum, the NRB specimens produced a much smaller amount of stable crack growth than notched C(T) specimens. However, the two geometries gave the same extrapolation line in a plot of apparent J_ρ versus ρ. In terms of calculating initiation fracture toughness, the NRB geometry is a suitable alternative to the C(T) geometry. If a substantial *J-R* curve is sought, the NRB does not provide sufficient stable crack growth. In this case, a planar specimen would be better than a NRB specimen.

Conclusions

The results presented in the previous section clearly demonstrated that the notched round bar geometry is a suitable alternative to the currently used planar specimen geometries. The NRB geometry is particularly well-suited for initiation fracture toughness testing where the construction of a *J-R*

curve is not required. The NRB geometry is a reasonable alternative for fracture toughness testing using the E 399 test method. Instead of determining K_{Ic}, a J_c value should be determined and then converted to K_{Jc}. This change in methodology is needed because of the larger amount of plasticity that develops in a notched versus a precracked specimen.

For *J-R* curve testing, the NRB is probably not as useful as the planar specimens because the NRB does not develop a large amount of stable crack growth. However, if initiation fracture toughness J_{Ic} is required, the methodology presented here can be used. In other words, the NRB geometry should provide enough stable crack growth to support a J_{Ic} construction similar to the E 813 test method. For materials like the overaged aluminum, which do not have observable surface crack growth, the J_{Ic} construction in the E 813 test method must be modified. The proposed change is to forego the use of the 0.2-mm offset line for determining J_{Ic}. Instead, J_{Ic} should be taken from the actual blunting line.

Overall, the NRB geometry should be attractive to industries that do not currently use precracked, planar specimens. The notched round bar does not require a servohydraulic testing machine because precracking is not necessary. If the normalization method is used for determining crack length, then unloading compliance is not required. In fact, the NRB geometry is no more difficult to test than a straight tensile bar. Two key issues must be remembered when using the NRB geometry. First, proper alignment must be maintained. The alignment requirements in the E 602 test method was found to be sufficient in this research program. Second, the notch root radius of each specimen should be carefully measured before testing. The extrapolation procedure may be sensitive to the measurement of notch root radius.

In terms of a cost savings over using precracked planar specimens, the NRB geometry may provide an advantage. When compared on a per-test basis, the NRB is significantly cheaper to test. However, the multispecimen approach presented here requires the use of several notch root radii and, at least, duplicate tests at a given notch root radius. For example, the E 399 test method recommends that at least three precracked specimens be used. If notched round bars are used with duplicate tests at three notch root radii, then six specimens would be needed. It is estimated that a single NRB specimen costs about one half the amount of a planar specimen. Thus, manufacturing six notched round bars would cost the same as three precracked, planar specimens. The real savings in using notched round bars is that fatigue precracking is not required. In addition, it is not necessary to use a servohydraulic testing system. In fact, the same test setup used for tensile tests should be adequate for fracture toughness testing with notch round bars.

References

[1] "Rapid Inexpensive Tests for Determining Fracture Toughness," report of The Committee on Rapid Inexpensive Tests for Determining Fracture Toughness, National Materials Advisory Board, National Academy of Science, Washington, DC, 1976.

[2] Brown, W. F., Jr. and Srawley, J. E., "Fracture Toughness Testing," *Fracture Toughness Testing and Its Applications, ASTM STP 381,* 1965, pp. 143–198.

[3] Brown, W. F., Jr., "The Circumferentially Notched Cylindrical Bar as a Fracture Toughness Test Specimen," *Linear Fracture Mechanics,* Envo Publishing, Lehigh Valley, PA, 1975, pp. 175–187.

[4] Stark, H. L. and Ibrahim, R. N., "Estimating Fracture Toughness from Small Specimens," *Engineering Fracture Mechanics,* Vol. 25, No. 4, 1986, pp. 395–401.

[5] Ibrahim, R. N. and Stark, H. L., "Validity Requirements for Fracture Toughness Measurements Obtained from Small Circumferentially Notched Cylindrical Specimens," *Engineering Fracture Mechanics,* Vol. 28, No. 4, 1987, pp. 455–460.

[6] Ibrahim, R. N. and Stark, H. L., "Establishing K_{Ic} from Eccentrically Fatigue Cracked Small Circumferentially Grooved Cylindrical Specimens," *International Journal of Fracture,* Vol. 44, 1990, pp. 179–188.

[7] Giovanola, J. H., Homma, H., Lichtenberger, M., Crocker, J. E., and Klop, R. W. "Fracture Toughness Measurements Using Small Cracked Round Bars," *Constraint Effects in Fracture Theory and Applications: Second Volume, ASTM STP 1244,* 1995, pp. 255–285.

[8] Beremin, F. M., "Calculation and Experiment on Axisymmetrically Cracked Tensile Bars: Prediction of Initiation, Stable Crack Growth and Instability," *Transactions of the Sixth International Conference on Structure Mechanics in Reactor Technology,* 17–21 Aug. 1981, pp. L6/2 1–7.

[9] Devaux, J. C., Rousselier, G., Mudry, F., and Pineau, A., "An Experimental Program for the Validation of Local Ductile Fracture Criteria Using Axisymmetrically Cracked Bars and Compact Tension Specimens," *Engineering Fracture Mechanics,* Vol. 21, No. 2, 1985, pp. 273–283.

[10] Devaux, J. C., Mudry, F., Pineau, A., and Rousselier, G., "Experimental and Numerical Validation of a Ductile Fracture Local Criterion Based on a Simulation of Cavity Growth," *Nonlinear Fracture Mechanics: Vol. II—Elastic-Plastic Fracture, ASTM STP 995,* 1989, pp. 7–23.

[11] Rousselier, G., Devaux, J. C., Mottet, G., and Devesa, G., "A Methodology for Ductile Fracture Analysis Based on Damage Mechanics: An Illustration of a Local Approach of Fracture," *Nonlinear Fracture Mechanics: Volume II—Elastic-Plastic Fracture, ASTM STP 995,* 1989, pp. 332–354.

[12] Rice, J. R. and Tracey, D. M., "On the Ductile Enlargement of Voids in Triaxial Stress Fields," *Journal of the Mechanics and Physics of Solids,* Vol. 17, 1969, pp. 201–217.

[13] Irwin, G. R., "Structural Aspects of Brittle Fracture," *Applied Materials Research,* Vol. 3, No. 2, April 1964, pp. 65–81.

[14] Wilshaw, T. R., Rau, C. A., and Tetelman, A. S., "A General Model to Predict the Elastic-Plastic Stress Distribution and Fracture Strength of Notched Bars in Plane Strain Bending," *Engineering Fracture Mechanics,* Vol. 1, 1968, pp. 191–211.

[15] Begley, J. A., Logsdon, W. A., and Landes, J. D., "Ductile Rupture Blunt-Notch Fracture Criterion," *Flaw Growth and Fracture, ASTM STP 631,* 1977.

[16] Reiff, K. and Ernst, P., "$CTOD_i$ Measured by Means of a Modified Charpy-V Specimen," *Fatigue and Fracture of Engineering Materials and Structures,* Vol. 20, No. 1, 1997, pp. 29–39.

[17] Paris, P. C., Ernst, H., and Turner, C. E., "A *J*-Integral Approach to Development of η-Factors," *Fracture Mechanics: Twelfth Conference, ASTM STP 700,* ASTM, 1980, pp. 476–502.

[18] Ernst, H. A., Paris, P. C., and Landes, J. D., "Estimations on *J*-Integral and Tearing Modulus *T* from a Single Specimen Test Record," *Fracture Mechanics: Thirteenth Conference, ASTM STP 743,* 1981, pp. 338–351.

[19] Landes, J. D. and Herrera, R., "A New Look at *J-R* Curve Analysis," *International Journal of Fracture,* Vol. 36, 1988, pp. R9–R14.

[20] Landes, J. D. and Herrera, R., "Calculation of *J* from Test Records for the Growing Crack," *International Journal of Fracture,* Vol. 36, 1988, pp. R15–R20.

[21] Wilson, C. D., "Fracture Toughness Testing with Notched Round Bars," doctoral dissertation of The University of Tennessee, Knoxville, TN, 1997.

Session II

Arne S. Gullerud,[1] *Robert H. Dodds, Jr.,*[1] *Roy W. Hampton,*[2] *and David S. Dawicke*[3]

3-D Finite Element Modeling of Ductile Crack Growth in Thin Aluminum Materials

REFERENCE: Gullerud, A. S., Dodds, R. H., Jr., Hampton, R. W., and Dawicke, D. S., **"3-D Finite Element Modeling of Ductile Crack Growth in Thin Aluminum Materials,"** *Fatigue and Fracture Mechanics: 30th Volume, ASTM STP 1360,* P. C. Paris and K. L. Jerina, Eds., American Society for Testing and Materials, West Conshohocken, PA, 2000, pp. 85–101.

ABSTRACT: This work describes the development and verification of a 3-D model to predict stable, Mode I crack growth in thin, ductile aluminum alloys. The model extends the standard 2-D form of the crack tip opening angle (CTOA) methodology, which determines crack extension based on obtaining a critical angle at the crack tip. When the CTOA reaches the critical value, all the nodes along the current, 3-D crack front are released simultaneously, thereby growing the crack in a self-similar manner. Evaluation of the CTOA occurs at a specified distance behind the crack tip; this decouples CTOA evaluation from mesh refinement. The CTOA-based model also includes adaptive load control strategies to minimize the effects of discrete load increments on the growth response. To evaluate the effectiveness of the described approach, this work describes a validation study using load-crack extension data from 2.3-mm-thick Al 2024-T3 specimens tested at NASA-Langley. The test matrix includes C(T) and M(T) specimens, with varying widths (50 to 600 mm), a/W ratios, and levels of constraint to suppress out-of-plane bending. Comparisons of load-crack extension curves from experiments and analyses of a constrained 150-mm C(T) specimen provide a calibrated critical CTOA value of 5.1°. Analyses using the calibrated CTOA value for constrained and unconstrained specimens provide predictions of peak load in good agreement with the experimental values.

KEYWORDS: stable crack growth, CTOA, 2024-T3 aluminum, 3-D, finite element analysis, out-of-plane bending

The ductile tearing behavior of thin sheet aluminum is critical to a number of engineering applications, most notably in safety assessments of aging aircraft [*1,2*]. These structures employ aluminum components only a few millimeters thick, while in-plane dimensions span several meters. During service, fatigue at rivet holes and lap joints, for example, generates through-thickness cracks in the components. These small cracks may experience significant ductile tearing and coalescence into longer cracks prior to component failure during an overload condition. Effective computational techniques that accurately predict ductile crack growth can greatly assist initial design and subsequent fracture assessments of these structures. Much of the current research on modeling ductile crack growth in metals centers on damage mechanics approaches, such as the Gurson-Tvergaard model [*3–5*], which characterize the void nucleation, growth, and coalescence process driving crack growth. This approach is highly effective in modeling crack growth in ferritic steels, where typically thick sections generate high levels of stress triaxiality that drive the damage process. In thin aluminum panels where

[1] Graduate research assistant and Nathan Newmark professor, respectively, Department of Civil Engineering, University of Illinois, 205 N. Mathews, Urbana, IL 61801.

[2] Structural analysis and verification group leader, MS 213-4, NASA Ames Research Center, Moffett Field, CA 94035-1000.

[3] Materials research engineer, NASA Langley Research Center, Hampton, VA 23681.

crack extensions are many times the thickness, through-thickness stresses are necessarily reduced, often leading to through-thickness slant fracture along bands of large plastic strain. Current approaches that rely on high triaxiality to damage the material have limited applicability for thin specimens. Modeling approaches for thin materials often use a simpler macroscale measure of near-tip deformation to control crack growth, such as the crack tip opening angle (CTOA) [*6–8*].

With CTOA-controlled crack growth, the crack front advances by a prescribed amount (usually one element size in a finite element model) when the CTOA reaches a specified, "critical" value. Constitutive models for material ahead of the crack tip generally use J_2 flow theory of plasticity; consequently, no material damage occurs ahead of the tip. Early researchers to adopt this modeling procedure include Rice and Sorensen [*9*], Sham [*10*], and Sorensen [*11*]; these studies focus on ductile growth under plane-strain, small-scale yielding conditions. Subsequent researchers have employed various CTOA criteria to investigate ductile tearing in fracture specimens in a 2-D setting (plane-strain or plane-stress conditions) [see, for example, Refs *12–14*]. These studies demonstrate that crack growth in thin aluminum components cannot be modeled properly with simple 2-D analyses. Despite the thin material, sufficient stress triaxiality develops just ahead of the crack front to make the response 3-D in character even for materials of 1 to 2-mm thickness. Furthermore, out-of-plane bending in unrestrained panels strongly affects crack growth, reducing peak loads by as much as 40% [*15*]. Full 3-D analyses become necessary to model adequately the fracture behavior of such thin components—near the crack front, the response has a 3-D character with thin shell behavior remote from the crack front. Studies that use 3-D models remain relatively rare. Dawicke et al. [*6,7*] describe 3-D crack growth analyses of thin panels with anti-buckling guides that use CTOA-controlled growth with enforced uniform extension along the crack front. To model the effects of local out-of-plane bending, Starnes et al. [*16*] and Young et al. [*17*] employ a thin shell model of the cracked component with a CTOA criterion to control crack growth. However, to match the measured experimental response, the shell model needs an adjustable plane-strain "core" along the crack plane to introduce some through-thickness constraint. In all of these studies, crack growth occurs at a fixed (critical) value of the CTOA. A number of factors may affect the applicability of a constant, critical CTOA value, including sheet thickness, crack, and loading geometry, absolute specimen size, buckling behavior, and the influence of multiple cracks. For the CTOA approach to offer a fracture parameter having general transferability between different configurations, it must be reasonably invariant of these factors.

This study explores the application of a fully 3-D model for ductile crack growth in thin aluminum sheets using a CTOA criterion, including the strong effects of out-of-plane bending. The first section outlines the CTOA modeling strategy in a 2-D framework, then discusses extension of the CTOA approach for 3-D analyses of planar (Mode I) growth and as an approximation for slant fracture. Evaluation of the CTOA occurs at a fixed, specified distance (L_c) behind the crack front, thereby divorcing CTOA evaluation from mesh resolution. Given a specific L_c value, the predicted growth response converges to a unique result with continued mesh refinement. The analyses also include adaptive loading strategies to insure results independent of load increment sizes specified in the analyses. A validation study demonstrates application of this new modeling approach to predict crack growth in the thin aluminum panels tested by Dawicke and Newman [*7,8*] at NASA-Langley. These tests on thin Al 2024-T3 panels covered a range of absolute sizes, specimen types, crack length to width (a/W) ratios, and levels of out-of-plane bending suppression. The validation procedure involves a calibration using a 150-mm C(T) specimen to provide the critical CTOA value, which then remains fixed for prediction of crack growth in all other tests. In all cases, the predictions of load-crack growth responses are in good agreement with experimentally measured responses.

CTOA Models For Crack Growth

Key Features in 2-D and 3-D Settings

Figure 1 illustrates the essential features of crack growth modeling with a critical CTOA criterion in a 2-D setting. The crack plane coincides with the symmetry plane. Nodes constrained to remain on

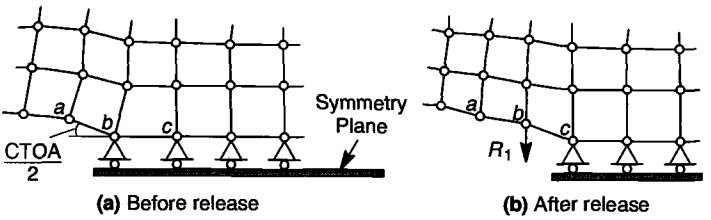

FIG. 1—*Crack advance in Mode I by node release in a 2-D setting.*

this plane define the remaining ligament, unconstrained nodes define the crack face, and the current crack tip node is the constrained node between the two sections. Crack growth occurs by release of the constraint in the direction normal to the crack plane for the current crack tip node. The crack tip node also serves as the vertex of the angle, with the unconstrained node adjacent to the crack tip typically providing the second point required for calculation of the CTOA. In a 3-D framework, however, the complexity increases significantly even for growth limited to Mode I conditions. The notion of a crack "tip" generalizes to a crack "front," which can be a closed loop (an embedded flaw) or a curved line (a through crack or surface crack). As in 2-D, multiple crack fronts may exist simultaneously and may grow together, forming new crack fronts. The local "direction" of crack growth in the symmetry plane at a point on the front now comes into question. To provide a simple extension of CTOA to 3-D applicable for through-crack configurations, the analyses described in this study determine the growth of an entire front based on the angle at a defined single "master" node (Fig. 2). When the CTOA at the master node reaches the critical value, all nodes on the crack front are released simultaneously. The analyst selects the master node for use at each crack front. The node at mid-thickness is typically selected as the master node since constraint effects make it the controlling location for crack growth in these thin sheet analyses. This implementation appears applicable to model thin structures where the remaining ligament size and the amount of crack growth are both much greater than the thickness.

Each time a growth event occurs, the nodes within a specified distance, L_c, of the crack tip are released (Fig. 3). Releasing a node removes the constraint in the normal direction of the crack plane; other constraints, if any, remain unchanged. The reaction force in the normal direction becomes an applied nodal force that must relax to zero gradually to prevent numerical difficulties. The traditional procedure that suspends external loading changes during node release becomes prohibitively expensive in large-scale 3-D analyses with multiple crack fronts; the node release process and further external loading must proceed concurrently. Conventional implementations of CTOA-controlled growth reduce such forces to zero over a fixed number of load steps. This approach, however, often introduces a dependence on the step size defined in the analysis. In this work, a traction-separation

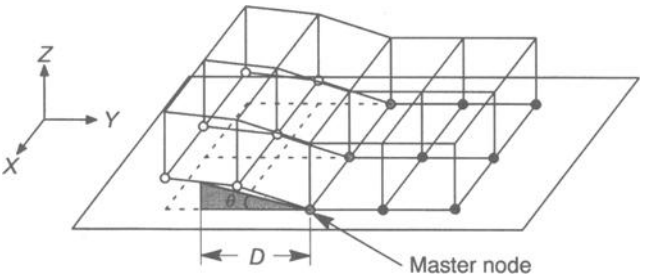

FIG. 2—*CTOA mechanism in 3-D illustrating enforced, uniform growth.*

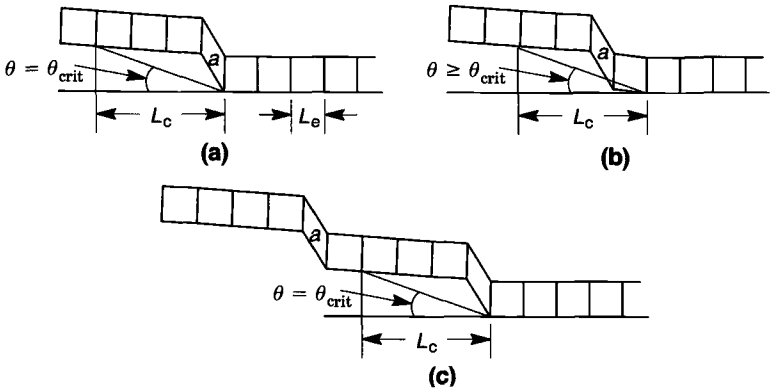

FIG. 3—*Definition of CTOA at a specified distance,* L_c, *to minimize meshing sensitivity of computed response.*

model lessens this dependence by placing the force reduction process on a more physical basis, as illustrated in Fig. 4. At release, the forces are decreased immediately by 20% to prevent the newly released nodes from penetrating the crack plane. Thereafter, the forces decrease gradually to zero following a linear relationship expressed in terms of the continued opening displacement of the master node. The reaction forces reach zero when the opening displacement of the master node increases to the value denoted $\overline{H}$. Numerical experiments show that use of $\overline{H} \approx 0.3 \times (\theta_c L_c)$ removes the step size dependence while preserving stability of the finite element analysis.

Mesh Dependence

Standard 2-D implementations typically define the current CTOA based on the geometry of the element adjacent to the crack tip. In Fig. 1, the vertical displacement of Node *a,* which shares an element edge with the crack tip Node *b,* sets the CTOA. This practice generally introduces a strong mesh dependency. Due to crack-face curvature, the CTOA value depends on the distance behind the tip used in the angle computation. With the CTOA definition illustrated in Fig. 1*a,* an element with a different size defines the angle at an alternate location, thereby requiring a different critical CTOA value for each mesh refinement. To avoid this problem, the present implementation defines the CTOA at a specified distance behind the crack tip, L_c. The specification of a critical CTOA value for analysis thus also includes the distance L_c at which it is defined. Distances are defined on the deformed configuration; linear interpolation permits CTOA calculation when the L_c distance does not correspond

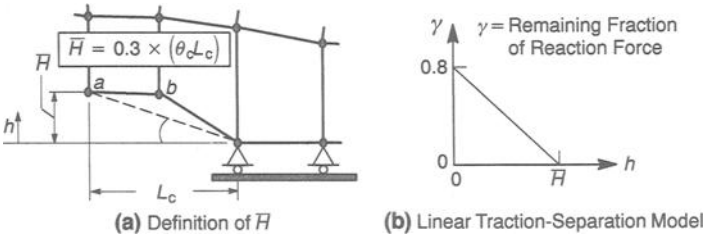

FIG. 4—*Traction-separation model for release of nodal reaction forces. Reaction forces for Nodes* a *and* b *relax to zero when opening displacement of master Node* a *reaches a height of* H.

directly to a node location in the deformed configuration. When the crack face becomes curved in the out-of-plane direction (due to bending), the L_c distance lies along the arc that follows the curvature of the crack face. Specifying a distance for definition of CTOA implicitly introduces a length scale in the fracture process and opens the possibility to divorce the mesh refinement from the fracture criterion. The distance L_c should ideally correspond to a physically meaningful length scale, perhaps related to the material's microstructure. However, the microstructural features (e.g., spacing of larger voids) of aluminum are far too small (~10 to 20 μm) for a connection with L_c. The selection of L_c remains an open issue, although it is clear that L_c should lie beyond the very highly curved region immediately adjacent to crack front nodes.

When the distance L_c corresponds to more than one element length behind the crack front, the node release process requires further modification; otherwise, problems with convergence and load step size dependency generally arise. Figure 3 shows the elements near the crack front at several stages during an analysis. Evaluation of the CTOA occurs at a distance, L_c, which is four times the element size (L_e) in this example. In 3*a*, the CTOA at the current crack front reaches the critical value, θ_c, requiring release of the crack front nodes. Due to the high stress levels, the elements adjacent to the crack front, marked as *a*, contribute the majority of deformation producing the CTOA. Figure 3*b* shows the deformation one load step after the release of the crack front nodes. The released nodes displace upwards only a small amount, yet the CTOA immediately exceeds the critical value. Since elements *a* are fully plastic, their deformations still control the CTOA value. The sudden release severely degrades convergence rates of the nonlinear solution in the finite element model and can cause the subsequent response to depend strongly on the load step size. This process continues until evaluation of the CTOA no longer includes elements *a;* this occurs when crack extension from the original crack front exceeds the CTOA measurement distance, L_c (see Fig. 3*c*). To eliminate problems ensuing from such growth events, the alternative approach adopted here releases all nodes within L_c ahead of the crack front. Using this method, crack growth occurs in increments of L_c, and the problems of convergence and load step size no longer occur.

To demonstrate that a fixed L_c value eliminates the dependence of crack opening profile on mesh resolution, Fig. 5 shows crack opening profiles from a mesh convergence study for a C(T) specimen with anti-buckling plates, $W = 50$ mm, $a/W = 0.4$, $B = 2.3$ mm. The material properties correspond to those for Al 2024-T3, which has a yield stress of 345 MPa and a Young's modulus of 71.3 GPa (see Fig. 5*b*) for stress-strain curve). The 3-D meshes for this study define quarter-symmetric models of the specimen and use 8-noded solid elements with two elements through the half thickness. The analyses differ in the mesh resolution along the crack plane, with elements ranging in size from L_e = 0.0625 to 1 mm. The small-displacement theory analyses evaluate the CTOA using $L_c = 1$ mm. Figure 5 shows the corresponding crack opening profiles for the different meshes after ten crack growth increments ($\Delta a = 10$ mm). The models that have two or more elements defined over the CTOA evaluation distance, L_c, predict virtually identical crack opening profiles. This demonstrates that converged predictions of the crack opening profile are obtained through the use of an explicit length-scale parameter, L_c.

These analyses also provide insight into the sensitivity of predicted crack growth to the specified L_c value. Since the element directly adjacent to the crack tip supplies the majority of the deformation forming the CTOA, an L_c value smaller than 1 mm produces a higher CTOA at the same load level and crack tip deformation. This suggests that reducing L_c while maintaining the same critical CTOA generates in a lower-resistance curve. However, each calibrated pair of L_c and CTOA values may not be unique, i.e., they may provide similar predictions of crack growth for the same specimen geometries.

Adaptive Load Control Strategies

Predictions of crack growth response generated with a CTOA criterion often show a dependence on sizes of the computational load steps. Two types of load step size dependencies have been identified. The first type arises from a simple "overshoot" of the critical angle. When a load step is too

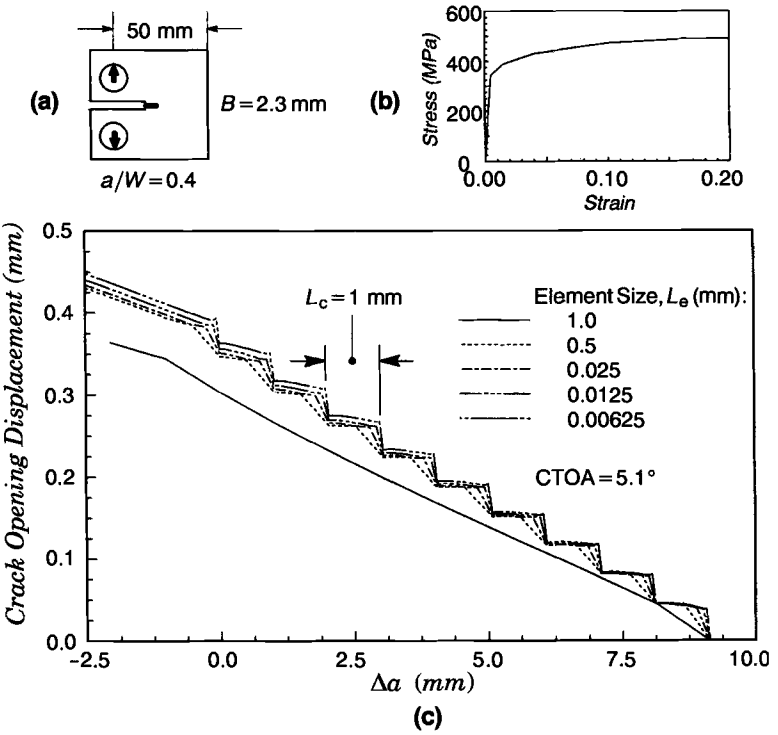

FIG. 5—*Analyses of 50-mm C(T) specimen,* a/W = *0.4, with out-of-plane bending prevented:* (a) *diagram of specimen,* (b) *engineering stress-strain curve from tensile data,* (c) *crack profiles from analyses with varying mesh densities.*

large, the resulting deformation causes the CTOA to exceed the critical angle before the corresponding crack front nodes are released. This is equivalent to momentarily increasing the critical CTOA, which leads to an elevation of the fracture resistance. If such overshoots occur frequently, the predicted response can be significantly different from an analysis that performs releases at the specified critical CTOA. To insure more precise enforcement of the critical CTOA, the crack growth algorithms employed here predict the CTOA resulting from the application of the next load step. If an overshoot condition arises, the load step is reduced an appropriate amount to achieve a CTOA very near the predicted critical value. This simple mechanism effectively eliminates the overshoot problem, reliably enforcing the CTOA at release to within 1% of the critical value.

The second type of load step size dependency arises when a large load increase, which if properly resolved would cause several growth increments, is applied in a single load step. Since the algorithms allow only one growth increment at each crack front during a load step, a model subjected to very large load steps may have spurious, additional resistance to crack growth simply due to the size of a large load step. As crack growth extends through a model that has a naturally decreasing fracture resistance, the definition of load step sizes becomes even more important to prevent this phenomenon. The adaptive loading strategy employed here enforces a minimum number of load steps, usually 10, between growth increments. Each violation of this requirement leads to a 50% permanent reduction in subsequent load step sizes.

Computational Procedures

The finite element program WARP3D provides the necessary framework for implementation of the 3-D CTOA-controlled crack growth procedures [*18*]. WARP3D includes a robust large strain formulation, nonlinear material response using Mises plasticity theory, and parallel execution via message-passing. The code provides both 8-noded and 20-noded solid elements, with a full complement of transition elements to bridge between the 8- and 20-noded elements in the same mesh. The 8-node element formulation uses the $\overline{B}$ methodology proposed by Hughes [*19*] to prevent mesh locking under fully plastic conditions. Solution for an applied increment of load follows in an iterative manner, using full Newton iterations to solve the nonlinear equilibrium equations. The code includes both iterative (conjugate gradient) and direct linear solvers; the direct sparse solver proved the most efficient for solution of the thin problems in this study.

Validation Procedures

Validation studies of the 3-D CTOA methodology described previously compare computational predictions of crack growth with a large dataset of tests on thin sheet 2024-T3 aluminum alloy. Conducted as part of the Aging Aircraft program at NASA-Langley, this testing program measures crack extension with applied load in a variety of specimen configurations. Table 1 summarizes the test matrix, which includes three material thicknesses (2.3, 1.6, and 1 mm), two specimen types (C(T) and M(T)), and a range of absolute sizes (50 to 150 mm for C(T), 75 to 1000 mm for M(T)). The tests also include specimens in both L-T and T-L orientations. This study focuses on tests of the 2.3-mm-thick specimens with the L-T orientation; a forthcoming publication describes a similar validation study using the 1.6-mm-thick specimens, also with L-T orientation [*15*]. Figure 5*b* shows the measured engineering stress-strain curve for the 2.3-mm-thick material as determined by tension tests. The testing protocol provides at least two tests for each configuration; the measured load-crack extension responses show excellent repeatability, with a maximum difference of 6% in peak load for identical configurations. For large M(T) specimens, the presence of the crack induces compressive stresses parallel to the crack plane (*T*-stress). These compressive stresses cause out-of-plane bending that reduces the failure (maximum supported) load by up to 24% in the 2.3-mm-thick specimens. Most of the tests employ a system of guide plates to minimize the out-of-plane deformation. Additional tests without guide plates for the M(T) specimens enable characterization of the bending effects on crack growth. Experimental data in the form of crack extension versus applied load records provide the basis for calibration/validation of the CTOA model. Additional information about the testing program is available in separate publication [*7,8*].

TABLE 1—*Matrix for NASA-Langley testing program for thin sheet Al 2024-T3.*

Thickness, mm	C(T), W (mm) $a/W = 0.4$	M(T), $2w$ (mm) $2a/2w = 0.333$	M(T), $2w$ (mm) $2a/2w = 0.42, 0.50$
2.3[c]	50.8, 101.6, 152.4	76.2, 304.8,[a] 609.6[a]	304.8[a]
1.6	152.4	76.2, 304.8,[a] 609.6,[a] 1016[a]	...
1.0[b]	152.4	76.2, 304.8	...

[a] Buckling allowed in test.

[b] Tests for this thickness also include 450-mm-diameter pressurized cylinders with 50-, 75-, and 100-mm cracks.

[c] Tests for this thickness also include 300-mm panels with multiple co-planar cracks.

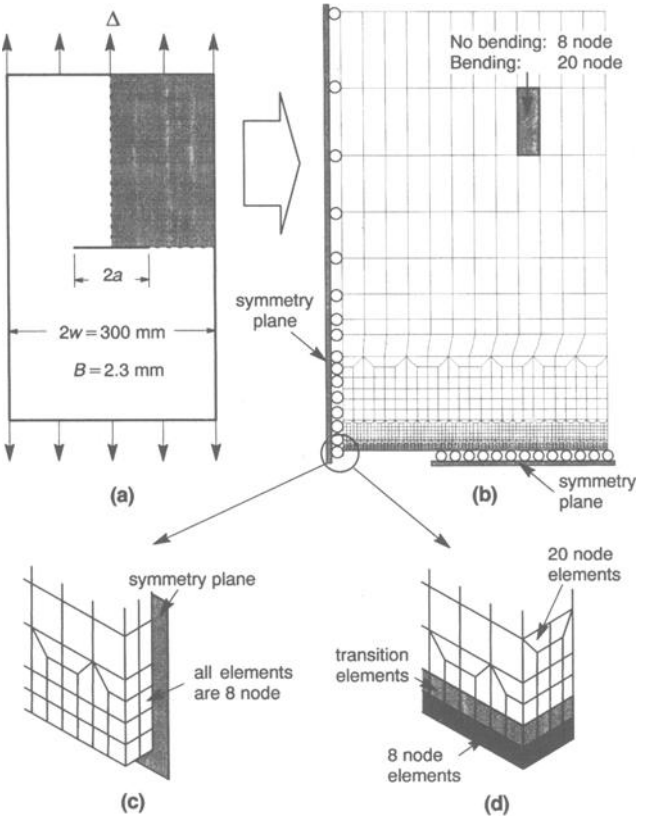

FIG. 6—*Typical mesh for 3-D CTOA analyses: M(T), 2w = 300 mm:* (a) *diagram of specimen;* (b) *quarter symmetric mesh for analyses with and without bending;* (c) *closeup of mesh without bending;* (d) *closeup of mesh with bending.*

The validation study of the 3-D CTOA model for the 2.3-mm-thick specimens proceeds as follows. The 3-D finite element model is calibrated to set the critical CTOA using the measured load-crack extension response for the 150-mm C(T) specimens with guide plates (constrained). Analyses of the remaining constrained C(T) and M(T) specimens employ the same critical CTOA. Comparisons of the load-crack extension response with the experimental results permit evaluation of the CTOA criterion for the constrained cases. In all the analyses, the CTOA is defined using L_c = 1 mm for consistency with previous studies [*6*]; this work does not explore the sensitivity of the predicted growth to L_c value. The analyses for each configuration use several meshes with increasing element density along the plane of crack growth, until additional mesh refinement yields no appreciable change in the response. Meshes for the constrained specimens are ⅛ symmetric models that employ all 8-node brick elements. Previous studies indicate that two elements through the half-thickness produce converged solutions [*20*]. Converged meshes require between 1300 to 5000 elements and use 500 load steps to generate the complete load-crack extension response measured in the tests. Figure 6 shows a typical mesh for the analyses with guide plates.

Additional analyses using the same calibrated CTOA value also predict the fracture behavior of the tests without guide plates (unconstrained). Meshes for the unconstrained models are ¼ symmetric. They utilize 20-node bricks (reduced integration) with one element through the thickness in regions outside

the crack front to capture out-of-plane bending (8-node bricks exhibit shear locking response in bending). To better model near-front conditions, 8-node elements with four elements through the thickness are defined along the crack plane. Transition elements serve to bridge between the crack plane elements and the remainder of the mesh. Analyses of the unconstrained tests use 4000 to 9400 elements and 500 to 800 load steps. Figure 6 shows a typical mesh for the unconstrained analyses. To trigger out-of-plane bending, meshes for the unconstrained specimens include an initial out-of-plane perturbation of the nodal coordinates that corresponds to the first buckling mode shape. Previous work indicates that perturbing the mesh with a buckling mode shape better captures the out-of-plane bending effect [*21*]. The maximum magnitude of the perturbation corresponds to 1% of the specimen thickness; parametric studies show a minor sensitivity of the response to the magnitude of the perturbation.

Results and Discussion

Calibration of the critical CTOA follows from matching the predicted with measured fracture behavior of the 150-mm C(T) specimen. Figure 7 shows the load versus crack extension results from the two experimental tests and from several analyses using different CTOA values. The experimental results have a small difference in failure (peak) load of 3.5%, allowing for a range of potential calibrated CTOA values. Given the difficulty of completely suppressing out-of-plane deformations in the tests, the small difference in the two tests may be due to limited buckling of the specimen having the lower resistance curve. The calibrated CTOA value is thus chosen to best match the upper curve. Each of the analyses uses 0.5-mm size elements (L_e = 0.5 mm) along the crack plane, providing two elements over the distance L_c used to define the CTOA. The analysis for an angle of 5.1° provides the best overall agreement with the test, yielding a failure load 1% lower than the experimental value. The analysis fails to match the early part of the response. Experimental studies indicate that steady crack growth, with a constant CTOA, does not occur until the crack grows a distance equivalent to one to two times the thickness of the specimen [*6*]. For this case, this distance roughly corresponds to the region where the maximum error in the analysis occurs. Figure 8 illustrates the effect of increasing mesh resolution along the crack plane using element sizes (L_e) of 1.0, 0.5, and 0.25 mm and a critical CTOA of 5.1°, along with the experimental results. The analyses with L_e = 0.5 mm and L_e

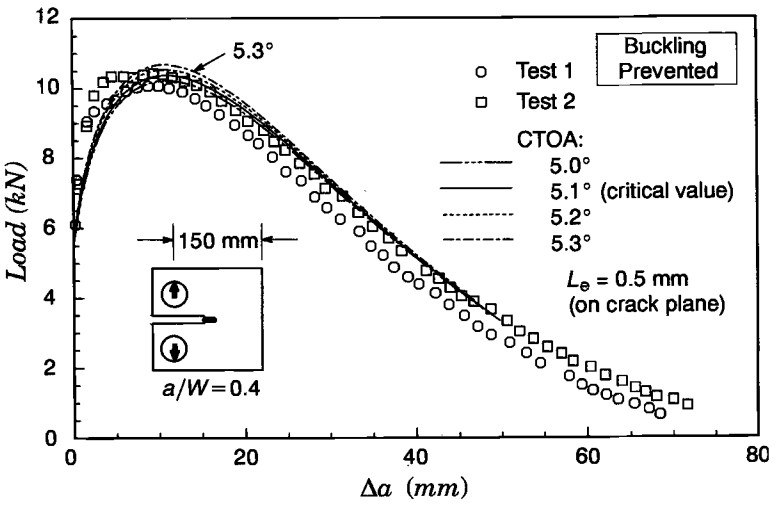

FIG. 7—*Load-crack extension response for constrained, 150-mm C(T),* a/W = *0.4. Curves are used to calibrate critical CTOA.*

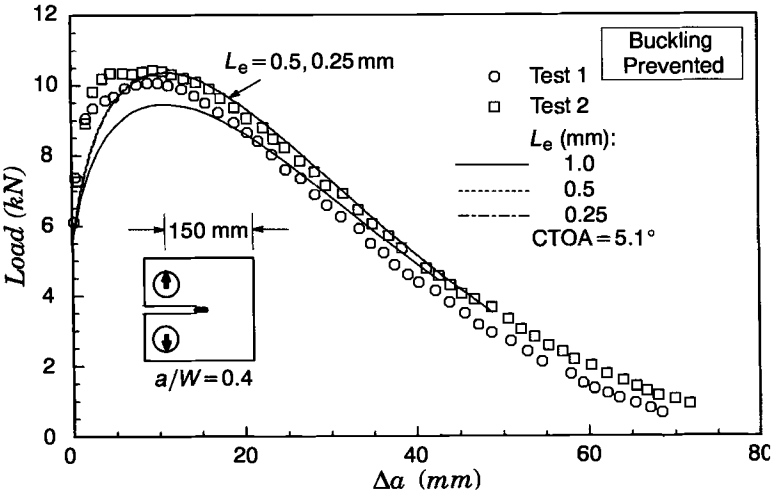

FIG. 8—*Element size effects on predicted load-crack growth response for constrained 150-mm C(T),* a/W = *0.4.*

= 0.25 mm produce nearly identical fracture behavior, indicating that the L_e = 0.5 mm analysis provides a converged solution for L_c = 1 mm.

Using 5.1° as the critical CTOA value for this material and thickness, additional analyses generate predictions for the 50- and 100-mm C(T) specimens, as well as the 75-, 300-, and 600-mm guide plate (constrained) M(T) tests. Table 2 compares the predicted failure (maximum) loads and measured experimental maximum loads for the C(T) tests. The analyses underpredict the 50- and 100-mm M(T) failure loads. Figures 9 and 10 show that in both of these cases the peak load occurs within the zone of transition from initiation of crack growth to steady growth, where a constant CTOA assumption becomes questionable. Despite the differences early in the response, the error in peak load prediction is 9 and 7% for the 50- and 100-mm C(T) specimens, respectively. Analysis of the 50-mm C(T) specimen requires 0.25-mm size elements (L_e) to reach a converged solution, while the 100-mm C(T) specimen requires 0.5-mm elements to reach convergence. The use of different angles for the initiation and continuation of crack growth may offer a simple approach to improve predictions of the initial tearing response. However, exploratory analyses performed early in this study indicate that specimen size and geometry have a strong effect on the initial CTOA value.

Predictions for the M(T) specimens show better agreement with experimental data. Table 3 compares the predicted failure loads with the experimental values. Figures 11–13 show the applied (remote) stress versus crack extension response and analysis predictions for each of the tests. The errors in predicted peak loads range from less than 1 to 4.4%, with an average error of 3%. All of the M(T)

TABLE 2—*Comparisons of predicted and measured peaks loads for constrained C(T) specimens* (a/W = *0.4).*

W, mm	Element Size, L_e, mm	Peak Load, WARP3D, kN	Peak Load, Experiment, kN	P_{WARP}/P_{EXP}
50	0.25	3.95	4.32	0.913
100	0.5	7.29	7.85	0.929
150	0.5	10.38	10.07/10.43	1.030/0.995

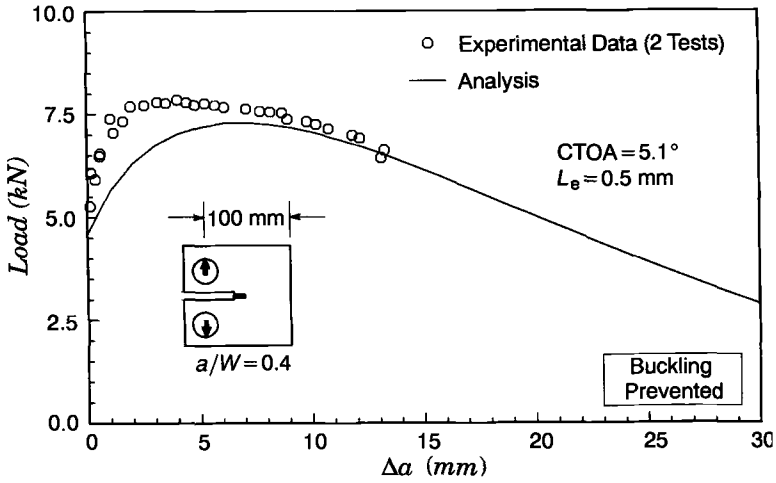

FIG. 9—*Predicted and measured load-crack growth response for constrained 100-mm C(T) specimen,* a/W = *0.4.*

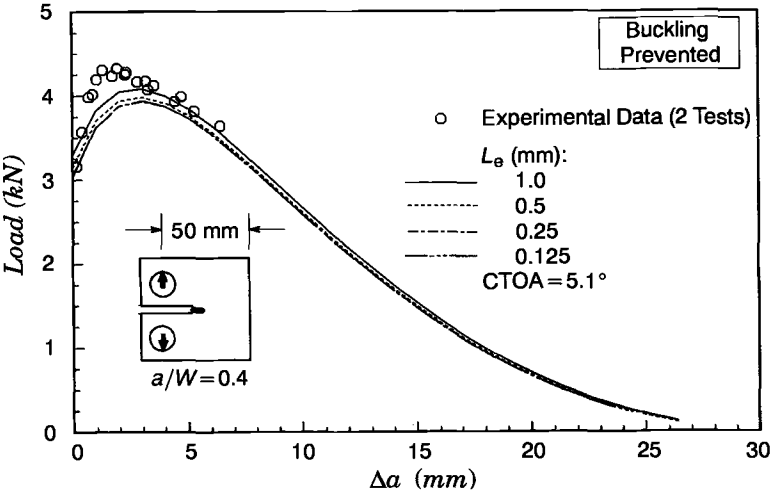

FIG. 10—*Predicted and measured load-crack growth response for constrained 50-mm C(T) specimen,* a/W = *0.4.*

TABLE 3—*Comparisons of predicted and measured peaks loads for constrained M(T) specimens.*

2*w*, mm	2*a*/2*w*	Peak Stress, WARP3D, MPa	Peak Stress, Experiment, MPa	P_{WARP}/P_{EXP}
75	0.33	229.6	239.9	0.957
300	0.33	210.6	215.34	0.978
300	0.42	184.5	190.7/186.0	0.967/0.992
300	0.50	156.5	160.8	0.973
600	0.33	202.8	194.3/197.2	1.044/1.029

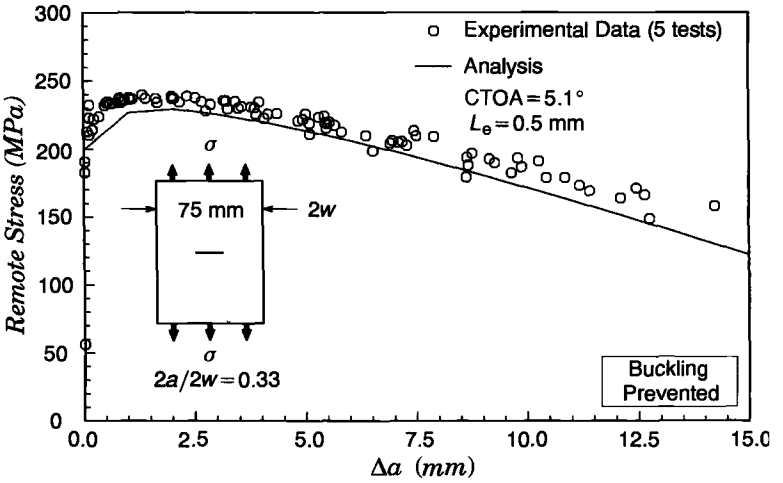

FIG. 11—*Predicted and measured load-crack growth response for constrained 75-mm M(T) specimen,* 2a/2w = *0.33.*

analyses reach convergence with 0.5-mm size elements (L_e) on the crack plane. The analyses underestimate the 75-mm M(T) peak load, underestimate the peak load slightly less on the 300-mm M(T) results, and overestimate the 600-mm specimen peak load. A possible cause for this trend is the failure to eliminate fully the out-of-plane displacements from the large panel tests. Since out-of-plane bending causes a significant reduction in peak load, any amount of such bending allowed by the guide plates lowers the corresponding resistance curve for the test. Some of the wide panel tests exhibited significant out-of-plane bending with the guide plates attached [*15*]. There also could be a slight dependence of the critical CTOA on absolute specimen width. However, the overall error appears sufficiently small to support use of the CTOA methodology for this range of specimen sizes.

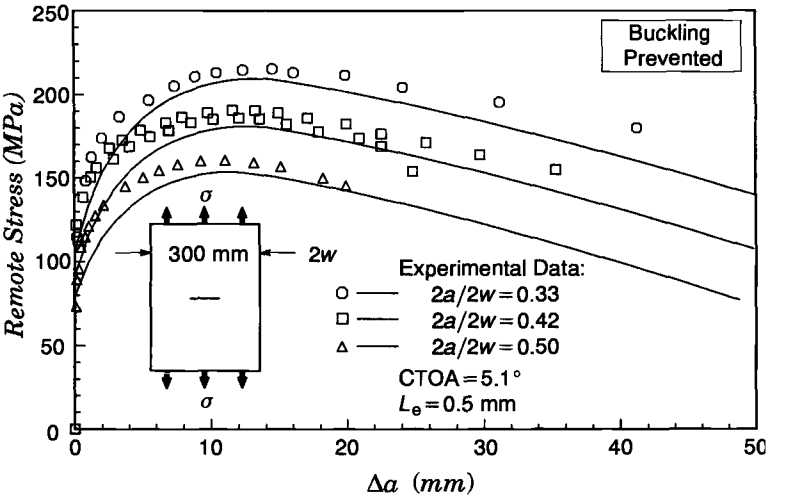

FIG. 12—*Predicted and measured load-crack growth response for constrained 300-mm M(T) specimens,* 2a/2w = *0.33, 0.42, 0.50.*

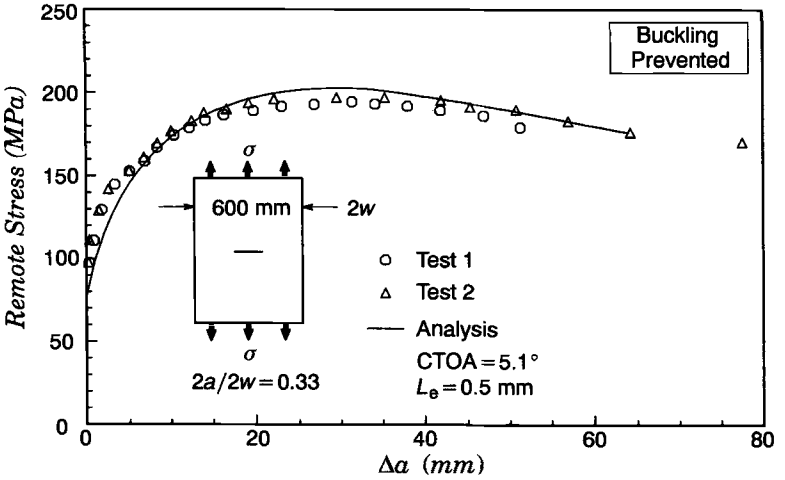

FIG. 13—*Predicted and measured load-crack growth response for constrained 600-mm M(T) specimen,* 2a/2w = *0.33.*

These results demonstrate that the CTOA-based growth model provides an effective engineering tool to predict ductile fracture behavior in thin specimens with constrained out-of-plane bending. Assessment of the applicability of the 3-D CTOA methodology to specimens that experience significant out-of-plane bending requires additional analyses. The testing program generated results for the $2w$ = 300-mm M(T) geometries and the $2w$ = 600-mm M(T) without guide plates. The specimens in these tests exhibit several centimeters of out-of-plane displacement and peak loads smaller by 10 to 25% compared to the constrained tests. To model these cases, the analyses use meshes with 20-node and 8-node solid elements. To verify the ability of such models to capture effectively the bending behavior, consider the instrumented test of a 600-mm M(T) specimen with a thickness of 1.6 mm conducted without guide plates [*22*]. The experiment conducted by Dawicke at NASA-Langley includes 4.8-mm holes at each crack tip to prevent crack extension under loading. A digital image correlation technique measured out-of-plane displacement of the specimen along a line parallel to the crack, 30 mm above the crack plane [*23*]. The analysis for this specimen has the same mesh as used for the unconstrained 600-mm M(T) test, with 0.5-mm elements (L_e) along the crack plane, but scaled to have a 1.6-mm thickness. An applied initial perturbation corresponding to the first buckled mode shape triggers the out-of-plane bending; the maximum value of the perturbation is 10% of the thickness, or 0.16 mm. Figure 14 compares the out-of-plane displacements at several applied loads for the experiment and the analysis. The out-of-plane displacements predicted by the analysis agree very well with the experimental results, indicating that the model used in this study is effective in capturing the correct bending behavior.

Table 4 compares the failure loads for the unconstrained tests and the corresponding analyses. Figure 15–16 show the applied load versus crack extension responses for the unconstrained tests. Analyses show that 0.5-mm elements (L_e) along the crack plane provide a converged prediction for the 300-mm M(T), $2a/2w$ = 0.33; all bending analyses use crack plane elements of that size. The analyses predict failure loads with errors ranging from 0.2 to 8.5% for the unconstrained M(T) tests. Again, these results display a trend observed in the constrained tests; the analyses increasingly overestimate the peak load with increasing specimen size. This trend may be due to slight dependence of the critical CTOA on specimen size. Nevertheless, the predictions and experimental results compare very well, indicating that the 3-D CTOA method described here shows significant promise as an engineering tool for assessing the fracture resistance of thin aluminum components.

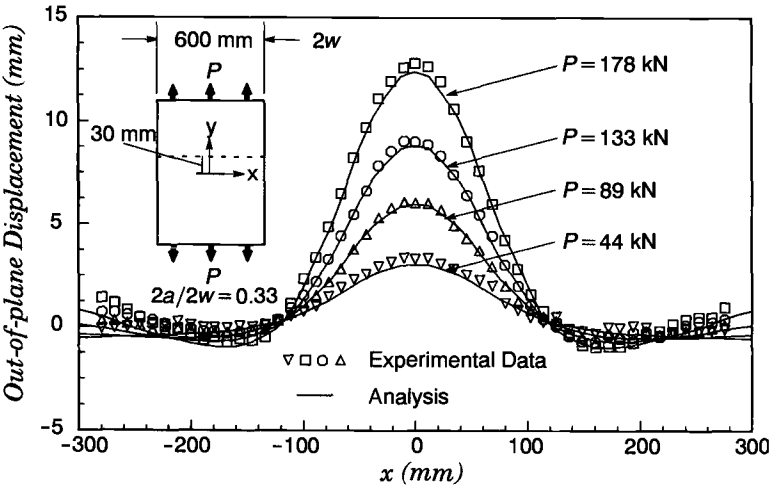

FIG. 14—*Comparison of predicted and measured out-of-plane displacements for unconstrained 600-mm M(T), thickness = 1.6 mm, 2a/2w = 0.33. Crack growth suppressed using blunt notch tips. Displacements measured 30 mm above crack plane as indicated.*

TABLE 4—*Comparisons of predicted and measured peaks loads for unconstrained M(T) specimens.*

2w, mm	2a/2w	Peak Stress, WARP3D, MPa	Peak Stress, Experiment, MPa	P_{WARP}/P_{EXP}
300	0.33	194.5	194.9	0.998
300	0.42	162.1	161.6	1.002
300	0.50	133.1	136.1/129.8	0.977/1.025
600	0.33	168.2	155.0	1.085

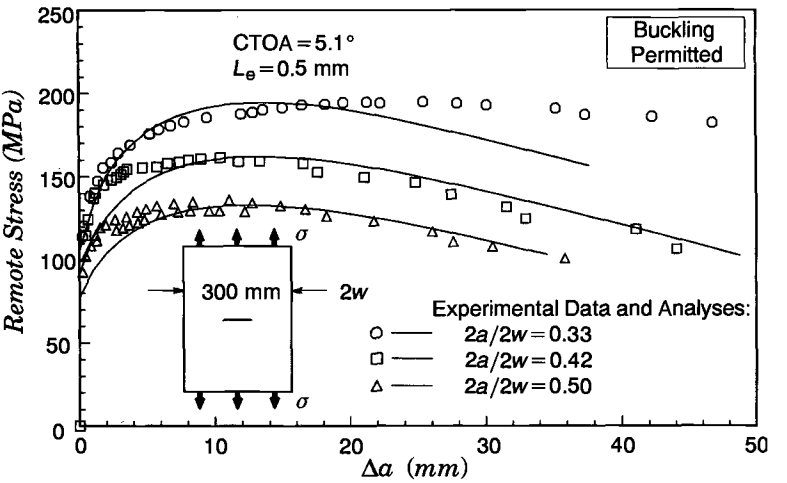

FIG. 15—*Predicted and measured load-crack growth response for unconstrained 300-mm M(T) specimens, 2a/2w = 0.33, 0.42, 1.50.*

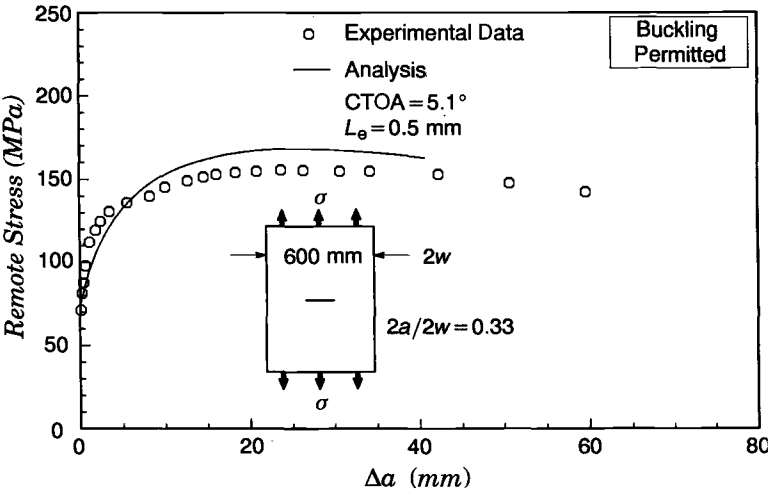

FIG. 16—*Predicted and measured load-crack growth response for unconstrained 600-mm M(T) specimens, 2a/2w = 0.33.*

Summary and Conclusions

This study describes an extension into a 3-D setting of the CTOA approach for finite element modeling of stable crack growth in thin ductile metals. The CTOA is defined at an analyst-specified distance (L_c) behind each crack front, thereby eliminating restrictions on the mesh refinement along the crack plane and enabling convergence studies to insure that crack growth predictions are not dependent on the mesh resolution. To eliminate dependence of predicted crack extension on computational load step size, this work introduces adaptive load control strategies and a traction-separation model for the reduction of release forces. Verification studies of the 3-D modeling strategy for crack growth use measured load-crack extension responses generated in a testing program on Al 2024-T3 conducted at NASA-Langley. The experimental program tested C(T) and M(T) specimens of 2.3-mm thickness over a range of absolute sizes and a/W ratios. The program includes a full set of tests with guide plates to constrain out-of-plane bending, and additional tests on large M(T) specimens with extensive out-of-plane bending. Calibration of the 3-D model using a 150-mm constrained C(T) specimen and L_c = 1 mm yields a critical CTOA value of 5.1°. Additional analyses use the calibrated CTOA value with L_c = 1 mm to predict failure load and load-Δa response for both constrained and unconstrained specimen.

This study provides several conclusions about the efficacy of the presented methodology for modelling crack growth in a thin, ductile fracture specimen:

- Use of a fixed value for L_c (distance behind crack tip to define CTOA) removes the dependence of predicted growth behavior and crack opening profile on mesh resolution.
- The newly developed adaptive load control algorithms and the traction-separation model for force release minimize the dependence of predicted growth behavior on the sizes of computational load steps.
- The calibrated CTOA value of 5.1° coupled with L_c = 1 mm enables predictions of the failure (maximum) loads for the constrained C(T) and M(T) specimens within 9% (worst case) of the experimental values. The analyses increasingly overpredict the failure load as specimen size increases. This may be due to either failure of the buckling guides to fully prevent out-of-plane displacements or a mild dependence of the critical CTOA on absolute specimen size.

- Analyses of the M(T) specimens that exhibit extensive out-of-plane bending predict out-of-plane displacements and load-crack extension responses that agree very well with experimental results.
- The 3-D CTOA mechanism based on uniform crack front extension holds significant promise to improve engineering models for prediction of crack growth in thin aluminum components.

Acknowledgments

This investigation was supported principally by grants from the NASA-Ames Research Center through Grant NAG2-1126, and through a Graduate Research Fellowship from the Office of Naval Research for the first author. This work was also supported by National Computational Science Alliance under Grant MSS970006N that made available computer resources on the NCSA SGI/CRAY Origin 2000. We also wish to thank Dr. Jim Newman, whose guidance and encouragement was vital to the success of this work.

References

[1] *Proceedings of the FAA-NASA Symposium on Continued Airworthiness of Aircraft Structures,* July 1997.

[2] *Proceedings from the Second Joint NASA/FAA/DoD Conference on Aging Aircraft,* Williamsburg, VA, 1998.

[3] Gurson, A. L., "Continuum Theory of Ductile Rupture by Void Nucleation and Growth: Part I—Yield Criteria and Flow Rules for Porous Ductile Media," *Journal of Engineering Materials and Technology,* Vol. 99, pp. 2–15.

[4] Tvergaard, V., "Material Failure by Void Growth to Coalescence," *Advances in Applied Mechanics,* Vol. 27, 1990, pp. 83–151.

[5] Xia, L. and Shih, C. F., "Ductile Crack Growth—I. A Numerical Study Using Computational Cells with Microstructurally-Based Length Scales," *Journal of the Mechanics and Physics of Solids,* Vol. 43, 1995, pp. 233–259.

[6] Dawicke, D. S., Newman, J. C., Jr., and Bigelow, C. A., "Three-Dimensional CTOA and Constraint Effects During Stable Tearing in a Thin-Sheet Material," *Fracture Mechanics: 26th Volume, ASTM STP 1256,* W. G. Reuter, J. H. Underwood, and J. C. Newman, Jr., Eds., American Society for Testing and Materials, Philadelphia, 1995, pp. 223–242.

[7] Dawicke, D. S. and Newman, J. C., Jr., "Residual Strength Predictions for Multiple Site Damage Cracking Using a Three-Dimensional Finite Element Analysis and a CTOA Criterion," submitted to *Fatigue and Fracture Mechanics: 29th Volume, ASTM STP 1321,* T. L. Panontin and S. D. Sheppard, Eds., American Society for Testing and Materials, 1998.

[8] Dawicke, D. S. and Newman, J. C., Jr., "Evaluation of Fracture Parameters for Prediction Residual Strength of Multi-Site Damage Cracking," *Proceedings from the First Joint NASA/FAA/DoD Conference on Aging Aircraft,* July 1997.

[9] Rice, J. R. and Sorensen, E. P., "Continuing Crack-Tip Deformation and Fracture for Plane-Strain Growth in Elastic-Plastic Solids," *Journal of the Mechanics and Physics of Solids,* Vol. 26, 1978, pp. 163–186.

[10] Sham, T. L., "A Finite-Element Study of the Asymptotic Near-Tip Fields for Mode I Plane-Strain Cracks Growing Stably in Elastic-Ideally Plastic Solids," *Elastic-Plastic Fracture: Second Symposium. Volume I—Inelastic Crack Analysis, ASTM STP 803,* C. F. Shih and J. P. Gudas, Eds., American Society for Testing Materials, 1983, pp. I-52–I-79.

[11] Sorensen, E. P., "A Numerical Investigation of Plane Strain Stable Crack Growth Under Small-Scale Yielding Conditions," *Elastic-Plastic Fracture, ASTM STP 668,* J. D. Landes, J. A. Begley, and G. A. Clarke, Eds., American Society for Testing and Materials, Philadelphia, 1979, pp. 151–174.

[12] Newman, J. C., Jr., "An Elastic-Plastic Finite Element Analysis of Crack Initiation, Stable Crack Growth, and Instability," *Fracture Mechanics: Fifteenth Symposium, ASTM STP 833,* R. J. Stanford, Ed., American Society for Testing and Materials, Philadelphia, 1984, pp. 93–117.

[13] Newman, J. C., Booth, B. C., and Shivakumar, K. N., "An Elastic-Plastic Finite-Element Analysis of the J-resistance Curve Using a CTOD Criterion," *Fracture Mechanics: Eighteenth Symposium, ASTM STP 945,* D. T. Read and R. P. Reed, Eds., American Society for Testing and Materials, Philadelphia, 1988, pp. 665–685.

[14] Shih, C. F., deLorenzi, H. G., and Andrews, W. R., "Studies on Crack Initiation and Stable Crack Growth," *Elastic-Plastic Fracture, ASTM STP 668,* J. D. Landes, J. A. Begley, and G. A. Clarke, Eds., American Society for Testing and Materials, 1979, pp. 65–120.

[15] Dawicke, D. S., Gullerud, A. S., Dodds, R. H., Jr., and Hampton, R. W., "Residual Strength Predictions with Crack Buckling," to appear in *Proceedings from the Second Joint NASA/FAA/DoD Conference on Aging Aircraft,* Williamsburg, VA, in press.

[16] Starnes, J. H., Jr. and Rose, C. A., "Stable Tearing and Buckling Responses of Unstiffened Aluminum Shells with Long Cracks," *The 2nd Joint NASA/FAA/DoD Conference on Aging Aircraft,* Williamsburg, VA, 1998.

[17] Young, R. D., Rouse, M., Ambur, D. R., and Starnes, J. H., Jr., "Residual Strength Pressure Tests and Nonlinear Analyses of Stringer- and Frame-Stiffened Aluminum Fuselage Panels with Longitudinal Cracks," *The 2nd Joint NASA/FAA/DoD Conference on Aging Aircraft,* Williamsburg, VA, 1998.

[18] Koppenhoefer, K., Gullerud, A., Ruggieri, C., Dodds, R., and Healy, B., "WARP3D: Dynamic Nonlinear Analysis of Solids Using a Preconditioned Conjugate Gradient Software Architecture," *Structural Research Series (SRS) 596,* UILU-ENG-94-2017, University of Illinois at Urbana-Champaign, 1994.

[19] Hughes, T. J. "Generalization of Selective Integration Procedures to Anisotropic and Nonlinear Media," *International Journal for Numerical Methods in Engineering,* Vol. 15, 1980, pp. 1413–1418.

[20] Dawicke, D. S., "Residual Strength Predictions Using a CTOA Criterion," DOT/FAA/AR-97/2, *Proceedings of the FAA-NASA Symposium on Continued Airworthiness of Aircraft Structures,* July 1997, pp. 555–566.

[21] ABAQUS, Hibbit, Karlsson and Sorensen, Inc., "Example Problems Manual: Volume I," Version 5.5, Section 3.2.12, 1995.

[22] Dawicke, D. S., private communication.

[23] Johnston, W. M. and Helm, J. D., "Experimental Results from the FAA/NASA Wide Panel Fracture Tests," to appear in *Proceedings from the Second Joint NASA/FAA/DoD Conference on Aging Aircraft,* Williamsburg, VA, in press.

Christian Thaulow,[1] *Zhiliang Zhang,*[2] *Øyvind Ranestad,*[3] *and Mons Hauge*[4]

J-Q-M Approach for Failure Assessment of Fusion Line Cracks: Two-Material and Three-Material Models

REFERENCE: Thaulow, C, Zhang, Z. L., Ranestad, Ø., and Hauge, M., **"*J-Q-M* Approach for Failure Assessment of Fusion Line Cracks: Two-Material and Three-Material Models,"** *Fatigue and Fracture Mechanics: 30th Volume, ASTM STP 1360,* P. C. Paris and K. L. Jerina, Eds., American Society for Testing and Materials, West Conshohocken, PA, 2000, pp. 102–114.

ABSTRACT: The theoretical background for the *J-Q-M* approach for quantifying the constraint in weldments for fusion line cracks is presented. In this model, *Q* quantifies the geometry effects and *M* the material mismatch effects. Initially the approach was developed for a two-material modified boundary level (MBL) model, but later was extended to include three materials: weld metal, heat-affected zone and base material, and more realistic specimen geometries. The analysis with MBL models showed that the effect of mismatch was rather independent of the *T*-stress for both bi- and tri-material models, indicating that *Q* and *M* could be treated independently. However, analysis of fracture mechanics tension specimens made of three materials revealed that the mismatch effect in some cases could depend on the geometry effects. New calculations have demonstrated that the dependence/independence is related to load level, ratio of mismatch, and the local geometry.

KEYWORDS: constraint, weldments, transferability, failure assessment, fusion line cracks, unstable fracture

Weldments are often the most critical part of a welded structure with regard to unstable fracture. Proper design and selection of materials are of vital importance to secure structural integrity. Current fabrication practice in industry adopts a weld metal strength overmatch (with respect to the base material) approach. The overmatch weld has the advantage of increasing the structural resistance in the case of shallow- and medium-sized cracks located in the weld metal. However, for cracks located in the HAZ it has been demonstrated that weld metal overmatch can have detrimental effects [*1–3*]. With the introduction of new high-strength structural steels, undermatched welds may be expected. The new steels have obtained their strength and toughness properties by advanced manufactoring processes, while the demand for increased strength in the weld metal has to be met by adding more alloying elements. Hence, the increased strength in the weld metal is obtained at the expense of weldability and toughness.

There is a need to quantify the effect of weld mismatch on fracture toughness and failure assessment. This has been the topic for the last 6–7 years, including two international symposia, "Mis-Matching in Welds," in 1993 and 1996, and the organization of a special sub-committee within the International Institute of Welding. Much of the work has, however, concentrated on cracks located in the middle of the welds, and the aim has been to indicate when the existing testing standards have to be modified to take the material mismatch effect into account.

[1] Professor, NTNU, N-7034 Trondheim, Norway.
[2] SINTEF, N-7034 Trondheim, Norway.
[3] Kværner Oil & Gas, N-1324 Lysaker, Norway.
[4] Statoil, N-7005 Trondheim, Norway.

FIG. 1—*Two constraints in a weldment: geometry constraint caused by crack size, specimen dimension and loading mode, and material mismatch constraint due to inhomogeneous material plastic properties.*

In order to derive a more complete understanding of the mismatch effect, models must be developed where the mismatch can be related to both the geometry effects (specimen geometry, crack size, crack location in the weldment, mode of loading) and material effects (yield strength, hardening exponent, local versus global mismatch). In 1993 *welding mechanics* was coined to identify this direction of research [*4*].

In this paper the recently developed *J-Q-M* approach for quantifying the constraint effects on the crack tip stress field is reviewed [*5–11,16–17*]. In the model, Q quantifies the geometry effect and M the material mismatch effect. Initially the approach was developed for a two-material modified boundary level (MBL) model, but has later been extended to include three materials: weld metal, heat-affected zone and base material, and more realistic specimen geometries, see Fig. 1. The theoretical development and the dependence between Q and M will be emphasized in the presentation.

Geometry Constraint

It has been observed for a long time that material fracture toughness is dependent on crack size, specimen dimension and loading mode, i.e., shallow cracks usually display better toughness than deep cracks. The factor that influences the transferability and invalidates the one-to-one relation between crack driving force J and the crack tip stress field is called *constraint.* For specimens made of homogeneous materials, the constraint is termed *geometry constraint.* It has been proposed in Refs *5–8* that the stress field at different levels of geometry constraint can be characterized by the *J-Q* theory, where J is the J integral and Q is a hydrostatic parameter that indicates the level of geometry constraint. According to the *J-Q* theory, the crack tip field deep inside the plastic zone can be separated into two parts. The first part is called reference field (σ_{ij}^{0}) that is still controlled by the J, or the one-to-one relation between the J and stress field is maintained in the reference field. Because the actual stress field is influenced by the constraint level at the crack tip, it will deviate from the reference field. The second part is called **difference field** ($\sigma_{ij}^{Diff\_Q}$) that is practically controlled by the hydrostatic parameter Q. The complete stress field can therefore be written:

$$\sigma_{ij} = \sigma_{ij}^{0}(J) + \sigma_{ij}^{Diff\_Q}(Q) \tag{1}$$

By carrying out detailed investigations using the modified boundary layer (MBL) model, O'Dowd and Shih [*5,6*] observed that the difference field for a wide range of constraint levels is relatively independent of both the normalized distance and angular position in the forward sector of the crack tip region ($|\theta| \leq \pi/2$), and the difference field for the shear stress is approximately zero. Furthermore, the two normal stress components of the difference field are approximately the same. Equation 1 is then simplified to the following form,

$$\sigma_{ij} \approx \sigma_{ij}^{0}(J) + Q\sigma_0\delta_{ij} \tag{2}$$

where δ_{ij} is the Kronecker delta, and σ_0 is the yield stress. Equation 2 shows that the difference field

caused by different levels of constraint can be approximated by a hydrostatic stress field and can be described by a single parameter Q. In the J-Q-M formulation [*11*], a more general approximation for the difference field that neglects the radial dependence but keeps the angular dependence has been used,

$$\sigma_{ij} = \sigma_{ij}^{Ref}(J) + Q\sigma_0 \tilde{f}_{ij}^{Q}(\theta) \tag{3}$$

where $\tilde{f}_{ij}^{Q}(\theta)$ are the normalized angular functions. Details for Eq 3 can be found in Ref *11*.

Material Mismatch Constraint

The material strength distribution in a real weldment is complicated, Fig. 1, and certain simplifications of the weldment crack problem are needed for basic examinations.

For a specimen made of inhomogeneous materials with an interface crack, the observed fracture toughness of a reference material is obviously influenced by the mismatch properties of the material on the other side of the interface. For materials with identical elastic properties, there are three types mismatch, strength mismatch, hardening mismatch, and both strength and hardening mismatch. Recently, extensive numerical studies have been carried out to investigate the effect of material mismatch constraint on the interface crack tip stress field of bi-material and tri-material boundary layer models [*9–18*]. Figure 2 shows the interface crack bi-material boundary layer model used for the investigation.

Material 1 is termed reference material, and Material 2 is termed mismatch material. The crack tip stress field for a given crack-driving force, J, was separated into two parts: one is a reference field of the reference material (σ_{ij}^{Ref}) controlled by J and a difference field due to the mismatch constraint. The radial and angular dependence of the difference field by material mismatch constraint has been thoroughly studied. It was found that the difference field is approximately independent of the normalized radial distance for a wide range of strength mismatch levels. The difference field is dependent on the angle. However, for each stress component, the angular dependence can be normalized by its corresponding amplitude, and the normalized angular functions depend only on the reference material, to a large extent independent of the mismatch material. Furthermore, the amplitudes of the normal stress components and the maximum principal stress are almost the same, while the absolute amplitude for the shear stress component is half of the one for the normal stress component. This finding indicates that the difference field of material mismatch constraint is self-similar and can be scaled by a mismatch constraint parameter M. M is defined as the amplitude of the difference field. Figure

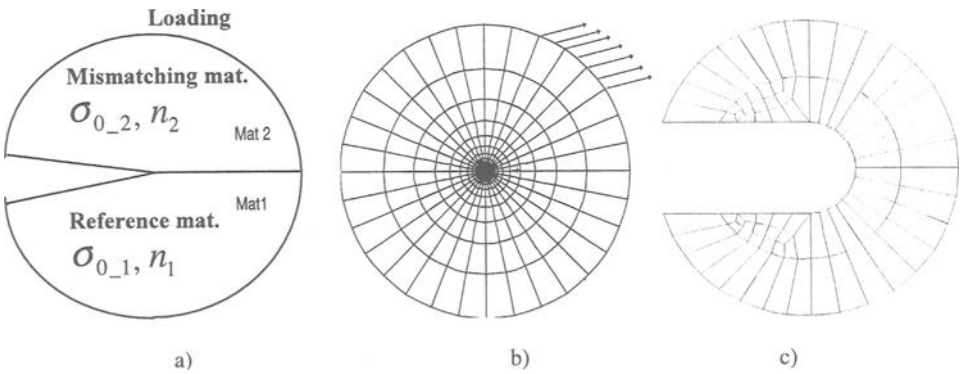

FIG. 2—(a) *Interface crack model used for deriving the* J-Q-M *formulation,* (b) *the global finite element mesh, and* (c) *mesh at the crack (initial small notch) tip.*

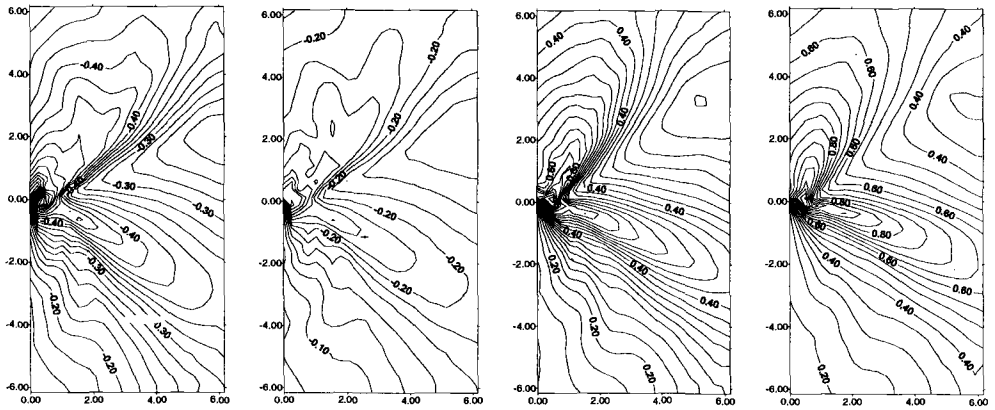

m=0.75 **m=0.85** **m=1.5** **m=2.0**

FIG. 3—*Self-similarity of the difference fields of the maximum principal stress at different mismatch levels* (m = $\sigma_{0\_2}/\sigma_{0\_1}$, *see Fig. 2). The number inside the figures indicates the level of the difference stress normalized by the yield stress. The horizontal and vertical co-ordinates represent the normalized distance from the crack tip.*

3 shows one example of the similarity of the difference field at different mismatch levels for materials with same elastic properties and strain-hardening exponent ($n = 0.2$).

Based on the above finding, a *J-M* formulation has been proposed [*9–11*]. According to the *J-M* theory, the interface crack tip field in a material system with identical elastic properties can be written:

$$\sigma_{ij} \approx \sigma_{ij}^{Ref}(J) + M\sigma_{0\_1}\tilde{f}_{ij}^{M}(\theta + 12\beta) \tag{4}$$

where $\beta = 0$ for mismatch ratio $m = \sigma_{0\_2}/\sigma_{0\_1} \geq 1$, and $\beta = 1$ for $m < 1$, σ_{0_1} is the yield stress of the reference material, and $\tilde{f}_{ij}^{M}$ represents the angular functions of the difference fields that depend only on the properties of the reference material. Equation 4 is valid for both the reference material and the mismatch material, but is most accurate for the reference material. Similar formulation has been obtained for an interface crack in a tri-material system [*16,17*].

Geometry Constraint and Material Mismatch Constraint

MBL Model

The *J-M* formulation, Eq 4, was obtained from the study of a boundary layer model, where the effect of geometry constraint was excluded. In a real weldment, both the geometry and material mismatch constraints are available. Numerical studies have been carried out to investigate the effect of the two constraints together on the crack tip stress field [*10,16*]. Modified boundary layer bi-material and tri-material models with varying values of T stress applied at the boundary, representing different levels of geometry constraint, have been analyzed. It is found that for a given material mismatch, the T stress shifts the near tip stress level of the interface crack up and down without significantly affecting the M. The results from the bi-material are presented in Fig. 4.

For the case of a tri-material system four yield strength combinations, with fixed hardening exponent $n = 0.07$, were compared together with the homogeneous reference solution (e.g., the whole specimen defined as HAZ material). For all T/σ_0 ratios and mismatch configurations, Q was calcu-

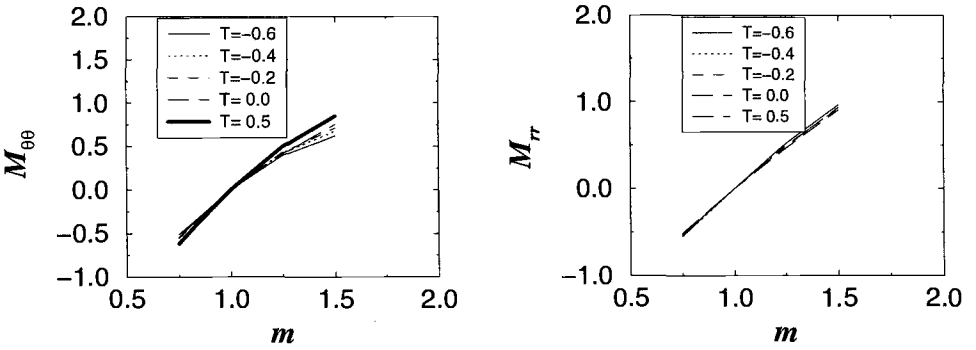

FIG. 4—*Effect of* T-*stress on the mismatch effect in angular and radial direction. Bi-material MBL model [11].*

lated as the difference between the maximum principal stress distribution for $T \neq 0$ and the corresponding distribution for $T = 0$ at the normalized distance $r = 2(J/\sigma_{0\_HAZ})$ close to the fusion line in the HAZ material. In Fig. 5 the calculations for the homogenous model (6-6-6) is compared with the mismatch cases. The results show that Q is very weakly dependent on the mismatch, confirming that the mismatch constraint and the geometry constraint can be separated in the MBL model. Based on these observations, a *J-Q-M* formulation is presented:

$$\sigma_{ij} \approx \sigma_{ij}^{M=0,T=0} + Q\sigma_{0\_1}\tilde{f}_{ij}^{Q}(\theta) + M\sigma_{0\_1}\tilde{f}_{ij}^{M}(\theta + 12\beta) \tag{5}$$

Equation 5 indicates that in the mixture of the two constraints the geometry constraint does not significantly disturb the difference field caused by material mismatch and the three parameter formulation can be used for describing the interface crack tip stress field.

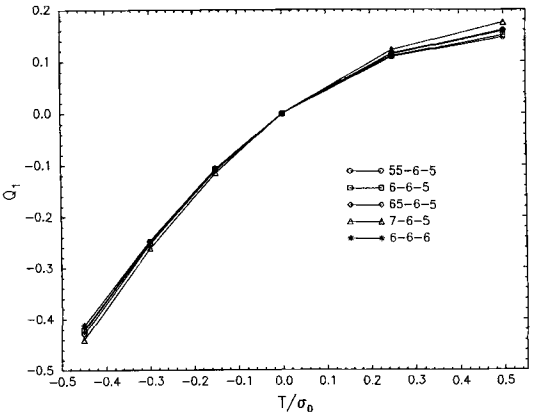

FIG. 5—*Mismatch effect on the* Q-T-*stress relation. Tri-material MBL model. The base material and HAZ have a constant yield stress of 500 and 600 MPa respectively, while the weld metal varies from 700 to 550 MPa [17].* Q_1 *means the* Q *calculated from the maximum stress. 55-6-5 in the legend means the combination of 550 MPa for weld metal, 600 MPa for HAZ, and 500 MPa for base metal, and so on.*

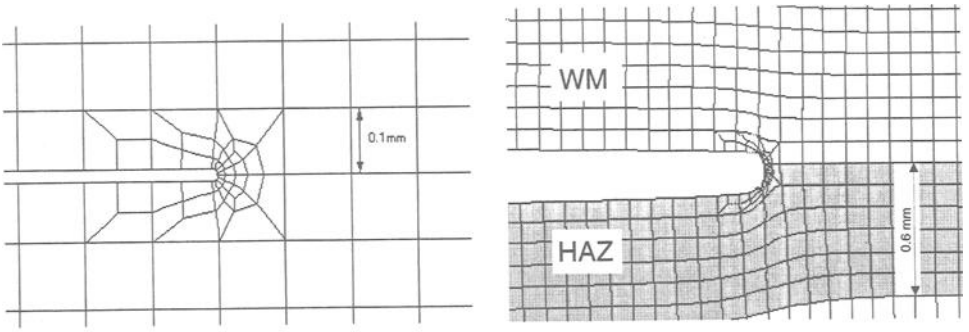

FIG. 6—*Finite element mesh at the crack tip* (a) *underformed and* (b) *deformed at* J = *200 N/mm for the SENT specimens [17].*

Fracture Mechanics Specimens

The MBL model is limited to small-scale yielding. Fracture mechanics test geometries have also been studied to investigate the effect of finite geometry and mode of loading on the mismatch stress fields. Two cases with 2D tri-material models have been re-examined:

- Wide plate in-tensile loading, $W = 70$ mm, $a/W = 0.1$ and 0.3, specimen geometry as shown in Fig. 1, and element mesh at the crack tip as shown in Fig. 2*c* [*14*]. The crack hits the fusion line under an angle.
- SENT specimens, $W = 26$ mm, $a/W = 0.17$ and 0.5; the element mesh is shown in Fig. 6. The crack is parallel with the fusion line.

The calculations in the case of wide plates are presented in Fig. 7. In Fig. 7 the $Q + M$ is calculated from the normalized differences of $\sigma_{\theta\theta}$ measured at $\theta = 2.37°$ (e.g., the integration points clos-

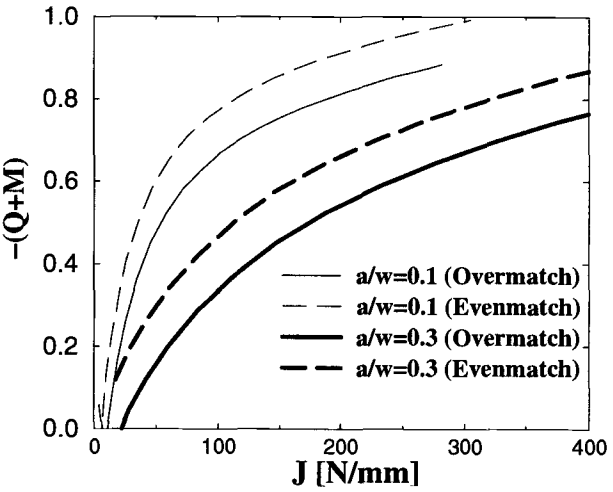

FIG. 7—Q + M *as a function of local over- and evenmatch at the crack tip. The yield strength of the base material and HAZ are 506 and 566 MPa, respectively, and the weld metal 643 and 566 MPa.*

est to the interface line, in this case located in the HAZ) at normalized distance $r = 2(J/\sigma_{0\_HAZ})$ are presented as a function of the applied crack tip loading for material over- and evenmatch and $a/W = 0.1$ and 0.3. It should be emphasized that in the calculation of the difference field, the HAZ material is the reference material. The geometry constraint shifts the level of the difference field, but the mismatch effect at a given geometry constraint is rather constant.

The change in total constraint $(Q + M)$ of the SENT specimens for four mismatch cases are presented in Fig. 8.

In this case the reference solution is the local evenmatch, 6-6-5. For each geometry the mismatch scales the constraint up or down rather independent of the crack tip loading.

After this rather qualitatively demonstration of the mismatch effect as a function of the crack tip loading for a given geometry, the next step was to replot the data in Figs. 7 and 8 to examine the mismatch effect in dependence of geometry, Fig. 9.

For each investigation the mismatch effect is rather independent of the geometry. The wide plate is also independent of the load level, while the mismatch effect for the SENT specimen decreases as the load is increased. This is caused by the effect of the finite size of the HAZ and weld metal zones. At low loads, yielding will be contained to the HAZ and weld metal, but after "break through" [3], the base material properties will dominate and the effect of local mismatch will decrease. The crack in the wide plate model, however, hits the interface fusion line between weld metal and HAZ at an angle, Fig. 1. The near-crack region will therefore be surrounded by more HAZ material than weld metal, and, more important, the plastic zone will include HAZ material as it develops and not constitute the "break through" observed in models where the crack is parallel to the fusion line.

The two investigations presented did not originally aim for an examination of the independence between Q and M. The wide plate model has a very fine mesh that gradually is coarsened and is well suited for detailed numerical analysis, while the SENT model has a regular mesh (mesh size 0.1 mm) over the crack tip region in order to model the different material zones.

In order to reach more definite conclusions, and include a bi-material model, it was necessary to develop new FE models and perform new calculations.

New Calculations

New SENT FE models were constructed, Fig. 10. The radial mesh arrangement from the wide plate has been rearranged in order to be able to define zones with specific material properties, e.g., weld metal, HAZ, and base material. In this way the preferred mesh can be combined with a crack-oriented parallel with the fusion line and a tri-material definition.

Small deformation formulation with eight-node elements and a reduced integration scheme in ABAQUS was used. Power law strain-hardening materials were assumed. For a material

$$\sigma_i = \sigma_{i0}\left(1 + \frac{\bar{\varepsilon}_i^p}{\varepsilon_{i0}}\right)^{n_i} \tag{6}$$

where σ_i is the flow stress, $\bar{\varepsilon}_i^p$ is the equivalent plastic strain, σ_{i0} is the yield stress, ε_{i0} is the yield strain $\varepsilon_{i0} = \sigma_{i0}/E$, and n_i is the strain-hardening exponent for material i.

The bi-material system examined has constant yield strength for the reference material (e.g., HAZ) of 400 MPa, while weld metal included 300, 400, 500, and 600 MPa, giving mismatch ratios from 0.75 to 2. For the tri-material system, the yield strength of the base material and HAZ was kept constant as 300 and 400 MPa, and the weld metal varied as for the bi-material case, resulting in the same local mismatch ratios. In all cases the hardening exponent was fixed at $n = 0.1$ in Eq 5. The geometry constraint was varied by changing the crack depths of a/W from 0.1, 0.3 to 0.5.

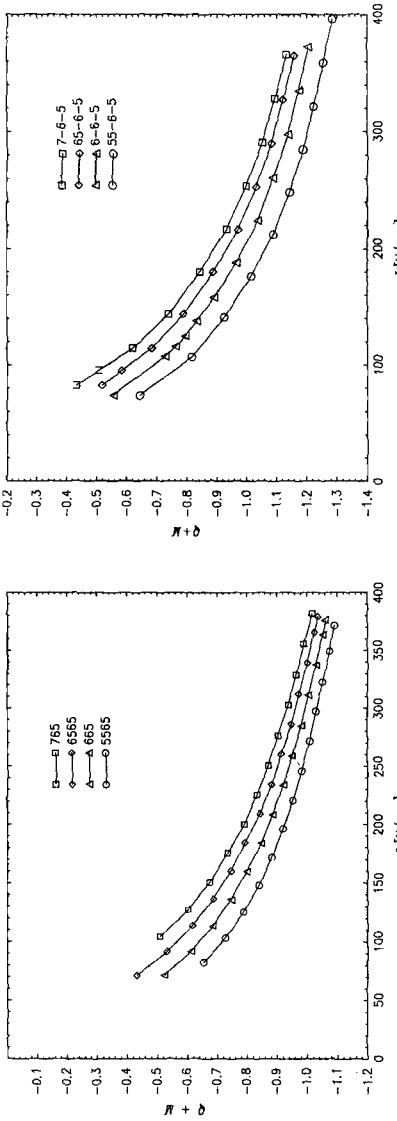

a) a/w=0.17 *b) a/w=0.5*

FIG. 8—*Loss of constraint for four cases of mismatch SENT specimens with a/W = 0.17 and 0.5. The base material and HAZ have a constant yield stress of 500 and 600 MPa, respectively, while the weld metal is varied from 700 to 550 MPa. 55-6-5 in the legend means the combination of 550 MPa for weld metal, 600 MPa for HAZ, and 500 MPa for base metal, and so on.*

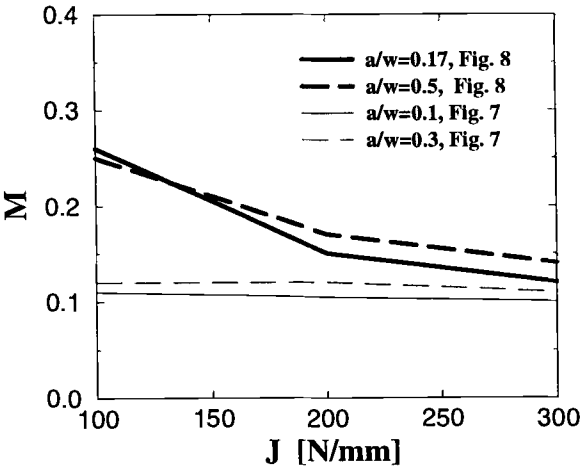

FIG. 9—*Mismatch effect,* M, *as a function of crack tip loading for the cases reported in Figs. 7 and 8. The results from Fig. 8 refer to the difference between the weld metal yield strength of 700 and 550 MPa. The bold lines are the results for SENT specimens, while the single lines are for wide plate specimens.*

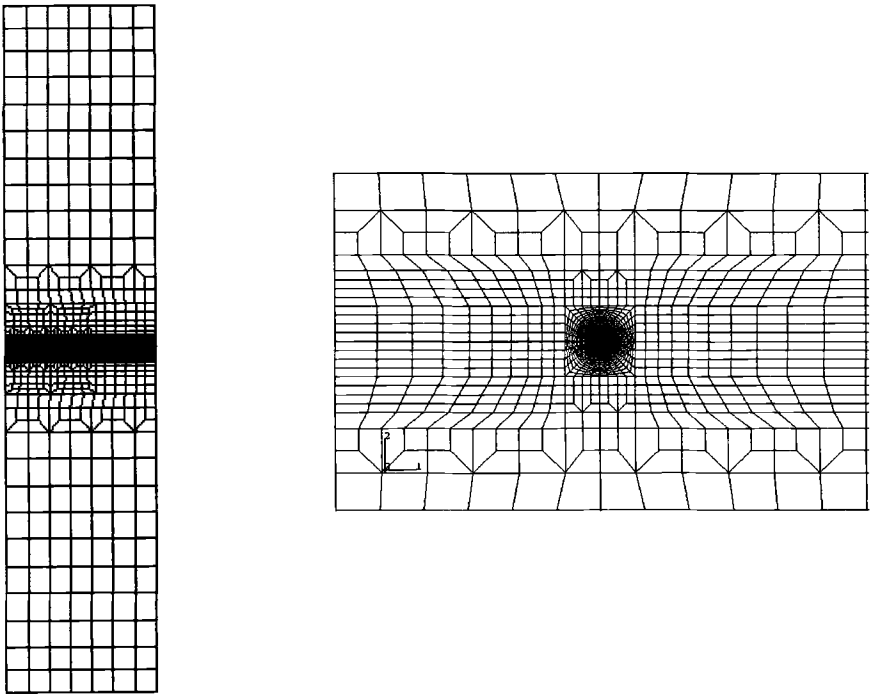

a) *b)*

FIG. 10—*Tri-material SENT specimen FE model for* a/w = *0.3,* (a) *global mesh and* (b) *local crack tip mesh arrangement.*

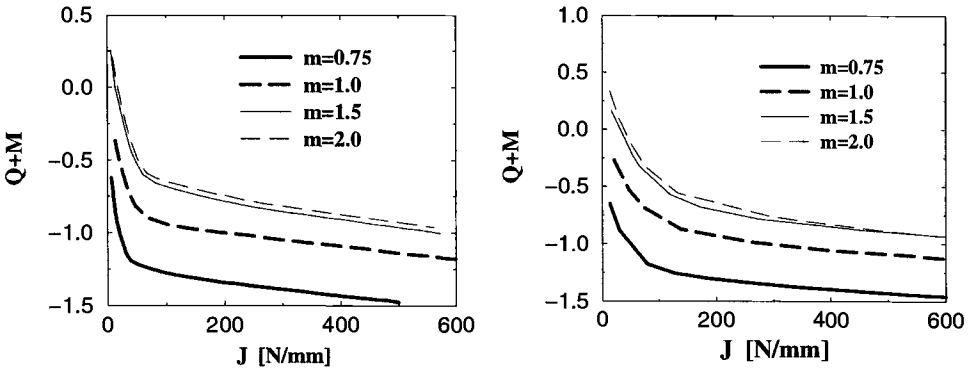

a) *b)*

FIG. 11—*Geometry and material constraint as a function of crack tip loading* (a) a/w = *0.1 and* (b) a/W = *0.3. Bi-material.*

Bi-Material

First the bi-material case was examined. The specimen was loaded in tension with $a/W = 0.1$ and 0.3 and mismatch ratios from 0.75 to 2, Fig. 11. It is demonstrated that the mismatch constraint is rather parallel with the homogeneous reference solution.

The effect of the mismatch constraint at a crack tip loading of $J = 200$ N/mm reveals no effect of the geometry constraint, Fig. 12.

The development of the mismatch constraint as a function of the crack tip loading is shown in Fig. 13. For the undermatch cases it is observed that for low J values the mismatch constraint will be more negative as the geometry constraint is increased. For the overmatch there is an opposite tendency with increased mismatch effect for the deepest crack, but the effect is small compared with the undermatch.

For both mismatch cases the shallow crack is most stable with respect to the homogenous solution as a function of J.

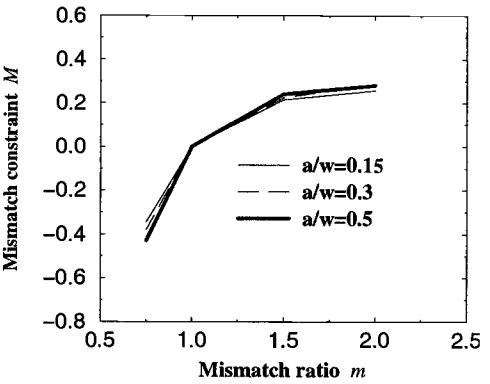

FIG. 12—*Mismatch constraint as a function of mismatch ratio for three crack depths. Crack tip loading* J = *200 N/mm.*

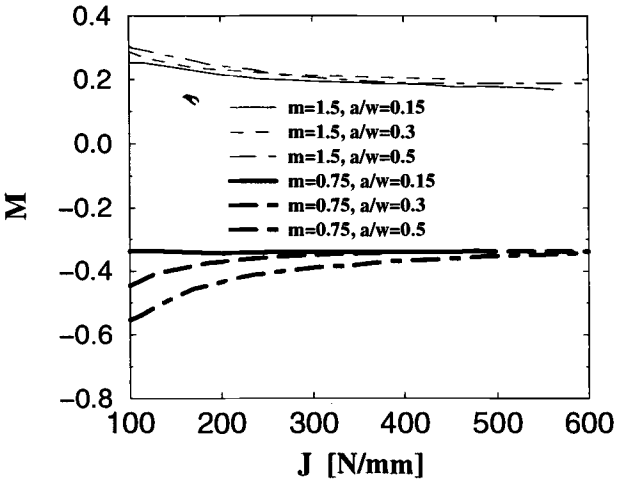

FIG. 13—*Mismatch constraint relative to homogenous specimen as a function of crack tip loading.*

Tri-Material

The development of $Q + M$ as a function of J for $a/W = 0.3$ reveals that the mismatch effect decreases with loss in geometry constraint, Fig. 14. This effect is caused by the "break through" as explained in the previous chapter.

The development of the mismatch constraint as a function of the crack tip loading for two mismatch cases and three crack depths is shown in Fig. 15. The tendencies are the same as observed for the bi-material, Fig. 13, but the independence of Q is reached at lower J. It can also be observed for the case of undermatch that the mismatch constraint is lower (e.g., less negative) for the tri-material than the bi-material case.

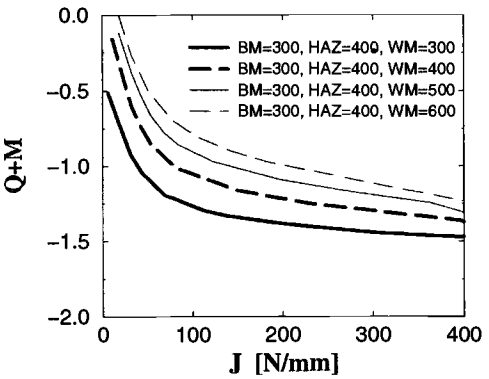

FIG. 14—*Geometry and material constraint as a function of crack tip loading for* a/W *= 0.3. Tri-material model.*

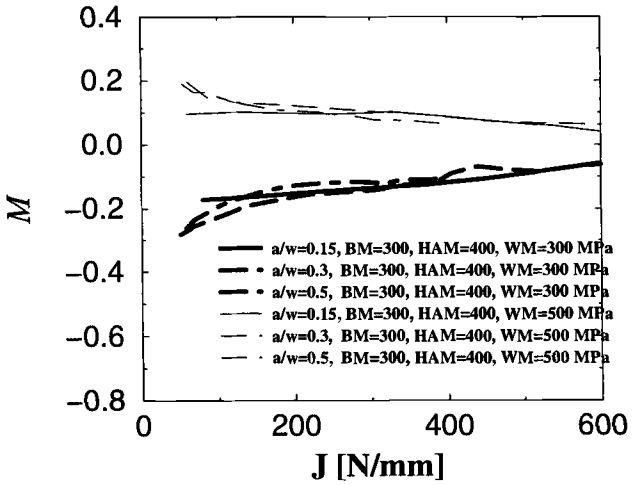

FIG. 15—*Mismatch constraint relative to local evenmatch as a function of crack tip loading. The mismatch ratios plotted are 0.75 and 1.25.*

Discussion

The aim with the analysis was to examine the dependence between geometry- and material constraint related to the *J-Q-M* theory. This theory is based mainly upon observations from FE calculations of so-called self-similarity in the crack tip stress fields and does not rely on exact analytical solutions. Hence, the definition of dependence must also be related to the accuracy of the theory itself. In Eqs 3 and 4 normalized angular functions have been introduced to shift the stress field. For the mismatch case a distinction is made between under- and overmatch.

In small-scale yielding, represented by the MBL models, the tri-material calculations demonstrated almost independence between the Q and M, Fig. 5, while some dependence is observed in the case of bi-material, Fig. 4. This trend is consistent with the new calculations, where the most pronounced dependence between Q and M was found for the bi-material, Fig. 13. The reason for this trend has not been investigated so far, but the first step will be to consider the basic theory again, as described above.

Except for the case of bi-material undermatch, Fig. 15, it can be concluded that in an engineering sense, the effect of material mismatch can be independently added to the geometry constraint. The effect of "break through" and the geometry in the vicinity of the crack tip must, however, be born in mind.

Conclusions

A rather good independence between the geometry constraint and the material mismatch constraint has been demonstrated. The best independence was obtained for tri-material models, representing the weld metal, HAZ, and base material. For models with the crack oriented parallel with the fusion line, the mismatch constraint in the case of overmatch decreased as the load was increased, while for the models with an angle between the crack tip and the fusion line, independence was maintained during loading. This is caused by the effect of the finite size of the HAZ and weld metal zones and the development of the plastic zones.

The calculations have been limited to tensile loading and the equal-hardening exponent for all materials. Both the effect of bending and hardening mismatch needs to be explored before the *J-Q-M* framework can be simplified for practical engineering use.

References

[1] Minami, F., Toyoda, M., Thaulow, C., and Hauge, M., "Effect of Strength Mis-Match on Fracture Mechanical Behaviour of HAZ-Notched Weld Joint," *Proceedings of the 2nd Workshop on Constraint Effects on the Structural Performance of Welded Joints,* Osaka, Japan, 1994.

[2] Toyoda, M., Minami, F., Ruggieri, C., Thaulow, C., and Hauge, M., "Fracture Property of HAZ-Notched Weld Joint with Mechanical Mis-Matching—Part I. Analysis of Strength Mis-Matching of Welds on Fracture Initiation Resistance of HAZ-Notched Joint," *Mismatching of Welds,* ESIS 17, K.-H. Schwalbe and M. Kocak, Eds., Mechanical Engineering Publications, London, 1994, pp. 399–415.

[3] Thaulow, C., Paauw, A. J., Hauge, M., Toyoda, M., and Minami, F., "Fracture Property of HAZ-Notched Weld Joint with Mechanical Mis-Matching—Part II. Effect of Local Mechanical Mis-Matching on Fracture Initiation in Steel Weldment," *Mismatching of Welds,* ESIS 17 K.-H. Schwalbe and M. Kocak, Eds., Mechanical Engineering Publications, London, 1994, pp. 417–432.

[4] Toyoda, M., Thaulow, C., and Blauel, J. G., "Strength Mis-Matching and Its Influence on the Performance of Welded Structures," *Mis-Matching of Welds,* ESIS Publ. 17, K.-H. Schwalbe and M. Kocak, Eds., 1994, pp. 335–350.

[5] O'Dowd, N. P. and Shih, C. F., "Family of Crack-Tip Fields Characterised by a Triaxility Parameter: Part I—Structure of Fields. *J. Mech. Phys. Solids,* Vol. 39, 1991, pp. 989–1015.

[6] O'Dowd, N. P. and Shih, C. F., "Family of Crack Tip Fields Characterised by a Triaxility Parameter—Part II. Fracture Applications," *J. Mech. Phys. Solids,* Vol. 40, 1992, pp. 939–963.

[7] Dodds, R. H., Shih, C. F., and Anderson, T. L., "Continuum and Micro-Mechanics Treatment of Constraint in Fracture," *International Journal of Fracture,* Vol. 64, 1993, pp. 101–133.

[8] Dodds, R. H., Anderson, T. L., and Kirk, M. T., "A Framework to Correlate a/w Ratio Effects on Elastic-Plastic Fracture Toughness (Jc)," *International Journal of Fracture,* Vol. 48, 1991, pp. 1–22.

[9] Zhang, Z. L., Hauge, M., and Thaulow, C., "Two-Parameter Characterisation of the Near Tip Stress Fields for a Bi-Material Elastic-Plastic Interface Crack," *International Journal of Fracture,* Vol. 79, 1996, pp. 65–83.

[10] Zhang, Z. L., Hauge, M., and Thaulow, C., "Assessment of Material Mismatch Constraint in a Bi-Material Elastic Plastic Interface Crack," *Proceedings of the International Symposium on Mismatching of Welds, Luneburg, Germany,* 1996.

[11] Zhang, Z. L., Hauge, M., and Thaulow, C., "The Effect of T Stress on the Near Tip Stress Field of an Elastic-Plastic Interface Crack," *Proceedings of the 9th International Conference on Fracture,* Sydney, 1–5 April 1997, B. L. Karihaloo, Y.-W. Mai, M. I. Ripley, and R. O. Ritchie, Eds., pp. 2643–2650.

[12] Thaulow, C, Hauge, M., and Zhang, Z. L., "Transferability of Fracture Mechanics Test Results of Weldments to Structure Behaviour; Application of the J-Q-M Approach," *Proceedings of the International Symposium on Safety in Application of High Strength Steel,* Trondheim, Norway, 1–2 July 1997.

[13] Hauge, M. and Nyhus, B., "Geometry and Mismatch Constraint in Engineering Fracture Assessment," *Proceedings of the International Symposium on Safety in Application of High Strength Steel,* Trondheim, Norway, 1–2 July 1997.

[14] Zhang, Z. L., Thaulow, C., and Hauge, M., "Effects of Crack Size and Weld Metal Mismatch on the HAZ Cleavage Toughness of Wide Plates," *Engineering Fracture Mechanics,* Vol. 57, No. 6, 1997, pp. 653–664.

[15] Zhang, Z. L., Thaulow, C., and Hauge, M., "On the Constraint Effects in HAZ-Cracked Wide Plate Specimens," *Proceedings of the International Symposium on Mismatching of Welds, Luneburg, Germany,* 1996.

[16] Ranestad, Ø., Zhang, Z. L., and Thaulow, C., "Quantification of Mismatch Constraint for an Interface Crack in an Elastic Plastic Tri-Material System," *Proceedings of the International Symposium on Mismatching of Welds, Luneburg, Germany,* 1996.

[17] Ranestad, Ø., Zhang, Z. L., and Thaulow, C., "Two-Parameter (J-M) Description of Crack-Tip Stress-Fields for an Idealised Weldment in Small Scale Yielding," submitted to *International Journal of Fracture.*

[18] Thaulow, C., Hauge, M., Zhang, Z. L., Burget, W., and Memhard, D., "Constraint Effects on Crack Tip Stress Fields for Cracks Located at the Fusion Line of Weldments," *Computational Materials Science,* Vol. 15, 1999; pp. 275–284.

Dennis M. Lambert[1] *and Hugo A. Ernst*[2]

Fracture Mechanics Validity Limits and Physical Evidence of Constraint in Fracture

REFERENCE: Lambert, D. M. and Ernst, H. A., **"Fracture Mechanics Validity Limits and Physical Evidence of Constraint in Fracture,"** *Fatigue and Fracture Mechanics: 30th Volume, ASTM STP 1360,* P. C. Paris and K. L. Jerina, Eds., American Society for Testing and Materials, West Conshohocken, PA, 2000, pp. 115–138.

ABSTRACT: The consideration of fracture behavior should be a matter of vital concern in current design efforts. Many materials exhibit grossly different behavior when discontinuities are present in the structure. These may be inherent in the material or may stem from poor manufacturing, handling, and/or design practices. Inclusion of fracture behavior in the design models is the subject of fracture mechanics. Ultimately, a knowledge of fatigue and fracture becomes very important in avoiding disaster.

This paper is written with two primary purposes: to characterize the physical nature of fracture, and to dramatize the need to characterize the central flat fracture differently from the surface, shear fracture. To this end, the contents of the paper are organized as follows: (1) validity limits of fracture mechanics: this information was originally developed for the purpose of extracting similar fracture data and will be used here to help characterize bulk constraint effects and to establish the existence of the surface effect; (2) analysis of crack face displacements of planar specimens subjected to loads: this includes actual crack-, separation-, and stretch-profiles; and (3) consideration of three-dimensional fracture in light of the existence of two distinct fracture zones that exhibit different failure mechanisms; for this purpose, G and J as a function of depth below surface are discussed, as well as several constraint factors as a function of depth.

KEYWORDS: EPFM, fracture, fracture mechanics, constraint, COD, CTOD, displacement-based fracture characterization, J-integral, modified J-integral, metals

Nomenclature

a,b,B,W	Specimen dimensions: the crack length, remaining ligament length, and remaining ligament thickness, and overall width in the direction of crack growth, respectively
a_o, b_o	Initial crack length and remaining ligament, respectively
C	Unloading compliance, i.e., the linear rate of change of displacement for a change of load
CT or CCT	Specimen configurations used to evaluate fracture behavior: specifically, compact tension, center-cracked tension, respectively
CTOD	Crack tip opening displacement
G	Griffith's G, the energy release rate for crack formation, assumes linear elastic material behavior
J	Rice's J-integral, the energy release rate for crack formation, assumes nonlinear elastic material behavior

[1] Assistant professor of Engineering Studies, Georgia Southern University, Statesboro, GA 30460-8047.
[2] Head, Mechanical Technology Department, Center for Industrial Research, Techint Organization, Buenos Aires, Argentina.

J_{Ic}	Value of J at crack initiation under plane strain conditions
J_{el}	The elastic component of J: $J_{el} = G$
J_{pl}	The nonlinear (plastic) component of J
K	Stress intensity factor
P, P_o, P_{max}	Load, limit load, and maximum load observed, respectively
v	Load-line displacement
v_{el}	Linear component of v, arising if load-versus-displacement is nonlinear
v_{pl}	Deviation of displacement from linearity
Δ	Change of the variable that follows the symbol, e.g., Δa is the change in the crack length (from the initial value), i.e., crack growth
ρ	Estimate of plastic zone size
ρ_J	Dimensionless parameter relating CTOD to the initial remaining ligament length
σ_o	Flow stress: $\sigma_o = (\sigma_y + \sigma_u)/2$, a convenient material property derived from an assumption of perfectly plastic behavior
σ_u	Ultimate tensile strength, a material property
σ_y	Yield strength, a material property
ω	Estimate of the size of the zone of nonproportionality

Subscripting

"el"	Component of the subscripted parameter that follows linear behavior
"o"	Indicates initial quantities of the subscripted parameter (with exception of σ_o)
"pl"	Component of subscripted parameter that is the deviation from linear behavior: the use of pl is to imply that the behavior is plastic, i.e., nonconservative
"AL" or "IN"	aluminum or nickel, respectively

Introduction

Structural safety and reliability have always been matters of vital concern to the aerospace industry as well as other manufacturers, and fracture mechanics has been especially useful in providing a quantitative description of the capability of structural parts to tolerate flaws. An evolution of fracture parameters has occurred, allowing the evaluation of the new structural materials being used. The first attempts at fracture mechanics characterization of materials imposed quasi-linear elastic conditions (LEFM), a restriction that is rare in practical structural materials. The parameters developed for use in the LEFM technology, G and K, are only effective as fracture-predicting tools as long as the material responds in a linear elastic manner. This has been shown to occur when the plastic zone present at the tip of the crack is much smaller than the ligament dimensions. This was been expressed as follows [*1*]:

$$\rho \equiv \frac{\pi}{8}\left(\frac{K}{\sigma_o}\right)^2 \ll B, b, a \tag{1}$$

Equation 1 gives an estimate of the plastic zone size, ρ; σ_o is the flow stress, and a, b, and B are specimen dimensions. The parameter, ρ, must be small versus the specimen dimensions for K to be valid.

The original fracture mechanics approaches were adapted to allow solution in cases where plasticity was more widespread and not confined to a small region of the fracturing object. To consider this more realistic class of structures and materials, elastic-plastic fracture mechanics (EPFM) methods were developed. Rice's J-integral [*16*] required an assumption of non-linear elasticity: this restriction to elastic behavior also produced a limitation in the range of applicability of the J parameter. Nonlinear elasticity does not faithfully represent actual structural material behavior, where energy is dissipated and permanent deformation occurs. The elasticity assumption may still be acceptable as long

as unloading is avoided. The requirements for J-control include small crack tip displacement (CTOD), proportional loading, and small crack extension. These are given by Eqs 2 and 3, below:

$$\rho_J \approx \frac{b_o}{\text{CTOD}} = \frac{b_o \sigma_o}{J} \gg 1 \tag{2}$$

$$\Delta a \leq 0.1 \times b_o \tag{3}$$

In the equations, ρ_J is the dimensionless parameter associated with crack tip displacement, b_o is the initial remaining ligament, and Δa is the length the crack has extended. The limitation of crack extension was established to avoid crack growth to the point that the constraint environment controlling fracture changed. Constraint as used here means the degree of triaxiality of the stress field. A minimum value of $\rho_J \geq 20$ to 25 is generally accepted to be the limit of J-controlled behavior.

Other limits of J exist. Though crack growth causes unloading and pronounces the permanent deformation behavior, the deviation from nonlinear elasticity can be kept to an acceptable level if certain limits are held. The ω-parameter was defined [*14*] that evaluated the degree of non-proportionality. The significance of this was that some unloading could be tolerated while using J within the limits of the ω criterion as:

$$\omega \equiv \frac{b}{D} = \frac{b}{J_{\text{Ic}}} \frac{dJ}{da} \gg 1 \tag{4}$$

In Eq 4, b is the current remaining ligament length, D defines the area associated with non-proportional loading, J_{Ic} is the value of J at crack growth initiation under plane strain conditions, and dJ/da is the slope of the JR-curve, i.e., a plot of the resistance to fracture, J, versus crack extension, Δa.

The J-integral was later modified [*2*] to overcome a difficulty associated with the use of J as a fracture parameter, i.e., the time-rate of change of an appropriate fracture parameter could not be a function of the time-rate of crack growth [*17*]. The *modified J* parameter (J_M) of Ernst was formed by a decomposition of J into two parts, one associated with the evolution of plasticity and one associated with the advance of the crack (as shown in Eqs 5a to 5c).

$$J = G + J_{\text{pl}}(v_{\text{pl}}, a) \tag{5a}$$

$$J = \left[G + \int \frac{\partial J_{\text{pl}}}{\partial v_{\text{pl}}}\bigg|_a dv_{\text{pl}} \right] + \int \frac{\partial J_{\text{pl}}}{\partial a}\bigg|_{v_{\text{pl}}} da \tag{5b}$$

$$J_M = J - \int \frac{\partial J_{\text{pl}}}{\partial a}\bigg|_{v_{\text{pl}}} da \tag{5c}$$

In the equations, the subscript "pl" indicates the nonlinear component of the variable; G and J_{pl} are the linear and nonlinear portions of J, respectively; v is the load-line displacement; and a is the crack length. The last term in Eq 5b was discarded in the J_M formulation of Eq 5c, removing the crack rate functionality. This modification may seem somewhat arbitrary, but it is reasonable that a parameter that correctly reflects fracture should not include the historic details of the change of the parameter as the crack grew to the current configuration.

J_M assumes real plasticity and follows the actual, irreversible process, with the change in plastic displacement always greater than or equal to zero, i.e., $dv_{\text{pl}} \geq 0$ [*6*]. Whereas J_{pl} is the area between two "calibration" (i.e., non-growing crack) curves (load-versus-plastic displacement) of two specimens that are identical except for infinitesimally different crack lengths, $J_{M,\text{pl}}$ was defined as the change in area between the load-versus-plastic displacement curves of these two specimens with

growing cracks where an infinitesimal difference in the crack length is always maintained. J_M meets the Rice criterion and includes some of the irreversibility of the fracture event. This allows fracture characterization to a much greater extent of crack growth. J_M appeared to correlate fracture data to a much higher degree: what are the limitations of J_M, though? This has been suggested to be at a crack extension of about 40% of the initial remaining ligament length. None of the various fracture parameters can be expected to describe fracture in an environment of gross plasticity, in which case the process is better described by deformation parameters, e.g., stress and strain. In the current study, various schemes to identify the onset of this plasticity-dominated behavior, i.e., the end of fracture mechanics validity, are presented. Each validity limit parameter is developed in detail, and then data are presented and the various schemes for establishing a limit of the validity are compared. The selected limiting parameter is applied to a set of fracture data showing the improvement of correlation gained.

The study of validity limits provides insight into the evolution of both the fracture event and the prevailing constraint, and this paper will further develop this theme regarding the evolution of the constraint as evidenced in physical crack measurements of planar specimens. Many have attempted to develop a displacement-based fracture resistance curve [*10,8,19*], and these have produced some success. The methods stem from the theoretically derived proportionality between energy-related parameters, such as G or J, and crack displacements, e.g., COD, CTOD, or δ_5. Displacement methods have been used successfully in predicting fracture resistance, but appear to lose effectiveness with extensive crack growth: the crack growth moves the fracture process zone further and further from the point of measurement of the displacement; thus, the parameter becomes progressively less sensitive. If a displacement parameter could be devised that was continually updated as the crack grew, it would not be expected to lose effectiveness. One effort of the overall investigation was to produce a displacement-based fracture model using far-field displacements as inputs.

A procedure to properly separate the region of fracture-dominated behavior from that of plasticity-dominated material behavior must be established. Two active modes of the fracture process have been identified: (1) plane strain fracture in the central zone of the ligament, a process that is J- or J_M-based, and (2) plane stress fracture at the surfaces, a process that is stress-based and is best characterized by plasticity. Any model should account for both the center and surface zones. One approach would be to consider enforced elasticity and then to relax the structural ligament into an elastic plastic behavior: in essence, adding a plastic displacement to the elastic displacement while maintaining a constant load. This is the conceptual essence of the ASTM Test Method for Measuring of Fracture Toughness E 1820-96.

Testing Results

Fracture tests were conducted on 6061-T651 aluminum alloy and IN718-STA1 nickel-base superalloy according to ASTM E 1820. Specimen configurations included compact tension (CT) and center crack tension (CCT) specimens for various thicknesses of the two materials. Intermediate crack lengths were determined by using unloading compliance data. Cracks were grown to approximately 50% of the initial remaining ligament, and the final crack fronts had considerable curvature. Figure 1 has been included as an example of crack front curvature. A linear averaging was used in all cases to produce unambiguous initial and final *average* crack lengths. The curvature can affect the crack-length-versus-compliance relationship, and the crack lengths produced by the crack length/compliance function were subsequently adjusted to provide agreement with the initial and the final average crack lengths using the curvature correction discussed in ASTM E 1820. These functions are highly nonlinear, and in the case of a few specimens, data suggested that the crack jumped in at a very low value of J_M. In any case, a slight shift of the resistance curves in these cases provided good agreement.

Figure 2 shows a typical resistance curve (R-curves that plot crack extension versus loading parameters) of the aluminum alloy and has been included at this point to show the similarity of *GR, JR,*

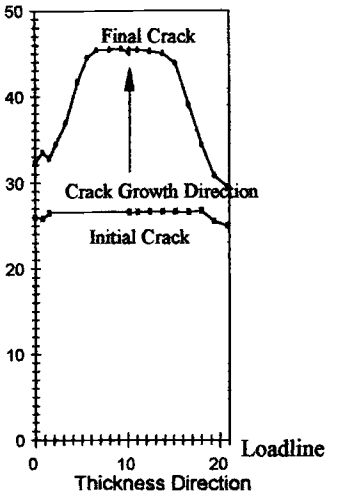

FIG. 1—*Curvature of the final crack front as seen in an aluminum compact tension specimen that has been broken open, exposing the fracture surface. Dimensions are in millimeters.*

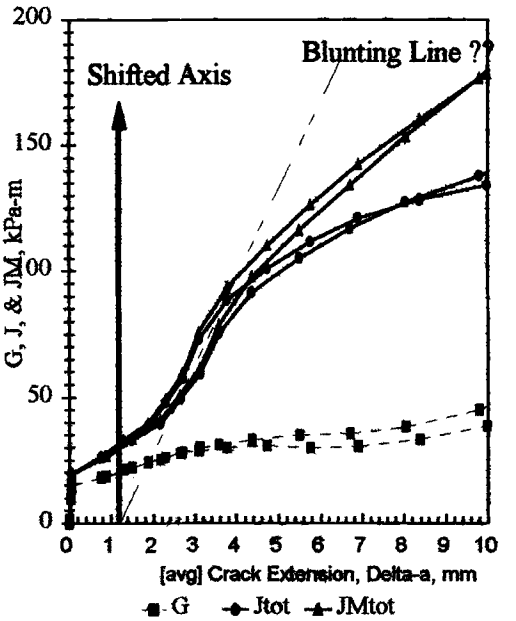

FIG. 2—*An example of fracture resistance curves.* GR-, JR-, *and* J_MR-*curves are shown for a 6061-T651 compact tension specimen. Note that average and greatest crack lengths are shown using the same symbols to suggest that both formulations are equivalent. Specimen C9, AL, CT:* B = *21.6 mm, 0% SG,* W = *50.8 mm,* $a_o/W = 0.52$.

and J_MR data formulated using average crack lengths and using the greatest length of the crack. Both the average and the greatest lengths are plotted and share the same symbols. *G, J,* and J_M are shown. Note that the average crack and the deepest crack formulations produce very similar results, so that essentially three curves are indicated. The *GR* curve shows a wider deviation at higher crack growths. This consistency is true of all of the specimens tested across both alloys, with the exception of three that deviate significantly at high crack growths. The average crack length was selected for use in this article because the data appeared to be smoother than the greatest-length data.

Figures 3*a* and 3*b* show the J_M-resistance (J_MR) data for the aluminum alloy and the nickel alloy, respectively. The J_MR-curve format was selected for this treatment, because J_MR-curves correlated data to a higher level of crack extension and because the *JR*-curves progressed towards constant *J*. If the resistance curve becomes constant, this suggests instability of the cracking object or a growing insensitivity of *J* with extensive crack growth.

Figure 4*a,* showing plots of the quotients *J*/*G* and J_MR against normalized crack extension for the aluminum alloy, further suggests the advantage of using J_MR-curves. The fractions *J*/*G* and J_M/G provide a simple measure of the relative amount of plasticity compared to the linear component. Normalized crack extension is used and is the fraction of the initial ligament that has been subsequently cracked. Notice in Fig. 4*a* that a linear region exists, and *J* and J_M agree in this zone. Further notice that while *J* falls away from the linear behavior at the point marked *J*/*G*, J_M remains consistent and linear to a higher degree of crack extension at *JM*/*G*. This response was true for all specimens in this test matrix, although a couple had more scatter than the others. It must be mentioned that the plots are "log/log" plots that tend to hide certain trends by their nature, but the linearity is clearly present, and this is evidence that J_M correlates the fracture phenomenon for more crack growth that does *J*.

Returning to the J_MR-curves of Figs. 3*a* and 3*b,* three observations can be made of the resistance curves presented in these graphs: (1) a broad range resistance behavior exists, (2) a clearly separated upper curve appears to exist for both materials, as well as a range of lower curve behaviors for both materials, and (3) after some degree of crack growth, many of the J_MR-curves exhibit an inflection

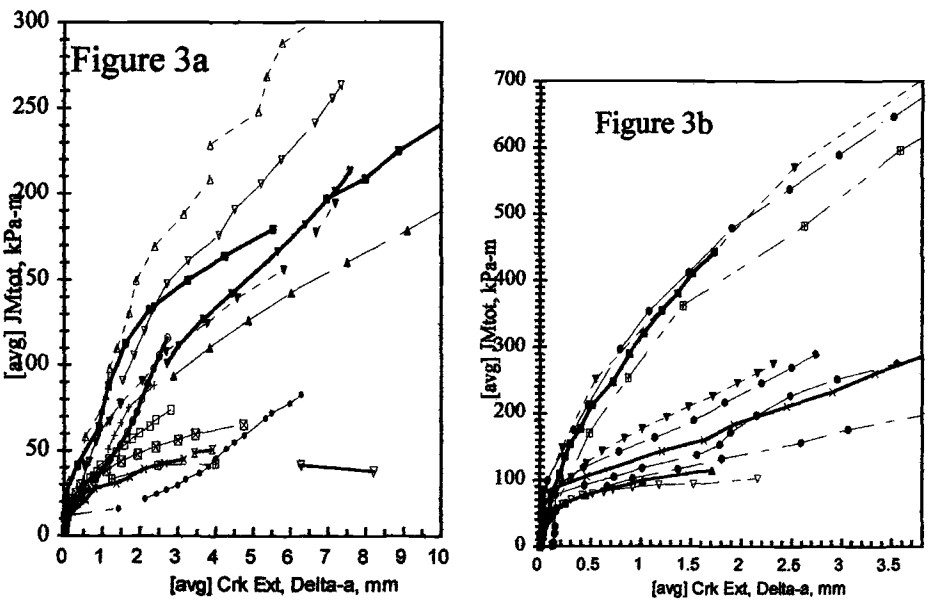

FIG. 3—*Fracture resistance curves (*J_MR*-curves) of a wide variety ligament configurations of compact tension specimens for:* (a) *6061-T651 and* (b) *IN718-STA1 alloys.*

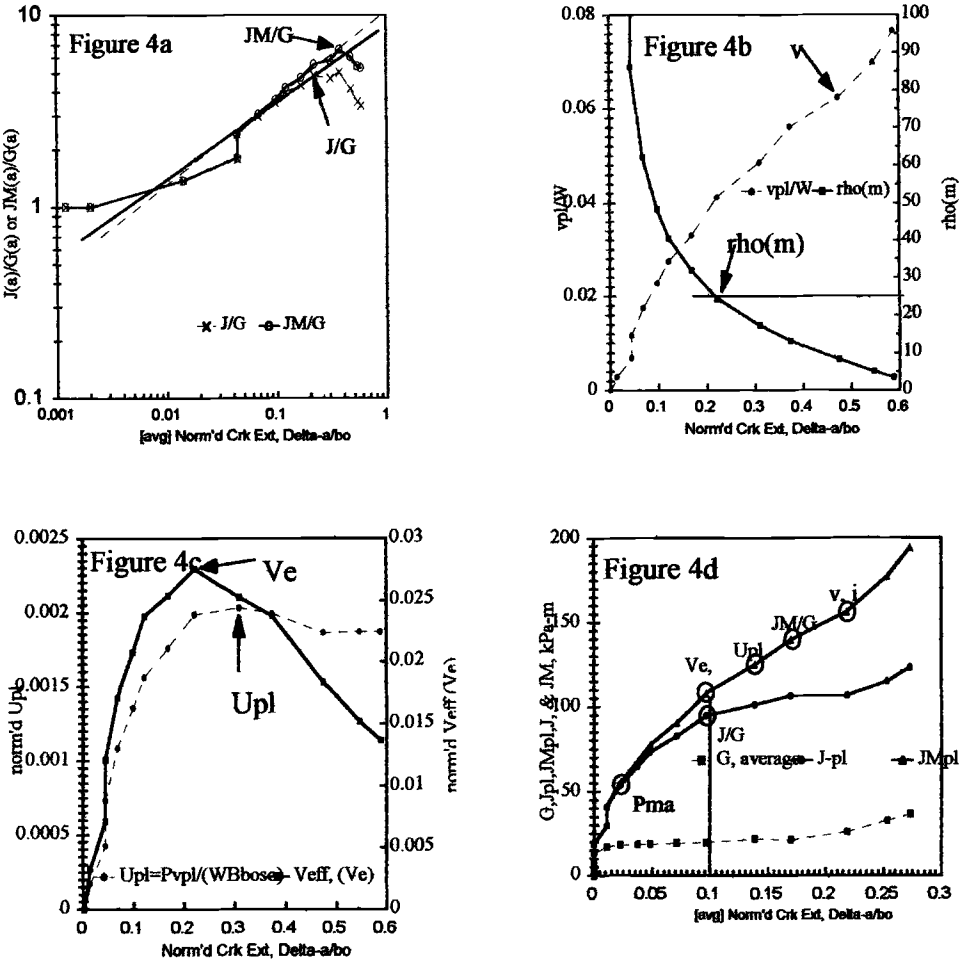

FIG. 4—*Plots illustrating the different fracture mechanics validity limits candidates and a comparison of all VL candidates evaluated for one specimen and plotted on the "raw"* R-*curves:* (a) *relative plasticity parameters,* J/G *and* J_M/G, (b) *inflection point of plastic displacement,* v_{pl}/W *and* ρ_M, (c) *plastic strain energy,* U_{pl} *and constant effective volume,* V_e, *and* (d) *an example of* G-, J-, *and* J_M-*resistance curves for an aluminum CT specimen (Specimen 66, AL, CT:* B = *6.4 mm, 0% SG,* W = *50.8 mm,* a_o/W = *0.76).*

point and become concave upwards. *R*-curve inflection is thought to be the signaling of a change of behavior from a regime controlled by fracture mechanics into one dominated by plasticity. To properly evaluate the effect of constraint in fracture requires that the data be qualified as representative of fracture mechanics behavior, such that the only variation observable is the constraint and not a change in the behavioral mode.

Validity Limits Analysis

It has been observed [*3,5,6*] that with sufficient crack growth, the J_M*R*-curve will pass from a concave-downwards shape to one that is concave-upwards. The upwards inflection is thought to be due

to a change in the deformation character. Specifically, the specimen has passed into a regime where deformation and crack growth are better described by abandoning local fracture mechanics parameters to use stress-strain relationships that considering the full-field problem instead. The point at which fracture mechanics methods are no longer effective in describing the fracture event is termed herein as the fracture mechanics validity limit (symbolized VL). This change of dominant behavior suggests that the two regimes should be separated for evaluation. This is not a new concept. Ernst and Pollitz [*6*] discussed ways of extrapolating J_M in order to allow estimation of the behavior of large, thick structures from the behavior of small specimens. The extrapolation makes use of an apparent improvement of correlation derived from using J_M instead of the *J*-integral parameter. They considered two options for establishing the limit of the J_M data to be used in the extrapolation: (1) the inflection point of the J_MR curve or (2) the inflection point of a plot of the plastic displacement-versus-crack extension. An assortment of schemes were then used to extend the truncated resistance curve to estimate much greater crack extension.

The inflection point observed in the J_MR-curve is often subtle and can be difficult to determine. This suggests that other parameters might be devised to better identify the validity limit of fracture mechanics. Eleven candidates were considered early in this investigation, although only the ones showing the most promise will be discussed in detail. Along with these, the location on the *JR*-curves corresponding to the maximum load during the test was determined, and certain comments will be made at an appropriate time regarding the observations.

Validity Limit Parameters Considered

The first candidate fracture mechanics validity limiting (VL) parameter was the inflection point of the J_MR-curve. This has been discussed as an indication in the *R*-curve of the onset of a new behavior, and the location is labeled "*i*," as in *inflection point* of the J_MR-curve in Fig. 4*d*.

One parameter that has been discarded as a candidate is the point at which the J_MR-curve becomes straight. The proper scaling associated with fracture mechanics is thought to be $a_1 = a_2$ at $J_1 = J_2$. Earlier work by Ernst [*4*] suggests that if fracture parameters can be scaled in the same way as plastic deformation processes, then the behavior has become plasticity-dominated, and fracture mechanics treatments are invalid. Ernst further showed that this case would be manifested as a straight line in the *JR*-curve format, i.e., if the behavior has become proportional crack growth (PCG), then it is characterized by a constant slope in the *R* curves. Constant slope, the second candidate parameter, has proved to be difficult to evaluate and appears to be at the same location as the inflection point.

A third candidate is the inflection point of the curve of plastic displacement-versus-crack extension (symbol "*v*" in Fig. 4*b*). In the course of fracture tests, the load, total displacement, and the unloading compliance are recorded (*P*, *v*, and *C*, respectively). From these, and the assumption that the displacement can be decomposed into linear (v_{el}) and nonlinear (v_{pl}) parts, the nonlinear (plastic) displacement can be calculated, as follows:

$$\begin{aligned} v &= v_{el} + v_{pl} \\ v_{el} &= P \times C \\ v_{pl} &= v - v_{el} = v - P \times C \end{aligned} \tag{6}$$

Graphs of normalized nonlinear displacement versus crack extension were produced (Fig. 4*b*). The use of the inflection point of the v_{pl}-versus-a curve as a VL parameter was discussed by Ernst and Pollitz [*5*]. They used a point where v_{pl}/W had grown to 5% above the amount inferred by linearly extrapolating from the inflection point using the slope at the inflection point. Again, the phenomenological change is thought to be a transition from fracture-driven processes to plasticity. As with the *i*-criterion, this point is often subtle and not easily established.

The fourth candidate (symbolized by "U_{pl}") is the product of load-times-plastic displacement (Fig. 4*c*). In this case, the attempt was to define an energy-type parameter and look for a change of behavior in the specimen data. In general, an increment of external work, Pdv, comes from crack growth plus a change in strain energy:

$$P\,dv = Jda + \Delta U \tag{7}$$

The terms in Eq 7 can be decomposed into elastic and plastic components, and the plastic portion of the expression will be considered further. This plastic portion is written as:

$$P\,dv_{pl} = dU_{nl} + BJ_{pl}da, \text{ with } dU_{nl} \geq 0 \tag{8}$$

In this equation, U_{nl} is the nonlinear (plastic) strain energy, and if $dU_{nl} = 0$, the end of validity has been reached. This can be developed further to give a simple expression for U_{nl} by using a Ramberg-Osgood constitutive form ($P \propto v_{pl}^{N}$):

$$U_{nl} = \frac{Pv_{pl}}{N+1} \tag{9}$$

Looking at Eqs 8 and 9, a plateau in load times plastic displacement is expected to signal a limit to fracture mechanics validity, i.e.,

$$\text{as } dU_{nl} \rightarrow 0,\ P \times v_{pl} \rightarrow \text{constant} \tag{10}$$

The criterion shown in Eq 10 is symbolized "U_{pl}." The curve in Fig. 4*c* has been normalized to produce a non-dimensional quantity.

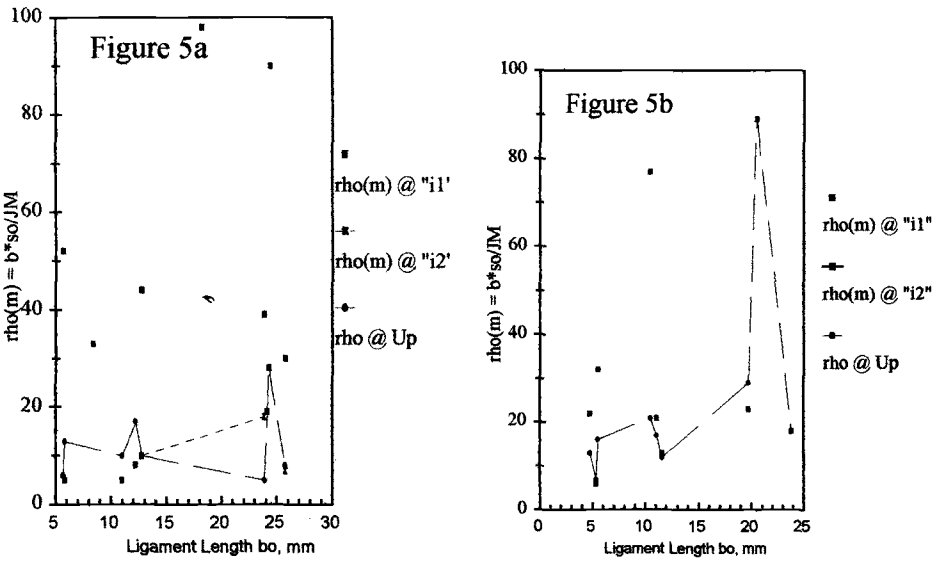

FIG. 5—*VL parameters* i *and* U_{pl}, *expressed as* ρ_M: (a) *aluminum specimen data plotted against initial ligament length,* b_o, *and* (b) *nickel data plotted against initial ligament length,* b_o.

The last candidate for a fracture mechanics regime limit is the onset of constant effective volume (symbol "V_e" in Fig. 6*d*). Plastic deformation is often assumed to be a constant volume process. Constant volume deformation is commonly assumed for plastic deformation, and the onset of plasticity would be expected to exhibit this behavior. This behavior might be applicable as a VL parameter,

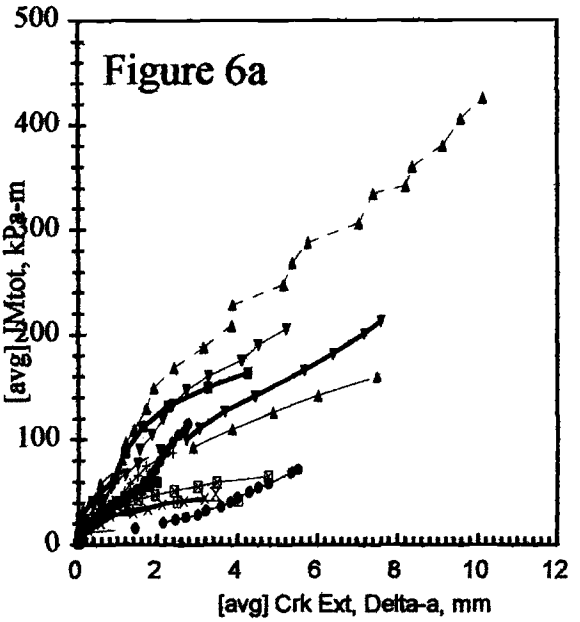

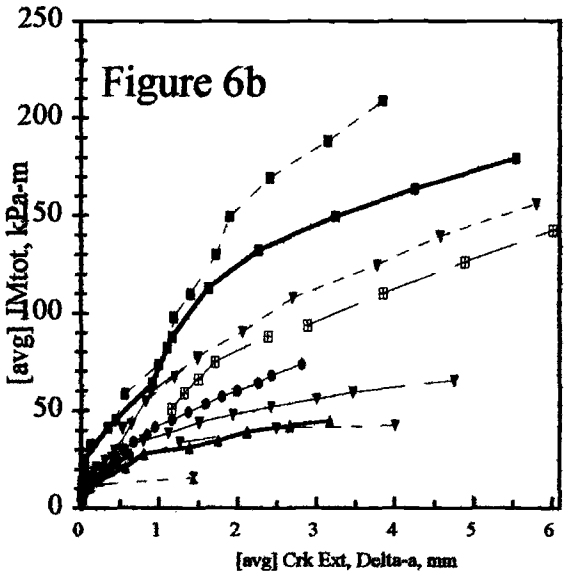

FIG. 6—*"Valid" J_MR-curves for 6061-T651:* (a) *validated by maximum plastic energy criterion,* U_{pb} *and* (b) *validated by first inflection point criterion.*

given an appropriate volume. Using the work functions or η-factors, an effective area can be defined. Note first that the η-factor arises from the assumption that the load can be separated into one function of crack length and one of plastic displacement:

$$P = g(a) \times F(v_{pl})$$
$$\eta \equiv \frac{\partial P}{\partial b}\frac{b}{P} \tag{11}$$

In the case of compact tension (CT) specimens,

$$\eta = 2 + 0.522\frac{b}{W} = \frac{\partial P}{\partial b}\frac{b}{P} \tag{12}$$

Separating variables and integrating the last equation produces a logarithmic form that can be rewritten as

$$P = C \times b^2 \exp\left(0.522\frac{b}{W}\right) \tag{13}$$

C is a constant of the integration with respect to b and could be a function of plastic displacement. Thus, C contains $F(v_{pl})$. By using the definition of stress, an effective area can be suggested:

$$A_{eff} = \frac{P}{\sigma} = \frac{C}{\sigma} \times b^2 \exp\left(0.522\frac{b}{W}\right)$$
$$V_{eff,CT} = l_{eff} \times A_{eff} = v_{pl} \times b^2 \exp\left(0.522\frac{b}{W}\right) \tag{14}$$

The appropriate length was assumed to be the plastic displacement. The effective volume criterion has been labeled "V_e" in Fig. 4*c*.

Validity Limits Analysis Results

Parameters ρ_M (similar to ρ_J, except that the current ligament and J_M are used in the formulation shown in Eq 2 instead of the initial ligament and J_{Ic}) and ω were tracked in addition to the VL parameters discussed above, but no clear minimum was observed, and apparent inflections in log-log plots were not considered reliable; thus, the data are omitted from consideration here. Of the other parameters, the inflection points of the J_MR curve, i, and the plastic displacement curve, v, were identical; although other possibilities for i did exist for some specimens, v always indicated the same value as one inflection point on the J_MR-curves. The plastic energy parameter, U_{pl}, was also identical or occurred immediately before i. The location of $\rho_M = 25$ was considered, and the results are very similar to those of U_{pl}, although more scatter was present. The results have been cast in two different ways: using J_M cast as ρ_M and the normalized crack length, $\Delta a/b_o$. The resulting limits were fairly consistent for the two materials:

$$\text{CT Specimens: } \left(\frac{\Delta a}{b_o}\right)_{AL} \approx 0.35, \text{ and } \left(\frac{\Delta a}{b_o}\right)_{IN} \approx 0.34 \tag{15}$$

The values of ρ_M associated with i and U_{pl} are plotted in Figs. 5*a* and 5*b* for 6061-T651 and for IN718-STA1, respectively. In Fig. 5*a*, two values for i are plotted, showing the first occurrence of a

J_MR-curve inflection and then a second occurrence, when two were present. It should be noted that the improvement of correlation of i and U_{pl} with the second occurrence is dramatic. In fact the only exceptions are the side-grooved specimens, and the reason for this is unknown. The correlation of limit of validity for the aluminum alloy that is suggested by Fig. 5*a* is by the ligament proportion, B/b_o. The correlation between i and U_{pl} is also good for the nickel alloy shown in Fig. 5*b*, although the correlation seems to be related to ligament length in this case, although correlations with ligament proportion, B/b_o, and with ligament length, B, also seemed reasonable.

The U_{pl}-qualified J_MR-curves for 6061-T651 appear in Fig. 6*a*. The presence of another inflection point reduces the apparent effectiveness of the parameter, leaving J_MR-curves that cross each other. Because of this, plots of J_MR using the first inflection point of J_M have been plotted in Fig. 6*b*, and the improvement is better. Substantial consideration has been given to the behavior exhibited in Fig. 2, i.e., the presence of multiple inflection points. The early inflection phenomenon may not be associated with nonlinearity of the compliance versus crack length functions, but *may* be an expression of the development of the crack in the interior of the ligament with no appreciable accumulation of plasticity. This appears as J and J_M values that are approximately equal to G in that early part of the curve in Fig. 2. Plots of J_M decomposed into G and J_{Mpl} (terms are evaluated per Eq 5c) appear in Figs. 7*a* and 7*b* for the aluminum alloy. It should be noted that all G behavior and all J_{Mpl} behavior are very similar. The GR-curves stack according to the ligament proportion, except for the lowest curve, and the J_{Mpl}, curves might be identical, with the exception of the delay of the beginning of evolution.

Crack Face Displacements

Two active modes of the fracture process have be identified: (1) plane strain fracture in the central zone of the ligament, a process that is J- or J_M-based, and (2) plane stress fracture at the surfaces, a process that is stress-based and is best characterized by plasticity.

A displacement-based fracture model would require the development of a procedure to *apportion* the structure into center and surface zones. One approach would be to consider enforced elasticity that is subsequently relaxed in the structural ligament into an elastic plastic behavior: in essence, adding a plastic displacement to the elastic displacement. This is the conceptual essence of the ASTM E 1820.

Crack face displacement data were taken at different depths for 6061-T651 specimens (CT and CCT) after wedging them at the final displacement achieved during the fracture test. The data mapped the relative positions of the crack faces throughout the entire crack cavity: from the notch root through the pre-crack region plus the monotonic fracture region to the final crack tip. A series of these mappings were produced for cross sections from the surface to the center line of the specimens. Figure 8 shows the data generated for one of the aluminum compact tension specimens. In this figure, consistent with a shear-type fracture mechanism, the "surface" crack profile deflects from flat fracture. Moving away from the surface crack profile, each subsequent profile is at approximately equal increments of depth (0.76 mm) from the previous. The inner-most profile is essentially flat fracture. The greater extension of the inner profiles is also obvious.

The displacement of the two surfaces relative to each other was calculated, and a series of "separation profiles" for one specimen appear in Fig. 9. Note that the center profile seems relatively straight, while the ones closer to the surface deviate at the same point to a greater and greater extent to where the surface is reached. This common point is the location of the initial crack tip. After the initial "deviation" from the center profile, each profile is relatively parallel to the center profile up to the point where the crack tip in each case is reached.

Theoretical "calibration" displacement functions were devised [*14*] to predict the shape of crack face profiles in specimen cross sections using far-field displacement or load. The calibration displacement functions predict the crack face displacement arising from the final load as if the crack had always been at the final (*current*) configuration, i.e., no crack growth was considered in loading to

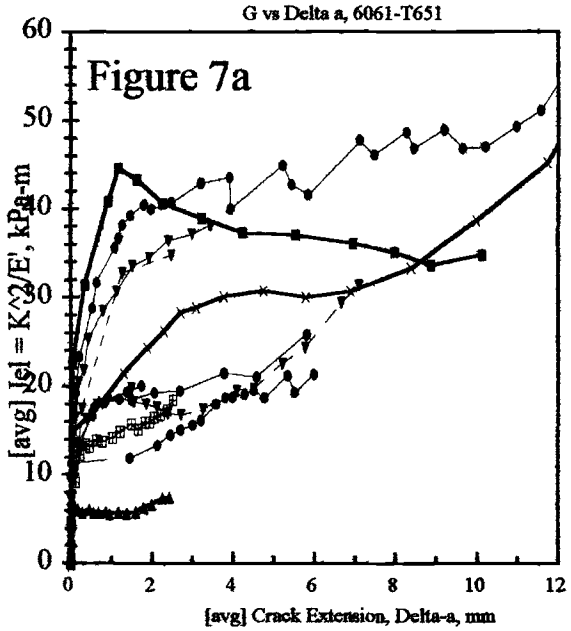

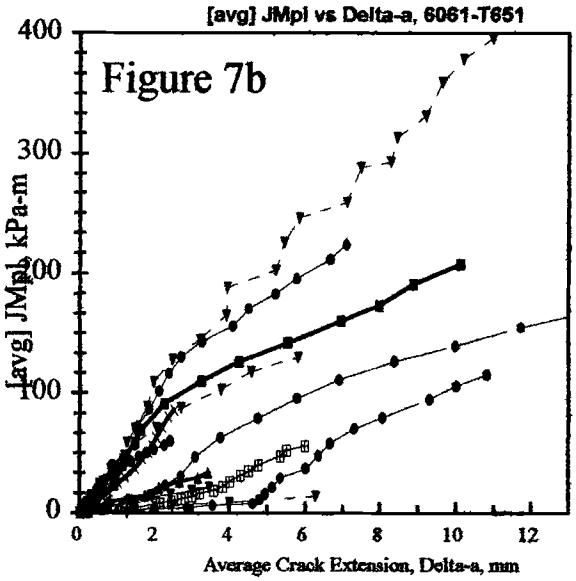

FIG. 7—*"Component resistance curves" of 6061-T651 compact tension specimens:* (a) *GR-curves (elastic component of* J_M*), and* (b) J_{Mpl}*R-curves (plastic component of* J_M*).*

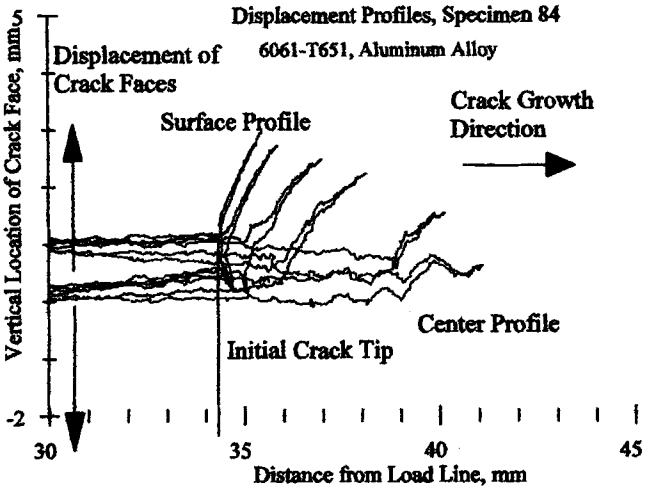

FIG. 8—*Crack face profiles for a typical aluminum specimen. The fatigue pre-crack is to the left side, and the monotonic fracture zone is on the right side. Note the deviation of the surface profiles from the flat fracture.*

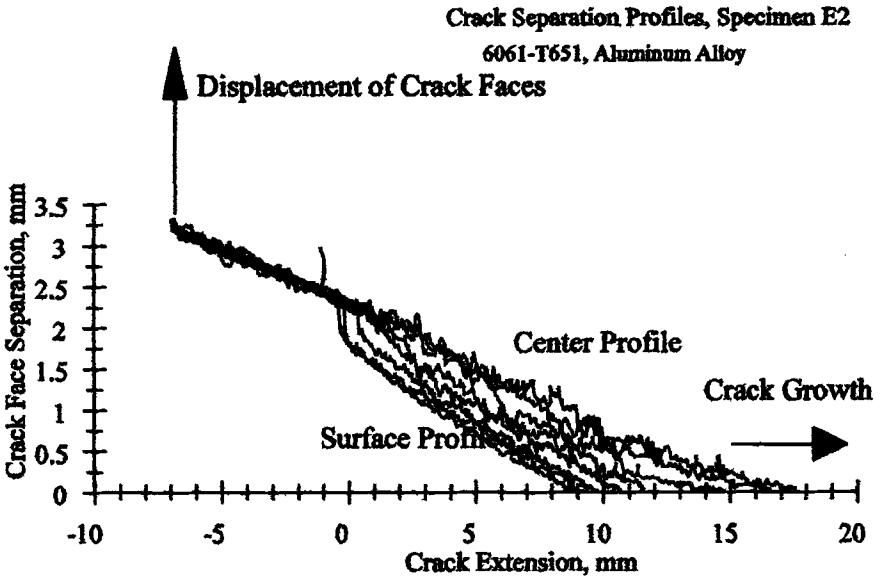

FIG. 9—*Crack face separation profiles for an aluminum compact tension specimen. Note the initial stretch associated with surface profiles and the relative parallelism of the profiles to the center profile after the initiation event.*

the final configuration. These calibration functions were the summation of elastic plus plastic displacement components. The first attempts at defining these calibration functions were primitive and needed improvement, including more terms from the power-series expansion of the displacement as a function of J; these calibration displacements were compared to the actual displacements in the pre-crack region, and, because of this, a one-term approximation was ineffective.

When the calibration functions are compared to actual crack displacements, any difference between the two in the fractured region was considered to be the result of the crack growth in the presence of the elastic and plastic displacements. Two differences between the plane strain calibration displacement and the actual profile were expected because of earlier efforts [*14*]. A first difference arises because of the gradient of constraint: far-field displacements are expected to be somewhere *between* plane strain and plane stress, and a multiplicative factor applied to the plane strain solution was found to be effective as an adjustment. A second difference expected is the effect of the crack growth, and this difference might yield a displacement criterion for fracture in the presence of varying constraint, i.e., depth below a free-surface, and the adjusted plane-strain J-field displacement. An example of a separation profile with the calibration profile included is shown in Fig. 10. To facilitate calculation of the calibration profile, the crack growth direction is reversed. Notice how well the calibration profile matches the actual separation profile in the pre-crack region in the upper right of the figure. This was typical of most of the profiles, although a few specimens did not exhibit such good agreement. One other detail must be mentioned: the position of the crack tip that was used for the calibration profile was the greatest extension of the crack tip. This is an unfortunate philosophical variation from the intended direction of this investigation, which was to use the end of the crack in each profile. This choice provided the best fit by far. If the specimens that provided poor agreement in the pre-crack region had been fitted using a crack tip that was deeper than the greatest extent of the crack, the agreement would have been improved, but this would have been impossible to defend.

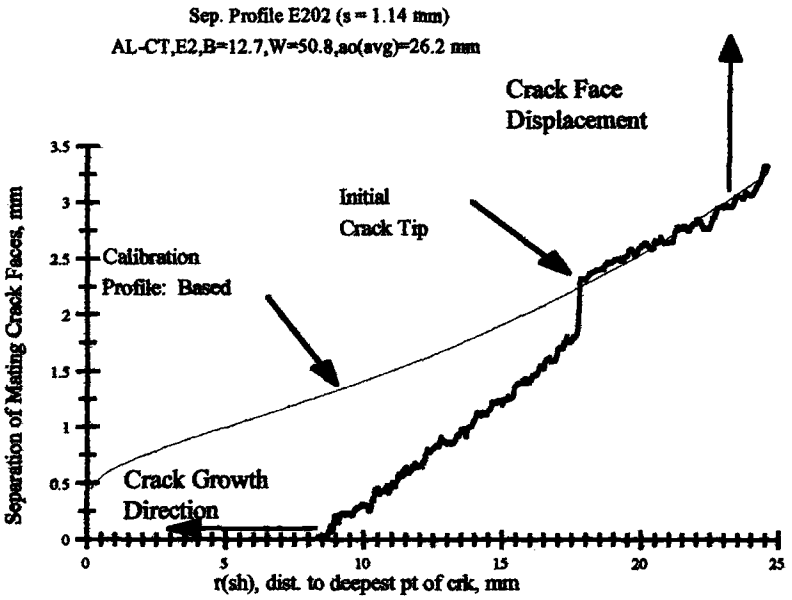

FIG. 10—*Individual separation profile of a typical cross section, showing the actual separation and the corresponding calibration displacement function. Note how well the two agree in the pre-crack region in the upper right portion of the profile. Crack growth direction has been reversed from earlier exhibits.*

The results presented above suggest that the deformation and crack growth character of the 6061-T651 material (and the IN718-STA1) could be divided into two components, specifically, surface plasticity plus flat fracture. These two correspond to physical zones in the ligament cross section, i.e., the surface and the center, respectively, where the deformation and fracture behavior differ. Planar specimens, ones with a constant profile throughout the cross section, were used in the development. This choice allowed the easy evaluation of the *JR*-, $J_M R$-curves and the corresponding calibration displacement profiles, since J, J_M and the relationships of calibration displacement to J or J_M were known for these configurations.

Displacement Calibration Functions

The profile analysis compared the theoretical, calibration displacement with that observed in the pre-crack region, away from the crack tip. The calibration functions approximate the displacement associated with the final crack configuration, loaded to the final load point, with no crack growth. These functions are the sum of the theoretical displacement expected from a cracked object where no plasticity is expressed plus the theoretical displacement expected from the cracked object if the ligament were fully plastic. Earlier efforts [*14*] had shown that the calibrations were dissimilar to actual crack profiles when the crack had sustained little crack growth. As a result of this, different effective crack lengths were considered [*13*]. Using the tip of the crack at the point of the greatest extension (at the center plane) as the *effective* crack tip location, the results were dramatically improved.

Elastic Displacement Calibration Function—The elastic calibration functions were taken from a development by Tada et al. [*18*], and a summary will be presented herein. The method is summarized here. For Mode I loading, the crack face displacement can be estimated by using Castigliano's theorem, with a resulting elastic displacement estimate as follows:

$$\delta_{el} = \delta_F = \frac{4}{E'}\sqrt{\frac{2}{\pi}}\left[K_{IP}\, r^{1/2} + \frac{1}{3}\frac{\partial K_{IP}}{\partial a} r^{3/2} + \frac{1}{10}\frac{\partial^2 K_{IP}}{\partial a^2} r^{5/2} + \frac{1}{42}\frac{\partial^3 K_{IP}}{\partial a^3} r^{7/2}\right] \tag{16}$$

K_{IP} is the *applied* stress intensity factor, a is the crack length, and r is the distance from the crack tip. Again, as mentioned above, r was referenced to the greatest extension of the crack throughout the cross section. E' is taken to be $E/(1 - \nu^2)$, assuming plane strain in all cases. The equations for K_{IP} and subsequent derivatives with respect to crack length for compact tension (CT) specimens have been appended to this paper. Several center-cracked tension (CCT) specimens were included in the profile analysis. No CCT calibration functions have been included, though. Actual displacements for these specimens were observed to be far below the theoretical, single-term expansion, and since the final loads were large relative to the CT specimens, it was theorized that the wedges used to secure the specimens at the final displacement had been crushed by the prevailing loads. As such, for the current work, and with the trend noted that the stretch characteristics were very similar for CCT and CT specimens [*14*], only the compact tension specimens were considered in this investigation.

Plastic Displacement Calibration Function—The form of the plastic displacement calibration function was taken from Hutchinson [*11*] and is, as follows:

$$\delta_{pl} = C_e J_{pl}^{\frac{n}{n+1}} r^{\frac{1}{n+1}} \tag{17}$$

Additional terms in the plastic displacement were considered, but it was not thought to be necessary to include more terms, because the plasticity was confined to the vicinity of the crack tip. C_e came as

an average of the residual displacement throughout the pre-crack region divided by r raised to the $1/(n + 1)$ power, i.e., from a linear regression analysis. This procedure is, as with the earlier attempt to find an elastic calibration function [*14*] empirical, since C_e is not related explicitly to the loading parameters, but the contribution of the plastic displacement component was small in most cases, and the correlation of the calibration functions to the actual pre-crack displacements appeared to be improved with the one-term plastic calibration function included as compared with the results where the term was omitted.

Bulk Constraint Factor, f(i)—The first calibration profiles that were analyzed compared well to the actual profiles. However, after these profiles were analyzed, subsequent profiles were found to have calibration displacements that were less than the actual profiles. With surface plasticity, the effective thickness is expected to be less than the actual thickness, and subsequently a multiplicative factor, $f(i) \equiv$ bulk constraint factor was inserted into Eq 16. The significance of $f(i)$ is thought to be that by taking $E' = E/(1 - \nu^2)$ in Eq 16, thus assuming plane-strain, $1/f(i)$ was the fraction of the ligament that was in plane-strain, i.e., if $f(i) = 4$, then the portion of the ligament thickness expressing plane strain was ¼ of the actual thickness. $f(i)$ is considered to be an indication of the loss of out-of-plane constraint. The bulk constraint factor was used for all profiles and was kept constant for profiles of a given specimen. The basis for the comparisons was a visual inspection of the fit in the pre-crack region.

Coefficient of the Plastic Displacement Term, C_e—The value of C_e was relatively constant for each specimen, and this is thought to express the presence of plasticity in front of the crack tip. For the specimens from the multiple specimen tests with lower load-line displacement, C_e was on the order of 10^{-6}, whereas for most of the other profiles, C_e was on the order of 10^{-5}. The exception was the thinnest specimen, where $B = 6.4$ mm, $a_o/W = 0.5$, with C_e on the order of 10^{-7}. Several comments should be made about this observation. First, the "other specimens" with a higher value of C_e had very large crack extension, and it can be speculated by the occurrence of an inflection point in the J_MR-curve that plasticity had become saturated to the back face of the specimen ligament; this was not the case for the lower final displacement specimens; thus, C_e is dramatically larger for the "other specimens" than for the specimens from the intermediate final load-line displacement of the multiple specimen tests. Second, the thin specimen is thought to have saturated the ligament from the *side* faces. The side-face saturation (or out-of-plane constraint) effect is described by $f(i)$, and for this specimen, the inflection point of the J_MR-curve had not been reached.

Results of the Profiling Analysis

The $f(i)$ data have been plotted as a function of the thickness of the ligament in Fig. 11. This figure plots $f(i)$ against linear thickness and shows the quality of a fit function derived. Note that Specimen No. 08 deviates dramatically; this is not considered a discrepancy, since No. 08 was a side-grooved specimen, a condition that tends to produce plane-strain conditions in the ligament. As such, No. 08 acted as if it were much thicker. The $f(i)$-versus-thickness data were fitted as follows:

$$f(i) = 12.17 \exp(-84.1B) \tag{18}$$

Comparison of f(i) *with Slope of the* J_MR*-Curves*—Comparison of $f(i)$ to other constraint parameters was desired, e.g., the slope of the J_MR-curve. The basis for comparison of J_MR-curves was R_L, the ligament length-to-thickness proportion ($R_L = b_o/B$). All but one specimen selected for the profile analysis had an initial ligament length of 25 mm, and Eq 18 was recast as $f(i)$-versus-R_L. This will allow comparison of $f(i)$ with other indications of the bulk constraint. This functionality

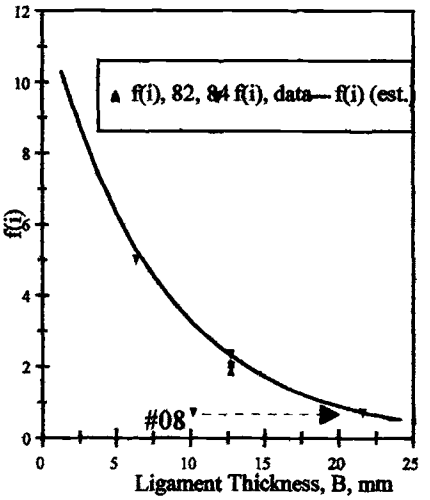

FIG. 11—*Plot of the bulk constraint factor* f(i), *used in calibration profiles versus ligament thickness, and including fit function developed. Note that side-grooved Specimen No. 08 is in plane strain conditions and acts like a much thicker specimen.*

is as follows:

$$f(i) = 12.17 \exp\left[-3.31 \cdot \left(\frac{B}{b_o}\right)\right] \tag{19}$$

A partitioning technique was used [*14*] to adjust the average values to give estimates of the $J_M R$-curves expected at the center plane of the specimens tested. This provides some measure of the prevailing constraint at the center of the specimen. These center $J_M R$ data were sparse and subject to statistical scatter, but the difference was small, and thus the whole set of data was used to fit a single center-plane $J_M R$-curve. The correlation seen in the center plane $J_M R$-curves was as a function of $1/R_L = B/b_o$, and the results were normalized using the $B/b_o = 2$ (short, thick ligaments) and the side-grooved specimen data with $J_M^{(\mathrm{REF})} = 175.2$, with units to provide consistency in the equation below. Thus, power law fits for the center-plane $J_M R$-curves of each configuration were of the form shown below:

$$J_M^{(c)}(R_L) = \phi_i \times J_M^{(\mathrm{REF})} = \phi_i \times 175.2\,(\Delta a)^{0.586} \tag{20}$$

This produces a nondimensional constraint factor, ϕ_i, that can be used for comparison to other constraint factors, e.g., the bulk constraint factor, $f(i)$, as cast in Eq 19 and constraint factor, ϕ_i, as derived from Eq 20, and this appears in Fig. 12. A comparison clearly exists. The bulk constraint factor, $f(i)$, provides a measure of the effective thickness of the ligament as compared with plane strain response. The factor has been derived for 6061-T651, aluminum alloy, from specimens in the compact tension configuration, and matches the load with a theoretical displacement associated with the final crack length in the absence of crack growth.

Stretch Resistance

After fitting the calibration displacement to the pre-crack region, the displacements within the growing-crack region could be considered. This is the portion of the actual crack separation profiles

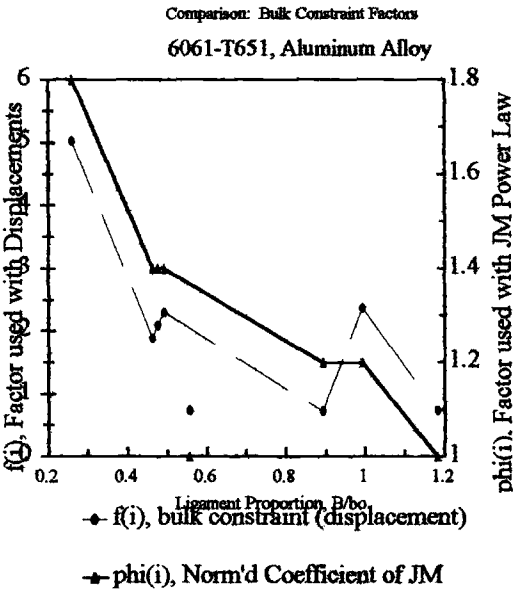

FIG. 12—*Plot of bulk constraint factor,* f(i) *and of* ϕ(i)*, a dimensionless factor derived from a power law fit of qualified* J_MR *curve data plotted against ligament proportion,* B/b_o.

that deviates from the calibration displacement functions as discussed earlier. At the free, side surfaces of the specimens, the deviation was substantial, while near the center-plane section of the specimens the deviation was negligible [*14*].

A quantity, termed the *stretch,* was defined as the difference between the calibration displacement function [*14*], as defined earlier, minus the actual profile displacement. Two examples of stretch profiles have been included in Fig. 13. The first is for short growth, being from among the multiple specimens, while the second is from long growth. This stretch was found to have identifiable characteristics: a stretch quantity could be seen at the beginning of crack extension (at the end of the pre-crack). This was termed the *initiation stretch* and could be seen as a deviation from the calibration displacement function with no corresponding crack growth. At some value of the stretch, the crack was seen to begin advancing. The change from initiation to crack extension was not discontinuous, although it did occur with relatively short extension. After the transition, the crack extended at a constant rate with respect to further stretch, i.e., a plot of stretch-versus-crack extension yielded a straight line after initiation.

Initiation Stretch—The initiation stretch, δ_i, was defined as the deviation of the actual displacement profile from the calibration displacement profile at the pre-crack tip (before any appreciable crack extension had occurred). δ_i was found to vary as a function of the depth beneath the surface normalized as the fraction of the distance from the surface to the center-plane cross-section: $S = 2s/B$. The depth below the *original* surface is "s" (most specimens experienced some dimpling or necking at the surface at the crack tip), B is the thickness of the ligament, and S is the fraction of depth beneath the surface and has a value of 0 at the surface and 1 at the center-plane.

The δ_i data have been plotted against S in Fig. 14. Included in the figure is a sigmoidal-curve fit of the data. This fit comes from linear regression analysis and fits the logarithm of δ_i to S^2. This fit was selected because it provided a maximum value of δ_i at $S = 0$, and the value of δ_i changes asymptotically towards a constant as $S \rightarrow 1$ approaching the center plane. Two other fits were considered: one

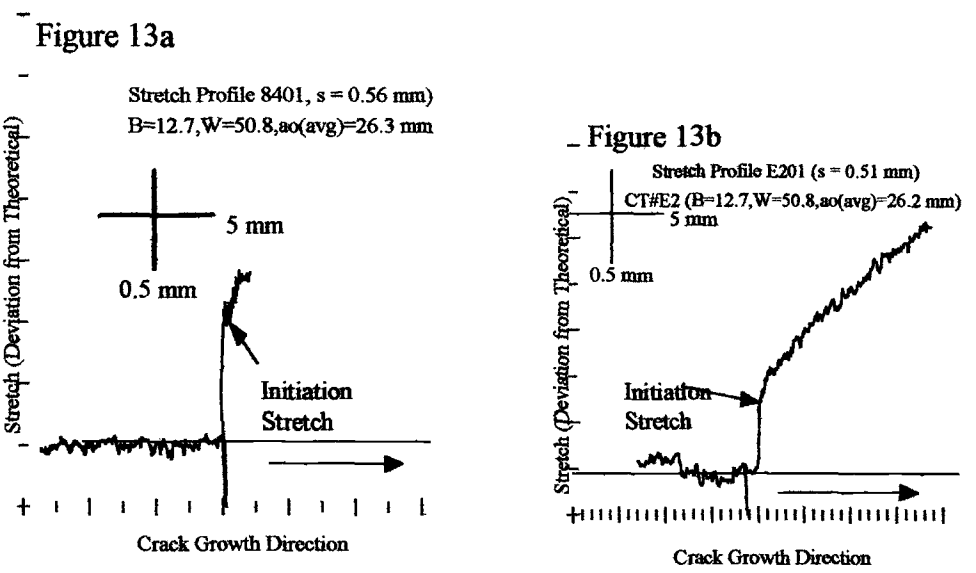

FIG. 13—*Two plots of stretch (surface profiles):* (a) *short crack growth from intermediate load-line displacement specimen from multiple specimen test, and* (b) *long growth specimen.*

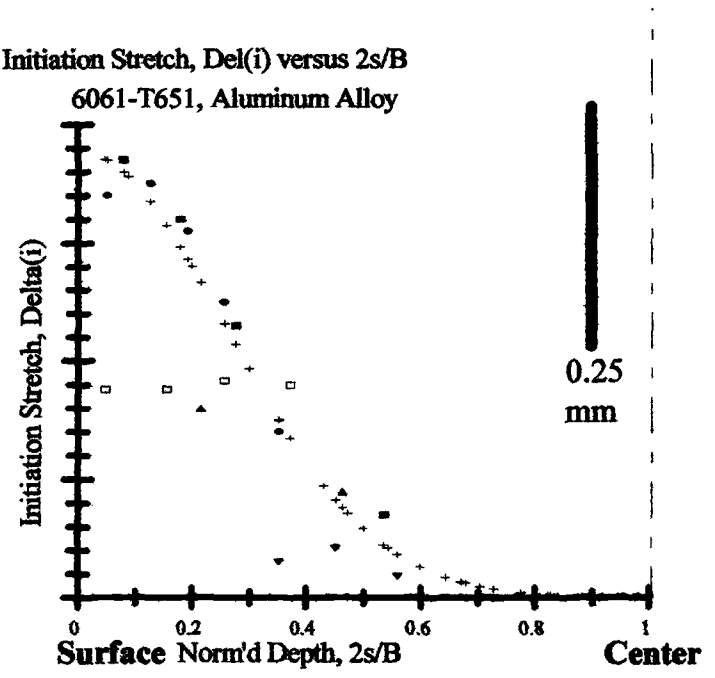

FIG. 14—*Plot of initiation stretch,* δ_i *as a function of the fractional depth below the free (side) surface. Included in the plot is a fit function. The smooth data are the fit function.*

was a linear fit of δ_i-versus-S, and one was a linear fit of $\ln(\delta_i)$-versus-S (exponential). The first of these is discontinuous at $S = 0.662$, which is undesirable. The second is relatively good, but exhibits singular behavior as $S \rightarrow 0$, again an undesirable trait. The sigmoidal fit for δ_i is as follows:

$$\delta_i = 0.479 \exp\left[-\left(\frac{2s/B}{0.367}\right)^2\right] = 0.479 \exp\left[-\left(\frac{S}{0.367}\right)^2\right] \tag{21}$$

This sigmoidal fit appears effective in quantifying the initiation stretch, as can be seen in Fig. 14. The data varied from the fit in three cases: (1) the side-grooved specimen, No. 08, exhibited little initiation stretch throughout the ligament (this was as anticipated: the cutting of side-grooves in a fracture specimen has been said to remove the plane strain region [*11*], (2) No. 51 (the thinnest specimen, discussed earlier at $B = 6.4$ mm and $a_o/W = 0.5$), may or may not have followed the curve, and (3) one of the multiple specimen tests with low load-line displacement ($B = 12.7$ mm and $a_o/W = 0.5$) apparently had not been subjected to sufficient displacement, and the observed displacement, taken as δ_i, is uniform up to the point where it joins the fitted curve, i.e., at the onset of crack growth. These exceptions seem consistent with the consideration of δ_i as a displacement-based criterion for crack initiation. The linearity of the extension-versus-stretch curve subsequent to initiation suggests that, as a function of the location in the cross-section, S, δ_i might describe the fracture *after* initiation as well, i.e., when any point within the flawed object reaches $\delta_i = \delta_i(S)$, fracture is imminent. The presence of a *slope* in the stretch curves could reflect an inability of the profiling techniques to completely quantify the evolving crack. Efforts to establish a rate of crack extension as a function of the load-line displacement using the calibration functions has been omitted here.

Summary of Two-Dimensional Analysis

The findings in the two-dimensional "planar" analysis are to be adapted to three-dimensional configurations, specifically to semi-elliptical surface cracks in plates subjected to tension (SCT specimens). The following sections have been inserted to further discuss and clarify the various outcomes of the 2D analysis for that purpose.

Interaction of Flat Fracture and Plasticity—In the one material subjected to the profile analysis and with the final consideration of only the compact tension configuration studied with the profiling techniques, the displacement in the flat fracture region appeared to be almost completely characterized by the linear elastic component alone. The plasticity component was *not* zero but, in general, represented only a slight correction from the linear elastic displacement. This was the behavior seen in the center of the cross section. Outside of the flat fracture region, and approaching more closely to the side-surfaces, the fracture character expresses progressively more plasticity, and fracture was no longer on a plane perpendicular to the load-line, but, instead, on a plane inclined to the side planes. This is the so-called *shear lip fracture* character.

To accommodate this change of character, the plasticity that is found at the surface, i.e., stretch prior to fracture, decreases in a smooth fashion at ever-increasing depth below the side surfaces. Comparing data from different specimens, this decrease occurs as a function of the fractional depth from the side surface of the ligament thickness. This is thought to be evidence of plasticity-based deformation character, since it is not attributable to the J-character of the configuration otherwise. The zone was expected to evolve such that the depth of plasticity would become greater as the loading parameter was increased. This was not the case: the depth associated with the change was clearly characterized by the initial remaining ligament dimensions and *not* the loading, P_o/P_{max}, here (a result that is only mentioned here). P_o is the limit load calculated assuming perfectly plastic behavior and using the initial specimen dimensions, while P_{max} is the maximum load observed in the test record.

Although the evidence discussed herein was derived from the crack face displacements, the limits of validity of fracture mechanics as exhibited by the inflection point of the $J_M R$-curve *also* showed evidence of a zone of plasticity: the initial remaining ligament length could be matched with the end of validity; the validity limit was reached when the average crack extension was 34% of the initial remaining ligament.

Bulk Constraint—Since the actual thickness was affected by the presence of a surface plasticity zone, a bulk constraint factor, $f(i)$, was inserted, "adjusting" to an effective thickness. This bulk constraint factor expressed functional dependence with the ligament thickness alone.

One important detail that should be discussed is the comparison of the bulk constraint factor with that of the initiation stretch. The initiation stretch results suggest that the basis for plasticity behavior and crack growth was independent of the thickness of the ligament, but a function of the fractional depth below the surface of the ligament, which would suggest that the bulk constraint factor, $f(i)$ should be constant. This was not the case, and it is thought to be so because the greater degree of crack extension at the center essentially separates the two phenomena into shear lip formation and flat fracture. For the thinnest specimen (No. 51, B = 6.4 mm, a_o/W = 0.5), the initiation stretch was virtually zero from the center to the surface, and $f(i)$ was very high. In this case, the bulk properties are effective in characterizing the fracture alone. The crack faces showed only shear lip zones. For the 12.7-mm-thick specimens, it should be noted that the flat fracture zone was virtually nonexistent.

The explanation to the apparent paradox is thought to be that the displacement characteristics, i.e., the shape of the profile, is defined by the elastic component, which is "allowed" by the surface plasticity. Thus, both the flat fracture and the surface plasticity zones contribute to the bulk constraint factor.

Application to Three-Dimensional Configurations—All of the configurations considered in this investigation were, in essence, three-dimensional. The compact tension, the center-cracked tension, and the single-edged notch tension specimens have been termed two-dimensional for convenience, and, strictly speaking, the results of testing such specimens should not be used if the crack front is not straight or is angled with respect to the side surfaces, conditions that do not suggest the degeneration of the problem to a two-dimensional analysis.

The current investigation considered such configurations that did not necessarily meet the straightness requirements and compared the results associated with averaged crack lengths to results that used the greatest extension of the crack with relative success. When the crack face displacements were considered, the apportioning of the components of the fracture event into two distinct regions, flat fracture and surface plasticity, was suggested. The apportioning was done using a methodology developed by Green and Knott [*9*] and modified by Gibson et al. [*7*], and the resulting analysis was ineffective in characterizing J_M or J. By looking further at an estimate of the $J_M R$-curve associated with the center plane, the fitted data were compared with $f(i)$, the bulk constraint factor, and this comparison suggested a similarity.

Conclusions

1. Two distinct zones of different fracture behavior were observed for the planar and the surface crack configurations [*14*], and these included a surface, shear-lip fracture zone and a central, flat-fracture zone.

2. The bulk constraint factor, $f(i)$, was a function of the ligament thickness only for the planar configurations tested, and $f(i)$ provides a measure of an effective thickness as compared to the full thickness subjected to plane strain conditions. The bulk constraint factor, $f(i)$, compared well with the coefficient, ϕ_i, derived to index the center-plane $J_M R$-curves. $f(i)$ was recast as a function of ligament proportion, R_L, for the purpose of the comparison.

3. Stretch resistance was defined as the deviation of the actual profile containing crack growth from that of a calibration profile at the final crack position with no crack extension.

4. The initiation stretch, δ_i, was characterized in the article and was a function of the depth beneath the side surfaces. The best correlation was produced with reference to the fractional depth of the cross section from the surface to the center plane.

Acknowledgments

Many should be thanked for their support and help in the development of the data and approaches used in this article. Messrs. Chris Wilson of Tennessee Tech and Wayne Gregg of NASA Marshall Space Flight Center must be noted for providing fracture specimens and funding this work through Grants NGT-50641 and NA G8-243.

APPENDIX

Definitions of Derivatives of K_{Ip} for Use in Equation 16

$$K_{IP} = \frac{P}{BW^{1/2}} \frac{\left(2 + \frac{a}{W}\right)\left(0.886 + 4.64\left(\frac{a}{W}\right) - 13.32\left(\frac{a}{W}\right)^2 + 14.72\left(\frac{a}{W}\right)^3 - 5.6\left(\frac{a}{W}\right)^4\right)}{\left[1 - \frac{a}{W}\right]^{3/2}} \tag{A}$$

$$\frac{\partial K_{IP}}{\partial a} = \frac{P}{2BW^{3/2}(1 + a/W)^{5/2}} \cdot 22.104 - 98.166\left(\frac{a}{W}\right) + 162.72\left(\frac{a}{W}\right)^2 - 52.44\left(\frac{a}{W}\right)^3 - 80.64\left(\frac{a}{W}\right)^4 + 50.4\left(\frac{a}{W}\right)^5 \tag{B}$$

$$\frac{\partial^2 K_{IP}}{\partial a^2} = \frac{P}{2BW^{5/2}(1 - a/W)^{7/2}} \cdot \left[-42.906 + 178.191\left(\frac{a}{W}\right) - 75.96\left(\frac{a}{W}\right)^2 - 296.34\left(\frac{a}{W}\right)^3 + 372.96\left(\frac{a}{W}\right)^4 - 126\left(\frac{a}{W}\right)^5\right] \tag{C}$$

$$\frac{\partial^3 K_{IP}}{\partial a^3} = \frac{P}{2BW^{7/2}[1 - a/W]^{9/2}} 329.1 - 954.5\left(\frac{a}{W}\right) - 471.2\left(\frac{a}{W}\right)^2 + 3418\left(\frac{a}{W}\right)^3 - 3427\left(\frac{a}{W}\right)^4 + 1071\left(\frac{a}{W}\right)^5 \tag{D}$$

References

[1] Dugdale, D. S., "Yielding of Steel Sheets Containing Slits," *Journal of the Mechanics and Physics of Solids*, Vol. 8, 1960, pp. 100–104.

[2] Ernst, H. A., "Material Resistance and Instability Beyond J-Controlled Crack Growth," *Elastic Plastic Fracture: 2nd Symposium, ASTM STP 803*, Vol. 1, 1984, pp. I-191–I-213.

[3] Ernst, H. A., "Study on the Deformation and Modified J-Integrals for Fracture Toughness Characterization," Final Report, ORNL RP-SB670-17, 1988.

[4] Ernst, H. A., "Recent Developments in Elastic Plastic Crack Growth Characterization," *Fracture Mechanics: 22nd Symposium, ASTM STP 1131, Vol. I,* H. A. Ernst, A. Saxena, and D. L. McDowell, Eds., 1992, pp. 136–157.

[5] Ernst, H. A. and Pollitz, E. T., "Methods to Characterize Crack Growth Under Elastic Plastic Conditions," circa 1988.

[6] Ernst, H. A. and Pollitz, E. T., 1989, "Fracture Toughness from Surveillance Data," EPRI RP-2975-10, Final Report.

[7] Gibson, G. P., Druce, S. G., and Turner, C. E., "Effect of Specimen Size and Geometry on Ductile Crack Growth Resistance in C-Mn Steel," *International Journal of Fracture,* Vol. 32, 1987, pp. 219–240.

[8] Goodier, J. N. and Field, F. A., *Fracture of Solids,* D. C. Drucker and J. J. Gilman, Eds., Wiley, New York, NY, 1963, pp. 103–118.

[9] Green, G. and Knott, J. F., "On the Effects of Thickness on Crack Growth in Mild Steel," *Journal of the Mechanics and Physics of Solids,* Vol. 23, 1975, pp. 167–183.

[10] Hellmann, D. and Schwalbe, K.-H., "Geometry and Size Effects on JR- and δR-Curves under Plane Stress Conditions," *Fracture Mechanics, 15th Symposium, ASTM STP 833,* 1984, pp. 577–605.

[11] Hutchinson, J. W., "Plastic Stress and Strain Fields at the Crack Tip," *Journal of the Mechanics and Physics of Solids,* Vol. 16, 1968, pp. 337–347.

[12] Hutchinson, J. W. and Paris, P. C., "Stability Analysis of J-Controlled Crack Growth," *Elastic Plastic Fracture: 2nd Symposium, ASTM STP 803,* Vol. 1, 1984, pp. 191–213.

[13] Irwin, G. R., "Analysis of Stresses and Strains Near the End of a Crack Traversing a Plate," *Journal of Applied Mechanics,* Vol. 24, 1957, pp. 361–364.

[14] Lambert, D. M., "*Three Dimensional Aspects of Elastic-Plastic Crack Growth,*" Ph.D. dissertation, Georgia Institute of Technology, 1994.

[15] Milosevic, Z., Bathias, C., and Pellessier-Tanon, A., "Ductile Crack Growth of Surface Cracks in Thin Welded Joints of an Aluminum Alloy 7020T6," *Engineering Fracture Mechanics,* Vol. 26, No. 1, 1987, pp. 33–43.

[16] Rice, J. R., "A Path Independent Integral and the Approximate Analysis of Strain Concentration by Notches and Cracks," *Journal of Applied Mechanics,* June 1968, pp. 379–386.

[17] Rice, J. R., Drugan, W. J., and Sham, T.-L., "Elastic-Plastic Analysis of Growing Cracks," *Fracture Mechanics, 12th Conference, ASTM STP 700,* 1980, pp. 189–221.

[18] Tada, H., Paris, P. C., and Irwin, G. R., *The Stress Analysis of Cracks Handbook,* Del Research Incorporated, St. Louis, MO, 1973.

[19] Wells, A. A., "Applications of Fracture Mechanics at and Beyond General Yielding," *British Welding Journal,* Vol. 10, 1963, pp. 563–570.

Thomas Siegmund[1] *and Wolfgang Brocks*[1]

The Role of Cohesive Strength and Separation Energy for Modeling of Ductile Fracture

REFERENCE: Siegmund, T. and Brocks, W., **"The Role of Cohesive Strength and Separation Energy for Modeling of Ductile Fracture,"** *Fatigue and Fracture Mechanics: 30th Volume, ASTM STP 1360,* P. C. Paris and K. L. Jerina, Eds., American Society for Testing and Materials, West Conshohocken, PA, 2000, pp. 139–151.

ABSTRACT: Barenblatt's idea of modeling the crack process zone by means of a cohesive zone has attracted considerable attention for predicting ductile crack growth. The model allows separation of the energy necessary for material separation from global plastic work. This has been a key problem in ductile fracture when searching for reasons for the geometry dependence of crack growth resistance curves. When using cohesive zone models, the correct determination of the cohesive zone material parameters is of eminent importance. In the past these parameters—the cohesive strength and the separation energy—were assumed to be material constants. However, micromechanical considerations show that this assumption is only an approximation in the case of ductile fracture. Here, the underlying mechanisms of void nucleation, growth, and coalescence are dependent on the stress triaxiality. This effect is accounted for in the new constitutive equation for cohesive zone models as presented here. In this new "triaxiality-dependent cohesive zone model," the cohesive material properties are taken to be dependent on the stress triaxiality in the solid element adjacent to the cohesive element. For low triaxiality, low values of cohesive strength and large values of the separation energy are observed; the opposite holds true for cases of high triaxiality. Ductile crack growth in a mild steel under quasistatic loading was investigated. The results from the use of the triaxiality-dependent cohesive zone model are compared to those of the Gurson-Tvergaard-Needleman (GTN) model as well as to the cohesive zone model with constant material parameters. The dissipation rate is shown to be a favorable measure for the characterization of the crack growth resistance. It allows the description of both the (global) plastic dissipation and the (local) work of fracture.

KEYWORDS: ductile fracture, micromechanical models, *J*-integral, dissipation rate, geometry effects, computational aspects, Gurson model, cohesive zone model

In the description of fracture, two important questions are discussed in the scientific community. The first one is the issue of providing a correct and physically meaningful picture of the processes occurring at the crack tip. The second question is on how the fracture toughness of a material in a specific structural geometry can be described. With the focus on a specific modeling approach, both issues have to be addressed to make possible model predictions reliable to the user.

One of the main requirements for a correct model description of fracture is that it must allow to predict the energy dissipation both due to global plastic deformation and due to the material failure itself separately. While material models for plastic deformation are well understood, much less is known about models for material separation. For ductile metals, such models have to capture the loss of stress-carrying capacity at the crack tip due to void nucleation, growth, and coalescence. Further-

[1] Scientist and professor, respectively, Institute of Materials Research, GKSS Research Center, Geesthacht, Germany.

more, from dimensional considerations, a length scale has to enter the constitutive formulation for material separation.

In a computational framework, two types of approaches were established throughout the last years. The use of the Gurson-Tvergaard-Needleman (GTN) model for the prediction of ductile fracture is, today, widely accepted [*1–4*]. Thereby, the material separation characteristics are described within a softening volumetric constitutive equation. This approach is attractive since it incorporates several of the features of the processes of void nucleation, growth, and coalescence into the constitutive description. In view of a computational realization, this model, however, has the main drawback that its solutions are mesh dependent [*5*]. The size of the elements in the crack growth region of the finite element mesh is conveniently being introduced as a material parameter of the constitutive description. This approach is not always accepted as satisfactory since it does not allow for convergent solutions with respect to the FE mesh. This issue is of importance when considering the coupling of the crack propagation analysis with Weibull statistics [*6*] in the analysis of the ductile-brittle transition.

An approach for modeling ductile fracture circumventing this problem is the application of the so-called cohesive zone models. Here, a set of cohesive surfaces elements is introduced into the finite element discretization [*7*]. The processes of void nucleation, growth, and coalescence are now no longer directly taken into account. Instead, it is the effective mechanical behavior of the failing material elements in front of the crack tip that is described by the constitutive relation of the cohesive zone. A cohesive strength, σ_{max}, and a cohesive energy, Γ, are the parameters that set the properties of the cohesive zone. This approach is able to provide convergent solutions for fracture [*8*]. Despite this very attractive feature, rather little effort has been undertaken in the scientific community to develop cohesive zone models appropriate for ductile fracture processes [*9*]. Cohesive zone models in their application to ductile fracture were based mainly on the assumption of cohesive strength and cohesive energy being material constants [*10–12*]. In the view of studies on the micromechanics of ductile failure, this assumption appears to be an approximation. Numerous studies have demonstrated that material separation based on void nucleation, growth, and coalescence strongly depends on the deformation history applied to the material under consideration [*13–15*]. The correct determination of the cohesive zone parameters is, however, of major importance within the cohesive zone modeling approach. In Ref *12*, in a study of dynamic crack growth, it was shown that the crack propagation behavior can shift from fast crack propagation to crack arrest if only a 15% change in the cohesive strength was taken into account.

A step to improve the constitutive equations for cohesive zone models for applications in the modeling of ductile fracture was undertaken in Ref *16* and subsequently applied to specimens of different geometries and size in Ref *17*. In this approach, the cohesive strength was taken to be dependent on the amount of plastic straining in the vicinity of the crack tip. Following this approach, the mesh size along the crack path turned out to be a model parameter, and the attractive feature convergence with respect to the finite element discretization was lost. The dependence of the cohesive zone parameters on the local conditions at the crack tip was also realized in Ref *18*, but no quantification of the effect was presented for inelastic material behavior.

We present a different way to improve the cohesive zone model for ductile fracture. The conditions at the crack tip are characterized in terms of the stress triaxiality, i.e., the ratio of hydrostatic stress to effective stress. The cohesive strength and energy are introduced in dependence on this quantity. The relationship between the stress triaxiality and the cohesive material parameters is found by studying material failure uncoupled from the crack problem.

With an appropriate material separation model at hand, the question arises on how to measure or predict, respectively, the tearing toughness of a certain material in a specific structure or specimen. The J-integral is the most widely used measure for this purpose. It has, however, the disadvantage that it does not allow distinguishing between the energy dissipated as (global) plastic deformation energy and (local) fracture energy, i.e., the cohesive energy. Furthermore, J is a cumulative quantity and

hence in general depends on the loading history. Additional complexities in its application arise when considering crack extension of several meters as in pipelines.

A different type of analysis can be performed considering the energy balance for an incremental process of crack extension, $\dot{A}$, under quasistatic loading:

$$\dot{W}_{ex} = \dot{U}_{el} + \dot{U}_{plas} + \dot{U}_{sep} \tag{1}$$

Here, W_{ex} is the work done by external forces, $\dot{U}_{el}$ and $\dot{U}_{plas}$ are the elastic and plastic components, respectively, of the internal energy of the body. Finally, $\dot{U}_{sep}$ is the energy required for material separation in the process zone. $\dot{U}_{sep}$ is related to the cohesive energy by:

$$\dot{U}_{sep} = \Gamma \dot{A} \tag{2}$$

It appears to be an attractive approach to define the tearing resistance of a material in a given specimen in terms of the energy dissipation rate, R [*19–21*]:

$$R = \frac{dU_{dis}}{dA} = \frac{dU_{plas}}{dA} + \Gamma \tag{3}$$

where $\dot{U}_{dis}$ is the dissipated energy per increment of crack area, $\dot{A}$. With micromechanical models as described above, it is possible to split R into global plastic dissipation, $\dot{U}_{plas}$, and the local cohesive energy, Γ. In addition, this approach becomes attractive since advanced analysis of fracture experiments by stereophotogrammetry recently demonstrated the possibilities of the determination of experimental values Γ [*22–23*].

This paper is intended to introduce the triaxiality-dependent cohesive zone model and to compare its capabilities to the GTN model and the cohesive zone model with constant material parameters, respectively. Both the J-integral and the energy dissipation rate are evaluated to demonstrate that combined efforts in the two issues of models for material separation and characterization of tearing resistance appear to be necessary to advance in the analysis of ductile fracture.

Material Separation Models

The Gurson-Tvergaard-Needleman-Model

Based on the analysis of a material element containing a void, the GTN model provides a set of equations describing the processes of void nucleation, growth, and coalescence. The set of equations includes a flow potential, Φ, relations for void evolution, and void coalescence. These relations are summarized in the following:

$$\begin{aligned}
\Phi &= \left(\frac{\sigma_e}{\sigma_M}\right)^2 + 2q_1 f^* \cosh\left(\frac{3q_2\sigma_h}{\sigma_M}\right) - [1 + q_3 (f^*)^2] \\
\dot{f} &= \dot{f}_{growth} + \dot{f}_{nuc},\ \dot{f}_{growth} = (1 - f)\,\dot{\varepsilon}_{kk}^{plas},\ \dot{f}_{nuc} = B\dot{\bar{\varepsilon}}^{plas} \\
B &= \frac{f_N}{s_N\sqrt{2\pi}} \exp\left\{-\frac{1}{2}\left[\frac{\bar{\varepsilon}^{plas} - \varepsilon_N}{s_N}\right]^2\right\}
\end{aligned} \tag{4}$$

$$f^*(f) = f \text{ for } f \le f_c \text{ and } f^* = f_c + k(f - f_c) \text{ for } f > f_c$$

σ_e denotes the effective and σ_h the hydrostatic stress. $\dot{\varepsilon}_{ij}^{plas}$ and $\dot{\bar{\varepsilon}}^{plas}$ are the increments in plastic strains

and equivalent plastic strain, respectively. f is the void volume fraction and f^* the modified void volume in the void coalescence stage. The material parameters to be determined are: the properties of the continuum surrounding the void (the elastic constants E, ν, the plastic deformation behavior $\sigma_M(\bar{\varepsilon}^{plas})$); the initial void volume (f_0); the void nucleation parameters (the volume of void that can nucleate, f_N, the plastic equivalent strain where the nucleation rate possesses is maximum value, ε_N, and the standard deviation of the assumed nucleation distribution function, S_N); the adjustment factors for void growth (q_1, q_2, q_3); and finally the parameters for void coalescence (the void volume fraction at the onset of void coalescence, f_c, and the growth acceleration factor, k). These parameters can be determined by the analyses of tests on round tensile bars. In addition, the use of this strain-softening constitutive relation must be combined with a length scale, D, to resolve the issue of localization. In most engineering applications of the GTN model, the length scale, D, is taken equal to the size of the elements in front of the crack tip [*2–4*]. The length scale then represents the height of the fracture process zone and is often assumed to be in the range of several hundreds of micrometers.

A ferritic steel (German designation StE460) [*2*] was used as a reference material. A possible set of material parameters that allows for the description of both tension tests on round bars as well as fracture mechanics tests in several specimen geometries was determined [*2*]: $E = 210\,000$ MPa, $\nu = 0.3$, $f_0 = 0.0025$, $f_N = 0.02$, $\varepsilon_N = 0.3$, $S_N = 0.1$, $q_1 = 1.5$, $q_2 = 1.0$, $q_3 = 2.25$, $f_c = 0.021$, $k = 3.4$, $D = 0.2$ mm. The plastic flow properties for the GTN model are taken from the true stress-strain curve of the steel under investigation (see Fig. 1). In the model realization of the fracture mechanics specimen, only the single row of elements in front of the initial crack tip is described by the GTN relation. The remaining part of the specimen is modeled as a material following the J_2-flow theory. Its elastic and plastic properties are taken to be identical to those of the matrix material surrounding the voids in the fracture process zone.

The Cohesive Zone Model with Constant Material Parameters

In the cohesive zone models, the material separation characteristics are given in the form of the effective relation between the tractions and displacement jumps across a set of predefined cohesive elements. For Mode I crack growth, the relation between the crack opening displacement, u_n, and the crack opening stress, σ_n, is given by [*7*]:

$$\sigma_n = \sigma_{\max}\, e\, z \frac{u_n}{\delta} \exp\left(-z\frac{u_n}{\delta}\right),\ \Gamma = \frac{9}{16}\sigma_{\max}\,\delta \text{ with } e = \exp(1),\ z = \frac{16e}{9} \tag{5}$$

Besides the specific form of the function (Eq 5), this approach needs two material parameters: the co-

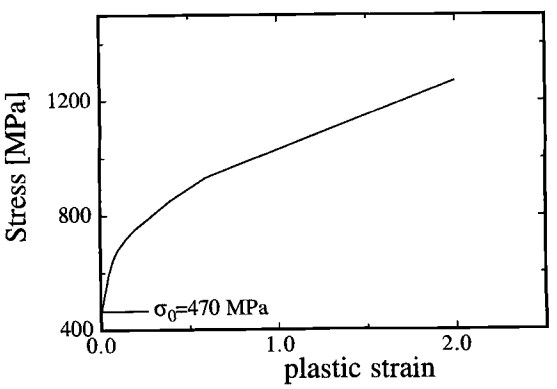

FIG. 1—*Plastic flow properties of the material under consideration.*

hesive strength, σ_{max}, and the cohesive energy, Γ. The resulting material length scale, δ, is embedded within the cohesive elements. No further introduction of a length scale linked to the finite element mesh becomes necessary. Constant values for σ_{max}, Γ, and δ, respectively, are commonly used in the application of this model to ductile fracture.

In the present application, a phenomenological approach described in Ref *24* for the determination of the cohesive zone material parameters was used for the cohesive zone model with constant material parameters. Γ was chosen such that the J-integral at crack growth initiation was represented; σ_{max} is fitted so that the slope of the $J - \Delta a$ is represented correctly.

The Triaxiality Dependent Cohesive Zone Model

Detailed studies of material unit cells containing voids [*13*] show that the behavior of such a material depends on the triaxiality of the stress state applied. The assumption of constant values for σ_{max}, Γ, and δ can, thus, only be an approximation. A micromechanically motivated approach for the determination of the cohesive zone parameters is thus to study failure of "unit" material elements uncoupled from the crack problem. Here, the properties of the material investigated in the unit cells are described by the GTN model. In Ref *10* the dependence of σ_{max} and Γ on the parameters $f_0, \sigma_0/E$ and N was studied. This study, however, considered only uniaxial straining of the unit cells in plane strain. Here, loading in plane strain under various constant applied stress ratios, $\rho = \sigma_1/\sigma_2$, is considered. The parameters of the GTN model are kept fixed. Typical results using the parameter set for the GTN model as described in the previous section are depicted in Fig. 2*a*.

The cohesive strength, σ_{max}, is taken as the maximum value reached by σ_2; the cohesive energy is equal to the areas under the curves in Fig. 2*a*. The shapes of the traction-separation curves obtained from the GTN model are different from those obtained from Eq 5. This difference is neglected in the remainder of the investigation. In fracture mechanics, the quantity stress triaxiality, T, defined as the ratio between hydrostatic stress and effective stress, is commonly used to quantify constraint at the crack tip. In plane strain the stress ratio, ρ, relates to T by:

$$\max(T) \approx \frac{1 + \rho}{\sqrt{3}\,(1 - \rho)} \tag{6}$$

For the small initial porosity considered here, Eq 6 describes well the maximum values of T reached during the loading process of the unit (see Fig. 2*b*). Only at large values of applied stress ratios the values of T reached during loading are slightly smaller than the values obtained by Eq 6. The depen-

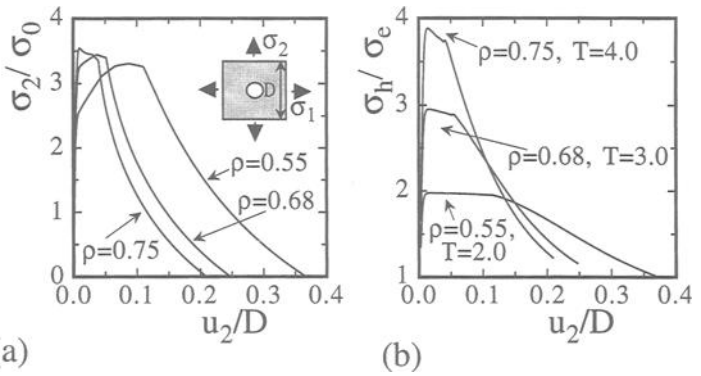

FIG. 2—*Behavior of a unit cell with a constitutive behavior described by the GTN model:* (a) *traction-separation behavior,* (b) *triaxiality-separation behavior.*

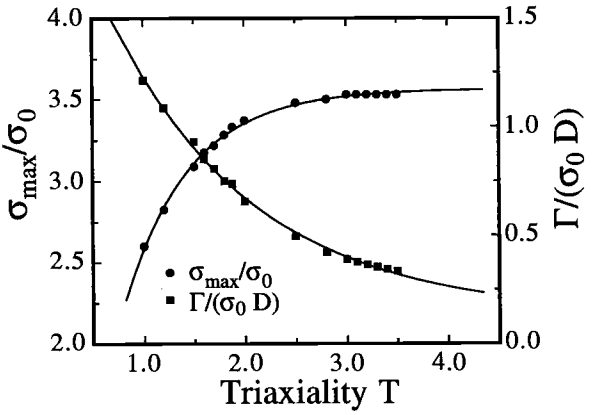

(a)

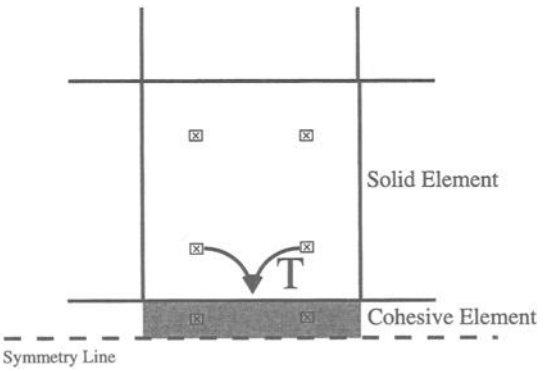

(b)

FIG. 3—(a) *The dependence of the cohesive zone material parameters on the stress triaxiality:* (b) *the finite element discretization set up for the triaxiality-dependent cohesive zone model.*

dence of the cohesive material parameters on T is given in Fig. 3*a*. These dependencies can well be described using the following functions:

$$\frac{\sigma_{max}}{\sigma_0} = -4.8 \cdot \exp\left[\frac{\max(T) + 0.032}{0.52}\right] + 3.56$$

$$\frac{\Gamma}{\sigma_0 D} = 0.57 \cdot \exp\left[\max(T) + 0.169\right] + 0.24 \tag{7}$$

Low values of cohesive strength and large values of cohesive energy are found at low applied values of T; the opposite is true for large values of T.

To incorporate the effects of local crack tip constraint into the cohesive zone model, both the cohesive strength and the cohesive energy are introduced as being dependent on the stress triaxiality

(see Fig. 3*b*). Within the finite element discretization of the cracked specimen, a row of cohesive surface elements is located along the assumed line of crack extension. The triaxiality dependence of the cohesive zone parameters is achieved by a coupling of the cohesive elements to the solid elements adjacent to the crack line. For each four-node solid element adjacent to the crack line, the values of the triaxiality at the two integration points closest to the crack line are averaged and transported into the corresponding cohesive element. Several different averaging procedure were tried, but very little influence on the predicted results was observed. The initial value of T was taken to be 1.0. Again, the bulk of the specimen is modeled as a material that follows the J_2-flow theory.

Results

The micromechanical models for material separation as presented in the previous section were applied to calculate crack growth in a M(T) and a C(T) specimen under the condition of plane strain. The geometries of the specimens are: M(T): $w = 50$ mm, $a_0/w = 0.5$; and C(T): $w = 50$ mm, $a_0/w = 0.59$. The numerical simulations use the micromechanical models for material separation as described in the previous section. In the finite element calculations, due to symmetry conditions, only half a specimen is considered for the C(T) specimen and a quarter of the complete specimen for the M(T) specimen. The size of the elements in front of the initial crack tip is taken to be ($D/2 \times D/2$).

The results obtained by the computational analysis are compared to experiments on specimens with the above-specified geometries. The specimens were sidegrooved with nominal thicknesses: M(T): $B_n = 16$ mm and C(T): $B_n = 20$ mm, respectively. The crack growth experiments were performed at the German Federal Institute of Materials Testing, BAM, Berlin [25].

The crack growth resistance of the material in the two types of specimen as quantified by the J-Δa curves is depicted in Fig. 4. The experimentally determined crack growth resistance is strongly dependent on the specimen geometry, with the C(T) specimen displaying a considerably lower resis-

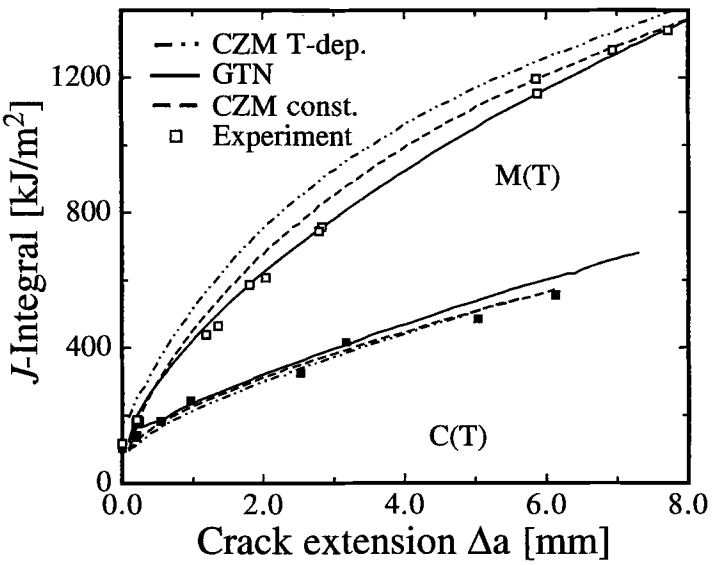

FIG. 4—*The crack growth resistance in form of* J-Δa *curves for the M(T) and C(T) specimen. Comparison of the experimental results to predictions from the GTN model, the cohesive zone model with triaxiality dependent, and constant parameters, respectively.*

tance than the M(T) specimen. Both the triaxiality-dependent cohesive zone model as well as the GTN model can predict this geometry dependence of the J-Δa curves well.

For the C(T) specimen, the experimentally determined and computationally predicted values from both computational models values are very close to each other. For the M(T) specimen, the GTN model also leads to very good predictions. For the triaxiality-dependent cohesive zone model, a deviation from the experimental values is observed for this specimen geometry, mainly in the intermediate range of the analyzed Δa range. This difference in the predictions of the two models for the M(T) specimen is due to the fact that in the triaxiality-dependent cohesive zone model, the quantity σ_{max}/σ_0 reaches a steady state value more rapidly than the corresponding quantity, $\max(\sigma_{22}/\sigma_0)$, in the GTN model. This difference in the numerical behavior of the models is subject of further investigation.

In addition to the GTN model and the triaxiality-dependent cohesive zone model, the crack growth analysis was also performed using the cohesive zone model with constant cohesive material parameters. Following the previously described approach to obtain the cohesive zone parameters, the best fit between experiments and the computational was achieved by using the following values for the cohesive zone parameters: $\sigma_{max}/\sigma_0 = 3.36$, $\Gamma/(\sigma_0 D) = 0.567$. This choice of parameters again results in a good prediction of the geometry dependence of the crack growth resistance; only in the M(T) specimen again a small deviation from the experimental curve is observed. It should be noted that these cohesive zone parameters determined by fitting experiments and simulation do not correspond to any pair of data in Fig. 3*a*; they can only be considered as phenomenological parameters without connection to the triaxiality-dependent micromechanical processes underlying the process of material separation.

In addition to the J-integral, contributions to the dissipation rate were determined and used as a measure for material toughness. In the finite element analysis, both contributions to this quantity—the global plastic dissipation rate and the work of separation—can be determined. For an incremental crack extension of area, $\dot{A}$, the rate of the plastic dissipation in the bulk of the specimen is given from the values of the effective stress, σ_e, and the rate of effective plastic strain, $\dot{\varepsilon}_{plas}$:

$$\dot{U}_{plas} = \int_v \sigma_e \dot{\bar{\varepsilon}}^{plas} dV \tag{8}$$

The volume integral is performed over that region of the specimen that is described by J_2-flow theory. For the GTN model, the work of separation, $\dot{U}_{sep}$, in an incremental crack advance, $\dot{A}$, is given by:

$$\dot{U}_{sep} = \int_v (1 - f)\, \sigma_e \dot{\bar{\varepsilon}}_{plas} dV \tag{9}$$

Here, the volume integral is performed over the single row of elements in front of the crack tip being described by the GTN model. For the cohesive zone model $\dot{U}_{sep}$ is found from:

$$\dot{U}_{sep} = \Gamma \dot{A} = \int \sigma_n du_n \cdot \dot{A} \tag{10}$$

To obtain the contributions to the dissipation rate, successive five-point least square linear fits were used in the numerical differentiation scheme from the energy versus crack extension records.

The two contributions to the dissipation rate, dU_{plas}/dA and Γ, are depicted separately in Fig. 5 and Fig. 6, respectively. Figure 5 shows the plastic dissipation rate as determined for the M(T) and C(T) specimen using the three different approaches for the material separation process at the crack tip. Just as for the J-integral the plastic dissipation rate is strongly dependent on the specimen geometry, the plastic dissipation rate is largest at the beginning of crack growth. For small amounts of crack growth, the M(T) specimen displays a considerably larger dissipation rate than the C(T) specimen. The absolute val-

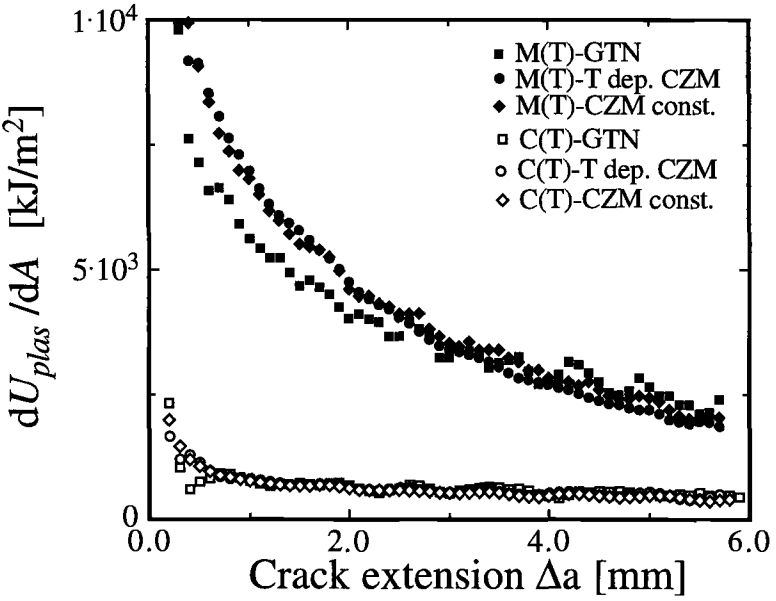

FIG. 5—*The plastic dissipation rate* dU_{plas}/dA *versus crack extension* Δa *curves for the M(T) and C(T) specimen. Comparison of predictions from the GTN model, the cohesive zone model with triaxiality dependent, and constant parameters, respectively.*

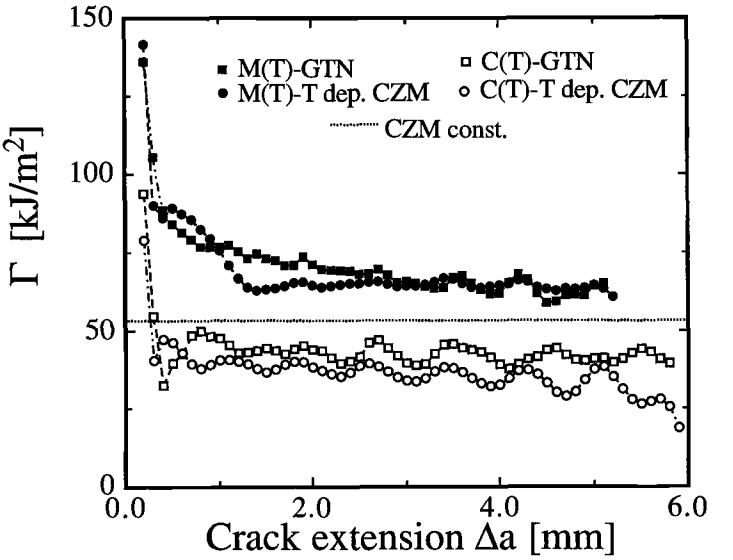

FIG. 6—*The local fracture energy (i.e., the cohesive energy,* Γ*) versus crack extension,* Δa*, for the M(T) and C(T) specimen. Comparison of predictions from the GTN model, the cohesive zone model with triaxiality-dependent and constant parameters, respectively.*

ues of dU_{plas}/dA as well as the difference in the values obtained for the C(T) and M(T) specimen subsequently diminishes in a transition stage. For the C(T) specimen, this transition phase is short, and only a small reduction in the plastic dissipation rate occurs. Nearly constant values of dU_{plas}/dA are obtained after a crack extension of approximately 2 mm. For the M(T) specimen the transition region is extended over a larger amount of crack growth. Also, the reduction in dU_{plas}/dA is considerably larger. All three modeling approaches result in very similar values of the plastic dissipation rate. Similar computational results on dU_{plas}/dA were already given in Ref *20* based on a $J(\Delta a)$ controlled crack growth simulation. Here, however, the investigation can proceed further. The introduction of the micromechanical models for material separation allows for evaluation of the amount of local fracture energy, Γ. Results on Γ in its dependence on Δa are depicted in Fig. 6. This diagram clearly shows that both the GTN model as well as the triaxiality-dependent cohesive zone model predict the local quantity Γ being dependent on the specimen geometry, too. Γ is predicted to be rather constant throughout the crack extension except for the very first stage of crack growth. Just as in the case of dU_{plas}/dA, there is a transition in the initial stage of crack growth where Γ is reduced from its initial values. The transition stage is again short in the C(T) specimen and larger in the M(T) specimen. The predictions of the two models are in good agreement with each other. The average value for Γ in the M(T) specimen is approximately 63 kJ/m^2, while it is approximately 36 kJ/m^2 in the C(T) specimen. For the triaxiality-dependent cohesive zone model, these values can be related to the triaxiality through Fig. 3*a*. For the M(T) specimen, $T = 1.9$, and for the C(T) specimen, $T = 3.0$, respectively. These values are in excellent agreement with the maximum values of the triaxiality reached in elements described by the GTN model in the respective specimen geometry. The computations using the cohesive zone model with constant model parameters are, on the other hand, not able to predict this effect. This unique and constant value of Γ used by the input data is approximately equal to the average of Γ in the M(T) and C(T) specimen.

The comparison of the two diagrams clearly shows that in the present case of crack growth under fully plastic conditions, the dissipation rate is dominated by the plastic dissipation rate. The ratio between dU_{plas}/dA and Γ in the C(T) specimen is initially 20 and after $\Delta a = 6$ mm approximately 12 to 15. This ratio is larger for the M(T) specimen; it is initially nearly about 100 and subsequently falls to 40.

For a detailed understanding and evaluation of the fracture processes, it is, in addition, of interest to evaluate the local material separation behavior at the crack tip. This part of the specimen response is not directly accessible by experiments. The material separation behavior is investigated at the location $\Delta a = 4$ mm. At this location, a steady state of the relation between the opening stress and the displacement jump across the crack surfaces has already been reached. Figure 7 depicts the material separation behavior for the M(T) and C(T) specimen as predicted by the triaxiality-dependent cohesive zone model, GTN model, and the cohesive zone model with constant material parameters. The physically process-based GTN model clearly predicts a material separation curve for the C(T) specimen different from that in the M(T) specimen. The peak stress reached in the C(T) specimen is only slightly larger than in the M(T) specimen. This is due to the initially moderate strain hardening of the matrix material (Fig. 1). The displacement after which the stress falls to zero is nearly twice as large in the M(T) specimen compared to the C(T) specimen. The geometry dependence of the material separation in the fracture process zone cannot be captured by the use of the cohesive zone model with constant material parameters. In this case, the material separation is independent of the specimen geometry. Introducing, however, σ_{max} and Γ as dependent on the triaxiality, the predictions improve considerably, and a geometry dependence of the material separation is again predicted. As seen from Fig. 7, the predictions of the material separation from the triaxiality-dependent cohesive zone model are in very good agreement with those from the GTN model.

The issue of mesh size dependence was widely discussed in the use of the material separation models for crack growth. This issue was investigated in the present case for the C(T) specimen. This specimen was analyzed using the GTN model as well as the triaxiality-dependent cohesive zone model in three different meshes. The element sizes in the homogeneously meshed zone in front of the initial crack tip are: $h_{min} = 0.2$, 0.1, and 0.05 mm. Results of crack growth simulations for these three different meshes are depicted in the form of J-Δa curves (Fig. 8). The results from computations for h_{min}

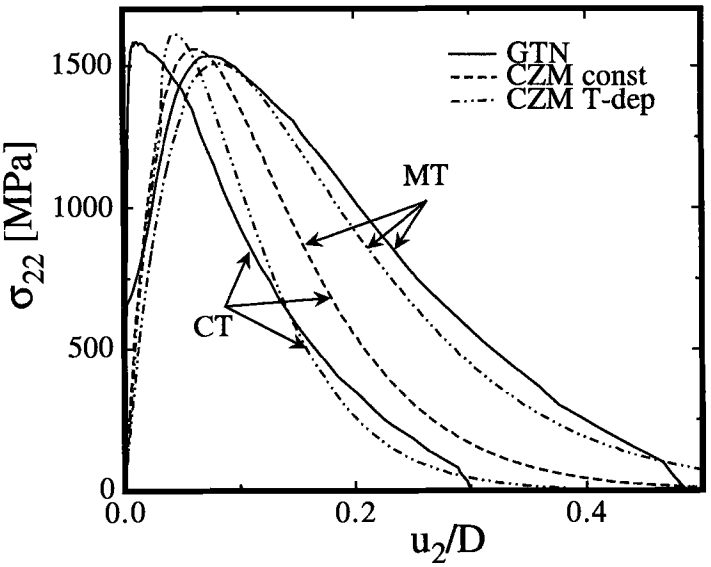

FIG. 7—*The traction-separation relations at the location Δa = 4 mm for the M(T) and C(T) specimen. Comparison of predictions from the GTN model, the cohesive zone model with triaxiality dependent, and constant parameters, respectively.*

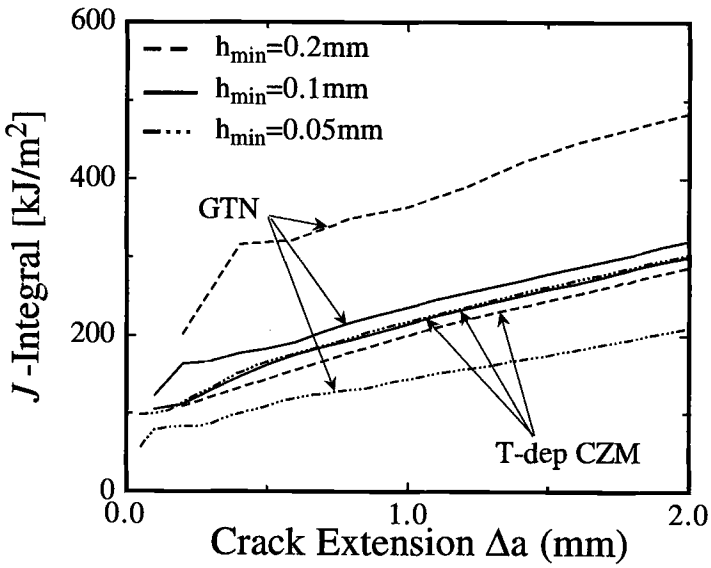

FIG. 8—*The crack growth resistance curve for the C(T) specimen as predicted by the GTN model and the triaxiality-dependent cohesive zone model influence of the element size in the homogeneously meshed zone in front of the initial crack tip.*

= 0.1 mm are identical to those already depicted in Fig. 3. This element size, h_{min}, in the case of the GTN model corresponds to half the height of the process zone, D, and is part of the material description. For the GTN model, the results of the crack growth simulation are thus strongly dependent on the mesh size. A decrease in mesh size results in a considerable reduction of the predicted crack growth resistance. The triaxiality cohesive zone model, on the other side, exhibits a very different behavior to a change in mesh size. A reduction in the element size leads to convergence of the obtained J-integral values. The finest mesh results in the highest values of crack growth resistance. The coupling of the cohesive elements to the solid elements via the stress triaxiality does not introduce a new additional mesh dependence of the solution.

Conclusion

Ductile crack growth in a mild steel was investigated using a newly developed triaxiality-dependent cohesive zone model. The model is micromechanically motivated and calibrated by studying material failure on unit cells separated from the actual crack problem. The computational results from the use of this model are in very good agreement with those obtained from the GTN model. This is true, both on the level of global specimen behavior as well as for local quantities at the crack tip. An agreement in the predictions for the process within the fracture process zone between the GTN model and the cohesive zone models cannot be obtained considering constant cohesive material parameters. It is important to note here that the feature of mesh convergence is not lost using the stress triaxiality as a measure to adjust the cohesive zone material parameters. This is in contrast to the strain-dependent cohesive zone model of Ref *16* and is due to the fact that the stresses at the crack tip remain bounded by the cohesive strength.

The new model can be understood as an intermediate step between the physically motivated GTN model and the more phenomenologically motivated cohesive zone models. The model is thus promising as it combines the most attractive features of both modeling approaches to ductile fracture. The present approach may help in a further understanding of elastic-plastic fracture mechanics since it allows for the splitting of the energy dissipation terms. For the C(T) specimen investigated here, the ratio between the global plastic dissipation rate and the cohesive energy is in the same range as recently determined experimental values [*22*].

However, in the present case of crack initiation under full plastic deformation of the specimens, the influence of the local quantities in the fracture process zone of the global specimen response is negligible, and all three approaches predicted very similar J-Δa curves that are in good agreement with the experimentally obtained values for the crack growth resistance. The effect of the cohesive zone parameters on the global behavior of a specimen is expected to be much larger in contained or small-scale yielding situations; the triaxiality dependence of the cohesive parameters will be retained there. There, the ratio between cohesive energy and the J-integral or the energy dissipation rate, respectively, is much smaller than in the specimen investigated here [*10*]. Thus, the necessity of a correct determination and calibration of the cohesive material parameters will be of even more importance.

References

[*1*] Needleman, A. and Tvergaard, V., "An Analysis of Ductile Rupture Modes at a Crack Tip," *Journal of the Mechanics and Physics of Solids,* Vol. 35, No. 2, 1987, pp. 151–183.

[*2*] Brocks, W., Klingbeil, D., Künecke, G., and Sun, D.-Z., "Application of the Gurson Model to Ductile Tearing Resistance," *Proceedings,* ASTM Conference on Constraint Effects in Fracture: Theory and Applications, M. Kirk and A. Bakker, Eds., Constraint Effects in Fracture Theory and Applications, Second Volume, *ASTM STP 1244,* 1995, pp. 232–252.

[*3*] Xia, L., Shih, C. F., and Hutchinson, J. W., "A Computational Approach to Ductile Crack Growth under Large Scale Yielding," *Journal of the Mechanics and Physics of Solids,* Vol. 43, 1995, pp. 389–413.

[*4*] Ruggieri, C., Dodds, R. H., and Panontin, T. L., "Numerical Modeling of Ductile Crack Growth in 3-D Using Computational Cell Elements," *International Journal of Fracture,* Vol. 82, No. 1, 1996, pp. 67–95.

[5] Needleman, A. and Tvergaard, V., "Mesh Effects in the Analysis of Dynamic Ductile Crack Growth," *Engineering Fracture Mechanics,* Vol. 47, No. 1, 1994, pp. 75–91.

[6] Mudry, F., "A Local Approach to Cleavage Fracture," *Nuclear Engineering and Design,* Vol. 105, 1987, pp. 65–76.

[7] Needleman, A., "An Analysis Decohesion Along an Imperfect Interface," *International Journal of Fracture,* Vol. 42, 1990, pp. 21–40.

[8] Needleman, A., "Numerical Modeling of Crack Growth Under Dynamic Loading Conditions," *Computational Mechanics,* Vol. 19, 1997, pp. 463–469.

[9] Broberg, K. B., "The Cell Model of Materials," *Computational Mechanics,* Vol. 19, 1997, pp. 447–452.

[10] Tvergaard, V. and Hutchinson, J. W., "The Relation between Crack Growth Resistance and Fracture Process Parameters in Elastic-Plastic Solids," *Journal of the Mechanics and Physics of Solids,* Vol. 40, No. 6, 1992, pp. 1377–1397.

[11] Lin, G., Kim, Y.-J., Cornec, A., and Schwalbe, K.-H., "Fracture Toughness of a Constrained Metal Layer," *Computational Materials Science,* Vol. 9, 1997, pp. 36–47.

[12] Siegmund, T. and Needleman, A., "A Numerical Study on Dynamic Crack Growth in Elastic-Viscoplastic Solids," *International Journal of Solids and Structures,* Vol. 43, No. 7, 1997, pp. 769–787.

[13] Koplik, J. and Needleman, A., "Void Growth and Coalescence in Porous Plastic Solids," *International Journal of Solids Structures,* Vol. 24, No. 8, 1988, pp. 835–853.

[14] Brocks, W., Sun, D.-Z., and Hönig, A., "Verification of the Transferability of Micromechanical Parameters by Cell Model Calculations with Visco-Plastic Materials," *International Journal of Plasticity,* Vol. 11, No. 8, 1995, pp. 971–989.

[15] Faleskog, J. and Shih, C. F., "Micromechanics of Void Coalescence-I. Synergistic Effects of Elasticity, Plastic Yielding and Multi-Size-Scale Voids," *Journal of the Mechanics and Physics of Solids,* Vol. 45, No. 1, 1997, pp. 21–50.

[16] Tvergaard, V. and Hutchinson, J. W., "Effect of Strain-Dependent Cohesive Zone Model on Predictions of Crack Growth Resistance," *International Journal of Solids and Structures,* Vol. 33, Nos. 20–22, 1996, pp. 3297–3308.

[17] Tvergaard, V., "Relations Between Crack Growth Resistance and Fracture Process Parameters under Large Scale Yielding," *Nonlinear Analysis of Fracture,* J. R. Willis, Ed., Kluwer Academic Publishers, 1997, pp. 93–104.

[18] Gao, H. and Klein, P., "Numerical Simulation of Crack Growth in an Isotropic Solid with Randomized Internal Cohesive Bonds," *Journal of the Mechanics and Physics of Solids,* Vol. 46, No. 2, 1998, pp. 187–218.

[19] Turner, C. E., "A Re-Assessment of Ductile Tearing Resistance, Part I: The Geometry Dependence of J-R Curves in Fully Plastic Bending, Part II: Energy Dissipation Rate and Associate R-Curves on Normalized Axes," *Proceedings,* Fracture Behavior and Design of Materials and Structures, 8th European Conference on Fracture, D. Firrao, Ed., EMAS, Warley, UK, 1990, pp. 933–949, 951–968.

[20] Memhard, D., Brocks, W., and Fricke, S., "Characterization of Ductile Tearing Resistance by Energy Dissipation Rate," *Fatigue and Fracture of Engineering Materials and Structures,* Vol. 16, No. 10, 1993, pp. 1109–1124.

[21] Kolednik, O., Shan, G., and Fischer, F. D., "The Energy Dissipation Rate—A New Tool to Interpret Geometry and Size Effects," *Fatigue and Fracture Mechanics: 27th Volume, ASTM STP 1296,* R. S. Piascik, J. C. Newman, and N. E. Dowling, Eds., American Society for Testing and Materials, Philadelphia, 1997, pp. 126–151.

[22] Stampfl, J., Scherer, S., Gruber, M., and Kolednik, O., "Reconstruction of Surface Topologies by Scanning Electron Microscopy for Application in Fracture Research," *Applied Physics A,* Vol. 63, 1996, pp. 341–346.

[23] Stüwe, H. P., "The Work Necessary to Form a Ductile Fracture Surface," *Engineering Fracture Mechanics,* Vol. 13, 1980, pp. 231–236.

[24] Tvergaard, V. and Hutchinson, J. W., "Effect of T-Stress on Mode I Crack Growth Resistance in a Ductile Solid," *International Journal of Solids and Structures,* Vol. 31, 1994, pp. 823–833.

[25] Häcker, R., Gerwien, P., Thiemich, K.-D., Wossidlo, P., and Baer, W., "Comparison of Results of Fracture Investigations on C(T) and M(T) Specimen of Material StE 460," Report No. BAM-V.33 98/2, German Federal Institute of Material Testing, Berlin, Germany, 1998.

I. C. Howard,[1] *Z. H. Li,*[2] *M. A. Sheikh*[3]

Modeling the Ductile to Cleavage Transition in Steels and Structures

REFERENCE: Howard, I. C., Li, Z. H., Sheikh, M. A., **"Modeling the Ductile to Cleavage Transition in Steels and Structures,"** *Fatigue and Fracture Mechanics: 30th Volume, ASTM STP 1360,* P. C. Paris and K. L. Jerina, Eds., American Society for Testing and Materials, West Conshohocken, PA, 2000, pp. 152–168.

ABSTRACT: The process of ductile damage and subsequent crack growth and of cleavage in ferritic steels occur in steps whose controlling microstructural features are quite different. Useful models of these can, therefore, be attempted by associating the mechanisms of ductile damage or cleavage with an appropriate, microstructurally controlled, cell size. Furthermore, the cell size for ductile damage is typically too large to be used for the crack-tip finite elements that are required for accurate resolution of the large strain gradients in the continuum field that represents the deformation there prior to significant damage development. What is required is a finite-element code that allows (at least potentially) the presence of cells of more than one size.

These considerations have led to mesh-independent damage mechanics modeling, and a model of the ductile-to-brittle transition that has appropriate cell sizes for each failure mechanism. The complexity of these refined models demands very large computational times for technically interesting problems. Accordingly, our predictions of the outcome of engineering tests have used a compromise single-size cell model chosen to balance the conflicting requirements for each failure process. The paper describes the proving of this, and its use in predicting two of the large-scale spinning cylinder tests.

The work illustrates the potential conflict that may arise between the detailed accuracy required for rigorous physical representation and the pragmatism needed to capture the essentials of application-driven research programs. The paper ends with a discussion of the possible relations between these approaches and their areas of effectiveness.

KEYWORDS: damage mechanics, local approach, ductile-to-brittle transition, pressure vessel steels, multi-cell modeling, cell modeling, large-scale tests

This paper describes the development of ideas for modeling various mechanical aspects of the ductile and brittle fracture behavior of ferritic steels and encapsulating it in a structural analysis code. In a major sense, the work is dedicated to the study of how to extract data from laboratory-sized tests and use it in models of material micro-behavior that are sufficiently robust to allow the prediction of tests that are very different in terms of geometry, scale, and loading. This is a tall order.

Despite this, results emerging from the work of several laboratories worldwide show that it can be accomplished in a variety of different ways. This fact alone is indicative of the anticipated robustness of the approach, which gives hope that tools developed from these studies will be useful and reliable in the future for the purposes of engineering assessment of critical structures.

[1] Reader, SIRIUS, Department of Mechanical Engineering, the University of Sheffield, Mappin Street, Sheffield S1 3JD, UK.

[2] Research assistant, SIRIUS, now at BAe, Airbus Division, Filton, Bristol, UK.

[3] Research assistant, SIRIUS, now at the Department of Mechanical Engineering, UMIST, Manchester, UK.

* SIRIUS is the Structural Integrity Research Institute of the University of Sheffield.

Basic Physical Principles

It has been well known for some considerable time that the fracture behavior of ferritic steels is dominated by two main effects, ductile rupture and cleavage. Ductile rupture results from void growth associated with the larger inclusions (typically MnS) in the steel. Cleavage is due to the propagation of micro-cracks that are born in the failure of particles (like grain-boundary carbides). This particle failure is induced by the plastic strains imposed on the particles as the macroscopic plastic zone sweeps over them. These underlying physical causes impose fundamental size scales on any models, particularly those using continuum mechanics, that attempt to describe or predict these phenomena. In particular, metallurgical observations combined with mechanical modeling (for example, [*1*] and [*2*]) suggest that the scale for cleavage modeling should be around 50 μm. On the other hand, studies towards the same end in the ductile regime suggest that the scale is much larger. Our own work has concentrated upon scales of the order of 250 to 500 μm, based upon metallographic study of particle sizes and distributions, and the effectiveness of modeling the influence of ductile damage on the deformation of notched round bars. Whatever the detailed choices of the scale for each of these processes, it is clear that they are probably substantially different.

Within this scenario, the modeling of these processes via continuum mechanics-based finite-element methods proceeds by identifying certain cell sizes in the crack tip region of the finite-element mesh. Figure 1 indicates the thinking behind this.

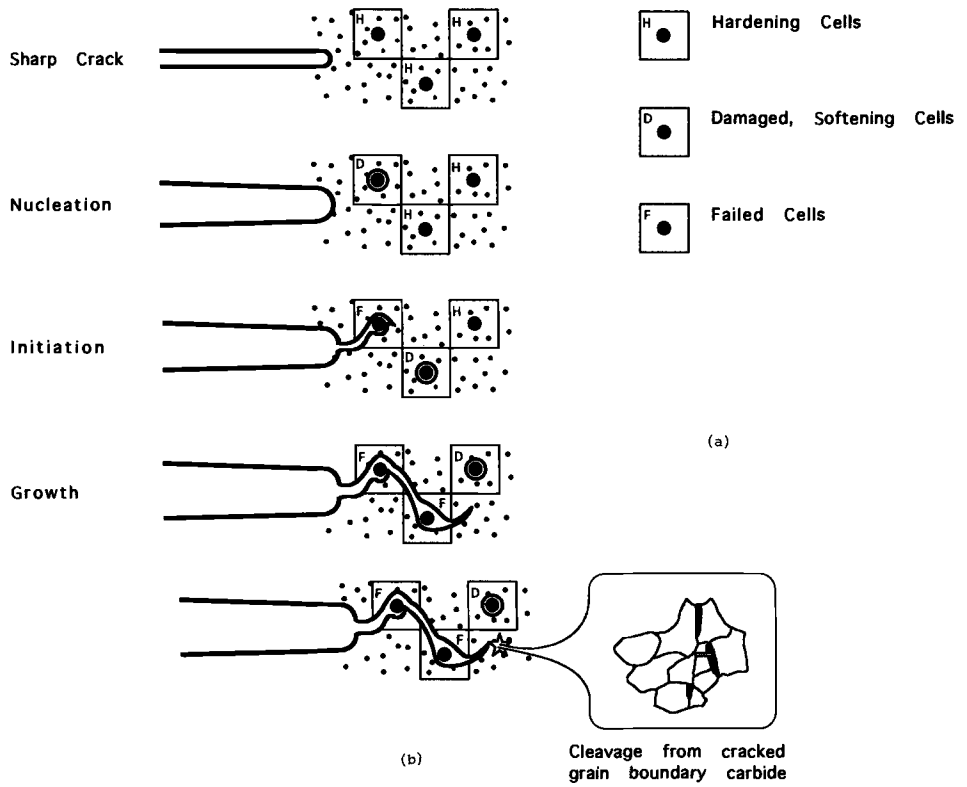

FIG. 1—*The structure of "local approach" cells in the crack-tip region.* (a) *Ductile damage mechanics cells, indicating the cell behavior as it hardens, softens, and fails, thereby providing the mechanism for crack advance.* (b) *The sampling, in the field ahead of the current crack tip, of the parameters that influence the probability for cleavage.*

For cleavage fracture, the Beremin [*1*] local approach model references a two-parameter Weibull description of the cumulative probability of cleavage initiation, p:

$$p = 1 - \exp\{-(\sigma_W/\sigma_u)^m\} \tag{1}$$

where σ_W is the Weibull stress that characterizes the severity of applied crack-tip loading, σ_u and m are material-specific parameters that respectively describe the intrinsic resistance of the material to cleavage (Weibull scale parameter) and the material scatter (Weibull shape parameter). The Weibull stress is calculated from a knowledge of the crack-tip stress and strain fields calculated with respect to a characteristic cell size. This cell size (typically 50 μm) is directly linked to the distribution of potential cleavage initiation sites within the microstructure [*1*]. When implemented in a finite-element model, the procedures evaluate the Weibull stress as

$$\sigma_W = \left\{ \sum_{\text{plastic zone}} \sigma_1^{\text{m}} \frac{\Delta \text{V}}{\text{V}_u} \right\}^{1/m} \tag{2}$$

in terms of the maximum principle stress σ_1 in each cell (of volume ΔV) throughout the plastic zone.

For ductile fracture, the Rousselier damage model [*3*] is based on the use of a constitutive equation to represent the mechanical properties with reference to an appropriate failure criterion. The model uses a modified plastic potential of the form:

$$F = \frac{\sigma_{eq}}{\rho} - H + \sqrt{3}DB(\beta)\exp\left\{\frac{C\sigma_m}{\rho\sigma_Y}\right\} \tag{3}$$

where H characterizes material work hardening, σ_{eq} is the von Mises equivalent stress, and ρ is the material density. Together, the first two terms represent yielding by the usual von Mises flow theory. The third term represents softening of the material due to the growth and coalescence of micro-voids. The parameters C and D are material-specific constants whose values control the sensitivity of softening to imposed hydrostatic stress and to strain. Beta (β) is the damage variable and $B(\beta)$ is a function that depends parametrically on C, the yield stress (σ_Y) and the initial void volume fraction (f_0). (The work described in this paper could have described the mechanics of ductile failure by any model with similar predictive properties to that of Rousselier. In particular, a suitable tuning of the Gurson-Tvergaard [*4,5*] model would have been equally useful.)

In the crack-tip region, the computation is performed in respect of a characteristic cell size, representative of the spacing between the largest second-phase particles within the microstructure (typically 250 to 500 μm, as previously mentioned).

Multi-Cell Modeling

This work arose from an attempt [*6*] to remove the mesh-dependency of the solution for ductile damage mechanics assessments of cracked specimens and components. The test-bed for demonstrating whether or not the techniques were successful was the study of the first of the spinning cylinder tests, which had already been shown [*7*] to be interpretable through the use of ductile damage mechanics. Essentially, the idea was to create meshes fine enough for each individual damage mechanics cell to include a number (the size of which would define the degree of refinement of any particular multi-cell model) of finite elements. The principles of this are shown in Fig. 2, where the crack-tip cell is highlighted for a model with one element per cell and one with 64 elements per cell. There were three types of model assessed in this study:

(a) the crudest, the one that has been the workhorse of virtually all applications of ductile dam-

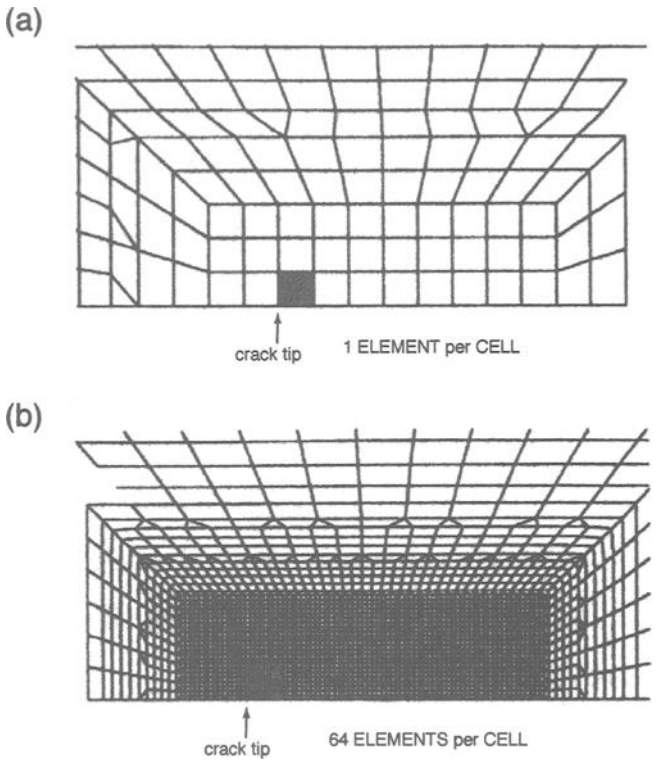

FIG. 2—*The undeformed meshes for two multi-cell models, where the crack tip cell is highlighted for* (a) *a model with one element per cell, and* (b) *one with 64 elements per cell. Note that the cell size is identical for each model.*

age mechanics, where the crack-tip mesh is identical with the cell structure there;

(b) two refinements, where each damage mechanics cell contained a number of internal finite elements, but where the behavior of the cell depended on different ways of sampling the fields in the elements within the cell;

(b1) the "fixed-cell" model, in which initiation was identified by 75% of the cell Gauss points having passed through the maximum of opening stress,

(b2) the "mesh-independent" model where the point of "significant damage" in the cell was identified by 75% of the cell Gauss points reaching the critical β-value obtained from studies on the behavior of notched bars. Once this point had been reached, all the stress and strain values in the elements within that cell were constrained to have the same value, which then changed with further deformation.

The behavior of these three models can be gaged from Fig. 3, where increasing realism of the blunted crack-tip shape is associated clearly with refinement of the model. Furthermore, the initiation of ductile crack growth can be estimated by the failure point of the first ductile cell. Table 1 sets out these predictions and shows unequivocally that the "mesh independent" model has the physical characteristics of its name. It is this model that held promise for an attempt at realistic modeling of the transition regime of ferritic steels by allowing the proper incorporation of different length scales for each of the ductile and cleavage processes.

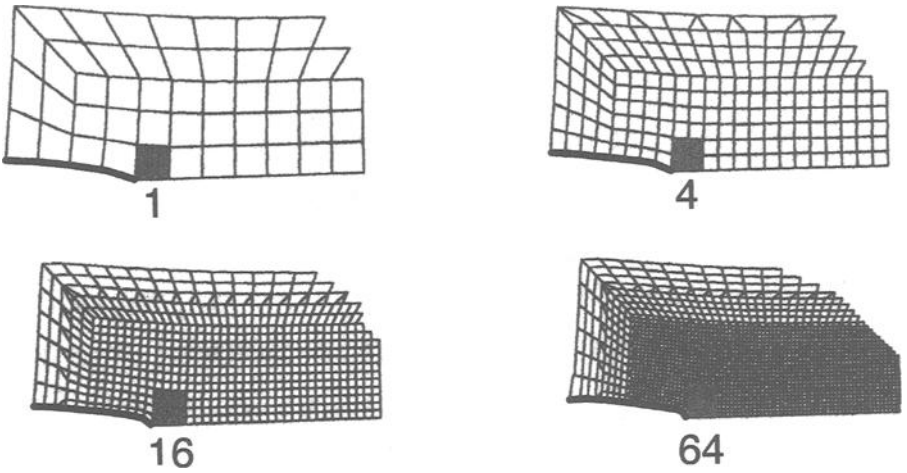

FIG. 3—*The deformed, near-tip, mesh configurations for each of the four models studied. In particular, the quality of modeling of the blunted crack shape increases noticeably with model refinement. The highlighted crack-tip cell is annotated with the number of internal elements in the finite-element mesh.*

TABLE 1—*Predicted results for the initiation value of* J *(MJ/m^2) as a function of mesh refinement for the different models for the mechanics of the ductile damage cell.*

	0.5-mm Mesh	0.25-mm Mesh	0.125-mm Mesh	0.0625-mm Mesh
Same mesh and cell size	0.171	0.100	0.063	
Cell size fixed: variable mesh	0.103	0.130	0.095	0.051
Mesh-independent cells	0.160	0.151	0.148	0.148

Coupled Models

Our approach to describing fracture in the transition regime, where cleavage initiation is preceded by ductile tearing, has been to couple the Beremin and Rousselier models in the same computational procedure. The work began by studying the relative performance of two models of doing this. The first of these, a "pragmatic" model, Type I, was chosen to combine the cell modeling in a computational procedure with practically acceptable turn around times. The second, Type II, dealt with the different scales for ductile failure and cleavage by suitable developments of the multi-cell models described above. The essential difference between the models is that Type I models have the same cells for evaluating both ductile processes and the approach to cleavage, while those of Type II do this in different cells of sizes appropriate to the underlying process. Figure 4 illustrates the two approaches [*8*]. In brief, for the A508 Class 3 steel [*9*] from which the fracture specimens were made, suitable local approach parameters are the following:

$$\text{Beremin model: } \sigma_u = 3141\ MPa \qquad m = 19 \qquad \lambda = 50\ \mu m$$

$$\text{Rousselier model: } C = 0.65 \qquad D = 1.3 \qquad f_0 = 6.71 \times 10^{-5} \qquad L = 500\ \mu m$$

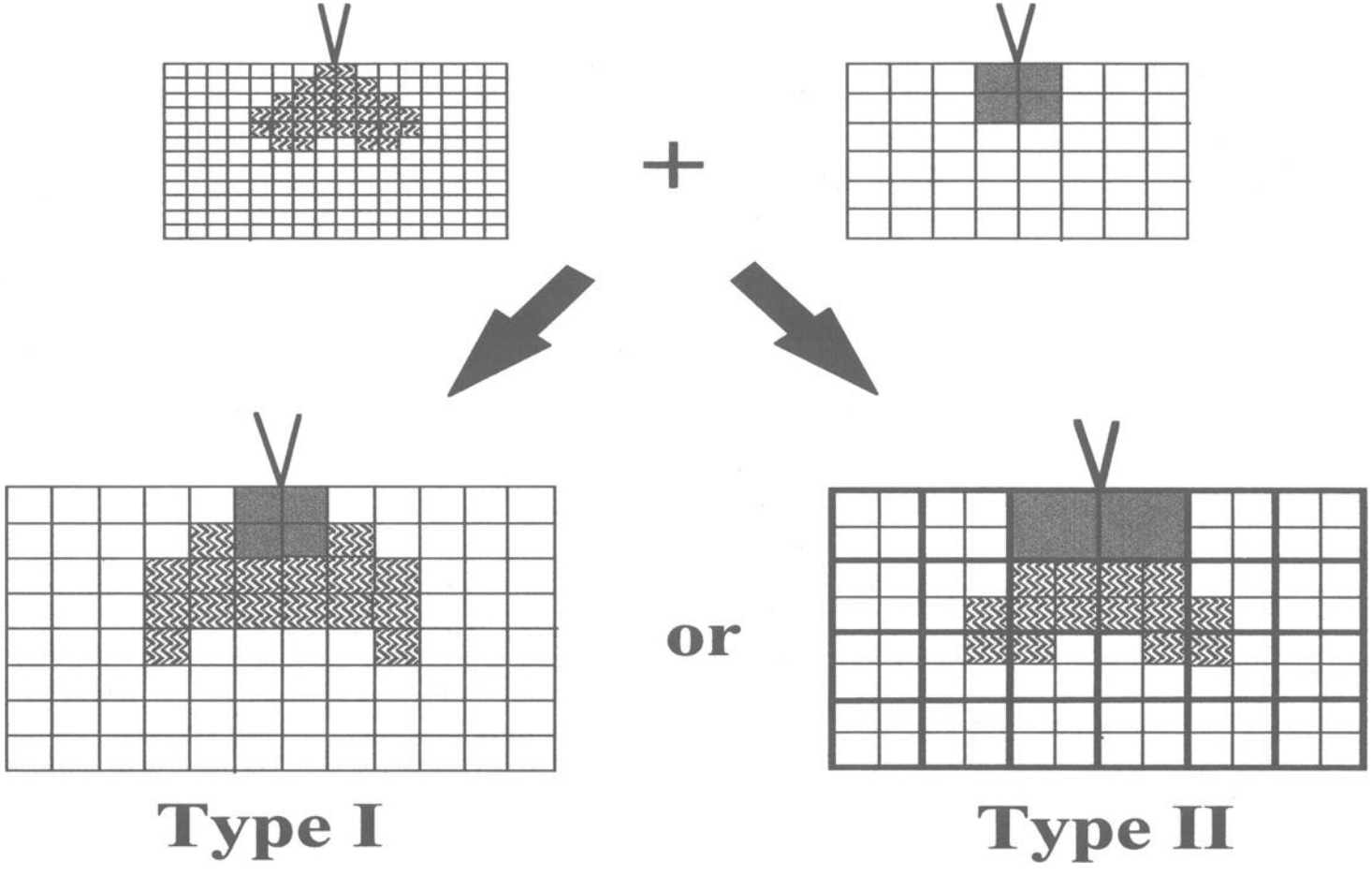

FIG. 4—*Schematic illustration of the coupling of the Beremin model of cleavage to the Rousselier model of ductile damage to either a Type I or Type II coupled model. In Type I models, the cell sizes are forced to the same value, while in Type II models they retain their individual values.*

Taking the models in reverse order, the Type II model is a straightforward extension of the ductile multi-cell model described above. Each 500 × 500-μm ductile damage cell is subdivided into a suitable number, here 10 × 10, of elements each of which represents a cleavage cell. The calculation of σ_W is continually updated by evaluation over this fine mesh. The instant when 75% of the Gauss points in the elements within a larger ductile cell have achieved a value of the damage variable $\beta \geq 0.6$ (this value having been established from an independent simulation of plain tensile test data) defines the attainment of the state of significant damage within that cell. This point is where softening begins to dominate the response of the cell, and henceforth the elements within it have their variables constrained to respond identically so that the cell behaves as a single entity. The calculation of the cumulative failure probability excludes the elements in the cells that have passed into the flanks of the crack as it advances by ductile growth.

The Type I model is simpler; it assumes that the cell sizes for cleavage and ductile damage are the same. In the present case, this size is 125 μm, and the crack tip is surrounded by elements of this size that deal simultaneously with both potential failure processes. From the previous point of view, this approach is one of pragmatic compromise. Even so, it is necessary to recalibrate the local approach parameters since they are both sensitive to cell size. The retuned values are:

$$\sigma_u = 3278\ MPa \qquad m = 28.6$$

$$C = 0.66 \qquad D = 1.39$$

The analysis proceeds from the current state by assessing the element immediately ahead of the tip to discover whether or not sufficient ductile damage has accumulated for it to move forward. If so, it does. The cumulative probability of cleavage is then updated by sampling all the cells, having previously recorded the peak value from cells where σ_W drops by virtue of them passing into the crack flanks.

The effectiveness of these two approaches was tested by using each to predict the transition curve of an A508 Class 3 steel for which a reasonably full set of data was available [*9*]. Figure 5 shows the results, where it is difficult to discriminate between the performance of the two models. From the "scientific" point of view, the similarity of the Type II predictions to those of Type I is quite disappointing, for the incorporation of what appears to be the essential physics of the cell modeling seems to have little effect in practice. When one recognizes the extra computational costs in using Type II models (an order of magnitude slower in turning a job around), the disappointment is increased further. On the other hand, the comparison shows the practical usefulness of the Type I model in addressing real data and provides real evidence in support of the pragmatic use of the Type I model in the prediction of the large-scale structural tests that will now be described. A comparison between the two models is set out in Table 2.

Once this point had been reached, the potential usefulness of the Type I strategy could only be gaged by trying it out on a real structural test. The data for that was available for Test 4 in the AEA Technology program of spinning cylinder tests, and what follows describes the attempt.

TABLE 2—*Comparison of the two coupled transition models.*

Type I	Type II
Approximate crack-tip fields	Accurate crack-tip fields
"Proxy" cell sizes	Representative cell sizes
Pragmatic approach	Impractical for large models

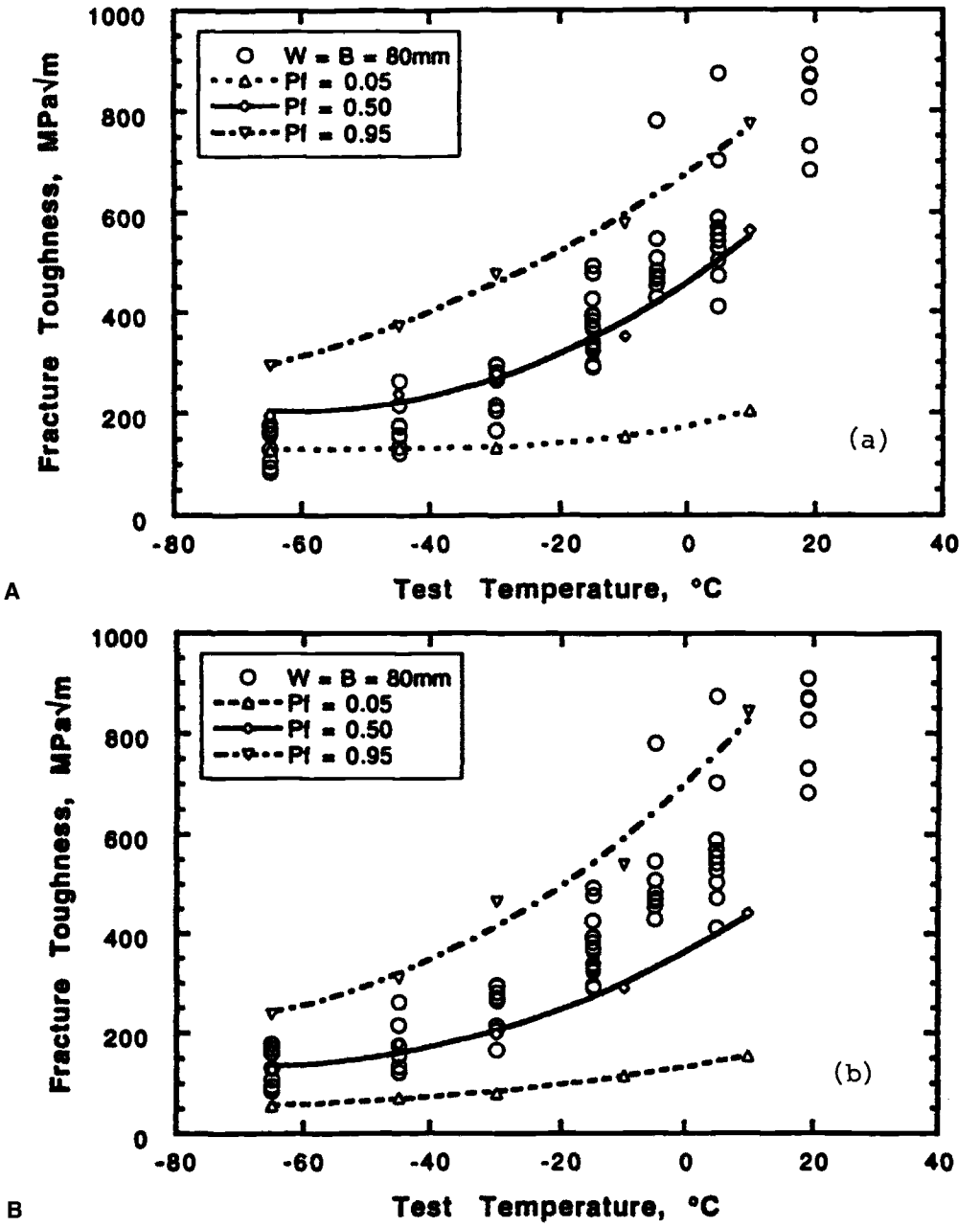

FIG. 5—*Experimental and predicted fracture toughness for an A508 Class 3 steel (SENB;* W = B *= 80 mm,* $a_0/W = 0.5$, *SG = 0%). Predicted curves show 5, 50, and 95% lines of probability of failure.* (a) *Predictions based on a Type I coupled Beremin-Rousselier model.* (b) *Predictions based on a Type II coupled Beremin-Rousselier model.*

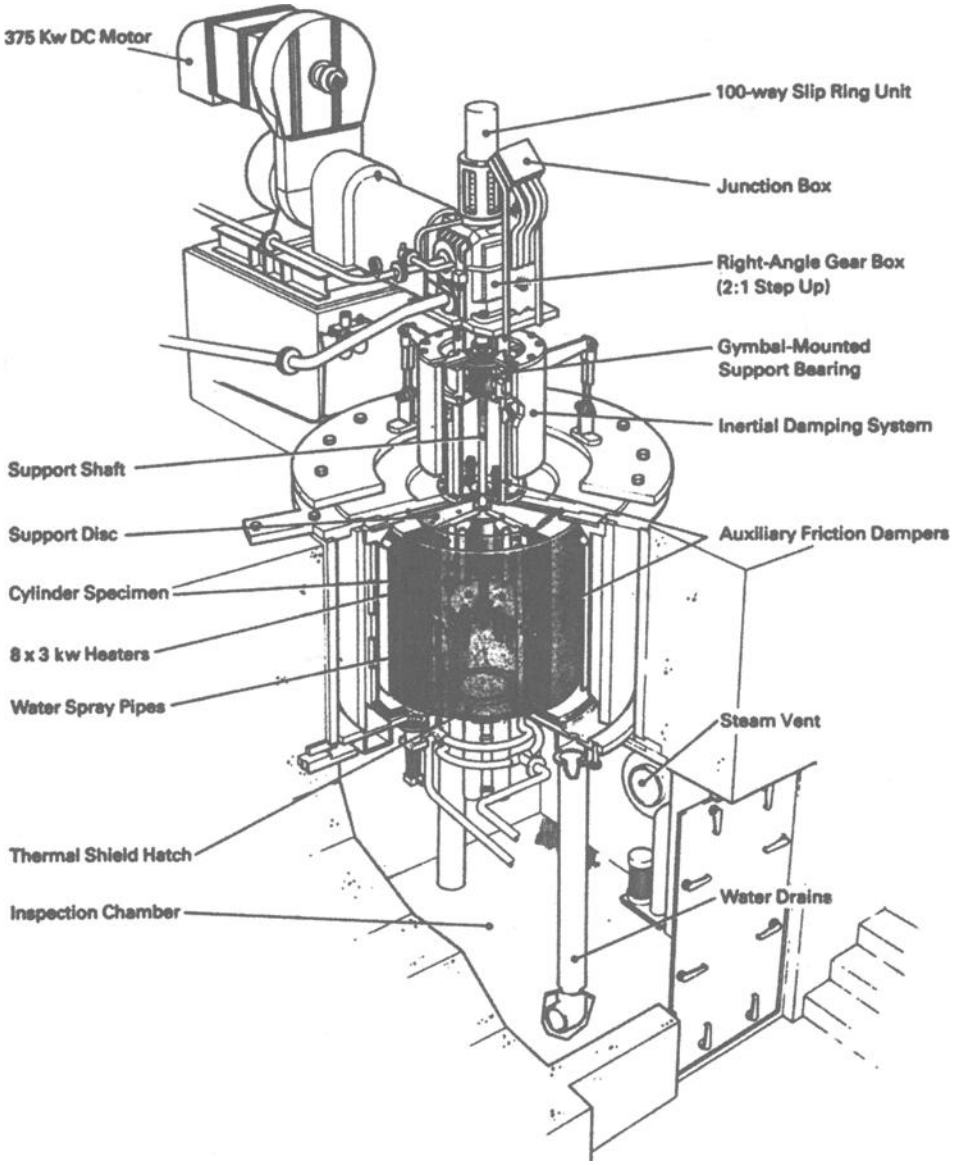

FIG. 6—*The spinning cylinder test rig at AEA Technology, Risley, UK.*

The Spinning Cylinder Test Facility

The spinning cylinder test facility is described fully by Clayton et al. [*10*]. Briefly, the general arrangement of the apparatus is as shown in Fig. 6. An 8-ton cylindrical test specimen is suspended by a flexible shaft from a single pivoted bearing so that it is free to rotate about the vertical axis. The driving power comes from a 375-kW d-c motor mounted on a horizontal pedestal and is transmitted via a right-angle gearbox with 2:1 step-up ratio (maximum design speed of 3500 rpm at the rotor). The cylinder is suspended in a reinforced underground enclosure for safety containment. Eight 3-kW

heaters mounted vertically within the test enclosure allow the temperature of the cylinder to be raised up to pre-test values of around 300°C.

Crack growth during the test is measured primarily by the alternating current potential difference technique (ACPD). In addition, data from thermocouples and strain gages indicate the development of temperature and strain fields during the test.

Spinning Cylinder Test 4 (SC4)

The details of this test and its prediction using the local approach have been given by Howard et al. [*11*]. However, since its successful prediction via the pragmatism of using Type I coupled models was a major prerequisite to its use for predicting the more complex NESC [*12*] (Network For Evaluating Steel Components) test, some description is necessary here. The test was primarily one of thermal shock, with the cylinder at an initial temperature of 305°C being quenched internally by water at 7°C. The specimen was made from an A508 Class 3 forging, with two semi-circular defects running from the inner surface on axial planes separated by 135°. The defects were located midway along the length of the cylinder and were 60 and 40 mm deep. Since the loading for this test was primarily thermal shock, the predictive work concentrated on the more susceptible 40-mm-deep defect. Post-test destructive examination revealed that cleavage had initiated after a small amount (0.2 to 0.4 mm) of tearing some 6 to 8 mm deep along the border of the 40-mm defect. There was no crack growth at the surface. During the test, the ACPD data outputs indicated a sudden increase of crack size of about 0.6 mm at 240 s into the thermal shock.

The modeling of spinning cylinder test 4 was fully three-dimensional, with Type I transition combined model cells of size 125 μm along the crack border. Tuning to compact data produced the following local approach parameters, based on the common cell size noted immediately above.

$$\text{Beremin model: } \sigma_u = 2296 \text{ MPa} \qquad m = 49$$

$$\text{Rousselier model: } C = 0.95 \qquad D = 1.80 \qquad f_0 = 5.531 \times 10^{-4}$$

To ease the computational load, these cells were highly elongated in the crack border direction, taking advantage of the expectation that gradients in this direction would be much smaller than those in a direction directly ahead of the crack tip. Even so, the resultant model had more than 40 000 degrees-of-freedom, requiring, for the completion of each load step of the analysis, about 1 h of run-time on a high-performance workstation cluster.

The outcome of the simulation was most instructive in what it said about the behavior of the cells ahead of the 20 mm of crack border inwards from the inner surface of the cylinder. There were five cells occupying this length. Irrespective of cleavage, the analysis predicted that these cells contained the ductile crack growth, with the cell nearest the inner wall and the one furthest from it having a predicted amount of growth of no more than 0.06 mm. On the other hand, the three cells between these outer two had predicted growth of 0.19 mm. This maximum occurred at 240 s into the predicted thermal shock, after which the thermo-mechanical driving force for further crack growth diminished. So 240 s was the time for both maximum possible ductile crack growth and the maximum probability of cleavage. Furthermore, at 240 s the predicted cumulative probability of failure was 0.95, a value that compares interestingly with the observed indicated cleavage event in the test. The successful outcome of this use of the Type I transition model in the prediction of SC4 gave considerable assurance that an attempt to predict the much more complex (both in terms of loading and material behavior) of the NESC experiment would be worthwhile.

The NESC Experiment

Since the details of this and its prediction via the local approach have recently been provided by Sherry et al. [*13*], only an outline is given here.

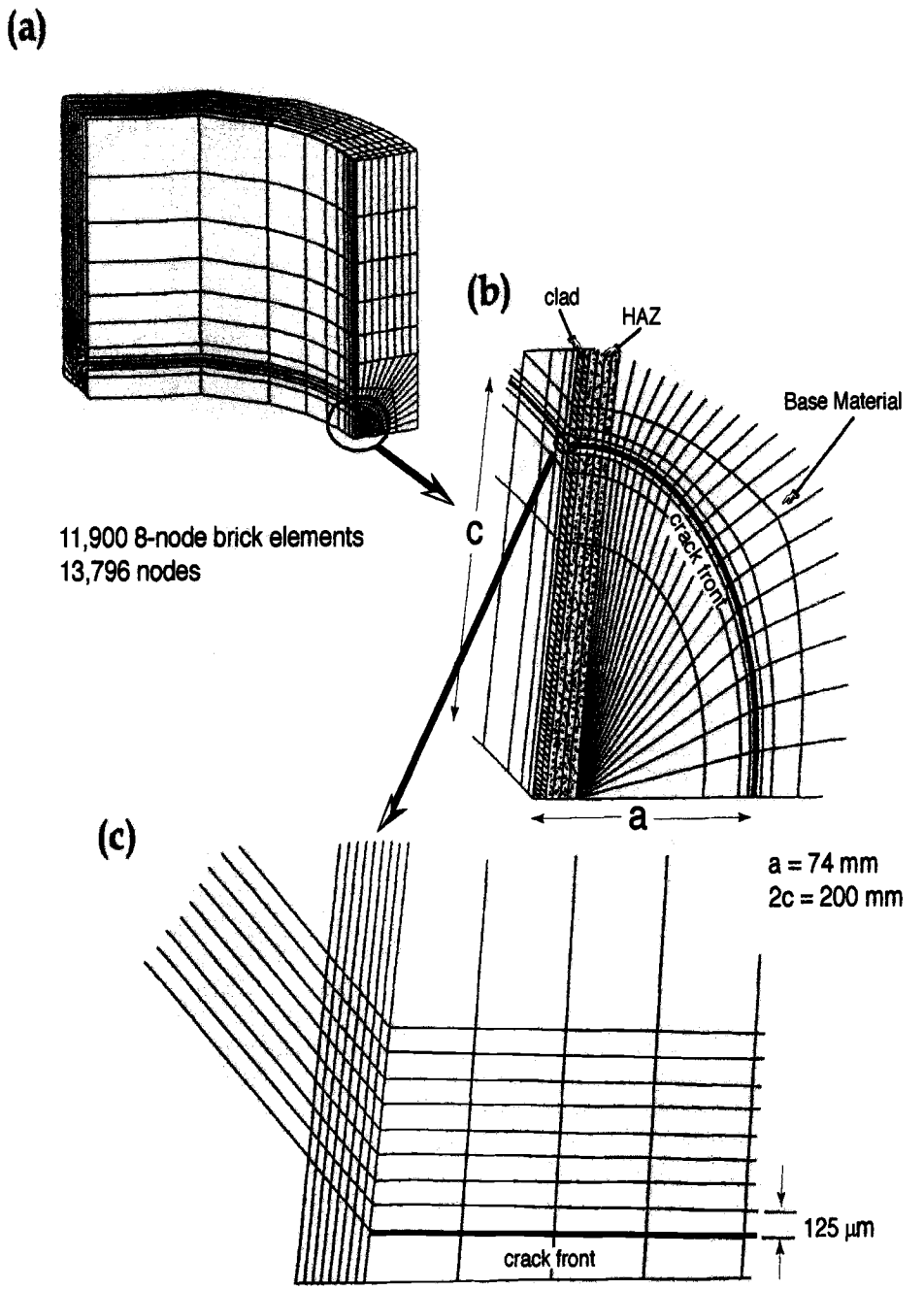

FIG. 7—*The geometry and meshing of the NESC spinning cylinder:* (a) *One eighth of the cylinder, showing the plane containing the 40-mm-deep defect.* (b) *Details of the semi-circular defect assessed.* (c) *Schematic of the near-tip cell structure along the crack border used for the Type I modeling of the transition behavior of the ferritic components of the NESC cylinder wall. Note that the length of the cells along the border are not to scale (they are larger than indicated in the figure).*

TABLE 3—*Details of the NESC thermo-mechanical loading.*

Initial temperature	290°C
Quench temperature	5°C
Rotational speed	2100 rpm increased to 2300 rpm over 360 s
Commence quench	2100 rpm, rate 725 L/min
Total test time	12 min
Heat transfer coefficient	10 000 $W/m^2/°C$

Figure 7 shows the geometry of the model used to simulate the test. In outline, it is similar to that of SC4, particularly in regard to the body of the cylinder being the same material as that of SC4, but differs from it in several important aspects. Firstly, the NESC cylinder had 4 mm of austenitic cladding welded onto the inner surface. This induced 10 mm of heat affected zone (HAZ) in the ferritic material immediately underneath the cladding. The modeling of this is shown in Fig. 7. The cylinder contained a number of defects, the most significant two being a surface breaking through-clad defect and a semi-elliptical under-clad defect. The assessment described here was for the surface-breaking defect, and the geometry modeled is also shown in Fig. 7. Also, the loading was more complex than that of SC4. It was a thermo-mechanical loading, designed to produce cleavage events preceded by ductile tearing. The details are given in Table 3.

The local approach parameters chosen to describe the failure of the different materials in this test are set out in Tables 4 and 5. Those for the base material can be seen to be the same as those previously chosen for SC4, since the material was the same. The tuning followed well established practice. In particular, the following facts and issues emerged during the process. We performed the tuning at Sheffield (SIRIUS) using raw experimental data obtained from tests undertaken at AEA Technology.

(i) The ductile parameters were tuned using notched bar data.
(ii) The tuned model predicts the *J-R* curves.
(iii) The cleavage parameters were tuned using data from precracked fracture toughness tests. These were:
  CTS 10 specimens for the base material—the same as for SC4,
  SECB 10 for the HAZ.
(iv) Cleavage data tuned on notched bar data could not predict that from precracked specimens.
(v) The cell sizes for all three material phases of the test were chosen to be the same.

The core of the prediction for this test is contained in the history of the combined probability p of cleavage for the cylinder as a whole for a model that automatically takes account of the evolving crack growth through ductile damage. Up to the time of 190 s into the experiment, the evolution of p in the HAZ and base materials is significantly different (details are available in Ref *13*), and p in the base material dominates the combined probability of cleavage. This is so despite the crack-driving force being consistently highest in the HAZ, a reflection of the enhanced resistance to cleavage of the

TABLE 4—*Ductile damage parameters for the materials of the NESC cylinder.*

Material	C	D	L_c (mm)	f_0
Base	0.98	2.0	0.125	5.53×10^{-4}
HAZ	0.80	1.8	0.125	5.53×10^{-4}
Clad	0.75	1.9	0.125	15.1×10^{-4}

TABLE 5—*Beremin cleavage parameters for the materials of the NESC cylinder.*

Material	m	σ_u (MPa)	V_0 (mm^3)
Base	49	2296	$(0.125)^3$
HAZ	44	2850	$(0.125)^3$

HAZ. After 190 s, the cleavage probability is similar for both materials, which then contribute similarly to the combined probability of cleavage. The time of around 190 s is a clear transition from steady and rapid rise with time of p in both phases to an approximately constant and high combined probability throughout the rest of the test. At the critical time of $t = 190$ s the combined probability is 0.975, with a slightly greater contribution from the HAZ than from the base material. Figure 8 shows the prediction for the region of crack border where interesting effects are predicted to happen. The predicted cleavage comes from a region where prior ductile crack growth is predicted, with the pre-cleavage growth being a definite function of distance along the crack border from the inner surface of the cylinder.

This pre-test prediction compares well with the preliminary results obtained from the NESC spinning cylinder test, which was performed on 20 March 1997. Strain gage data from the test indicate a rapid change in surface strain at $t = 213$ s into the thermal transient. This is consistent with a crack growth event, most probably cleavage. The close proximity of the test time of 213 s and the time, 190 s, of qualitative change in the predicted history of the cleavage probability p is very encouraging in its implied support for the use of transitional cell models of the type described here.

Discussion

The approach to combining ductile and cleavage cell models that has been presented in this paper began with the belief that the fundamental scales for ductile fracture and for cleavage of steels differed by about an order of magnitude. The tools for carrying out this approach were developed in studies of how to remove the mesh-dependence in the continuum part of the crack-tip field that is imposed by identifying the finite-element mesh with the microstructural cell size. In principle, the technique allowed arbitrary mesh refinement everywhere that had not yet been overwhelmed by a ductile damage cell in its phase of significant damage and subsequent rupture. One could then produce an apparently realistic combined ductile-cleavage model by identifying the refined mesh with suitably sized cleavage cells. In these, the probability of cleavage can be calculated (through the relations of Eqs 1 and 2) as it changes naturally as the component or structure suffers deformation and crack growth by the successive failure of the crack-tip ductile damage cells.

That thinking produced the Type II combined model. As a matter of historical fact, the Type II model was developed shortly after the simpler Type I model. The latter had been conceived as an engineer's "pragmatic" attempt to bring the Beremin and ductile damage models together in the easiest way in order to interpret the ductile-to-brittle transition curve. At the time, the Type II model appeared to contain essential aspects of the micromechanics of the two competing processes and therefore should be treated as a much more physically realistic test-bed on which to judge the performance of the Type I modeling. The inability of the Type II model to produce qualitatively more accurate predictions than those from the Type I model was, at the time, something of a disappointment. Since then, that inability has gradually shed, with other considerations, useful light on the provenance of the Type I modeling, whose practical usefulness has proved itself in the predictions of the SC4 and NESC tests.

Firstly, it is now apparent that our original estimates (based on microstructural information) of the size of the ductile damage cell was too large for the assessment of ductile crack growth from initially sharp cracks. For example, contemporary studies [*14,15*] have reported successful two-dimensional

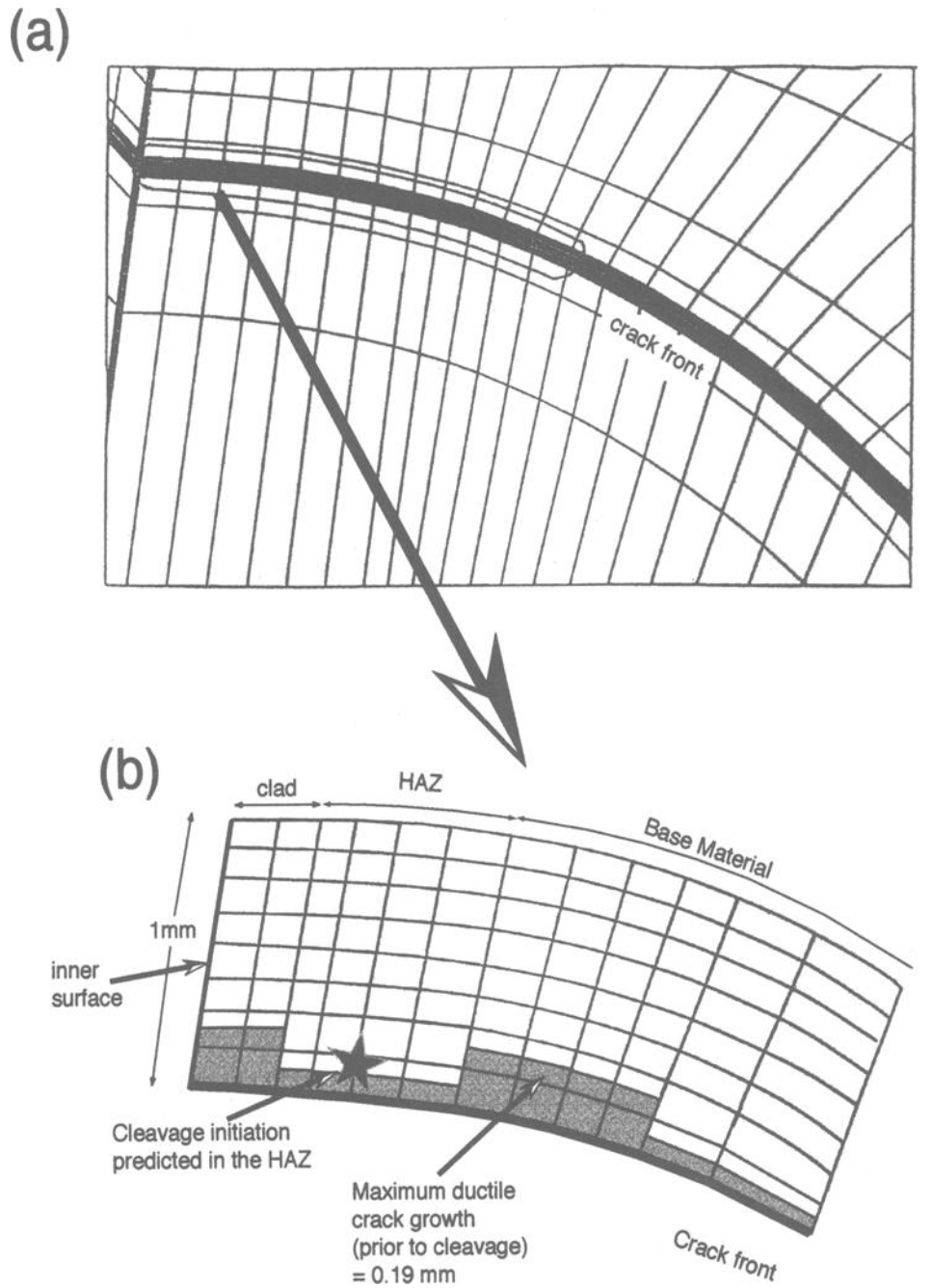

FIG. 8—*Details of the predictions of ductile crack growth and probability of cleavage in the simulation of the NESC experiment.* (a) *The segment of the crack border where growth is predicted.* (b) *Schematic of the detailed prediction of the Type I modeling.*

analyses predicting the performance of common structural steel with ductile cell sizes in the range 50 to 200 μm. This is consistent with observed values of crack tip opening displacement (CTOD) for such steels. Since any simple model of cell failure predicts that the CTOD is about the cell size, this consistency is unsurprising.

Secondly, the finite elements used to represent the cells in our (and others') models are four-noded isoparametric elements in two dimensions. Stress (and other) data are stored at the four Gauss points in these elements. Hence, the volume element in calculating the Weibull stress is that associated with each Gauss point, that is, approximately one-quarter of that of the finite element. In other words, the cleavage cell size is about one half of the length of the finite element used to calculate the stresses from which the Weibull stress, σ_W, is obtained. (Others [*16,17*] have also noted this point.) With a combined-model cell size of 125 μm, this makes the size of the fundamental cleavage integration volume slightly greater than 50 μm. This is consistent with recent metallurgical studies, for example [*18*].

The upshot of all this is that, for the pressure vessel steels simulated in these studies, the simpler combined model Type I now appears to be much closer to the underlying physics than was originally imagined. This heartening conclusion should be tempered by the thought that the underlying cell size for ductile damage is likely to be much less of a constant than that for cleavage in ferritic steels. Recall that contemporary work suggests that the ductile cell size can range from 50 to 200 μm. At the upper extreme, there is a 2:1 mismatch in the ductile/cleavage cell representation. At the lower extreme, this ratio reverses. These observations suggest that cell modeling of the type reported here should still be treated as a potentially fruitful exercise in engineering pragmatism. This note of caution comes from several dark areas in the practicalities of cell modeling. Some of them are discussed below.

The NESC cylinder was composed of three main material phases, the base material, the austenitic cladding, and the HAZ. The model, described above, that was used to simulate the test used a cell size that was the same for all three phases. This is forced on the physics by the need to compute with conventional finite elements. For these, elements that are of constant size in each phase, but differ phase-to-phase, are incompatible at the phase boundaries. The apparent success of the NESC simulation is strong evidence that there is value in this level of pragmatism. It is significantly reinforced by other work [*19,20*] using uniform cell sizes where simulation of a transition weld between a ferritic and an austenitic steel successfully reproduces the complex (nonplanar) patterns of ductile crack growth. Even so, there is important research to be done in this area.

In tuning the local approach parameters for the material of SC4, we initially used only notched bar data. This was successful for the ductile regime, as the tuned model then reproduced the experimental CTS resistance curve. This success was not repeated in the cleavage regime, leading us to the conclusion, as others have found, that cleavage data tuned on notched bar tests cannot straightforwardly reproduce the results of tests on precracked specimens, using the methods set out in Eqs 1 and 2. As a result, the Weibull parameters for the base material were tuned directly from the precracked test data. This raises another open question on the subject. Is it possible to transfer cleavage data from one specimen type to another, and, if so, how is it to be done? The question concerns practical matters as well as the fundamental mechanics of the subject. If we are to use the local approach in more sophisticated assessments than the ones already undertaken, where the simulated crack should automatically find its own nonplanar path through the component, we need to be able to deal with differing balances between hydrostatically dominated deformation and that dominated by shear. Confidence in transferring cleavage data from one specimen type to another would be an enormous help in underpinning attempts of this kind.

Conclusions

The fundamental scales for ductile and cleavage fracture of steels are different. This suggests that cell models of these processes should have different sizes.

Complex models using different cell sizes for each process did not predict transition data that was significantly better than that derived from simpler, uniformly sized cell models.

The first validation of the uniform cell modeling was derived from comparison with the results of the fourth spinning cylinder test (SC4). Confidence derived from this allowed a detailed analysis and blind prediction of the seventh spinning cylinder test, the NESC experiment. The prediction was subsequently shown to compare well with the initial test data.

Further successful research on the transferability of cleavage data from one specimen type to another is essential if nonplanar crack growth is to be simulated with confidence.

Acknowledgments

Collaboration between AEA Technology and SIRIUS on damage mechanics modeling began some ten years ago. The work described in this paper would not have been possible without the cooperation between Drs. D. P. G. Lidbury and A. H. Sherry of AEA Technology and the authors of the present paper. In particular, Drs. Lidbury and Sherry have made very significant contributions to the work reported in this paper, and the authors wish to record here this substantial input to the work.

References

[1] Beremin, F. M., "A Local Criterion for Cleavage Fracture of a Nuclear Pressure Vessel Steel," *Metallurgical Transactions,* Vol. 14A, 1983, pp. 2277–2287.

[2] Knott J. F., "The Transition from Fibrous Fracture to Cleavage Fracture," *International Journal of Pressure Vessels and Piping,* Vol. 64, 1995, pp. 225–234.

[3] Rousselier, G., "Ductile Fracture Models and their Potential in Local Approach of Fracture," *Nuclear Engineering and Design,* Vol. 105, 1987, pp. 97–111.

[4] Gurson, A. L., "Continuum Theory of Ductile Rupture by Void Nucleation and Growth: Part I—Yield Criteria and Flow Rules for Porous Ductile Media," *Journal of Engineering Materials and Technology,* Vol. 99, 1977, pp. 2–15.

[5] Tvergaard, V., "Influence of Voids on Shear Band Instabilities under Plane Strain Conditions," *International Journal of Fracture Mechanics,* Vol. 17, 1981, pp. 389–407.

[6] Bilby, B. A., Howard, I. C., and Li, Z. H., "Mesh Independent Cell Models for Continuum Damage Theory," *Fatigue and Fracture of Engineering Materials and Structures,* Vol. 17, 1994, pp. 1221–1233.

[7] Lidbury, D. P. G., Sherry, A. H., Bilby, B. A., Howard, I. C., Li, Z. H., and Eripret, C., "Prediction of the First Spinning Cylinder Test using Continuum Damage Mechanics," *Nuclear Engineering and Design,* Vol. 152, 1994, pp. 1–10.

[8] Sherry, A. H., Beardsmore, D. W., Lidbury, D. P. G., Howard, I. C., Sheikh, M. A., and Li, Z. H., "Local Approach Prediction of Fracture Toughness—Interim Report, March 1996," AEAT-0226, AEA Technology Report, AEA Technology, Risley, 1996.

[9] Lidbury, D. P. G. and Moscovic, R., "Assessment of the Ductile-To-Brittle Transition Toughness Behavior of an A508 Class 3 PWR Pressure Vessel Steel by a Statistical Approach," ASME PVP-Vol. 250, Pressure Vessel Integrity, American Society of Mechanical Engineers, 1993, pp. 283–294.

[10] Clayton, A. M., Leckenby, R. E., Reading, K., Robbins, E. J., and White, W. P., "A Spinning Cylinder Tensile Test Facility for Pressure Vessel Steels," *Transactions, 8th International Conference on Structural Mechanics in Reactor Technology,* Vol. G, North Holland, Amsterdam, 1985, pp. 21–26.

[11] Howard, I. C., Li, Z. H., Sheikh, M. A., Lidbury, D. P. G., and Sherry, A. H., "The Simulation of the Fourth Spinning Cylinder Test using Damage Mechanics," *Fatigue and Fracture,* K. Yoon, Ed., ASME PVP-Vol. 324, American Society of Mechanical Engineers, 1996, pp. 251–265.

[12] Hurst, R. C., Boydon, F., Wintle, J., McGarry, D., and Hemsworth, B., *Severe Accidents and Topics in the NESC Project,* S. Bhandari, Ed., ASME PVP-Vol. 362, American Society of Mechanical Engineers, 1996, pp. 213–219.

[13] Sherry, A. H., Lidbury, D. P. G., Beardsmore, D. W., Sheikh, M. A., and Howard, I. C., "The Application of the Local Approach to Predict the Outcome of the NESC Experiment," *Fatigue, Fracture and High Temperature Design Methods in Pressure Vessels and Piping,* ASME PVP-Vol. 365, American Society of Mechanical Engineers, 1998, pp. 75–84.

[14] Xia, L. and Shih, F. S., "Ductile Crack Growth–I. A Numerical Study using Computational Cells with Microstructurally-Based Length Scales," *Journal of the Mechanics and Physics of Solids,* Vol. 43, 1995, pp. 233–259.

[15] Ruggieri, C. and Dodds, R. H., "A Transferability Model for Brittle Fracture Including Constraint and Ductile Tearing Effects—A Probabilistic Approach," *International Journal of Fracture,* Vol. 79, 1996, pp. 309–340.

[16] Xia, L. and Shih, F. S., "Ductile Crack Growth—III. Transition to Cleavage Fracture Incorporating Statistics," *Journal of the Mechanics and Physics of Solids,* Vol. 44, 1996, pp. 603–639.

[17] Xia, L. and Cheng, L., "Transition from Ductile Tearing to Cleavage Fracture: A Cell-Model Approach," *International Journal of Fracture,* Vol. 87, 1997, pp. 289–306.

[18] Lin, T., Evans, A. G., and Ritchie, R. O., "Stochastic Modeling of the Independent Roles of Particle Size and Grain Size in Trans-granular Cleavage Fracture," *Metallurgical Transactions,* Vol. 18A, 1987, pp. 641–651.

[19] Li, Z. H., Pugh, A., Howard, I. C., and Yates, J. R., "The Assessment of Cracks in Welds between Dissimilar Materials—An Application of the Ductile Damage Model," Departmental Report, Department of Mechanical Engineering, the University of Sheffield, 1996.

[20] Bassene, S., "Analysis of Crack Behavior in a Transition Weld," Final Year Report, Department of Mechanical Engineering, the University of Sheffield, 1998.

Stephanie C. TerMaath,[1] *Anthony R. Ingraffea,*[2] *and Paul A. Wawrzynek*[3]

A Computational Fracture Mechanics Approach for the Analysis of Facesheet-from-Core Disbond of Honeycomb Core Sandwich Panels

REFERENCE: TerMaath, S. C., Ingraffea, A. R., and Wawrzynek, P. A., **"A Computational Fracture Mechanics Approach for the Analysis of Facesheet-from-Core Disbond of Honeycomb Core Sandwich Panels,"** *Fatigue and Fracture Mechanics: 30th Volume, ASTM STP 1360,* P. C. Paris and K. L. Jerina, Eds., American Society for Testing and Materials, West Conshohocken, PA, 1999, pp. 169–182.

ABSTRACT: The modified crack closure method is combined with finite element analysis to study the damage mode of facesheet-from-core disbond of honeycomb core sandwich structure. Explicit panel models containing an initial disbond region are analyzed to better understand this type of failure. Calculation of energy release rates is used to determine loading conditions that will cause disbond propagation. The edge peel-off case is used as an example, and parameter studies are performed to determine the importance of key properties with regard to damage tolerance of the panels.

KEYWORDS: honeycomb core sandwich panel, disbond, energy release rate, facesheet, damage tolerance, fracture mechanics, modified crack closure method

Honeycomb core sandwich panels are being considered for use as primary structural members in the high-speed civil transport due to their high stiffness-to-weight ratios [*1–7*]. Composite panels are relatively light weight and high-temperature tolerant compared to their solid metallic predecessors, but are still able to withstand the same or greater levels of loading, making them an attractive alternative to their heavier, but more conventional counterparts. Since the use of these panels as primary structure for civilian aircraft is a fairly new concept, little is known regarding their damage tolerance during normal sub- and supersonic flight and under unexpected severe loading conditions. Therefore, a comprehensive understanding of the failure modes associated with damage of these panels is an essential prerequisite for their widespread use as primary structure. In particular, this paper addresses the damage mode of facesheet-from-core disbond. A comprehensive literature review for this project can be found in the final project report to the sponsor, the Boeing Commercial Airplane Company [*8*].

Honeycomb core sandwich panels consist of a honeycomb core attached to two facesheets with an adhesive (Fig. 1). Manufacturing defects or in-service loads can cause a condition in which a facesheet is partially disbonded from the core (Fig. 2). This disbond region may spread and cause panel failure during subsequent loading. Continuum fracture mechanics, used for conventional damage tolerance assessments, does not provide a fully realistic account of disbond propagation between the facesheet and the core, and a detailed study of this failure mechanism is necessary.

[1] Graduate research associate, Cornell University, 301 Hollister Hall, Ithaca, NY 14853.
[2] Dwight C. Baum Professor of Civil and Environmental Engineering, Cornell University, 643 Rhodes Hall, Ithaca, NY 14853.
[3] Senior research associate, Cornell University, 638 Rhodes Hall, Ithaca, NY 14853.

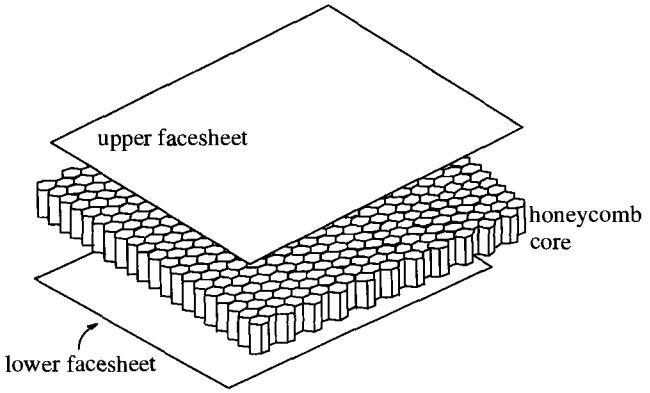

FIG. 1—*Honeycomb core sandwich panel.*

Finite element analyses with FRANC3D/STAGS [*9,10*] have been performed on panel models of various sizes and mesh configurations where the core and facesheet geometries were explicitly modeled. Through a combination of these analyses and fracture mechanics theory, disbond propagation was studied to better understand this mode of failure and to develop computer-based tools to aid in the analysis of this type of cracking.

An across-the-width, edge peel-off configuration was chosen for these studies, since the cracking mode of disbond could be isolated and only Mode I-like fracture occurs. In addition, the project sponsor, the Boeing Commercial Airplane Company, wanted to develop experimental methods to determine adhesive properties, such as fracture toughness (conventionally, only the common lap shear test had primarily been used). The experimental tests to validate this computational model as a test configuration were performed as Phase 2 of this project [*11*]. The results of Phase 2 and comparisons with previous experimental methods [*12,13*] will be reported in a subsequent paper.

Modified Crack Closure Theory

The modified crack closure method combined with finite element analysis, as developed by Rybicki and Kanninen [*14*], is used to calculate an energy release rate at the disbond front. This calculated value is then compared with the critical energy release rate of the adhesive, which bonds the face sheet to the core, to determine whether or not the disbond will propagate. This method has been successfully applied to the study of delamination of composite materials [*15*] and will be further extended in this paper to study the propagation of disbond regions in honeycomb core sandwich structure.

Crack closure theory, as introduced by Irwin [*16*], states that the energy released as a crack propagates from Length a to Length $a + \Delta a$ is equivalent to the amount of work required to close a crack from Length $a + \Delta a$ to Length a. Therefore, the energy required to propagate a crack in a material of

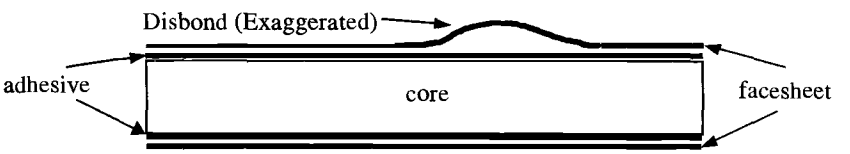

FIG. 2—*Embedded disbond region.*

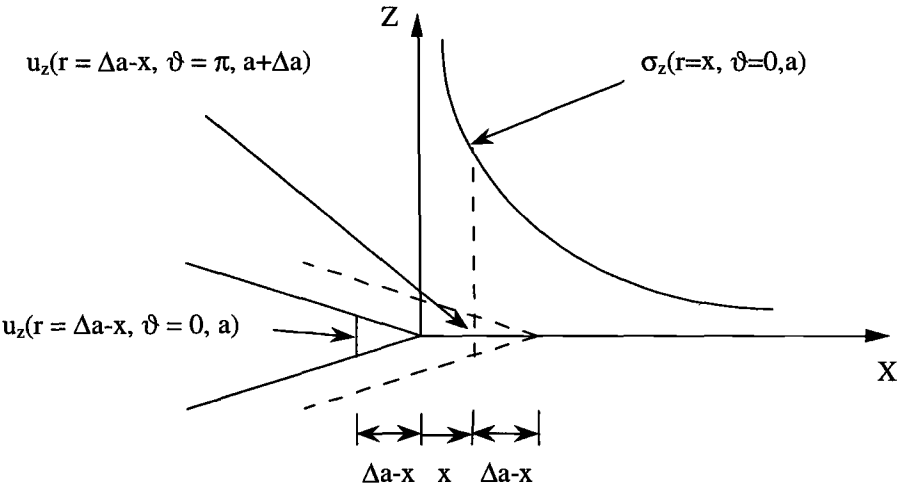

FIG. 3—*Pictorial representation of the stresses and displacements used in crack closure calculations.*

unit thickness in Mode I by an amount Δa is

$$W = \frac{1}{2}\int_0^{\Delta a} \sigma_z(r = x, \vartheta = 0, a)u_z(r = \Delta a - x, \vartheta = \pi, a + \Delta a)dx \tag{1}$$

where σ_z represents the normal stress at the front of a crack of Length a. In crack closure theory, this stress is caused by closing the crack from Length $a + \Delta a$ to Length a. In addition, u_z is the normal displacement or opening of a crack of Length $a + \Delta a$ (Fig. 3), and r and ϑ are the usual polar coordinates centered on the crack front.

Evaluation of the work integral (Eq 1) requires two analyses, one to determine stresses ahead of the crack front, and one with a virtual crack extension to determine the corresponding relative opening displacements in the region of the virtual extension. However, Irwin postulated that the crack front does not change shape for very small increments of crack growth. Therefore, the displacements immediately behind the crack front for a crack of Length a are the same as those behind the crack front for a crack of Length $a + \Delta a$ when Δa is infinitesimally small (Fig. 4).

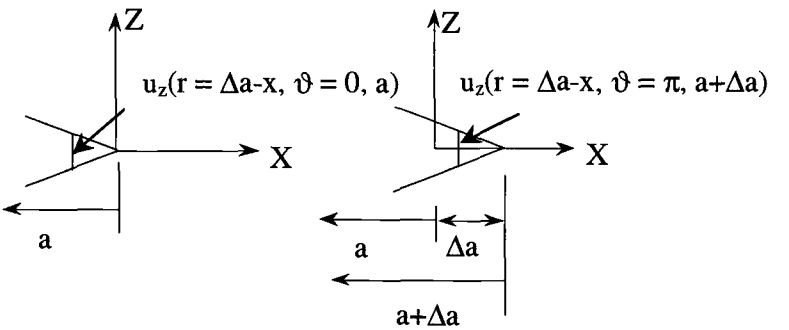

FIG. 4—*Pictorial representation of self-similar crack propagation.*

Under the assumption of self-similar crack growth

$$u_z(r = \Delta a - x, \vartheta = \pi, a) = u_z(r = \Delta a - x, \vartheta = \pi, a + \Delta a) \tag{2}$$

Therefore, the new integral to be evaluated is

$$W = \frac{1}{2}\int_0^{\Delta a} \sigma_z(r = x, \vartheta = 0, a) u_z(r = \Delta a - x, \vartheta = \pi, a) dx \tag{3}$$

Thus, this assumption of self-similar crack growth greatly reduces computation time, since this modified work integral (Eq 3) requires only one analysis.

The energy release rate, G, is expressed in terms of crack closure integrals as

$$G = \lim_{\Delta a \to 0} \frac{W}{t\Delta a} \tag{4}$$

where t is the thickness of the material. Therefore, the energy release rate for self-similar propagation as determined by the modified crack closure method is

$$G = \lim_{\Delta a \to 0} \frac{1}{2t\Delta a}\int_0^{\Delta a} \sigma_z(r = x, \vartheta = 0, a) u_z(r = \Delta a - x, \vartheta = \pi, a) dx \tag{5}$$

Finite Element Approach

The stresses and displacements in Eq 5 will be determined by a finite element analysis. It is therefore useful to express this equation in terms of nodal displacements and forces that are readily extracted from STAGS, the finite element program to be used for the analyses.

For this problem, the stresses in Eq 5 are developed in the adhesive, which attaches the facesheet to the core. Viewing a typical interface region (Fig. 5), the desired stresses are those along the facesheet-core interface between Nodes 1 and 2.

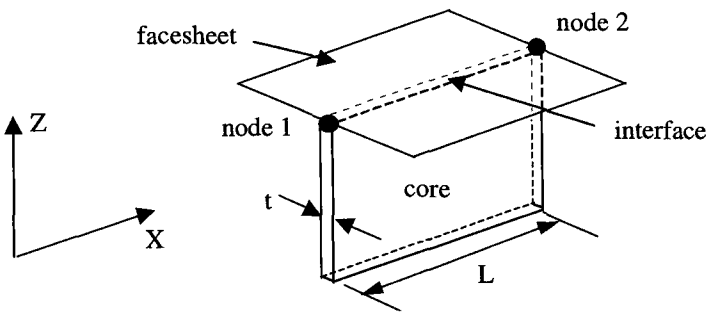

FIG. 5—*Typical connection between facesheet and four-noded element in core.*

For four-noded linear quadrilateral elements, the nodal stresses in the required direction are expressed in terms of nodal forces as

$$\begin{pmatrix} \sigma_z^1 \\ \sigma_z^2 \end{pmatrix} = \begin{pmatrix} \dfrac{2[2F_{z1} - F_{z2}]}{tL} \\ \dfrac{2[2F_{z2} - F_{z1}]}{tL} \end{pmatrix} \tag{6}$$

Upon substitution of these stresses into Eq 3, and utilizing linear shape functions, the expression for work along the interface connecting one core element to the facesheet in terms of nodal forces and displacements in the required direction becomes

$$W_{\text{element}} = \frac{F_{z1}u_{z1} + F_{z2}u_{z2}}{2} \tag{7}$$

Thus, for the modified crack closure formulation using finite element results, the energy release rate becomes

$$G = \frac{\sum_{i=1}^{\#\text{elements}} F_{zi+\Delta a}u_{zi}}{2\left(\sum_{i=1}^{\#\text{elements}} t_i L_i\right)} \tag{8}$$

where u_{zi} is the nodal displacement in the normal direction behind the disbond front, while $F_{zi+\Delta a}$ is the corresponding nodal force in the normal direction in front of the disbonded area. The sum in the denominator is the area of core that becomes separated due to the disbond propagation.

Application to Honeycomb Sandwich Structure

The correlation between the locations of nodal forces and displacements (with and without the assumption of self-similar growth) on the honeycomb core sandwich panels is shown for the across-the-width edge peel-off case in Figs. 6 and 7. The important difference is that only one finite element solution is required in the former case, while two are required for the latter. In the figures, black nodes represent nodal displacements and white nodes depict nodal forces.

When determining the energy release rate using self-similar crack propagation (Fig. 6), the forces at the white nodes (in front of the disbond area) are multiplied by the displacements at the black nodes

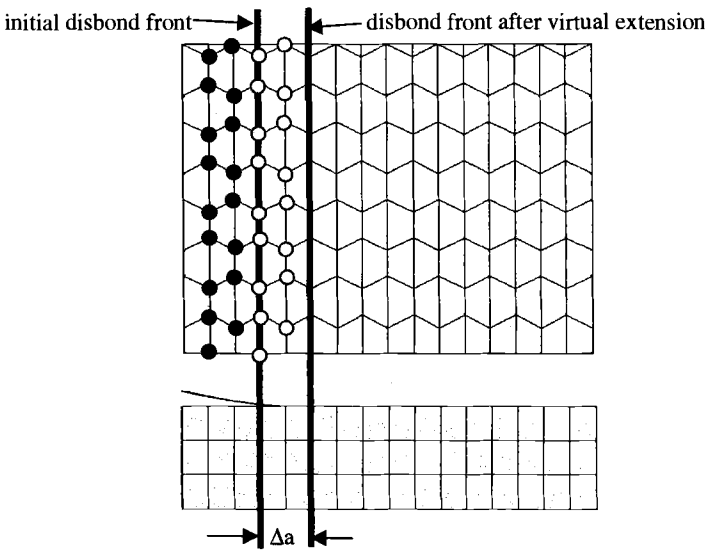

FIG. 6—*Correlation between locations of nodal forces (white nodes) and displacements (black nodes) assuming self-similar crack propagation.*

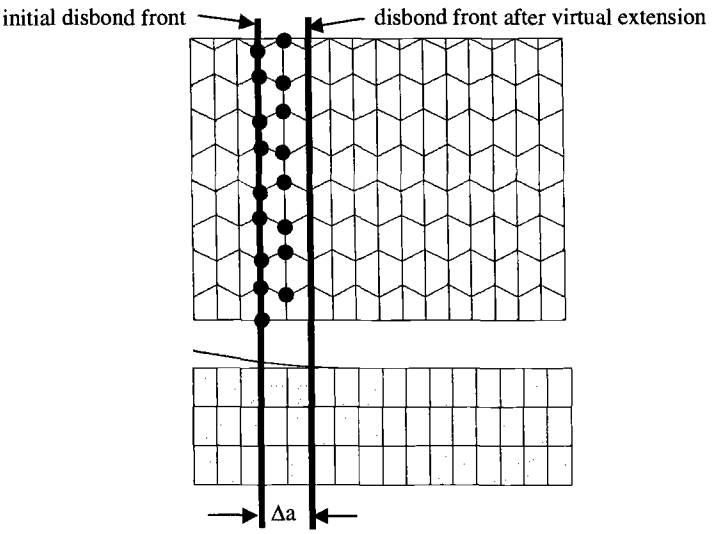

FIG. 7—*Correlation without assuming self-similar propagation (forces and displacements as coincident nodes).*

(behind the disbond front). If the energy release rate is calculated from two separate analyses without the assumption of self-similar crack propagation, the forces from the analysis of disbond Length a (white nodes from Fig. 6) are multiplied by the displacements from an analysis of disbond Length $a + \Delta a$ (black nodes from Fig. 7).

Implementation to Across-the-Width Peel-Off Case

Four-noded quadrilateral shell elements were used to model the facesheets and core (Fig. 8) of the honeycomb sandwich panel. The geometry of the core was explicitly modeled as a honeycomb, consisting of regular hexagons rigidly attached to two facesheets. The adhesive stiffness was neglected. The geometrical properties of the panel were as follows:

1. Thickness of facesheet = 0.254 cm.
2. Thickness of honeycomb cell walls = 0.00508 cm.

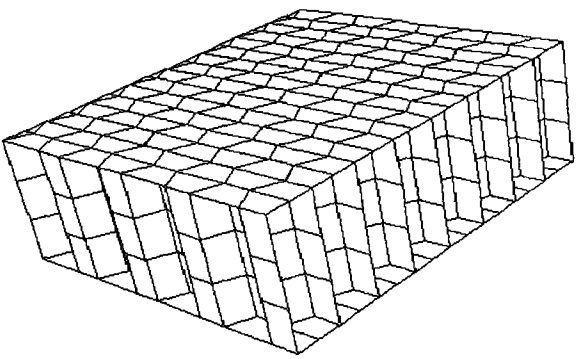

FIG. 8—*Finite element model of panel.*

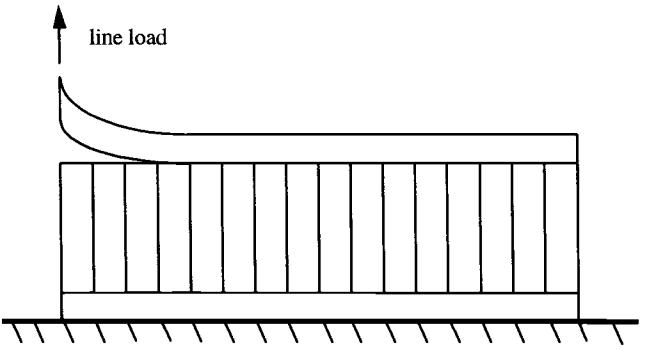

FIG. 9—*Boundary conditions on finite element model.*

3. Depth of core = 1.27 cm.
4. Cell size of hexagons = 0.47625 cm.

Both the facesheets and core were initially modeled as titanium. For the edge peel-off case, the upper facesheet was detached from the core in the disbond area (2 hexagons in length), the bottom of the panel was fixed, and an out-of-plane load of 17.5 N/cm was applied along the disbonded edge (Fig. 9).

Mesh Convergence

Three meshes were created to determine the effects of mesh refinement on the analysis. Linear four-noded quadrilateral shell elements were used for all meshes. The core was divided into three sections through the depth for all meshes. The main concern in the meshing process was the top facesheet, since it was expected that core determinations would be minimal and would therefore contribute negligibly to the change in strain energy as the disband propagated. Therefore, to determine the facesheet element density required for convergence, three levels of facesheet mesh refinement were studied. The first mesh (Mesh 1) consisted of two elements per hexagon on the facesheets (Fig. 8). The second mesh (Mesh 2) differed from the first in that the sides of each hexagon were divided into two, resulting in eight elements per hexagon (Fig. 10*a*). This mesh was then further refined such that each hexagon edge on the facesheet was divided into three (Mesh 3), resulting in 18 elements per hexagon (Fig. 10*b*).

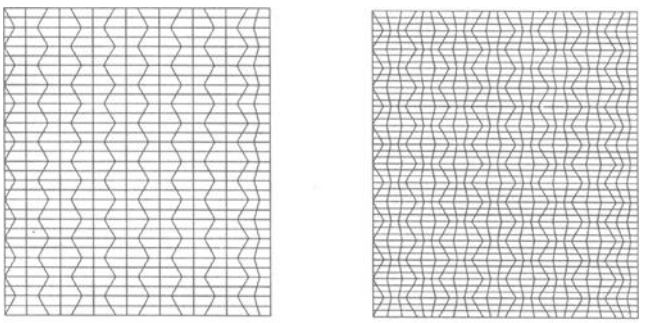

FIG. 10—*Mesh refinements of facesheets.*

TABLE 1—*Forces at disbond front.*

Mesh	Total Force at Disbond Front, N
1	68.15
2	55.78
3	52.18

In preliminary studies, significant free edge effects were noted in the results due to the small size of the panel. To eliminate all free edge effects, periodic boundary conditions were applied to opposite sides of the panel. These conditions constrain opposite panel edges to exhibit exactly the same deformations, thus causing the model to behave as though it were a much larger panel.

To test for convergence, the total force between the facesheet and core at the disbond front was determined for each mesh (Table 1). Based on the nature of the convergence for these three meshes, it was determined that Mesh 3 was adequate for this study, as a larger number of elements would not have yielded a significantly more accurate result worthy of the substantial increase in computation time.

Calculation of the Change in Strain Energy for Disbond Growth

To verify the finite element method for calculating the change in strain energy due to disbond growth (Eq 7), models were created and analyzed with disbond lengths of two and three cells in order to study a growth increment of one cell. The deformed shapes resulting from these two analyses are shown in Figs. 11 and 12.

The deformed panels appear as expected. Note that there is significant core displacement near the disbond front, so the amount of crack opening is equal to the facesheet displacement minus the core displacement. This relative displacement, not the facesheet displacement, is used in the strain energy calculations.

Based on these models, several values of W for the disbond growth of one cell were determined by different means. The work calculated using the crack closure method was computed in two basic ways, one assuming self-similar propagation and one where the disbond was propagated and the actual displacements used. Next, since STAGS computes the internal strain energy as part of a routine finite element analysis, a value of W was computed as the difference in internal strain energy be-

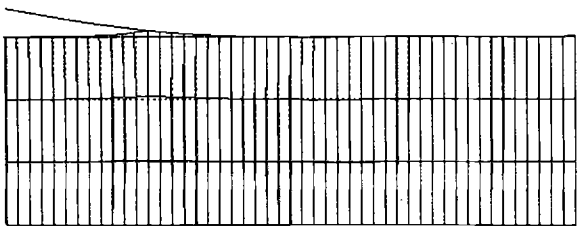

FIG. 11—*Deformed panel for initial disbond of 2 cells (Mesh 3).*

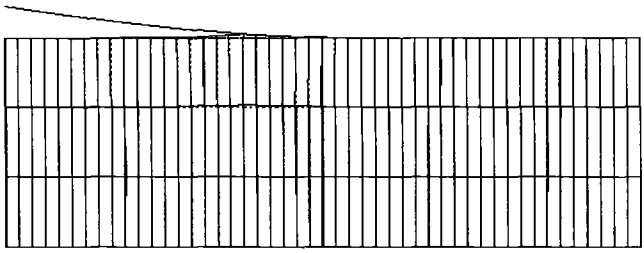

FIG. 12—*Deformed panel after an additional cell of disbond growth (Mesh 3).*

tween the two analyses. Finally, comparison was made to the simple analytical model shown as Eq 9 (the strain energy in a beam due flexure from basic mechanics).

$$E = \frac{1}{2}\int_0^L \frac{M^2}{EI}\,ds \tag{9}$$

Table 2 shows the values of W computed by the different methods. The crack closure theory is able to obtain the same value as the change in strain energy computed by STAGS. Furthermore, beam flexure theory predicts an acceptably close estimate, showing that the crack closure results are reasonable. Based on these results, it can be concluded that the crack closure theory accurately accounts for the change in strain energy due to disbond propagation. It can also be deduced that self-similar crack growth is not an accurate assumption for this particular model and growth increment. It is believed this assumption did not hold since the amount of crack propagation is not small relative to the other panel parameters (such as the initial disbond length). This aspect of disbond propagation will be examined in the next section.

Study of Self-Similar Assumption

When applied, the assumption of self-similar growth saves substantial computation time. Therefore, studies were performed on different growth increments to determine when this assumption becomes valid. It was believed that the self-similar growth assumption did not hold in the previous studies due to the fact that the disbond growth increment was not small relative to panel size. In addition, since the disbond front was near the edge of the panel, the growth was most likely experiencing free edge effects, and steady-state propagation had not yet been achieved. To determine when the self-similar assumption holds, a panel model 2 cells wide and 41 cells long was created using an element density equal to Mesh 3, with periodic boundary conditions on the opposing edges.

Disbonds of various lengths were placed in the model, and the growth was incremented by one element. Errors in accuracy based on self-similar growth versus performing two analyses were as large

TABLE 2—*Results from strain energy calculations. Change in strain energy as disbond propagates by one cell (J).*

Crack Closure	STAGS	Beam Flexure Theory	Self-Similar
0.000207	0.000206	0.000226	0.000150

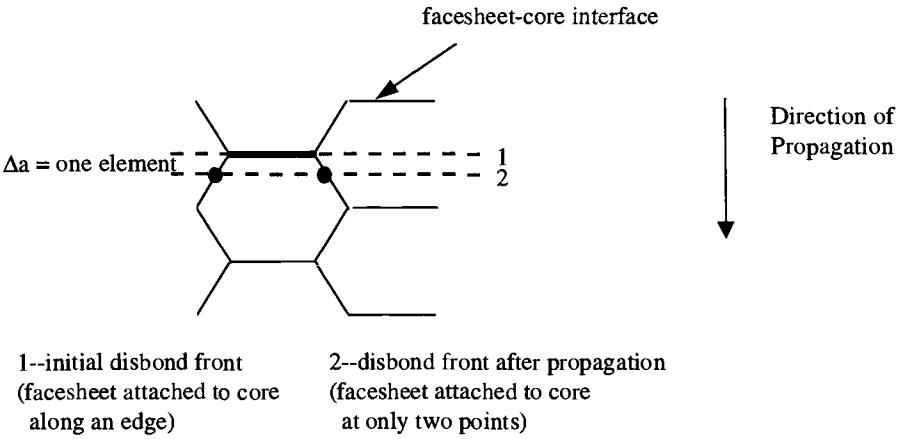

FIG. 13—*One element increment of growth.*

as 40%, occurring when the growth began or ended on an edge of a hexagon (Fig. 13). (Before propagation, the facesheet was constrained along an edge, whereas after it was held to the core at only two points and vice versa.) This finding led to the discovery that, in addition to requiring steady-state propagation and small increments of growth relative to panel size, the disbond front must also be self-repeating for all growth increments. In other words, the same pattern along the honeycomb lattice must be exhibited by the disbond front before and after propagation.

To explore self-repeating propagation, a growth increment of one cell (hexagon) was studied (Fig. 14*a*) with a disbond length of 20 cells (so that steady-state would be achieved). The error was found to be only 6%, a substantial improvement in accuracy although the growth increment was six times as large. Then, a self-repeating growth increment of ½ cell was studied (Fig. 14*b*). The error for a disbond length of 10 cells was only 5%, while for a disbond length of 20 cells the error was reduced to 1.7%, an acceptable value for accuracy.

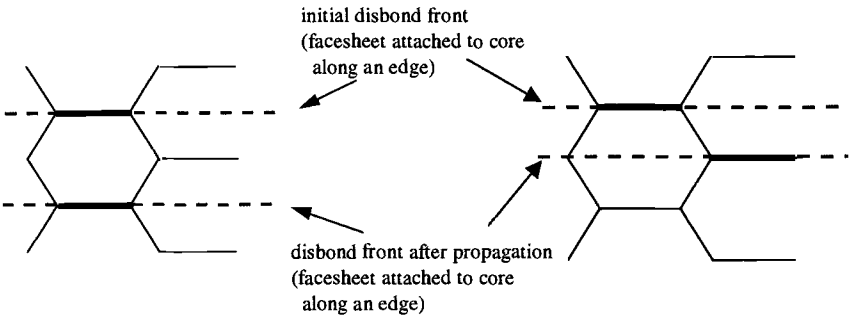

a--*One Cell Increment of Growth* b--*1/2 Cell Increment of Growth*

FIG. 14—*Self-repeating increments of growth.*

Therefore, for disbond growth that is self-repeating, relatively small, and sufficiently far from free edges, the self-similar assumption can be applied with reasonable accuracy.

Calculation of Energy Release Rate

The above verification shows that the modified crack closure method coupled with finite element analysis accurately predicts the strain energy released as a disbond propagates. Furthermore, the self-similar assumption has been validated for small, self-repeating growth increments sufficiently far from the edges. These findings will now be utilized to calculate energy release rates for across-the-width disbond regions in panels modeled in edge peel-off configurations.

The model analyzed is the same as that used in the self-similar growth studies (2 cells wide and 41 cells long, with periodic boundary conditions enforced on opposing edges). A disbond length of 20 cells was placed in the model and propagated by ½ cell using an edge load of 12.52 N/cm. This load was chosen because it produces an energy release rate equal to the critical energy release rate of a typical adhesive (2000 J/m^2). This critical energy release rate is the value at which the disbond will begin to propagate.

Under the assumption of self-similar growth, the change in strain energy is calculated as 0.001115 J (G = 2000 J/m^2). The actual change in strain energy as computed by two analyses is 0.001133 J (G = 2028 J/m^2). Therefore, the error resulting from the self-similar assumption is 1.7%, as previously computed. Next, a geometrically nonlinear analysis was performed to determine whether linear analysis yielded sufficient accuracy. The resulting change in strain energy under self-similar growth assumptions was calculated as 0.001113 J (G = 1993 J/m^2), a difference of only 0.1% from the linear analysis. Therefore, geometrically linear analysis was deemed adequate for this particular problem.

Parametric Studies

To determine the importance of key properties, parametric studies were performed to study the influence of core thickness, t_c, facesheet thickness, t_f, and facesheet material (in terms of Poisson's ratio, ν, and Young's modulus, E) with regard to damage tolerance. These parameters were varied one at a time, and the load at which the disbond would propagate, L_p, was computed.

Comparing facesheet thickness versus the load to propagate the disbond, it was determined that L_p was approximately proportional to $t_f^{3/2}$ (Fig. 15). Meanwhile, the core thickness affected the load approximately proportional to $t_c^{1/2}$ (Fig. 16).

Next, the effects of facesheet material were studied. First, Poisson's ratio was varied. As shown in Table 3, it can be expected that for small variations around 0.31, disbond propagation is not very sensitive to changes in ν; however, if extreme deviations from this value are anticipated, a higher ν will significantly improve performance. However, it is most likely that the facesheet material chosen for this type of panel will have a ν around 0.3 (typical for the materials under consideration for use in the high speed civil transit). Therefore, the effects of Young's modulus were studied for a representative range of ν varying from 0.26 to 0.33. As seen in Table 4, the load to propagate the disbond is almost linearly related to facesheet stiffness.

Variations in any of the parameters will effect the load required to propagate a disbond; however, facesheet thickness and stiffness appear to display the greatest significance in determining when the disbond will propagate. While higher values of these two properties will increase panel resistance to disbond, they also have the added benefit of reducing the possibility of facesheet buckling. Although not a topic discussed in this paper, disbond propagation is often coupled with facesheet buckling (particularly when the panel is loaded in compression or flexure).

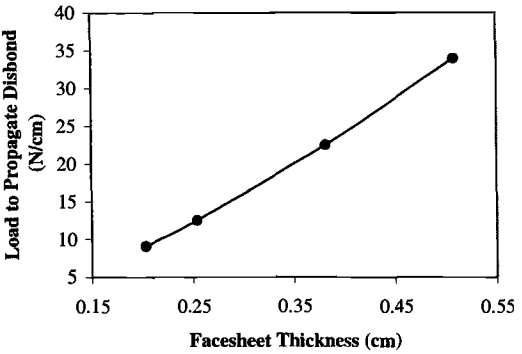

FIG. 15—*Effect of varying facesheet thickness on load required to propagate disbond.*

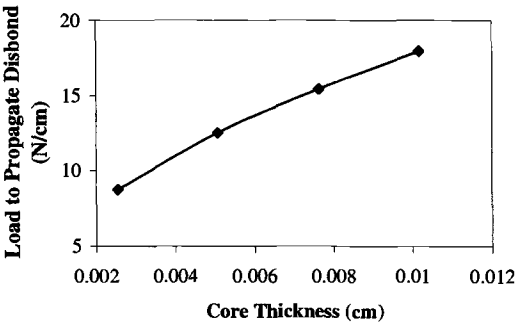

FIG. 16—*Effect of varying core thickness on load required to propagate disbond.*

TABLE 3—*Effect of varying Poisson's ratio on load required to propagate disbond.*

Poisson's Ratio, ν	Load to Propagate Disbond, N/cm
0.20	12.22
0.31	12.52
0.50	13.56

TABLE 4—*Effect of varying facesheet stiffness on load to propagate disbond (N/cm) for different values of Poisson's ratio.*

	Facesheet Stiffness ($\times 10^6$ Pa)		
ν	6.9	17.2	34.5
0.26	9.86	15.34	21.61
0.30	9.95	15.48	21.63
0.33	10.04	15.62	21.82

Conclusions

The modified crack closure method combined with finite element analysis was studied to determine its possible use as a computer-based tool for modeling and predicting disbond growth in honeycomb core sandwich structure. The preliminary results from disbond analyses performed using this method are promising (although further computational analysis and experimental work are required for full development of this method).

To save computation time, the self-similar assumption can be utilized when the disbond growth increment is self-repeating, relatively small, and sufficiently far from free edges. As with most finite element analyses, results are mesh dependent, so adequate mesh refinement to ascertain convergence is essential. While disbond growth exhibits sensitivity to variations in all panel properties, facesheet thickness and material appear to carry the most influence. Increasing facesheet thickness and stiffness has the additional advantage of decreasing the facesheet's tendency to buckle, another phenomenon often coupled with disbond propagation.

The method presented in this paper for studying disbond propagation appears to be an effective and efficient means to study this type of damage. With further research, this method may be applied to the general case of an arbitrarily shaped disbond region under arbitrary loading.

Acknowledgments

This material is based upon work supported under a National Science Foundation Graduate Fellowship and a grant from the Boeing Commercial Airplane Company. The authors thank Dr. Matthew Miller, Dr. Elaine Worden, Eric Cregger, Dr. Scott Burton, and Dr. Walter Dauksher for their assistance with this project.

References

[1] Miller, M., Rufin, A., Westre, W., and Samavedam, G., "High-Speed Civil Transport Hybrid Laminate Sandwich Fuselage Panel Test," *Fatigue and Fracture Mechanics: 29th Volume, ASTM STP 1321*, T. L. Panontin and S. D. Sheppard, Eds., American Society for Testing and Materials, 1998.

[2] Schultz, P., et al., "High-Speed Research Airframe Technology—Metals Durability," Boeing Document D6-81884, Final Report for NASA Contract NAS1-20220, Task 15, March 1996.

[3] Samavedam, G. and Hoadley, D., "Fracture and Fatigue Strength Evaluation of Multiple Site Damaged Aircraft Fuselages—Curved Panel Testing and Analysis," Final Report for FAA Contract DTRS-57-89-D-00009 Task VA9007, Foster-Miller, Inc., May 1991.

[4] Roebroeks, G., *Towards GLARE—The Development of a Fatigue Insensitive and Damage Tolerant Aircraft Material*, Delft University, 1991.

[5] Lawcock, G., et al., "Novel Fiber Reinforced Metal Laminates for Aerospace Applications—A Review," *SAMPE Journal*, Vol. 31, No. 1, 1995, pp. 23–31.

[6] Hoggatt, J. T., "Structural Reinforced Thermoplastic Laminates and Method for Using Such Laminates," U.S. Patent Number 3,939,024, 1976.

[7] Litzkow, M. A., "Foster-Miller 'Panel 30' Material Constant-Amplitude Fatigue Tests," Boeing Preliminary Test Report D122X850TR Number 1, September 1995.

[8] Ingraffea, A., TerMaath, S., and Ferguson, K., "An Investigation into Damage Tolerance of Honeycomb Structural Members," Final Report to Boeing Commercial Airplane Company, Purchase Contract Numbers ZA0079 and JG7634, November 1997.

[9] Carter, B. J., Chen, C.-S., Ingraffea, A. R., and Wawrzynek, P. A., "A Topology Based System for Modeling 3D Crack Growth in Solid and Shell Structures," *Advances in Fracture Research, Vol. 4*, Ninth International Congress on Fracture, Sydney, Australia, Elsevier Science Publishers, New York, 1997, pp. 1923–1934.

[10] Brogan, F. A., Rankin, C. C., Cabiness, H. D., and Lodenlu, A., *STAGS User Manual Version 2.3*, Lockheed Martin Missiles and Space Co., Inc., Advanced Technology Center, Palo Alto, CA, July 1994.

[11] Ural, A., Han, T., Chen, C., Zehnder, A., Ingraffea, A., and Wawrzynek, P., "Continuing Investigations into Damage Tolerance in Honeycomb Structural Members," Final Report to the Boeing Commercial Airplane Company, Purchase Contract Numbers ZA0079 and JG7634, January 1999.

[12] ASTM Standard Designation D5528-94a, "Standard Test Method for Mode I Interlaminar Fracture Toughness of Unidirectional Fiber-Reinforced Polymer Matrix Composites," 1994.

[*13*] Devitt, D. F., Schapery, R. A., and Bradley, W. L., "A Method for Determining the Mode I Delamination Fracture Toughness of Elastic and Viscoelastic Composite Materials," *Journal of Composite Materials,* Vol. 14, 1980, pp. 270–285.

[*14*] Rybicki, E. F. and Kanninen, M. F., "A Finite Element Calculation of Stress Intensity Factors by a Modified Crack Closure Integral," *Engineering Fracture Mechanics,* Vol. 9, 1977, pp. 931–938.

[*15*] Mukherjee, Y. X., Gulrajani, S. N., Mukherjee, S., and Netravali, A. N., "A Numerical and Experimental Study of Delaminated Layered Composites," *Journal of Composite Materials,* Vol. 28, No. 9, 1994, pp. 837–870.

[*16*] Irwin, G. R., "Fracture," *Handbuch der Physik VI,* 1958, pp. 551–590.

Session III

J. Keith Donald,[1] *Guy M. Connelly,*[2] *Paul C. Paris,*[3] *and Hiroshi Tada*[4]

Crack Wake Influence Theory and Elastic Crack Closure Measurement

REFERENCE: Donald, J. K., Connelly, G. M., Paris, P. C., and Tada, H., **"Crack Wake Influence Theory and Elastic Crack Closure Measurement,"** *Fatigue and Fracture Mechanics: 30th Volume, ASTM STP 1360,* P. C. Paris and K. L. Jerina, Eds., American Society for Testing and Materials, West Conshohocken, PA, 2000, pp. 185–200.

ABSTRACT: Experimental and analytical evidence indicates that "closure" or interference of crack faces does not entirely isolate the crack tip from damaging strains. To account for the contribution of the cyclic crack tip strain below the opening load, a new analysis technique has been developed for estimating ΔK_{eff}. This technique is based on crack wake influence theory (the relationship between the effect of crack wake interference on a displacement or strain measurement location and the corresponding effect at the crack tip). Solving the distribution and position functions provides a method of equating remote compliance measurements to reduction in crack tip elastic strain. The experimental method involves determining the ratio of the compliance of the shielded crack to that of the fully open crack (CR). This relationship remains elusive until it is recognized that $1 - CR$ is directly related to the influence of the closure mechanism on both the measurement location and the crack tip. The verification of this method includes experimental measurements of a large center crack panel with multiple displacement and strain gage measurement locations. The standard crack has been replaced with a milled slot, allowing precision blocks to be inserted at specific positions to simulate crack wake interference. Finite element analysis and theory of elasticity are linked to the experiment to better understand the measurement requirements for crack tip closure. The estimation of ΔK_{eff} using the ratio of influences from the theory of elasticity can be directly compared with other approximation techniques such as the adjusted compliance ratio or opening load.

KEYWORDS: crack wake influence, effective stress intensity, crack closure, compliance ratio

In 1970, the understanding of fatigue crack growth was enhanced with the discovery of crack closure by Elber [*1,2*]. However, correlating stress ratio effects using closure has been hampered by nonrepeatable measurements of closure and contradictory results [*3-10*] is experimental and analytical evidence indicating that closure or interference of crack faces does not entirely isolate the crack tip from damaging strains. In an attempt to account for the contribution of the cyclic crack tip strain below the opening load, a new analysis technique has been recently proposed for estimating ΔK_{eff} [*11–14*]. This method is referred to as the adjusted compliance ratio (ACR) technique. An extensive evaluation of the method on 6013-T651, 2324-T39, and 7055-T7511 aluminum alloys shows an improved correlation of fatigue crack growth rate stress ratio effects under steady-state conditions and at near-threshold growth rates [*15*]. However, the analytical understanding of the ACR concept has until now been limited. If the ACR concept is to be used, proper modeling will be necessary to validate it, to identify its limitations, and to incorporate adjustments based on theory.

In this investigation, finite element (FEM) analysis and theory of elasticity were linked to the experimental compliance measurements of a large center crack panel with multiple displacement and

[1] Director, Fracture Technology Associates, 2001 Stonesthrow Road, Bethlehem, PA 18015.
[2] Director, Connelly Applied Research, 4683 Oakwood Lane, Nazareth, PA 18064.
[3] Professor, Washington University, St. Louis, MO 63130.
[4] Affiliate professor, Washington University, St. Louis, MO 63130.

strain gage measurement locations. A milled slot replaced the traditional crack to allow crack closure or crack wake interference to be simulated by locating precision steel blocks of varying heights, lengths, and positions in the wake of the crack (or slot). Attempts to model the ACR method remained elusive until it was recognized that the compliance ratio (CR) is an indirect result of the closure mechanism. But influence $(1 - CR)$ is the direct result of the closure mechanism and is the true correlating parameter that relates modification of the crack tip elastic strain magnitude with the corresponding displacement (or strain) modification of a remote measurement location. It is this realization that set the stage for crack wake influence (CWI) theory.

Solving the influence functions provides a method of equating remote compliance measurements to reduction in crack tip elastic strain, where there is a direct impact on the magnitude of the "damaging" cyclic plastic crack tip strains. The experimental method involves determining the ratio of two compliances, that of the shielded crack to that of the fully open crack, then subtracting this from 1 to obtain influence $(1 - CR)$. The complete solution for estimating ΔK_{eff} from influence functions requires knowledge of the distribution of the crack wake forces. Measurement of the magnitude of the crack forces is not necessary since the influence relationships derived are non-dimensional functions that depend only on the crack wake interference position. Evidence to date suggests that CR is a key parameter for experimental estimation of ΔK_{eff}. However, further effort is required to model distribution using both predictive models and experimental techniques.

Technical Approach

Certainly a long-term goal is to characterize both the extrinsic and intrinsic nature of the long crack fatigue crack growth rate (FCGR) curve, especially in the near-threshold regime. An intrinsic or "closure free" relationship should provide a basis for a better understanding of the small crack phenomena and the transition from small-crack behavior to long-crack behavior. To this end, an experimental and analytical verification program has been conducted to enhance the understanding of crack-wake influence. Consideration of crack-wake influence is necessary to relate a remote compliance measurement to near-crack tip elastic strain behavior. Since experimental measurement procedures can only provide an estimate of ΔK_{eff}, proper modeling of crack-wake influence should improve the accuracy of these measurements.

ΔK_{eff} *Estimation Method*

The estimation of ΔK_{eff} from opening load implies that the crack progressively "peels open" as load is applied. The opening load is defined as the minimum load at which the fatigue crack is completely open to the tip during the increasing-load part of a fatigue cycle. ΔK_{eff} is assumed to be based on the cyclic load range above the opening load. In this case, the compliance below opening load is generally neglected. Consequently, a "true" measurement of the opening load would provide a lower boundary on the determination of ΔK_{eff} simply because the strain contribution below the opening load is ignored.

The estimation of ΔK_{eff} using either crack wake influence theory or the ACR method is based on an interpretation of crack closure as a stress redistribution (or load transfer) using a different model. Therefore, the opening load marks a transition point where the applied load is no longer directly proportional to the magnitude of the local crack tip strain field. However, the calculation of ΔK_{eff} includes the full range of the applied load and therefore does not depend upon a precise determination of the opening load. The ΔK_{eff} computed from this interpretation will be larger than that based on opening load since additional crack tip strain is included below the opening load.

The interpretation of the load versus displacement/strain records is illustrated in Fig. 1. From this figure it can be shown that the reduction in elastic strain magnitude due to crack wake interference is based on the ratio between the secant compliance (or actual strain/displacement magnitude) to the fully open compliance (or strain/displacement magnitude that would have occurred in the absence of

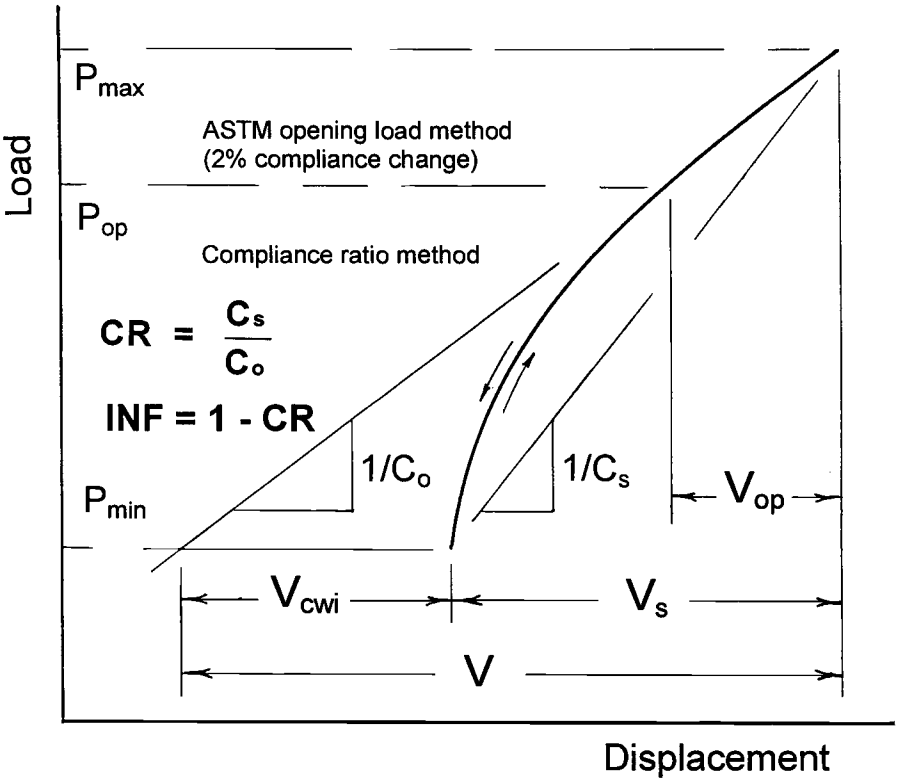

FIG. 1—*Diagram of load-remote displacement curve showing compliance ratio and crack wake influence.*

closure) as follows:

$$CR = \frac{C_s}{C} \tag{1}$$

where:

CR = compliance ratio,
C_s = V_S/P (compliance of secant drawn between minimum load-strain/displacement and maximum load-strain/displacement), and
C = V/P (compliance of load-strain above opening load).

However, this relationship would be useful only if near-crack tip elastic strain could be monitored. Since measurement of local crack tip strain is not practical, an alternative method, the ACR technique, has been devised to accomplish the same end using remote compliance measurements. ACR is determined by substracting the compliance prior to the initiation of a crack (C_i) from both the secant compliance (C_S) and the compliance above the opening load (C) as follows:

$$ACR = \frac{C_s - C_i}{C - C_i} \tag{2}$$

where:

ACR = adjusted compliance ratio, and
$C_i = V_i/P_i$ (compliance of load-displacement with notch but no crack).

This results in a compliance that is due solely to the presence of the crack extension beyond the notch. The adjustment parameter, C_i, is the compliance of the specimen (including the notch) as measured from a remote location and compensates for much of the measurement location sensitivity.

Experimental Procedure and Finite Element Analysis

The primary motivation behind the experimental approach was to provide a means of verifying formulations for crack wake influence. Proposed methodologies could then be tested against experimental data. For this purpose, a center crack panel was prepared from 6.40-mm (0.252-in.)-thick 2024-T351 aluminum plate having a width (2W) of 305 mm (12.0 in.) and a total height (2H) of 787 mm (31.0 in.). After allowing for fixturing, the total ungripped height of the plate was 610 mm (24.0 in.). The sample included a 2.54-mm (0.100-in.) milled slot having a length (2a) of 152 mm (6.0 in.) and a notch tip radius of 1.27 mm (0.050 in.). The sample stresses were applied using a servo-controlled, hydraulically actuated, closed-loop mechanical test machine interfaced to a computer system for control and data acquisition.

A close-up photograph of the displacement and strain gage measurement locations is shown in Fig. 2. Five measurement locations were recorded as a function of applied load for various interference configurations. Of these, only the centerline displacement gage (No. 5) and the near-notch tip strain gage (No. 3) were thoroughly investigated. However, the remaining measurement locations will provide future verification of both experimental and predictive models for crack wake force distribution. For each displacement measurement location, the average response of two clip gages (one on each side of the sample) increased sensitivity and linearity. Gage Location 5 used a gage length (2y) of 27.9 mm (1.10 in.) for most measurements. However, a gage length extension fixture provided a gage length of 305 mm (12.0 in.) for some of the measurements. This additional measurement location provided vital verification of the principles of the crack wake influence theory. A pair of strain gages

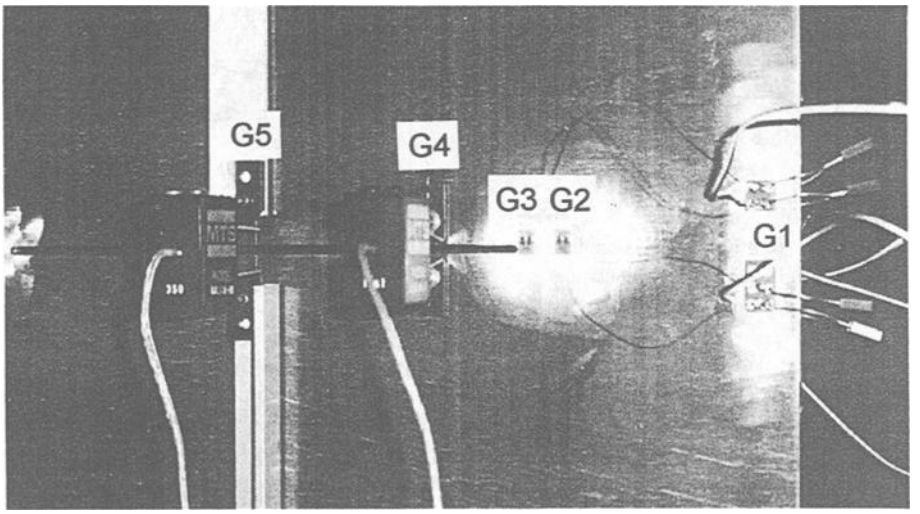

FIG. 2—*Close-up photograph of M(T) sample showing measurement locations.*

(one on each side at Gage Location 3) having a square grid measuring 0.81 mm (0.032 in.) per side was located 2.54 mm (0.10 in.) from the notch tip.

Custom software was prepared to record simultaneous load versus displacement/strain curves for each measurement location. Each record consisted of 500 digitized data pairs from a single loading and unloading interval. Measurements were recorded while the sample was cycled to between 0.31 kN (70 lb) and 31.14 kN (7000 lb) using a sinusoidal waveform with a frequency of 0.1 Hz. The load was selected to be just below the elastic limit at the notch tip. The interference blocks (one or more) were installed while the specimen was at maximum load. A summary of selected compliance measurements is shown in Table 1. The measurements were selected on the basis of being representative of both point load and distributed load. Most of the measurements are based on loading the specimen with asymmetric placement of the interference block. Two measurements were based on a centerline gage length of 305 mm.

A finite element (FEM) analysis of the center-notch specimen was performed using FRANC2D/L [*16*]. Two distinct types of FEM grids were employed, one grid representing the plate specimen with

TABLE 1—*Selected compliance measurements with interference.*

Thickness:	6.4 mm (0.252 in.)
Total width ($2W$):	305 mm (12.0 in.)
Total slot length:	152 mm (6.00 in.)
Notch (slot) tip radius:	1.27 mm (0.05 in.)
P_{max}:	31.14 kN (7000 lb)
P_{min}:	0.31 kN (70 lbs)
Modulus of elasticity	71.02 GPa (10.3×10^6 psi)
Method of interference	Steel blocks
Symmetry	Asymmetric loading unless otherwise noted
Centerline gage length (GL)	27.9 mm (1.10 in.) unless otherwise noted

	Interference Parameters[a] (position and height of blocks)			
Record No.	Initial b, mm	Final b, mm	Height, mm	Comments
MT2 7[2]	−4.4	4.4	2.565	GL = 305 mm (12.0 in)
MT2 8[2]	46.6	55.2	2.540	GL = 305 mm (12.0 in)
MT4 11	−4.4	4.4	2.565	
MT4 25	−4.4	4.4	2.591	
MT5 11	8.3	17.1	2.565	
MT5 25	8.3	17.1	2.591	
MT6 11	21.0	29.8	2.565	
MT6 25	21.0	29.8	2.591	
MT7 11	33.7	42.5	2.565	
MT7 25	33.7	42.5	2.591	
MT8 11	46.4	55.2	2.565	
MT9 17	59.1	67.9	2.560	
MT10 1	46.4	55.2	2.560	Symmetric
MT10 13	35.8	65.8	2.591	
MT12 4	0.0	68.8	2.540	
MT12 5	0.0	68.8	2.558	Foil shim added
MT12 7	0.0	59.9	2.558	Foil shim added
MT12 9	0.0	59.9	2.565	Brass shim added
MT12 11	30.0	59.9	2.565	
MT12 13	0.0	30.0	2.565	
MT12 15	0.0	30.0	2.591	

[a] Final initial gives block width; position is measured from centerline.

[b] P_{max} = 22.24 kN (5000 lb), P_{min} = 2.22 kN (500 lb), position of shims—symmetric.

a machined slot, the other representing a plate of the same overall dimensions with a crack rather than a slot. When analytical predictions of the slotted specimen compare favorably with experimental displacement and strain measurements, extension of this method to an analysis of a cracked specimen is more reliable, in particular values at other locations, such as very near the crack tip. An analysis was also made to investigate the effects of both point and finite-width crack wake interference for the notched and cracked specimens.

Closed-Form Solutions

The primary thrust of this investigation was to link the experimental observations and FEM analysis with theory of elasticity. From the *Stress Analysis of Cracks Handbook* [*17*], closed-form solutions are available for stress intensity and remote centerline displacements as a function of remote stress and a concentrated force on the crack surface. These solutions are shown for the infinite and finite width plate in a slightly modified form in the Appendix. The solutions for applied K and ΔK are based on remote stress and are relatively straightforward. However, solutions for ΔK_{eff} or K_{eff} (R = 0.0) require that the stress intensity (K_{cwi}) due to a force on the crack surface be subtracted from the applied K as follows:

$$K_{eff} = K - K_{cwi} \tag{3}$$

For a concentrated force at a given position in the wake of the crack (assuming R = 0.0), the centerline displacement, V_{cwi}, and the corresponding K_{cwi} at the crack tip are readily available as follows:

$$V_{cwi} = \frac{4P}{\pi E} \cdot f_{Vcwi}\left(\frac{b}{a}, \frac{y}{a}, \frac{a}{W}\right) \tag{4}$$

$$K_{cwi} = \frac{2P}{\sqrt{\pi a}} \cdot f_{Kcwi}\left(\frac{b}{a}, \frac{a}{W}\right) \tag{5}$$

where:

V_{cwi} = displacement at centerline due to concentrated force P on crack surface,
K_{cwi} = stress intensity due to concentrated force P,
E = modulus of elasticity,
P = concentrated force per unit thickness.
a = crack length,
b = distance from centerline of concentrated force P,
y = ½ gage length (for V_{cwi}),
W = ½ panel width, and
$f()$ = a function of geometry (subscript related quantities, see Appendix).

Combining terms yields a relationship for K_{cwi} as a function of V_{cwi} as follows:

$$K_{cwi} = \frac{V_{cwi} \cdot \pi E \cdot f_{Kcwi}\left(\frac{b}{a}, \frac{a}{W}\right)}{2\sqrt{\pi a} \cdot f_{Vcwi}\left(\frac{b}{a}, \frac{y}{a}, \frac{a}{W}\right)} \tag{6}$$

From the remote load versus displacement curve, V_{cwi} represents the offset from the linear response of the closure-free crack and is computed as follows:

$$V_{cwi} = V(1 - CR) \tag{7}$$

If no remote stress were to be applied, V_{cwi} would simply represent the offset or change in displacement due to the concentrated force P on the crack at Position b. The entire relationship between the remote load versus displacement response and the modification of crack tip stress field can be easily normalized by including the relationships for V and K for remote stress as follows:

$$V = \frac{\sigma}{E}\left(y + 2f_V\left(\frac{y}{a}, \frac{a}{W}\right)\right) \tag{8}$$

$$K = \sigma\sqrt{\pi a}\, f_K\left(\frac{a}{W}\right) \tag{9}$$

where:

V = displacement at centerline due to remote stress,
K = stress intensity due to remote stress, and
σ = remote stress.

Combining terms yields a relationship for K as a function of V as follows:

$$K = \frac{VE\sqrt{\pi a} \cdot f_K\left(\frac{a}{W}\right)}{y + 2\, f_V\left(\frac{y}{a}, \frac{a}{W}\right)} \tag{10}$$

Combining Eqs 6 and 10 results in the non-dimensional relationship between a remote load displacement curve and the crack tip stress intensity as follows:

$$IFR = \frac{\frac{V_{cwi}}{V}}{\frac{K_{cwi}}{K}} = \frac{2a \cdot f_K\left(\frac{a}{W}\right) \cdot f_{Vcwi}\left(\frac{b}{a}, \frac{y}{a}, \frac{a}{W}\right)}{y + 2\, f_V\left(\frac{y}{a}, \frac{a}{W}\right) \cdot f_{Kcwi}\left(\frac{b}{a}, \frac{a}{W}\right)} \tag{11}$$

This equation is referred to as the influence ratio (IFR). It represents the relative impact of crack wake interference on the displacement measurement compared to the effect of this same interference on the crack tip. The non-dimensional nature of this expression eliminates the need for knowing the magnitude of concentrated forces. From Eqs 7 and 11:

$$\frac{K_{cwi}}{K} = \frac{1 - CR}{IFR} \tag{12}$$

From Eqs 3 and 12, either K_{eff} or ΔK_{eff} can be solved for a known value of K or ΔK.

The above method works for crack wake interference at a known position. For a given crack size and measurement location influence, $1 - CR$, is a function of the height and stiffness as well as the

position of the interference. However, the influence ratio, IFR, depends only on position. By itself, a concentrated load solution for crack wake influence is not very useful. Closure is typically a distributed force effect over part of or the entire wake of the crack and depends on stress ratio, load history, and other considerations. However, numerical integration of the above solutions allows incorporating a force distribution effect. The distribution might be successfully modeled and predicted keeping in mind that distribution, not magnitude, needs to be determined.

Comparison Between Closed Form Solutions and the ACR Method

Since previous work on 6013-T651, 2324-T39, and 7055-T7511 aluminum alloys shows an improved correlation of FCGR stress ratio effects at near-threshold growth rates [*12,15*], it makes sense to compare the ACR method to the closed-form solutions. The first step is to re-arrange the terms of the ACR relationship to be compatible with CWI, as in Eq 2 and repeated here:

$$ACR = \frac{C_s - C_i}{C - C_i} \tag{13}$$

It has been postulated that ACR represents an approximation of the ratio of ΔK_{eff} to ΔK_{app} or of K_{eff} to K. This assumption, in addition to removing P from all compliance terms, results in:

$$\frac{K_{eff}}{K} \cong \frac{V_s - V_i}{V - V_i} \tag{14}$$

From influence relationships:

$$K_{eff} = K - K_{cwi} \tag{15}$$

and:

$$V_s = V - V_{cwi} \tag{16}$$

therefore:

$$\frac{K - K_{cwi}}{K} \cong \frac{V - V_{cwi} - V_i}{V - V_i} \tag{17}$$

or:

$$1 - \frac{K_{cwi}}{K} \cong 1 - \frac{V_{cwi}}{V - V_i} \tag{18}$$

or:

$$\frac{K_{cwi}}{K} \cong \frac{V_{cwi}}{V - V_i} \tag{19}$$

An equivalent form of the IFR function as shown in Eq 11 will now be derived as follows:

$$\frac{\frac{V_{cwi}}{V}}{\frac{K_{cwi}}{K}} \cong \frac{V_{cwi}}{V} \cdot \frac{V - V_i}{V_{cwi}} = \frac{V - V_i}{V} \tag{20}$$

$$1 - \frac{V_i}{V} = 1 - \frac{y + 2f_V\left(\frac{y}{a_i}\right)}{y + 2f_V\left(\frac{y}{a}\right)} \tag{21}$$

This equation is referred to as the ACR equivalence of the IFR. This allows a comparison between the closed-form solutions and the approximate ACR solutions. For $\Delta a \ll a_i$ (in this case, a_i represents the notch length) the ACR method is equivalent to the CWI method for a concentrated force located midway between *ai* and *a*, or a distributed force starting from a_i that linearly tapers to zero at the crack tip. Obviously, with knowledge of how ACR behaves, improvements to the ACR method for determining ΔK_{eff} may be practical.

Results

Given the above background on three evaluation methods of CWI, it is appropriate to compare the experimental, finite element, and closed-form solutions. For the centerline clip gage (gage length = 27.9 and 305 mm) under remote stress, experimental data, FEM analysis, and theory agree within 2%. Three positions of influence and two measurement locations (centerline clip Gage 5 and near-notch tip strain Gage 3) were plotted as a function of shim height in Fig. 3. The expected linear relationship between shim height and influence was confirmed.

Figure 4 shows the ratio of the influence of the centerline clip gage to the influence of the near-crack tip strain gage using both experimental measurements as depicted in Fig. 3, and other experimental measurements to simulate point loading. FEM analysis of a notch and a crack is also included using the same measurement locations as in the experiment. The theory curve as depicted in Eq 11 represents the influence of the centerline clip gage divided by the crack tip stress intensity influence.

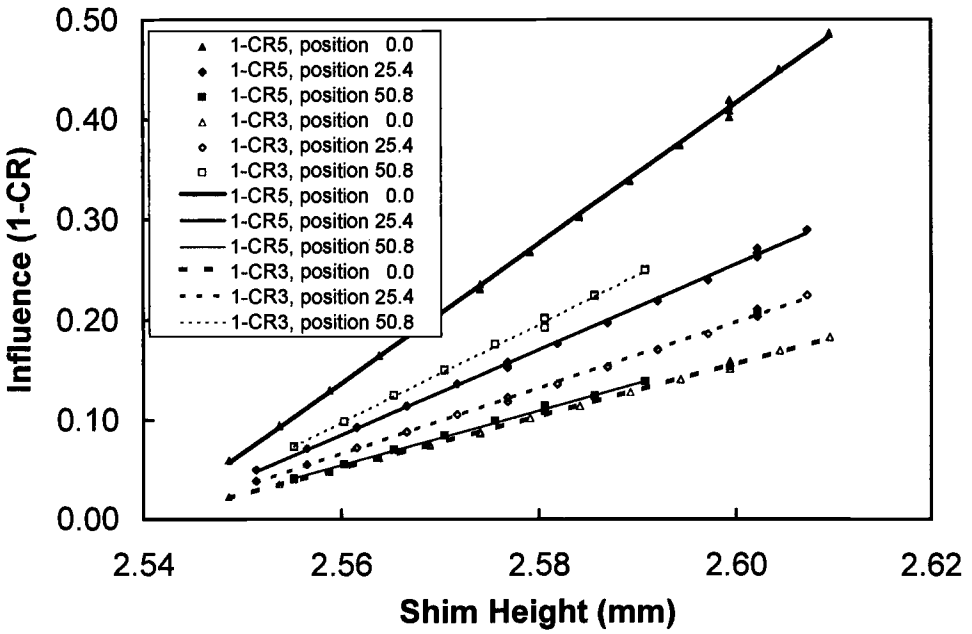

FIG. 3—*Influence versus shim height for two measurement locations and three influence positions.*

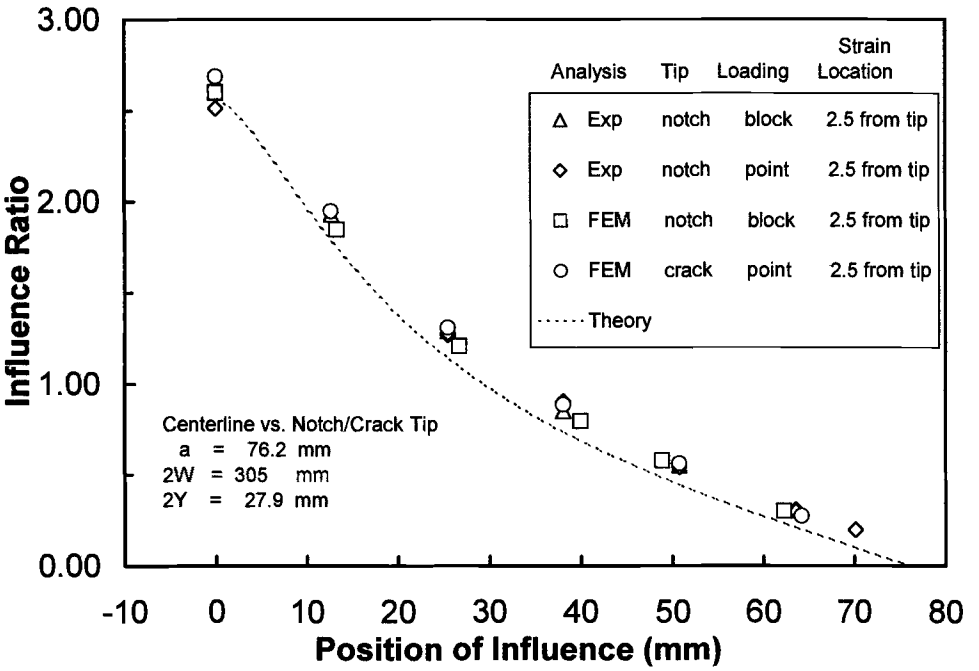

FIG. 4—*Influence ratio versus position showing experimental data, FEM analysis, and theory.*

This influence ratio is position-sensitive only and is thus independent of the height or stiffness of the shim. Figure 5 shows the same theory curve compared to FEM analysis with strain measurements either at the crack tip or 0.25 mm (0.01 in.) in front of the crack tip. These observations are in excellent agreement with the theory curve. Figure 6 shows the theory curve shifted 2.5 mm (0.1 in.) to the right (the same distance as strain Gage Location 3 from the notch tip). The experimental and FEM analysis data from Fig. 4 are now in good agreement with the theory curve. This provides strong evidence that the closed-form solutions have been properly interpreted.

Having establish a link between experiment, FEM and theory, the selected compliance records of Table 1 were analyzed to see how the three methods of ΔK_{eff} estimation compare. In all cases, the centerline clip gage (Gage Location 5) was used to predict the measured strain range of the near-notch tip strain gage (Gage Location 3). The three methods are: the closed form solutions, the ACR method, and the 2% ASTM opening load method. These results are presented as a ratio of $\Delta K_{eff}/\Delta K_{app}$ for the measured value of the near-notch tip strain as well as predicted values of near-notch tip strain using the centerline clip gage and three methods of evaluation in Table 2. For the closed-form solutions, the position of the interference blocks was offset 2.5 mm (0.1 in.), consistent with the observations depicted in Fig. 6. All distributed forces were considered uniform except for the instances where the contact surface length included most of the slot. In this case, an arbitrary assumption was made that the force exerted by the blocks on centerline would be 50% of the force exerted near the notch tip.

The normalized $\Delta K_{eff}/\Delta K_{app}$ from Table 2 are plotted in Fig. 7 showing how closely each method predicts the measured values of the near-notch tip gage. Perfect agreement is represented by a bar height of 1.0, with over-predictions above 1.0, and under-predictions below 1.0. Clearly, opening load substantially under-predicts the true elastic strain range near the notch tip. The ACR method is an improvement over opening load, but it fails to account for the intricacies of CWI. Finally, the

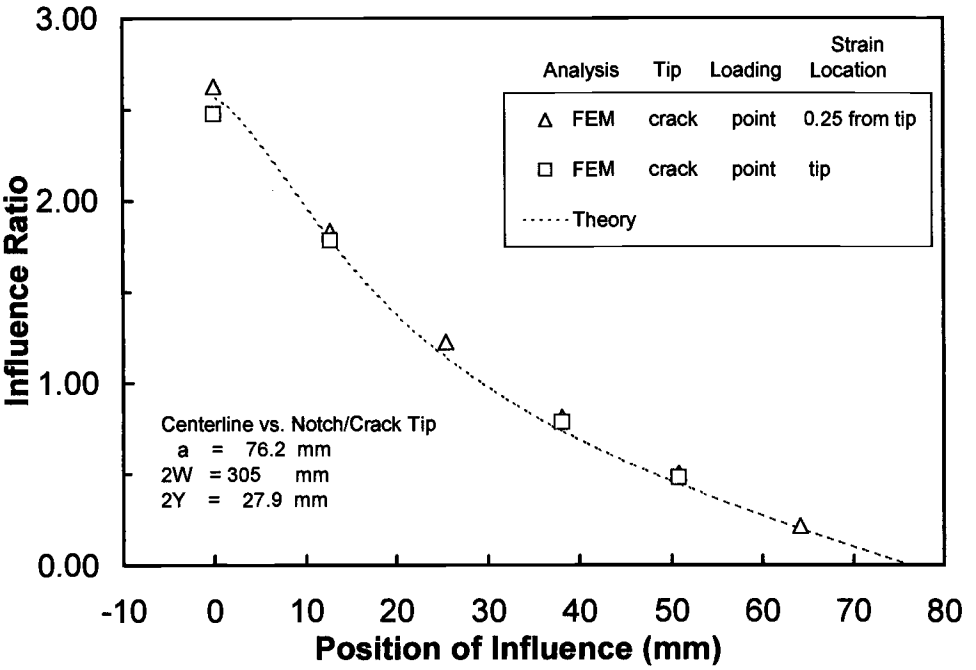

FIG. 5—*Influence ratio versus position comparing FEM analysis on crack with theory.*

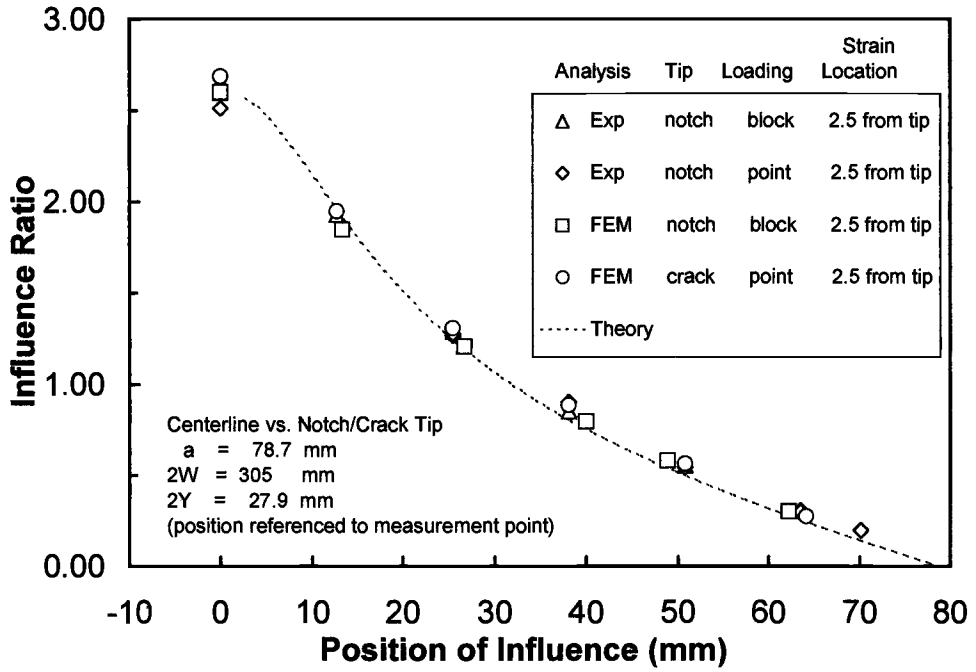

FIG. 6—*Influence ratio versus position comparing experimental data and FEM analysis with theory offset line.*

TABLE 2—*Summary of test results.*

Record No.	$\Delta K_{eff}/\Delta K_{app}$ [a] Measured (G3)	$\Delta K_{eff}/\Delta K_{app}$ [b] CWI (theory)	ACR	2% OP	Normalized $\Delta K_{eff}/\Delta K_{app}$ [c] CWI (theory)	ACR	2% OP
MT2 7	0.886	0.875	0.785	0.305	0.988	0.886	0.344
MT2 8	0.905	0.915	0.853	0.568	1.011	0.942	0.628
MT4 11	0.912	0.907	0.745	0.444	0.994	0.817	0.487
MT4 25	0.842	0.835	0.546	0.137	0.992	0.648	0.163
MT5 11	0.895	0.897	0.773	0.438	1.002	0.864	0.489
MT5 25	0.820	0.822	0.607	0.128	1.002	0.740	0.156
MT6 11	0.877	0.874	0.792	0.415	0.997	0.903	0.473
MT6 25	0.789	0.783	0.641	0.090	0.992	0.812	0.114
MT7 11	0.850	0.840	0.788	0.336	0.988	0.927	0.424
MT7 25	0.743	0.729	0.634	0.050	0.981	0.853	0.067
MT8 11	0.798	0.771	0.746	0.223	0.966	0.935	0.279
MT9 17	0.762	0.710	0.734	0.123	0.932	0.963	0.161
MT10 1	0.804	0.799	0.638	0.299	0.994	0.794	0.372
MT10 13	0.646	0.642	0.701	0.111	0.994	1.085	0.172
MT12 4	0.865	0.874	0.899	0.589	1.010	1.039	0.681
MT12 5	0.695	0.694	0.754	0.266	0.999	1.084	0.383
MT12 7	0.767	0.757	0.758	0.377	0.987	0.988	0.492
MT12 9	0.682	0.668	0.669	0.175	0.979	0.981	0.257
MT12 11	0.704	0.697	0.713	0.160	0.990	1.013	0.227
MT12 13	0.839	0.835	0.692	0.428	0.995	0.825	0.510
MT12 15	0.712	0.705	0.449	0.084	0.990	0.631	0.118

[a] Values determined from measured *CR* of near-notch tip strain Gage 3.
[b] Values predicted from centerline gage using CWI theory, ACR, or ASTM 2% OP.
[c] Normalized by dividing $\Delta K_{eff}/\Delta K_{app}$ [2] by $\Delta K_{eff}/\Delta K_{app}$ [a].

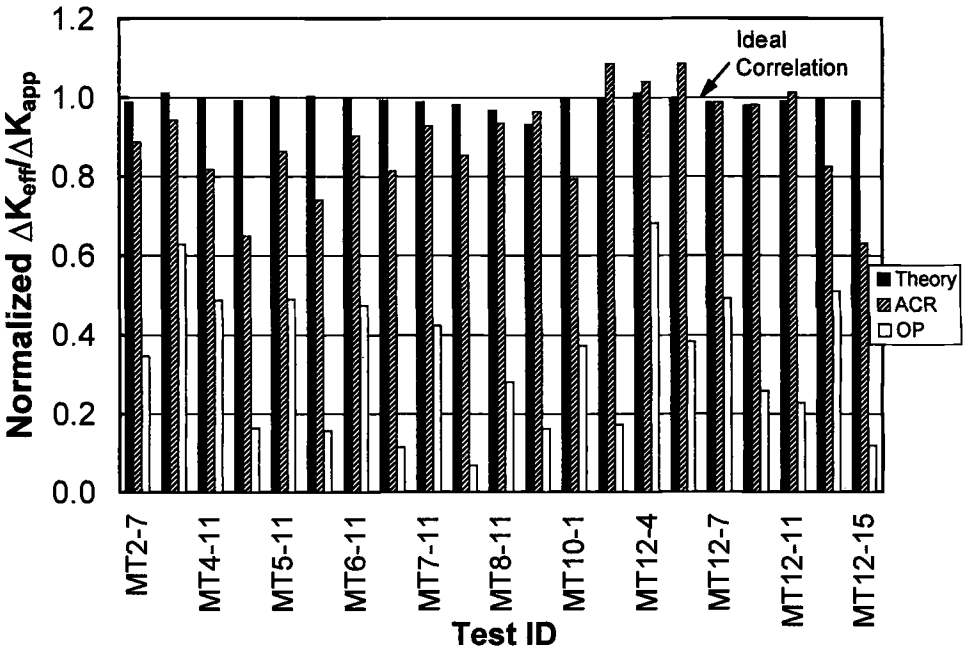

FIG. 7—*Summary of test results and analysis.*

closed form solutions (CWI) give the best prediction of near-notch tip behavior over the widest range of conditions, in particular, the 305-mm centerline gage length (Records MT2-7 and MT2-8), the point load simulations (Records MT4 through MT9), and the distributed force cases (Records MT12).

Summary and Conclusions

The experimental and analytical evidence shows that crack wake influence (CWI) is a method of linking the interpretation of remote load-displacement curves to crack tip strain behavior. If the distribution of crack wake forces is known, the method provides a direct measure of the reduction in strain at the crack tip due to closure. If the distribution is not known, estimates of the distribution combined with CWI theory should provide better estimates of ΔK_{eff} than do either opening load or the ACR method.

The development of closed-form solutions for measurement locations other than the centerline location should provide the means of experimentally determining an estimate of the crack wake force distribution through the use of influence relationships between two strategically placed measurement locations. For example, the influence relationships for clip Gage Location 4 and strain Gage Location 2 should provide valuable information of near-crack tip force distribution as long as the area of interest lies between the measurement locations.

The experimental approach includes fairly large gaps near the notch tip. This tends to exaggerate the mismatch associated with the opening load method. However, even small gaps, both near the crack tip and throughout the crack wake, can have a pronounced effect that the CWI theory can capture. Examples of this are:

1. Mismatch associated with roughness-induced closure can produce large gaps. The rougher the surface, the less the contact area.
2. Plasticity-induced closure may only be a surface effect under plane-strain. Therefore, a large gap may exist in the interior of the sample.
3. Crack tip stretch may result in a gap near the crack tip.
4. The ASTM procedure for decreasing K to determine threshold has its limitations. If the test is started at a K level that is too high, a false threshold may occur due to plasticity in the crack wake. This also creates a large gap near the crack tip.
5. Interference associated with overloads eventually ends up in the wake creating a gap near the crack tip.
6. Residual stresses may cause the crack to clamp shut at the notch but not necessarily near the crack tip.
7. The notion that small cracks and long cracks behave differently because of wake effects strongly suggests that CWI is important.

The experimental and analytical procedures have so far focused on stress ratios near zero ($R = 0.0$). But CWI should work at any stress ratio, including negative ones. In all cases, the basis for determining influence is the minimum load of the fatigue cycle. Of course, the force distribution in the wake of the crack will be modified by stress ratio since the crack profile will be influenced by the remote stress. This has to be considered in any attempts to model force distribution. The knowledge gained during this phase of research should enhance our ability to interpret remote load versus displacement records and provide better experimental estimates of ΔK_{eff}.

Acknowledgments

The authors wish the acknowledge Fracture Technology Associates, Alcoa Technical Center, and the Office of Naval Research for their support of this effort.

APPENDIX

Closed Form Solutions

Terminology:

V = displacement at centerline due to remote stress,
K = stress intensity due to remote stress,
V_{cwi} = displacement at centerline due to concentrated force P on crack surface,
K_{cwi} = stress intensity due to concentrated force P,
σ = remote stress,
E = modulus of elasticity.
P = concentrated force,
a = crack length,
b = distance from centerline of concentrated force P,
y = ½ gage length (for V and V_{cwi}),
W = ½ panel width, and
v = Poisson's ratio.

Infinite plate, remote stress

$$K = \sigma\sqrt{\pi a}$$

$$V(0,y) = \frac{\sigma y}{E} + \frac{2\sigma}{E}\left[\sqrt{a^2 + y^2} \cdot \left(1 - A\frac{y^2}{a^2 + y^2}\right) - (1 - A)y\right]$$

$$A = \frac{1}{2}(1 + v)$$

Infinite plate, concentrated force (symmetric)

$$K_{cwi} = \frac{2P}{\sqrt{\pi a}} \cdot \frac{1}{\sqrt{1 - (b/a)^2}}$$

$$V_{cwi}(0,y) = \frac{4P}{\sqrt{\pi E}}\left(\tanh^{-1}\sqrt{\frac{a^2 - b^2}{a^2 + y^2}} + A\frac{y^2}{b^2 + y^2}\sqrt{\frac{a^2 - b^2}{a^2 + y^2}}\right)$$

$$A = \frac{1}{2}(1 + v)$$

Finite width, remote stress, horizontal edge constraint

$$K = \sigma\sqrt{\pi a} \cdot \sqrt{\frac{2W}{\pi a} \cdot \tan\frac{\pi a}{2W}}$$

$$V(0,y) = \frac{\sigma y}{E} + \frac{2\sigma}{E} \cdot \frac{W}{\pi}$$

$$\times \left[\cosh^{-1} \left(\frac{\cosh \frac{\pi y}{2W}}{\cos \frac{\pi a}{2W}} \right) - A \frac{\pi y}{2W} \cdot \frac{\sinh \frac{\pi y}{2W}}{\sqrt{\left(\sin \frac{\pi a}{2W} \right)^2 + \left(\sinh \frac{\pi y}{2W} \right)^2}} - (1 - A)y \right]$$

$$A = \frac{1}{2}(1 + v)$$

Finite width, concentrated force (symmetric), horizontal edge constraint

$$K_{cwi} = \frac{2P}{\sqrt{\pi a}} \cdot \sqrt{\frac{\pi a}{2W} \cdot \tan \frac{\pi a}{2W}} \cdot \frac{\cos \frac{\pi b}{2W}}{\sqrt{\left(\sin \frac{\pi a}{2W} \right)^2 - \left(\sin \frac{\pi b}{2W} \right)^2}}$$

$$V_{cwi}(0,y) = \frac{4P}{\pi E} \left(\tanh^{-1} \sqrt{\frac{1 - \left(\cos \frac{\pi a}{2W} / \cos \frac{\pi b}{2W} \right)^2}{1 - \left(\cos \frac{\pi a}{2W} / \cosh \frac{\pi y}{2W} \right)^2}} + A \frac{\pi y}{2W} \cdot \frac{\sinh \frac{\pi y}{2W}}{\left(\sin \frac{\pi b}{2W} \right)^2 + \left(\sinh \frac{\pi y}{2W} \right)^2} \cdot \sqrt{\frac{\left(\sin \frac{\pi a}{2W} \right)^2 - \left(\sin \frac{\pi b}{2W} \right)^2}{\left(\sin \frac{\pi a}{2W} \right)^2 + \left(\sinh \frac{\pi y}{2W} \right)^2}} \right)$$

$$A = \frac{1}{2}(1 + v)$$

References

[1] Elber, W., "Fatigue Crack Closure Under Cyclic Tension," *Engineering Fracture Mechanics,* Vol. 2, 1970, pp. 37–45.

[2] Elber, W., "The Significance of Fatigue Crack Closure," *Damage Tolerance in Aircraft Structures, ASTM STP 486,* American Society for Testing and Materials, 1971, pp. 230–242.

[3] Hertzberg, R. W., Newton, C. H., and Jaccard, R., "Crack Closure: Correlation and Confusion," *Mechanics of Fatigue Crack Closure, ASTM STP 982,* American Society for Testing and Materials, 1988, pp. 139–148.

[4] Phillips, E. P., "Results of the Round Robin on Opening-Load Measurement," NASA Technical Memorandum 101601, 1989, Langley Research Center, Hampton, VA.

[5] Phillips, E. P., "Results of the Second Round Robin on Opening-Load Measurement," NASA Technical Memorandum 109032, 1993, Langley Research Center, Hampton, VA.

[6] Sadananda, K. and Vasudevan, A. K., "Analysis of Fatigue Crack Closure and Thresholds," *Fracture Mechanics: 25th Volume, ASTM STP 1220,* Erdogan and Hartranft, Eds., American Society for Testing and Materials, Philadelphia, PA, 1995.

[7] Sadananda, K. and Vasudevan, A. K., "Short Crack Growth Behavior," *Fatigue and Fracture Mechanics: 27th Volume, ASTM STP 1296*, R. Piascik, N. Dowling, and J. Newman, American Society for Testing and Materials, West Conshohocken, PA, 1997.

[8] Chen, D. L., Weiss, B., and Stickler, R., "Contribution of the Cyclic Loading Portion Below the Opening Load to Fatigue Crack Growth," *Materials Science and Engineering*, Vol. A208, 1996, pp. 181–187.

[9] Macha, D. E., Corbly, D. M., and Jones, J. W., "On the Variation of Fatigue-Crack-Opening Load with Measurement Location," *Experimental Mechanics*, June 1979, pp. 207–213.

[10] Allison, J. E. and You, C. P., "Problems Associated with the Quantification of Fatigue Crack Closure," *Proceedings*, Fatigue '90, H. Kitigawa and T. Tanaka, Eds., Materials and Components Engineering Publications, Ltd., United Kingdom, 1990, pp. 1249–1255.

[11] Donald, J. K., "Introducing the Compliance Ratio Concept for Determining Effective Stress Intensity," *International Journal of Fatigue, Elsevier Science Ltd.*, Vol. 19, Suppl. 1, 1997, pp. 191–195.

[12] Donald, J. K., Bray, G. H., and Bush, R. W., "An Evaluation of the Adjusted Compliance Ratio Technique for Determining the Effective Stress Intensity Factor," *29th National Symposium on Fatigue and Fracture Mechanics, ASTM STP 1332*, T. L. Panontin and S. D. Sheppard, Eds., American Society for Testing and Materials, West Conshohocken, PA, 1998.

[13] Donald, J. K., Bray, G. H., and Bush, R. W., "Introducing the K_{max} Sensitivity Concept for Correlating Fatigue Crack Growth Data," *High Cycle Fatigue of Structural Materials (Professor Paul C. Paris Symposium)*, W. Soboyejo and T. S. Srivatsan, Eds., The Minerals, Metals & Materials Society (TMS), Warrendale, PA, 1997.

[14] Donald, J. K. and Phillips, E. P. "Analysis of the Second ASTM Round Robin Program on Opening-Load Measurement Using the Adjusted Compliance Ratio Technique," *Advances in Fatigue Crack Closure Measurement and Analysis: Second Volume, ASTM STP 1343*, R. C. McClung and J. C. Newman, Jr., Eds., American Society for Testing and Materials, West Conshohocken, PA, 1998.

[15] Bray, G. H. and Donald, J. K. "Separating the Influence of K_{max} from Closure-Related Stress Ratio Effects Using the Adjusted Compliance Ratio Technique," *Advances in Fatigue Crack Closure Measurement and Analysis: Second Volume, ASTM STP 1343*, R. C. McClung and J. C. Newman, Jr., Eds., American Society for Testing and Materials, West Conshohocken, PA, 1998.

[16] James, M. and Swanson, D., "FRANC2D/L: A Crack Propagation Simulator for Plane Layered Structures," available from http://www.mne.ksu.edu/~franc2d/.

[17] Tada, H., Paris, P. C., and Irwin, G. R., *The Stress Analysis of Cracks Handbook*, 2nd ed., Paris Productions Incorporated, 1985.

Markus Lang[1] *and James M. Larsen*[2]

Fatigue Crack Propagation and Load Interaction Effects in a Titanium Alloy

REFERENCE: Lang, M. and Larsen, J. M., **"Fatigue Crack Propagation and Load Interaction Effects in a Titanium Alloy,"** *Fatigue and Fracture Mechanics, 30th Volume, ASTM STP 1360,* P. C. Paris and K. L. Jerina, Eds., American Society for Testing and Materials, West Conshohocken, PA, 2000, pp. 201–213.

ABSTRACT: An experimental investigation of load interaction effects in Ti-6Al-2Sn-4Zn-2Mo is presented. Simple variable amplitude loading spectra were applied to test samples, and the crack propagation stress intensity factor, K_{PR}, was subsequently measured. The data were condensed to two equations ("master curves") that describe the influence of an unloading cycle after constant amplitude loading and a single overload cycle, respectively. The results suggest that load interaction effects are caused by residual compressive stresses ahead of the crack front, whereas the influence of crack closure is minor.

KEYWORDS: fatigue crack propagation, crack closure, residual stresses, titanium, load interaction, life prediction

Nomenclature

$K_{max,OL}$	Maximum stress intensity factor of an overload
K_{PR}, F_{PR}	Crack propagation stress intensity factor (-load)
$K_{PR,C}$, $K_{PR,OL}$	Crack propagation stress intensity factor after unloading following constant amplitude loading and an overload, respectively
K_{op}, F_{op}	Crack opening stress intensity (-load)
K_{ul}	Unloading stress intensity factor
K_w, F_w	Stress intensity factor experienced by the crack tip at minimum load
R	Stress intensity factor ratio ($R = K_{min}/K_{max}$)
R_{BL}	Stress intensity factor ratio of base loading
R_{tip}	Stress intensity factor ratio experienced by the crack tip
UR	Unloading ratio
ΔK	Stress intensity factor range
ΔK_B	Cyclic amplitude during the CPLM procedure
ΔK_{eff}	Effective part of ΔK
ΔK_{tip}	Stress intensity amplitude experienced by the crack tip
ΔK_T	Intrinsic threshold value
δ	Incremental step in mean stress intensity factor during the CPLM procedure

The design of dynamically loaded engineering structures would be relatively easy if there were no load interaction phenomena. These are irregularities in the growth rate of a fatigue crack caused by

[1] Air Force Research Laboratory, Materials and Manufacturing Directorate, Wright-Patterson Air Force Base, OH 45433-7817, USA, National Research Council-Associate. Now with IABG, Department of Fatigue & Failure Analysis, 85521 Ottobrunn, Germany.

[2] Air Force Research Laboratory, Materials and Manufacturing Directorate, Wright-Patterson Air Force Base, OH 45433-7817.

variations in the maximum and minimum load. A tensile overload retards the crack growth rate, while a compressive overload accelerates it. In contrast, fatigue crack propagation under constant amplitude loading (CA) is relatively easy to understand, since the crack growth rate is constant (K-controlled test) or continuously accelerates from crack initiation to final failure (stress-controlled test). A life management program for any kind of irregularly loaded structure needs the capability of predicting load interaction effects due to variable amplitude loading, the most common loading pattern in aircraft, cars, offshore structures, and so forth.

The discovery of load interaction effects around 1960 [*1*] triggered extensive research activities in many countries. Much progress has been made in understanding the consequences of load interaction, i.e., the retardation or acceleration of a crack after a tensile or compressive overload, respectively. It was demonstrated that the retardation period increases with magnitude [*2–5*] and number of tensile overloads [*6,7*] as well as with decreasing sheet thickness [*7,8*]. Those are only a few examples of publications that present the variations in crack growth rate with the number of load cycles or time after one or more overloads. Numerous attempts also addressed the problem from a crack closure [*9,10,11*] perspective and the effective part of the amplitude (ΔK_{eff}) after an overload was studied [*12–14*]. These investigations quantified specific overload cases and contributed to the understanding of the phenomenon but did not yield a generalized description of the problem. Consequently, no complete methodology yet exists that reliably predicts fatigue crack propagation due to the general case of variable amplitude loading. Many industrial organizations, therefore, conduct extensive and costly test programs and develop their own crack growth prediction codes to solve specific problems. Consequently, when we try to characterize load interaction effects, we should keep the term *generality* as primary requirement in view of a later implementation in a life prediction method. A solution for the problem would be of great value to damage-tolerant life management of aging aircraft and engine structures, an important issue in the United States [*15,16*] and many other countries. Critical decisions, e.g., whether an aircraft structural part should be replaced or can continue to operate safely, are based on crack growth predictions due to expected loading conditions. The need for improved spectrum-load life prediction methods is certain to grow, considering the increasing number of older commercial and military aircraft to be managed and additional industries that are adopting damage-tolerant design philosophies.

It is sufficient to investigate simple loading sequences, such as a single overload, since it can be assumed that a general mechanism is responsible for the mechanical response of metallic materials to changes in loading. If the condition after the sequence is independent of the loading history before that sequence and if is possible to describe those simple cases on a general basis, it should be possible to describe complicated loading sequences, since they consist of an array of simple sequences. This paper presents an experimental program wherein simple loading sequences are investigated in the titanium alloy Ti-6Al-2Sn-4Zn-2Mo (Ti-6242). This is a continuation of the work in Refs *17–20,* where different experimental studies of load interaction effects in an aluminum alloy were presented. These studies resulted in a new approach and a set of simple equations that describe load interaction effects. Moreover, it was asserted that the form of those equations is qualitatively valid for all homogeneous metallic materials. This paper supports this assertion. Some immanent conceptual details are explained in the following section. Then, the experimental program for Ti-6242 is presented and the results are discussed.

Conceptual Approach

The approach used here is the same as explained in Refs *17* and *18.* For the sake of self-consistency of the present paper, the approach shall be briefly explained.

Crack Closure

In contrast to Elber's way to implement crack closure into the ΔK_{eff} concept [*9–11*], crack closure is treated as proposed in Ref *21,* which is itself a further development of Ref *22.* Crack surface con-

tact, which can be caused by a variety of mechanisms, shields the crack tip and therefore increases the minimum stress intensity factor experienced by the crack tip at minimum remote load. This is illustrated in Fig. 1, where the relation between the applied load F and the stress intensity factor K (Fig. 1*b*) is plotted for the respective compliance curve (Fig. 1*a*). If we insert an artificial rigid shim at F_{max} (that fills the space between the crack halves) and unload the specimen to F_{min}, the crack tip still "sees" K_{max}, even though the remote load of the specimen is F_{min}. Inserting a shim at any other load level would result in similar behavior. The surplus wake material between the crack flanks is a "natural wedge" that conserves the stress intensity factor K_w (w stands for wedging action) at the applied load F_{min}. Therefore, at F_{min} the crack tip region does not experience K_{min}, but the higher K_w. The amplitude and the R value that are "seen" by the crack tip are determined by

$$\Delta K_{tip} = K_{max} - K_w \tag{1}$$

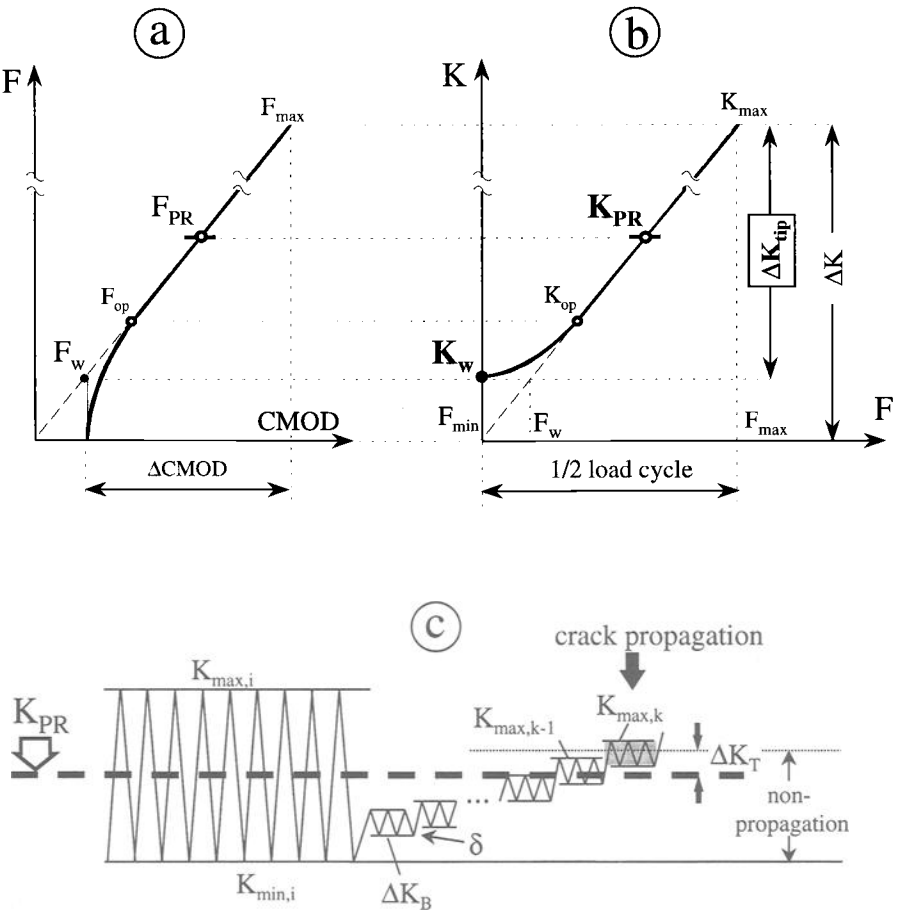

FIG. 1—*Determination of* ΔK_{tip} *and* R_{tip}. (a) *A compliance curve of a crack that exhibits crack closure and* (b) *the respective relation between the applied load* F *and the stress intensity factor* K *experienced at the crack tip.*

and

$$R_{tip} = (K_w/K_{max}) \tag{2}$$

respectively. Any compliance curve representing the behavior of the whole specimen body (clip gage remote from the crack tip or back face strain (BFS)) directly yields K_w as the intersection point of a vertical line through K_{min} and the elongation of the linear part of the compliance curve (see Fig. 1*a*). Note that K_{op} is not the term of interest, but K_w. See Refs *17–21* for a full explanation of this point. All following test results are treated accordingly.

The Effective Amplitude, ΔK_{eff}

To determine the effective part of the load amplitude, a simple criterion is employed: The load level above which a crack propagates during the loading cycle determines the lower bound of the effective amplitude, ΔK_{eff}. The respective stress intensity factor level is called K_{PR}, the *crack propagation stress intensity factor* [*17–19*]. K_{PR} can be determined experimentally by measuring the onset of crack growth after any loading sequence of interest. The procedure is called crack propagation load measurement method (CPLM) and goes back to Refs *23* and *25*. After the sequence being investigated is applied (Fig. 1*c*), the specimen is cycled with a small amplitude ΔK_B (which must be greater than the intrinsic threshold stress intensity factor range, ΔK_T) above the last minimum load before CPLM ($K_{min,i}$ in Fig. 1*c*), and sufficiently below the expected K_{PR}. If the crack does not propagate during the first loading block (i.e., $da/dN < 1 \times 10^{-7}$ mm/cycle), the mean load of the small amplitude cycles is increased by a small amount δ (e.g., 0.2 MPa$\sqrt{m}$ in terms of K). This procedure is repeated until the crack starts to grow in the k^{th} block (shaded block in Fig. 1*c*). It shall be noted that the result of the CPLM technique is independent of ΔK_B, as long as its minimum is above K_{min} ($K_{min,i}$ in Fig. 1*c*) of the sequence to be investigated [*21,23,24*]. Once the onset of crack growth is detected, K_{PR} can be calculated as

$$K_{PR} = (K_{max,k} + K_{max,k-1})/2 - \Delta K_T \tag{3}$$

With a correction for the intrinsic threshold value ΔK_T [*25*] (material dependent), which is the "elastic resistance of the crack tip," the effective amplitude is determined by

$$\Delta K_{eff} = K_{max} - K_{PR} - \Delta K_T \tag{4}$$

Even though the right side of Eq 4 differs from Elber's expression, ΔK_{eff} is still used in the conceptual scope of the similarity approach proposed by Elber [*9–11*], which predicts equal crack growth increments for the same ΔK_{eff}. The application of ΔK_{eff} to constant and variable amplitude loading requires the determination of K_{PR} on a cycle by cycle basis.

Experimental Program

The titanium alloy Ti-6Al-2Sn-4Zn-2Mo (σ_y = 1067 MPa, σ_u = 1112 MPa) was used in this investigation. C(T) specimen (W = 40 mm, B = 10 mm) were cut out of rolled plates in the LT direction. Three categories of tests were conducted. First, K_{PR} was measured after different constant amplitude loading sequences (Table 1*a*). Then a series of tests was conducted where K_{PR} was determined after sequences where the last minimum load (K_{ul}) was either above or below $K_{min,BL}$ (see Table 1*b*). In the third part of the test program, K_{PR} was measured after single overload cycles with different subsequent unloading level, K_{ul}, as shown in Table 1*c*. Note that all parameters such as R values or overload maxima, were varied. After these sequences, the CPLM procedure was performed as shown schematically in Table 1 and Fig. 1 (ΔK_B = 3 MPa$\sqrt{m}$, δ = 0.2 MPa$\sqrt{m}$). Each loading block con-

TABLE 1—*The testing program.* K_{PR} *measurements after* (a) *constant amplitude loading,* (b) *an unloading cycle following constant amplitude loading, and* (c) *a single overload with different subsequent unloading levels,* K_{ul}.

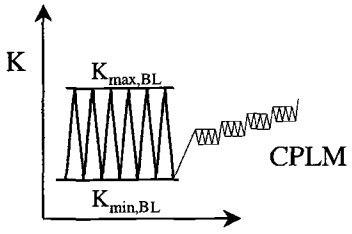

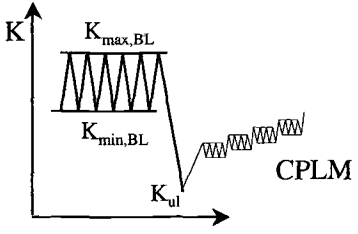

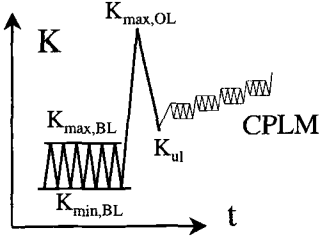

(a)

Constant Amplitude Loading	
R_{BL}	$K_{max,BL}$ [MPa√m]
0.05	15, 25
0.33	20, 30
0.47	20, 30
0.68	30, 40
0.8	40

(b)

Unloading After Constant Amplitude Loading		
R_{BL}	$K_{max,BL}$ [MPa√m]	K_{ul} [MPa√m]
0.05	20	10.1
	30	20.7
0.47	30	3
	40	8
0.68	40	13.2
0.8	30	18
	30	3

(c)

Unloading After a Single Overload			
R_{BL}	$K_{max,BL}$ [MPa√m]	$K_{max,OL}$ [MPa√m]	K_{ul} [MPa√m]
0.05	16	40	0.8, 6.1, 8
0.1	12	33.6	1.2, 10.8
	16	33.6	15.8, 22.9, 31.8
		40	22
0.33	16	33.6	5.3
0.5	20	40	10
0.7	30	40	21

sisted of 200 000 cycles. The onset of crack growth was detected by a potential difference measurement system and monitored by a computer program. A second computer controlled the loads of the test machine. Prior to an overload or unloading cycle, the specimens were precracked for 1 mm with the base-loading sequence to establish steady-state conditions (CA loading with R_{BL} and $K_{max,BL}$, see Table 1). Crack extension during precracking was monitored optically, and the loads were adjusted after every 0.125 mm to keep K constant during precracking. During all tests a clip gage was mounted at the mouth of the C(T) specimens, and the compliance curves were recorded. The frequency during base loading was 10 to 50 Hz (depending on the amplitude), 0.05 Hz during an overload or unloading cycle (recording compliance curves), and 50 Hz during the CPLM procedure. All tests were run in controlled laboratory air environment at room temperature and approximately 30% relative humidity. The specimen temperature was continuously monitored during the CPLM procedure to distinguish an increase in potential difference due to physical crack extension from an increase due to a rise in specimen temperature.

Results

K_{PR} *after CA Loading and a Subsequent Unloading Cycle*

The K_{PR} data due to the tests from Table 1*a* and 1*b* were normalized by the respective K_{max} value of the prior CA loading sequence and plotted in Fig. 2*a* versus R_{tip} of the unloading cycle, $R_{tip,ul}$, which is called the unloading ratio, UR (the expression UR is used for consistency with the nomenclature used in Refs *17,18,20,* where the tension and compression range was investigated for Al 7475-T7351 and UR was used to unify different scales). *UR* (= $R_{tip,ul}$) is the R value of the last unloading cycle that is experienced by the crack tip. This correction is necessary to account for the increase in minimum stress intensity factor from K_{min} to K_w due to crack closure shielding (Eq 2). In those cases where closure was detected, the parameter K_w, and consequently *UR,* was determined as described previously. The data can be seen in Table 2. The K_{PR} data from the tests with constant amplitude loading in Fig. 2*a* (Table 1*a*) are marked by filled circles; those from tests with different unloading levels above or below $K_{max,BL}$ (Table 1*b*) are marked by open diamonds. As obvious from Fig. 2*a,* all data points fall upon a single curve. This is the same observation as in Ref *17* for an aluminum alloy. The consequences that arise from this agreement are discussed later in this paper.

K_{PR} *after a Single Overload with Different Subsequent Unloading Level*

The K_{PR} data from the overload experiments in Table 1*c* are treated analogously to those from Table 1*a,b.* The K_{PR} data are divided by the respective $K_{max,OL}$ value and plotted versus the crack closure corrected unloading ratio, *UR.* It should be stressed that *UR* is the R value of the unloading cycle following the peak of the overload. Adjustments for crack closure were necessary only for $R_{ul} < 0.15$ and $K < 3.5$ MPa$\sqrt{m}$ (that applies also for all the other tests, see Table 2). K_w was 0.2 to 0.8 MPa$\sqrt{m}$ above K_{ul}, which is a minor correction. Figure 2*b* shows that all normalized K_{PR} data points lie along a single curve, as observed in Ref *18* for an aluminum alloy.

Discussion

The results of the entire test program (Table 1) can be expressed by two simple functions. K_{PR} after constant amplitude loading, $K_{PR,C}$, is given as

$$K_{PR,C} = (0.433 + 0.311 \cdot UR + 0.09 \cdot UR^2 + 0.16 \cdot UR^3) \cdot K_{max} \qquad [0 \leq UR \geq 1] \qquad (5)$$

and K_{PR} after a single overload, $K_{PR,OL}$, is given as

$$K_{PR,OL} = (0.391 + 0.393 \cdot UR + 0.03 \cdot UR^2 + 0.184 \cdot UR^3) \cdot K_{max,OL} \qquad [0 \leq UR \geq 1] \quad (6)$$

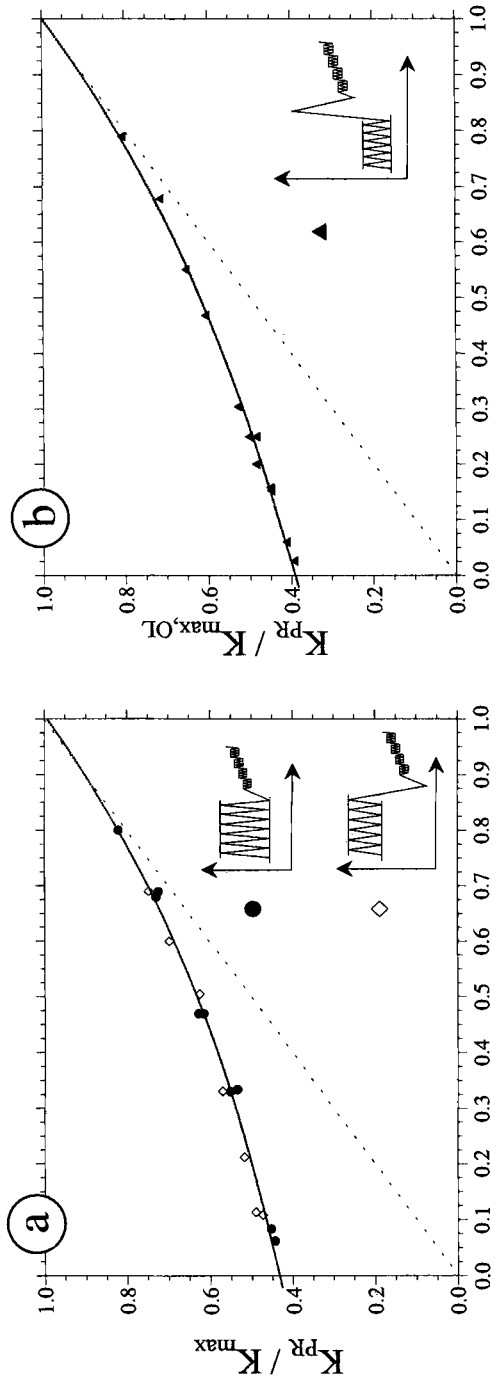

FIG. 2—*Results of* K_{PR} *measurements for* (a) *the loading sequences in Table 1a and* b; *and* (b) *the sequences in Table 1c.*

TABLE 2—*The crack closure data for the tests in Table 1 due to the experimental procedure explained in the section "Crack Closure" and in Fig. 1*a, b.

R_{BL}	$K_{max,\,BL}$ [MPa√m]	$K_{max,\,OL}$ [MPa√m]	K_{ul} [MPa√m]	R_{ul}	$K_{w,ul}$ [MPa√m]	UR ($R_{tip,ul}$)
Constant Amplitude Loading						
0.05	15	-	0.75	0.05	1.25	0.083
	25	-	1.25	0.05	1.55	0.062
Unloading After Constant Amplitude Loading						
0.47	30	-	3	0.1	3.23	0.108
0.8	30	-	3	0.1	3.06	0.102
Unloading After Single Overload						
0.05	16	40	0.8	0.02	1.03	0.026
0.1	12	33.6	1.2	0.036	2	0.06

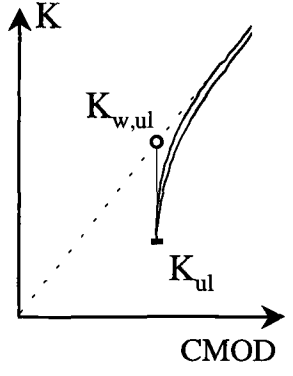

It is obvious that Eqs 5 and 6 are of the same form, namely

$$K_{PR} = f(UR) \cdot K_{max} \tag{7}$$

where K_{max} is the last maximum stress intensity factor. It is obvious that K_{PR} after any of the sequences investigated depends only on two variables: *the maximum and minimum stress intensity factor of the last unloading cycle.* This is illustrated in Fig. 3 where Eqs 5 and 6 are shown along with some examples that visualize their significance.

The diagonal line connecting the point $(K_{PR}/K_{max} = 1)/(UR = 1)$ with $(K_{PR}/K_{max} = 0)/(UR = 0)$ in the graph in Fig. 3 represents the stress intensity factor experienced at the crack tip (normalized by K_{max}) during an unloading cycle in any of the respective sequences. Sequence (1) consists of a CA loading block with a high R_{BL}, followed by a single unloading cycle to nearly zero. Sequence (2) is pure CA loading. Since K_{max} and K_{ul} (probably K_w due to closure at low R_{ul}) of the last unloading cycle in Sequences (1) and (2) are identical, the same K_{PR} value is yielded. Sequences (3) and (4) contain the same CA loading block as Sequences (1) and (2) but with an insufficient last unloading cycle reaching only to $K_{ul,3,4}$. Cases (3) and (4) result in the same K_{PR}, since K_{max} and $K_{ul,3,4}$ are identical. However, $K_{PR,3,4}$ is higher than $K_{PR,1,2}$, according to Eq 5. Equation 6 for the single overload has identical conceptual consequences. Sequences (5) and (6) have different CA sequences but the same overload sequence in the sense that $K_{max,OL}$ and $K_{ul,6,7}$ (and K_w) are identical. Consequently, K_{PR} is the same. Sequences (7) and (8) have again the same CA loading part as sequences (5) and (6) but a higher unloading level after the peak. Accordingly, K_{PR} is the same after Sequences (7) and (8) but higher than after (5) and (6).

These examples demonstrate the significance of the test results and their impact on the conceptual view of fatigue crack propagation. K_{PR} after a single overload or a single unloading cycle following CA loading (Table 1*b,c*) is independent of the prior R_{BL} and ΔK_{BL} value. Therefore, the "history" before these events is wiped out by the last unloading cycle. The extent of cyclic plasticity in front of the crack tip due to different ΔK_{BL}, the crack growth rate, or the level of K_{PR} before these events are without impact. The K_{PR} value is set solely by the last unloading cycle and is uniquely described by Eqs 5 and 6 using only K_{max} and UR. Equation 5 is the *master curve* for the case of unloading during and after CA loading, and Eq 6 is the *master curve* for a single overload. This confirms the results and conclusions in Refs *17* and *18* where the same properties were observed for the aluminum alloy Al 7475-T7351. The only differences between Eqs 5 and 6 and the respective equations in Refs *17* and *18* are the constants (the two curves are also further apart in Al 7575-T7351). The qualitative form of the equations, given by Eq 7, is identical. It should be noted that Eq 6 yields K_{PR} directly after a single overload. The changes in K_{PR} due to subsequent loading, e.g., multiple overloads (a transitional increase in K_{PR}) or the case where the same amplitude continues after the overload (the decline in K_{PR}, while the overload effect fades away) can be described in the same general way as the loading cases here. However, these issues are beyond the scope of this paper.

Another important result is that Eqs 5 and 6 describe a *dynamic* process. The upper curve in Fig. 3 (Eq 5) describes the level of K_{PR} at any stage during an unloading cycle after constant amplitude loading. The curve is practically followed starting from the point $(K_{PR}/K_{max} = 1)/(UR = 1)$ (which refers to K_{max}) down to the respective unloading ratio UR (or K_{ul}). As a further consequence, Eq 5 describes the unloading process for *every* unloading cycle during constant amplitude loading, beginning at K_{max} and ending at K_{min}. It also describes the unloading process below the minimum load of a constant amplitude sequence (an underload), only K_{max} must be the same.

As mentioned above, the criterion for plastic crack extension during the loading cycle is that K exceeds K_{PR} ($K_{PR} + \Delta K_T$ if we implement the threshold value, Eq 4). This K_{PR} value, though, is set by the *previous* unloading cycle. In the case of a single overload, the lower curve in Fig. 3 (Eq 6) is "dynamically" followed during the unloading cycle after the peak of the overload. Equation 6 is the

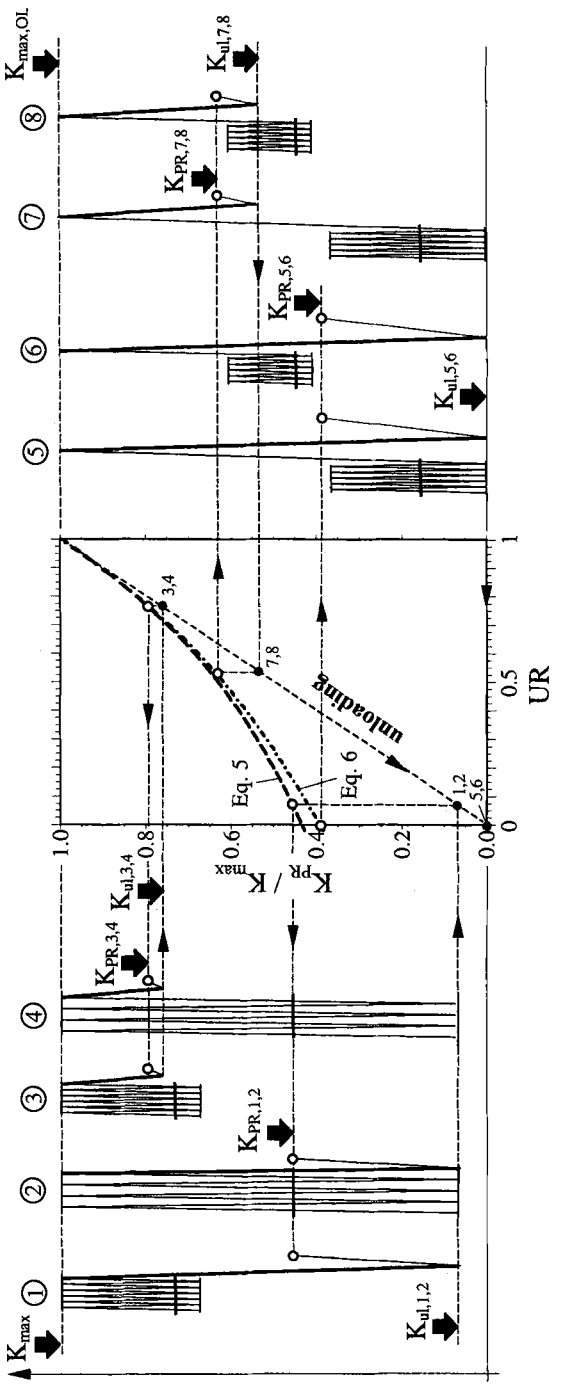

FIG. 3—*Demonstration of the conceptual consequences and applicability of the two master curves, given by Eqs 5 and 6.*

master curve for a single overload that directly yields K_{PR} after *any* single overload sequence in the Ti-6242 alloy investigated.

Equations 5 and 6 directly predict acceleration and retardation. If the CA loading in Sequences (5) and (6) in Fig. 3 would resume after the overload, the same overload would cause crack arrest in Sequence (5), while it would cause acceleration in Sequence (6). Please find the K_{PR} levels in the CA sequences indicated as horizontal lines in Fig. 3. Additionally, it is easy to calculate *UR* necessary to establish the same K_{PR} after sequence (6) (Fig. 3) as before the overload. There are various combinations of $K_{max,OL}$ and K_{ul} that produce this K_{PR} value. In this case we have no load interaction, and the crack continues growing unaffected. This demonstrates the capabilities of Eqs 5 and 6 for implementation in life prediction methodologies.

The immediate changes in K_{PR} are an important indication for attempting a mechanistic explanation of the experimental results. As already mentioned, the data in Fig. 2 were modified for crack closure, and this correction was not necessary for $R > 0.15$ and $K > 3.5$ MPa$\sqrt{\text{m}}$. Therefore, crack closure can not be the physical reason for the changes in K_{PR}, especially at high R values where crack closure is absent. For example, an overload at a high R value increases K_{PR} according to Eq 6 (see, for example, Sequence (8) in Fig. 3), which can not be explained by crack closure. The authors are subscribers of the idea that such immediate changes in K_{PR} can only happen if the responsible mechanism is a stress-governed process. In Refs *17* and *18* residual compressive stresses (RCS) in front of the crack tip were claimed responsible for variations in K_{PR} after overloads and compressive loads. This idea, however, is not new; it was the original explanation for load interaction effects in the 1960s [*1,2*], long before crack closure was discovered.

Figures 2 and 3 demonstrate another property of fatigue crack propagation, namely that K_{PR} during any load cycle is always higher than the last K_{min} (or K_w if closure occurs).

$$K_{PR} \geq K_{min} \tag{8}$$

This is easy to see in Figs. 2 and 3. The minimum load (dashed line between $(K_{PR}/K_{max} = 1)/(UR = 1)$ and $(K_{PR}/K_{max} = 0)/(UR = 0)$ is always lower than K_{PR} (or K_{PR}/K_{max}). As a result, ΔK_{eff} must always be smaller than the applied ΔK, even at very high R values (see also Refs *17* and *18*). This is different in the crack closure concept [*11*], where the absence of closure at high R values would force ΔK_{eff} to be equal to the applied ΔK, which is disproved by the current results.

The difference between K_{ul} and K_{PR} is thought to be proportional to the magnitude of residual compressive stresses in front of the crack tip, such that

$$\Delta K_{res} = K_{PR} - K_{ul} \tag{9}$$

or $\Delta K_{res} = K_{PR} - K_w$ if closure occurs. The lower a specimen is unloaded, the more it must be reloaded in the next cycle to propagate the crack ($K_{PR} - K_{ul}$ increases). The absolute value of K_{PR}, though, decreases during the unloading process.

We can conclude that we have separated the processes occurring behind and in front of the crack tip, i.e., crack face closure and residual compressive stresses, respectively. Crack closure is an *extrinsic* effect that can be present or not. There are several factors that can enhance crack face closure, as can be found in any textbook in this field. The relation between K_{PR} and the loading parameters of the last unloading cycle for the cases investigated (Eqs 5 and 6) reflects an *intrinsic* response of the material. The level of crack face closure decides only the "window" or range that is used in Eqs 5 and 6 (Fig. 3). However, Eqs 5 and 6 are still valid and the material reacts intrinsically to the load range it experiences, as explained in Fig. 3.

In Refs *17* and *18* the qualitative form of the equivalent equations to Eqs 5 and 6 was claimed to be valid for all homogeneous metallic materials. This investigation supports this statement. If residual compressive stresses govern fatigue crack propagation, Eqs 5 and 6 must exist for all metal al-

loys, even though they might be quantitatively different (other constants in the equations). Residual stresses in general, compressive or tensile, are based on the elastic-plastic interaction in metallic materials. Most engineering alloys for damage tolerant applications are designed to exhibit substantial elastic and plastic deformation and will consequently be susceptible to the introduction of residual compressive stresses. Even more "brittle" alloys show some plastic deformation and will, therefore, follow the same functional description.

Summary

An experimental investigation of load interaction effects in Ti-6242 is presented. The parameter K_{PR} (crack propagation stress intensity factor) was measured after various load sequences involving constant amplitude loading and a subsequent unloading cycle, as well as single overload sequences. The CPLM method was used to measure K_{PR}. The experimental results yield two equations (*master curves*) that describe the general case of the unloading process after constant amplitude loading and a single overload, respectively. The master curves are of a simple nature and quantitatively valid for the Ti-6242 alloy investigated. The qualitative form of the master curves is considered valid for all homogeneous metallic materials. The investigation also shows that load interaction effects are controlled by residual compressive stresses in front of the crack tip where as the influence of crack closure is small.

Acknowledgments

We gratefully acknowledge the help of Mr. George A. Hartman (AFRL/MLLN) for writing the computer software to run the tests. Additionally, we would like to thank Bob E. deLaneuville from Pratt & Whitney, West Palm Beach, Florida, for supplying the specimens for this investigation. The first author greatly acknowledges support by the United States National Research Council.

References

[1] Schijve, J., "Fatigue Crack Propagation in Light Alloy Sheet Material and Structures," *Advances in Aeronautical Sciences,* Pergamon Press, Oxford, 1961.

[2] Schijve, J., Broek, D., and de Rijk, P., "Crack Propagation under Variable Amplitude Loading," NLR Report M 2094, 1962.

[3] Rice, R. C. and Stevens, R. I., "Overload Effects on Subcritical Crack Growth in Austenitic Manganese Steel," *ASTM STP 536,* American Society for Testing and Materials, West Conshohocken, PA, 1973, pp. 95–114.

[4] Wei, R. P., Shih, T. T., and Fitzgerald, J. H., "Load Interaction Effects on Fatigue Crack Growth in Ti-6A1-4V Alloy," NASA Report CR-2239, 1973.

[5] Vargas, L. G. and Stephens, R. I., "Subcritical Crack Growth under Intermittent Overloading in Cold-Rolled Steel," *Proceedings, 3rd International Conference on Fracture,* Munich, Germany, 1973.

[6] Trebules, V. W., Jr., Roberts, R., and Hertzberg, R. W., "Effect of Multiple Overloads on Fatigue Crack Propagation in 2024-T3 Aluminum Alloy," *ASTM STP 536,* American Society for Testing and Materials, West Conshohocken, PA, 1973, pp. 115–146.

[7] Mills, W. J. and Hertzberg, R. W., "Load Interaction Effects on Fatigue Crack Propagation in 2024-T3 Aluminum Alloy," *Engineering Fracture Mechanics,* Vol. 8, 1967, pp. 657–667.

[8] Daiuto, R. A. and Hillberry, B. M., "Effect of Thickness on Fatigue Crack Propagation in 7475-T731 Aluminum Alloy Sheet," NASA-CR-172367, 1984.

[9] Elber, W., "Fatigue Crack Propagation under Random Loading: An Analysis Considering Crack Closure," *International Conference of Aeronautical Fatigue,* Stockholm, Sweden, 19–23 May 1969.

[10] Elber, W., "Einfluß der plastischen Zone auf die Riβausbreitung unter Schwingbelastung," *DVM, Materialprüfung,* Vol. 12, No. 6, 1970, pp. 189–220.

[11] Elber, W., "The Significance of Fatigue Crack Closure," *ASTM STP 468,* American Society for Testing and Materials, West Conshohocken, PA, 1971, pp. 230–242.

[12] Robin, C., Chehimi, C., Louah, M., and Pluvinage, G., "Influence of Overloads on the Subsequent Crack Growth of a Fatigue Crack in a E36 Steel," *Proceedings of the 4th European Conference on Fracture,* 1982, pp. 488–494.

[13] Bernard, P. J., Lindley, T. C., and Richards, C. E., "Mechanisms of Overload Retardation During Fatigue Crack Propagation," *Fatigue Crack Growth Under Spectrum Loads, ASTM STP 595,* American Society for Testing and Materials, West Conshohocken, PA, 1976, pp. 78–97.

[14] Brown, R. D. and Weertmann, J., "Effects of Tensile Overloads on Crack Closure and Crack Propagation Rates in 7050 Aluminum," *Engineering Fracture Mechanics,* Vol. 10, 1978, pp. 867–878.

[15] *First joint DoD/FAA/NASA Conference on Aging Aircraft,* Ogden, UT, 1997.

[16] *Aging of U.S. Air Force Aircraft,* Publication NMAB-488-2, National Academic Press, Washington, DC, 1997.

[17] Lang, M. and Huang, X., "The Influence of Compressive Loads on Fatigue Crack Propagation in Metals," *Fatigue & Fracture of Engineering Materials and Structures,* Vol. 21, No. 1, 1998, pp. 65–84.

[18] Lang, M., "Description of Load Interaction Effects by the ΔK_{eff}-Concept," *Advances in Fatigue Crack Closure Measurement and Analysis, ASTM STP 1343,* American Society for Testing and Materials, West Conshohocken, PA, in press.

[19] Lang, M. and Marci, G., "The Influence of Single and Multiple Overloads on Fatigue Crack Propagation," *Fatigue and Fracture of Engineering Materials and Structures,* Vol. 22, 1998, pp. 257–271.

[20] Lang, M. and Marci, G., "Reflecting on the Mechanical Driving Force of Fatigue Crack Propagation," *Fatigue and Fracture: 29th Volume, ASTM STP 1332,* T. L. Panontin and S. D. Sheppard, Eds., American Society for Testing and Materials, West Conshohocken, PA, 1997, pp. 474–495.

[21] Marci, G., "The Effects of the Plastic Wake Zone on the Conditions for Fatigue Crack Propagation," *International Journal of Fracture,* Vol. 16, No. 2, 1980, pp. 133–153.

[22] Westergaard, H. M., "Bearing Pressures and Cracks," *Transactions of ASME,* Vol. 61, ASME, New York, 1939, pp. A49–A53.

[23] Pellas, J., Baudin, G., and Roberts, M., "Fatigue Crack Growth Model Prediction with Two Coupled Differential Equations," *International Conference on Fracture,* Waterloo, Canada, Vol. 2, 19–24 June 1977, pp. 1353–1360.

[24] Marci, G., Castro, D. E., and Bachmann, V., "Closure Measurements Via a Generalized Threshold Concept," *Fracture Mechanics: Twenty-First Symposium, ASTM STP 1074,* American Society for Testing and Materials, West Conshohocken, PA, 1990, pp. 563–580.

[25] Marci, G., "Effect of the Active Plastic Zone on Fatigue Crack Growth Rates," *Fracture Mechanics, ASTM STP 677,* American Society for Testing and Materials, West Conshohocken, PA, 1979, pp. 168–186.

Hsing-Ling Wang[1] *and Alten F. Grandt, Jr.*[1]

Fatigue Analysis of Multiple Site Damage in Lap Joint Specimens

REFERENCE: Wang, H.-L. and Grandt, A. F., Jr., **"Fatigue Analysis of Multiple Site Damage in Lap Joint Specimens,"** *Fatigue and Fracture Mechanics: 30th Volume, ASTM STP 1360,* American Society for Testing and Materials, West Conshohocken, PA, 2000, pp. 214–226.

ABSTRACT: This paper describes research to determine the influence of multiple-site damage on the fatigue life of lap joint specimens. Multiple-site damage is an important concern in aging aircraft and deals with determining failure conditions for multiple crack configurations. The goal of this paper is to determine the fatigue life for a mechanically fastened joint with multiple fatigue cracks located along one row of rivet holes. A predictive model for the fatigue life is evaluated with the results of several pre-cracked specimens tested to failure under constant amplitude loading. Predictions for the growth and coalescence of individual cracks in specimens with various initial crack configurations and applied stress levels agree well with the experimental results.

KEYWORDS: lap joints, load transfer mechanism, hole expansion, rivets, multiple site damage, fatigue crack propagation, life prediction

The multiple site damage (MSD) issue [*1–7*] deals with assuring structural integrity after extended periods of service when many small cracks have formed at multiple locations. The MSD problem is of particular concern in lap joint structure where the many fastener holes provide likely locations for MSD to form, propagate, coalesce, and finally lead to catastrophic failure. Predicting failure involves complicated analysis of load transfer through the fasteners [*3,7–11*], residual stresses from rivet installation [*12*], interface contact [*7,8*], bending due to fuselage curvature [*13,14*], and biaxial loading [*15*]. One must also consider crack formation at the fastener holes [*15*], crack propagation, interaction between adjacent crack tips [*2–7,16*], and residual strength criteria to reach the final life prediction [*2–7*].

This paper demonstrates analysis procedures developed to evaluate MSD in single lap joint structure. The approach includes formulating a load transfer model that considers MSD in the lap joint, determination of stresses associated with rivet installation and bending, and computation of stress intensity factors. Residual strength and fatigue crack growth lives are then computed for the joint. The analysis procedure is experimentally evaluated with a set of fatigue tests. The particular experiments discussed here involve 2.29-mm-thick 2024-T3 aluminum sheets joined with three rows of eight 4.76-mm-diameter countersunk aluminum rivets. As discussed later, the rivets are installed with a force-controlled riveting process that results in 1.15% hole expansion. Five such specimens are pre-cracked along one row of holes to simulate MSD and then cycled to failure under constant amplitude loading. (Details of the precracking procedure are described in a later section.) A fracture mechanics analysis is then used to predict the growth, coalescence, and final fracture resulting from the initial MSD in the lap joint.

[1] Former graduate research assistant and professor, respectively, School of Aeronautics and Astronautics, 1282 Grissom Hall, Purdue University, West Lafayette, IN 47907-1282.

Analysis

This section briefly summarizes the procedure used to determine the stress intensity factors and subsequent fatigue life of a lap joint that contains MSD. Further details of the analysis procedure are given in Ref *7*.

Load Transfer Analysis for a Riveted Lap Joint

The analysis begins with an elastic load transfer solution proposed by Barrois [*17*] to determine the force applied by individual fasteners in a mechanical joint. There are two assumptions in this model. First, beam theory is used to determine the deformation of a rivet lying on elastic foundation, and, second, there is no interference or clearance between the rivet and the foundation contact surfaces. The load transferred by two adjacent rivets can be determined by considering displacement compatibility associated with changes in the dimensions δ and Λ shown in Fig. 1.

$$\delta_i - \delta_{i+1} = \Lambda_{ai} - \Lambda_{bi} \tag{1}$$

Two boundary conditions are used to account for two extremely different deflections on the contact surface between the rivet head and panels. One approach is to assume a perfectly clamped rivet head, and the other is to assume a pinned head that allows rotations at this location. These two boundary conditions induce different fastener flexibilities and result in different rivet load transfer ratios. The benefit of the Barrois analysis over other empirical load transfer models is that it provides an analytical method to extend load transfer calculations to more complicated structural geometries and different types of rivet heads (including countersinks). Several empirical load transfer solutions [*11*] for an uncracked lap joint are compared with the Barrios model in Fig. 2. This particular case is for a three-row, single-lap joint with equal sheet thicknesses and a rivet / panel stiffness ratio (E_{rivet}/E_{panel}) of 3. Note that all of the empirical load transfer ratios for this case are encompassed by the two extreme boundary conditions considered in the Barrois model. Load transfer experiments conducted with "neat fit" pins indicate that the Barrois model gives good results for the pinned end condition [*7*].

The relative displacement terms, δ_i, given in Eq 1 are based on an analytic solution for a beam on an elastic foundation and do not allow interference or clearance between the rivet and the elastic foundation contact surfaces. In reality, installation of practical countersink rivets involves interference fit during the rivet-squeezing process and creates plastic deformation that invalidates the elastic assumptions. In order to apply the Barrois analysis to the interference fit countersunk fasteners employed in the experimental program, the joint flexibility was determined experimentally with the setup described below.

Single-lap joint specimens with a single rivet (Fig. 3) were tested, and an extensometer (MTS Model 632.11B-20) was used to obtain the load-deflection curve across the joint. The relatively long (102-mm) gage length was selected to minimize bending effects in the single lap joint. Four different squeeze forces were used to install the rivets (17.80, 15.58, 13.35, and 11.13 KN) in order to determine the in-

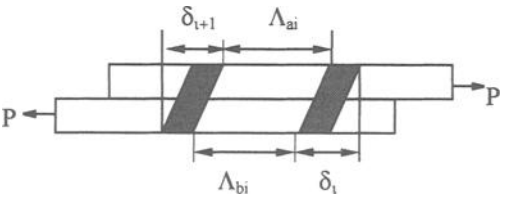

FIG. 1—*Displacement compatibility of two adjacent rivets.*

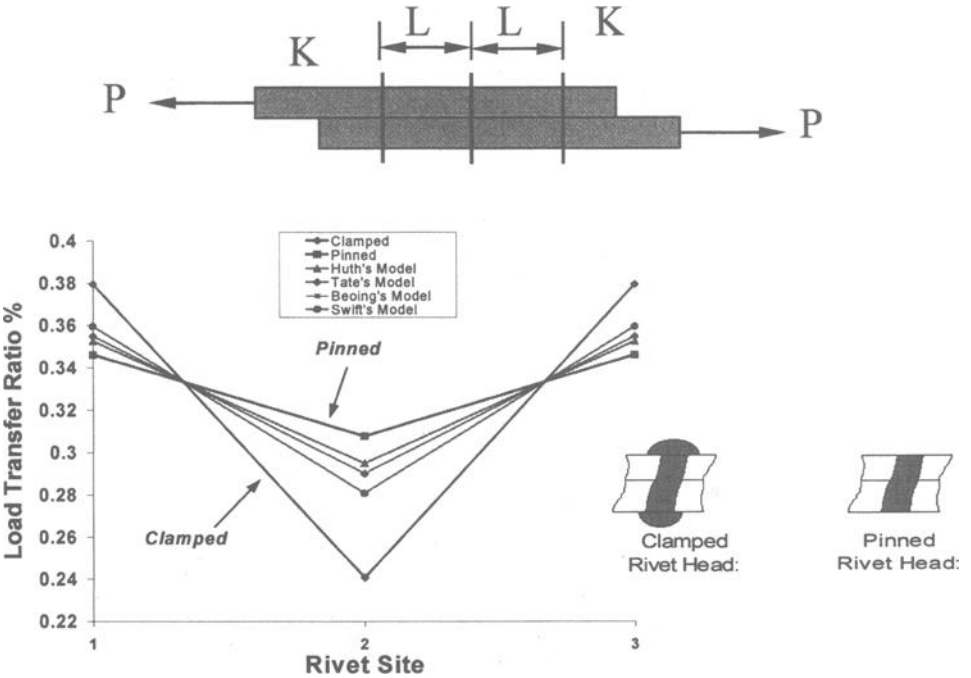

FIG. 2—*Load transfer ratio (elastic solution) and boundary conditions.*

fluence of fastener interference. (As discussed later, hole expansion was experimentally related to the rivet installation squeeze force.) In addition, the displacement was measured on both sides of replicate specimens (*front side* with countersunk head and *rear side* with driven head) to ensure that consistent behavior was obtained from the load-displacement tests. The specimens were loaded in tension in a 90-KN (20-kip) servo-hydraulic MTS test machine until the force-displacement curve slightly exceeded yield, and then the specimen was unloaded. The specimen was then reloaded and unloaded ten more times in the elastic regime. The average slope of the deflection-force curves is the joint flexibility and

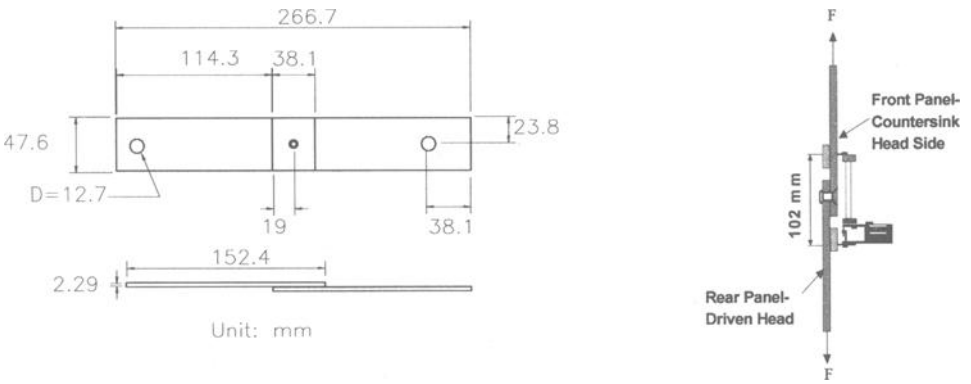

FIG. 3—*Setup for joint flexibility measurement.*

TABLE 1—*Joint flexibility versus deformed rivet head.*

Rivet Squeeze Force			
KN	Kip	D/D_0	Joint Flexibility (JF), mm/MN
17.80	4.0	1.186	54.39
15.58	3.5	1.257	53.94
13.35	3.0	1.321	52.80
11.13	2.5	1.386	58.11

is reported in Table 1 for the four-rivet squeeze forces. Note that joint flexibility initially decreases as the squeeze force is increased (and the lap faces are held more tightly together), resulting in a stiffer joint. The flexibility increases again, however, for large squeeze forces, indicating that there is an optimum value of squeeze force with respect to joint stiffness. Similar behavior has been reported in Ref *18*.

A parametric study for a three-row, countersunk, single-lap joint structure was conducted to determine the influence of squeeze force on load transfer. For higher rivet-squeezing forces, the plastic deformation becomes more severe and the joint flexibility is smaller (less flexible). It is, therefore, plausible that more load can be transferred from this "tighter" clamping condition. Figure 4 shows the load transfer ratios for rivet rows installed with different rivet squeeze forces. As shown by Case I, if rivets in all three rows are squeezed with the same force (15.58 KN = 3.5 kip), the top and the bottom rivet rows transfer the same load, while the middle row carries less force. Case II considers different squeeze forces for all three rows, with the top row installed with the largest force (15.58 KN = 3.5 kip) and the middle with the smallest force (11.13 KN = 2.5 kip). Note that in this example the load transfer ratio for the top row increases, while the middle row decreases. If, as in Case III, the middle row rivets are installed with the highest squeeze force and the top row has the lowest installation force, the changes in load transfer ratios are reversed from Case II.

Another load transfer issue is associated with the growth of cracks at various fastener holes. As these cracks grow, the structural compliance will increase (i.e., become less stiff), inducing additional displacement in the joint. This effect can cause load shedding from cracked to uncracked rows of riv-

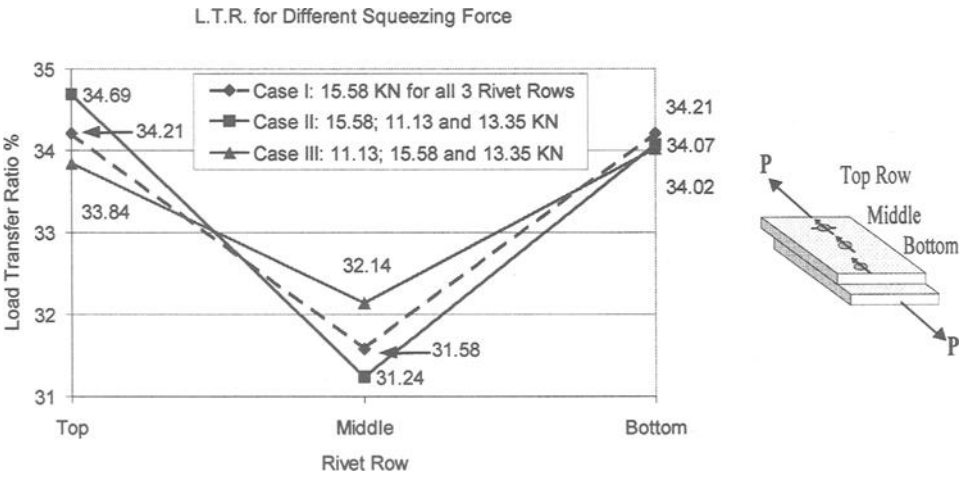

FIG. 4—*Load transfer ratio for a 3-row riveted joint.*

ets and change the load transfer mechanism. In order to analyze this load-shedding effect, the displacement compatibility given by Eq 1 can be rewritten as

$$\delta_i - \delta_{i+1} = \Lambda_{ai} - \Lambda_{bi} - \delta_{due\_to\_crack} \tag{2}$$

Here $\delta_{due\_to\_crack}$ is the product of the applied force P and the structural compliance C for the cracked member. The structural compliance is a function of the load transfer ratio, the stress intensity factor, and geometry [*4,7,19*]. The SIF solutions used here are from Ref *20* and employ the solutions for a plate with a row of through-cracked holes (case TCO5) and for a crack at an offset hole in a plate (Case TCO3). Reference *7* presents example results for the change in load transfer associated with crack growth and provides more details about the calculations.

Stress Intensity Factor for Interference Fit Rivets

Interference fit fasteners are often used to increase fatigue life since hole expansion produces residual stresses that delay fatigue crack formation and growth. As discussed later, interference fit can also affect the load transfer in a riveted joint. Two interference fit models proposed by Rich and Impellizzeri [*12*] and by Hsu and Forman [*21*] are used for this study. The major difference between the Rich-Impellizzeri and the Hsu-Forman stress analyses is that the former assumes elastic-perfectly plastic material behavior, while the latter applies work-hardening plasticity. Comparison of residual stresses predicted by these two models for various interference levels are given in Ref *7*.

Residual stresses created by the interference fit can reduce the effective hoop stress at the fastener hole and cause significant improvement in fatigue life. Cathey and Grandt [*22*] showed that stress intensity factors obtained by a relatively simple weight function method could be used to obtain reasonable fatigue crack growth lives for open, cold-worked holes in 7075-T6 aluminum specimens. The SIF K_R due to the residual stresses can be calculated from a tabulated weight function [*23*] if the uncracked stress distribution is known. The total SIF K_{tot} associated with load transfer and the interference-fit plasticity analysis of the riveted structure is given by superposition as

$$K_{tot} = K_{by\text{-}pass\ loading} + K_{pin\text{-}loading} \pm K_R \tag{3}$$

Here the $K_{by\text{-}pass\ loading}$ and the $K_{pin\text{-}loading}$ terms are the stress intensity factors from Ref *20* for the bypass and pin-loading cases and employ the load transfer analysis described previously. The $+/- K_R$ term in Eq 3 adds or subtracts the interference fit SIF depending on whether the residual stress field is tension or compression. Thus, when the interference fit results in compressive residual stresses, the SIF due to remote loading is reduced, and crack formation and propagation are delayed. Example calculations for these stress intensity factors are reported in Ref *7*.

An experimental program was conducted to determine the appropriate hole expansion for the installed rivets employed for the present work. Once the interference fit level is established, the plastic deformation and the compressive stress around the rivet hole can be estimated and stress intensity factors computed by Eq 3. A controlled squeeze force riveting procedure was employed here to ensure consistent quality of the riveted specimens [*18*]. Since inconsistent installation will affect the level of interference fit and corresponding stress field around the rivet holes, force-controlled riveting processes are commonly recommended for aviation manufacturing [*18,24–25*]. The current work employed a controlled squeeze-force rivet apparatus based on a 22-KN (5-kip) MTS testing system.

Hole expansion measurements were performed on the specimen shown in Fig. 5. Here three rows of 9 rivets were used to join two 2.29-mm (0.09-in.)-thick 2024-T3 aluminum sheets. The distance between holes and free edges was five times the 4.87-mm (0.192-in.) rivet diameter to avoid interaction during the riveting process. The countersunk rivets (100° flush head) were made from 2117 aluminum alloy, had a shank diameter D_0 = 4.76 mm (0.187 in.), and had the following identification

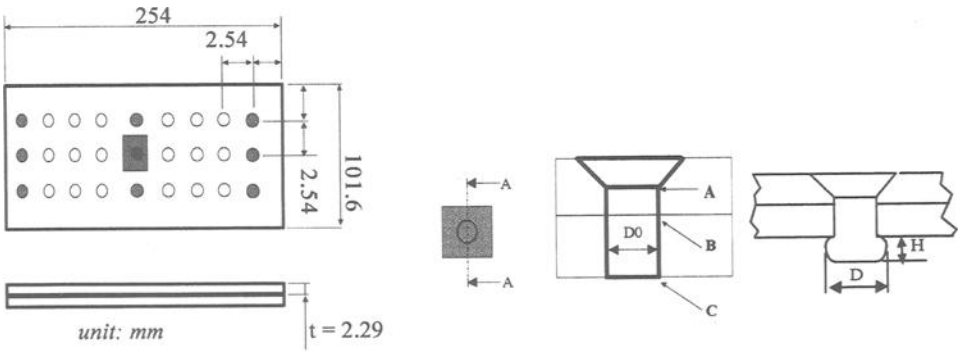

FIG. 5—*Specimen setup for hole expansion measurement (dimension in mm).*

number: MS20426-AD-6-6 [*25*]. Four different squeezing forces were examined (11.13, 13.35, 15.58, and 17.80 KN), with all 27 rivets in a given specimen installed with the same squeeze force.

Nine of the twenty-seven installed rivets were cut from each assembly, sectioned, carefully polished, and measured to determine the expansion diameters at three locations [*7*]. Table 2 and Fig. 6 give results for the average expansion D measured at the three locations shown in Fig. 5: A = the root of countersink head, B = the interference between two plates, and C = driven head. Note that the expansion level increases with the applied rivet squeeze force.

Secondary Bending Effect

Secondary bending considerations also play a role for SIF calculations in single-lap joint specimens. A bending stress calculation proposed by Schijve [*26*] is given by Eq 4 in the form of an estimated bending ratio k.

$$k = \frac{\sigma_{bend}}{\sigma_{remote}} = \frac{6}{t_1} \times \frac{e - T_2 \dfrac{\beta}{\alpha_2}}{1 + \dfrac{\alpha_1}{\alpha_2}\dfrac{T_2}{T_1}} \tag{4}$$

Here, as shown in Fig. 7,

t_1 = plate thickness, mm,
e = eccentricity of two jointed plates,
β = rivet rotational angle,
P = Remote load, KN,

TABLE 2—*Deformed rivet diameter and height versus squeezing force.*

Squeezing Force						
KN	Kip	D, mm	Standard Development, mm	D/D_0	H, mm	Standard Development, mm
17.80	4.0	6.6	0.00127	1.386	2.48	0.00194
15.58	3.5	6.29	0.00141	1.321	2.69	0.00199
13.35	3.0	5.99	0.00153	1.257	3.00	0.00248
11.13	2.5	5.65	0.00115	1.186	3.33	0.00278

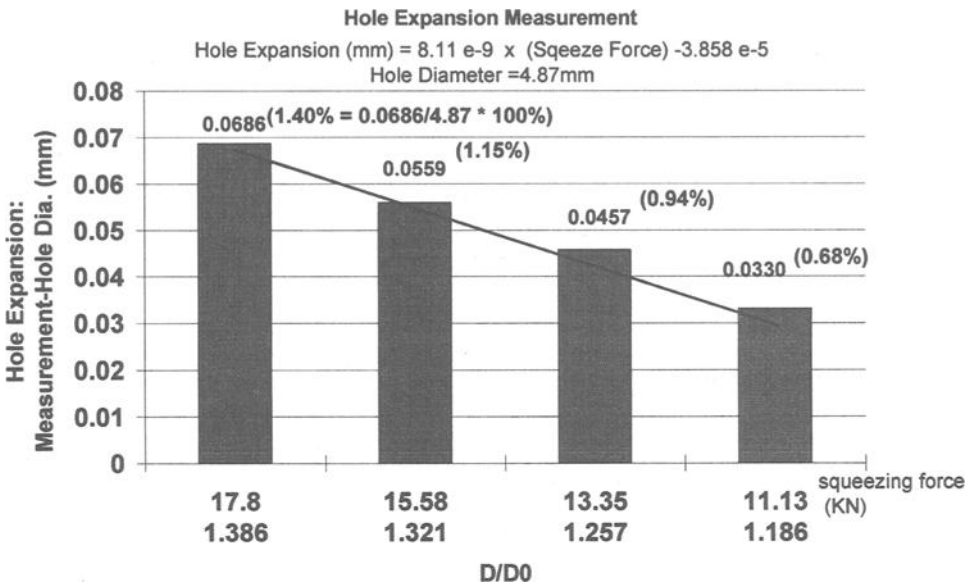

FIG. 6—*Hole expansion measurements as a function of rivet squeeze force.*

E_i, I_i = Young's modulus and moment of inertia of i^{th} plate,
$\alpha_i = P/(E_i I_i)$,
L_i = the distance between the rivet to the boundary or the spacing between the rivets, mm, and
$T_i = \text{Tanh}(\alpha_i L_i)$.

With the aid of Eq 4, the bending stress σ_{bend} can be calculated, and the SIF due to secondary bending can be estimated by the following equations [*14*].

$$K_{bend} = \beta_{ben} k \sigma_{remote} \sqrt{\pi a_{eff}}$$
$$\beta_{ben} = 0.39 \times \left(1.0 + 0.16 \left(\frac{a_{eff}}{W_{eff}}\right)^2\right) \text{ with } v = 0.3 \tag{5}$$

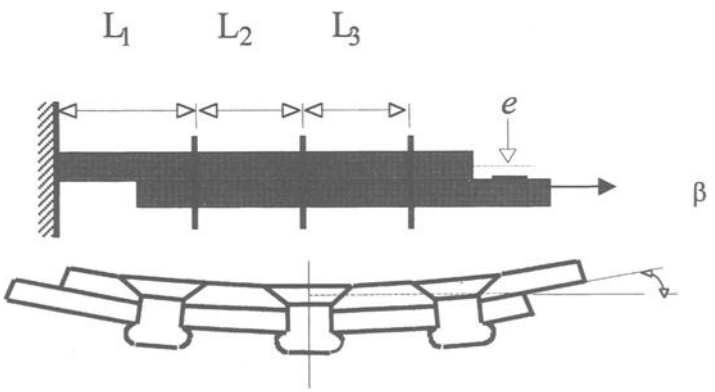

FIG. 7—*Schematic representation of the secondary bending (rivet rotation) model.*

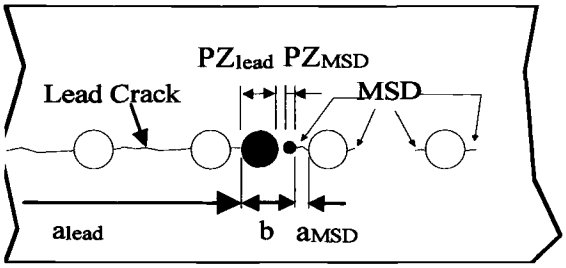

FIG. 8—*Schematic of the ligament yield criterion proposed by T. Swift [1].*

Here W_{eff} is the hole spacing and $2a_{eff}$ is an effective crack length that includes the hole diameter and radial crack lengths. Rewriting Eq 3, the total SIF for a single lap joint specimen is:

$$K_{tot} = K_{by\text{-}pass\ loading} + K_{pin\text{-}loading} \pm K_R + K_{bend} \tag{6}$$

Failure Criteria

While several failure criteria have been proposed for the MSD problem, this research employs the net section yield and Swift's ligament yield criteria [*1*]. The net section yield criterion states that failure will occur when the failure load P_{Cnet} causes the net section stress to equal or exceed the tensile yield stress (σ_{ys}). This condition may be expressed as follows:

$$\begin{aligned} P_{Cnet} &= \sigma_{ys}\,(W - nD - n_{MSD}a_{avg} - 2a_{lead})t \\ &= \sigma_{ys}W_{net}t \end{aligned} \tag{7}$$

Here W is the panel width, n is the total number of rivet holes, D is the average rivet hole diameter, n_{MSD} is the number of MSD cracks, a_{avg} is the average crack length, a_L is the half-crack length of the central lead crack, and t is the panel thickness.

The Swift ligament yield failure criterion [*1*] states that the failure occurs when the plastic zones of two approaching crack tips "touch" each other as shown schematically in Fig. 8. This failure load, P_{CLY}, is given by Eq 8.

$$P_{CLY} = \sigma_{ys}tW_{net}\left[\frac{2b}{(a_{MSD}\beta_h^2\beta_{iMSD}^2 + a_{lead}\beta_{ilead}^2)}\right] \tag{8}$$

In Eq 8, W_{net} is the net width of the specimen, defined in Eq 7, a_{MSD} and a_{lead} are the two approaching MSD and lead crack lengths, β_{ilead} and β_{iMSD} are the Kamei-Yokobori [*16*] interaction factor for two approaching cracks, β_h is the TC05 SIF solution [*20*], and b is the crack tip separation shown in Fig. 8.

Fatigue Tests of Lap Joint Specimens and Life Predictions

Five lap joint fatigue tests were conducted to evaluate the ability to predict the growth and coalescence of MSD cracks. The single lap specimens were joined by three rows of eight countersunk rivets as shown in Fig. 9. All specimens were precracked along the top rivet row where experience (and the load transfer model) indicates that the most severe cracking occurs. The specimens were then

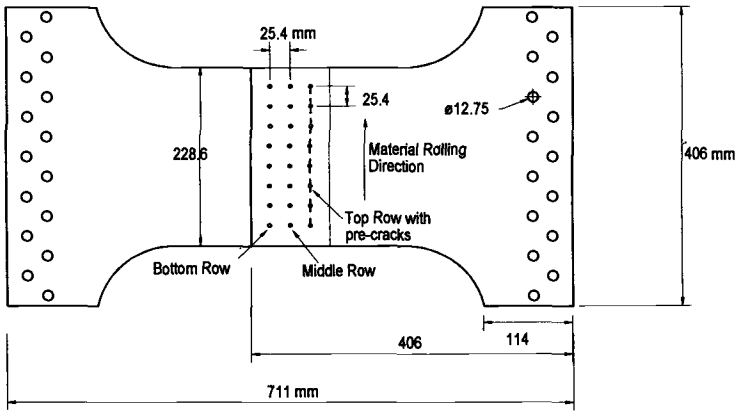

FIG. 9—*Schematic of single lap joint specimen.*

tested under constant amplitude loading, and the growth, coalescence, and final fracture resulting from individual cracks were recorded and compared with the numerical analysis.

All specimens were made from 2.29-mm (0.09-in.)-thick 2024-T3 bare aluminum alloy loaded in the T-L rolling direction. Specimen preparation consisted of two steps. First, 812-mm long by 406-mm (32 by 16-in.)-wide panels were constructed with a "dogbone" test section that was 228.6 mm (9 in.) wide. A single row of eight 3.97-mm ($^5/_{32}$-in.)-diameter holes were then drilled in these specimens, and a jeweler's saw (blade thickness = 0.33 mm = 0.013 in.) was used to cut a pair of small notches on the opposite sides of each hole (average length = 0.381 mm = 0.015 in.). The two outside holes were not notched, however, since it is known that more load is taken by rivets located near free edges than by other rivets in wide lap joint specimens [*18,27*], and it was desired to prevent premature failure at those locations. The panels were then cyclically loaded to develop cracks at the saw cuts. This precracking was conducted at a frequency of 5 Hz and employed a load-shedding procedure that ended when the SIF for the longest crack tip reached 6.6 MPa$\sqrt{\text{m}}$ (6 ksi$\sqrt{\text{in.}}$). The lengths of these cyclic MSD cracks ranged from 4.57 mm (0.18 in.) to zero (including the saw cut).

The next step was to cut each panel in half, leaving one member of each pair with the precracked row of holes. These two halves were then drilled to the desired 8 × 3 rivet hole pattern, reamed to a final hole diameter of 4.85 mm (0.191 in.), and countersunk on one side. This final drill and ream removed the initial saw cuts, leaving only small fatigue cracks in one panel at the initial row of holes. Finally, 4.76-mm (0.187-in.)-diameter countersunk rivets (MS20426-AD-6-6) were installed with a fixed 15.58-KN (3.5-kip) squeeze force. Since the specimens were riveted after precracking, some of the shorter cracks were contained within the residual stress field formed during the rivet crimping procedure. In addition, portions of some cracks were removed by the countersinking, leaving an internal crack that was hidden from view by the rivet head. The average radial precracks were typically on the order of 0.34 to 1.12 mm (0.0134 to 0.044 in.) long and emanated from both sides of the countersunk rivet holes. The average MSD precrack lengths and the applied fatigue loads are summarized in Table 3 for the five experiments reported here.

Comparison of Analysis and Experiment

Cyclic extension of all MSD cracks resulting from the $R = 0.05$ constant amplitude fatigue loading were measured by means of a traveling microscope and were recorded as a function of elapsed cycles. Fatigue crack growth lives were then computed by a fracture mechanics-based algorithm that incrementally grows individual cracks based on their current stress intensity factor and the fatigue

TABLE 3—*Summary of specimen initial conditions and failure data.*

Test Specimen ID	Avg. Crack Length, mm	Max Applied Stress KN	Max Applied Stress ksi	Total Life/ Prediction Life, Cycles	Delayed Cycles	Difference, %
Slap 1	0.98	55.1	8	99 143/126 281	56 000	27.4%
Slap 2	1.00	96.5	14	9028/7801	0	13.6%
Slap 3	0.34	68.9	10	50 489/42 629	10 000	15.6%
Slap 4	1.12	55.1	8	97 655/109 266	40 000	11.9%
Slap 5	0.82	55.1	8	160 024 /147 350	70 000	8.0%

crack growth rate behavior for the test materials (see Ref *7* for the fatigue crack growth properties of the 2024-T3 material tested here). The initial growth, coalescence, and final fracture is predicted in this manner, and the algorithm has been quite successful in predicting fatigue lives for other MSD specimens that contain open holes in stiffened and unstiffened panels [*2,4–6*]. The predictive algorithm was modified in the present case to include the stress intensity factor and load transfer solutions described previously for the lap joint configuration. Since the current life prediction model is based on through-cracked stress intensity factor solutions and does not consider three-dimensional effects associated with part-through cracks or the countersink, the average hole diameter and through-crack length were used as input for the MSD life prediction program.

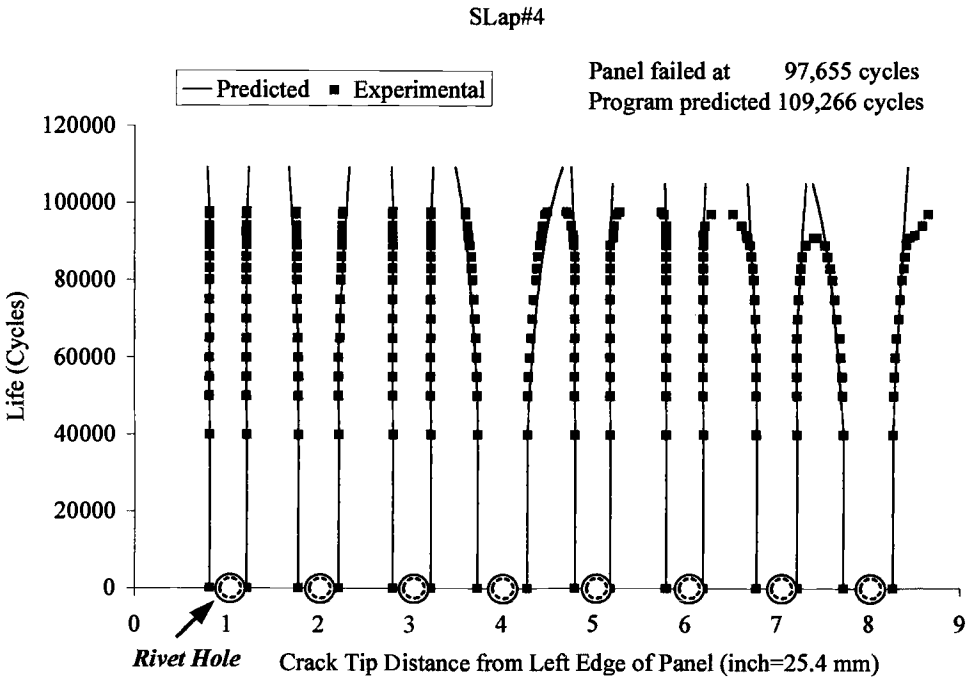

FIG. 10—*Comparison of experimental and predicted fatigue crack propagation for a single lap joint specimen SLap 4 (3 rows of 8 rivets) tested at a cyclic stress level of 55.1 MPa (8 ksi) (the size of rivet hole is not to scale).*

As mentioned previously, some of the small precracks were hidden under the rivet heads or contained in the plastic zone around the installed rivet and did not immediately grow, resulting in a period of "crack retardation." (The measured delay cycles are listed in Table 3.) Note that specimen SLap 5 exhibited significant delay, and the observed fatigue crack growth period is relatively long compared to SLaps 1 and 4, which were also tested at the same 55.1-MPa (8-ksi) cyclic stress level (note, however, that the average MSD size was smaller for this specimen). Since the algorithm assumes MSD cracks at all hole locations, and a few of the smaller precracks were removed following the final ream and countersink, it was decided to assume a small 0.127-mm (0.005-in.) crack length at those locations. Figure 10 plots crack tip position versus elapsed cycles for SLap 4 (see Ref 7 for similar plots for the other specimens), and Fig. 11 summarizes the measured and predicted fatigue crack growth lives for all five lap joint tests. The average difference between the measured and predicted lives for these five fatigue tests is 15%, varying between 8.0 and 27.4%.

As indicated previously, the initial fatigue crack growth was "retarded" by two mechanisms—the clamping pressure between the cracked plates and plasticity-induced compressive stress around the rivet holes. If the crack lengths are long enough, or the applied remote stress is large enough, the cracks will propagate immediately upon applied cyclic loading, and the life prediction agrees well with the experimental results. Specimen SLap 2, for example, contained relatively short precracks, but was tested to the largest applied cyclic stress (96.5 MPa = 14 ksi), and the cracks began growing immediately without a delay period. The predicted and measured lives agreed within 14% for this case. In the other tests, it was necessary to start computations after the cracks were observed to begin growing in the fatigue test in order to obtain a reasonable fatigue life. The experimental data do indicate, however, that it is possible to obtain excellent life predictions once the cracks have started to grow. Thus, the load transfer analysis and stress intensity factor solutions developed for the lap joint problem give reasonable crack growth lives when the crack retardation effect is experimentally ac-

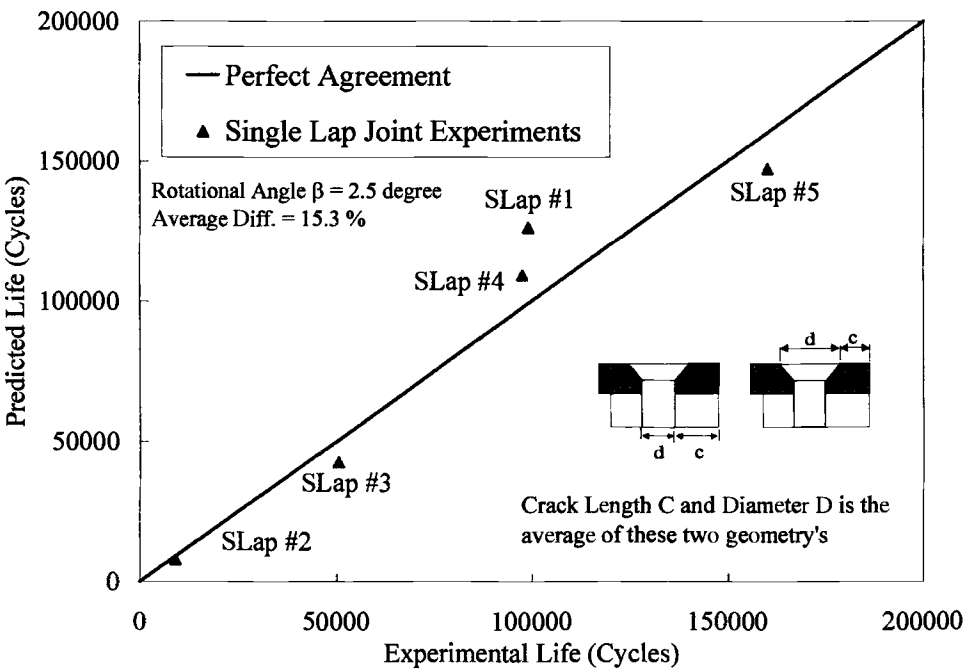

FIG. 11—*Measured and predicted fatigue panel failure lives for tests.*

counted for. Continuing research is focusing on developing techniques to predict the delay period for analysis purposes.

References

[1] Swift, T., "Widespread Fatigue Damage Monitoring Issues and Concern," *The 5th International Conference on Structural Airworthiness of New and Aging Aircraft,* Hamburg, Germany, 16–18 June 1993.

[2] Moukawsher, E. J., Grandt, A. F., Jr., and Neussl, M. A., "Fatigue Life of Panels with Multiple Site Damage," *Journal of Aircraft,* Vol. 33, No. 5, September-October 1996, pp. 1003–1013.

[3] Wang, H. L., Buhler, K., and Grandt, A. F., Jr., "Evaluation of Multiple Site Damage in Lap Joint Specimens," *Proceedings of the 1995 USAF Structural Integrity Program Conference,* ASIP, Vol. 1, August 1996, pp. 21–38.

[4] Heinimann, M. B. and Grandt, A. F., Jr., "Analysis of Stiffened Panel with Multiple Site Damage," *Proceedings of the 1996 USAF Structural Integrity Program Conference,* San Antonio, TX, 3–5 Dec. 1996.

[5] Grandt, A. F., Jr., Sexton, D. G., Golden, P. J., Bray, G. H., Bucci, R. J., and Kulak, M., "A Comparison of 2024-T3 and 2524-T3 Aluminum Alloys under Multi-Site Damage Scenarios," *ICAF 97 Fatigue in New and Aging Aircraft,* Vol. II, Poster Papers, R. Cook, and P. Poole, Eds., *Proceedings of the 19th ICAF Symposium, International Committee on Aeronautical Fatigue,* 18–20 June 1997, Edinburgh, Scotland, pp. 659–669.

[6] Heinimann, M. B. and Grandt, A. F., Jr., "Fatigue Analysis of Stiffened Panels with Multiple Site Damage," *First Joint DoD/FAA/NASA Conference on Aging Aircraft,* Ogden, Utah, 8–10 July 1997.

[7] Wang, H. L., "Evaluation of Multiple Site Damage in Lap Joint Specimens," Ph.D. thesis, School of Aeronautics and Astronautics, Purdue University, West Lafayette, IN, December 1998.

[8] Beuth, J. L. and Hutchinson, J. W., "Fracture Analysis of Multiple Site Cracking in Fuselage Lap Joints," *Durability of Metal Aircraft Structures, Proceedings, International Workshop on Structural Integrity of Aging Airplane,* Atlanta, GA, 31 March-2 April 1992, Atlanta Technology Publications, 1992.

[9] Beuth, J. L. and Hutchinson, J. W., "Fracture Analysis of Multi-Site Cracking in Fuselage Lap Joints," *Computational Mechanics,* Vol. 13, 1994, pp. 315–331.

[10] Lee, E. U., "Effect of Load Transfer on Fatigue of Mechanically Fastened Metallic Joints," *Fatigue in Mechanically Fastened Composite and Metallic Joints, ASTM STP 927,* Philadelphia, 1986, pp. 95–117.

[11] Huth, H., "Influence of Fastener Flexibility on the Prediction of Load Transfer and Fatigue Life for Multiple-Row Joints," *Fatigue in Mechanically Fastened Composite and Metallic Joints, ASTM STP 927,* Philadelphia, 1986, pp. 221–250.

[12] Rich, D. L. and Impellizzeri, L. F., "Fatigue Analysis of Cold-Worked and Interference Fit Fastener Holes," *Cyclic Stress-Strain and Plastic Deformation Aspects of Fatigue Crack Growth, ASTM STP 637,* ASTM, Philadelphia, 1977, pp. 153–175.

[13] Singh, R., Park, J. H., and Atluri, S. N., "Growth of Multiple Cracks and Their Linkup in a Fuselage Lap Joint," *AIAA Journal,* Vol. 32, No. 11, November 1994, pp. 2261–2268.

[14] Sampath, S. and Broek, D., "Estimation of Requirements of Inspection Intervals for Panels Susceptible to Multiple Site Damage," *Structural Integrity of Aging Airplanes,* Springer-Verlag, Berlin, Heidelberg, 1991, pp. 339–389.

[15] Vleiger, H., "Results of Uniaxial and Biaxial Tests on Riveted Fuselage Lap Joint Specimens," *FAA/NASA International Symposium on Advanced Structural Integrity Methods for Airframe Durability and Damage Tolerance,* 4–6 May 1994, Hampton, VA.

[16] Kamei, A. and Yokobori, T., "Two Collinear Asymmetrical Elastic Cracks," Report of the Research Institute for Strength and Fracture of Materials, Tohoku University, Vol. 10, Section 1–4, December 1974, pp. 41–42.

[17] Barrois, W., "Stress and Displacements Due to Load Transfer by Fasteners in Structural Assemblies," *Engineering Fracture Mechanics,* 1978, Vol. 10, pp. 115–176.

[18] Muller, R. P. G., "An Experimental and Analytical Investigation on the Fatigue Behavior of Fuselage Riveted Lap Joints—The Significant of the Rivet Squeeze Force and a Comparison of 2024-T3 and Glare 3," Ph.D. dissertation, Delft University of Technology, Faculty of Aerospace Engineering Structures and Materials Laboratory, The Netherlands.

[19] Grandt, A. F., Jr. and Sinclair, G. M., "Stress Intensity Factors for Surface Cracks in Bending," *Stress Analysis and Growth of Cracks, Proceedings of the 1971 National Symposium on Fracture Mechanics, Part I, ASTM STP 513,* Philadelphia, 1972, pp. 37–58.

[20] Fatigue Crack Growth Computer Program "NASA/FLAGRO" Version 2.0, Appendix C, December 1992.

[21] Hsu, Y. C. and Forman, R. G., "Elastic-Plastic Analysis of an Infinite Sheet Having a Circular Hole Under Pressure," *Journal of Applied Mechanics,* June 1975, pp. 347–352.

[22] Cathey, W. H. and Grandt, A. F., Jr., "Fracture Mechanics Consideration of Residual Stresses Introduced by Coldworking Fastener Holes," *Journal of Engineering Materials and Technology,* January 1980, Vol. 102, pp. 85–91.

[23] Kullgren, T. E. and Grandt, A. F., Jr., "Tabulated Stress Intensity Factor Solutions for Flawed Fastener Holes," *Engineering Fracture Mechanics,* Vol. 18, No. 2, 1983, pp. 435–451.

[24] *Standard Aircraft Handbook,* 5th ed., L. Reithmaier, Ed., originally compiled and edited by S. Leavell and S. Bungay, TAB /AERO, Division of McGraw-Hill, Inc., Blue Ridge Summit, PA.

[25] *Military Handbook, Metallic Materials and Elements for Aerospace Vehicle Structures,* MIL-HDBK-5G, 1 Nov. 1994.

[26] Schijve, J., "Some Elementary Calculations on Secondary Bending in Simple Lap Joints," NLR TR 72036 U, 1972.

[27] Newman, J. C., Jr., Harris, C. E., James M. A., and Shivakumar, K. N., "Fatigue-Life Prediction of Riveted Lap-Splice Joints Using Small-Crack Theory," *ICAF 97 Fatigue in New and Aging Aircraft,* Vol. I, Poster Papers, R. Cook, and P. Poole, Eds., *Proceedings of the 19th ICAF Symposium, International Committee on Aeronautical Fatigue*, 18–20 June 1997, Edinburgh, Scotland, pp. 523–552.

John D. Dougherty,[1] *T. S. Srivatsan,*[2] *and J. Padovan*[3]

A Combined Experimental and Finite Element Study of Crack Closure Effects in Modified 1070 Steel

REFERENCE: Dougherty, J. D., Srivatsan, T. S., and Padovan, J., **"A Combined Experimental and Finite Element Study of Crack Closure Effects in Modified 1070 Steel,"** *Fatigue and Fracture Mechanics: 30th Volume, ASTM STP 1360,* American Society for Testing and Materials, West Conshohocken, PA, 1998, pp. 227–239.

ABSTRACT: The significance and even the existence of crack closure is being questioned by several researchers. The objective of this study was to determine if crack closure occurs and to quantify its significance. An approach combining experimental measurement techniques with finite element analysis techniques was utilized. For two values of compact tension specimen thickness, a series of tests were conducted to determine the effect of maximum stress intensity, load ratio, constraint, and single tensile overload on the crack closure and fatigue crack growth behavior of a modified 1070 steel. Test results indicated that constraint has a significant influence on crack closure and crack growth rate behavior. Thin specimens exhibited consistently lower crack growth rates and higher crack closure levels than the thick specimens, except for tests conducted at a high load ratio, where crack closure did not occur. The thin specimens also exhibited a more significant overload effect. A new finite element modeling technique, which uses substructuring techniques to model the load cycling and crack propagation of an entire compact tension specimen, was developed. Comparison of stationary crack and propagating crack finite element models revealed that plasticity-induced crack closure produces a significant amount of crack tip shielding, which effectively reduces the strain range and mean strain experienced at the crack tip.

KEYWORDS: crack propagation, crack closure, finite element model, substructuring, crack tip shielding, strain range, mean strain, overload effects

The phenomenon of crack closure has been intensely studied for over two decades. Most researchers have addressed the problem either purely experimentally, through a variety of measurement techniques, or purely numerically, through finite element techniques or analytical approaches. There have been very few studies that have attempted to combine experimental and numerical techniques into a more comprehensive investigation of crack closure. This study was initiated to help fill this void in fracture mechanics research. The objective of this study was to determine if crack closure occurs and to quantify its significance.

Traditional means of experimentally measuring crack closure, such as the crack mouth opening displacement (CMOD) and the back face strain gage (BFSG) methods, are relatively insensitive, resulting in difficulty extracting the crack closure and opening loads from the load versus deflection (or strain) data. More recently, surface strain gage (SSG) techniques have been developed that are more sensitive to crack closure, but only when the strain gage is a small distance from the crack tip. Sur-

[1] Product development specialist, Timken Research, The Timken Company, Mail Code RES-09, 1835 Dueber Ave., S. W., P.O. Box 6930, Canton, OH 44706.
[2] Department of Mechanical Engineering, The University of Akron, Akron, OH 44325
[3] Department of Mechanical and Polymer Engineering, The University of Akron, Akron, OH 44325.

face strain gages need to be located outside of the crack tip plastic zone to avoid a nonlinearity in stress-strain behavior overshadowing the nonlinearity due to crack closure. A new combined surface strain gage technique, called the SSGC method, was developed to overcome the above limitations. A series of surface strain gages are mounted on the compact tension (CT) specimen at a vertical location outside of the plastic zone created by the advancing crack tip. Combining the output of this series of strain gages enables relatively sensitive measurement of crack closure and opening loads over a wide range of crack lengths.

The application of finite element (FE) methods for modeling plasticity-induced crack closure requires solution of a nonlinear material problem with contact. A fine mesh is needed to accurately depict the material behavior near the crack tip, and small crack extensions must be used to adequately model crack propagation. Computational limitations result in most researchers simplifying the model to a small region near the crack tip, with approximated boundary conditions being applied to simulate the behavior of the entire structure. For this study, a new 2-D FE method was developed that utilizes substructuring techniques to reduce the number of degrees of freedom required in the elastic-plastic contact solution, while accurately modeling the stiffness and behavior of the entire structure. FE models of entire CT specimen experiments, including precracking, were performed to provide direct comparisons with experimentally measured values of displacement, strain, and crack closure and opening loads.

The Crack Closure Controversy

Crack closure reduces the amount of the applied stress intensity range (ΔK) that is experienced by the crack tip, resulting in a reduction in crack growth rate. Crack closure was discovered by Elber [*1*], who attributed the phenomenon to the mechanism of plasticity-induced crack closure. Other closure mechanisms have been introduced by various researchers. Oxide-induced and surface-roughness-induced crack closure mechanisms were introduced by Ritchie and Suresh [*2*]. Viscosity-induced and phase-transformation-induced crack closure mechanisms were introduced by McEvily [*3*].

Experimental studies have identified and quantified the impact of several of these crack closure mechanisms. The level of closure has also been shown to be affected by intrinsic microstructural effects, specimen geometry, crack geometry, loading conditions, and environmental conditions. For the sake of brevity, the interested reader is referred to the following papers, which cover various aspects of crack closure in detail.

1. Mechanisms of crack closure—McEvily [*3*].
2. Significance of crack closure near threshold—Liaw [*4*].
3. Crack closure measurement techniques—Schijve [*5*].
4. Results of experimental studies—Dougherty, Srivatsan, and Padovan [*6*].
5. Application of FE methods—Dougherty, Srivatsan, and Padovan [*7*].

Recently, the significance and even the existence of crack closure has been the subject of much debate. The significance of plasticity-induced crack closure, except for cases of overload, was questioned by McEvily [*3*], who based his view on the testing of specimens with different thickness not having shown significant changes in crack growth rates. Due to the thickness effect (plane strain versus plane stress) on plastic zone size, slower crack growth rates would be anticipated for the thin specimens, which have larger plastic zone sizes and thus should experience more plasticity-induced crack closure. For overload cases where predominantly plane strain conditions prevail, Suresh [*8*] further questioned the significance of plasticity-induced crack closure due to the reduced plastic zone size associated with plane strain. Vasudevan, Sadananda, and Louat [*9*] went as far as to suggest that plasticity-induced crack closure does not occur at all unless aided by oxide formation.

Finite Element Model

A new finite element modeling technique for simulating plasticity-induced crack closure was developed that utilized substructuring techniques to enable modeling an entire CT specimen in a computationally efficient manner. The finite element code used in this study is the commercially available general purpose FE code called ABAQUS, which is a product of Hibbitt, Karlsson, and Sorensen. The pre- and post-processing package used to create the FE mesh and process the model results is the commercially available software program called FAM, which is a product of FEGS, Limited. A detailed study of the impact of mesh density, crack advance scheme, crack closure modeling method, element type, and crack plane element aspect ratio was conducted. Details of the development of this new FE technique are available elsewhere [7]; therefore, only a brief summary will be presented here.

A new crack plane spring modeling method was developed that utilizes a constant element edge stiffness approach as opposed to a lumped nodal stiffness approach. For each element along the crack plane, a constant stiffness per unit area was selected. This element edge stiffness was divided up among the nodes along the element edge based on the element edge area associated with each node. For each node along the crack plane: (a) tension-only springs are used to restrain nodes, at and ahead of the crack tip, from moving away from the crack plane during loading, and (b) compression-only springs are used to prevent overclosure along the crack plane during unloading. Crack advance is achieved by eliminating all of the tension-only springs attached to the element edge being released and reducing the spring forces to zero. This is done at constant load so the redistribution of stresses and strains are accurately represented. Utilizing this crack advance scheme results in each load cycle consisting of three steps.

1. Loading up to maximum load.
2. Advancing the crack at maximum load.
3. Unloading from maximum load to minimum load.

The mesh refinement and element aspect ratio studies were performed to assure that the mesh used in the CT specimen FE models would appropriately capture the plasticity behavior of the advancing crack tip. A study of the impact of element type was conducted using four-node bilinear (Q4) and eight-node biquadratic (Q8) elements. The Q4 element type was selected because the displacement functions used for the Q8 element results in the element stiffness not being uniform along the element edge, which resulted in a nonuniform residual stress pattern in the wake of the advancing crack. Comparison of analyses conducted using 2-D plane strain and 2-D plane stress formulations revealed that crack closure occurred in both cases. The 2-D plane stress formulation was selected for use in the CT specimen FE models because it resulted in K_{cl} values that were in much closer agreement with experimentally measured values.

The material model selected for the FE model was a rate-independent isotropic hardening plasticity model. The Von Mises yield criterion was used, with the normality principle being used to define the expansion of the yield surface. Comparison of FE model results of analyses conducted using isotropic and kinematic hardening plasticity models revealed that the isotropic hardening model matched the experimental data more closely. The kinematic hardening plasticity model resulted in large differences between K_{cl} and K_{op} values, while experimentally measured K_{cl} and K_{op} values were nearly identical. Cyclic stress-strain tests revealed that the steady-state response of this material was indicative of isotropic hardening behavior. The stress-strain material behavior, used in the FE model, was based on a combination of the monotonic and cyclic stress-strain curves. For low strains (up to 0.0175), the stress-strain behavior was approximated from the cyclic stress-strain curve. For strains above cyclic stress-strain data points, the stress-strain behavior was approximated using the monotonic stress-strain curve.

Compact Tension Specimen FE Model

The CT specimen was split into a near field crack tip region, which must be included in the main model, and a far field region, which can be accurately represented by a super element. The near field crack tip region is where the material behavior such as elastic-plastic, nonlinear elements such as tension-only and compression-only springs are utilized, and crack advance is modeled by elimination of tension-only springs. The far field region exhibits purely elastic material behavior; therefore, a super element can be created that accurately depicts the linear stiffness behavior of the entire far field region. A super element is constructed by forward eliminating the global stiffness matrix down to a reduced stiffness matrix associated with only the degrees of freedom corresponding to the retained nodes of the super element. The retained nodes were as follows.

1. All nodes which connect to the main model.
2. All nodes along the loading pin hole that come into contact with the loading pin.
3. All nodes associated with the locations of the CMOD, BFSG, and SSGC gages.

The boundary condition, used for the super element, was that all nodes along the crack plane were constrained from moving normal to the crack plane. The boundary conditions used for the main model were as follows: (a) the node located at the top dead center of the loading pin hole was constrained to move only normal to the crack plane, and (b) the tension-only and compression-only springs along the crack plane were between a crack plane node and a fixed node.

The cyclic loading of the CT specimen was accomplished by performing Hertzian contact analyses of the loading pin/hole interaction [7]. The total load used in the Hertzian contact model was obtained using the CT specimen relationship between load and stress intensity (see Eq 1).

$$K = \frac{P}{B \cdot W^{1/2}} \cdot \frac{(2 + \alpha)}{(1 - \alpha)^{3/2}} \cdot (0.886 + 4.64 \cdot \alpha - 13.32 \cdot \alpha^2 + 14.72 \cdot \alpha^3 - 5.6 \cdot \alpha^4) \quad (1)$$

where

K = applied stress intensity,
P = applied load,
B = specimen thickness,
α = (a/W) crack length ratio,
W = specimen width, and
a = crack length.

The results of these contact analyses provided the nodal forces that were applied to the upper portion of the loading pin hole in the main model. A FORTRAN computer program was written to perform the above calculations and automatically write all of the ABAQUS loading step input data required to cycle the loads and propagate the crack for an entire test simulation.

Material and Specimen Processing

The material selected for this investigation was modified 1070 steel, denoted as 1070M. The chemical composition of this steel, in weight percent, is presented in Table 1. All specimens were machined from hot-forged blanks. Forging preforms were machined from 63.5-mm-diameter hot-rolled solid rounds, heated to 1218°C, hot forged to a 50% reduction in height, and then air cooled to ambient temperature. These hot forgings were then subjected to a quench and temper process consisting of: (a) heating to 843°C for 1 h, (b) quenching in oil, and (c) tempering at 709°C for 3 h. The above processing resulted in a fine-grained tempered martensitic microstructure with slight spheroidization of the carbides

TABLE 1—*Chemical composition of the 1070M steel.*

C	Mn	P	S	Si	Cr	Ni	Mo	Cu	Al	Sn	Ti	Fe
0.680	0.950	0.009	0.022	0.170	0.130	0.110	0.050	0.190	0.035	0.009	0.001	Balance

present in the microstructure. X-ray diffraction measurements revealed that the microstructure contained a negligible amount of retained austenite. The grain size ranged from 0.011 to 0.022 mm, and the resulting hardness ranged from 96 to 98 HRB. The CT specimens were machined such that the crack plane was perpendicular to the rolling direction. All material property specimens were machined accordingly to evaluate the material behavior perpendicular to the crack plane of the CT specimens.

For this material, the monotonic tension test properties, cyclic stress-strain behavior, low-cycle fatigue properties, and fracture characteristics have been previously reported [*10*]. The monotonic tensile test properties are summarized in Table 2. Tests conducted under fully reversed total strain control revealed the material to exhibit significant amounts of cyclic strain-softening behavior at low strain amplitudes, small amounts of cyclic strain softening at intermediate strain amplitudes, and a combination of cyclic strain hardening followed by cyclic strain-softening behavior at high strain amplitudes. The cyclic yield point is estimated to be 328 MPa.

The CT specimens were designed and manufactured in accordance with ASTM Test Method for Measurement of Fatigue Crack Growth Rates (E 647) specifications. A specimen width of 50.8 mm was used with the length of the machined notch being 15.24 mm. Specimen thickness values of 3.175 and 12.70 mm were selected for this study, both of which fall within the range specified in the above standard. For the CMOD method, the displacement gage was located in a V-notch at the mouth of the machined notch in the CT specimen. For the BFSG method, the strain gage is positioned in the geometric center of the back surface of the CT specimen. For the SSGC method, a series of four strain gages were placed on the side of the CT specimen at a vertical distance of 1.5 mm from the expected crack plane. The four gages were positioned at crack lengths corresponding to 16.26, 19.51, 24.89, and 30.40 mm. The displacement and strain data obtained by the above gages enable direct comparisons with the results of the FE models.

Experimental Procedures

All tests were conducted in accordance with ASTM E 647 specifications using a fully automated closed loop servohydraulic structural test machine. The test conditions chosen were a cyclic frequency of 20 Hz, a sinusoidal waveform, and a room temperature (23°C) lab air environment with 50% relative humidity. All tests were conducted under load control with a PC-based computer program being used to conduct the test and store test results of: (a) cycle number, (b) maximum load, (c) minimum load, and (d) crack length. This software calculates crack length based on CMOD gage displacements and automatically adjusts the minimum and maximum loads in accordance with the type

TABLE 2—*Monotonic tensile test results for the 1070M steel.*

Yield Strength		Ultimate Strength		Elongation to Failure, ε_f (%)	Reduction in Area, RA (%)
MPa	ksi	MPa	ksi		
589.0	85.5	721.0	104.6	25.9	59.7

of test being conducted. Visual crack length measurements were periodically taken to verify that crack front curvature was within acceptable limits.

A two-level factorial test matrix was set up to study the influence of the following parameters on crack closure and crack growth rate behavior.

1. Specimen thickness (T = 3.175 and 12.70 mm).
2. Maximum stress intensity (K_{max} = 16.5 and 33.0 MPa·m$^{1/2}$).
3. Load ratio ($R = K_{max}/K_{min}$ = 0.10 and 0.55).
4. Overload (0 and 100%).

These tests, conducted under constant K_{max} and R conditions, enable crack closure measurement comparisons between the CMOD, BFSG, and SSGC methods under constant test conditions. Conventional fatigue crack propagation (FCP) tests were also conducted at load ratios of R = 0.10 and 0.55 to establish the crack growth rate (da/dN) versus stress intensity range (ΔK) curves for this material. All of the CT specimens were precracked under constant load and constant R = 0.10 conditions such that the final value of K_{max} was 16.5 MPa·m$^{1/2}$ at the crack length of 17.53 mm.

A four-channel PC-based data acquisition system was used to periodically store the output from the load cell and the CMOD, BFSG, and SSGC gages for complete load cycles. The data acquisition rate was 100 kHz, which results in 1250 data points per channel for each load cycle. Despite every effort to minimize noise, the impact of noise on the signal was of sufficient magnitude that it could not be neglected during data analysis. The ability to readily discern the value of K_{cl} is dependent on the competing influences of the sensitivity and the signal-to-noise ratio. For the CMOD and BFSG methods, this ability is expected to slightly increase with crack length because only the signal-to-noise ratio is increasing with crack length. For the SSGC method, each strain gage has two distinct regions of crack length where both the sensitivity and signal-to-noise ratio are high. Therefore it is expected that each gage will result in K_{cl} values that have a bimodal appearance when represented as a function of crack length. By having a series of strain gages for which these regions overlap, the value of K_{cl} can be readily determined for a wide range of crack lengths.

Several existing methods are available for objectively determining the point in the load-displacement or load-strain curve that corresponds to the stress intensity at closure (K_{cl}). These methods have been shown to be effective for analysis of data obtained from the CMOD and BFSG methods. However, these methods are not sufficiently robust for surface strain gage methods, where: (a) the adverse effect of noise on the signal can not be neglected, and (b) the slope can change from positive to zero to negative in a single interval of load range. Based on these concerns, a new method was developed [*11*] that utilizes a combination of the following statistical approaches:

1. Statistical methods to minimize noise impact.
2. Linear least squares regression to calculate local slopes for each data point.
3. A probability test of statistical significance to assure that the local slop variation is outside of the population of normally distributed slope variations.

This new method was compared to the existing slope offset methods and found to be a quite robust data analysis technique for the CMOD, BFSG, and SSGC methods. The use of the same method for determining K_{cl} and K_{op} also provided an objective comparison to rate the relative sensitivity of each crack closure measurement technique under various test conditions.

Results: Experimental

For the crack mouth opening displacement (CMOD) method, the shape of the load-displacement curves varies only slightly over a wide range of crack lengths. However, the curves resulting from the

surface strain gage method change shape considerably, depending on whether the strain gage is positioned ahead of, or behind, the advancing crack tip [6]. The crack closure results, obtained from the CMOD and BFSG methods, were virtually identical. Also, no significant difference between crack closing (K_{cl}) and crack opening (K_{op}) values were found.

A comparison of the K_{cl} results from the CMOD and SSGC measurement methods is presented in Fig. 1 for two levels of K_{max} (16.5 and 33.0 MPa·m$^{1/2}$) and two specimen thickness values (T = 3.175 and 12.70 mm). These four tests were all conducted under constant K_{max} and R = 0.10 test conditions. To facilitate ease of comparison, the results are plotted as load ratio of crack closure (R_{cl} = K_{cl}/K_{max}) versus crack length (a). Comparison of these results enable the following observations of crack closure behavior and measurement to be made:

1. The SSGC method provided consistently higher R_{cl} values.
2. The R_{cl} values exhibited an increasing, then decreasing behavior versus crack length.
3. The R_{cl} values were higher for the high K_{max} tests.
4. The CMOD R_{cl} results exhibit a greater dependence on specimen thickness, particularly at high K_{max} levels and longer crack lengths.

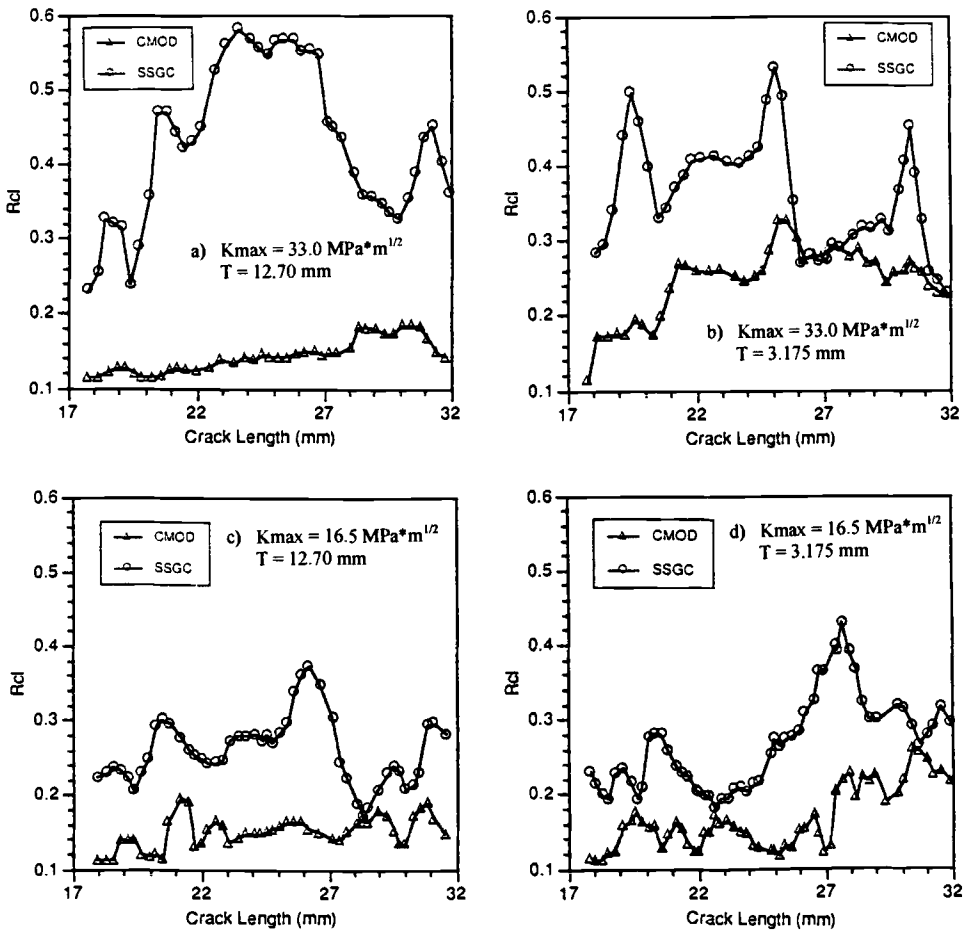

FIG. 1—*Comparison of measured* R_{cl} *values for the constant* K_{max} *and* R *tests.*

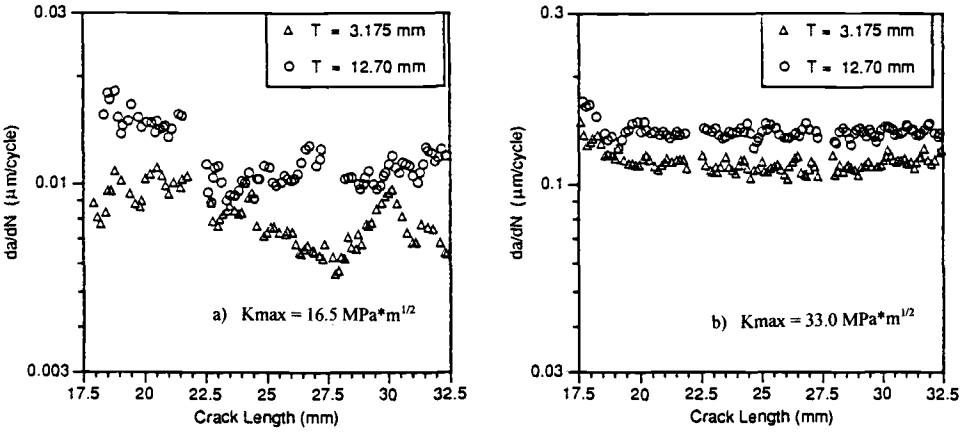

FIG. 2—*Comparison of* da/dN *values for the constant* K_{max} *and* R *tests.*

The fatigue crack growth rate data, obtained from these four tests, are compared in Fig. 2. For both $K_{\max}$ levels, the thin specimen exhibited consistently lower crack growth rates than the thick specimen. Also, for both $K_{\max}$ levels and both specimens, the *da/dN* values exhibited a decreasing, then increasing behavior versus crack length. Since the crack growth rate is related to the crack closure behavior by Eqs 2 and 3, these crack growth rate behaviors qualitatively agree with the experimentally measured crack closure behavior, which showed higher R_{cl} values for the thin specimens and an increasing, then decreasing behavior of R_{cl} versus crack length.

$$da/dN = C(\Delta K_{eff})^n \tag{2}$$

$$\begin{aligned} \Delta K_{eff} &= (1 - R_{cl}) \cdot K_{\max} \text{ (for } R_{cl} > R) \\ \Delta K_{eff} &= (1 - R) \cdot K_{\max} \text{ (for } R_{cl} \leq R) \end{aligned} \tag{3}$$

Further evidence of the significance of crack closure was obtained from the constant $K_{\max} = 33.0$ MPa·m$^{1/2}$ and $R = 0.55$ test, for which the value of K is identical to that of the constant $K_{\max} = 16.5$ MPa·m$^{1/2}$ and $R = 0.10$ test. The value of $R = 0.55$ is at or above the level of R_{cl} measured during tests conducted at $R = 0.10$. Therefore, the effect of closure on the crack growth rate of the $R = 0.55$ tests is minimal, and any difference in *da/dN* values between these tests arises as a direct result of the closure behavior of the $R = 0.10$ test condition. For both the thin and thick specimens subjected to the $R = 0.55$ test, a crack growth rate of approximately $2.0 \cdot 10^{-8}$ m/cycle was exhibited for all crack lengths. The *da/dN* values for the $R = 0.10$ tests were consistently less than this and showed a dependence on both specimen thickness and crack length.

Single Tensile Overload Tests

The crack closure results obtained from the single tensile overload tests are presented in Fig. 3. Here, the results are plotted as R_{cl} versus distance from the overload. This test is conducted at constant $K_{\max} = 16.5$ MPa·m$^{1/2}$ and $R = 0.10$, with a single tensile overload of 100% being applied at the start of the test. The CMOD method was found to be relatively insensitive to any overload effect on closure. The SSGC method was found to be much more sensitive to the overload effect and was able to capture the subtle features of crack closure behavior following application of the single tensile

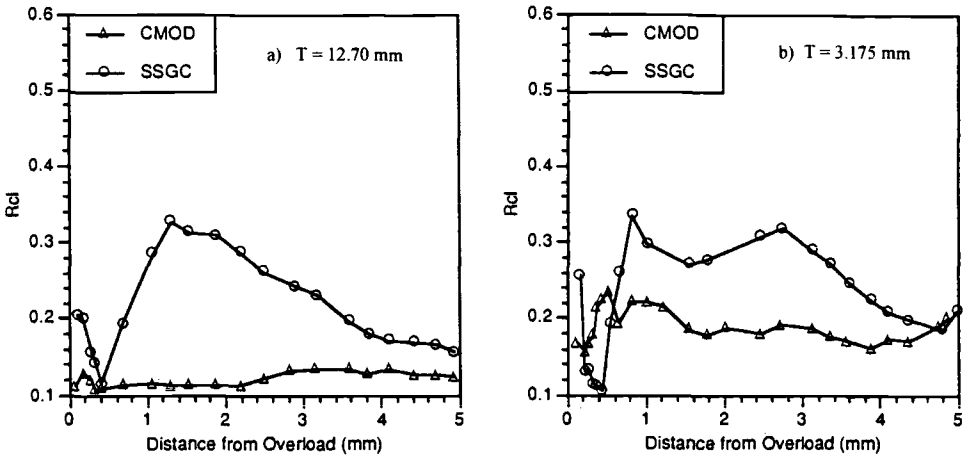

FIG. 3—*Comparison of measured* R_{cl} *values for the overload tests.*

overload:

1. The values of R_{cl} initially decrease immediately following the tensile overload.
2. As the crack grows further into the plastic zone created by the overload, the values of R_{cl} progressively increase to a level higher than that of the baseline test.
3. As the crack grows out of the overload plastic zone, the value of R_{cl} gradually decreases to a level at or below that of the baseline test.
4. The thin specimen exhibited both a more substantial initial reduction in R_{cl} values, and the subsequent increase in R_{cl} values occurred over a greater distance.

The crack growth rate results of the overload tests are compared to the baseline tests in Fig. 4. Both the thin and the thick specimens exhibit accelerated crack growth rates immediately following the

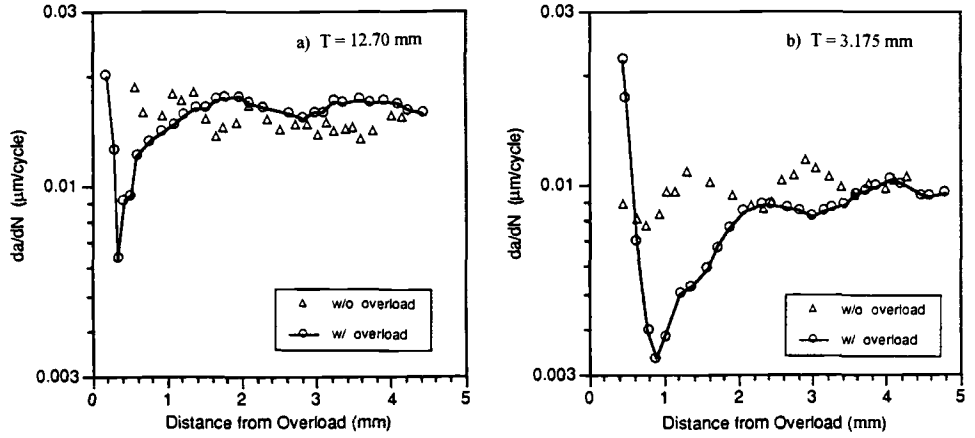

FIG. 4—*Comparison of* da/dN *values for the overload and baseline tests.*

overload. The distance over which the increased *da/dN* values occurred was greater for the thin specimen. Both specimens exhibit decelerated growth rates as the crack tip advances further into the plastic zone created by the overload. The distance over which the decreased *da/dN* values occurred was greater for the thin specimen. As the crack grew beyond the overload plastic zone, the growth rates became equal to or greater than that of the baseline test. All of these observations of crack growth rate behavior directly correspond to the previously discussed observations of measured crack closure behavior following the overload, thus providing further evidence of the significance of crack closure.

Crack Closure Mechanisms

After each test, the crack was propagated until specimen fracture under constant load and constant R test conditions. This enabled visual observation and scanning electron microscope (SEM) examination of the fatigue fracture surfaces. Inspections of the crack curvature and the crack plane angle were made to verify that the test conformed with ASTM E 647 specifications. No indication of wetting of the fracture surfaces was observed, which eliminates viscosity-induced closure as an operative mechanism. The microstructure contained a negligible amount of retained austenite, thus eliminating the mechanism of phase transformation-induced closure. For all test conditions, the fracture surfaces were found to be relatively smooth, planar, and featureless. Oxidation of the fracture surface was detected only in the near-threshold region just prior to crack arrest. No oxide debris were observed in the region of stable crack growth. No appreciable influence of K_{max} on surface roughness was observed. The above SEM observations indicate the following material and test condition characteristics, which are pertinent to the mechanisms of closure operative in this microstructure.

1. Crack path meandering only occurred during crack initiation at the notch root.
2. Oxide-induced closure was only significant in the near-threshold region, where low crack growth rates and small crack tip opening displacements occur.
3. Surface roughness was not appreciably affected by K_{max} level; therefore, this mechanism does not explain the effect of K_{max} on R_{cl} observed in this study.
4. By process of elimination, plasticity-induced closure is the sole closure mechanism that dominates the Region II crack closure behavior of this microstructure.

Results: Finite Element Model

The starting point for all test simulations was the final load step of the FE model used to simulate the precracking sequence. For the constant K_{max} = 16.5 MPa·m$^{1/2}$ and R = 0.10 test simulation, the first load cycle is identical to the final precracking cycle. For the other two test simulations, the first load cycle is identical K_{max} = 33.0 MPa·m$^{1/2}$ and R = 0.10. For the constant K_{max} and R test simulation, this condition is held constant throughout. For the overload test simulation, this condition represents the single tensile overload, after which the loading is reduced to K_{max} = 16.5 MPa·m$^{1/2}$ and R = 0.10. The FAM pre/post processing software package enables results from different load steps to be combined in equation form. This capability was used to combine results from P_{max} and P_{min} conditions into the cyclic parameters of strain range and mean strain. Comparisons of results between propagating crack FE models and the corresponding stationary crack FE models were made to highlight the impact of crack tip shielding produced by plasticity-induced crack closure. Note: no crack closure occurs for the stationary crack model under positive R loading because there is no crack wake plasticity to produce closure. Therefore, comparisons between stationary crack and propagating crack models enables the impact of crack closure to be quantified.

For the constant K_{max} = 16.5 MPa·m$^{1/2}$ and R = 0.10 test condition, the strain range results for the stationary crack and propagating crack FE models were 0.0051 and 0.0036, respectively. This indi-

cates that a 30% reduction in the strain range was produced by closure-induced crack tip shielding. Comparison of mean strain values revealed a 16% reduction, from 0.0099 to 0.0083. For the constant K_{max} = 33.0 MPa·m$^{1/2}$ and R = 0.10 test condition, a similar comparison revealed a 56% reduction in strain range, from 0.0161 to 0.0070, and a 7% reduction in mean strain, from 0.0337 to 0.0315. The load ratio values of crack closure (R_{cl}) and crack opening (R_{op}) were identical, which qualitatively agree with the experimental measurements previously discussed. For both of the these test simulations, crack closure was continuous starting immediately behind the crack tip and gradually progressing along the crack wake.

For the single tensile overload test, the changes in strain range and mean strain as the crack tip propagates into and out of the overload plastic zone were monitored to quantify the overload effect. The baseline conditions in terms of R_{cl}, strain range, and mean strain were 0.41, 0.0036, and 0.0078, respectively. Immediately following the single tensile overload, the value of R_{cl} decreased, while the strain range and mean strain increased to values of 0.0055 and 0.0243, respectively. As the crack tip propagates into the overload plastic zone, the value of R_{cl} increases above the baseline level, which results in an increased amount of crack tip shielding and corresponding reduction in strain range (0.0018) and mean strain (0.0040). As the crack tip emerges from the overload plastic zone, the values of R_{cl}, $\Delta\varepsilon_{yy}$, and ε_{yym} steadily approach those of baseline conditions. These findings agree with measured crack closure results, which exhibited:

1. A reduced crack closure level immediately following the overload.
2. An increased closure level as the crack propagated into the overload plastic zone.
3. Crack closure levels returning to baseline levels, as the crack propagated out of the overload plastic zone.

Direct Comparisons with Experimental Results

Comparison of the load ratio of crack closure (R_{cl}) between the FE model and experimental results, obtained using the SSGC method, revealed excellent agreement for the constant K_{max} and constant R tests. For the K_{max} = 16.5 MPa·m$^{1/2}$ and R = 0.10 test, the FE model resulted in a constant value of R_{cl} = 0.41. The experimental results in the region of high gage sensitivity, for both the thin and thick specimens, were in the range of $0.37 \leq R_{cl} \leq 0.43$. For the K_{max} = 33.0 MPa·m$^{1/2}$ and R = 0.10 test, the FE model resulted in R_{cl} = 0.59, while the experimental results were in the range of $0.53 \leq R_{cl} \leq 0.58$.

Figure 5 provides a direct comparison between FE model and experimental results of strain ratio versus load curves for the surface strain gage located at a = 19.51 mm. For the SSGC method, the measured strain versus applied load behavior changes as the crack propagates. When the strain gage is ahead of the crack tip, the slope of the strain versus load curve decreases when crack closure occurs, while, for a strain gage in the wake of the crack, the slope increases as closure occurs. A direct comparison of CMOD versus crack length results revealed that the FE model results fell between the experimental results of the thin and thick specimens. These comparisons reveal that the FE model results match the experimental results quite well both qualitatively and quantitatively.

Use of FE results for the total strain range and the mean strain has been shown to be an effective means of elucidating the fatigue conditions at the crack tip. Traditional fatigue life calculations, such as the Coffin-Manson strain-life relationship, utilize these two cyclic strain parameters. Combining experimental results of crack growth rate with experimentally verified FE simulations would enable future crack growth rate laws to be based on the strain range ($\Delta\varepsilon_{yy}$) and mean strain (ε_{yym}) instead of the traditional fracture mechanics approach, which uses the effective stress intensity range (ΔK_{eff}). Adopting this approach would enable a merging of data from strain controlled low cycle axial fatigue tests and load-controlled CT specimen crack propagation tests.

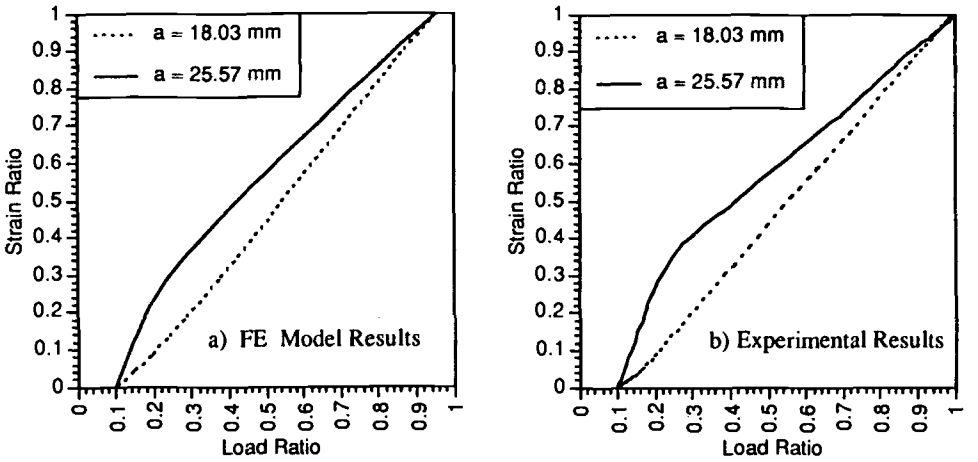

FIG. 5—*Comparison of FE model and experimental results for SSGC gage located at* a = *19.51 mm, under* K_{max} = *16.5 MPa* · $m^{1/2}$ *and* R = *0.10 test conditions.*

Conclusions

1. For this microstructure, the existence of crack closure was verified through CMOD, BFSG, and SSGC experimental measurements, and crack closure was found to have a significant impact on crack growth rates.
2. A specimen thickness effect on crack closure behavior and crack growth rate behavior was observed.
3. The single tensile overload effect on crack growth rates was readily explained by the measured crack closure behavior. The thin specimen exhibited a more significant overload effect.
4. The crack closure behavior and the crack growth rate behavior exhibited a slight dependence on crack length under constant K_{max} and $R = 0.10$ test conditions.
5. The SSGC method resulted in consistently higher R_{cl} values than the CMOD and BFSG methods. Part of this is attributed to the SSGC method measuring closure at the specimen surface where R_{cl} is highest. The SSGC method was shown to be particularly superior for the overload test.
6. By process of elimination, plasticity-induced closure dominates Region II crack closure behavior in this microstructure. Crack path meandering, oxide-induced, and surface roughness-induced closure are significant only during crack initiation at the notch root and/or at near-threshold crack growth rates.
7. Plasticity-induced closure results in a significant amount of crack tip shielding that effectively reduces the cyclic strain range and mean strain occurring at the crack tip.
8. Comparison of FE model and experimental results revealed excellent agreement.

Acknowledgments

The authors would like to thank The Timken Company for supporting this research effort. Dr. John D. Dougherty would like to thank Mr. Michael J. Leap for his assistance with specimen preparation, Mr. Charles A. Mozden for his assistance with SEM examinations, and Mr. Mark J. Ostapack and Mr. Al K. Pierce for their assistance with strain gage installation and instrumentation. Lastly, sincere thanks and appreciation are expressed to the late Mr. Peter S. Orvos, who was always supportive of this vast effort and offered encouragement throughout this lengthy research project.

References

[1] Elber, W., "The Significance of Fatigue Crack Closure," *Damage Tolerance in Aircraft Structures, ASTM STP 486,* American Society for Testing and Materials, Philadelphia, 1971, pp. 230–242.

[2] Ritchie, R. O. and Suresh, S., "Some Considerations on Fatigue Crack Closure at Near-Threshold Stress Intensities Due to Fracture Surface Morphology," *Metallurgical Transactions A,* Vol. 13A, May 1982, pp. 937–940.

[3] McEvily, A. J., "On Crack Closure in Fatigue Crack Growth," *Mechanics of Fatigue Crack Closure, ASTM STP 982,* American Society for Testing and Materials, Philadelphia, 1988, pp. 35–43.

[4] Liaw, P., "Overview of Crack Closure at Near-Threshold Fatigue Crack Growth Levels," *Mechanics of Fatigue Crack Closure, ASTM STP 982,* American Society for Testing and Materials, Philadelphia, 1988, pp. 62–92.

[5] Schijve, J., "Fatigue Crack Closure: Observations and Technical Significance," *Mechanics of Fatigue Crack Closure, ASTM STP 982,* American Society for Testing and Materials, Philadelphia, 1988, pp. 5–34.

[6] Dougherty, J. D., Srivatsan, T. S., and Padovan, J., "Fatigue Crack Propagation and Closure Behavior of Modified 1070 Steel: Experimental Results," *Engineering Fracture Mechanics,* Vol. 56, No. 2, 1997, pp. 167–188.

[7] Dougherty, J. D., Srivatsan, T. S., and Padovan, J., "Fatigue Crack Propagation and Closure Behavior of Modified 1070 Steel: Finite Element Study," *Engineering Fracture Mechanics,* Vol. 56, No. 2, 1997, pp. 189–212.

[8] Suresh, S., "Micromechanisms of Fatigue Crack Growth Retardation Following Overloads," *Engineering Fracture Mechanics,* Vol. 18, No. 3, 1983, pp. 577–593.

[9] Vasudevan, A. K., Sadananda, K., and Louat, N., "Reconsideration of Fatigue Crack Closure," *Scripta Metallurgica et Materialia,* Vol. 27, 1992, pp. 1673–1678.

[10] Dougherty, J. D., Srivatsan, T. S., and Padovan, J., "Cyclic Stress Response, Strain Resistance, and Fracture Behavior of Modified 1070 Steel," *Engineering Fracture Mechanics,* Vol. 53, No. 6, 1996, pp. 829–847.

[11] Dougherty, J. D., "Combined Experimental and Finite Element Study of Fatigue Crack Closure in 1070M Steel," Ph.D. dissertation, The University of Akron, 1994.

Hong-Yan Zhang,[1] *Ralph I. Stephens,*[2] *and Gregory Glinka*[3]

Subsurface Fatigue Crack Initiation and Propagation Behavior of Induction-Hardened Shafts under the Effect of Residual and Applied Bending Stresses

REFERENCE: Zhang, H.-Y., Stephens, R. I., and Glinka, G., **"Subsurface Fatigue Crack Initiation and Propagation Behavior of Induction-Hardened Shafts under the Effect of Residual and Applied Bending Stresses,"** *Fatigue and Fracture Mechanics: 30th Volume, ASTM STP 1360,* American Society for Testing and Materials, West Conshohocken, PA, 2000, pp. 240–260.

ABSTRACT: The Society of Automotive Engineers Fatigue Design and Evaluation (SAEFDE) Committee has been conducting a long-term program aimed at the development of a predictive capability for fatigue life of SAE 1045 induction-hardened shafts. As a part of a larger-scale investigation provided by the SAEFDE committee, this research provided an analytical model capable of predicting the total fatigue life, both crack initiation and crack propagation, of an induction-hardened shaft under applied bending stress. The analysis procedure incorporated the effects of residual stresses. Total stress intensity factors were calculated and superimposed using applied bending stress intensity factors and residual stress intensity factors along the subsurface elliptical crack front. Fatigue tests were conducted using SAE 1045 induction-hardened shafts to verify the analytical models of subsurface fatigue crack growth. The total fatigue life calculations of subsurface failure showed a factor from 0.6 to 0.8 compared with the experimental results. The analytical model and experimental data confirmed that the majority of the total fatigue life is spent in the crack propagation phase.

KEYWORDS: 1045 steel bars, induction hardening, residual stresses, elliptical subsurface crack, cyclic bending, stress intensity factor, fatigue crack initiation, fatigue crack growth

In some industries, fatigue critical components such as axle shafts, transmission shafts, and hydraulic cylinder pins are induction hardened [*1*]. By the primary processes of induction hardening, namely, heating and quenching, hardened components can be created that exhibit a hard, phase-changed, and property-changed case, as well as the most important development of large surface compressive residual stresses combined with a tough core with tensile residual stresses. SAE 1045 induction-hardened solid steel bars of many sizes are used in the ground vehicle industry. As shown in Fig. 1, these shafts often have an induction case depth from 1 to 6 mm with a Brinell hardness of 563 (Rockwell C is 55) in the case, and a Brinell hardness of 192 (Rockwell C is 11) in the core. Loading conditions of these shafts can be bending, torsion, or a combination of bending and torsion. Both surface and subsurface cracks have been found during service and experimental tests [*2–3*]. However, most of the fatigue failures of induction-hardened shafts are due to subsurface cracks, which are associated with a longer fatigue life than surface cracks. The SAEFDE committee has been conducting a long-term program aimed at the development of a predictive capability for fatigue life and fracture behavior of SAE 1045 induction-hardened round shafts. As a part of a larger-scale investigation pro-

[1] Engineer, Deere & Company Technical Center, 3300 River Drive, Moline, IL 61265-1792.
[2] Professor, Mechanical Engineering Department, The University of Iowa, Iowa City, IA 52242.
[3] Professor, Mechanical Engineering Department, University of Waterloo, Waterloo, Ontario, Canada.

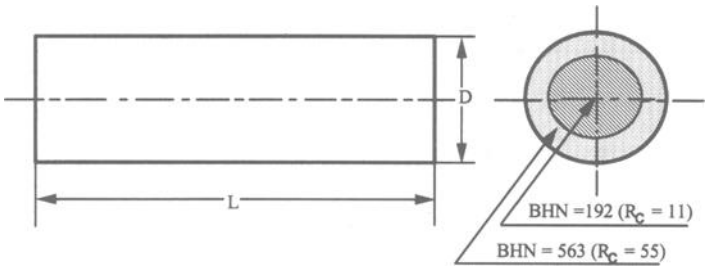

FIG. 1—*Induction-hardened 1045 steel bar geometry.*

vided by the SAEFDE committee, the goal of this research is to analytically, numerically, and experimentally investigate the fatigue behavior of induction-hardened round shafts under the effects of residual and applied bending stresses in order to construct fatigue life prediction procedures to aid in the design of cheaper and more dependable components in their service lives. Accordingly, subsurface crack initiation and propagation behavior of induction-hardened shafts under bending load were investigated and analytically predicted. Discriminating three-point bending fatigue tests were performed to verify the usefulness of the analytical fatigue life prediction methods.

As is well known, the total fatigue process is normally divided into two parts, an initiation phase where microcracks form and grow through the first few grains, and a propagation phase where the crack has grown through many grains and formulae for fracture mechanics apply. Five aspects were considered in modeling the fatigue life of induction-hardened shafts under bending load in this research as follows: (a) estimation of the initial subsurface crack size, site, and initiation life; (b) derivation of accurate stress intensity factors under linear bending stress and nonlinear residual stresses for subsurface cracks; (c) integration of the fatigue crack propagation life; (d) determination of the final critical subsurface crack sizes; and (e) discriminating experimental verification of subsurface fatigue crack growth behavior of SAE 1045 induction-hardened shafts.

Materials/Specimens

The material used in this study is SAE 1045 steel and was provided by the SAEFDE committee. This is a medium carbon steel and is widely used in the ground vehicle industry for round bars of many sizes, which in many cases experience bending loads. The composition of the SAE 1045 steel includes as few as two primary elements, iron and 0.46% of carbon. The normalized 1045 material provided by the SAEFDE committee was formed by hot rolling bar stock to a diameter of approximately 63.5 mm. The normalizing temperature was 900°C followed by air-cooling. The microstructure of the normalized 1045 steel consisted of 80% lamellar pearlite in a 20% ferrite matrix.

The round shaft specimens used in this research have a diameter of 35 mm and a nominal induction-hardened case depth of 6 mm. As shown in Fig. 2, flats (machined prior to the induction-hardening process) at the ends of the shafts were added to facilitate the test setup and to eliminate point loads that would occur between the specimen and support rollers if no flats were present. The flats were not modeled in the analyses, nor was this required since the flats decrease the specimen volume by less than 0.1% and since the material was removed in areas remote from the critical region, Section A-A. The specimens were first machined from the hot-rolled bar stock to a diameter of approximately 35 mm and a length of 390 mm, and then the flats were machined. Then, the machined 1045 steel specimens were induction hardened. After induction hardening, the specimens were tempered at 180°C for 1 h, which gave a nominal Rockwell C hardness of 55 to 60 in the case. The specimens were oil polished after the induction heat treatment to remove the surface roughness and microcracks caused by the hardening process.

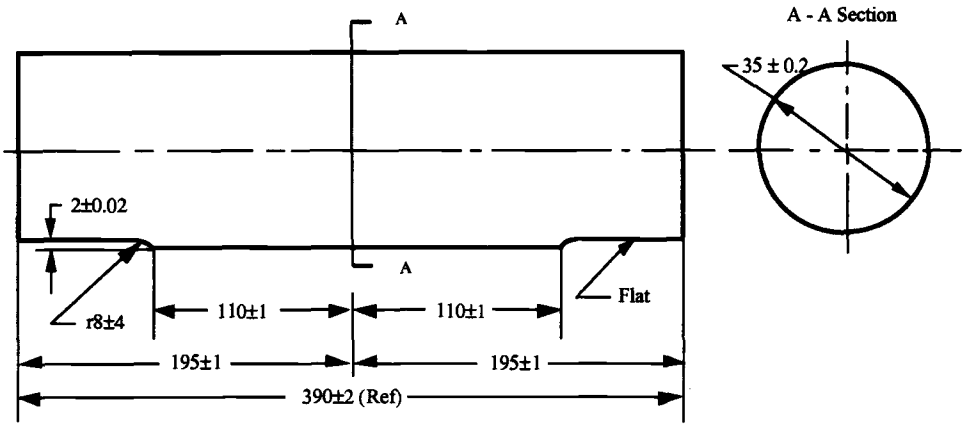

FIG. 2—*Dimensions and specifications of the specimens.*

Figure 3 shows a typical hardness profile that presents the hardness distribution versus normalized radial distance of an induction-hardened shaft specimen. Three areas are defined in this figure for the cross section of the induction-hardened shaft, as normalized core, transition zone, and hardened case. Table 1 presents the corresponding monotonic, cyclic, and low-cycle fatigue properties for the SAE 1045 normalized material (exists as core in an induction-hardened shaft), four levels of through-hardened material, R_c = 29, 36, 44 (exists as the transition zone in a induction-hardened shaft) and R_c = 55 (exists as the hardest case in the induction-hardened components) [*4*].

The exact pattern of the residual stress distribution depends on the size of the component, the heat-treating temperatures employed, the depth of hardening, and the type of quench and tempering. In fact, no prototype residual stress distribution exists. For the convenience of analysis, the actual residual stress distribution of a particular component was usually obtained from a component of measured residual stresses with similar size and hardness. The typical residual stress distribution [*5–7*] of SAE 1045 induction-hardened shaft specimens is given in Fig. 4.

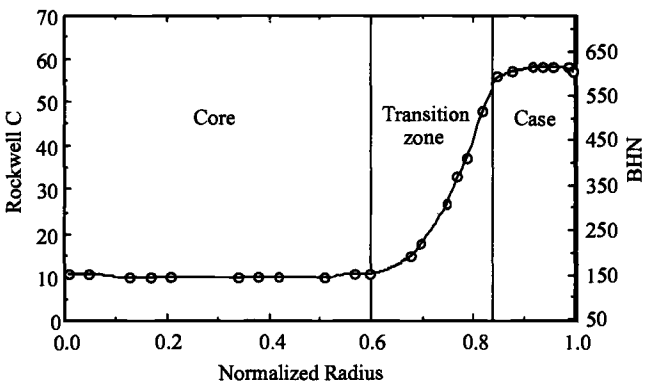

FIG. 3—*Hardness profile of an SAE 1045 induction-hardened shaft specimen.*

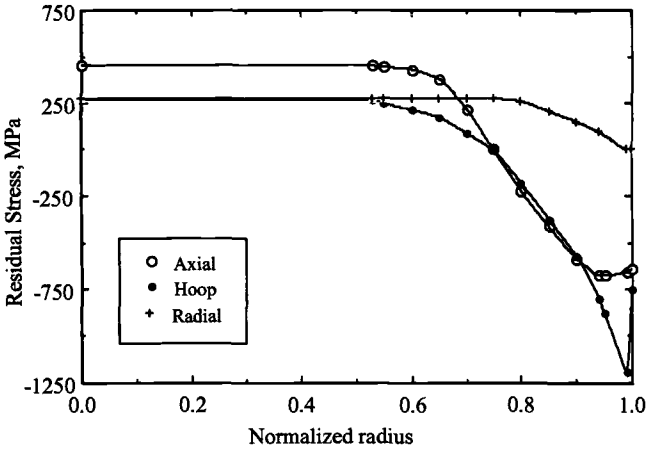

FIG. 4—*Typical residual stress distribution of SAE 1045 induction-hardened shaft specimens.*

Analytical Life Prediction Procedures

Crack Initiation

The fatigue process is commonly generalized as consisting of a "crack initiation (formation or nucleation)" stage followed by a "crack propagation" stage. A major concern in both experimental and modeling aspects of fatigue is the definition of "crack initiation." The reason for this concern is due to the fact that fatigue crack propagation is usually analyzed using fracture mechanics with the assumption that cracks already exist in the components. So, the following questions are raised. Under what loading conditions will a subsurface crack initiate, where exactly will the subsurface crack initiate, what is the subsurface crack initiation life, and most importantly, what is the size of the initial subsurface crack at the beginning of crack propagation.

Three conclusions were obtained from the literature review [*8–10*] on subsurface crack initiation studies of hardened shaft specimens: (1) cracks tended to initiate in the subsurface for the surface-hardened components in long-life "high-cycle-fatigue" situations; (2) a surface-hardened component with subsurface crack initiation would have longer fatigue life than with surface crack initiation; and (3) subsurface cracks initiate at the core and case interface. These conclusions qualitatively interpret the subsurface fatigue failure in a surface-hardened component, but do not quantitatively answer the specific questions that need to be solved in this research for the fatigue crack propagation study.

Assumptions—The local strain-life approach was used to predict fatigue initiation life of induction-hardened shafts in this research. The shafts were considered as having radial hardness layers with each layer having unique cyclic stress-strain and low-cycle fatigue properties, as given in Table 1. The procedure incorporated the effects of residual stresses to analyze and determine fatigue initiation life and damage.

The basic assumption of the analysis procedure in this research is that if the stress-strain history at the subsurface crack initiation site of an induction-hardened shaft and that applied to a smooth laboratory specimen under uniaxial tension load are the same, then the fatigue life of the smooth laboratory specimen will be equal to the fatigue crack initiation life at the subsurface initiation site (illustrated in Fig. 5). This assumption may somewhat underestimate the initiation life of a subsurface crack at the core and case interface because of different boundary conditions between the smooth specimen and the subsurface initiation site.

TABLE 1—*Monotonic and cyclic properties of SAE 1045 steel.*[a]

Property	Core	Transition Zone			Case
Hardness	$R_C = 11$	$R_C = 29$	$R_C = 36$	$R_C = 44$	$R_C = 55$
Converted Brinell hardness	192	277	336	410	563
ASTM grain size	9	7.5	7.5	7	8
Elastic modulus, E (GPa)	207	206	209	205	204
Ultimate tensile strength, S_u (MPa)	718	942	1323	1516	2297
Yield strength, $S_{y0.2\%}$ (MPa)	424	619	787	865	1636
Fatigue (limit) strength, σ_f (MPa)	250	400	560	600	860
Cyclic yield strength, σ_y' (MPa)	390	510	755	865	1724
Fatigue strength coefficient, σ_f' (MPa)	1439	2978	3902	4593	5786
Fatigue strength exponent, b	−0.13	−0.16	−0.16	−0.17	−0.15
Fatigue ductility coefficient, ε_f'	0.54	0.70	0.56	0.38	1.57
Fatigue ductility exponent, c	−0.53	−0.58	−0.60	−0.59	−0.99
Cyclic strength coefficient, K' (MPa)	1325	1743	2051	2381	3702
Strain hardening exponent, n'	0.203	0.189	0.163	0.172	0.100

[a] SAEFDE 1045 Data, Ref *4*.

For a smooth induction-hardened round shaft specimen under an applied bending load, the complete local stress analysis shows a triaxial stress state because residual stresses are triaxial. Since a local triaxial condition in the induction-hardened specimen exists, one might argue that a multiaxial fatigue life analysis is needed. Fortunately, however, since the subsurface crack is mostly initiated in the interface between the core and case, where the hoop residual stress is nearly equal to zero and the radial residual stress is negligible compared with the total stress in the axial direction, uniaxial fatigue analysis for the crack initiation study in the interface of core and case is still applicable.

Stress Mapping—Figure 6 is an example of stress mapping for an induction-hardened shaft that undergoes constant amplitude $R = 0$ cyclic bending stress of $\sigma_b = 743$ MPa. The stress fluctuation between residual stress and bending cyclic stress constitutes the unique cyclic stresses at each subsur-

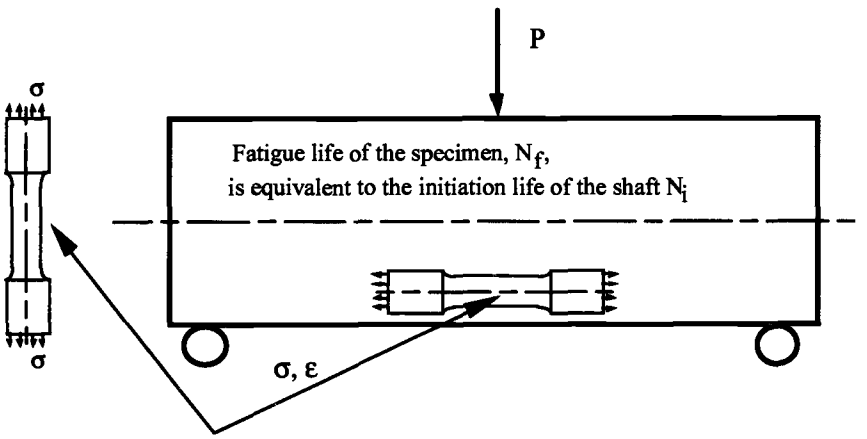

FIG. 5—*Assumption of local stress-strain approach to fatigue initiation life prediction based on smooth specimen data.*

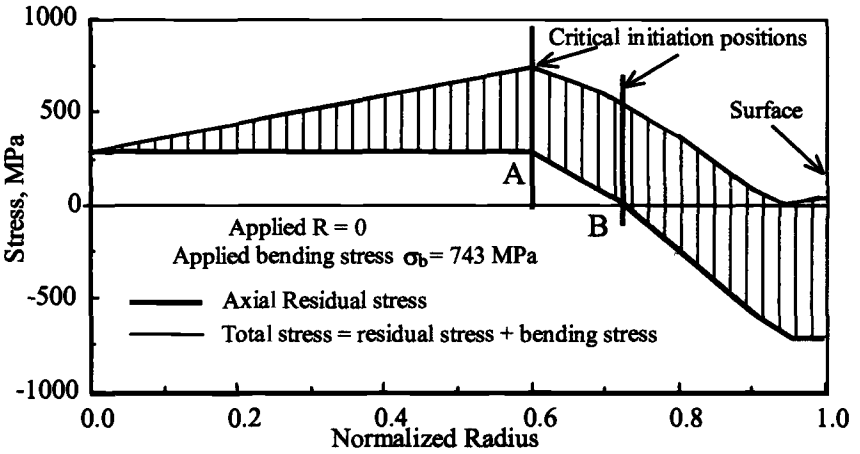

FIG. 6—*Cyclic stress at each position fluctuating between axial residual stress and total stress for applied* σ_b *= 743 MPa.*

face position of the shaft cross section, and this unique cyclic stress at each position on the specimen's cross section is also shown in Fig. 6.

From this stress mapping figure, three points were specifically examined for crack initiation based on the following engineering judgment:

1. The surface of the shaft should be examined to see if the crack would initiate on the surface. Although cyclic-applied compressive stresses are not very important for crack propagation, they are of importance to crack initiation.
2. Location B in Fig. 6 should be examined because it has the largest cyclic stress range. The axial residual stress in this location nearly equals zero.
3. Location A in Fig. 6 should be examined. Although the cyclic stress range is not as large as the one at Location B, it has the highest mean tensile stress.

Morrow and Smith-Watson-Topper (SWT) mean stress correction models were used with the local strain-life approach to determine the initiation lives at the above three locations.

Subsurface Crack Initiation Life and Initiation Site—The calculated crack initiation lives N_i are listed as follows:

1. Surface $N_i = 3.9 \times 10^7$ cycles (Morrow)
   $N_i = 3.0 \times 10^{10}$ cycles (SWT)
2. Location A at Normalized radius, $2r/D = 0.6$
   $N_i = 6.6 \times 10^5$ cycles (Morrow)
   $N_i = 7.6 \times 10^4$ cycles (SWT)
3. Location B at Normalized radius, $2r/D = 0.7$
   $N_i = 4.6 \times 10^5$ cycles (Morrow)
   $N_i = 8.9 \times 10^4$ cycles (SWT)

The initiated crack will first form on the point where the fatigue life calculation shows the lowest number of cycles. Therefore, from the above example, (1) a crack will not initiate on the surface of

the induction-hardened shaft under the applied bending load of $\sigma_b = 743$ MPa at $R = 0$; (2) a crack will initiate at Location B by using Morrow's approach, and the initiation life is 4.6×10^5 cycles; (3) a crack will initiate at Location A by using SWT's approach, and initiation life is 7.6×10^4 cycles.

Estimation of Initiated Crack Sizes—A major concern in both experimental and modeling aspects of fatigue is the definition of "crack formation" because of the fact that fatigue crack propagation is analyzed using fracture mechanics with the assumption that cracks already exist in the components. For an induction-hardened shaft used in the ground vehicle industry, there is no regular nondestructive crack inspection for subsurface cracks. The safe and effective usage of induction-hardened shafts can depend upon the relatively accurate analytical fatigue propagation life prediction, which will strongly rely on the initiation size investigation.

Two criteria were considered to determine the initiation crack sizes for SAE 1045 induction-hardened shafts, such as intrinsic crack size of the material at the fatigue crack initiation site and ASTM LCF smooth laboratory specimen size.

If considering crack initiation and propagation as two connected phases in one process under the lowest critical stress such as fatigue limit stress range $\Delta\sigma_f$, there is a transition point where the crack goes from $\Delta\sigma_f$ control to ΔK_{th} control. Kitagawa and Takahashi defined the crack size at such a transition point as the intrinsic crack size [*11*]. Therefore, the following relation can determine the intrinsic crack size:

$$a_{\text{intrinsic}} = \frac{1}{\pi}\left(\frac{\Delta K_{th}}{\Delta\sigma_f F}\right)^2 \tag{1}$$

where

F = the dimensionless stress intensity correction factor.

For a subsurface elliptical crack in an induction-hardened shaft, F (will be described in the next section) is a function of specimen and crack geometry a/D, a/b, t/D, and ϕ (a, b, t, ϕ, and D are defined in Fig. 7). The threshold stress intensity factor, ΔK_{th}, for SAE 1045 core material at $R = 0$ was determined by Werner and Stephens [*12*]. Fatigue limit σ_f for SAE 1045 core material given in Table 1 was obtained at $R = -1$. The Goodman relation of correcting the mean stress effect was used to determine the fatigue limit σ_f for other R ratios.

For SAE 1045 induction-hardened shafts with a diameter of 35 mm, the calculated intrinsic crack size for a subsurface elliptical crack under bending load at $R = 0$ is

$$a_{\text{intrinsic}} = \frac{1}{\pi}\left(\frac{\Delta K_{th}}{\Delta\sigma_f F}\right)^2 = \frac{1}{3.14}\left(\frac{4.8}{530 \times 0.4925}\right)^2 \tag{2}$$

$$= 0.000106 \text{ m} \approx 0.1 \text{ mm (for } D = 35 \text{ mm shaft)}$$

This result was calculated based on the assumption that the crack aspect ratio is $a/b = 0.8$. Stress intensity factor at $\phi = 90°$ was chosen for the representative stress intensity factor of the subsurface crack. For terms and calculation details of intrinsic crack size, refer to Ref *13*.

It can be seen from Eqs 1 and 2 that the intrinsic crack size of SAE 1045 core material is independent of different applied loading levels, but depends on size of the shaft through the dimensionless stress intensity factor, F. 0.1 mm was set as the low boundary of the estimated initiation crack sizes for induction-hardened shafts with a subsurface elliptical crack at a normalized radius of 0.7.

It is also reasonable to assume that the initiated subsurface crack size in the induction-hardened shaft is equal to the final crack size (before breaking into two pieces) of the ASTM standard labora-

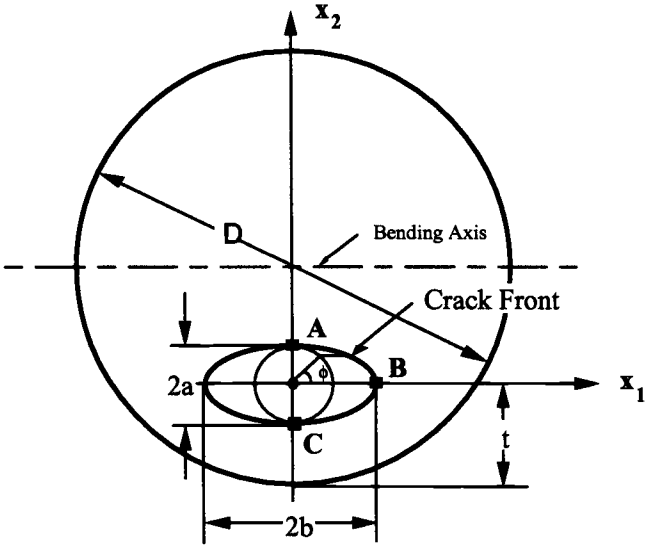

FIG. 7—*Definition of an elliptical subsurface crack in a round shaft.*

tory ε-N specimen. The diameter of 6 to 8-mm smooth laboratory specimens are used for the determination of the ε-N curve. Often, 80 to 95% of the specimen lives are spent to create a crack size of 0.5 to 1 mm deep. Knowing that crack initiation size is smaller than the crack size, and for the purpose of finding the smallest crack size as the high boundary of crack initiation size, 0.5 mm was set for the high boundary of the estimated crack sizes for induction-hardened shafts.

From the above two methods, therefore, the initiation crack sizes a_i for SAE 1045 induction-hardened shafts with a diameter of 35 mm, the calculated intrinsic crack sizes for a subsurface elliptical crack (located at $2r/D = 0.7$) under bending load at $R = 0$ can be assumed to be within the range of

$$a_{\text{intrinsic}} (=0.1) < a_i < 0.5 \text{ mm} \tag{3}$$

Crack Propagation

Stress Intensity Factor Solutions of Elliptical Subsurface Cracks—The subsurface crack geometry considered, and as shown in Fig. 7, is defined by the main axes of the ellipse, $2a$ and $2b$. The crack center is situated at a distance t from the closest boundary in the minor axis direction. A parametric angle, ϕ, was defined to present the different positions along the crack front. Points A, B, and C in Fig. 7 are the characteristic positions of the subsurface ellipse, with $\phi_C = -90°$, $\phi_B = 0°$, and $\phi_A = 90°$. It was assumed that the elliptical subsurface crack in the induction-hardened shaft was fully open under the bending load, so the superposition technique was used to determine the total stress intensity factors.

The basic equation of stress intensity factor K_I for the subsurface elliptical crack under bending load is defined as Eq 4, and F_I is a function of a/D, a/b, t/D, and ϕ.

$$K_I = \sigma_b F_I \sqrt{\pi a} \tag{4}$$

Numerical calculations were made for a wide range of all available geometric parameters that influence the location and shape of the elliptical crack using K-solver software [*14–16*]. For that pur-

pose, Mode I stress intensity factor solutions for the subsurface elliptical crack were calculated using *K*-solver at various points along the crack front for crack depth *a*/*D* ratio from 0.005 up to 0.15, crack location *t*/*D* ratios of 0.15 and 0.2 (the subsurface crack will be initiated at this position for the components studied in this research). These stress intensity factors for subsurface elliptical cracks under bending load have been compared with Chen, Nisitani, and Mori's solutions [*17*], who used a body force method at the limited crack depth of $a/D \leq 0.08$ and limited crack front of Points A and C. The differences are less than ±0.5%. For $a/D > 0.08$, however, there are no available solutions for comparison. A selection of stress intensity factor results were plotted and given in Fig. 8 and Fig. 9 under a bending load.

Stress intensity factors for residual stresses in the induction-hardened round shaft with an elliptical subsurface crack, see Fig. 7, were also calculated using the *K*-solver software [*14–16*]. Nonlinear distributed axial residual stresses, as given in Fig. 4, were expressed up to three order double-power series under the Cartesian coordinate system in the *K*-solver software. The Taylor two-dimensional expansion technique was used to transform the residual stress from the polar coordinate system to the Cartesian coordinate system at the center of the ellipse ($x_1 = 0, x_2 = 0$). The calculated Mode I residual stress intensity factors expressed as S (MPa) $= K_{res}/\sqrt{\pi a}$ along the crack front were obtained for various combinations of elliptical crack ratios. A selection of these results were plotted and given in Fig. 10 and Fig. 11. They are plotted against the crack front from $\phi = -90°$ to 0° to 90°, as C to B to A in Fig. 7. There are no available residual stress intensity factor solutions for the elliptical subsurface crack in the round shaft from the literature; therefore, the comparison of the results from *K*-solver with the others can not be done.

It was assumed that the elliptical subsurface crack in the induction-hardened shaft was fully open under the bending load, so the superposition technique was used to determine the total stress intensity factors calculated based on the linear elastic fracture mechanics.

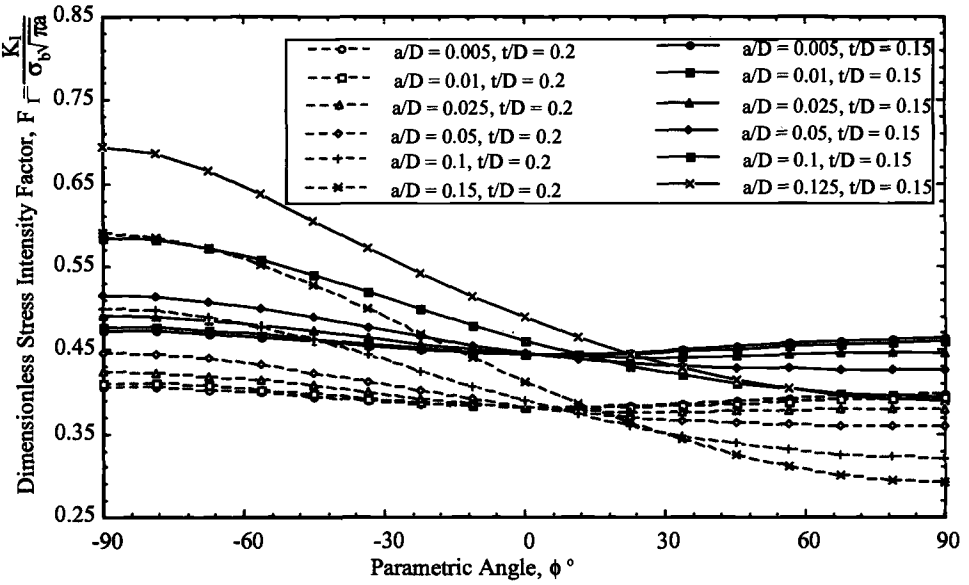

FIG. 8—*Dimensionless stress intensity factor* (F_I) *of an elliptical subsurface crack as a function of the parametric angle* (ϕ) *for different crack sizes with* a/b = *0.9, and* t/D = *0.15 and 0.2 (round shaft under bending load).*

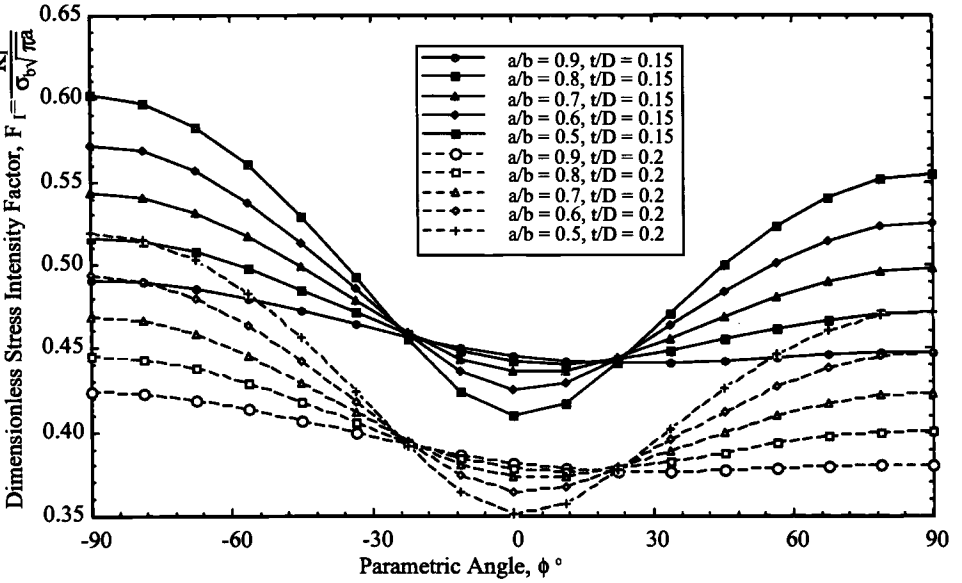

FIG. 9—*Dimensionless stress intensity factor* (F_I) *of an elliptical subsurface crack as a function of the parametric angle* (ϕ) *for different aspect ratios with* a/D = *0.025, and* t/D = *0.15 and 0.2 (round shaft under bending load).*

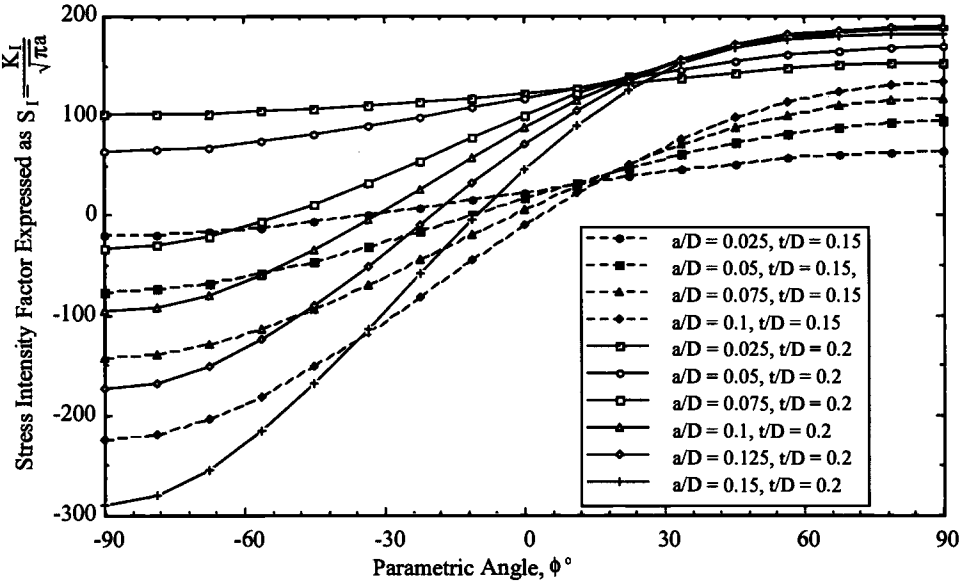

FIG. 10—*Mode I residual stress intensity factor (expressed as* S_I) *of an elliptical subsurface crack as a function of the parametric angle* (ϕ) *for different crack sizes with* a/b = *0.9, and* t/D = *0.15 and 0.2.*

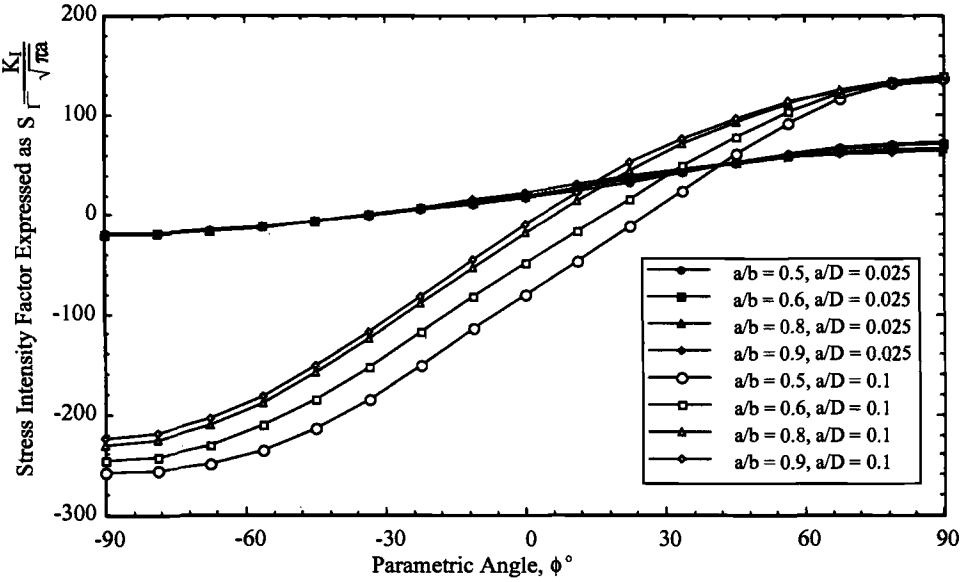

FIG. 11—*Mode I residual stress intensity factor (expressed as* S_I*) of an elliptical subsurface crack as a function of the parametric angle (*ϕ*) for different aspect ratios with* t/D = *0.15, and* a/D = *0.025 and 0.1.*

Fatigue Crack Growth Rates of SAE 1045 Steel in the Induction-Hardened Specimens—The fatigue crack growth rates of the SAE 1045 through hardened material (Rockwell C = 56) that existed as the case in the induction-hardened shafts were obtained in this research [*13*] and are given in Fig. 12 for R = 0.05 and 0.5. The fatigue crack growth properties of SAE 1045 normalized material that existed as the core in the induction-hardened shafts were available from the study by Werner and Stephens [*12*] and are listed in Table 2.

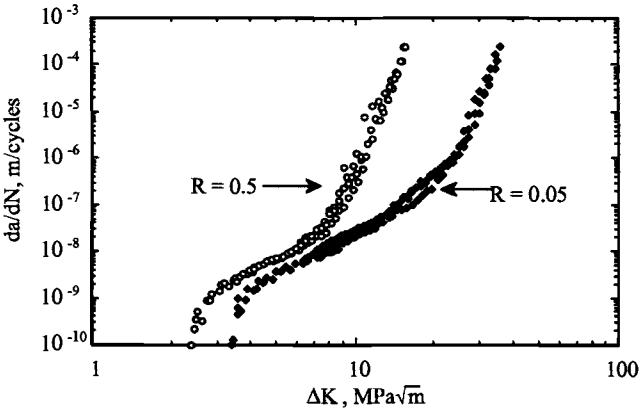

FIG. 12—da/dN-ΔK *for SAE 1045 through hardened material (Rockwell C = 56) for* R = *0.5 and* R = *0.05.*

TABLE 2—*Threshold stress intensity values and Region II fatigue crack growth for SAE 1045 normalized steel.*

	$R = 0.05$		$R = 0.5$	
	ΔK_{th} (MPa $\sqrt{m}$) = 3.5		ΔK_{th} (MPa$\sqrt{m}$) = 2.4	
R ratio	da/dN Range, m/cycle	ΔK Range, MPa$\sqrt{m}$	Paris Equation Coefficient	Paris Equation Exponent
$R = 0.05$	$10^{-9} - 10^{-6}$	9–40	8.2×10^{-13}	3.5
$R = 0.5$	$10^{-9} - 10^{-6}$	6–40	6.4×10^{-12}	3

Material fatigue and fracture properties are usually studied on standard specimens with through-the-thickness cracks for which the stress state is characterized by a single fracture mechanics parameter, stress intensity factor. For a standard specimen under cyclic loading with a constant stress ratio, there is usually a one to one relationship between the stress intensity factor range (ΔK) and the fatigue crack growth rate (da/dN). In two-dimensional surface or subsurface crack growth analyses, such as semi-elliptical surface cracks or elliptical subsurface cracks, where the stress intensity factor varies along the crack front, different approaches are used to establish the da/dN and ΔK relation.

Analytical Model of Subsurface Fatigue Crack Growth—The detailed mechanism of the residual stress effect on fatigue crack growth in induction-hardened shafts is very complicated. As a consequence, to model the fatigue crack growth in the induction-hardened round shaft, assumptions were made in order to simplify the problem. The basic assumption was that the crack propagation occurred due to the combined action of residual stresses and applied bending stress. The most important assumption was that, for the induction-hardened shaft under bending, Mode I crack growth caused by the opening mode stresses in the axial direction tended to dominate the crack growth. The crack growth was calculated by assuming that each local point along the crack front grew independently by obeying the local material fatigue crack growth rates. The local effective stress intensity factor ranges were calculated at each applied loading level to predict the local crack growth pattern through the use of the SAE 1045 core and case fatigue crack growth rate properties (Table 2 and Fig. 12). The concept (called "Non-Self-Similar" growth) is shown in Fig. 13 as

$$\text{Calculate local crack growth:} \qquad \delta a_i = \left.\frac{da}{dN}\right|_i dN \tag{5}$$

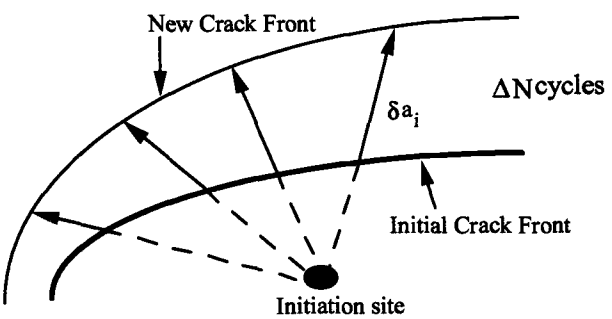

FIG. 13—*"Non-self-similar" crack growth.*

where

$$\left.\frac{da}{dN}\right|_i = f(\Delta K_{eff}, R_{eff})_i \tag{6}$$

A new elliptical crack front automatically advanced to the new position. This sequence was repeated in an iterative manner, thus modeling the progression and development of the initial elliptical subsurface crack. The process was repeated incrementally, and the size and shape of the initial elliptical crack was changed as a function of residual and applied bending stress intensity factors.

Crack growth was assumed to take place only for the positive part of the range of the stress intensity factor, as

1. If $(K_{res,i} + K_{\min,i}) > 0$ $\Delta K_{eff,i} = \Delta K_{ext,i}$ (7a)

2. If $(K_{res,i} + K_{\min,i}) < 0$ and $(K_{res,i} + K_{\max,i}) > 0$ $\Delta K_{eff,i} = K_{res,i} + K_{\max,i}$ (7b)

3. If $(K_{res,i} + K_{\max,i}) < 0$ $\Delta K_{eff,i} = 0$ (7c)

Because Mode I is operative under the bending load, the crack grew at Points A, B, and C during ΔN cycles by an increment Δa_A, Δa_B, and Δa_C in the directions orthogonal to the starting elliptical crack contour. The new crack contour was again approximated by an ellipse with the Vertices A, B, and C points, the axes of the new ellipse crack and location are:

$$a = a + (\Delta a_A + \Delta a_C)/2 \tag{8a}$$

$$b = b + \Delta a_B \tag{8b}$$

$$t = t + (\Delta a_C - \Delta a_A)/2 \tag{8c}$$

The crack growth calculations at any point on the elliptical crack front were based on the stress intensity factors calculated, at a total of $n = 9$ points equally spaced with $\Delta\phi = 22.5°$.

The current algorithm for computing subsurface crack propagation life and patterns for an induction-hardened shaft under the bending load was based on the above propagation model and the following failure criteria:

1. The $K_{\max} + K_{res}$ is greater than the fracture toughness K_Q value 59 MPa$\sqrt{\text{m}}$ for core material or the fracture toughness K_{Ic} value 38 MPa$\sqrt{\text{m}}$ for case material [*18*].
2. The ΔK_{eff} is greater than 40 MPa$\sqrt{\text{m}}$ for core material because the available fatigue crack growth rates of core material are for Region I and Region II only (Table 2).
3. The crack has grown so near the surface that a penetration of the crack through the surface may be realistic. In this case, the distance between the boundary of the crack and the boundary of the free surface is less than 2 mm.

The critical size of the crack was then determined from the occurrence of either of the three cases.

Excerpts from the analytical calculation output of the given initiated subsurface crack growth analyses are presented in Table 3. Five calculation steps were used. Information shown in this table are nine rows of data for each propagation step, which represent the data for each point on the crack front

TABLE 3—*Sample output of predicted subsurface crack growth of SAE 1045 induction hardened shafts D = 35 mm.*

starting subsurface elliptical crack and loading condition: $t = 6.55$ mm, $a_0 = 0.1$ mm, $b_0 = 0.125$ mm; $\sigma_b = 743$ MPa, Applied stress ratio R = -1						
Φ Degrees	$K_{bending}$ MPa$\sqrt{m}$	K_{res} MPa$\sqrt{m}$	Effective R_{eff}	$K_{max}+K_{res}$ MPa$\sqrt{m}$	Predicted Growth Δ(mm)	Accumulated Crack Size (mm)
After N = 510 000 cycles						
-90	5.0	0.5	-0.8	5.5	0.34	0.44
-67.5	4.9	0.5	-0.8	5.4	0.32	0.42
-45	4.7	0.5	-0.8	5.2	0.29	0.40
-22.5	4.5	0.5	-0.8	5.0	0.25	0.37
0	4.4	0.5	-0.8	4.9	0.24	0.36
22.5	4.5	0.5	-0.8	5.0	0.25	0.37
45	4.7	0.5	-0.8	5.2	0.29	0.39
67.5	4.9	0.5	-0.8	5.4	0.32	0.42
90	4.9	0.5	-0.8	5.4	0.33	0.44
After N = 535 000 cycles						
-90	11.3	0.4	-0.9	11.7	0.11	0.55
-67.5	11.5	0.4	-0.9	12.0	0.12	0.50
-45	11.9	0.5	-0.9	12.4	0.13	0.50
-22.5	12.1	0.7	-0.9	12.8	0.15	0.51
0	13.4	0.9	-0.9	14.2	0.21	0.59
22.5	13.2	1.0	-0.9	14.2	0.21	0.59
45	12.6	1.1	-0.8	13.7	0.18	0.57
67.5	11.9	1.1	-0.8	13.0	0.16	0.59
90	11.2	1.2	-0.8	12.4	0.13	0.51
After N = 545 000 cycles						
-90	16.2	-0.9	-1.1	15.3	0.19	0.90
-67.5	16.1	-0.8	-1.1	15.3	0.19	0.76
-45	15.9	-0.5	-1.1	15.4	0.19	0.77
-22.5	15.6	0.0	-1.0	15.5	0.20	0.78
0	15.3	0.5	-0.9	15.8	0.21	0.78
22.5	15.2	1.0	-0.9	16.2	0.22	0.80
45	15.1	1.5	-0.8	16.6	0.24	0.81
67.5	15.2	1.7	-0.8	16.9	0.26	0.79
90	15.2	1.8	-0.8	17.0	0.26	0.84
After N = 550 000 cycles						
-90	18.0	-0.6	-1.1	17.4	0.25	1.12
-67.5	18.0	-0.5	-1.1	17.6	0.25	1.15
-45	18.0	-0.1	-1.0	17.9	0.27	1.17
-22.5	18.0	0.4	-1.0	18.4	0.29	1.19
0	17.8	1.1	-0.9	18.9	0.31	1.20
22.5	17.5	1.7	-0.8	19.2	0.32	1.21
45	17.2	2.2	-0.8	19.4	0.33	1.22
67.5	16.9	2.6	-0.7	19.4	0.33	1.20
90	16.8	2.7	-0.7	19.4	0.33	1.22
After N = 557 000 cycles						
-90	23.4	-0.5	-1.0	22.9	1.97	3.15
-67.5	23.4	-0.4	-1.0	23.0	1.42	2.61
-45	23.4	-0.1	-1.0	23.4	0.73	1.93
-22.5	23.4	0.4	-1.0	23.7	0.76	1.96
0	23.1	1.1	-0.9	24.2	0.80	1.99
22.5	22.7	2.4	-0.8	25.1	0.88	2.07
45	22.3	3.1	-0.8	25.4	0.90	2.09
67.5	21.9	3.6	-0.7	25.5	0.91	2.08
90	21.8	3.7	-0.7	25.5	0.91	2.10

of the ellipse, starting with Point C ($\phi = -90°$), through B ($\phi = 0°$) to A ($\phi = 90°$) (refer to Fig. 7 for the definition being used). The first column identifies the position of the crack front. The second column identifies the maximum positive linear elastic stress intensity factor under bending at each point of the crack front using *K*-solver. The third column presents the computed residual stress in-

tensity factor at each point of the crack front using K-solver. The fourth column presents the resultant effective stress ratio $R_{\text{eff}} = \dfrac{K_{\min} + K_{res}}{K_{\max} + K_{res}}$. The fifth column identifies the resultant maximum stress intensity factors by adding the maximum applied bending stress and residual stress components. By assuming only the positive part of the stress intensity factor will contribute to crack growth, Column 6 presents the calculated crack growth at each point along the crack front. Crack growth was integrated based on the material crack growth rates given in Table 2 and Fig. 12. Since the loading is of constant amplitude in this research, the integration was carried out sequentially in small steps. A crack increment of 10% of the current crack size was taken as the step size until the next crack size was reached. Finally, Column 7 identifies the accumulated crack growth at each point along the crack front. It should be noted that the evolution of the crack shape was determined only by Points A, B, and C to model the next ellipse. The growth data listed for other points along the crack front were for references.

The complete crack growth simulation results from the case just described are given graphically in Fig. 14 to show the growth pattern. It is evident from this figure that the initiated subsurface crack grew both toward the center of the shaft and the hardened case. The shape of the ellipse tended to be a circle. It was also noted that about 90% of the fatigue propagation life occurred to grow the crack

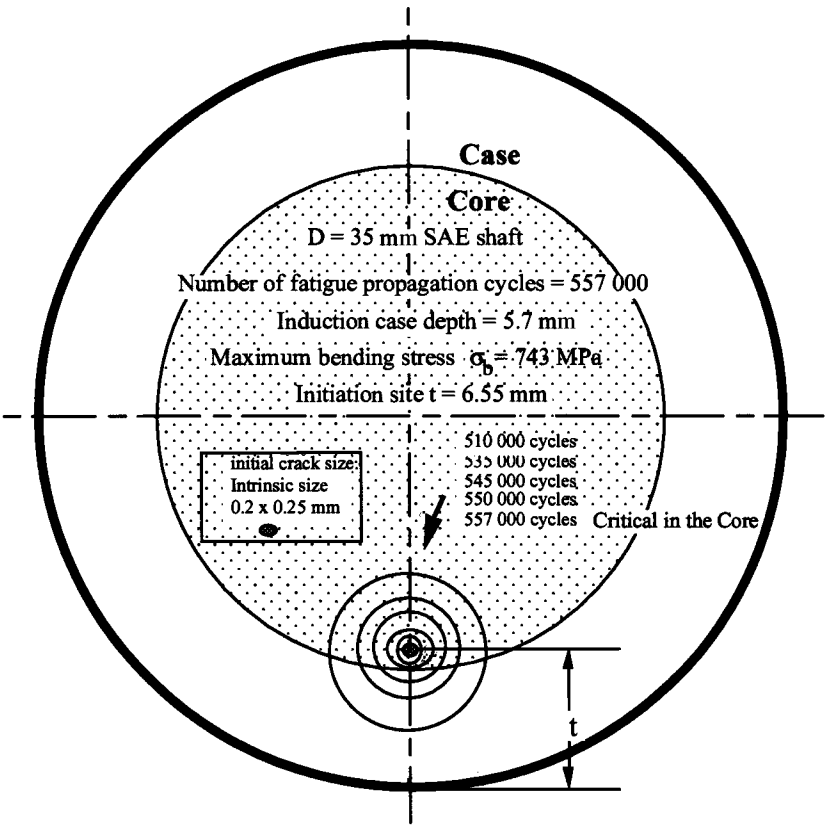

FIG. 14—*Predicted fatigue crack growth of subsurface elliptical crack in an SAE 1045 induction-hardened shaft of* D = *35 mm under bending load.*

up to $a = 0.5$ mm. The crack growth rate increased significantly with the increasing crack size. After 5.57×10^5 cycles, Point A ($\phi = 90°$) becomes critical due to the resultant final $K_{max} + K_{res}$ of 60 MPa$\sqrt{m}$ exceeded fracture toughness of the core material of $K_Q = 59$ MPa$\sqrt{m}$.

It was found from the above analysis that the time from the formation of the subsurface crack to a crack size of $a = 0.5$ mm could consume about 90% of the total fatigue life. The remainder of the fatigue life was the growth from $a = 0.5$ mm to the final fracture size of around $a_f = 2$ mm.

Discriminating Fatigue Crack Growth Testing

Testing Procedures

Three-point bending fatigue crack growth tests were performed using a computer-controlled 100-kN closed-loop electrohydraulic test system with sinusoidal constant amplitude loading waveform at about 5-Hz frequency. All fatigue crack growth tests were conducted in load control under loading stress ratio of $R = P_{min}/P_{max} = 0.05$, and in laboratory air at room temperature.

The experimental procedure consisted of the investigation of crack growth patterns under a designed loading history. For the purpose of verifying the analytical fatigue crack growth calculations of induction-hardened round shafts in the testing, the "beach mark technique" was used with the loading cycles in order to create underload markings during fatigue crack growth and to facilitate later measurement of the crack size during the fatigue crack growth. The underload markings can be obtained by dividing the constant amplitude loading cycles at several stages using the much lower loading cycles, which will leave underloading marks from the previous test loading cycles. For this purpose the load amplitude was reduced by 15 to 30%, while applied stress ratio R was kept the same; depending upon the fatigue crack growth rate, the beach mark procedure used $N = 3000$ to 10 000 cycles. After final fracture, the crack shape, size, and growth rate were determined based on the measurements from the fractographic and SEM studies. The resulting fatigue crack growth of this investigation was compared to the numerical/analytical analysis for verification.

Testing Results and Discussions

Two specimens with a 6-mm induction-hardened depth showed subsurface crack growth beach marks on the fracture surface. The detailed information of these test results is given in Table 4. Information included in these tables are the depth of the crack initiation site (t), testing load range (ΔP_l), marking load range (ΔP_m), the total fatigue life cycles (N_t) (neglects marking load cycles), and a brief description of the apparent cracked surface. Fracture surface of Specimen Bar-D35-6#2 was selected for failure analysis and for verifying the fatigue crack growth model in this paper.

Figure 15 presents the complete section of a fractured shaft of a specimen identified as Bar-D35-6#2 with a 6-mm hardening depth. This is a macroscopically flat fracture. The fracture originated at a subsurface location in the core region near the transition zone (induction-hardening heat effective area) between the core and the case. The subsurface fatigue crack resulted in the formation of a

TABLE 4—*Test results of speciments with a 6-mm induction-hardened depth.*

Specimen	Initiation Site	Surface Appearance	Loading Range, ΔP_l (kN)	Marking Range, ΔP_m (kN)	Loading Fatigue Life,[a] N_t (cycles)
Bar-D35-6#1	$t = 6.25$ mm	One beach mark	68-72-74	52	1.55×10^6
Bar-D35-6#2	$t = 6.5$ mm	One beach mark	70	56	1.18×10^6

[a] Marking load cycles were not included.

FIG. 15—*Macrofractograph of Specimen Bar-D35#6-2 (2×).*

smooth-textured, light-colored surface. No clear indication of an existing inclusion or a flaw was evident in the center of the initiation site. A higher magnification of the fatigue surface of the same specimen is given in Fig. 16. One beach mark is visible in this figure and is labeled.

The final fracture occurred at $P = 70$ KN, and the total loading cycles (excluding the beach-marking cycles) were $N_{total} = 1.18 \times 10^6$. Figure 17 shows the detail loading history. By tracing back the loading history from the final fracture, it was determined that the beach mark was obtained under $P = 56$ KN for 20 000 cycles (the last beach marking load that was performed on the specimen). This beach mark provided two analytical verification opportunities for comparing the experimental results with the provided fatigue crack growth model for a subsurface crack in the SAE 1045 induction-hardened shaft specimen; one is the beach mark caused under $P = 56$ KN for 20 000 cycles, and the other is after the beach mark to the final fracture caused under $P = 70$ KN for 17 790 cycles. For detailed information of the analytical verification refer to Ref *13*.

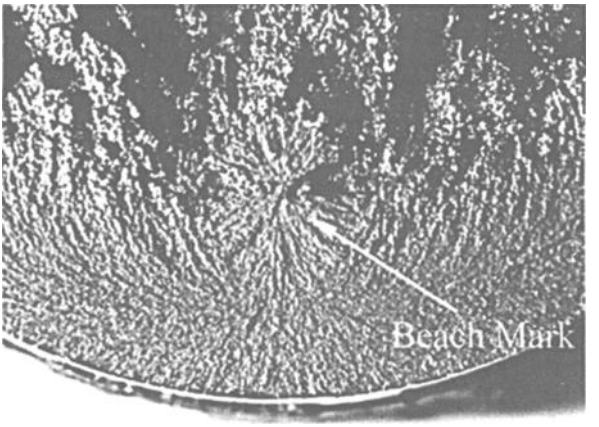

FIG. 16—*Macrofractograph of fatigue surface of the Specimen Bar-D35-6#2 (5×).*

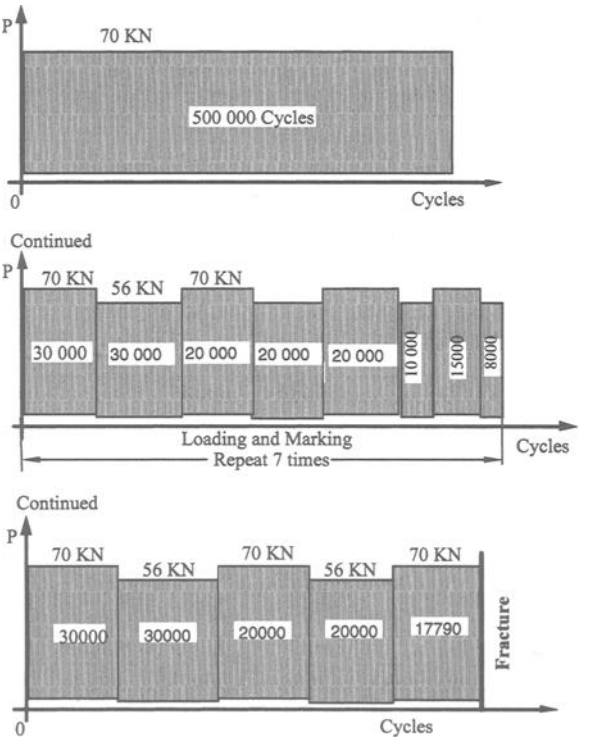

FIG. 17—*Loading history of Specimen Bar-D35-6#2.*

Comparison of Calculated and Experimental Fatigue Lives of SAE 1045 Induction-Hardened Specimens

The calculated total fatigue lives (initiation and propagation) of SAE 1045 induction hardened specimens (with a 6-mm induction-hardened depth) were compared with the experimental test results. The initiation crack sizes and sites used in the analytical calculations were measured from specimens under a microscope. Table 5 shows the comparison. SWT's approach was used to calculate the fatigue initiation life. Included in Table 5 are the applied bending stress (σ_b), measured initiation site (t), calculated fatigue crack initiation life (N_i), measured crack initiation size (a_0), calculated fatigue crack growth life (N_p), calculated total fatigue life (N_t), experimental total fatigue life (N_t), and the comparison factor between calculated and experimental total fatigue life. As can be seen from the table, the analytical models of fatigue crack growth agree with the experimental fatigue life of induction-hardened shafts very well. A general factor of 0.6 to 0.8 was obtained in the total fatigue life calculations in this research compared with the experimental results. Calculations were conservative.

It was demonstrated from the experimental verification results that the fatigue crack growth model developed in this study is capable of predicting fatigue crack propagation life in the SAE 1045 induction-hardened shafts under the bending loads. The total fatigue life calculations with a factor from 0.6 to 0.8 are quite encouraging. It was also found from the above table that fatigue crack propagation life dominated the total fatigue life for the SAE 1045 induction-hardened shaft specimens. The crack propagation could consume about 95% of the total fatigue life.

TABLE 5—*Comparison of calculated and experimental fatigue of life of 1045 induction-hardened specimens under bending at* R = *0.05.*

Specimen	Applied Bending, σ_b (MPa)	Initiation Site, t (mm)	Initiation Life, N_i (Cycles)	Initiation Size, a_0 (mm)	Crack Growth Life, N_p (cycles)	Calculated $N_t = N_i + N_p$ (cycles)	Experimental $N_t = N_i + N_p$ (cycles)	Calculated/Experimental
Bar-D35-6#1	1144 to 1245	6.25	2.4×10^4 (SWT)	$a_0/b_0 = 0.75$ $a_0 = 0.15$ mm $b_0 = 0.2$ mm	9.48×10^5	9.72×10^5	1.55×10^6	0.64
Bar-D35-6#2	1178	6.5	2.6×10^4 (SWT)	$a_0/b_0 = 0.75$ $a_0 = 0.15$ mm $b_0 = 0.2$ mm	9.54×10^5	9.8×10^5	1.18×10^6	0.83

Conclusions

An analytical procedure for the fatigue life prediction of induction-hardened shafts under the effect of residual and applied bending stresses has been developed. It has been demonstrated that the fatigue crack propagation life dominated the total fatigue life for the SAE 1045 induction-hardened shaft because of the large surface compressive residual stresses. It is clear from the experimental verification results that the fatigue crack growth model developed in this study is capable of predicting fatigue crack propagation life in the SAE 1045 induction-hardened shafts under the bending loads. The total fatigue life calculations with a factor from 0.6 to 0.8 are quite encouraging.

Acknowledgments

This work was sponsored by John Deere Dubuque Works. The authors wish to express their gratitude to John Deere engineers Greg Werner and Lee Tucker for their support, effort, and assistance in this investigation. The authors are particularly grateful to John Deere engineer Tom Cordes for his valuable discussions, time, and encouragement during the course of the study. The assistance provided by An-Yu Kuo of Optimal Corporation, Paul Prevey of Lambda Research, and Dan DeRoo of John Deere is also acknowledged.

References

[1] Boyer, H. E., *Practical Heat Treating,* American Society for Metals, Metals Park, OH, 1984.

[2] Kurath, P. and Jiang, Y., "Analysis of Residual Stresses and Cyclic Deformation for Induction Hardened Components," *SAE Technical Paper 950707,* SAE International, Warrendale, PA, 1995.

[3] Landgraf, R. W. and Chernenkoff, R. A., "Residual Stress Effects on Fatigue of Surface Processed Steels," *Analytical and Experimental Methods for Residual Stress Effects in Fatigue, ASTM STP 1004,* R. L. Champoux, J. H. Underwood, and J. A. Kapp, Eds., American Society for Testing and Materials, West Conshohocken, PA, 1988, pp. 1–12.

[4] Dindinger, P. M., "SAE 1045 Phase II Axial Fatigue Properties," SAE Fatigue Design and Evaluation Committee Minutes, Cincinnati, OH, March 1993, SAE, Warrendale, PA.

[5] Deere & Company, "Typical Residual Stress Depth Analysis for an SAE 1045 Induction Hardened Component," SAE Fatigue Design and Evaluation Committee Minutes, Tulsa, Oklahoma, October 1987, SAE, Warrendale, PA.

[6] Communication with Cordes, T., senior staff engineer, Deere & Company Technical Center, Moline, IL, December 1996.

[7] Prevey, P. S., "X-ray Diffraction Determination of the Triaxial Residual Stress State and Cyclic Relaxation in SAE 1045 Biaxial Fatigue Specimens," submitted for publication in *AE-14++*, SAE International, Warrendale, PA 1997.

[8] Starker, P., Wohlfahrt, H., and Macherauch, E., "Subsurface Crack Initiation During Fatigue as a Result of Residual Stresses," *Fatigue of Engineering Materials and Structures,* Vol. 1, 1979, pp. 319–327.

[9] Qian, J., Fatemi, A., and Cordes, T. S., "The Influence of Subsurface Nucleation on Uniaxial Fatigue Behavior of Ion Nitrided Specimens," *Fatigue 93,* J. P. Bailon and J. I. Dickson, Eds., EMAS, 1993, pp. 329–334.

[10] Lindner, M. J. and Elbella, A., "Fatigue Analysis of Induction Hardened Pins," *Reliability, Stress Analysis, and Failure Prevention,* ASME, New York, 1993, pp. 105–110.

[11] Kitagawa, H. and Takahashi, S., *Proceedings of 2nd International Conference on Mechanical Behavior of Materials,* Boston, MA, 1976.

[12] Werner, G. K. and Stephens, R. I., "Fatigue Crack Growth Properties of 1045 Hot-Rolled Steel," *Multiaxial Fatigue: Analysis and Experiments, AE-14,* G. E. Leese and D. Socie, Eds., 1989, pp. 81–96.

[13] Zhang Freking, H. Y., "Fatigue Crack Growth Behavior of Induction Hardened Shafts under the Effect of Residual and Applied Bending Stresses," Ph. D. dissertation, The University of Iowa, May 1998.

[14] Kuo, A. U., Shvarts, S., and Chen, K. L., "K-solver, A Stress Intensity Factor Calculator for a 3-D Crack under Arbitrary Mixed Mode Loading," *Structural Integrity Associates,* Inc., 1993.

[15] Chen, K. L., Kuo, A. Y., and Shvarts, S., "Stress Intensity Factor Solutions for Partial Elliptical Surface Cracks in Cylindrical Shafts," *Fracture Mechanics: Twenty-Third Symposium, ASTM STP 1189,* R. Chona, Ed., American Society for Testing and Materials, West Conshohocken, PA, 1993, pp. 394–416.

[16] Kuo, A. Y. and Shvarts, S., "An Analytical Solution for an Elliptical Crack in a Flat Plate Subjected to Arbitrary Loading," *Fracture Mechanics: Twenty-second Symposium, ASTM STP 1131,* Vol. 2, S. N. Atluri,

J. C. Newman, Jr., and J. S. Epstein, Eds., American Society of Testing and Materials, West Conshohocken, PA, 1992, pp. 347–367.

[17] Chen, D., Nisitani, H., and Mori, K., "Stress Intensity Factors for a Fish-eye in a Shaft," *Transaction of the Japan Society of Mechanical Engineers,* Vol. 57, 1991, pp. 1768–1774.

[18] Zhang, H. Y., "Stress Intensity Factors for Round Bars and Fracture Toughness of SAE 1045 Steel Round Bars under Three Different Heat Treatments," Master's thesis, The University of Iowa, May 1995.

Session IV

Richard W. Hertzberg[1]

Estimation Procedure for Determination of Fatigue Crack Propagation in Metal Alloys

REFERENCE: Hertzberg, R. W., **"Estimation Procedure for Determination of Fatigue Crack Propagation in Metal Alloys,"** *Fatigue and Fracture Mechanics: 30th Volume, ASTM STP 1360,* P. C. Paris and K. L. Jerina, Eds., American Society for Testing and Materials, West Conshohocken, PA, 2000, pp. 261–277.

ABSTRACT: Estimation of closure-corrected fatigue crack propagation (FCP) data in monolithic metal alloys was reported recently by the author, using a simple computational method. The quantity $E\sqrt{\mathbf{b}}$, where E = the modulus of elasticity, and **b**, the dislocation Burgers vector, is used to define a stress intensity factor, corresponding to an FCP rate of **b**/cyc. The remainder of the FCP curve at higher FCP rates (where $da/dN > \mathbf{b}$) is found to follow a relation of the form: $da/dN = (\Delta K/E)^3(1/\sqrt{\mathbf{b}})$. Good agreement is found between computed FCP data and recently reported experimental test results for various aluminum, titanium, and steel alloys. Such computations allow for a rapid and inexpensive way to estimate the FCP response of metals under both long and short crack growth conditions.

KEYWORDS: fatigue crack propagation, crack closure, fatigue calculations, K^c_{max} test methods

For the past 40 years, the use of fracture mechanics concepts in the design of structural components has led to their improved safety and reliability. Of particular note, the dynamics of fatigue crack propagation (FCP) were greatly clarified by Paris et al. [*1*], who demonstrated a strong relation between FCP rates and the prevailing stress intensity factor range at the advancing crack tip, wherein

$$da/dN = A\Delta K^m \tag{1}$$

where

da/dN = crack growth increment/loading cycle,
ΔK = stress intensity factor range ($K_{max} - K_{min}$), and
A,m = f (material, test, and environmental variables).

Various investigators determined that the fatigue response of different metallic alloy groups varied greatly from one another (e.g., aluminum versus steel versus titanium alloys) and that major differences in FCP behavior could exist within a particular metal group. Regarding the role of material variables, investigators determined that the fatigue resistance of metal alloys was dependent on both microstructure-sensitive and microstructure-insensitive properties. Regarding the latter, early success in reconciling substantial differences in FCP behavior between different classes of metals (e.g., aluminum, titanium, and ferrous alloys) involved the normalization of ΔK values for each alloy by the material's respective modulus of elasticity (E) [*2*]. In parallel fashion, Bates and Clark [*3*] determined that fatigue striation spacings, found on the fracture surfaces and relating to the incremental advance

[1] New Jersey Zinc professor of Materials Science and Engineering, Department of Materials Science and Engineering, 5 E. Packer Avenue, Lehigh University, Bethlehem, PA 18105.

of the crack with each loading cycle, also could be normalized by E with a relation of the form

$$\text{striation spacing} \approx 6\left(\frac{\Delta K}{E}\right)^2 \tag{2}$$

Equation 2 has proven useful in post-failure analyses of structural failures as well as in the understanding of fundamental material behavior.

Reconciling the FCP response of a particular metallic system in terms of microstructure-sensitive material properties and/or deformation characteristics has proven to be a more challenging task. For example, large differences in FCP rates for a given alloy system have been reported to depend on grain size; the size, chemistry, and distribution of second phase microconstituents, and changes in slip character [*4*]. Based on concepts proposed by Elber [*5,6*], the influences of these material variables on FCP response often have been reconciled by the extent of crack closure at the advancing crack tip. Regarding the latter, it has been shown that the crack may be partially closed during the loading cycle, even though the mean stress is greater than zero. Crack closure has been attributed to crack surface interference in association with residual tensile displacements from the plastic deformation process, oxide layer interference, and/or interference between mating fracture asperities [*7*]. Elber demonstrated that crack closure measurements may be used to define an *effective* crack tip stress intensity factor range, ΔK_{eff} (where $\Delta K_{eff} = K_{\text{maximum}} - K_{\text{open}}$), that characterizes the intrinsic fatigue crack growth response of a given alloy. Indeed, improved correlations in FCP data were found in numerous alloy systems when FCP data were compared, based on closure-corrected ΔK_{eff} values rather than on ΔK_{app} values [*4*].

Accelerated Experimental Test Methods

To date, uncertainties persist regarding the determination of the most correct method needed to determine ΔK_{eff}. These difficulties involve the precision of crack closure measurements, the identification of the relevant data for the determination of the closure event, and the proper definition of closure itself [*8*]. Work is continuing to resolve these experimental and analytical difficulties. For example, Donald and others [*9,10*] suggest that ΔK_{eff} may be determined in terms of certain load-strain compliance ratios without the need to define a specific K_{op} value. Alternatively, this author and co-workers [*11*] have determined that a convenient approximation of closure-free FCP data can be obtained when tests are conducted under constant $K_{\max}$ conditions. This so-called $K^c_{\max}$ test procedure leads to increasing load ratios (i.e., R values) which, in turn, result in decreased levels of crack closure. Accordingly, the $K^c_{\max}$ test rapidly generates a closure-free test environment as the crack lengthens, wherein ΔK_{app} rapidly approaches ΔK_{eff}. As such, this test procedure provides for a rapid and convenient method by which ΔK_{eff} data may be generated. For example, estimates of ΔK_{eff} data can be generated in half a day's testing time as compared with several days of testing time needed for more conventional constant-R ratio test procedures; also, the difficulties of obtaining reliable crack closure data are eliminated. It should be noted that some uncertainties remain as to the most appropriate value of $K_{\max}$ to use in the $K^c_{\max}$ test method, but both experimental and analytical progress is being made in this regard [*9,10,12*].

$K^c_{\max}$ testing procedures also provide a rapid and inexpensive method by which an upper bound estimate of short crack growth rate behavior may be identified [*13,14*]. Several examples of the use of $K^c_{\max}$ testing for the estimation of short crack behavior has been reported by the author (e.g., see Fig. 1). Meaningful ΔK_{eff} data can be generated in even less time through use of a step-down procedure [*15*]. Here, a small block of FCP data is generated at a high ΔK level and then $K_{\min}$ is raised abruptly to produce a sharply lower level of ΔK_{eff} (Fig. 2*a*). Since $K_{\max}$ remains the same, no overload interaction effect is experienced such that additional FCP data may be generated at a much lower ΔK level. As such, a few such blocks of data under $K^c_{\max}$ test conditions provide the investigator within a very

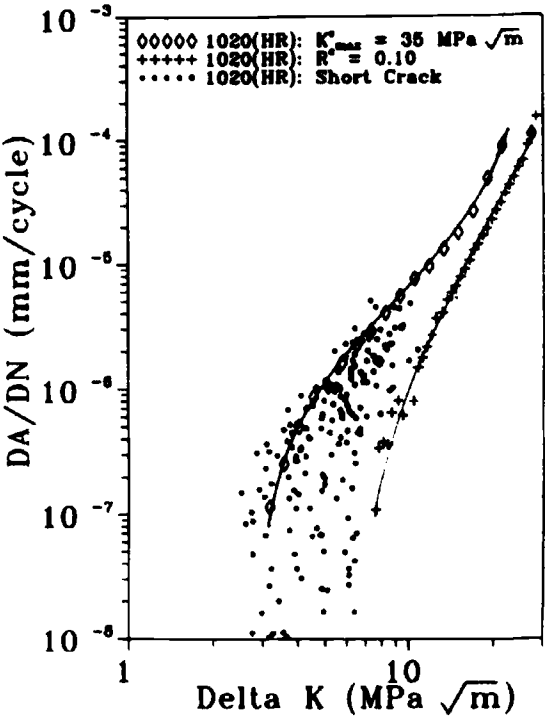

FIG. 1—*FCP data reveals that* K^c_{max} *data provide upper bound agreement with short crack results in 1020 steel [14].*

short period of time an outline of the material's closure-free FCP response (Fig. 2*b*). In a closely related manner, such K^c_{max} testing blocks introduce clearly defined marker bands on the fracture surface, while at the same time not interfering with the dynamics of the fatigue crack propagation process (Fig. 2*c*) [*15,16*].

Computational Methods

Proceeding further, the author [*17,18*] previously reported a simple computational method to estimate certain closure-corrected FCP data using only two fundamental microstructure-insensitive material constants—Young's modulus, E, and the dislocation Burgers vector, **b**. For the case of closure-corrected data, it was found that when ΔK_{th} values for several alloy systems (determined by ASTM Standard Test Method for Measurement of Fatigue Crack Growth Rates (E 647-95a) test procedures and corresponding to a growth rate of 10^{-10} m/cycle) were normalized by the respective material's modulus of elasticity, values of $(\Delta K_{th}/E)^2$ (units of m) were found to be comparable to the magnitude of the respective material's Burgers vector, **b** (see Ref *17*, Table 1). Accordingly, this author suggested the existence of a closely related ΔK level near ΔK_{th}, ΔK_b, where the macroscopic fatigue crack growth rate was equal to the size of the material's Burgers vector. (For the case of most commercial metallic alloys, **b** has numerical values in the range of $2.5 - 3.0 \times 10^{-10}$m.) Therefore,

$$\left(\frac{\Delta K_b}{E}\right)^2 = \mathbf{b} \tag{3}$$

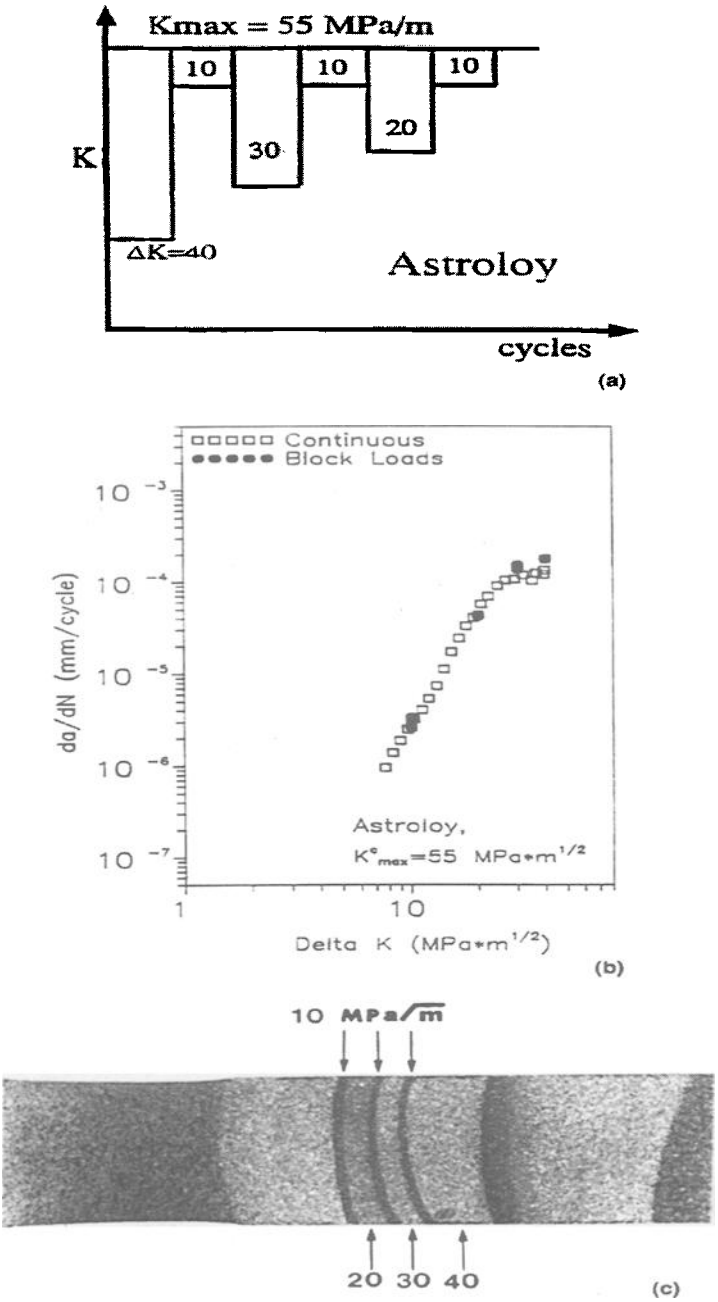

FIG. 2—*Influence of block loading on FCP response and fracture surface appearance in Astroloy nickel-base alloy [15]:* (a) *Block loading profile. Note that* K_{max} *remains constant;* (b) *agreement between FCP results based on continuous and block loading test conditions;* (c) *macroscopic fracture surface appearance revealing distinct marker bands corresponding to discrete load blocks (unstable fracture at left). Note dark fracture surface appearance in conjunction with both low and high* ΔK *loading conditions.*

where

ΔK_b = ΔK level near threshold where $da/dN = \mathbf{b}$
E = modulus of elasticity
$\mathbf{b}$ = Burgers vector

It follows from Eq 3 that a data point on the da/dN-ΔK plot (Point A) possesses coordinates of $da/dN = \mathbf{b}$ and $\Delta K_b = E\sqrt{\mathbf{b}}$, respectively (Fig. 3). This datum defines the point above which crack growth is continuous and equal to $n\mathbf{b}$ (where $n \geq 1$) and below which crack growth is discontinuous (where $n < 1$). In the latter instance, at any particular location along the crack front, growth does not occur with every loading cycle.

Further analysis of $K^c_{\max}$-generated closure-corrected FCP data reveals a third power crack growth rate dependence on ΔK with the form

$$da/dN = \boldsymbol{b}(\Delta K/\Delta K_b)^m = \boldsymbol{b}(\Delta K/\Delta K_b)^3 \tag{4}$$

When Eqs 3 and 4 are combined, it follows that

$$da/dN = \boldsymbol{b}(\Delta K/E\sqrt{\boldsymbol{b}})^3 = (\Delta K/E)^3(1/\sqrt{\boldsymbol{b}}) \tag{5}$$

Equation 5 can then be used to estimate the da/dN-ΔK plot for closure-corrected FCP data for crack growth rates $\geq \mathbf{b}$/cycle. Several examples of experimental and computed data for several alloys are shown in Fig. 3.

Note the agreement between the essentially closure-free $K^c_{\max}$ experimental test results and the computed data (see Line A-B), where Point B corresponds to 10 ΔK_b. It is also encouraging to note that Eq 5 serves as an upper bound estimate for short crack behavior and agrees well with $K^c_{\max}$ test results. For example, Fig. 1 is replotted along with computed data and shown in Fig. 3*c*.

In a recent publication, McClintock [*19*] examined a different group of data and arrived at a similar relation, with ΔK_b being empirically approximated by $E\sqrt{2\mathbf{b}}$ and the growth rate relation given as

$$da/dN = \boldsymbol{b}(\Delta K/E\sqrt{2\boldsymbol{b}})^{3.5} \tag{6}$$

Minor differences are found when Eqs 5 and 6 are compared; McClintock's relation contains an additional factor of $\sqrt{2}$ in the determination of ΔK_b and the estimation of the power dependence (m) is 3.5 versus 3 in the present study. These discrepancies may be related to the fact that much of McClintock's database pertained to ΔK_{app} information, whereas ΔK_{eff} data were used in earlier publications by this author. Since ΔK_{eff} data are believed to be a better reflection of a material's intrinsic fatigue response, their use in fundamental calculations is believed to be more meaningful. Nonetheless, these differences are considered to be minor, especially when compared with the fact that the two relations are of the same form and both offer a simple means by which experimental fatigue crack propagation data may be estimated.

Equations 5 and 6 provide a means by which fatigue crack propagation data near ΔK_{th} and above may be estimated prior to experimental verification. Many instances can be envisioned where FCP information is unavailable for needed design purposes, such as in estimation of short crack behavior in an alloy for which only long crack data exist and in material selection where FCP data are simply not available. To illustrate, it was the author's intent to estimate the fatigue response of a Cu-Be alloy prior to conducting experimental verification of the material's FCP behavior. Curve A-B, shown in Fig. 3*d*, represents data computed based on Eq 5. Excellent agreement is found between experimentally determined ΔK_{eff} test results, based on $K^c_{\max}$ test methods, and the computed data. In this instance, the average value of "m" was found to be 3.0, as predicted from Eq 5.

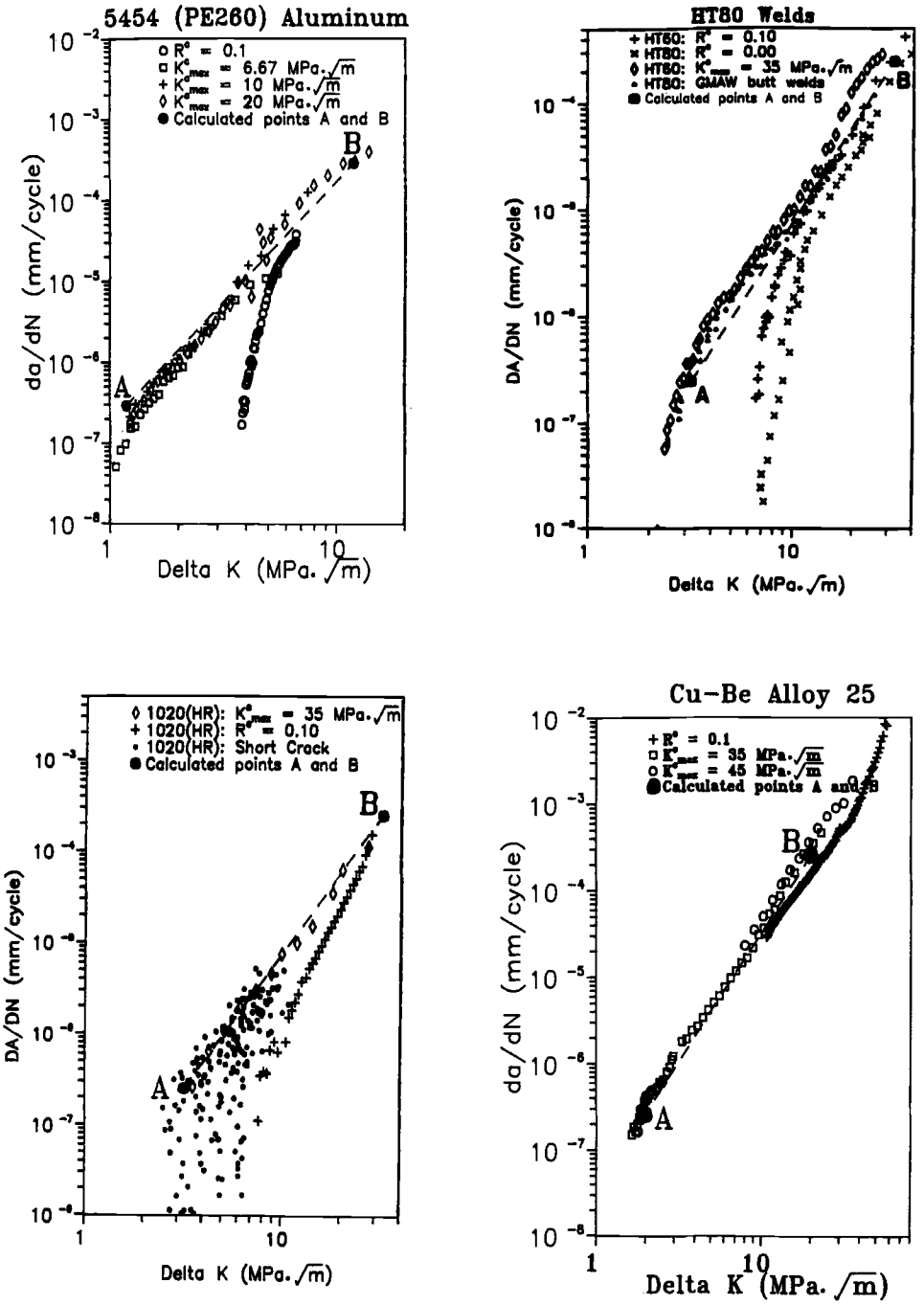

FIG. 3—*Agreement noted between* K^c_{max} *experimental data and calculated FCP results (Line A-B) based on Eq 5 [18]:* (a) *5454 (PE 260) aluminum;* (b) *HT 80 welds;* (c) *Fig. 1 replotted to include computed data (Line A-B);* (d) *calculated data for Cu-Be alloy and subsequent confirmation with experimental* K^c_{max} *test conditions.*

Additional Computational Results

To further verify the utility of Eq 5 in the computation of closure-free FCP data, this author identified additional ΔK_{eff} data from the recent literature for comparison [*9,10,12,16,20–25*]. Several examples of experimental versus computed test data are shown in Figs. 4 and 5 where the computed data are noted by a solid line A-B, corresponding to a range of ΔK values between ΔK_b and 10 ΔK_b, except where noted. Two examples for the case of 7075-T6 and AF42 cast aluminum alloys are shown in Figs. 4*a* and 4*b*. Due to the limited range of experimental data for the 7075-T6 alloy and the associated truncated plot, the computed data are shown between ΔK values of 4 and 20 MPa$\sqrt{m}$. The agreement is excellent at ΔK values of approximately 6 MPa$\sqrt{m}$ and above. For the case of the AF42 cast alloy, agreement is reasonably good when computed values are compared with experimental data, based on K^c_{max} test methods as compared with $R = 0.1$ data. This is to be expected since, as discussed above, the K^c_{max} data closely mirror ΔK_{eff} results.

Excellent agreement between experimental and computed data is shown in Figs. 4*c* and 4*d* for two closely related titanium alloys. The data shown in Fig. 4*d* are based on ΔK_{app} test results. It should be noted, however, that since Albertson et al. [*22*] reported essentially no crack closure in their tests, the ΔK_{app} data are essentially equal to ΔK_{eff} test results. Also note that in Fig. 4*d* the computed line is truncated at $\Delta K = 15$ MPa$\sqrt{m}$ since the value of 10 ΔK_b (i.e., 20 MPa$\sqrt{m}$) extends well beyond the axes of the original plot.

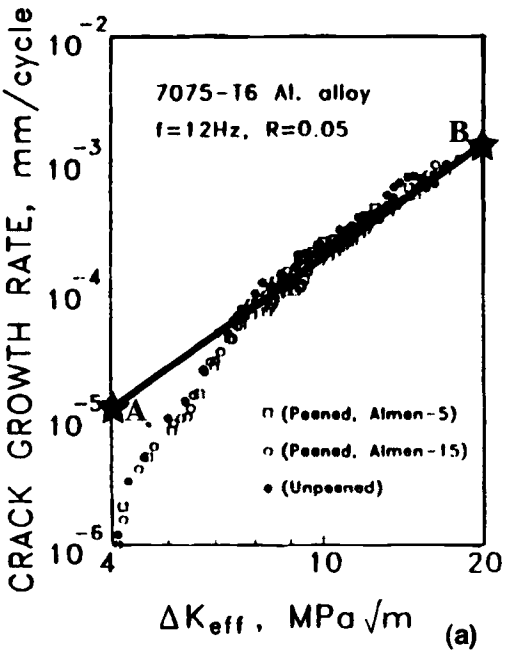

FIG. 4—*Comparison between* ΔK_{eff} *test results and computed FCP data (Line A-B) derived from Eq 5:* (a) *7075-T6 aluminum alloy* [*20*]; (b) *AF42 cast aluminum alloy* [*12*]; (c) *Ti 6246 titanium alloy* [*21*]; (d) *Ti-6222 titanium alloy* [*22*]; (e) *various steel alloys* [*23*]; (f) *dual phase steels containing continuous martensitic phase (M-C) and discontinuous martensitic phase (M-D)* [*24*]; (g) *HY 80 steel alloy* [*16*]; (h) *medium carbon steel* [*25*].

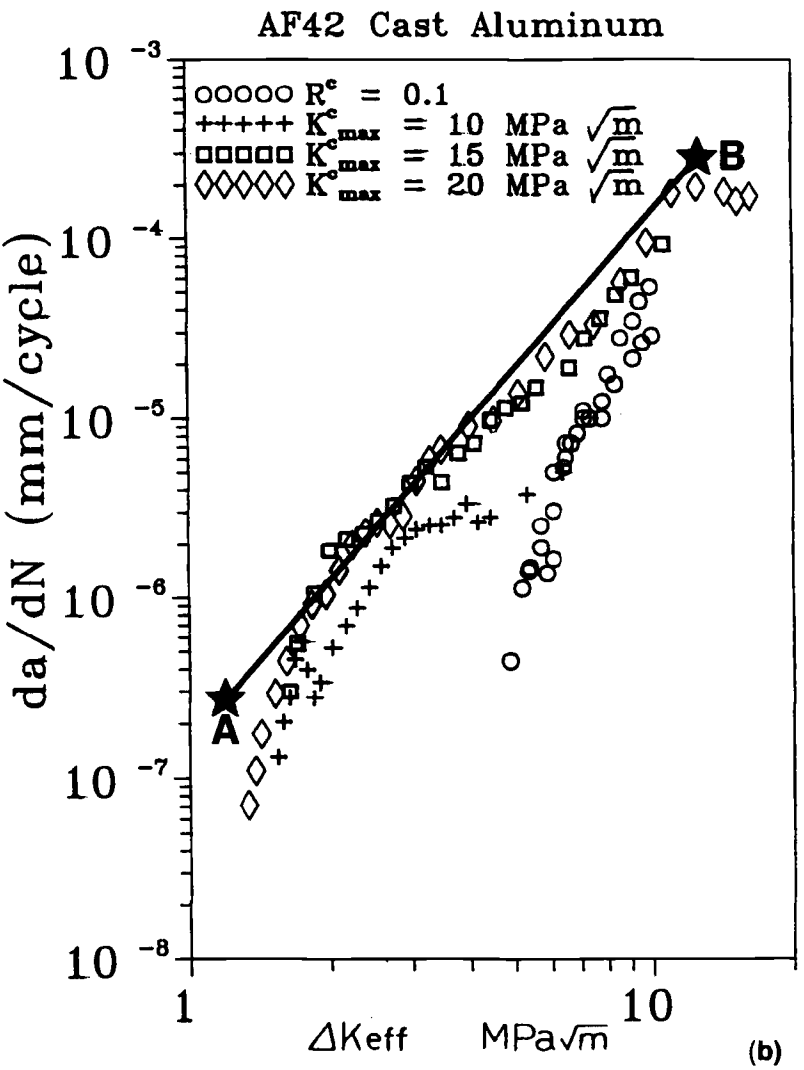

FIG. 4—*Continued*

Proceeding further, several additional experimental/computational comparisons are presented in Figs. 4*e–h* for various steel alloys. Equation 5 provides good agreement in Fig. 4*e* for ten steel alloys tested in ambient air at 20 to 50 Hz, based on data published by Petit et al. [*23*]. Figure 4*f* reveals that computed FCP data using Eq 5 serves as an upper bound for fatigue data from Nakajima et al. [*24*] for dual-phase steel alloys possessing both continuous (M-C) and discontinuous (M-D) martensitic phases. Encouraging comparisons are also found for two medium-strength steel alloys, based on results reported by Soboyejo and Knott [*16*] and Tsukada et al. [*25*] and shown in Figs. 4*g* and 4*h*, respectively.

Finally, recent ΔK_{eff} test results for three different aluminum alloys from the work of Donald and

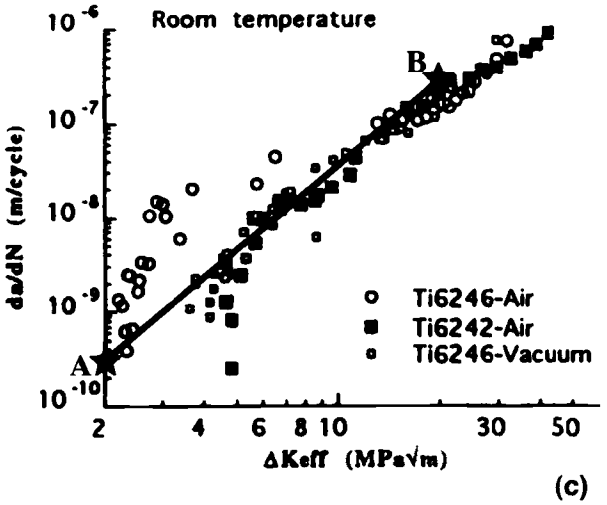

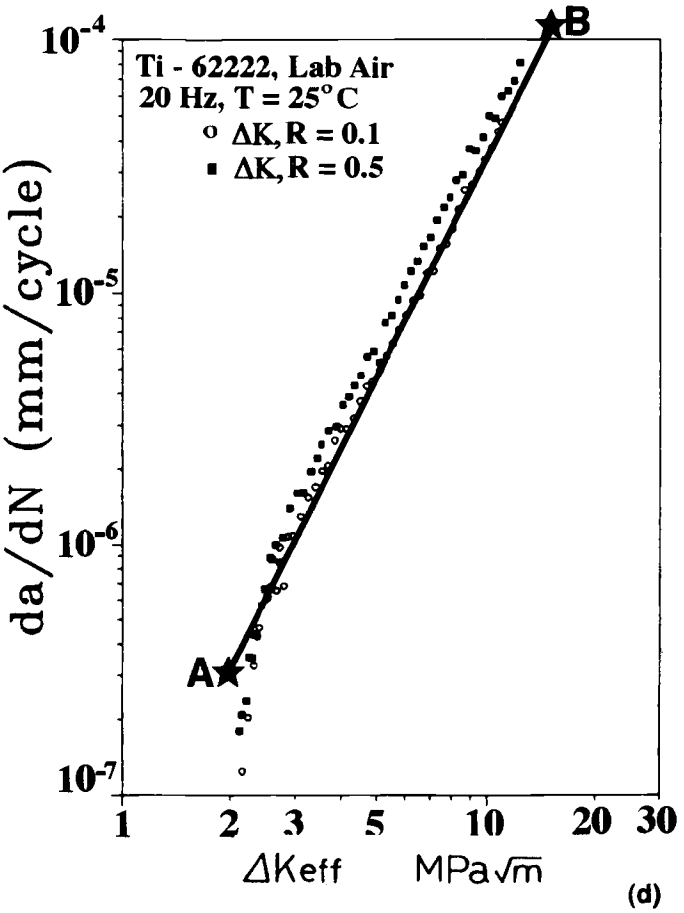

FIG. 4—*Continued*

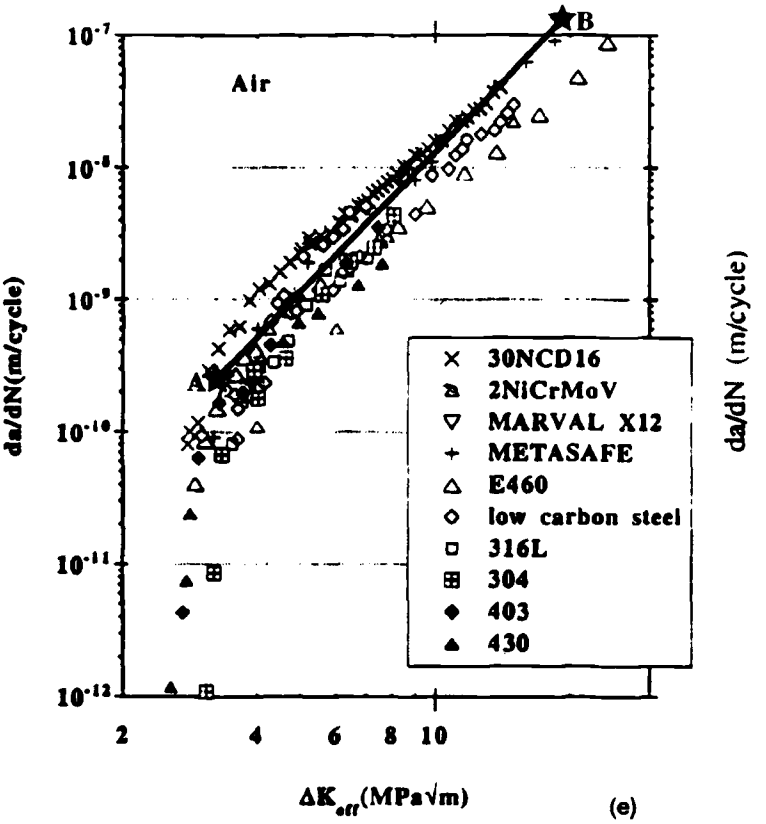

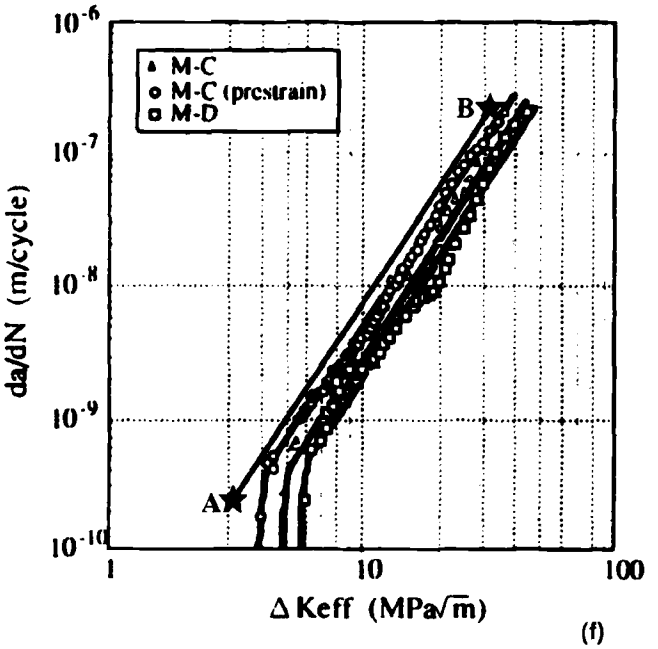

FIG. 4—*Continued73*

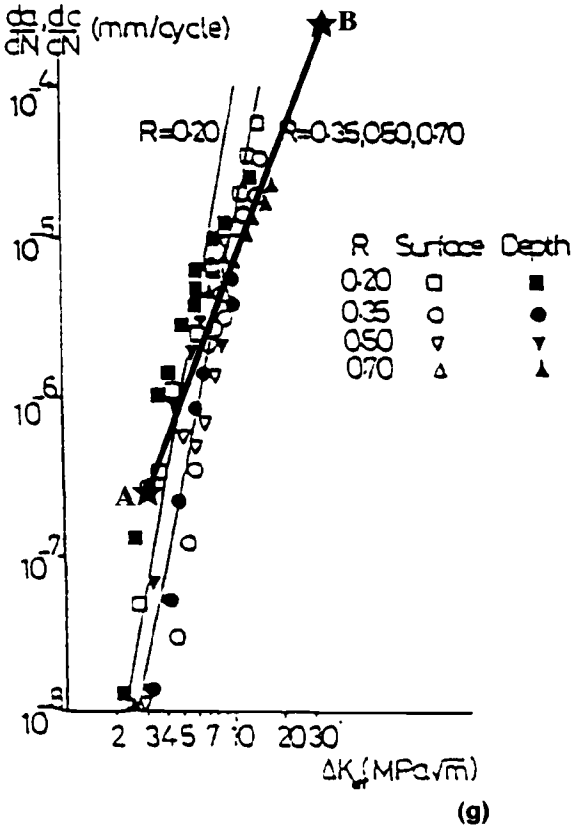

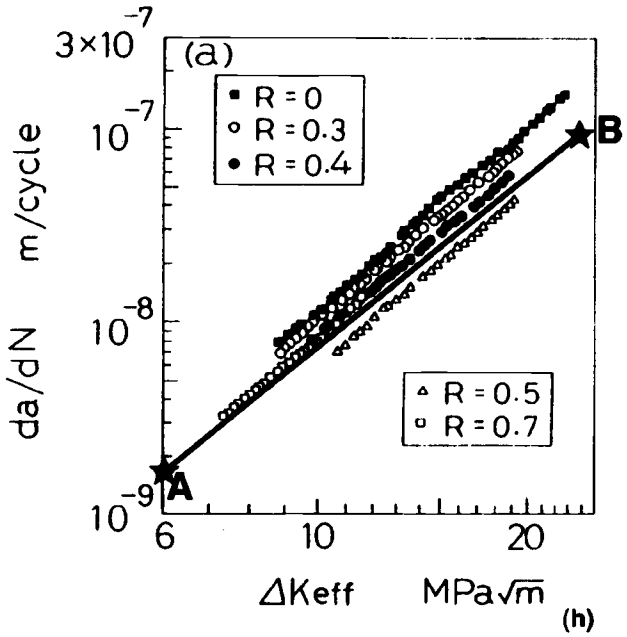

FIG. 4—*Continued*

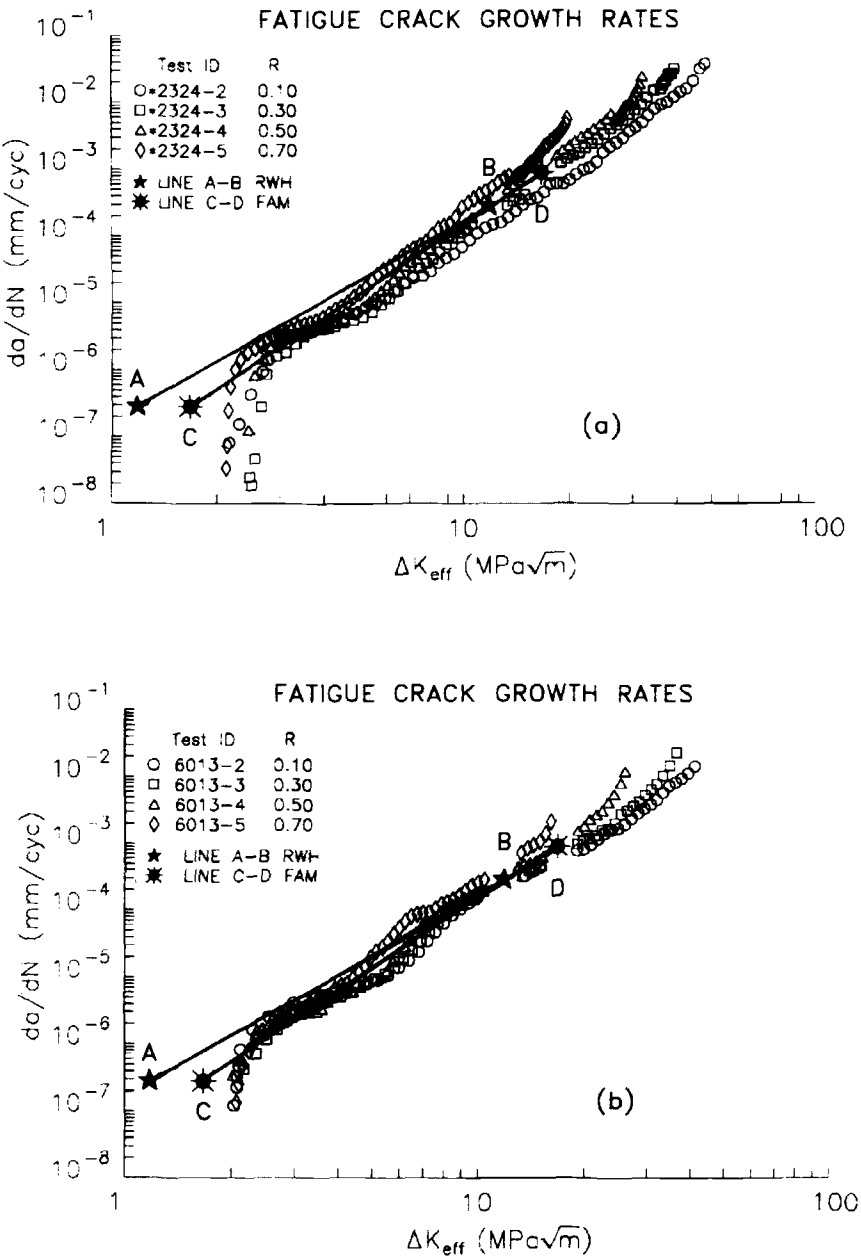

FIG. 5—*Comparison between* ΔK_{eff} *test results, based on the adjusted compliance ratio technique, and computed FCP data derived from Eq 5 (Line A-B) and Eq 6 (Line C-D). Good agreement is noted between experimental and both sets of computed data for:* (a) *2324;* (b) *6013; and* (c) *7055 aluminum alloys [9].*

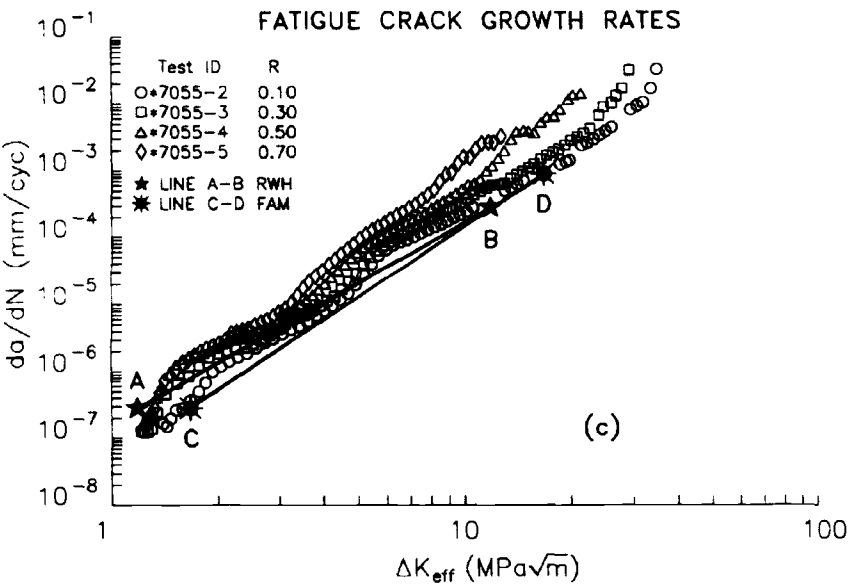

FIG. 5—*Continued*

co-workers [*9*] are shown in Fig. 5, based on their adjusted compliance ratio (ACR) technique for the determination of ΔK_{eff} conditions. Computed results are shown for both Eqs 5 and 6. As before, the simple computational method provides a useful and convenient method by which closure-corrected FCP data may be estimated.

Summary and Conclusions

Closure-corrected fatigue data provide an important means by which the fatigue crack propagation response of different metal alloys may be compared. Such data may be approximated by test results derived from time-saving K^c_{max} test methods. In a further simplification, closure-free fatigue data may be approximated by a simple calculation involving two fundamental material properties, E and **b.** A closure-corrected datum near ΔK_{th} may be computed at a crack growth rate of **b**/cycle in association with a stress intensity factor range, ΔK_b, equal to $E\sqrt{\mathbf{b}}$. Additional data at $da/dN >$ **b**/cycle are found to depend on ΔK^3, with the relation given by:

$$da/dN = (\Delta K/E)^3(1/\sqrt{b})$$

Good agreement is found between computed data and recently published ΔK_{eff} test results for various aluminum, titanium, and steel alloys. This relation provides a means by which fatigue crack propagation data near ΔK_{th} and above may be estimated prior to experimental verification. This may prove of value where FCP information is unavailable for needed design purposes, such as in estimation of short crack behavior in an alloy for which only long crack data exist and in material selection where FCP data are simply not available.

Acknowledgments

The author thanks Ms. Andrea Pressler and J. K. Donald for graphic superposition renditions of experimental and computed FCP data.

References

[1] Paris, P. C., Gomez, R. E., and Anderson, W. E., "A Rational Analytic Theory of Fatigue," *The Trend in Engineering,* Vol. 13, No. 1, 1961, pp. 9–14.

[2] Pearson, S., *Nature (London),* Vol. 211, 1966, p. 1077.

[3] Bates, R. C. and Clark, W. G., Jr., *Transactions Quarterly,* Vol. 62, No. 2, ASME, 1969, p. 380.

[4] Hertzberg, R. W., *Deformation and Fracture of Engineering Materials,* 4th ed., John Wiley and Sons, New York, 1996.

[5] Elber, W., "Fatigue Crack Closure Under Cyclic Tension," *Engineering Fracture Mechanics,* Vol. 2, 1970, pp. 37–45.

[6] Elber, W., "The Significance of Fatigue Crack Closure," *Damage Tolerance in Aircraft Structures, ASTM STP 486,* American Society for Testing and Materials, 1971, pp. 230–242.

[7] Suresh, S. and Ritchie, R. O., *Metallurgical Transactions,* Vol. 13A, 1982, p. 1627.

[8] Hertzberg, R. W., Newton, C. H., and Jaccard, R., "Crack Closure: Correlation and Confusion," *Mechanics of Fatigue Crack Closure, ASTM STP 982,* American Society for Testing and Materials, West Conshohocken, PA, 1988, pp. 139–148.

[9] Bray, G. H. and Donald, J. K., "Separating the Influence of K_{max} from Closure-Related Stress Ratio Effects Using the Adjusted Compliance Ratio Technique," *Advances in Fatigue Crack Closure Measurements and Analysis: Second Volume, ASTM STP 1343,* R. C. McClung and J. C. Newman, Jr., Eds., American Society for Testing and Materials, West Conshohocken, PA, 1997, pp. xxx.

[10] Donald, J. K., Bray, G. H., and Bush, R. W., "Introducing the K_{max} Sensitivity Concept for Correlating Fatigue Crack Growth Data," *High Cycle Fatigue of Structural Materials,* W. O. Soboyejo and T. S. Srivastan, Eds., The Minerals, Metals & Materials Society, 1997, pp. 123–141.

[11] Herman, W. A., Hertzberg, R. W., Newton, C. H., and Jaccard, R., "A Re-evaluation of Fatigue Threshold Test Methods," *Fatigue 87,* Vol. II, R. O. Ritchie and E. A. Starke, Jr., Eds., EMAS, 1987, pp. 819–828.

[12] Clark, T. R., Herman, W. A., Hertzberg, R. W., and Jaccard, R., "A Technical Note: Influence of Mean Stress on Fatigue in Several Aluminum Alloys Utilizing K^c_{max} Threshold Procedures," *Fatigue Fracture of Engineering Materials and Structures,* Vol. 19, No. 7, 1996, pp. 949–954.

[13] Herman, W. A., Hertzberg, R. W., and Jaccard, R., "A Simplified Laboratory Approach for the Prediction of Short Crack Behavior in Engineering Structures." *Journal of Fatigue of Engineering Structures and Materials,* Vol. 11, No. 4, 1988, pp. 303–320.

[14] Hertzberg, R. W., Herman, W. A., Clark, T. R., and Jaccard, R., "Simulation of Short Crack and Other Low Closure Loading Conditions," *Small Crack Test Methods, ASTM STP 1149,* J. M. Larsen and J. E. Allison, Eds., American Society for Testing and Materials, 1992, pp. 197–220.

[15] Ragazzo, C., Hertzberg, R. W., and Jaccard, R., "A Method for Generating Fatigue Marker Bands Using a Constant K_{max} Test Procedure," *Journal of Testing and Evaluation,* Vol. 23, No. 1, 1995, pp. 19–26.

[16] Soboyejo, W. O. and Knott, J. F., "An Investigation of Crack Closure and the Propagation of Semi-Elliptical Fatigue Cracks in Q1N (HY 80) Pressure Vessel Steel," *International Journal of Fatigue,* Vol. 17, No. 8, 1995, pp. 577–581.

[17] Hertzberg, R. W., "A Simple Calculation of da/dN-ΔK Data in the Near Threshold Regime and Above," *International Journal of Fracture,* Vol. 64, 1993, pp. R53–R58.

[18] Hertzberg, R. W., "On the Calculation of Closure-Free Fatigue Crack Propagation Data in Monolithic Metal Alloys," *Materials Science and Engineering,* Vol. A190, 1995, pp. 25–32.

[19] McClintock, F. A., "The Paris Law for Fatigue Growth in Terms of the Crack Tip Opening Displacement," *High Cycle Fatigue of Structural Materials,* W. O. Soboyejo and T. S. Srivastan, Eds., The Minerals, Metals & Materials Society, 1997, pp. 3–24.

[20] Zhu, X. Y. and Shaw, W. J. D., "Correlation of Fatigue Crack Growth Behavior with Crack Closure in Peened Specimens," *Fatigue and Fracture of Engineering Materials and Structures,* Vol. 18, No. 7/8, 1995, pp. 811–820.

[21] Sarrazin-Baudoux, C., Lesterin, S., and Petit, J., "Influence of Microstructure on the Fatigue Crack Growth Behavior of Titanium Alloys at High Temperature," *Advances in Fracture Research,* ICF9, Vol. 3, Pergamon, Amsterdam, 1997, pp. 1579–1586.

[22] Albertson, T. P., Stephens, R. R., and Bayha, T. D., "Fatigue Crack Growth of Two Advanced Titanium Alloys at Room and Elevated Temperature," *Elevated Temperature Effects on Fatigue and Fracture, ASTM STP 1297,* R. S. Piascik, R. S. Gangloff, and A. Saxena, Eds., American Society for Testing and Materials, 1997, pp. 140–161.

[23] Petit, J., Henaff, G., Sarrazin-Baudoux, C., and Lesterin, S., "Influence of Moist Atmospheres on Fatigue Crack Propagation," *Advances in Fracture Research,* ICF9, Vol. 3, B. L., Karihaloo, Y-W. Mai, M. I. Ripley, and R. O., Ritchie, Eds., Pergamon, Amsterdam, 1997, pp. 1309–1320.

[24] Nakajima, K., Yokoe, M., and Miyata, T., "The Effect of Microstructure and Prestrain on Fatigue Crack Propagation of Dual-Phase Steels," *Advances in Fracture Research,* ICF9, Vol. 3, B. L. Karihaloo, Y-W. Mai, M. I. Ripley, and R. O. Ritchie, Eds., Pergamon, Amsterdam, 1997, pp. 1541–1548.

[25] Tsukuda, H., Ogiyama, H., and Shiraishi, T., "Fatigue Crack Growth and Closure at High Stress Ratios," *Fatigue and Fracture of Engineering Materials and Structures,* Vol. 18, No. 4, 1995, pp. 503–514.

Fan Ye,[1] *Chris Mercer,*[2] *Diana Farkas,*[3] *and Winston O. Soboyejo*[4]

The Fracture and Fatigue Crack Growth Behavior of Forged Damage-Tolerant Niobium Aluminide Intermetallics

REFERENCE: Ye, F., Mercer, C., Farkas, D., and Soboyejo, W. O., **"The Fracture and Fatigue Crack Growth Behavior of Forged Damage-Tolerant Niobium Aluminide Intermetallics,"** *Fatigue and Fracture Mechanics: 30th Volume, ASTM STP 1360,* American Society for Testing and Materials, West Conshohocken, PA, 2000, pp. 278–298.

ABSTRACT: The micromechanisms of fracture and fatigue crack growth are elucidated for a new class of damage-tolerant niobium aluminide Nb_3Al-xTi intermetallics. Fatigue crack growth in alloys containing 10 and 25 at% Ti is shown to occur primarily by cleavage, while alloys containing ~40 at% Ti are shown to exhibit similar fracture and fatigue crack growth behavior to ductile metals and their alloys. Slower elevated-temperature (750°C) crack growth rates in the Nb_3Al-40Ti alloy are attributed largely to the effects of oxide-induced crack closure. The transition from cleavage fracture (in the Nb_3Al-10Ti and Nb_3Al-25Ti alloys) to ductile fracture in the Nb_3Al-40Ti is correlated with the onset of significant levels of crack-tip plasticity, which is predicted using atomistic simulations.

KEYWORDS: fatigue, fracture, niobium aluminide, atomistic simulation, toughness

The development of increased specific thrust in future aeroengines requires the use of new materials with lower density than existing nickel-base superalloys, which have typical densities in the range between 8 and 10 g/cm^3 [*1–3*]. The new materials must also have the combination of oxidation resistance and damage tolerance required for safe operation in future aerospace vehicles. Unfortunately, however, most of the alternative ceramic and intermetallic alloys have been shown to have limited damage tolerance [*4–6*]. High melting point refractory alloys have also been shown to have limited oxidation resistance at elevated temperature. There is, therefore, a need for new high-temperature structural materials with the potential to replace existing materials systems.

This paper represents the results of a recent study of fracture and fatigue crack growth in a new class of damage tolerant Nb_3Al-xTi (x = 10, 25, and 40Ti) intermetallics that was developed by Fraser and co-workers [*1*]. The transition from brittle cleavage to ductile dimpled fracture (in the 10 and 25Ti alloys) is associated with the onset of significant levels of crack-tip plasticity under monotonic loading. The onset of crack-tip plasticity is also predicted using atomistic simulations of crack-tip deformation via the embedded atom method. Similarly, the paper reports a transition from cyclic cleavage in the 10 and 25Ti alloys to ductile fatigue crack growth mechanisms in the 40Ti alloy. The Paris exponents in the 40Ti alloy are also shown to be comparable to those in ductile metals and their al-

[1] Post-doctoral research associate, Department of Materials Science and Engineering, The Ohio State University, 2041 College Road, Columbus, OH 43210-1179.

[2] Post-doctoral research associate, Department of Materials Science and Engineering, The Ohio State University, 2041 College Road, Columbus, OH 43210-1179.

[3] Professor, Department of Materials Science and Engineering, Virginia Polytechnic Institute and State University, 213 Holden Hall, Blacksburg, VA 24061-0237.

[4] Professor, Department of Mechanical and Aerospace Engineering, and the Princeton Materials Institute, Princeton University, Bowen Hall, 70 Prospect St., Princeton, NJ 08544.

loys. Slower fatigue crack growth rates in the 40Ti alloy are attributed largely to the effects of oxide-induced crack closure. The results suggest that alloys based on the 40Ti composition may soon become candidates for intermediate-temperature (700 to 800°C) structural applications.

Material

Processing and Microstructure

The Nb_3Al-xTi (x = 10, 25, and 40Ti) alloys that were examined in this study were produced by Teledyne Wah Chang, Albany, OR. Nominal and actual ingot compositions are listed in Table 1. Triple-melted ingots were produced by vacuum-arc casting in a 11.4-cm-diameter by 25.4-cm-high mold. Ingots of the 40Ti alloy were reduced to billet form by conventional upset forging processes. However, the 10 and 25Ti alloys cracked during conventional forging. These alloys were, therefore, processed using isothermal forging at 1250°C and a constant strain rate of 0.25 s^{-1}.

The resulting microstructures of the forged products are presented in Figs. 1*a*-1*d*. The forged 10Ti and 25Ti have microstructures consisting of A15 precipitates in a matrix of B2. Also, the composition of the B2 phase in the 10Ti and 25Ti alloys were Nb-6Al-10Ti and Nb-12Al-33Ti, respectively [*10*]. The compositions of the A15 phases in the 10Ti and 25Ti alloys were Nb-18Al-9Ti and Nb-21Al-24Ti, respectively [*10*]. An orthorhombic phase was also detected in the 25Ti alloy after annealing at 750°C for 25 h. The orthorhombic phase in the 25Ti alloy was distributed into star-shaped clusters in the B2 matrix. However, the 40Ti alloy contained only B2 grains in the as-forged condition. The amounts of A15 and orthorhombic phases present in these alloys were quantified using automated image analysis techniques. The results of the analysis are summarized in Table 2. The chemical composition of the orthorhombic phase was Nb-25Al-43Ti, while the B2 phase had a composition of Nb-10Al-34Ti in the 40Ti alloy [*10*]. All the alloys were tested in the as-forged condition and after annealing at 750°C for 25 h (DA). The behavior of the 40Ti alloy was also examined after solution treatment at 1150°C for 8 h and aging at 750°C for 25 h (STA). The 750°C anneal was used to stabilize the microstructure at the potential oxidation-temperature limit for the uncoated 40Ti alloy [*10*].

The as-forged microstructures of the 10Ti and 25Ti alloys consisted of elongated B2 grains. The grains are elongated in the direction perpendicular to the forging direction (Figs. 1*a* and 1*c*). Some needle-like orthorhombic grains were also identified to nucleate from the B2 grain boundaries in the 25Ti alloy. It is important to note here that the 10Ti and 25Ti alloys retained their elongated grain structure, along with a small fraction of A15 precipitates, following the 750°C stabilization anneal (Figs. 1*a*-1*d*). However, the B2 structure of the 40Ti alloy was not fully retained after annealing at 750°C for 25 h, followed by a furnace cool (DA). This resulted in the formation of a two-phase microstructure, consisting predominantly of Widmanstätten orthorhombic platelets in a matrix of B2 (Table 2).

Typical optical and transmission electron micrographs of the heat-treated 40Ti alloy are presented in Figs. 1*e* and 1*f*, respectively. Unlike the 25Ti alloy (Fig. 1*d*), the orthorhombic grains in the 40Ti alloy do not arrange themselves into star-shaped clusters (Fig. 1*f*). Instead, they form predominantly Widmanstätten structures that completely fill the prior B2 grains. The structure and composition of

TABLE 1—*Actual compositions of niobium aluminide alloys in atomic percent.*

Alloy	Nb	Al	Ti	O	N	H	C	Cu
Nb-15Al-10Ti	Bal	12.54	8.71	0.131	0.033	0.040	0.016	0.008
Nb-15Al-25Ti	Bal	15.12	25.12	0.250	0.021	0.085	0.016	0.004
Nb-15Al-40Ti	Bal	14.55	40.20	0.146	0.01	0.058	0.038	<.01

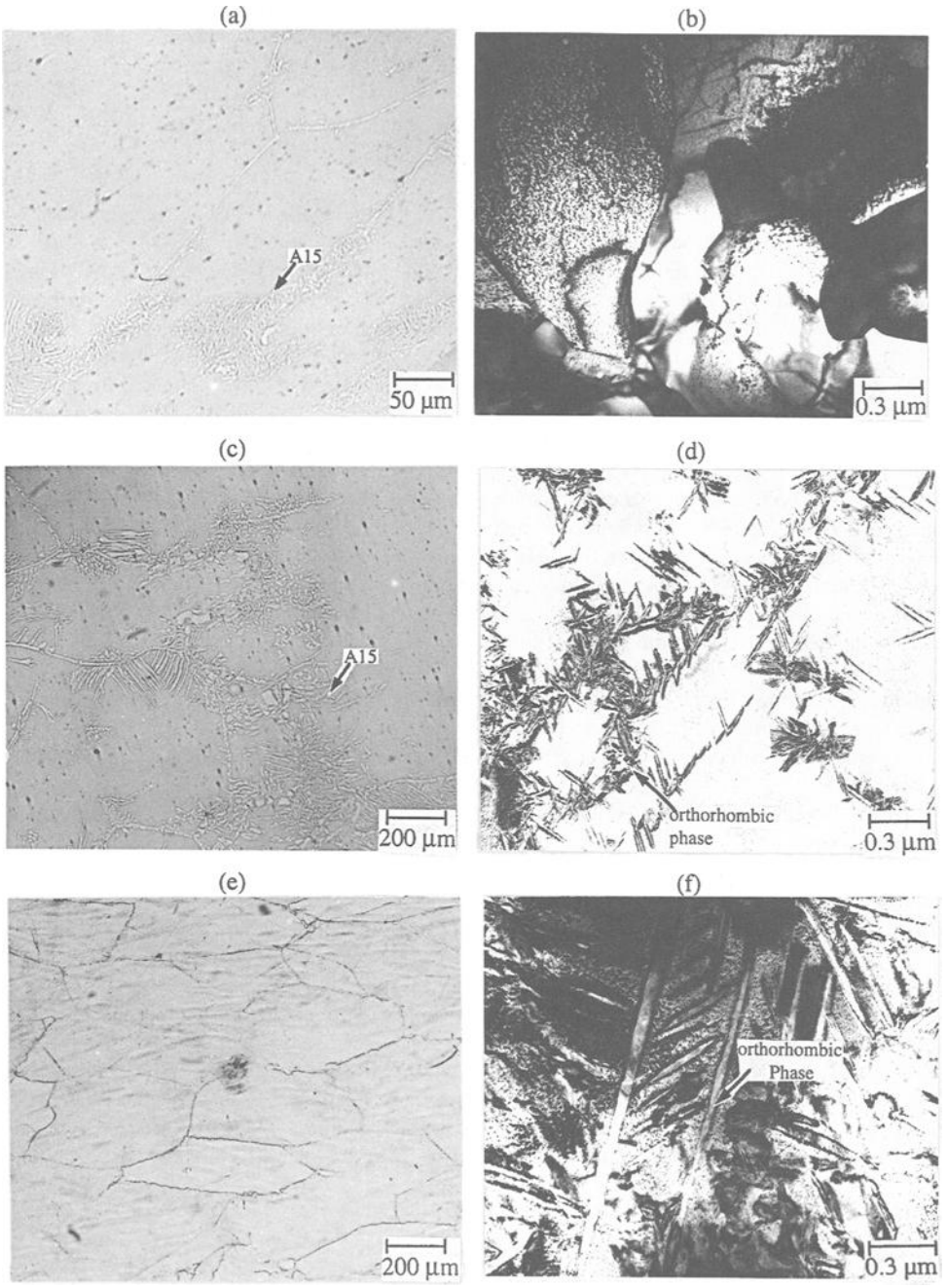

FIG. 1—*Typical microstructures of forged 10Ti* (a,b)*, 25Ti* (c,d)*, and 40Ti* (e,f) *(750°/25 h) (Figs. 1*a*, 1*c*, and 1*e *are optical micrographs; Figs. 1*b*, 1*d*, and 1*f *are bright field TEM micrographs).*

TABLE 2—*Volume fraction of phases present in niobium aluminide alloys.*

	10Ti Alloy		25Ti Alloy		40Ti Alloy	
Phases Present	As Forged	DA	As Forged	DA	As Forged	DA
A15	7 ± 1.5%	7 ± 1.5%	9 ± 2%	9 ± 2%	0	0
Orthorhombic	0	1 ± 0.5%	0	18 ± 2.5%	0	85 ± 5%

the orthorhombic phase in the 25 and 40Ti alloy were similar to those reported in earlier studies of cast niobium aluminides [*7*]. The chemical composition of the orthorhombic phase was Nb-25Al-43Ti, while the B2 phase had a composition of Nb-10Al-34Ti in the 40Ti alloy [*7–9*]. The orthorhombic phase was formed in both the 25 and 40Ti alloys after annealing at 750°C for 25 h (Figs. 1*c*-1*f*). However, the as-forged 40Ti alloy had a purely B2 structure.

Tensile Properties

The tensile properties of 10Ti, 25Ti, and 40Ti alloys are summarized in Table 3. Tension tests were performed on dog-bone specimens with 25.4 mm and a 3-mm-by-12.7-mm cross section. The results show that the 10Ti and 25Ti alloys exhibit limited ductility and low ultimate tensile strengths at room temperature. The 10Ti and 25Ti alloys also failed before bulk yielding. Fracture of these alloys occurred by brittle cleavage fracture modes in the as-forged and annealed conditions. However, the 40Ti alloy exhibits extensive ductility (~4 to 30%) and high yield strengths (695 to 904 MPa) at room temperature. The yield strengths of the 40Ti alloy also increased significantly upon annealing at 750°C for 25 h (DA). Furthermore, unlike most intermetallic materials, tensile fracture of the as-forged and annealed 40Ti alloy occurred by ductile dimpled fracture (Fig. 2). Similar behavior has been observed in the cast 40Ti alloy [*1*].

The 40Ti alloy also exhibited strain-softening behavior, and hence it does not have an ultimate tensile strength in the as-forged or heat-treated conditions. A typical stress-strain curve of the 40Ti alloy is shown in Fig. 3. Note that the as-forged alloy exhibits a plastic strain to failure of ~30% at room temperature. However, the ductility of the 40Ti alloy decreases to ~40% after annealing at 750°C for 25 h (DA). Also, almost zero ductility was observed after 1150°C/8 h + 750°C/25 h (STA) treatment,

TABLE 3—*Room temperature tensile properties of forged Nb-12Al-x Ti alloys.*

	10Ti		25Ti		40Ti	
Tensile Property	AF	DA	AF	DA	AF	DA
Young's Modulus, E (GPa)	125 ± 3.0	77.4 ± 1.5	106 ± 1.5	71.4 ± 1.1	64.6 ± 0.7	101 ± 1.0
0.2% offset yield stress, S_y (MPa)	...[a]	...[a]	...[a]	...[a]	695 ± 18	904 ± 14
Ultimate tensile strength, S_{UTS} (MPa)	200 ± 19	98 ± 17	193 ± 21	377 ± 50	...	...
Fracture strength, S_F (MPa)	200 ± 19	98 ± 17	193 ± 21	377 ± 50	1080 ± 37	951 ± 15
Total strain to failure, ε_{max} (%)	0.17 ± 0.08	0.15 ± 0.07	0.19 ± 0.08	0.51 ± 0.1	29.5 ± 0.6	3.9 ± 0.9

[a] Material fractured before yield (AF = As-forged, DA = As-forged + 750°C/25 h).
Note that the above tensile properties refer to engineering stress and engineering strain.

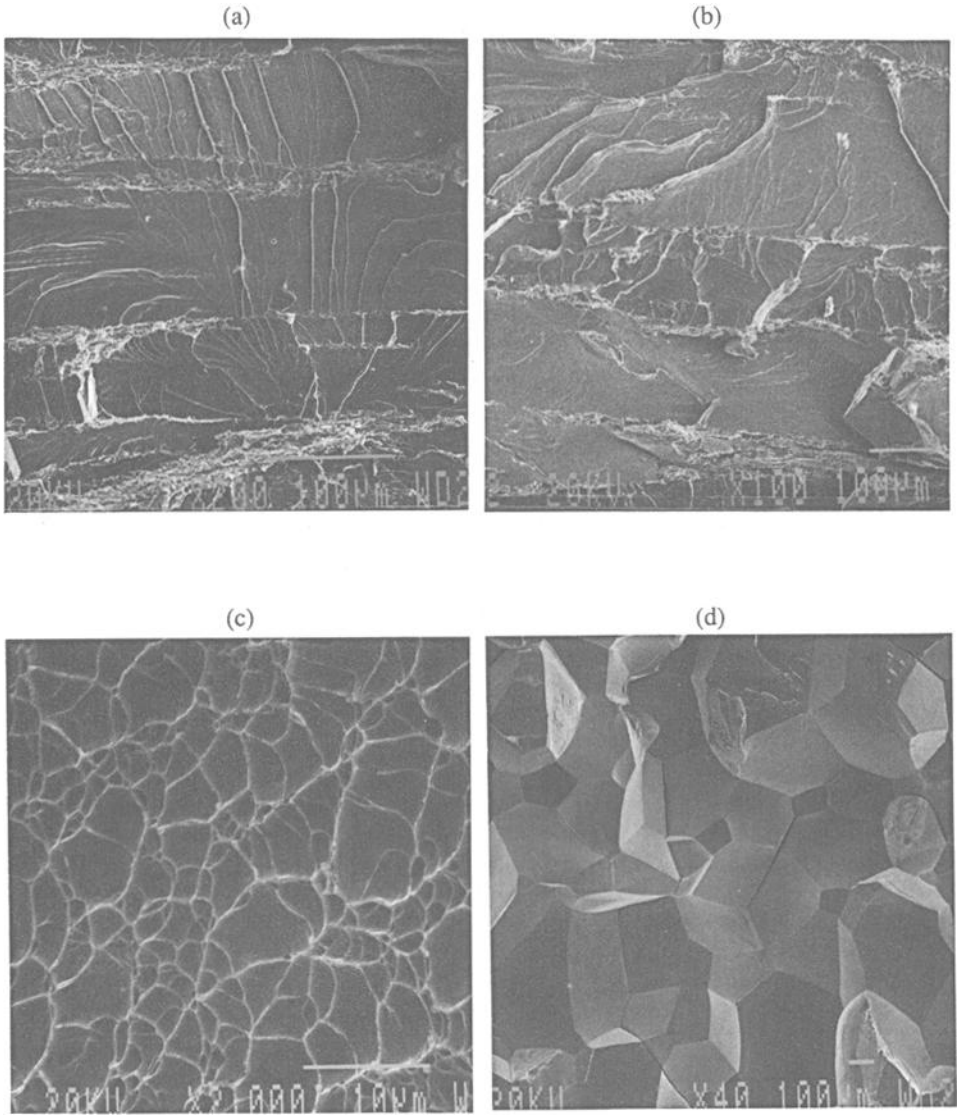

FIG. 2—*Typical tensile fracture modes in:* (a) *as-forged 10Ti;* (b) *as-forged 25Ti;* (c) *as-forged 40Ti; and* (d) *as-forged +1150°C/8 h +750°C/25 h heat-treated 40Ti.*

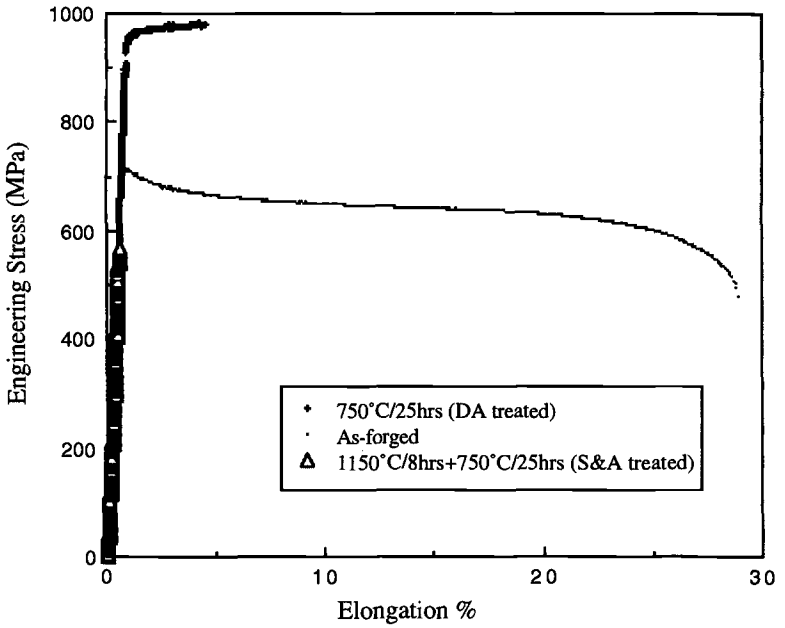

FIG. 3—*Elongation-engineering stress curves obtained for the Nb-15A1-40Ti alloy.*

which resulted in an intergranular fracture mode. A summary of room-temperature tensile properties of all the three alloys is presented in Table 3.

Experimental Procedure

Fracture Toughness

Fracture toughness tests were performed on single-edge-notched (SEN) bend test samples (2.54 by 2.54 by 10.16 cm). The relatively large specimen dimensions were selected to promote plane strain conditions and to ensure that at least 50 grains (average grain size ~250 μm) were sampled by the through-thickness crack fronts during stable crack growth. The samples were precracked under far-field compression loading [*11*] prior to fracture toughness testing under three-point bend loading. The fracture toughness tests were performed in accordance with the ASTM E 399 specifications [*12*]. A loading rate corresponding to a stress intensity factor increase rate of 1 MPa$\sqrt{\text{m}}$ · s^{-1} was used in these tests. The stress intensity factors were calculated using an expression provided in the ASTM E 399 code [*12*].

Fatigue Crack Growth

Fatigue crack growth studies were carried out on 6.25-cm-long single-edge-notched (SEN) bend specimens with square (25.4 by 25.4 mm) cross sections and lengths of ~6.25 cm. The initial notches were ~11 mm deep. The SEN specimens were produced by electro-discharge machining (EDM). All the fatigue crack growth experiments were carried out in a closed-loop servohydrallic testing machine. The SEN specimens were pre-cracked in air using computer-controlled load-shedding techniques under three-point bend loading. A cyclic frequency of 10 Hz and a stress intensity factor range,

ΔK, of ~20 to 25 MPa$\sqrt{m}$, were employed in the precracking. A load-shedding rate, C, of -0.08 (mm^{-1}) or -2 ($in.^{-1}$) was used in the fatigue crack growth testing, where C is given by [*12*]:

$$K_{max} = K_{max0}\exp[C(a - a_0)] \tag{1}$$

Note that K_{max} is the current stress intensity, K_{max0} is the initial stress corresponding to a_0, C is a constant with dimensions of 1/length, which is the controlling load shedding/increasing rate, a is the current crack length, and a_0 is the initial crack length.

After pre-cracking, the fatigue crack growth experiments were also conducted under three-point bend loading at a cyclic frequency of 10 Hz. A stress ratio, $R = K_{min}/K_{max}$, of 0.1 was used. Fatigue crack growth was also monitored using a high-resolution (2.5-μm) telescope connected to a video monitoring unit. This was used to verify the actual crack lengths during the tests. The fatigue thresholds were determined by load shedding. Note that the threshold was taken to correspond to a ΔK level at which no crack growth was detected after ~10^7 cycles.

After testing, the polished sides of the specimens were examined under a scanning electron microscope. The interactions between the fatigue cracks and underlying microstructures were thus elucidated. The SEN specimens were then deformed continuously to failure under monotonic loading. Finally, the fracture surfaces of the specimens were studied under a scanning electron microscope.

Atomistic Simulations

Atomistic simulations were carried out in an effort to identify the fundamental reasons for the improved toughness of 40Ti alloy. The simulations were carried out using molecular statics (embedded atom method). Details of the potentials and simulations procedure are provided in Ref *13*. The simulations employed aniotropic crack-tip fields for linear elastic solids developed by Sih and Liebowitz [*14*].

The criterion for dislocation emission (in single crystals) versus brittle fracture (cleavage) will be based on the work of Rice [*15*] and Zhou et al. [*16*]. The conditions for the onset of dislocation emission will be obtained by equating the critical loading for dislocation emission to that required for cleavage. The following critical condition for cleavage is given by Ref *15*:

$$K_{Ic} = \sqrt{\frac{4\mu\gamma_s}{1 - \nu}} \tag{2}$$

The critical condition required for dislocation emission is also given by Rice [*8*] to be:

$$K_{Ic} = \left[\frac{2\mu\gamma_{us}}{1 - \nu} \cdot \frac{8}{(1 + \cos\theta)\sin^2\theta\cos^2\phi}\right]^{1/2} \tag{3}$$

where μ is the shear modulus, ν is the Poisson's ratio, γ_s is the stacking fault energy, γ_{us} is the unstable stacking fault energy, θ is the inclination angle of the slip plane, and ϕ is the angle between the Burgers vector and the slip line. The condition for dislocation emission may thus be obtained by equating Eqs 2 and 3. This gives:

$$\frac{\gamma_{us}}{\gamma_s} = \frac{(1 + \cos\theta)\sin^2\theta\cos^2\phi}{4} \tag{4}$$

Similar expressions have also been developed by Zhou, Carlsson, and Thomson [*16*] to account for the effects of ledges at the crack-tip. Under such conditions, K_{Ic} remains unchanged. However, K_{Ie} is

now given by:

$$K_{Ic} \sim \left[\frac{50\mu\gamma_{us}\gamma_s}{b} \cdot \frac{8}{(1 + \cos\theta)\sin^2\theta}\right]^{1/2} \tag{5}$$

where b is the Burgers vector.

The transition from brittle to ductile behavior is then given by:

$$\frac{\gamma_{us}}{\mu b} = \frac{(1 + \cos\theta)\sin^2\theta}{100(1 - \nu)} \tag{6}$$

Atomistic simulations of the crack-tip deformation behavior in the 40Ti alloy were carried out for external Mode I loads of $K = 1.6$ MPa$\sqrt{m}$. The atomistic blocks used were quasi 3D. In this scheme, the boundary conditions along the direction of the crack front are periodic with a periodicity distance equal to that of the lattice in that direction. In the other two directions, fixed boundary conditions are used, with sizes of at least 30 nm. The blocks typically contain 25 000 to 30 000 atoms. This size was chosen after determining that a simulation cell of this size is sufficient to ensure that the relaxations obtained were independent of the cell size.

We constructed a polycrystalline array that contains different $\Sigma = 5$ grain boundaries. This array was generated by periodic repetition of four grains. These grains had two different orientations and created four variants of $\Sigma = 5$ grain boundaries, differing in their translational states. All the grains had the [001] axis in common, and this direction was chosen as the direction of the crack front for our simulations. The crack plane was oriented in various directions and positions with respect to the grain boundaries. The simulation cells were constructed starting with a block of Nb atoms and replacing 40% of them by Ti at random sites in both sub-lattices. Following the substitution of Ti for Nb, 15% of the niobium atoms were replaced by Al in only one sub-lattice, as indicated by the ordered B2 structure. The above criteria (Eqs 2-6) were used to determine whether dislocation emission occurs prior to the onset of cleavage fracture.

Results

Fracture Toughness

The fracture toughness data obtained from the forged alloys are summarized in Table 4. Fracture toughness increases from 10 to 20 MPa$\sqrt{m}$ in the 10Ti and 25Ti alloys to levels as high as ~100 to 110 MPa$\sqrt{m}$ in the 40Ti alloy. The latter values are some of the highest fracture toughness levels ever recorded for any ordered intermetallic alloy. The test conditions also generally satisfied the

TABLE 4—*Summary of fracture toughness values and fracture modes.*

Material	Processing/ Heat-Treatment	Phase(s)	Fracture Toughness (MPa $\sqrt{m}$)	Fracture Mode
Nb-15Al-10Ti	As-Forged	B2 + A15	17 ± 3	Cleavage
	As-forged + 750°C/25 h	B2 + A15	27 ± 5	Cleavage
Nb-15Al-25Ti	As-Forged	B2 + A15	18 ± 4	Cleavage
	As-forged + 750°C/25 h	B2 + A15 + O	29 ± 5	Cleavage
Nb-15Al-40Ti	As-Forged	B2	110 ± 10[a]	Ductile dimpled
	As-forged + 750°C/25 h	B2 + O	102 ± 13[a]	Ductile dimpled

[a] Specimen did fully satisfy ASTM E 399 specification for plane strain fracture toughness testing.

ASTM E 399 requirements. However, it is important to note that the specimen dimensions (25.4 by 25.4 by 100 mm) of the direct-aged 40Ti alloy did not fully satisfy all the ASTM E 399 criteria. Nevertheless, the fracture toughness of 100 to 110 MPa$\sqrt{m}$ that was obtained in the direct aged condition was essentially independent of specimen thickness for specimen thicknesses between 12.5 and 25.4 mm. The effects of thickness on fracture toughness therefore appear to be relatively small in this thickness regime.

Similar improvements in fracture toughness have also been obtained from a Nb-13Cr-37Ti alloy [*17–19*] that has fracture toughness levels between ~65 to 85 MPa$\sqrt{m}$. As in the case of the 40Ti alloy, the improved fracture toughness in the Nb-13Cr-37Ti alloy was associated with the onset of significant levels of crack-tip plasticity. These will be discussed later. In any case, the 750°C/25 h (DA) treated 10Ti and 25Ti alloys exhibit a significant increase in fracture toughness, from about 18 to 28 MPa$\sqrt{m}$. Fracture in the 10Ti and 25Ti alloys occurred by transgranular cleavage (Figs. 4*a-d*). In contrast, the as-forged and DA-treated 40Ti alloys exhibit predominantly ductile dimpled fracture modes (Figs. 4*e,* 4*f*). Ductile dimpled fracture was observed to occur in the forged 40Ti alloy along with secondary splitting along the grain boundaries of the forged direct-aged material (Fig. 4*f*).

Atomistic Simulations

The results of the atomistic simulations are presented in Figs. 5*a*-5*d*. Figure 5*a* shows the simulations of a crack running parallel to a grain boundary, along a (120) type plane within a grain. In this and subsequent figures, only the immediate region around the crack tips is shown in the figures, the actual simulations being larger. We show the results for a loading of 1.6 MPa$\sqrt{m}$, which is well above the Griffith cleavage value computed from Eq 2. Significant blunting and dislocation emission was observed in the crack/microstructure interaction for the 40Ti alloy.

Similar results were observed for the case where the crack propagates along a grain boundary. An example is shown in Fig. 5*b,* where significant blunting is observed, despite the fact that the crack is actually running along the grain boundary and encountering a perpendicular grain boundary along its path. In this case, the crack actually was more blunted as it encountered a region with a larger local concentration of Ti atoms. These results are consistent with increased ductility with increasing Ti content, as shown in previous work on Nb_3Al-xTi with Ti levels up to 33% Ti [*13*]. Similar behavior was observed for cracks along a cube plane, and for alloys the Al atoms were distributed randomly in both sub-lattices. Figure 5*c* shows an example of these simulations. The improved fracture toughness in the 40Ti alloy is, therefore, associated with the onset of crack-tip plasticity and crack-tip blunting, as shown in Figs. 5*a*-5*d*.

Past simulations of crack-tip deformation in alloys containing lower Ti levels (~16 at%) have shown that cleavage fracture is favored over dislocation emission and crack-tip blunting in such cases [*13*]. Previous simulations of B2 NiAl intermetallics have also indicated the preference for cleavage fracture over dislocation emission. In both cases, the relatively low fracture toughness of the low Ti-containing Nb_3Al-xTi alloys (17-29 MPa$\sqrt{m}$) and the low fracture toughness levels of NiAl (~4 to 6 MPa$\sqrt{m}$ [*20*]) were associated with brittle fracture modes and sharp crack tips that are predicted by the atomistic simulations [*21*].

In contrast, the current atomistic simulations of the 40Ti alloy indicate very high levels of Ti plasticity and crack-tip blunting, as shown in Figs. 5*a*-5*d*. The results of the simulations of the 40Ti alloy are also consistent with the experimental observations of ductile fracture modes in the 40Ti alloy (Fig. 4*e*). The results of the atomistic simulations therefore predict the occurrence of crack-tip dislocation motion as observed in the fracture toughness experiments. This suggests that further atomistic simulations may be used to guide the development of more complex niobium aluminide-based alloys with the potential for improved toughness via crack-tip dislocation activity. Hence, the use of atomistic simulations could result in a significant reduction in the alloy development cost that is required to optimize niobium-aluminide-based intermetallics for potential structural applications.

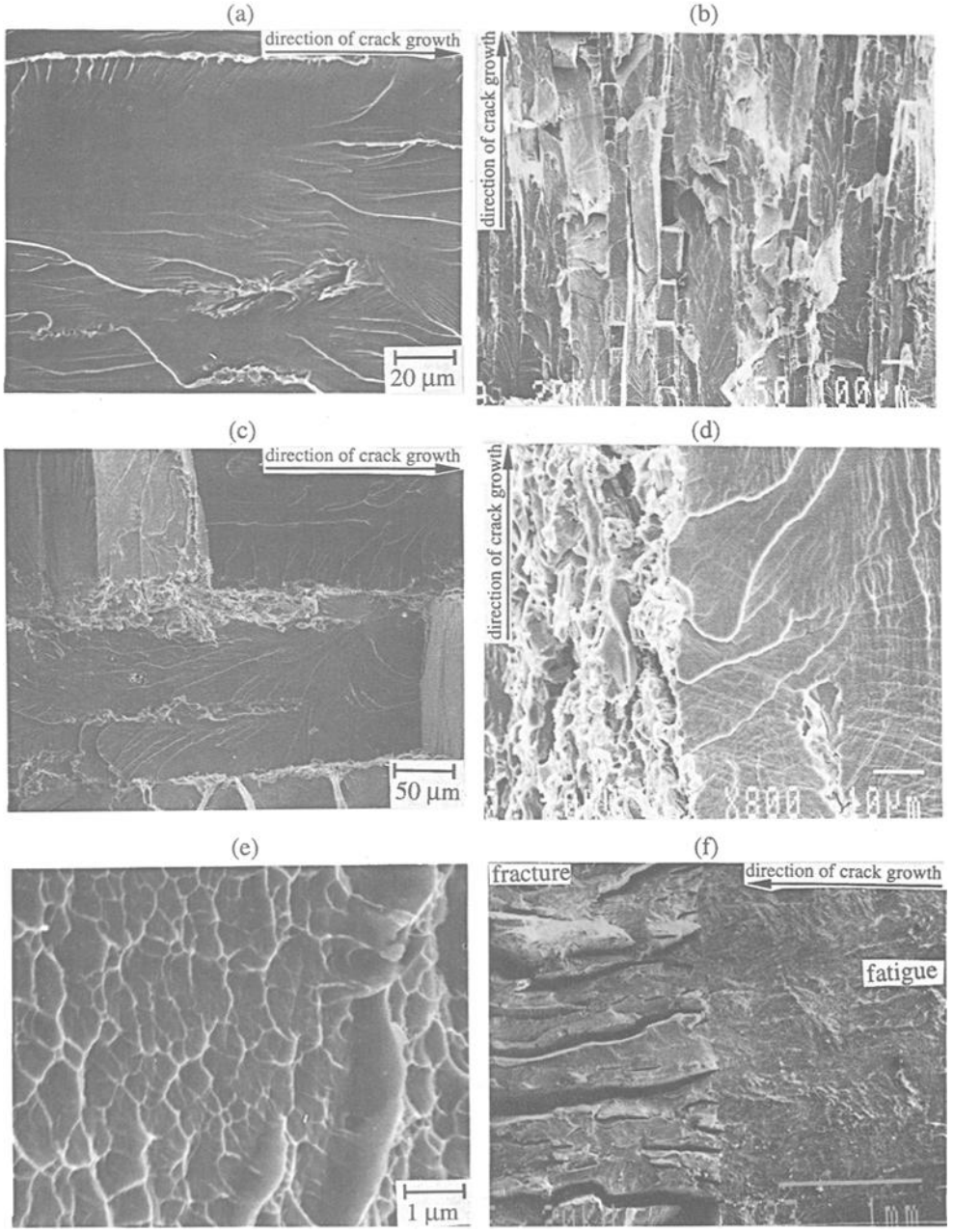

FIG. 4—*Typical fracture modes in SEN fracture toughness specimens: cleavage in Forged 10Ti alloy* (a) *as-forged and* (b) *as-forged+750°C/25 h cleavage in forged 25Ti alloy* (c) *as-forged and* (d) *as-forged+750°C/25 h; ductile dimpled fracture in 40Ti Alloy* (e,f).

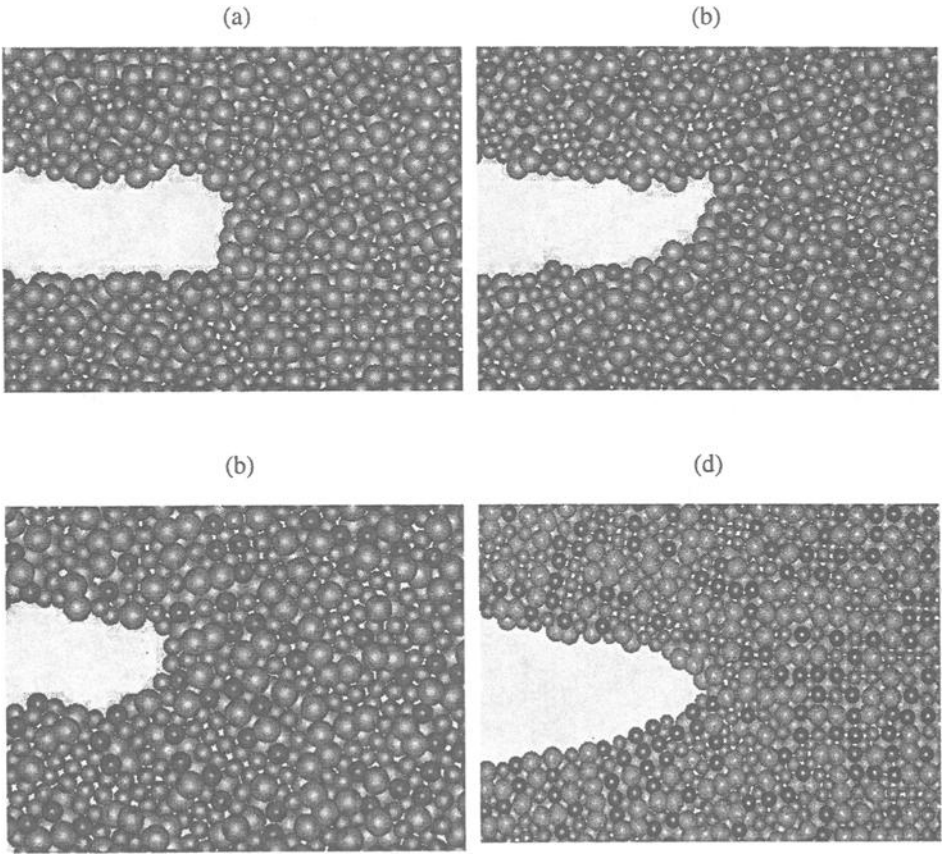

FIG. 5—*Results of the atomistic simulations of Nb-15A1-40Ti* (a), (b), *and* (c) *(small darker symbols represent A1; larger light gray symbols represent Ti):* (a) *crack along a ⟨210⟩ type plane within a single grain at a stress intensity;* (b) *crack along a ⟨210⟩[001] symmetrical tilt grain boundary;* (c) *crack along a ⟨100⟩[001] plane within grain;* (d) *crack along a ⟨100⟩[001] plane for 10% Ti alloy.*

Room-Temperature Fatigue Crack Growth and Thresholds

The room-temperature fatigue crack growth rates (for a stress ratio of 0.1) of the forged Nb-15Al-*x*Ti alloys are compared with those of forged mill annealed Ti-6Al-4V [*22*] and IN718 [*23*] and pure Nb [*24*] that were examined in this study (Figs. 6*a* and 6*b*). Stress ratios of 0.1 and 0.5 appear to have only a limited effect on fatigue crack growth rates in all of the alloys (Figs. 6*c* and 6*d*). The exponents of ΔK and K_{max} [$da/dN = C(\Delta K)^m(K_{max})^n$] are presented in Table 5. Note that the relative values of m and n provide an indication of the relative contributions from cyclic and static fracture modes. The 10Ti and 25Ti alloys exhibit faster crack growth rates and higher Paris exponents than the 40Ti alloy. The fatigue crack growth rates in the 40Ti alloy are faster than those of IN718 in the as-forged condition. However, the crack growth rates in the 40Ti alloy are comparable to fatigue crack growth rates in mill-annealed Ti-6Al-4V. It is particularly important to note that the 40Ti alloy has a Paris exponent of ~2, which is close to values of ~2 to 4 that are typically reported for ductile metals and their alloys [*23*].

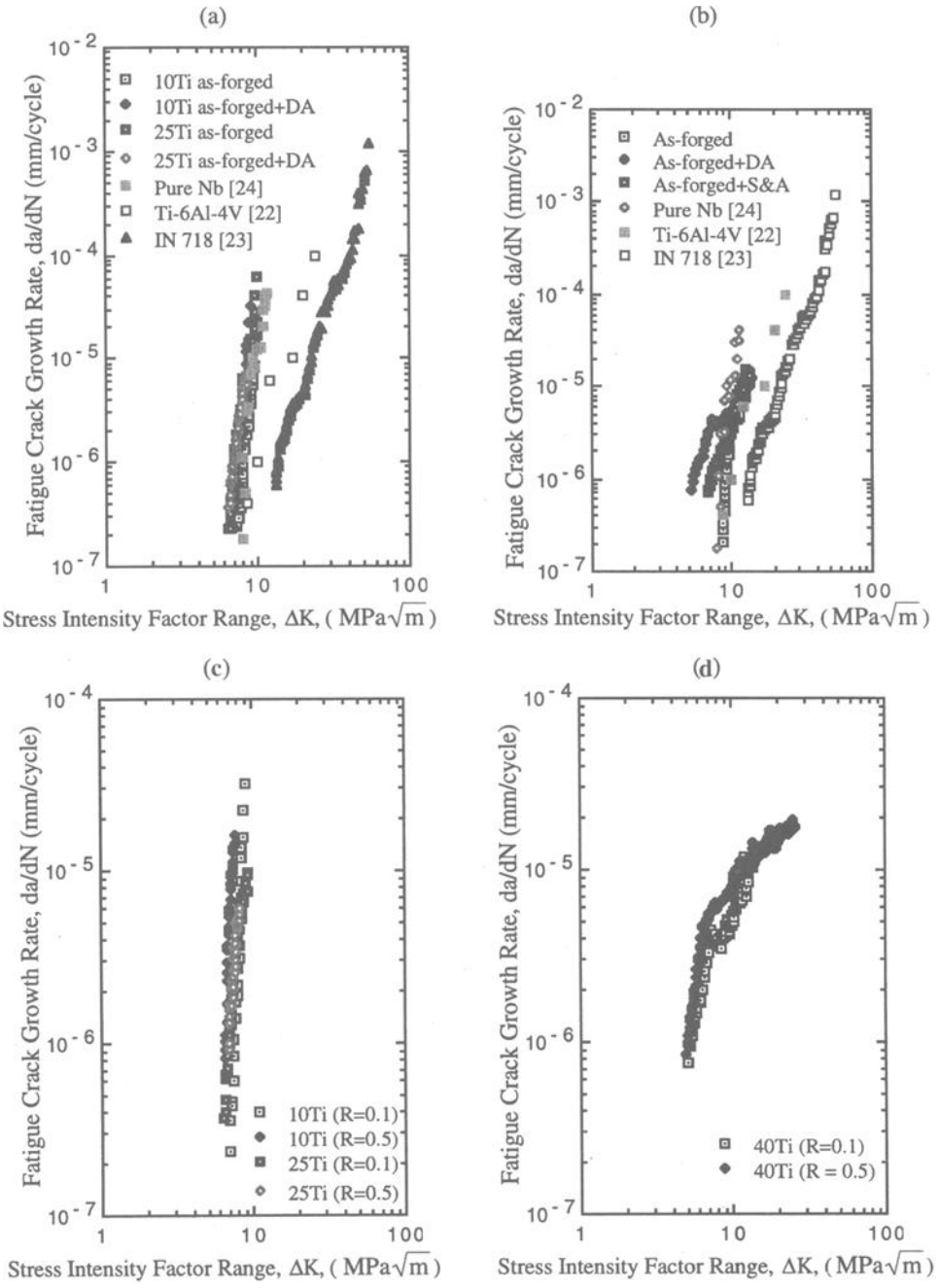

FIG. 6—*Summary of fatigue growth rate data obtained for:* (a) *forged 10Ti and 25Ti alloys and* (b) *forged Nb-15A1-40Ti alloy;* (c) *effects of R ratio on 10Ti and 25Ti;* (d) *effects of R ratio on 40Ti.*

TABLE 5—*Summary of Paris constants in Nb-15Al-xTi Alloys.*

Alloy	C mm/cycle	m	n
Nb-15Al-10Ti	$10^{-22.6}$	14.1	4.66
Nb-15Al-25Ti	$10^{-13.7}$	8.65	0.47
Nb-15Al-40Ti	$10^{-7.83}$	1.63	0.93

The fatigue crack growth threshold, ΔK_{th}, levels in the as-forged 25Ti and 10Ti alloys (~6.4 and ~7.1 MPa$\sqrt{m}$, respectively) are greater than those of the 40Ti alloy (~5.1 MPa$\sqrt{m}$) in the as-forged condition. However, the fatigue crack growth rates in the 40Ti alloy are generally slower than those obtained for the 10Ti and 25Ti alloys in the Paris regime. The DA treatment also appears to have only a small effect on the fatigue crack growth behavior of the 10Ti and 25Ti alloys. However, DA treatment has a significant effect on the 40Ti alloys in which the fatigue threshold drops from ~8.6 MPa$\sqrt{m}$ to ~6.7 MPa$\sqrt{m}$ after DA treatment.

Inspection of the fracture surfaces of the fatigue samples revealed faceted cleavage fracture modes in the 10Ti and 25Ti alloys (Figs. 7*a* and 7*b*). However, the DA-treated 40Ti alloy exhibits crystallographic fracture modes in the low- and mid-ΔK regimes, and fatigue striations in the high ΔK regime at a stress ratio of 0.1 (Fig. 8*b*). However, a faceted crystallographic fracture mode was observed in the DA 40Ti alloy at a stress ratio of 0.5 (Figs. 8*c* and 8*d*). The lower Paris exponents and slower fatigue crack growth rates in the 40Ti alloy were, therefore, associated with a transition from cyclic cleavage (in the 10Ti and 25Ti alloys) to fatigue crack growth mechanisms that are comparable to those observed in ductile metals and their alloys [*25*].

Elevated-Temperature Fatigue Crack Growth and Thresholds

The fatigue crack growth rate data obtained for the DA heat-treated 40Ti alloy at 750°C in air are presented in Fig. 9. The near-threshold crack growth rates obtained at 750°C were slower than those obtained in air at 25°C. Higher fatigue thresholds were also obtained at 750°C (~8.2 MPa$\sqrt{m}$) compared with corresponding fatigue threshold values of ~5.1 MPa$\sqrt{m}$ at 25°C. The high elevated-temperature fatigue thresholds were associated with the presence of thick oxide layers that were observed on the fracture surfaces of the 40Ti specimens that were tested at 750°C.

X-ray analysis of these fracture surfaces was carried out in a Scintag Pad-V X-ray diffractometer. The results (Fig. 10) revealed that the oxides on the fracture surface consisted predominantly of rutile (TiO_2). Evidence of fracture surface oxidation was also obtained from the microstructural and fractographic examination of the crack profiles shown in Figs. 11*a* and 11*b*. These show clearly that oxide debris (Fig. 11*a*) and an oxide layer (Fig. 11*b*) are formed on the fracture surfaces of the fatigue specimen that were tested at 750°C. Such oxide layers and debris can induce crack closure/wedging when the excess debris/oxide thicknesses are comparable to crack-tip opening displacements.

To explore this possibility, oxide-induced closure levels were estimated using a modified Dugdale-Barenblatt closure model [*26*]. The model accounts for the wedging induced by an oxide layer that forms behind the crack tip. Since the composition and thickness of the oxide layer must be known in any detailed oxide-induced closure analysis, the oxide layer on the fracture surfaces was characterized using X-ray and energy dispersive X-ray spectroscopy. The oxide layer was shown to consist solely of TiO_2. The excess oxide thicknesses and the wedge lengths of the oxide films were used in the estimation of the closure stress intensity factor, K_{cl}, which was estimated from the following ex-

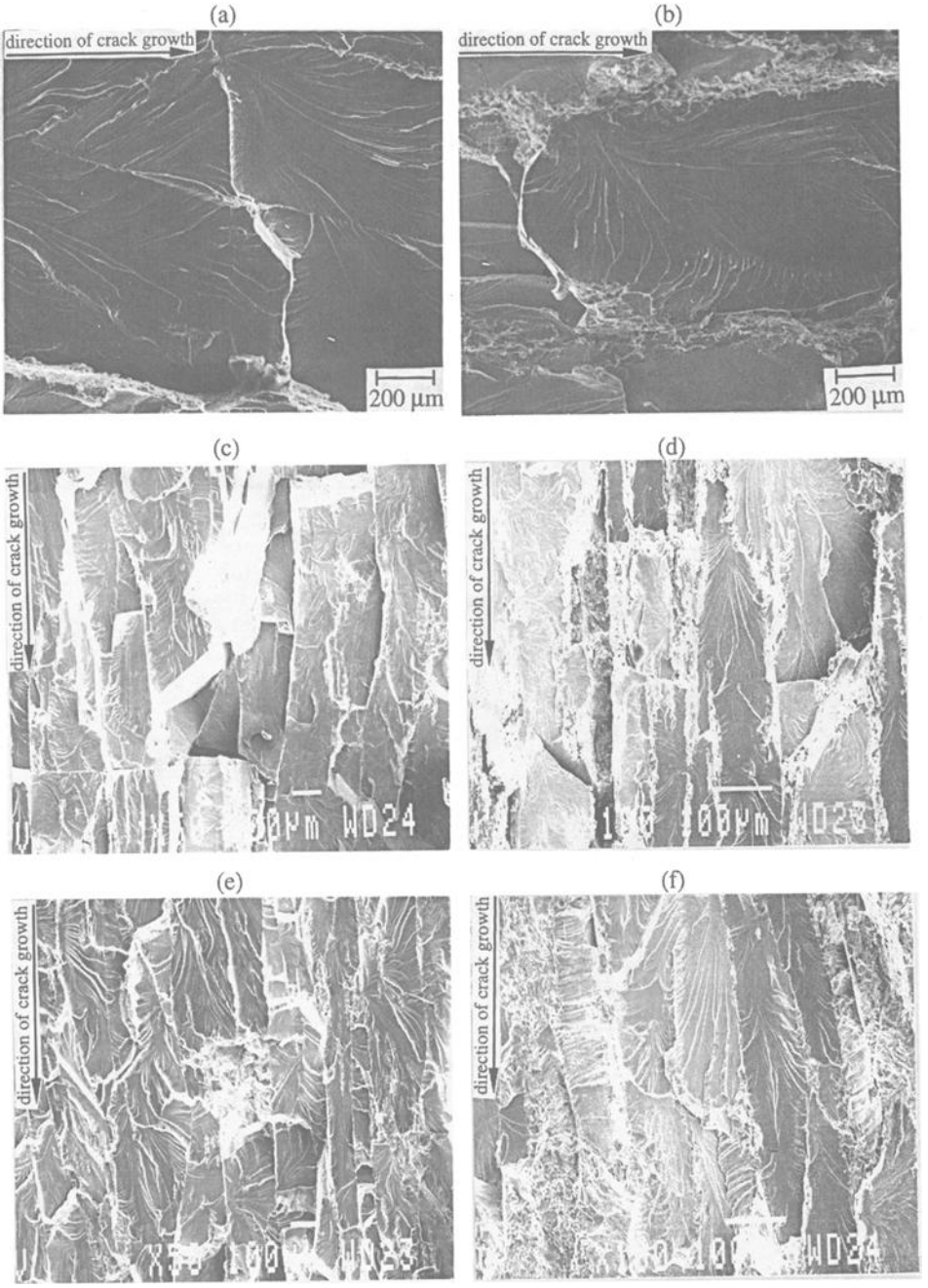

FIG. 7—*Cleavage modes in as-forged 10Ti alloy* (a), *25Ti alloy* (b); *as-forged+750°C/25 h (DA) treated 10Ti alloy;* (c) R = *0.1 and* (e) R = *0.5 and 25Ti alloy:* (d) R = *0.1 and* (f) R = *0.5.*

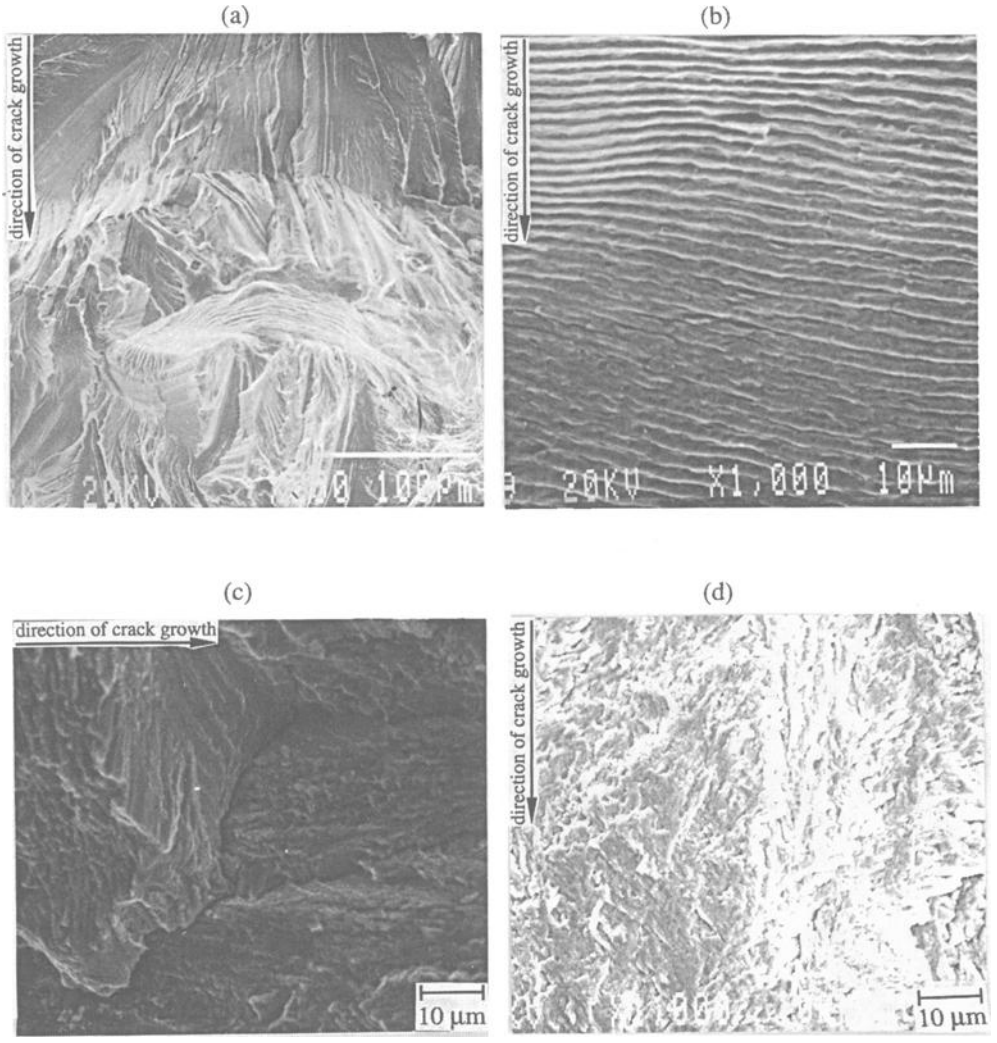

FIG. 8—*Typical fatigue fracture modes in as-forged 40Ti:* (a) *low* ΔK*;* (b) *high* ΔK*; and* (c) *secondary cracking in 40Ti (DA) at* $R = 0.1$ *and* (d) $R = 0.5$.

pression due to Suresh and Ritchie [*24*]:

$$K_{cl} = \frac{dE}{4(\pi l)^{1/2}(1 - \mu^2)} \tag{7}$$

where d is the excess oxide thickness, $2l$ is the wedge length of the oxide film, μ is Poisson's ratio of ~0.3, and E is the Young's modulus of ~105 GPa. The excess oxide thickness was estimated from the crack profiles of the 40Ti specimen. An average oxide of thickness of ~5 μm was measured in the 40Ti alloy following the threshold test. The wedge length, $2l$, was also measured at the end of the test. This was shown to be ~4.3 mm. With Young's modulus, $E = 105$ GPa, and Poisson's ratio assumed

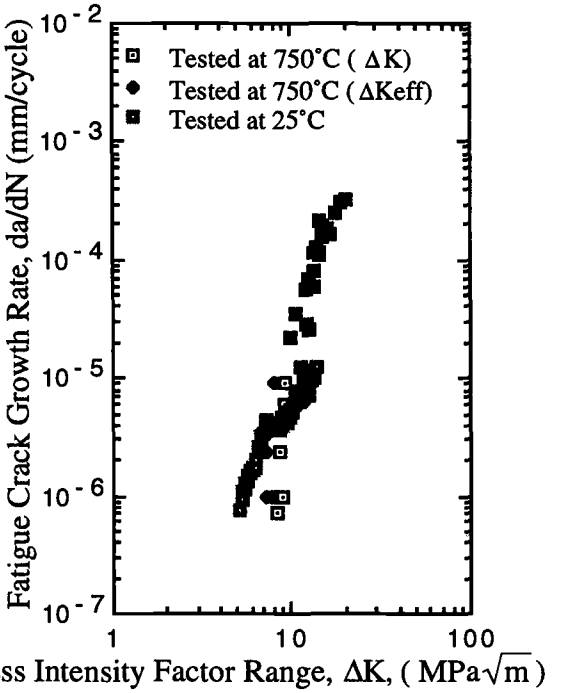

FIG. 9—*Fatigue growth rates in as-forged+DA treated Nb-15A1-40Ti alloy at 25 and 750°C.*

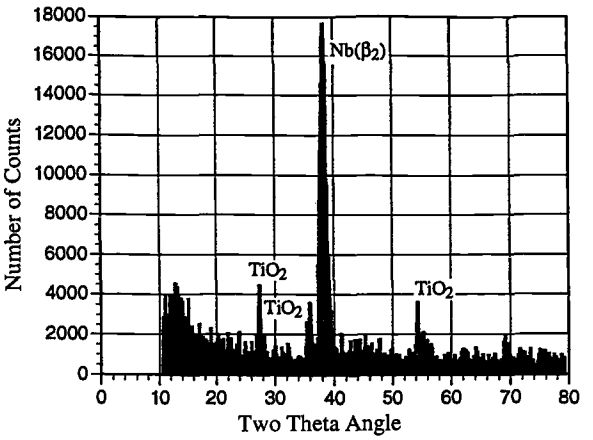

FIG. 10—*X-ray diffraction profile obtained from oxide layer on fracture surface of 40Ti fatigue crack growth specimen tested at 750°C.*

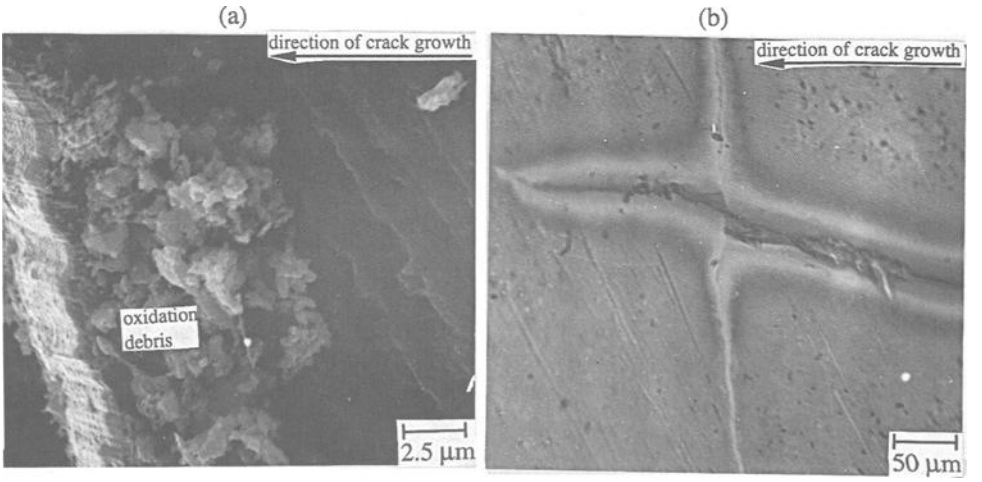

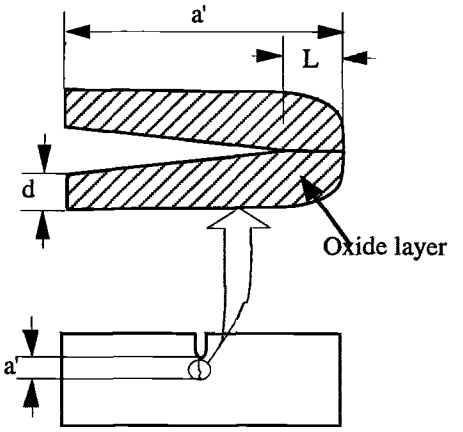

FIG. 11—*Fatigue crack growth in the 40Ti alloy at 750°C:* (a) *oxidation debris and striations on the fracture surface;* (b) *crack profile showing evidence of oxide layer and secondary splitting along intersecting grain boundary;* (c) *schematic illustration of oxide-induced crack closure.*

to be 0.3, the closure stress intensity level, K_{cl}, is thus estimated from Eq 7 to be ~1.8 MPa$\sqrt{m}$ at the threshold condition in the 40Ti alloy at 750°C. Hence, the effective fatigue threshold, $\Delta K = \Delta K_{app} - \Delta K_{cl}$, was estimated to be ~6.6 MPa$\sqrt{m}$ at 750°C. This is close to fatigue threshold obtained for the 40Ti alloy at room temperature. This suggests that the differences between the fatigue thresholds and near-threshold crack growth rates at 25 and 750°C are due partly to the effects of oxide-induced closure.

Consistent with the above arguments, the fatigue crack growth rates in the mid-ΔK and high ΔK regimes were comparable to those obtained at room temperature where oxide-induced closure was not observed. This suggests that oxide-induced closure does not occur in mid-ΔK and high-ΔK regimes where the crack opening displacements are much greater than the excess oxide thickness levels. The ineffectiveness of oxide-induced closure in this regime may also be attributed partly to higher crack-tip opening displacements, and the limited time available for fracture surface oxidation to occur in mid- and high-ΔK levels where the fatigue crack growth rates are relatively fast.

Discussion

Fracture Toughness

It is of interest to discuss the improvements in fracture toughness within the context of ongoing work on niobium base intermetallics. First, it is important to note that the significant improvements in fracture toughness of the 40Ti alloy are associated with the onset of significant levels of crack-tip plasticity and crack-tip blunting (Figs. 5*a*–5*d*). This is consistent with previous results of atomistic simulations of crack-tip plasticity by Farkas [*13*]. Her analysis shows that dislocation emission is favored over cleavage, as the Ti content is increased from 16 to 33 at%. Dislocation and crack-tip blunting were predicted by atomistic simulations of crack-tip deformation in {110} crystals oriented for crack growth in ⟨100⟩ and ⟨111⟩ directions. In contrast, the analysis of Farkas predicted that cleavage fracture was more likely to occur before dislocation emission occurred in an alloy containing lower amounts of Ti (16%).

The measured fracture toughness levels of 40 to 110 MPa$\sqrt{\text{m}}$ are clearly much higher than those reported previously for other intermetallic system such as gamma-based titanium aluminides [*5*] and $MoSi_2$ [*6*]. However, recent work on Nb-Cr-Ti alloys and in-situ composites [*17,19*] has shown that significant improvements in fracture toughness (~65 to 80 MPa$\sqrt{\text{m}}$) can also be engineered in these body-centered cubic alloys by the addition of ~40 at% Ti. The beneficial effect of ~40% Ti was correlated with the lower number of d + s electrons per atom in the Nb-Cr-Ti system [*17*]. In contrast, alloying elements that increase the number of d + s electrons per atom were shown to have lower ductilities. In any case, the Nb-Cr-Ti and Nb-Al-Ti alloys with ~40 at% Ti additions are of scientific and technological interest due to their high fracture toughness levels. These two alloy systems also appear to have the balance of properties required for structural applications at temperatures up to ~700 to 750°C.

Finally, it is of interest to compare the measured fracture toughness levels to those reported by other workers for niobium base alloys/intermetallics (Fig. 12). The Laves phase (Nb-Cr-Ti) intermetallics and composites generally have fracture toughness levels between ~8 to 20 MPa$\sqrt{\text{m}}$ at room temperature [*17,18*]. However, the fracture toughness levels may be as high as 65 to 85 MPa$\sqrt{\text{m}}$ in the body-centered cubic Nb-Cr-Ti alloys, which have lower elevated-temperature oxidation limits (~700°C) than the Laves phase intermetallics (~1000 to 1200°C). The fracture toughness levels in the Nb-Cr-Ti alloys also increase with increasing Ti content up to 40 at% Ti, while those of the Laves phase intermetallics decrease with Cr_2Nb content [*17*]. Fracture toughness data have also been reported for Nb-Si and Nb-Cr-Ti-Hf-Si alloys [*27*]. The niobium silicides have fracture toughness levels that are typically below ~35 MPa$\sqrt{\text{m}}$. The fracture toughness levels in these oxidation-resistant systems are due to the protective nature of complex mixed oxides [*27*] that are formed on exposed surfaces of Nb-Si and Nb-Cr-Ti-Hf-Si alloys. Typical fracture toughness levels for the toughest of the oxidation-resistant Nb-Cr-Hf-Ti-Si alloys are ~20 to 26 MPa$\sqrt{\text{m}}$ [*27*].

The fracture toughness levels of 40 to 110 MPa$\sqrt{\text{m}}$ reported in this paper for the 40Ti alloy are, therefore, greater than those reported for other high-temperature niobium-base intermetallics. However, the toughness levels in the 40Ti alloy are comparable to those reported for the Nb-13Cr-37Ti alloys. The latter alloy has a density of ~6.7 g/cm^3 [*18*] compared to the Nb-15Al-40Ti, which has a density of ~6.1 g/cm^3 [*1*]. Furthermore, the other properties of the Nb-13Al-37Cr and Nb-15Al-40Ti are generally comparable.

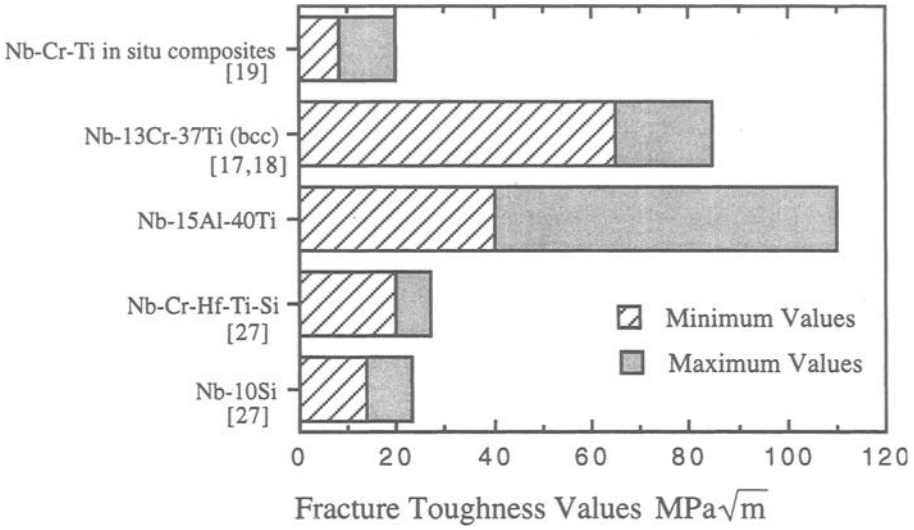

FIG. 12—*Comparison of fracture toughness values.*

Fatigue Crack Growth

The fatigue crack growth resistance of the 40Ti alloy is also attractive. Unlike most intermetallics, the Paris exponent of this alloy is close to 2. These relatively low (comparable to other intermetallics) Paris exponents are comparable to typical values for conventional structural metals and their alloys [*25*]. Standard damage-tolerant design philosophies [*28*] may, therefore, be used in the analysis and design of 40Ti structures and components. In contrast, most of the brittle intermetallics systems require initiation-based design concepts to prevent catastrophic failure due to fast fatigue crack growth rates [*29*] and short crack phenomena [*29*]. Such initiation-based methodologies may limit the structural benefits that can be achieved by the use of alternative high-temperature materials such as gamma-based titanium aluminides [*29*].

Finally, it is of interest to note that the slower fatigue crack growth rates at 750°C (Fig. 9) suggest that niobium aluminides may be used in the temperature regime between 25 and 750°C. However, further work is needed to fully explore possible creep-fatigue crack interactions that can occur in this temperature regime. Detailed studies of the effects of environment on fatigue crack initiation and fatigue crack growth are also needed. Nevertheless, the attractive combinations of fracture toughness and fatigue crack growth resistance reported in this paper suggest that niobium aluminides may soon become strong candidates for intermediate-temperature structural applications.

Conclusions

1. Fracture in the brittle 10Ti and 25Ti alloys occurs by brittle cleavage fracture modes under monotonic loading. These alloys have relatively low fracture toughness levels of ~10 to 20 MPa$\sqrt{m}$ at room temperature. In contrast, the tougher (40 to 100 MPa$\sqrt{m}$) 40Ti alloys exhibit ductile dimpled fracture modes (similar to those in metallic materials) in the as-forged and direct-aged conditions under monotonic loading. However, the 40Ti alloy fails by intergranular fracture after solid solution treatment and annealing. Reasons for the transition to intergranular fracture in the STA condition are unknown at present.

2. The fatigue crack growth rates in the 40Ti alloy are comparable to those in IN718, pure Nb, and Ti-6Al-4V at room temperature. The Paris exponents obtained for the 40Ti alloy is ~2. This is comparable to values reported for conventional structural metals and their alloys. However, the fatigue crack growth rates in the brittle 10Ti and 25Ti alloys are also much faster than those in the 40Ti alloy.

3. Fatigue crack growth in the 40Ti alloy occurs by a "faceted" fracture mode in the near-threshold regime. Fatigue striations are observed in the mid- and high-ΔK regimes in the 40Ti alloy. Fatigue crack growth in the 10Ti and 25Ti alloys occurs by cyclic cleavage in the low-, mid-, and high-ΔK regimes.

4. At 750°C, thick oxide (TiO_2) scales (excess oxide thickness ~5-μm thick) are formed on the fracture surfaces of the 40Ti alloy in the near-threshold regime. The slower fatigue crack growth rates in the regions closest to the fatigue threshold are due partly to the effects of oxide-induced closure, which occurs when the crack opening displacements are comparable to the measured oxide thicknesses.

Acknowledgments

The research was supported by The Office of Naval Research (Grant No. N00014-94-1-0501). The authors are grateful to the program manager, Dr. George Yoder, for his encouragement and support. Appreciation is also extended to Mr. Andy Culbertson of The Naval Air Warfare Center for providing additional financial support. The authors are also grateful to Prof. Hamish Fraser, Dr. Mel Jackson, Prof. T. S. Srivatsan, and Dr. Craig Wocjik for useful discussions on niobium alloys and niobium-base intermetallics.

References

[1] Hou, D. H., Shyue, J., Yang, S. S., and Fraser, H. L. in *Alloy Modeling and Design,* G. M. Stocks and P. Z. A. Turch, Eds., The Metallurgical Society, Warrendale, PA, 1994, pp. 291–298.

[2] DiPasquale, J., Gahutu, D., Konitzer, D., and Soboyejo, W. O. in *High Temperature Ordered Intermetallic Materials—VI,* J. A. Horton, I. Baker, S. Hanada, R. D. Noebe, and D. S. Schwartz, Eds., Vol. 364, MRS Proceedings, 1995, pp. 1347–1352.

[3] Srivatsan, T. S., Daniels, C., Sriram, S., Dhana Singh, K. P., Soboyejo, W. O., and Konitzer, D. in *Proceedings of The Symposium on Fatigue and Fracture of Ordered Intermetallics II,* W. O. Soboyejo, T. S. Srivatsan, and R. O. Ritchie, Eds., The Metallurgical Society, Warrendale, PA, 1995, pp. 287–308.

[4] Dauskardt, R. H., Ritchie, R. O., and Cox, B. N. in *Advanced Materials & Processes,* Vol. 144, 1993, pp. 30–35.

[5] Mercer, C. and Soboyejo, W. O. in *Acta Metallurgica et Materialia,* Vol. 45, 1996, pp. 961–971.

[6] Soboyejo, W. O., Ye, F., Chen, L.-C., Bahtishi, N., Schwartz, D. S., and Lederich, R. J. in *Acta Metallurgica et Materialia,* 1996, Vol. 44, pp. 2027–2041.

[7] Shyue, J., Hou, D.-H., Johnson, S. C., Aindow, M., and Fraser, H. L. in *Materials Research Society Proceedings,* 1993, Vol. 288, pp. 243–250.

[8] *Binary Phase Diagrams,* T. B. Massalski, Ed., American Society of Metals, Metals Park, OH, 1986.

[9] Das, S., Jewett, T. J., and Perepezko, J. H. in *Structural Intermetallics: Proceedings of 1st International Symposium on Structural Intermetallics,* R. Darolia, J. J. Lewandowski, C. T. Liu, P. L. Martin, D. B. Miracle, and M. V. Nathal, Eds., The Metallurgical Society, Warrendale, PA, 1993, pp. 35–44.

[10] Fraser, H. L., Research Report, Office of Naval Research, 1996.

[11] Suresh, S. and Brockenbrough, J. R. in *Acta Metallurgica et Materialia,* 1988, Vol. 36, pp. 1444–1470.

[12] "Metals Tests Methods and Analytical Procedures," *Annual Book of ASTM Standards,* Section 3, 1993.

[13] Farkas, D., "Atomistic Simulation of Fracture in the B2 Phase of the Nb-Ti-Al System," *Materials Science and Engineering,* 1997 (submitted).

[14] Sih, G. C. and Liebowitz, H., "Mathematical Theories of Brittle Fracture," *Fracture—An Advanced Treatise,* H. Liebowitz, Ed., Vol. II, Academic Press, New York, 1968, pp. 69–189.

[15] Rice, J. in *Journal of the Mechanics and Physics of Solids,* 1992, Vol. 40, pp. 239–271.

[16] Carlsson, A., Zhou, S. J., and Thomson, R. in *Physical Review Letters,* Vol. 72, 1994, p. 852.

[17] Davidson, D. L., Chan, K. S., and Anton, D. L. in *Metallurgica Materialia, Transactions A,* 1996, Vol. 27A, pp. 3007–3018.

[18] Davidson, D. L., Chan, K. S., and Anton, D. L. in *Metallurgica Materialia, Transactions A,* 1997, Vol. 28A, pp. 1797–1808.
[19] Chan, K. S. in *Metallurgical Materialia. Transactions A,* 1996, Vol. 27A, pp. 2518–2531.
[20] Miracle, D. in *Acta Metallurgica Materialia,* 1993, Vol. 41, pp. 649–684.
[21] Vailhe, C., Shastry, V., and Farkas, D., "Fatigue and Fracture of Ordered Intermetallic Materials: II," W. O. Soboyejo, T. S. Srivatsan, and R. O. Ritchie, Eds., The Metallurgical Society, Warrendale, PA, 1995, pp. 179–188.
[22] Dubey, S., Soboyejo, A. B. O., and Soboyejo, W. O. in *Acta Metallurgica Materialia,* 1997, Vol. 45, pp. 2777–2787.
[23] Mercer, C. and Soboyejo, W. O. in *Superalloy 718, 625, 706 and Various Derivatives,* E. A. Loria, Ed., 1997, pp. 577–586.
[24] N. Polvanich and K. Salama, *Hydrogen Embrittlement: Prevention and Control, ASTM STP 962,* L. Raymond, Ed., 1987, pp. 417–427.
[25] Suresh, S. in *Fatigue of Materials,* Cambridge University Press, 1991.
[26] Suresh, S. and Ritchie, R. O. in *Fatigue Crack Growth Threshold Concepts,* D. L. Davidson and S. Suresh, Eds., AIME, Warrendale, PA, 1984, pp. 227–261.
[27] Bewlay, B. P., Lewandowksi, J. J., and Jackson, M. R. in *Journal of Metals,* August 1997, pp. 44–67.
[28] Larsen, J. M., Worth, B. D., Annis, C. G. Jr., and Haake, F. K. in *International Journal of Fracture,* 1996, Vol. 80, pp. 237–255.
[29] Larsen, J. M., Worth, B. D., Balsone, S. J., Rosenberger, D. H., and Jones, J. W., *Proceedings, Fatigue' 96,* Elsevier Science Ltd., Oxford, U.K., 1996, Vol. III, pp. 1719–1730.

A. Varvani-Farahani[1] *and T. H. Topper*[2]

The Effect of Biaxial Strain Ratio and Periodic Compressive Overstrains on Fatigue Crack Growth Mode and Crack Growth Rate

REFERENCE: Varvani-Farahani, A. and Topper, T. H., **"The Effect of Biaxial Strain Ratio and Periodic Compressive Overstrains on Fatigue Crack Growth Mode and Crack Growth Rate,"** *Fatigue and Fracture Mechanics: 30th Volume, ASTM STP 1360,* P. C. Paris and K. L. Jerina, Eds., American Society for Testing and Materials, West Conshohocken, PA, 2000, pp. 299–312.

ABSTRACT: Biaxial fatigue tests were performed on thin-walled tubular 1045 steel specimens in a test fixture that applied internal and external pressure and axial load. There were two test series, one in which constant amplitude fully reversed strains were applied and another in which large periodic compressive strain cycles causing strains normal to the crack plane were inserted in a constant amplitude history of smaller strain cycles. Ratios of hoop strain to axial strain of $\lambda = -1$ (pure shear), $\lambda = -0.625$, $\lambda = -\nu$ (uniaxial straining), and $\lambda = +1$ (equibiaxial straining) were used in each test series. A confocal scanning laser microscopy (CSLM) image processing technique that gave a resolution of 0.25 μm was developed and used to obtain three-dimensional images of small cracks as they were opened under load. The information in the images was used to construct cross sections of cracks from which crack depth, shape and crack opening stress were obtained.

For pure shear straining tests ($\lambda = -1$) and for tests at a strain ratio of $\lambda - 0.625$ surface cracks rapidly initiated on planes of maximum shear in both constant amplitude and overstrain tests but did not increase significantly in length until near the end of the tests. Instead they grew into the specimen until they were semi-circular in shape. This phase occupied approximately 90% of the fatigue life. Then they began to grow in length as well as depth and linked up to cause failure.

In the uniaxial and equibiaxial straining tests, crack growth initiated on planes of maximum shear at 45° to the surface of the specimens (Stage I crack growth) before changing to Stage II growth perpendicular to the applied stress. The cracks once initiated grew continuously in both the length and depth direction until failure took place.

The magnitude and frequency of application of the periodic compressive overstrain cycles in the second test series was chosen to reduce the crack opening stress level below the minimum stress level of the constant amplitude cycles so that they experienced closure-free crack growth. The compressive overstrains significantly increased crack growth rates and decreased the threshold strain intensity for the smaller constant amplitude cycles. They also caused a large decrease in the small cycle fatigue resistance as measured by their equivalent strain-life curves.

KEYWORDS: biaxial fatigue, crack growth mechanism, periodic compressive overstrain, confocal scanning laser microscopy technique, effective fatigue life and crack growth rate

Compared to the large volume of information on the growth of fatigue cracks under uniaxial loading conditions, experimental studies on fatigue crack initiation and propagation in biaxial fatigue straining are comparatively rare in the literature. Some studies have been done on crack initiation and

[1] Assistant professor, Department of Mechanical Engineering, Ryerson Polytechnic University, 350 Victoria Street, Toronto, Ontario, M5B 2K3, Canada.

[2] Full professor, Civil Engineering Department, University of Waterloo, Waterloo, Ontario N2L 3G1, Canada.

initial growth under biaxial fatigue loading, for instance, Parson and Pascoe [*1*] showed that crack initiation and the direction of initial crack growth were dependent on the applied strain and biaxiality ratio. Brown and Miller [*2*] provided a comprehensive review of the literature on crack initiation and crack growth planes under biaxial loading. They considered nucleation and initial growth of fatigue cracks under torsion and biaxial tension and suggested the terms Case A and Case B cracks. In Case A (torsion), the initial crack growth was along the specimen surface. However, in Case B (biaxial tension), cracks grew into the specimen. Socie [*3*] reviewed the cracking behavior for different materials subjected to tension and torsion.

To the best of our knowledge, there has been no quantitative study of the progress of a crack as it grows into the interior of the material. This study provides quantitative information concerning crack growth rates and shapes as a crack grows into the interior of the specimen under biaxial strain ratios (hoop strain/axial strain) of $\lambda = -1, -\nu, -0.625$, and $+1$ obtained using a confocal scanning laser microscopy (CSLM) image processing technique. CSLM also provided accurate measurements of the height of asperities for constant amplitude straining and for periodic compressive overstrain histories. In this paper the effect of periodic compressive overstrains on fracture surface asperities, crack growth rate, and fatigue life for uniaxial and biaxial fatigue straining conditions are studied.

Experimental Procedure

Material, Properties, and Specimen Design and Preparation

The material examined in this investigation was an as-rolled 1045 steel with the following chemical composition (wt%): 0.46 C, 0.17 Si, 0.81 Mn, 0.027 P, 0.023 S, and the remainder Fe. This material is a medium carbon heat treatable steel that is widely used in the automotive industry. The microstructure of 1045 steel after final polishing showed pearlitic-ferritic features (average grain size of 50 μm) containing up to 30 μm long sulfide inclusions in the rolling direction. The modulus of elasticity is 206 GPa, and the cyclic yield stress is 448 MPa.

Figure 1 shows the solid uniaxial and tubular biaxial fatigue specimens used in this study. The specimens were machined from a 65 mm diameter bar with the axial loading axis parallel to the rolling direction. After machining, the specimens were polished using emery cloth of grit 240, 400, and 600. Final polishing was done with a diamond paste of 5 μm, and alumina particles of 1 and 0.25 μm.

Fatigue Crack Tests

Uniaxial Fatigue Tests—Uniaxial fatigue crack growth rate tests were performed in axial strain control in a servo-hydraulic test machine with a load-cell capacity of 111 kN. The crack growth tests under uniaxial constant amplitude straining (CAS) were performed with a strain amplitude of $\pm 0.075\%$. Periodic axial compressive overstrain crack growth tests were performed with compres-

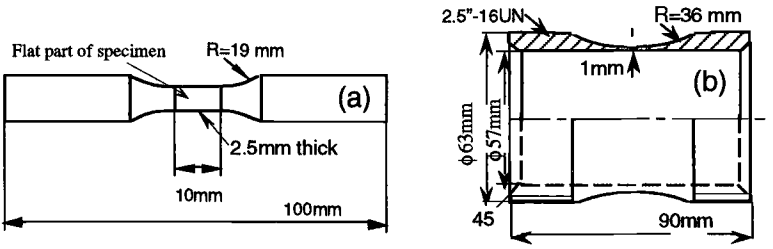

FIG. 1—(a) *Uniaxial plate specimen, and* (b) *biaxial tubular specimen.*

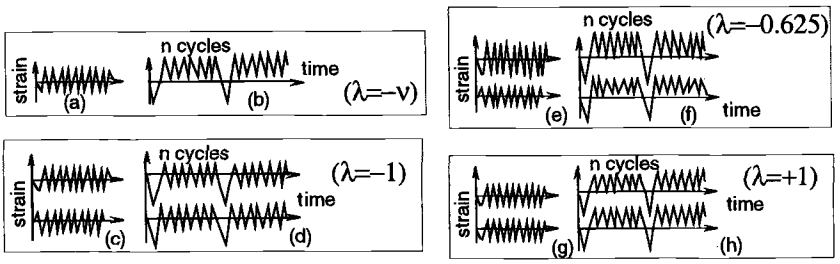

FIG. 2—*Straining histories for various uniaxial and biaxial CAS and PCO conditions.*

sive overstrains of −0.17, −0.24, and −0.381% followed by numbers of small cycles n equal to 50, 200, 500, and 1000 [*4*]. Figures 2*a–b* illustrate the crack growth test strain histories for uniaxial constant amplitude straining and a uniaxial strain history containing periodic compressive overstrains. Smooth specimens were used to determine the crack initiation plane and to measure Stage I crack growth rate under uniaxial straining. The same uniaxial specimen but with a crack starter notch with a radius of 0.25 mm was used to monitor the crack growth in Stage II.

Biaxial Fatigue Tests—Thin-walled tubular specimens were cyclically strained in the axial direction in the strain frame while pressure was alternately applied to the inside and outside of the specimen during each cycle. The biaxial fatigue machine is described in Ref *5*. Three biaxial principal strain ratios (hoop strain/axial strain) were used: $\lambda = -1$ (pure shear straining), a biaxial strain ratio of $\lambda = -0.625$, and $\lambda = +1$ (equibiaxial straining).

Constant amplitude biaxial fatigue tests and tests with strain histories containing periodic compressive overstrains (PCO) were performed in strain control at a frequency of 0.5 Hz. The axial strain (ε_a) and transverse (hoop) strain (ε_h) were controlled to provide the 180° out-of-phase biaxial strain ratio of $\lambda = -1$ and a strain ratio of −0.625. The strain histories used for biaxial shear fatigue tests for strain ratios of −1 and −0.625, respectively, are shown in Figs. 2*c–d* and 2*e–f*. One of the strain histories for each strain ratio is constant amplitude straining, and the other has blocks of a periodic compressive overstrain followed by n small cycles. Equibiaxial fatigue ($\lambda = +1$) tests were performed under strain control for both constant amplitude straining and for strain histories containing periodic overstrains. The axial strain and hoop strain were controlled to provide an in-phase biaxial strain ratio of $\lambda = +1$. The strain histories used in equibiaxial fatigue are shown in Figs. 2*g–h*. The number of small cycles per block at each strain level was chosen so that the overstrain damage was about 20% of the total damage [*4*].

Uniaxial and Biaxial Crack Depth and Crack Opening Measurements

Under uniaxial straining, a confocal scanning laser microscopy (CSLM) image processing technique was used to measure the crack depth of small cracks in the early stage of growth (Stage I) as the number of cycles increased. The CSLM system which is described in detail in previous studies [*6–7*] has a resolution of 0.25 μm. Crack growth in Stage II was measured on the surface of the plate specimen shown in Fig. 1*a* using an optical microscope with a ×500 magnification. Similarly, shear and equibiaxial fatigue crack lengths were measured using an optical microscope at the same intervals as the depth measurements were performed using CSLM.

Using a tensometer (tension machine) and a pressurizing device, respectively, for uniaxial and biaxial cracked specimens, cracked specimens were pulled to open the crack mouth under the CSLM system [*7*]. Then a laser beam was centered on the crack by direct observation through an attached optical microscope. The cracked specimen was scanned by the laser beam which was then reflected

to a detector. Images from different levels of crack depth were obtained by changing the specimen height using a piezo-electric stage. A set of confocal image slices at depth steps of 1 μm were acquired. Post-image processing was later used to combine all the images. Optical sectioning using post-image-processed crack data provided the crack depth and the crack mouth width at every point along the crack length for each tensile stress/internal pressure. Fatigue crack growth tests under strain histories presented in Fig. 2 were performed by measuring the crack depth and crack length at intervals of 1000 to 5000 cycles.

Fracture Surface Asperity Height Measurements

A fractographic examination of the fracture surface of short fatigue cracks was carried out after breaking the 1045 steel specimens in liquid nitrogen. The fracture surface and the variation in the height of asperities on the fracture surface were observed using a confocal scanning laser microscope. First, the laser beam was centered on the area of the fracture surface adjoining the crack tip by direct observation through an attached optical microscope. An area of 1 mm^2 of fracture surface at the crack tip was scanned by the laser beam and reflected to the detector. In order to make a three-dimensional profile of fracture surface asperities, a piezo-electric stage was used. The piezo-electric stage controls the distance between specimen and microscope. This provides successive images of level contours of the asperities from their peaks to their valleys. All images were combined to create an image of the configuration of the fracture surface profile. Taking different slices through this profile and determining an average value of fracture surface asperity height in each slice revealed that the asperity height is dramatically influenced by the magnitude of the compressive overstrain. In this study the fracture surface asperity heights of specimens under both constant amplitude straining and strain histories containing periodic compressive overstrain cycles were measured. The CSLM measurements of the fracture surfaces of small cracks revealed that there was little variation of asperity heights across the fracture surfaces. The maximum variation of asperity height in an area of 1 mm^2 did not exceed 10%. The fracture surface asperity heights reported in the results section of this study are the average values of asperity height measured on a 1-mm^2 area of the fracture surface.

Results and Discussion

Optical Sectioning to Construct a 3D Image of a Crack using the CSLM

Figure 3 shows an optical sectioning of a small crack and gives the crack cross section at Point i (where $L = L_i$ μm) from the left hand end of the crack. Each optical cross section is parallel to the X-Z plane (see Fig. 3). The difference in height between the peak and the valley in the X-Z plot gives the crack depth at that slice. The peak value in each slice was considered to be the average of peaks at the

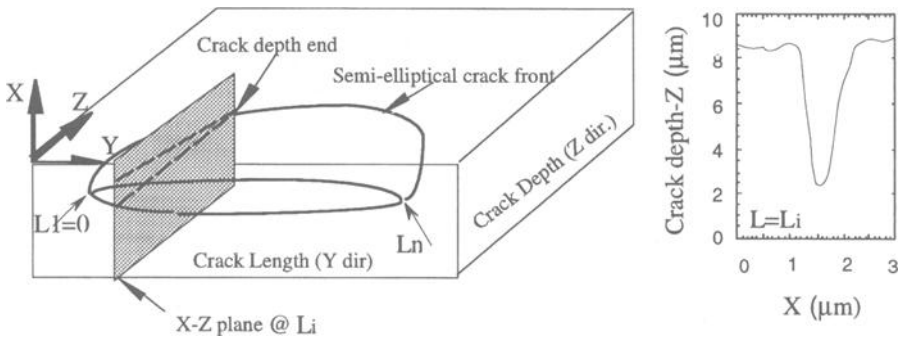

FIG. 3—*An optical section obtained from the 3D crack profile along the crack length.*

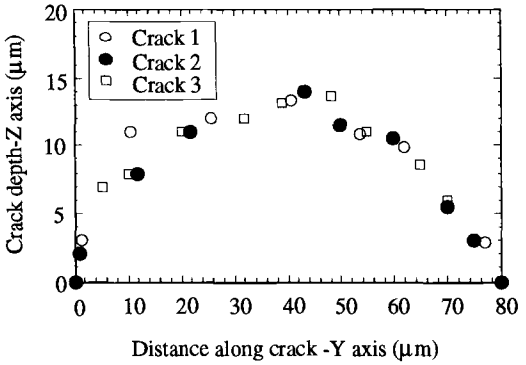

FIG. 4—*Profile of crack depth.*

crack mouth. Using images obtained at successive static strain levels of the pulling/pressurizing device provided crack mouth displacement measurements in the X-direction. Figure 4 presents the crack front shapes for two $\lambda = -1$ microcracks (Crack 1 and Crack 2) and an equibiaxial fatigue crack (Crack 3). The cracks all developed an approximately semi-elliptical front. Each datum point on this semi-elliptical crack front corresponds to deepest point at an optical slice such as that shown in Fig. 3.

Crack Growth under Constant Amplitude Straining

Uniaxial Fatigue Straining ($\lambda = -\nu$)—Under a uniaxial straining condition, cracks first initiated and grew into the specimen on the maximum shear plane at 45° to the specimen surface (Stage I growth). After growing through one or two grains into the specimen (in the depth direction) in Stage I, the crack plane (in the depth direction) rotated to become normal to the axis of straining (Stage II growth). The plane of crack growth in Stage II was observed from the fracture surface of the specimen after failure. Figure 5*a* illustrates the plane and direction of initial growth of a crack under uni-

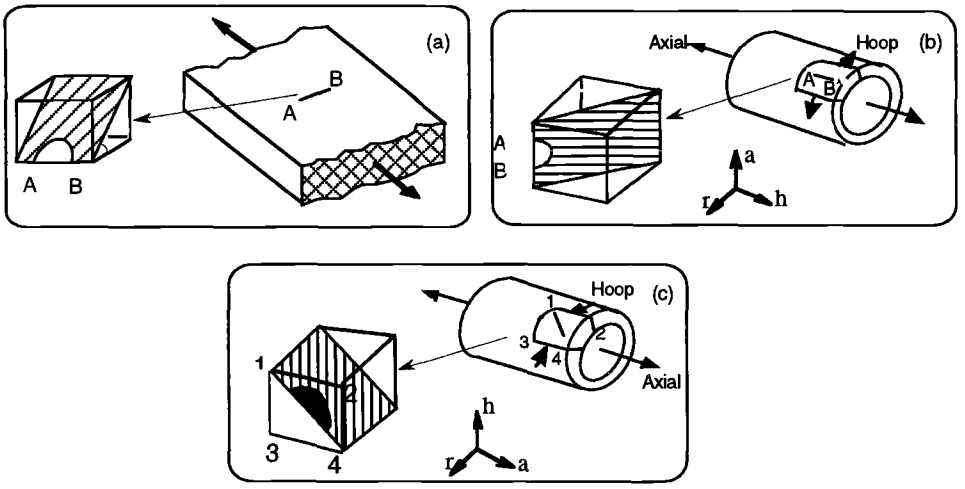

FIG. 5—*Crack initiation plane and initial growth under* (a) *uniaxial straining,* (b) *equibiaxial straining, and* (c) *shear straining.*

axial straining. The ratio of crack depth to half crack length (a/c) was obtained in 1045 Steel for short fatigue crack lengths of the order of 125 to 250 mm using CSLM [5]. Aspect ratios (a/c) of cracks that experienced fatigue straining just above the fatigue limit stress were found to be approximately 0.80. Using the CSLM technique, the crack depth profile (in Stage I crack growth) was also found to be semi-elliptical in shape.

Equibiaxial fatigue cracks ($\lambda = +1$)—In equibiaxial (in-phase biaxial) fatigue tests on tubular specimens, cracks initiated and grew along the specimen surface on the two maximum shear planes parallel and vertical to the specimen axis and propagated into the specimen on planes at 45° to the specimen axis. Figure 5*b* shows the plane of crack initiation and initial growth of an equibiaxial fatigue crack ($\lambda = +1$). About two thirds of the equibiaxial fatigue cracks initiated in the axial direction of the tubular specimen. The greater number of cracks in this direction that coincides with the direction of rolling is attributed to elongated sulfide inclusions parallel to the rolling direction. Equibiaxial cracks initiated on the planes of maximum shear strain at fractions of specimen fatigue life (N/N_f) of 0.074, 0.088, 0.086, 0.083, and 0.085 at biaxial strain amplitudes of 0.10, 0.135, 0.15, 0.22, and 0.30%, respectively.

Vertical equibiaxial cracks initiated at several points on the tubular specimen and propagated along and into the specimen. In most tests, failure defined by oil leaking through the specimen thickness occurred when the crack length exceeded 2 mm. Figure 6 shows photos of initial growth and failure of equibiaxial fatigue cracks. Figure 7*a* presents the crack depth measurement results on the plane of maximum shear strain as the number of cycles increase. These results show that as the magnitude of the strain amplitude increases, cracks grow faster into the specimen surface. The variation of aspect ratio (a/c) with crack depth for equibiaxial fatigue cracks ($\lambda = +1$) is given in Fig. 7*b*.

Biaxial shear cracks of ($\lambda = -1$) and ($\lambda = -0.625$)—In 180° out-of-phase biaxial straining tests on tubular specimens, cracks initially nucleated on an active slip band system that coincided with the maximum shear planes at ±45° to the axial direction of the specimen. Microcracks (shear planes) propagated into the surface of the specimen while their length remained unchanged. Under pure shear straining, microcracks of 3 μm initiated along slip bands on the crack plane at fractions of specimen fatigue life (N/N_f) of 0.05, 0.11, 0.095, and 0.09 at shear strain amplitudes of 0.3, 0.4, 0.6, and 1.0%, respectively. Similarly, initiation of cracks (3 μm) under a biaxial strain ratio of −0.625 occupied a fraction of specimen life (N/N_f) of 0.088, 0.074, 0.078, and 0.068 at axial and hoop strain amplitude pairs of (0.128%, −0.08%), (0.16%, −0.10%), (0.20%, −0.125%), (0.24%, −0.15%), and (0.29%, −0.18%), respectively. Figure 5*c* shows the plane of maximum shear strain and the direction of initial growth of microcracks ($\lambda = -1$ and -0.625).

To measure the depth of microcracks, fatigued tubular specimens were pressurized internally using a hydraulic device in the confocal scanning laser microscope. Hoop and longitudinal stresses due

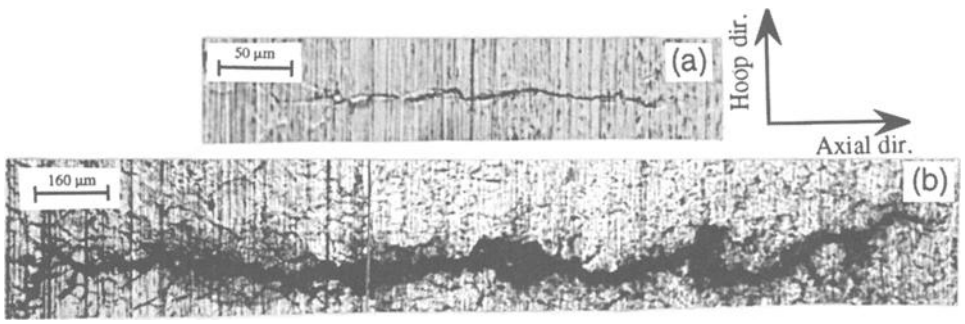

FIG. 6—*Micrographs of* (a) *initial growth, and* (b) *failure under equibiaxial fatigue straining.*

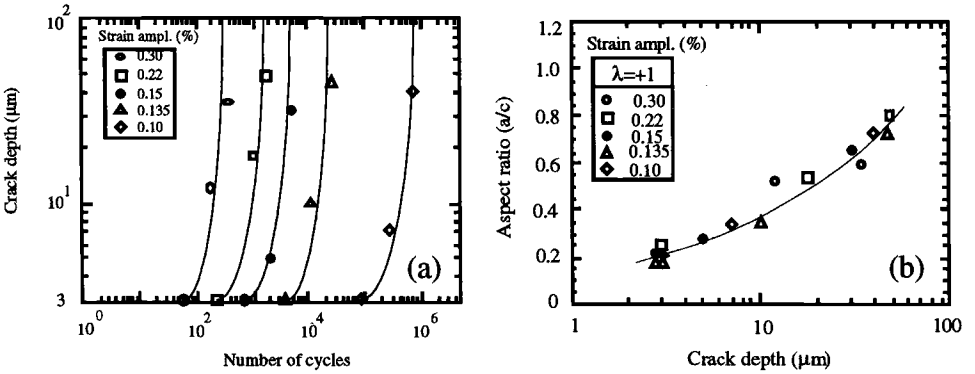

FIG. 7—(a) *Early crack growth results under equibiaxial CAS fatigue straining, and* (b) *crack aspect ratio versus the crack depth for* $\lambda = +1$.

to a progressive increase in the static internal pressure opened the crack along the maximum shear plane and three-dimensional images of the crack were acquired. The crack opened and the crack depth increased with internal pressure until it was fully open. Figure 8 shows a family of curves of the depth of a typical shear crack ($\lambda = -1$) at its deepest point versus the hoop stress due to internal pressure. The crack opening stress was defined as the static hoop stress at which the crack depth reached its maximum value (crack fully opened) during a progressive increase in internal pressure. The maxima of the curves (in Fig. 8) give the crack depths at various numbers of cycles for a shear microcrack formed under a cyclic shear strain amplitude of 0.3%.

Under both shear straining ($\lambda = -1$) and a biaxial straining of $\lambda = -0.625$, many microcracks initiated and grew into the specimens. In each specimen, about 10 microcracks were marked and the depth and length of these microcracks were measured as the number of cycles progressed. Then the average crack length and depth of the ten microcracks at given cycle numbers from initiation to failure were calculated. The scatter in the measured length and depth of cracks in a specimen did not exceed 15%. The propagation of microcracks can be characterized as R-system crack behavior using the terminology introduced first by Marco and Starkey [*8*]. In this system, cracks start at many points

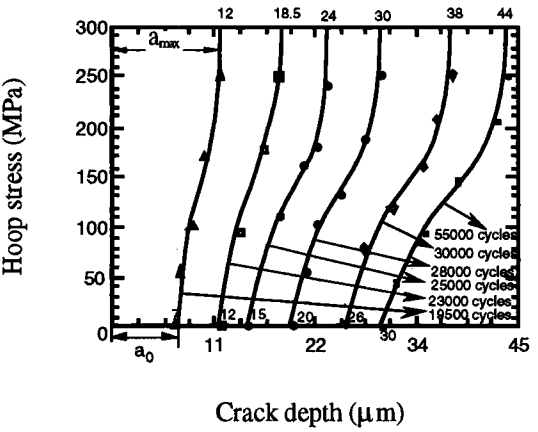

FIG. 8—*Crack depth measurements versus static hoop stress as the number of cycles increases.*

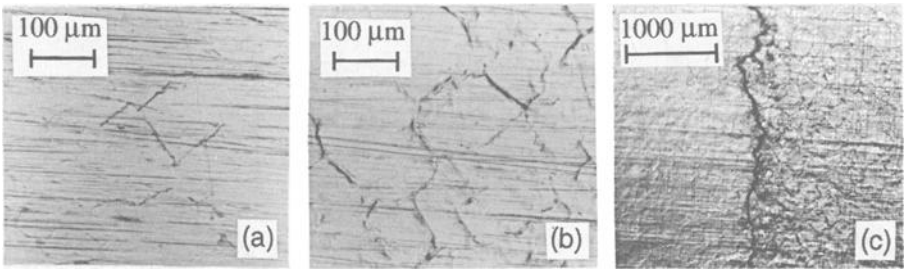

FIG. 9—*Microphotographs of shear cracks from initiation to failure.*

on a specimen and progress toward the interior of the material (depth direction). The number of microcracks increased as cycling progressed. Once a crack initiated it grew into the specimen as the number of cycles increased but, its surface length did not increase much until the specimen reached about 90% of its fatigue life. The microcracks were uniformly distributed on the surface of specimen. At 60 to 70% of the fatigue life, linking up of a few microcracks was observed (Fig. 9*a*). At 90 to 95% of the fatigue life when the shape ratio of crack depth to half crack length reached unity, the microcracks began to grow in the length as well as in the depth direction and began linking up on shear planes (Fig. 9*b*). This linking up of microcracks led to failure shortly thereafter (Fig. 9*c*). Typically during failure, inclined microcracks linked up in the longitudinal direction of a specimen to form a 2.0 to 5.0-mm crack.

Figure 10*a* shows crack depth versus cycles data for constant amplitude tests of the tubular 1045 steel specimen under pure shear straining from initiation (a slip band crack of 3 μm) to failure (a crack size of 1 mm). The solid part of the curves corresponds to crack growth on the plane of maximum shear strain and the dashed part of the curves corresponds to the period of rapid linking up of microcracks (shear planes) at the end of a test. The variation of aspect ratio (a/c) with crack depth for different shear strain amplitudes as a pure shear microcrack grew in the depth direction, with almost no increase in surface crack length (up to 90% of fatigue life), is given in Fig. 10*b*.

The growth mechanisms of shear fatigue cracks and equibiaxial fatigue cracks are schematically shown in Fig. 11. Under biaxial shear straining, the initiation and initial growth of cracks on planes of maximum shear strain occupied up to 90% of the fatigue life, and then failure occurred by a rapid

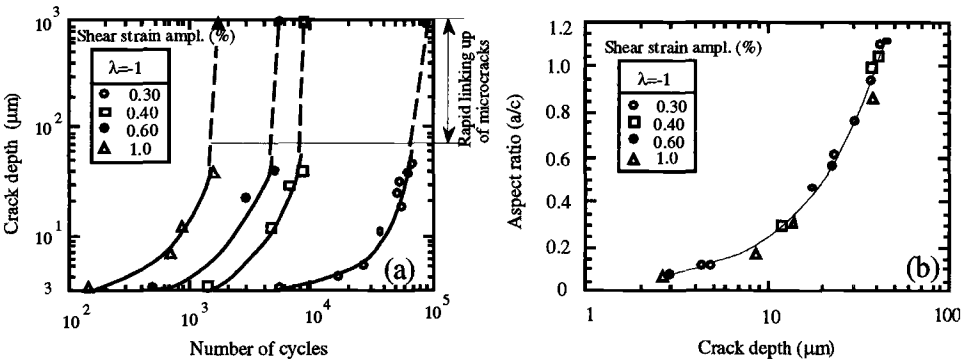

FIG. 10—(a) *Shear crack growth results from initiation to failure, and* (b) *shear crack aspect ratio versus the crack depth.*

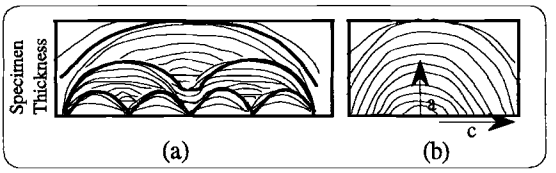

FIG. 11—*Crack growth mechanisms under* (a) *shear, and* (b) *equibiaxial fatigue straining.*

linking of cracks on shear planes. However, in equibiaxial fatigue straining ($\lambda = +1$), once a crack initiated, it grew in the length and depth directions until failure took place.

The Effects of Periodic Compressive Overstrains on Fracture Surface Asperities, Crack Growth Rate and Fatigue Life

Uniaxial Fatigue Straining ($\lambda = -\nu$)—An examination of the growth of short fatigue cracks under constant amplitude straining and during strain histories having periodic compressive overstrains of various magnitudes revealed that the fracture surface near the crack tip and the crack growth rate changed dramatically with the magnitude of the compressive overstrain. The height of the surface irregularities reduced as the compressive overstrain increased, progressively flattening fracture surface asperities near the crack tip.

CSLM image processing of the fracture surface in an area immediately behind the fatigue crack tip was used to measure the height of asperities for constant amplitude straining and for periodic compressive overstrains of −0.17, −0.24, and −0.38% (followed by 50 small fatigue cycles). Asperity height decreased from 28 μm in constant amplitude straining to 18, 13, and 8 μm for −0.17, −0.24, and −0.38% overstrains, respectively. A complementary investigation using a scanning electron microscope (SEM) revealed compression-induced abrasion marks. The abrasion marks corresponded to the region close to the crack tip location when the compressive overstrains were applied. Figure 12*b* is a scanning electron micrograph of an asperity immediately behind the crack tip showing the area flattened due to a compressive overstrain of −0.38%. This is compared to the height of an asperity in constant amplitude straining and a stress amplitude of 0.075% in Fig. 12*a*.

Figure 13*a* shows crack depth versus number of cycle plots for cracks for various magnitudes of the compressive overstrains. Figure 13*b* shows that as the magnitude of periodic compressive overstrain increases the height of fracture surface asperity reduces significantly.

The crack growth rate of short fatigue cracks in 1045 steel increases dramatically as the magnitude of compressive overstrain increases. A compressive overstrain led to a flattening of roughness asperities and therefore a reduction in closure stress. In this regard, Henkener et al. [*9*] reported that the crack growth rate increased as the magnitude of a compressive overload increased. The increased

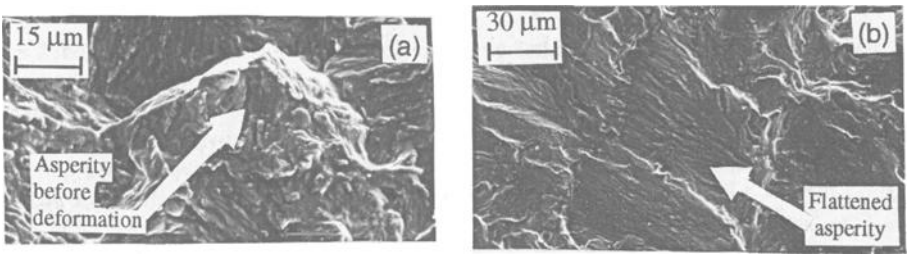

FIG. 12—*Fracture surface asperities before and after the application of uniaxial PCO.*

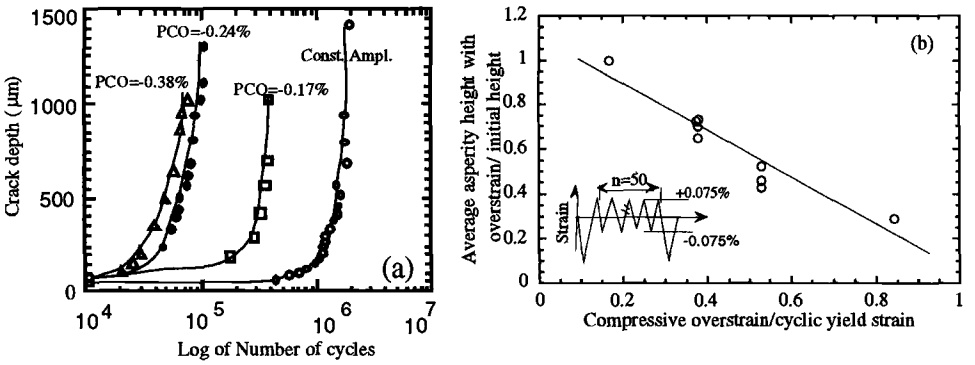

FIG. 13—(a) *Crack growth behavior under CAS and various PCO histories, and* (b) *asperity height versus various PCO magnitudes.*

compressive overload led to an increase in the range of the effective intensity factor. Herman et al. [*11*] and Hertzberg et al. [*10*] also showed that a low closure stress (due to compressive loads) is associated with the crushing of asperities in the crack wake.

The crack growth behavior of short fatigue cracks under three periodic compressive overstrains (Fig. 13*a*) shows that the increase in crack growth rate from −0.17 to −0.24% compressive overstrain is much higher than that for an interval from −0.24 to −0.38% compressive overstrain.

For a 1-mm increase in crack depth in this figure, a test at a −0.17% overstrain requires 8000 blocks (50 × 8000 = 400 000 cycles) while the tests with −0.24 and −0.38% overstrains correspond to about 1800 and 1500 blocks, respectively. In this regard, Kemper et al. [*12*] and Tack and Beevers [*13*] observed a similar saturation effect in which increases in compressive overstrain beyond a certain level did not result in additional increases in crack growth rate. Figure 14*a* plots fatigue lives versus maximum shear strain for uniaxial CAS and PCO histories. This figure shows that the fatigue strength reduced by a factor that ranged from 1.50 at short lives (10^4 cycles) to 2.0 at long lives (10^7 cycles) when periodic compressive overstrains of −0.38% were applied.

Biaxial Fatigue Straining—Figures 14*b–d* plot fatigue lives versus the maximum shear strain for biaxial strain ratios of −1, −0.625, and +1. These figures show a significant decrease in the biaxial fatigue strength of specimens that were subjected to the in-phase periodic compressive overstrains of −0.30%. The fatigue strength reduction due to the overstrains for $\lambda = -1$ straining varies from 1.40 at short lives (10^4 cycles) to 1.75 at long lives (10^7 cycles), for biaxial tests with a strain ratio of $\lambda = -0.625$ the reduction varied from 1.50 at short lives (10^4 cycles) to 1.90 at long lives (10^7 cycles); and for equibiaxial tests the reduction varied from 1.75 at short lives (10^4 cycles) to 2.80 at long lives (10^7 cycles).

CSLM measurements and SEM examination of crack fracture surfaces, which had experienced in-phase periodic compressive overstrains, revealed that for all strain ratios the fracture surface asperities at the crack tip were severely flattened, suggesting that the decreases in fatigue lives are mainly due to the crushing of fracture surface asperities by in-phase compressive overstrains. A typical SEM fractograph of a specimen subjected to in-phase biaxial compressive overstrains of −0.3% followed by 19 small $\lambda = -1$ (shear straining) tension-compression cycles of ±0.15% strains is shown in Fig. 15. A noticeable feature of the flattened asperities on the fracture surface of the in-phase PCO tests is the parallel abrasion lines. The deduction, that these lines are induced by the abrasion between

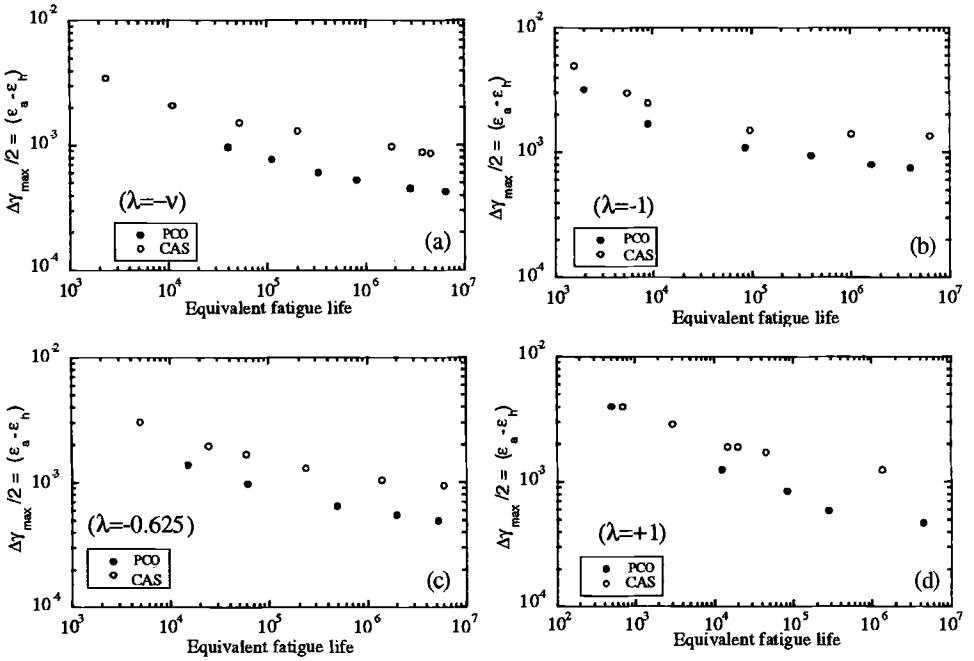

FIG. 14—*Fatigue life data versus maximum shear strain component for CAS and PCO histories:* (a) *uniaxial straining,* (b) *shear straining,* (c) *biaxial straining of −0.625 strain ratio, and* (d) *equibiaxial straining.*

crack flanks due to the compressive overstrain, is substantiated by the observation that parallel lines are formed in the same direction in all flattened areas. Similar reductions of asperity heights were observed for all other strain ratios.

For shear straining ($\lambda = -1$), CSLM observations showed that the application of a −0.3% com-

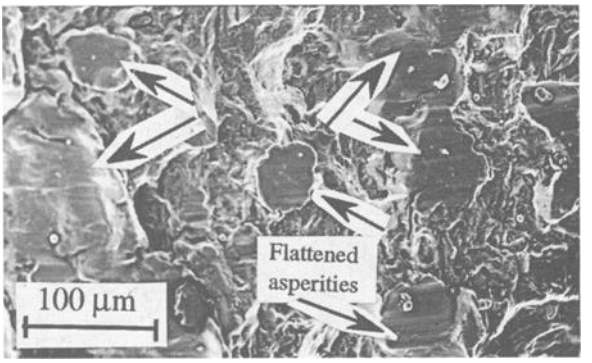

FIG. 15—*SEM microphotograph of flattened fracture surface asperity under PCO shear straining history.*

pressive overstrain crushed the fracture surface asperities and resulted in fully open crack growth with no crack face interference. Thus, the full range of applied strain intensity was effective. For equibiaxial straining ($\lambda = +1$), in-phase PCO cycles increase the portion of fatigue cycle that is effective. Small cycle numbers were chosen so that the crack opening stress remained below the minimum stress and the whole strain cycle was effective. For PCO biaxial fatigue straining of -0.625, there is both a decrease in crack face interference in the shear mode and an increase in the effective portion of the opening mode due to overstrains. Again small cycle numbers were chosen so that the crack face did not touch and the whole strain cycle was effective.

Closure Free Fatigue Lives and Crack Growth Rates under various Biaxial Strain Ratios

Various critical shear plane parameters have been used to correlate fatigue lives at different strain ratios [*14*]. All of them involve some combination of the shear strain range on the plane of maximum shear strain ($\Delta\gamma_{max}$) and the normal strain range ($\Delta\varepsilon_n$) acting on this plane. Reference *14* showed that these parameters could also be adapted to describe the strain intensity factor range. All of them showed roughly the same ability to correlate fatigue lives and crack growth rates. As mentioned in the previous section closure free crack growth was achieved in PCO tests by choosing a number of small cycles that maintained the measured crack opening stress below the minimum stress of small cycles. Figure 16 plots the fatigue lives versus the Brown and Miller parameter ($\Delta\gamma_{max}/2 + 0.3\Delta\varepsilon_n$) for various strain ratios. The upper curve gives fatigue lives under constant amplitude straining and the lower curve gives equivalent small cycles for strain histories containing periodic compressive overstrains in which the small cycles had no crack closure. Both fatigue lives obtained under constant amplitude straining and closure free fatigue lives for the various strain ratios are correlated within a factor of 3 in life by the parameter. Reference *14* showed that other critical plane theories gave similar correlations.

The effective strain intensity equivalent to the Brown and Miller fatigue life parameter is given [*14*] by $\Delta K_{eff} = QG\,(F_{II}\Delta\gamma_{max} + 0.78\,F_I\Delta\varepsilon_n)\sqrt{\pi a}$, where G is the shear modulus, F_I and F_{II} are geometry shape factors in tensile mode and shear mode respectively, and Q is a strain concentration factor for short cracks.

Crack growth rates for biaxial strain ratios of $-\nu$, -0.625, -1, and $+1$ versus the effective strain intensity factor range (ΔK_{eff}) values are plotted in Fig. 17.

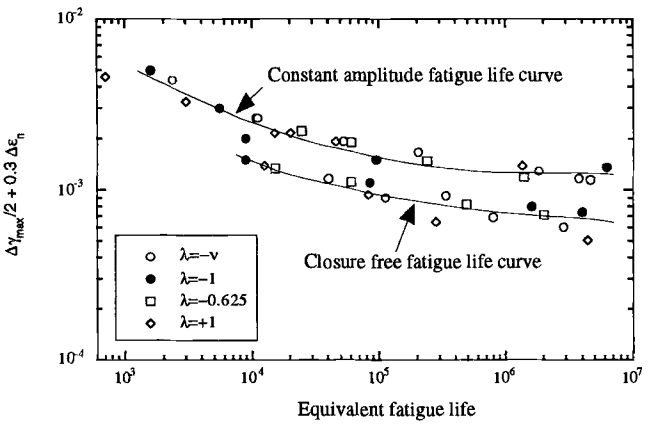

FIG. 16—*Fatigue lives for tests at various strain ratio versus the Brown and Miller parameter for constant amplitude straining and periodic compressive overstrain histories.*

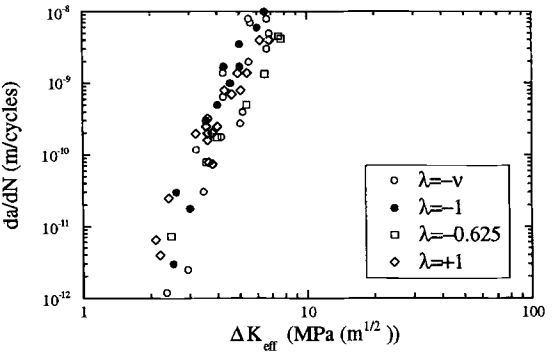

FIG. 17—*Crack growth rate versus effective strain intensity factor range of various strain ratios.*

Conclusions

In this paper crack growth mechanisms and crack growth rates under constant amplitude straining and periodic compressive overstrain histories were studied. Four principal strain ratios of $-\nu$, -0.625, -1, and $+1$ were chosen.

1. In uniaxial straining ($\lambda = -\nu$), cracks initiated along the maximum shear plane at 45° to the surface of the specimen (Stage I growth) and failure then took place by Stage II growth perpendicular to the axis of the specimen. In equibiaxial fatigue straining ($\lambda = +1$), cracks nucleated on the two maximum shear planes parallel and perpendicular to the specimen axis and initially propagated into the specimen on planes at 45° to the specimen surface (Stage I growth). They then propagated normal to the stress axis (Stage II growth). In both uniaxial and equibiaxial fatigue straining, a crack, once initiated, grew in the length and depth directions until failure took place.
2. In tests with biaxial strain ratios of $\lambda = -1$ and $\lambda = -0.625$, surface cracks initially nucleated on slip bands at 40° to 45° to the axis of the specimen. Then the growth of microcracks on shear planes into the specimen occupied up to 90% of the fatigue life during which time the surface length of the microcracks remained nearly constant. The microcracks started increasing in length after the crack became semi-circular ($a/c = 1$) at about 90% of fatigue life. Failure then occurred by a rapid linking of microcracks.
3. CSLM measurements and an SEM examination of the growth of short fatigue cracks under uniaxial and biaxial constant amplitude straining and during strain histories having periodic compressive overstrains revealed that the crack growth increased dramatically with the magnitude of the compressive overstrain. The height of the fracture surface irregularities reduced progressively as the compressive overstrain increased and flattened fracture surface asperities near the crack tip. This resulted in a reduced crack closure stress and a faster crack growth.
4. The magnitude and frequency of application of the periodic compressive overstrain cycles in the second test series was chosen to reduce the crack opening stress to a level below the minimum stress level of the constant amplitude cycles so that they experienced closure free crack growth. The compressive overstrains significantly increased crack growth rates and decreased the threshold strain intensity for the smaller constant amplitude cycles. They also caused a large decrease in the small cycle fatigue resistance as measured by their equivalent strain-life curves.

Acknowledgment

The authors wish to thank the Ministry of Culture and Higher Education of Iran for the financial support.

References

[1] Parson, M. W. and Pascoe, K. J., "Observations of Surface Deformation, Crack Initiation and Crack Growth in Low-cycle Fatigue under Biaxial Stress," *Material Science Engineering,* Vol. 22, 1976, pp. 31–50.

[2] Brown, M. W. and Miller, K. J., "A Theory for Fatigue Failure under Multiaxial Stress-Strain Conditions," *Proceedings of the Institution Mechanical Engineering,* Vol. 187, 1973, pp. 745–755.

[3] Socie, D., "Critical Plane Approaches for Multiaxial Fatigue Damage Assessment," *Advances in Multiaxial Fatigue, ASTM STP 1191,* D. L. McDowell, and R. Ellis, Eds., American Society for Testing and Materials, Philadelphia, PA, 1993, pp. 7–63.

[4] Varvani-Farahani, A. and Topper, T. H., "The Effect of Periodic Compressive Overstrain Excursions on Crack Closure and Crack Growth Rates of Short Fatigue Cracks-Measurements and Modelling," *Advances in Fatigue Crack Closure Measurements and Analysis, ASTM STP 1343,* accepted for publication, 1999.

[5] Varvani-Farahani, A. and Topper, T. H., "Crack Growth and Closure Mechanisms of Shear Cracks under Constant Amplitude Biaxial Straining and Periodic Compressive Overstraining in 1045 Steel," *International Journal of Fatigue,* Vol. 19, No. 7, 1997, pp. 589–596.

[6] Varvani-Farahani, A., Topper, T. H., and Plumtree, A., "Confocal Scanning Laser Microscopy Measurements of the Growth and Morphology of Microstructurally Short Fatigue Cracks in Al 2024-T351 Alloy," *Fatigue and Fracture of Engineering Materials and Structure,* Vol. 19, No. 9, 1996, pp. 1153–1159.

[7] Varvani-Farahani, A. and Topper, T. H., "Short Fatigue Crack Characterization and Detection using Confocal Scanning Laser Microscopy (CSLM)," *Nontraditional Methods of Sensing Stress, Strain and Damage in Materials and Structures, ASTM STP 1318,* G. F. Lucas and D. A. Stubbs, Eds., American Society for Testing and Materials, West Conshohocken, PA, 1997, pp. 43–55.

[8] Marco, S. M. and Starkey, W. L., "A Concept of Fatigue Damage," *Transactions of ASME,* Vol. 76, 1954, pp. 627–632.

[9] Henkener, J. A., Scheumann, T. D., and Grandt, A. F., "Fatigue Crack Growth Behaviour of Peakaged Al-2.6Li-0.09Zr Alloy," *Proceedings,* Fourth International Conference on Fatigue and Fracture Threshold, 1990, pp. 957–962.

[10] Herman, W. A., Hertzberg, R. W., and Jaccard, R., "Prediction and Simulation of Fatigue Crack Growth under Conditions of Low Cycle Closure," *Proceedings,* Advance Fracture Research, 7th International Conference on Fracture, 1989, p. 1417.

[11] Hertzberg, R. W., Herman, W. A., Clark, T., and Jaccard, R., "Simulation of Short Fatigue Crack and other Low Closure Loading Conditions Utilizing Constant $K_{max}\Delta K$-decreasing Fatigue Crack Growth Procedures" *Small-Crack Test Methods, ASTM STP 1149,* American Society for Testing and Materials, Philadelphia, PA, 1992, pp. 197–220.

[12] Kemper, H., Weiss, B., and Stickler, R., "An Alternative Prediction of the Effect of the Stress-Ratio on the Fatigue Threshold," *Engineering and Fracture Mechanics,* Vol. 4, 1989, pp. 591–600.

[13] Tack, A. J. and Beevers, C. J., "The Influence of Compressive Loading on Fatigue Crack Propagation in three Aerospace Bearing Steels," *Proceedings,* Fourth International Conference on Fracture and Fatigue Thresholds, 1990, pp. 1179–1184.

[14] Varvani-Farahani, A., "Biaxial Fatigue Crack Growth and Crack Closure under Constant Amplitude and Periodic Compressive Overload Histories in 1045 Steel," A Ph.D. thesis, University of Waterloo, Canada, 1998.

Jin Ho Lee,[1] *Young Jin Kim,*[1] *and Kee Bong Yoon*[2]

Determination of C_t-Parameter Considering Effects of Accumulated Creep Deformation During Loading Period

REFERENCE: Lee, J. H., Kim, Y. J., and Yoon, K. B., **"Determination of C_t Parameter Considering Effects of Accumulated Creep Deformation During Loading Period,"** *Fatigue and Fracture Mechanics: 30th Volume, ASTM STP 1360,* P. C. Paris and K. L. Jerina, Eds., American Society for Testing and Materials, West Conshohocken, PA, 2000, pp. 313–326.

ABSTRACT: Most of the assessment equations for C_t, which is a well-known fracture parameter characterizing creep and creep-fatigue crack growth rates, have limited applicability to constant load conditions. However, crack growth due to creep can also occur under varying load conditions when the load rate is slow enough such that accumulated creep deformation near the crack tip can't be neglected. An estimation equation of the C_t-parameter that can be applied to the case of slow load rising was derived by the authors and denoted as $(C_t)_r$.

In this paper, correlation between $(C_t)_r$ at the end of the load-rising period and C_t at the beginning of the succeeding load hold period is shown. And a new C_t estimation equation that can be applied to the load hold period following a slow load rising period is derived using the relation between $(C_t)_r$ and C_t. Finite-element analyses of several cases with various load-rising conditions were performed. The results support accuracy of the proposed C_t estimation scheme. General applicability of the equation is also discussed.

KEYWORDS: creep, fatigue, crack, time dependent fracture mechanics, C_t-parameter, C^*-integral

Nomenclature

a	Crack length, mm
A	Coefficient of Norton's creep law, $MPa^{-n} \cdot h^{-1}$
n	Exponent of Norton's creep law
B, W	Thickness and width of specimen, mm
C_P	Coefficient of loading equation, N/S^{ξ}
ξ	Exponent of loading equation
C^*, $C^*(t)$, $C(t)$, C_t	Creep fracture parameters, MPa · m/h
$(C_t)_r$	C_t - parameter under load-increasing condition, MPa · m/h
E	Modulus of elasticity, MPa
F	Calibration factor of stress intensity factor
$F_{cr}(\theta,n)$, $\tilde{r}_c(\theta,n)$	Dimensionless shape function of creep zone size under load increasing condition and under load hold condition
I_n	HRR integration constant
K, K_I, $K_I(t)$	Stress intensity factor, $MPa\sqrt{m}$
P, $P(t)$	Applied load, N
t_{TR}	Transition time under the load rising condition, s

[1] Ph.D. candidate and professor, respectively, Department of Mechanical Engineering, Sungkyunkwan University, 300 Chunchun-dong, Jangan-gu, Suwon 440-746, Korea.

[2] Associate professor, Department of Mechanical Engineering, Chung Ang University, 221, Huksuk, Dongjak, Seoul 156-756, Korea.

t_T Transition time under the constant load condition, s
t_{rs} Characteristic time, s
$\dot{V}_c$ Load-line displacement rate due to creep, mm/s
α, α_r Material-dependent constant under load-increasing condition and under load hold condition, respectively
β, β_r Irwin's crack length correction factor under load increasing condition and under load hold condition, respectively
η Geometry factor
ν Poisson's ratio

As high-temperature equipments are operated under a cycle of startup, steady operation, and shutdown, cracks existing in the components usually experience fatigue loading of trapezoidal waveshapes [*1,2*]. To simplify modeling of the creep-fatigue crack growth behavior, it was common to assume the trapezoidal waveshape as one with instantaneous loading and unloading. Under the assumption of this loading type, a cracked body will show only cycle-dependent fatigue crack growth during the load rising and decreasing period and will show only time-dependent creep crack growth during the load hold period. Hence, for this simplified waveshape, the stress intensity factor range ΔK has been used for characterizing the cycle-dependent fatigue crack growth rate, and the C_t-parameter has been used for characterizing the time-dependent creep crack growth rate [*3–7*]. However, when the load-rising period is long enough for allowing considerable creep deformation, crack growth behavior during the load-rising period can't be characterized just by ΔK. Additional crack growth due to creep during the load rising period also should be considered by introducing another characterizing parameter such as the C_t-parameter during the load-rising conditions. The authors derived an estimation equation of the C_t-parameter which can be applied to the case of slow load rising and denoted it as $(C_t)_r$ in the previous papers [*8,9*].

In this study extending the previous work, C_t behavior during the load hold period after slow loading is investigated. Correlation between $(C_t)_r$ at the end of the slow loading period and C_t at the beginning of the succeeding load hold period is shown. And a new estimation equation of the C_t-parameter reflecting the effect of the load rising time is proposed. In deriving the new estimation equation of C_t, the previous $(C_t)_r$ equation and the relation between $(C_t)_r$ and C_t are utilized. Finite-element analyses of several cases with various load-rising conditions were performed to show applicability and accuracy of the proposed estimation equation.

Background

For elastic-secondary creeping materials, Riedel derived estimation equations of $C(t)$-integral for the case with the load hold period following a slow load-rising period as well as the case with the slow load-rising period [*10*]. On the other hand, the authors [*8,9*] proposed $(C_t)_r$ as the C_t-parameter under the slow load-rising condition, and Yoon et al. [*11*] proposed an estimation equation of C_t-parameter during the load hold time reflecting the effect of the load rising time using the concept similar to the case of Riedel's $C(t)$-integral. In this section, these parameters are reviewed briefly.

C(t)-*Integral and* C_t-*Parameter Under Load-Rising Condition*

Riedel and Rice derived a C(t) equation during the load hold period after an instantaneous loading as follows [*12*]:

$$C(t) = \frac{1}{n+1}\frac{(1-\nu^2)K_I^2}{Et} + C^* \tag{1}$$

where n is the exponent of Norton's power creep law, ν is Poisson's ratio, E is Young's modulus, K_I is the stress intensity factor, and C^* is the C^*-integral [*13–15*].

Also Riedel [*10*] derived a $C(t)$ equation for the load-rising condition as shown in Eq 3 when the applied load increases in proportion to the power, ξ, of the time, t, as shown in Eq 2.

$$P = C_P t^{\xi} \tag{2}$$

$$C(t) = \frac{1}{n+1} \frac{(1-\nu^2)K_I^2(t)}{E\left\{\frac{1}{1+2\xi n} t\right\}} + C^*(t) \tag{3}$$

In these equations, C_P and ξ are loading constants. And, $K_I(t)$ and $C^*(t)$ are functions of time t. When the time elapses as long as the creep zone expands extensively throughout the whole specimen, $C(t)$ becomes equal to $C^*(t)$. A characteristic time for the transition from small-scale creep to extensive creep is defined as the transition time under the load-rising condition, t_{TR}, and is given by

$$t_{TR} = \frac{1+2\xi n}{n+1} \frac{(1-\nu^2)K_I^2(t_{TR})}{C^*(t_{TR})E} \tag{4}$$

As the applied load increases according to Eq 2, the authors denoted the C_t-parameter under the load rising condition as $(C_t)_r$. Estimation equations of $(C_t)_r$ were derived as follows [*8,9*]:

$$(C_t)_r = \frac{4\xi(n-1)}{4\xi(n-1)-n+3} \frac{P(t)\dot{V}_c}{BW} \frac{F'}{F} - C^*(t)\left\{\frac{1}{\eta} \frac{4\xi(n-1)}{4\xi(n-1)-n+3} \frac{F'}{F} - 1\right\} \tag{5}$$

$$(C_t)_r = \frac{4\alpha_r \beta_r F_{cr}(\theta,n)}{E(n-1)} \frac{(1-\nu^2)K_I^4(t)}{W} \frac{F'}{F} (EA)^{\frac{2}{n-1}} t^{-\frac{n-3}{n-1}} + C^*(t) \tag{6}$$

where B is the specimen thickness, W is the specimen width, $\dot{V}_c$ is the load-line displacement rate due to creep, $F = K_I B\sqrt{W}/P$, $F' = dF/d(a/W)$, η is the geometry factor, A is the coefficient of Norton's power creep law, β_r is Irwin's crack length correction factor, and $F_{cr}(\theta,n)$ is the dimensionless shape function of creep zone boundary under the load rising condition. α_r is the material-dependent factor defined as follows:

$$\alpha_r = \frac{n-1}{\pi}\left\{\frac{1}{1+2\xi n}\right\}^{\frac{2}{n-1}} \frac{\xi\{3\xi(n-1)+2\}}{4\xi(n-1)-n+3} \tag{7}$$

When the crack length and the applied load values are known, $(C_t)_r$ can be calculated from Eq 6. Equation 5 can be used for the case when the load-line displacement rate due to creep is measured.

C(t)-*Integral and* C_t-*Parameter Under Load Hold Condition After Slow Loading*

When the load rising time is t_r, the $C(t)$-integral at the end of the load rising period can be calculated by substituting t_r for t in Eq 3 [*10*]. Hence, when load waveshapes with the slow load-rising period and the succeeding load hold period are applied at the cracked body, the $C(t)$-integral during the load hold time can be derived by substituting $t - t_r + \{1/(1+2\xi n)\}t_r$ for t in Eq 1. The resulting equation is as follows [*10*]:

$$C(t) = \frac{1}{n+1} \frac{(1-\nu^2)K_I^2}{E\left\{t - t_r + \frac{1}{1+2\xi n} t_r\right\}} + C^* \tag{8}$$

Because the effect of the load-rising period is included in Eq 8, this equation may be used as a crack-tip fracture parameter under the load waveshape with the load hold period following a slow load-rising period.

Extending the concept of C^* to the transient creep condition, Saxena [*18*] proposed the C_t-parameter as a creep fracture parameter applicable to the wide range creep conditions. And Saxena et al. [*18,19*] proposed Eqs 9 and 10 as estimation equations of the C_t-parameter under the constant loading condition.

$$C_t = \frac{P\dot{V}_c}{BW}\frac{F'}{F} - C^*\left(\frac{1}{\eta}\frac{F'}{F} - 1\right) \tag{9}$$

$$C_t = \frac{4\alpha\beta\tilde{r}_c(\theta,n)}{E(n-1)}\frac{(1-\nu^2)K_I^4}{W}\frac{F'}{F}(EA)^{\frac{2}{n-1}}t^{-\frac{n-3}{n-1}} + C^* \tag{10}$$

where β is Irwin's crack length correction factor, and $\tilde{r}_c(\theta,n)$ is the dimensionless shape function of creep zone boundary under the constant loading condition. And α is the material-dependent factor defined as follows:

$$\alpha = \frac{1}{2\pi}\left\{\frac{(n+1)I_n}{2\pi(1-\nu^2)}\right\}^{\frac{2}{n-1}} \tag{11}$$

where I_n is the HRR integration constant. When time elapses until the creep zone expands extensively throughout the whole specimen, C_t becomes equal to C^*. A characteristic time for the transition from small-scale creep to extensive creep is defined as the transition time under the constant loading condition, t_T, and is given by

$$t_T = \frac{(1-\nu^2)K_I^2}{(n+1)EC^*} \tag{12}$$

For slow loading, Yoon et al. proposed the following equation for C_t estimation during the load hold time following a slow load-rising period [*11*]:

$$C_t = \frac{4\alpha\beta\tilde{r}_c(\theta,n)}{E(n-1)}\frac{(1-\nu^2)K_I^4}{W}\frac{F'}{F}(EA)^{\frac{2}{n-1}}\left(t - t_r + \frac{\delta}{1+2n}t_r\right)^{-\frac{n-3}{n-1}} + C^* \tag{13}$$

where δ is the scaling constant and is assumed as 1 for convenience. In the above equation, C_t was derived by substituting $t - t_r + \{\delta/(1+2n)\}t_r$ for t in Eq 10 like the case of $C(t)$. Because the effect of the load rising time is included in Eq 13 like Eq 8, this equation can also be used as a fracture parameter characterizing creep crack growth under the load waveshape with the load hold period following a load-rising period.

Theoretical Derivation

It has been a general practice to assume instantaneous loading. Hence, the creep deformation during the load-rising period that may cause additional crack growth could not be considered in the previous models. However, if Eqs 5 and 6, which represent the C_t-parameter during the load rising time, $(C_t)_r$, are used, it may be possible to assess the amount of crack growth due to creep during the slow load-rising period [*8,9*]. For the case of a trapezoidal fatigue loading, the total crack growth rate

$(da/dN)_{total}$ can be expressed as the summation of the cycle-dependent fatigue crack growth rate, the time-dependent creep crack growth rate during the load-rising period, and the time-dependent creep crack growth rate during the load hold period as follows:

$$\left(\frac{da}{dN}\right)_{\text{total}} = \left(\frac{da}{dN}\right)_{\text{fatigue}} + \left(\frac{da}{dN}\right)_{\text{creep/rise time}} + \left(\frac{da}{dN}\right)_{\text{creep/ hold time}} \tag{14}$$

In Eq 14, each term of the right-hand side can be characterized by different fracture parameters. That is, the first term, the cycle-dependent fatigue crack growth rate, can be characterized by the well-known stress intensity factor range ΔK. The second term, the time-dependent creep crack growth rate during the load-rising period, can be characterized by $(C_t)_r$ proposed by the authors [*8,9*]. And the third term, the time-dependent creep crack growth rate during the load hold period, is known to be characterized by the C_t-parameter during the load hold period. The last parameter, C_t, however, should be estimated by considering the accumulated creep deformation during the preceding load rising period. Therefore, the C_t estimation equation of this case is discussed further in this section.

To consider the creep effect during the preceding load rising period, Yoon et al. employed $t - t_r + \{\delta/(1 + 2n)\}t_r$ instead of t as shown in Eq 13 [*11*]. In this section, C_t equation during the load hold period after a slow loading is derived analytically by considering the relationship between $(C_t)_r$ at the end of the load rising period and C_t at the beginning of the succeeding load hold period. The relation was given as follows [*9*]:

$$\{(C_t)_r - C^*(t)\}|_{t=t_r} = \frac{4\xi(n-1)}{4\xi(n-1) - n + 3}(C_t - C^*)|_{t=t_r} \tag{15}$$

Then, the C_t-parameter at the beginning of the load hold period following a slow load rise, i.e., at $t = t_r$, can be rearranged as follows:

$$C_t = \frac{4\xi(n-1) - n + 3}{4\xi(n-1)}\{(C_t)_r - C^*(t_r)\} + C^* \tag{16}$$

By inserting Eq 6 into Eq 16, the C_t equation at $t = t_r$ is given by

$$C_t = \frac{4\xi(n-1) - n + 3}{4\xi(n-1)}\left\{\frac{4\alpha_r\beta_r F_{cr}(\theta,n)}{E(n-1)}\frac{(1-\nu^2)K_I^4(t_r)}{W}\frac{F'}{F}(EA)^{\frac{2}{n-1}}t_r^{-\frac{n-3}{n-1}}\right\} + C^* \tag{17}$$

By equating Eq 17 with Eq 10, we then obtain the following equation on time t when C_t values of both cases become equivalent.

$$t = \left\{\frac{4\xi(n-1)}{4\xi(n-1) - n + 3}\frac{\alpha\beta\tilde{r}_c(\theta,n)}{\alpha_r\beta_r F_{cr}(\theta,n)}\right\}^{\frac{n-1}{n-3}} \cdot t_r \tag{18}$$

Equation 18 shows that the C_t values after the load-rising time of t_r in the case of the loading condition described by Eq 2 becomes equivalent to the C_t values after the hold time of t shown by Eq 18 in the case of the instantaneous loading condition. In other words, stress relaxation due to creep at the characteristic time t defined by Eq 18 after instantaneous loading becomes the same as that which occurred during the load-rising time of t_r. This characteristic time t is denoted as t_{rs} in this paper and is rewritten as shown in Eq 19. This characteristic time, then, becomes conceptually similar to the term $\{\delta/(1 + 2n)\}t_r$ proposed by Yoon et al. [*11*]. Hence, Eq 19 shows clearer functional form than $\{\delta/(1 + 2n)\}t_r$ defined previously as an arbitrary scaling factor.

TABLE 1—*Material properties of the 1.25Cr–0.5Mo steel used for finite element calculation.*

Test Temperature, °C	Yield Strength, MPa	Tensile Strength, MPa	Young's Modulus, GPa	Creep Coefficient, A, ($MPa^{-n} \cdot h^{-1}$)	Creep Exponent, n
538	263	390	141	7.76×10^{-36}	13.63

$$t_{rs} = \left\{ \frac{4\xi(n-1)}{4\xi(n-1)-n+3} \frac{\alpha\beta\tilde{r}_c(\theta,n)}{\alpha_r \beta_r F_{cr}(\theta,n)} \right\}^{\frac{n-1}{n-3}} \cdot t_r = \frac{\delta}{1+2\xi n} \cdot t_r \tag{19}$$

Therefore, a generalized C_t estimation equation which can be applied during the load hold time following a slow load rising period is derived by employing the characteristic time t_{rs} as follows:

$$C_t = \frac{4\alpha\beta\tilde{r}_c(\theta,n)}{E(n-1)} \frac{(1-\nu^2)K_I^4}{W} \frac{F'}{F} (EA)^{\frac{2}{n-1}} (t - t_r + t_{rs})^{-\frac{n-1}{n-3}} + C^* \tag{20}$$

The characteristic time t_{rs} introduced in this equation reflects the reduction of C_t at the beginning of the load hold period, which occurs due to the creep deformation accumulated during the load rising period. Thus, the above equation can be used as a fracture parameter characterizing creep crack growth during the load hold period following a slow load-rising period like the generalized $C(t)$-integral proposed by Riedel [*10*].

Finite-Element Analysis

As the load waveshape with the slow load-rising period and the succeeding load hold period is applied to a cracked body, the characteristic time t_{rs} should be determined in advance to calculate the C_t-parameter reflecting the effect of the load rise time using Eq 20. Hence, finite-element analyses are performed to determine the value of t_{rs}. The material properties used in this analysis were measured from a 1.25Cr-0.5Mo steel plate. The tensile and creep properties of the material are summarized in Table 1 [*8,9*]. Two cases of analyses were carried out, one under the slow load-rising condition and the other under the load-holding condition after the instantaneous load increased as described in Table 2. In the former analysis, the applied load is increased linearly from 0 to 42 kN for 8.4 h as described in Table 2. In the latter case, the load is held constant at the value of 15 kN for 1×10^5 h as described in Table 3. The applied load is distributed along the upper portion of the pin hole over a span of 45°. ABAQUS Version 5.7 package was used in the analysis. Figure 1 shows the finite-element mesh of the C(T) specimen type. Only the upper half of the specimen is modeled using the symmetry. The finite-element mesh consists of 490 eight-node plane strain isoparametric elements and 1580 nodes. A crack ratio (a/W) of 0.44 was used. At the crack tip, r^{-1}-type singular elements were generated by collapsing three nodes along a side into one point.

Another set of analyses was performed to assess the accuracy of the C_t estimation scheme shown

TABLE 2—*Values for* $\beta_r \cdot F_{cr}(\theta,n)$ *determined under a load rising condition.*

P_{max}, kN	Load Rising Time, t_r (h)	Transition Time, t_{TR} (h)	Curve Fitting Range (h)	$\beta_r \cdot F_{cr}(\theta,n)$
42	8.4	8.1	0 to 3	1/10.4
			0 to 8.1	1/7.8
			Linear part	1/10.3

TABLE 3—*Values of* $\beta \cdot \tilde{r}_c(\theta,n)$ *determined under a load holding condition.*

P_{max}, kN	Load Holding Time, t_h (h)	Transition Time, t_T (h)	Curve Fitting Range (h)	$\beta \cdot \tilde{r}_c(\theta,n)$
15	1.0×10^5	8.01×10^4	0 to 3	1/14.0
			0 to 8.01×10^4	1/11.4
			Linear part	1/14.2

in Eq 20. As shown in Table 4, several cases of finite-element analyses were carried out with various load-rising periods, crack lengths, and applied load levels. By comparing the C_t values obtained from finite-element analysis with those obtained by Eq 20, the accuracy of the proposed equation is shown.

Results and Discussion

Determination of Characteristic Time t_{rs}

Values of α_r, α, β_r, β, $F_{cr}(\theta,n)$, and $\tilde{r}_c(\theta,n)$ should be known in advance in order to determine the characteristic time t_{rs}, which is necessary to calculate the C_t-parameter of Eq 20. Values of α_r and α can be determined from Eqs 7 and 11, respectively. However, more accurate definition is necessary for the values of β_r, β, $F_{cr}(\theta,n)$, and $\tilde{r}_c(\theta,n)$. By performing finite-element calculations, Bassani et al. [*19*] proposed β as $1/3$ by assuming that $\tilde{r}_c(\theta,n) = \tilde{r}_c(90°, n)$ and that the creep zone expands in a self-similar manner. In order to use $1/3$ as a value of β, the value of $\tilde{r}_c(\theta,n)$ should be determined consistently according to Bassani's definition. On the other hand, the value of $\tilde{r}_c(\theta,n)$ defined by Riedel and Rice in 1980 [*12*] is obtained qualitatively and is different from that derived numerically by Riedel in 1983 [*10*]. Besides, the value of $\tilde{r}_c(\theta,n)$ derived by Riedel is known only for the case of $\xi = 0$ and $n = 5$. The value of $F_{cr}(\theta,n)$ is also known only for the case of $\xi = 1$ and $n = 5$ [*10*]. And the value of β_r previously proposed by the authors is not known yet.

Therefore, at first we determined the value of $\beta_r \cdot F_{cr}(\theta,n)$ under the load-rising condition and also determined the value of $\beta \cdot \tilde{r}_c(\theta,n)$ under the load-holding condition following an instantaneous loading period. Efforts to determine each value of β_r, β, $F_{cr}(\theta,n)$, and $\tilde{r}_c(\theta,n)$ were not made.

Figure 2 shows the analysis results when the applied load increases linearly as indicated in Table 2. In Fig. 2, the $(C_t)_r$ values calculated from Eq 5 and $\dot{V}_c$ determined by finite-element analysis are compared with those calculated from the analytic equation, Eq 6, with the values of $\xi = 1$ and $\beta_r \cdot F_{cr}(\theta,n) = 1/4.05$. In this figure, $(C_t)_r$ is normalized by $C^*(t_r)$ and time t is normalized by t_{TR}. In order to determine the accurate value of $\beta_r \cdot F_{cr}(\theta,n)$, the average value of $(C_t)_r$ calculated by Eq 5 is compared with that calculated by Eq 6. Calculated results of $\beta_r \cdot F_{cr}(\theta,n)$ are shown in Table 2.

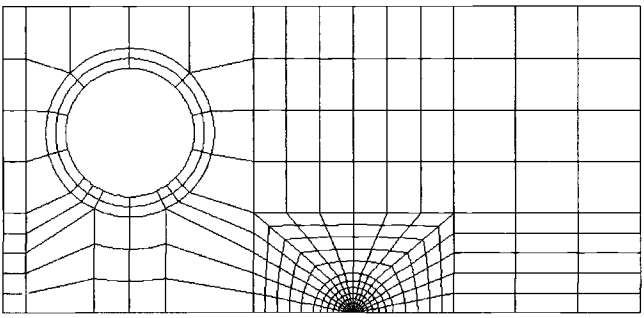

FIG. 1—*Finite-element model of a compact specimen.*

TABLE 4—*Finite-element analysis conditions for various load rising cases.*

Case	Load Rising Time, t_r, (h)	Load Holding Time, t_h, (h)	P_{max}, kN	R	a/W	B, mm	t_{rs} by Previous Model, Eq 13, s	t_{rs} by Current Model, Eq 20, s
Case 1	1/6	1/6	15	0	0.44	20.05	21	34
Case 2	3	1	15	0	0.44	20.05	382	618
Case 3	5	1	15	0	0.44	20.05	637	1029
Case 4	3	1	15	0	0.5	20.05	382	618
Case 5	3	1	15	0	0.55	20.05	382	618
Case 6	3	1	20	0	0.44	20.05	382	618
Case 7	3	1	25	0	0.44	20.05	382	618

Figure 3 shows analysis results when the load is applied instantaneously and is held constant as indicated in Table 3. In Fig. 3, the C_t values calculated from Eq 9 and $\dot{V}_c$ determined by finite-element analysis are compared with those calculated from the analytic equation, Eq 10, with the values of $\xi = 1$ and $\beta \cdot \tilde{r}_c(\theta,n) = 1/7.5$. In Fig. 3, C_t is normalized by C^* and time t is normalized by t_T. The average value of C_t obtained from Eq 9 was also compared with that obtained from Eq 10 to determine the value of $\beta \cdot \tilde{r}_c(\theta,n)$. The calculated results of $\beta \cdot \tilde{r}_c(\theta,n)$ are also summarized in Table 3.

As we can see from the tables, the values of $\beta_r \cdot F_{cr}(\theta,n)$ and $\beta \cdot \tilde{r}_c(\theta,n)$ vary according to the curve fitting range. Hence, in order to acquire reliable and reproducible values of $\beta_r \cdot F_{cr}(\theta,n)$ and $\beta \cdot \tilde{r}_c(\theta,n)$, an appropriate curve fitting range should be carefully selected in which the characteristics of curves obtained from the finite-element results and the analytically calculated results are well represented. In Fig. 2, the analysis results show the fluctuation of $(C_t)_r$ in the initial part. Except in this part, the results show linear variation of $(C_t)_r$ until the transition time is reached. After the transition time, the results show nonlinear variation of $(C_t)_r$. In Fig. 3, it can be seen that C_t shows the same trend as $(C_t)_r$

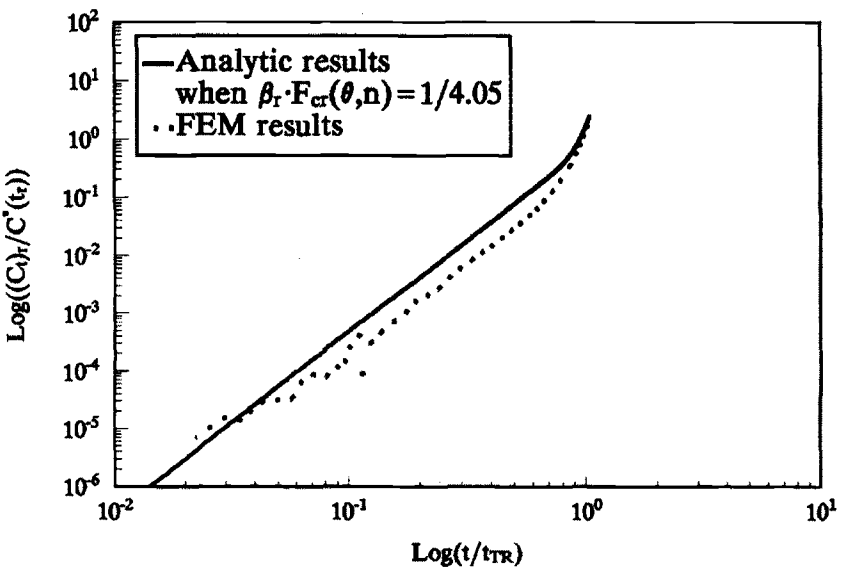

FIG. 2—*Comparison of* $(C_t)_r$ *value between finite-element analysis results and analytic results during load rising period.*

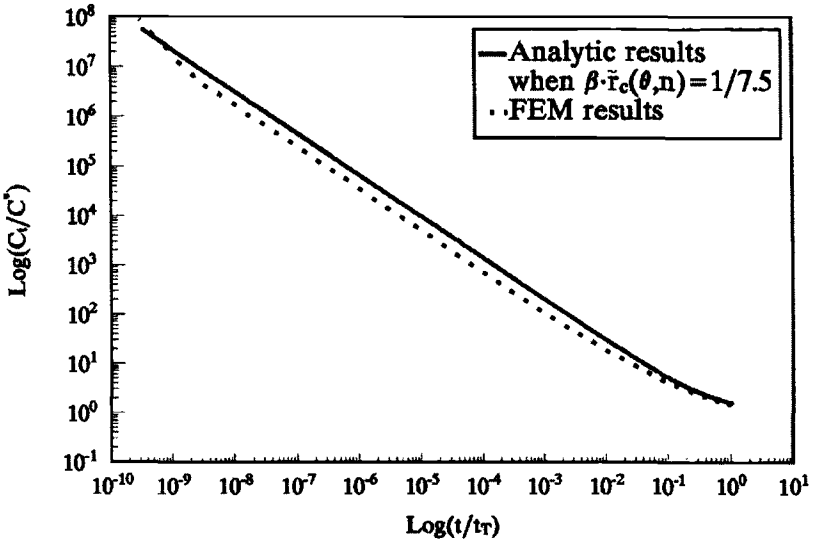

FIG. 3—*Comparison of* C_t *values between finite-element analysis results and analytic results during load holding period.*

of Fig. 2. The fluctuation of the analysis results in the initial part occurs because the creep deformation and the time increment in the initial part are too small to calculate accurately.

The analytical results derived from Eqs 6 and 10 show the continuous linear variation of the $(C_t)_r$ and C_t values until the transition time is reached. After the transition time, $(C_t)_r$ and C_t show clear nonlinear behavior as indicated in Figs. 2 and 3. However, it usually takes very long for a cracked body to reach the transition time as shown in Tables 2 and 3. Since one cycle of fatigue loading is usually short in comparison with the transition time, it is considered to be appropriate to select the linear part of Figs. 2 and 3 as a curve fitting range of assessing the values of $\beta_r \cdot F_{cr}(\theta,n)$ and $\beta \cdot \tilde{r}_c(\theta,n)$.

On the basis of the above arguments, we selected the linear variation part of $(C_t)_r$ and C_t values as the curve-fitting range and acquired 1/10.4 and 1/14.2 as proper values of $\beta_r \cdot F_{cr}(\theta,n)$ and $\beta \cdot \tilde{r}_c(\theta,n)$, respectively.

Accuracy of the Proposed C_t*-Estimation Scheme*

To show the usefulness of the proposed C_t estimation equation that can be applied during the load hold period following a slow load rising, finite-element analyses of several cases were carried out and the analysis results discussed here.

The finite-element analysis results and the analytic results for Case 1 of Table 4 are shown in Fig. 4. In this figure, data plotted before 600 s show the variation of $(C_t)_r$ and data after 600 s show the variation of C_t as a function of time. The finite-element results for the trapezoidal waveshape with the load-rising time of 600 s are compared with those for the trapezoidal waveshape with the instantaneous load rising. It was observed that the former showed considerably small C_t values in comparison with the latter, particularly in the initial part of the load hold period. This is because the creep deformation is accumulated near the crack tip during the load rising period and the crack-tip stress field is redistributed and relaxed. In Fig. 4, "previous model" [*11*] indicates the analytic results calculated from Eq 13 defined by Yoon et al., and "current model" indicates the analytic results calculated from Eqs 19 and 20 newly proposed in this paper.

Figure 4 shows some differences among the results of the previous model, the analytically calcu-

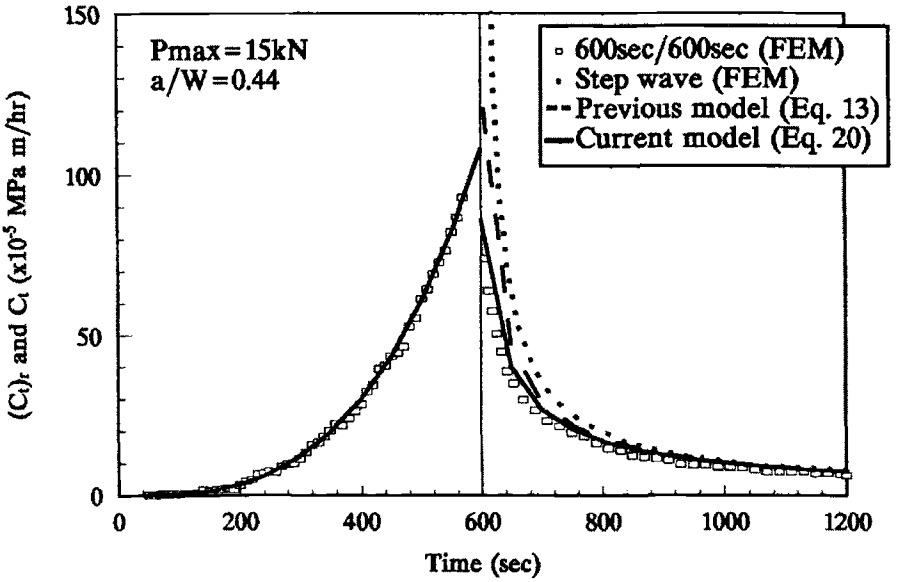

FIG. 4—*Comparison between FEM results and analytic results for Case 1.*

lated results of the current model, and the results of finite-element analysis. Good agreement was observed between the results of the current model and the results of finite-element analysis. On the other hand, the previous model shows some difference. This difference occurs because δ was arbitrarily assumed as 1. δ should be calibrated properly by considering the effect of the accumulated creep deformation during the load-rising period on crack-tip stress relaxation.

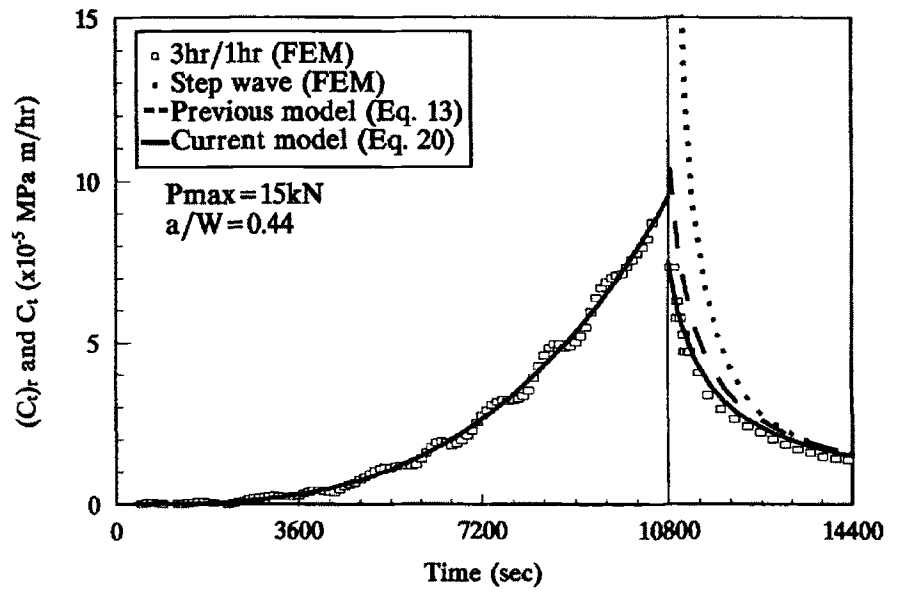

FIG. 5—*Comparison between FEM results and analytic results for Case 2.*

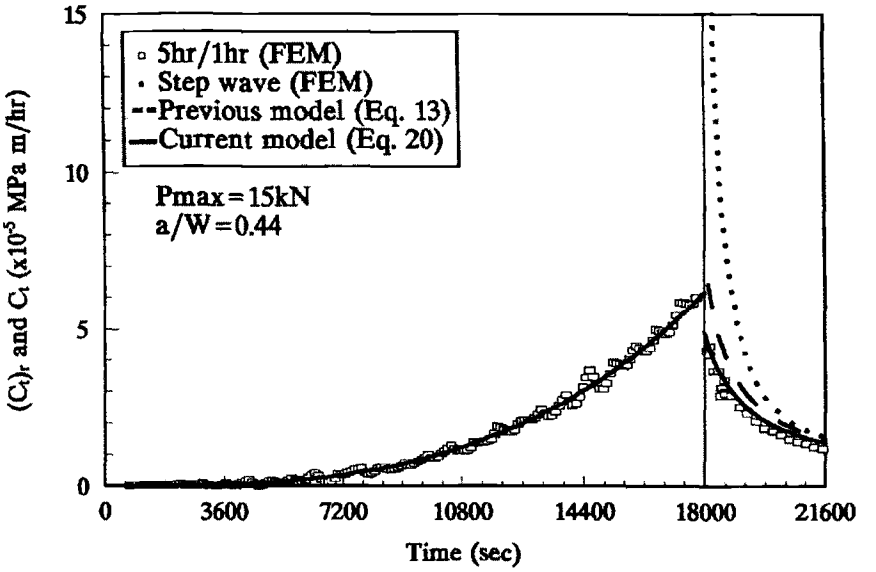

FIG. 6—*Comparison between FEM results and analytic results for Case 3.*

Figures 5 and 6 show the finite-element analysis results and the analytic results for Case 2 and Case 3 in which the load rising time of Case 1 was changed to 3 h and 5 h, respectively. In these cases, good agreement was also observed between the results of the current model and the results of finite-element analysis. Figures 7 and 8 show the analysis results and the analytic results for Case 4 and Case 5 in which the crack ratio (a/W) of Case 1 was changed to 0.5 and 0.55, respectively. Good agreement was observed between the results of the current model and the results of finite-element

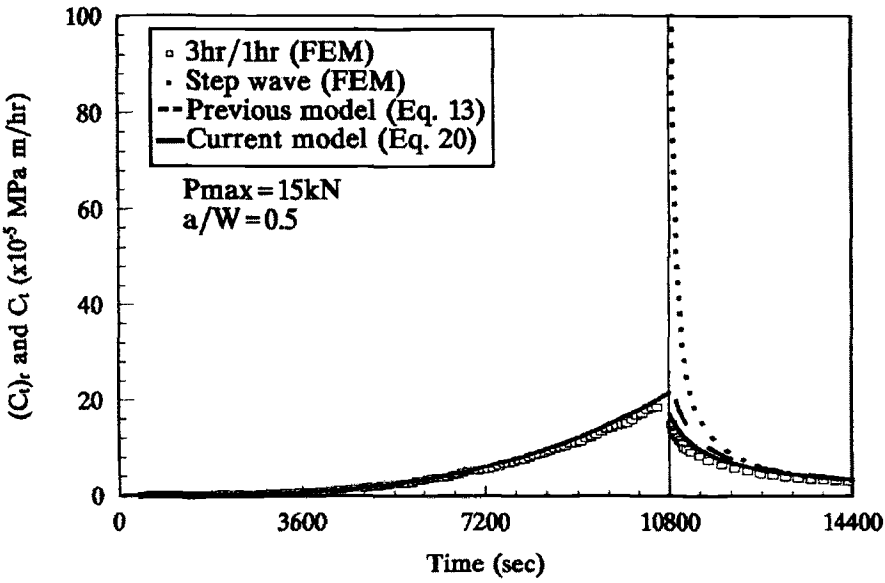

FIG. 7—*Comparison between FEM results and analytic results for Case 4.*

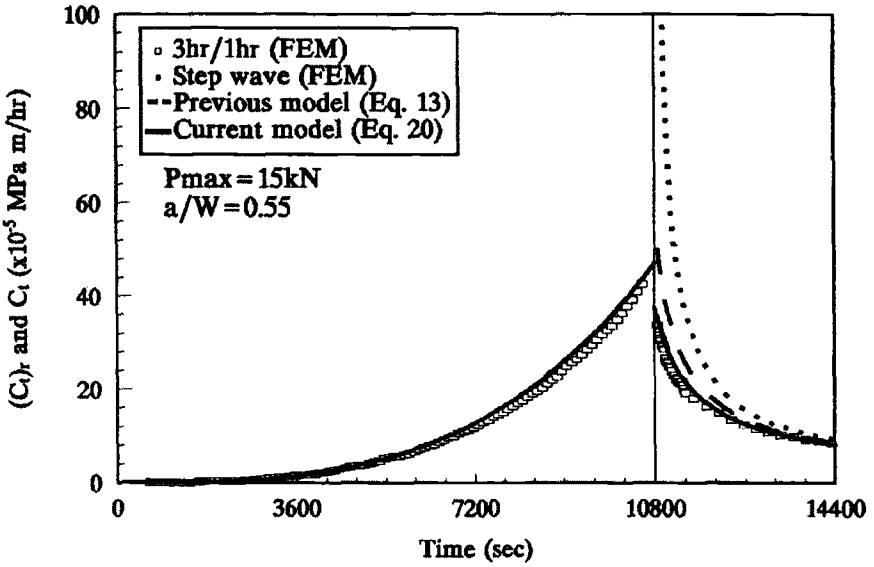

FIG. 8—*Comparison between FEM results and analytic results for Case 5.*

analysis, too. Figures 9 and 10 show the analysis results and the analytic results for Case 6 and Case 7 in which the maximum applied load of Case 1 was changed to 20 and 25 kN, respectively. Consequently, in all cases, good agreement was observed between the results of the current model and the results of finite-element analysis.

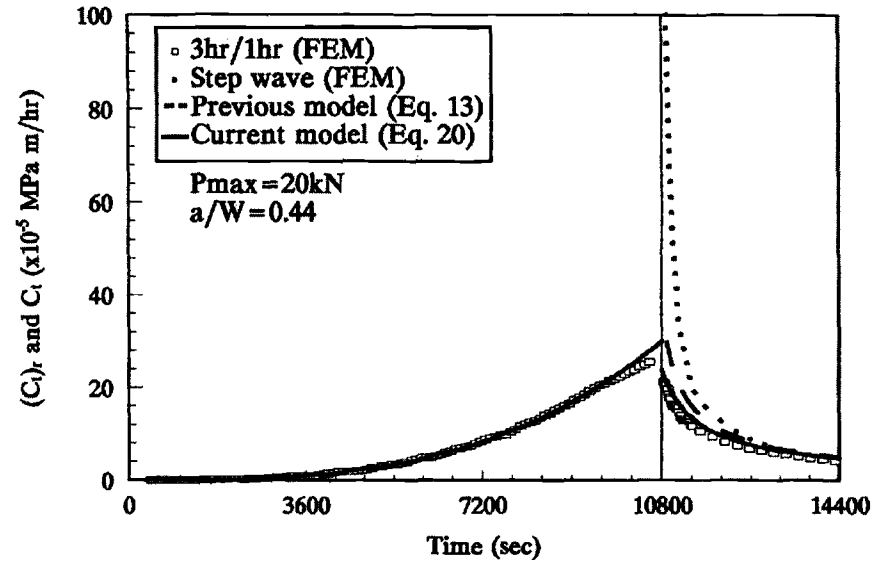

FIG. 9—*Comparison between FEM results and analytic results for Case 6.*

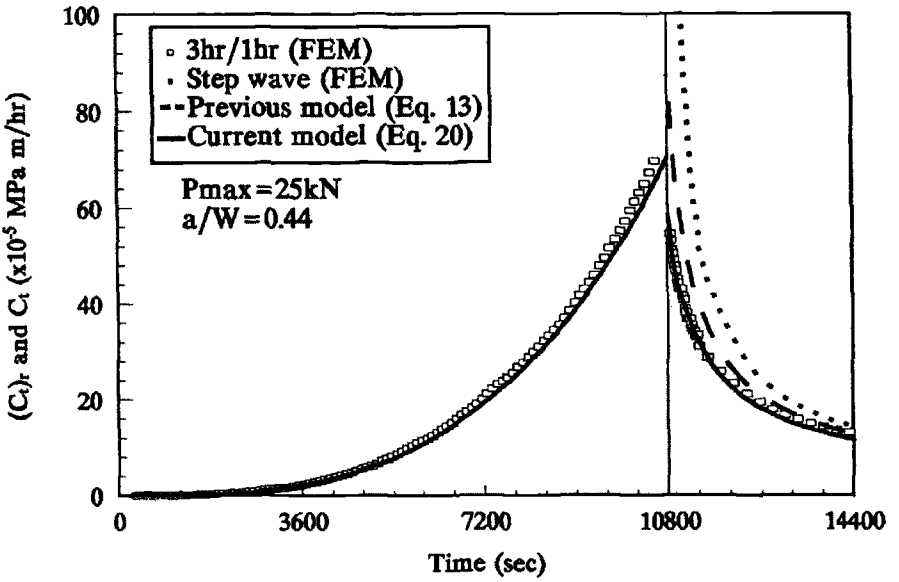

FIG. 10—*Comparison between FEM results and analytic results for Case 7.*

From the overall finite-element analysis results of Case 1 through Case 7, it can be argued that the generalized C_t estimation scheme derived in this paper be used as a useful method for determining creep fracture parameter that can characterize the crack growth behavior by creep deformation during the load hold period following a slow load-rising period.

Summary and Conclusions

In this study, an estimation scheme for the C_t-parameter is investigated considering the effect of accumulated creep deformation during the load rising period. Several cases of finite-element analyses were carried out. The following conclusions are drawn from this study.

1. The characteristic time t_{rs} is defined, which represents reduction of C_t due to the accumulated crack-tip creep deformation during the load-rising period.
2. By using the characteristic time t_{rs}, a new C_t estimation scheme that can be applied to the load hold period following a slow load-rising period is proposed.
3. To evaluate the characteristic time t_{rs}, values of $\beta_r \cdot F_{cr}(\theta,n)$ and $\beta \cdot \tilde{r}_c(\theta,n)$ should be determined in advance. A method of determining reliable and reproducible values of $\beta_r \cdot F_{cr}(\theta,n)$ and $\beta \cdot \tilde{r}_c(\theta,n)$ is proposed.
4. By performing finite-element analyses of several cases, it was shown that the C_t estimation scheme suggested in this paper gives accurate results.

Acknowledgment

The authors are grateful for the support provided by a grant from the Korea Science & Engineering Foundation (KOSEF) and Safety and Structural Integrity Research Center at the Sungkyunkwan University.

References

[1] Martin, H. F., "Cyclic-Duty Turbine and Boiler Operating Practice and Guidelines," EPRI CS-3800 Final Report, 1984.

[2] Saxena, A., "Fatigue Crack Growth in Elevated Temperature Power-Plant Materials and Components," *Fatigue '96,* Vol. II, 1996, pp. 729–740.

[3] Saxena, A., "Remaining Life Estimation of Boiler Pressure Parts-Crack Growth Studies," EPRI RP 2253-7, 1986.

[4] Yoon, K. B., Saxena, A., and McDowell, D. L., "Influence of Crack-Tip Cyclic Plasticity on Creep-Fatigue Crack Growth," *Fracture Mechanics, ASTM STP 1131,* 1992, pp. 367–392.

[5] Yoon, K. B., Saxena, A., and Liaw, P., "Characterization of Creep-Fatigue Crack Growth Behavior Under Trapezoidal Waveshape Using C_t-Parameter," *International Journal of Fracture,* Vol. 59, No. 2, 1993, pp. 95–114.

[6] Adefris, N., Saxena, A., and McDowell, D. L., "Creep-Fatigue Crack Growth Behavior in 1Cr-1Mo-0.25V Steels. Part I: Estimation of Crack Tip Parameters," *Fatigue and Fracture of Engineering Materials and Structures,* Vol. 19, No. 4, 1996, pp. 387–399.

[7] Adefris, N., Saxena, A., and McDowell, D. L., "Creep-Fatigue Crack Growth Behavior in 1Cr-1Mo-0.25V Steels. Part II: Crack Growth Behavior and Models," *Fatigue and Fracture of Engineering Materials and Structures,* Vol. 19, No. 4, 1996, pp. 401–411.

[8] Lee, J. H., Kim, Y. J., and Yoon, K. B., "A Study on the Creep Fracture Parameter for Characterizing Crack Growth Under the Load Rising Condition," *Proceedings,* KSME Materials and Fracture Division Meeting, February 1998, pp. 50–56.

[9] Lee, J. H., Kim, Y. J., and Yoon, K. B., "Mechanics Interpretation of C_t-parameter Under Load Rising Conditions," submitted for publication.

[10] Riedel, H., "Crack-Tip Stress Fields and Crack Growth Under Creep-Fatigue Conditions," *Elastic-Plastic Fracture, ASTM STP 803,* 1983, pp. 1505–1520.

[11] Yoon, K. B., Baek, U. B., and Suh, C. M., "Effects of Loading Rate on Creep Crack Growth During Succeeding Load-Hold Period Under Trapezoidal Fatigue Waveshape," *Elevated Temperature Effects on Fatigue and Fracture, ASTM STP 1297,* 1997, pp. 102–116.

[12] Riedel, H. and Rice, J. R., "Tensile Cracks in Creeping Solids," *Fracture Mechanics, ASTM STP 700,* 1980, pp. 112–130.

[13] Landes, J. D. and Begley, J. A., "A Fracture Mechanics Approach to Creep Crack Growth," *Mechanics of Crack Growth, ASTM STP 590,* 1976, pp. 695–700.

[14] Nikbin, K. M., Webster, G. A., and Turner, C. E., "Relevance of Nonlinear Fracture Mechanics to Creep Cracking," *Cracks and Fracture, ASTM STP 601,* 1976, pp. 47–62.

[15] Ohji, K., Ogura, K., and Kubo, S., *Transactions of JSME,* Vol. 42, 1976, pp. 350–358.

[16] Irwin, G. R., "Fracture," *Handbuch der Physik VI,* Springer, 1958, pp. 551–590.

[17] Irwin, G. R., "Plastic Zone Near a Crack and Fracture Toughness," *Proceedings,* 7th Sagamore Conference, 1960, p. IV–63.

[18] Saxena, A., "Creep Crack Growth Under Non-Steady State Conditions," *Fracture Mechanics, ASTM STP 905,* 1986, pp. 185–201.

[19] Bassani, J. L., Hawk, D. E., and Saxena, A., "Evaluation of the C_t-Parameter for Characterizing Creep Crack Growth Rate in the Transient Regime," *Nonlinear Fracture Mechanics, ASTM STP 995,* 1989, pp. 7–26.

[20] Saxena, A., Han, J., and Banerji, K., "Creep Crack Growth Behavior in Power Plant Boiler and Steam Pipe Steels," *Journal of Pressure Vessel Technology,* Vol. 110, 1988, pp. 137–146.

[21] Riedel, H. and Detampel, V., "Creep Crack Growth in Ductile, Creep Resistant Steels," *International Journal of Fracture,* Vol. 33, 1987, pp. 239–262.

A. B. O. Soboyejo,[1] *M. A. Foster,*[2] *C. Mercer,*[3] *J. C. Papritan,*[4] *and W. O. Soboyejo*[5]

A New Multiparameter Model for the Prediction of Fatigue Crack Growth in Structural Metallic Materials

REFERENCE: Soboyejo, A. B. O., Foster, M. A., Mercer, C., Papritan, J. C., and Soboyejo, W. O., **"A New Multiparameter Model for the Prediction of Fatigue Crack Growth in Structural Metallic Materials,"** *Fatigue and Fracture Mechanics, 30th Volume, ASTM STP 1360,* P. C. Paris and K. L. Jerina, Eds., American Society for Testing and Materials, West Conshohocken, PA, 2000, pp. 327–343.

ABSTRACT: A multiparameter model is proposed for the characterization of fatigue crack growth in structural metallic materials. The model assesses the combined effects of identifiable multiple variables that can contribute to fatigue crack growth. Mathematical expressions are presented for the determination of fatigue crack growth rates, da/dN, as functions of multiple variables, such as: stress intensity factor range, ΔK; stress ratio, R; closure stress intensity factor, K_{cl}; and the maximum stress intensity factor, K_{max}. A generalized empirical methodology is proposed for the estimation of fatigue crack growth rates as functions of these variables. The validity of the new methodology is then verified by making appropriate comparisons between predicted and measured fatigue crack growth data obtained from experiments on selected structural metallic materials. The multiparameter predictions are shown to be in close agreement with experimental data.

KEYWORDS: fatigue, crack growth, life prediction, multiparameter models, fracture mechanics, probabilistic methods

Since the pioneering work of Paul Paris and co-workers about 40 years ago, [*1,2*], the use of the Paris law has gained widespread acceptability in a wide range of industries. Paris' early work [*1*] was particularly important because it was the first to recognize the relationship between the fatigue crack growth rate and linear elastic fracture mechanics parameters based on Irwin's stress intensity factor, K. For fatigue crack growth in the mid-ΔK regime, Paris and co-workers [*2*] later suggested that the fatigue crack growth rate, da/dN, may be expressed as the following power law function

$$\frac{da}{dN} = C(\Delta K)^m \tag{1}$$

In Eq 1, C and m are material constants, and for metallic structural materials, the values of m are gen-

[1] Associate professor, Department of Food, Agricultural and Biological Engineering and Department of Aerospace Engineering, Applied Mechanics and Aviation, The Ohio State University, Columbus, OH 43210.

[2] Graduate research associate, Department of Aerospace Engineering, Applied Mechanics and Aviation, The Ohio State University, Columbus, OH 43210.

[3] Post-doctoral research fellow, Department of Materials Science and Engineering, The Ohio State University, Columbus, OH 43210.

[4] Associate professor, Department of Food, Agricultural and Biological Engineering, The Ohio State University, Columbus, OH 43210.

[5] Associate professor, Department of Materials Science and Engineering, The Ohio State University, Columbus, OH 43210.

erally between 2 and 4. Following the work of Paris et al. [*1,2*], Forman and co-workers [*3*] proposed an alternative empirical crack growth law for the assessment of the combined effects of the stress intensity factor range, ΔK, and stress ratio, R, on fatigue crack growth rate, da/dN. Walker [*4*] also developed a simple two-parameter crack growth law for the estimation of da/dN as a function of ΔK and the maximum stress intensity factor, K_{max}. Most recently, sigmoidal and logarithmic expressions [*5,6*] have been used to describe the dependence of fatigue crack growth on ΔK in the near-threshold, Paris, and high-ΔK regimes. However, most of the existing fatigue crack growth laws [*1–6*] are restricted to cases where fatigue crack growth is dependent on only one or two variables.

In this paper, we propose a multiparameter framework for the characterization of fatigue crack growth. Following an overview of the deterministic fracture mechanics framework for the assessment of the combined effects of multiple mechanical variables, a log-normal statistical distribution is proposed for the assessment of the possible variabilities in the fatigue crack growth behavior. The proposed multiparameter approach is validated for long fatigue crack growth in selected structural metallic materials (Inconel 718, HY80 pressure vessel steel, and Ti-6Al-4V).

Theoretical Modeling

(a) *Multiparameter Modeling of Fatigue Crack Growth*

We start by assuming that the fatigue crack growth rate, Y, is a function of k random variables X_i, $i = 1,2,\ldots,k$, with an initial value of $Y_0 = \alpha_0$. We also assume that the total fatigue crack growth rate, Y, is the contribution of the k random variables. These k random variables can be some or all of the following parameters that can contribute to fatigue crack growth rate in structural metallic materials: stress intensity factor range, ΔK, stress ratio R, crack closure stress intensity factor K_{cl}, specimen thickness t, microstructural and environmental conditions, composition of the material and temperature, among other essential physical, chemical, and environmental parameters of the problem. The assumption that can be justified experimentally is also made that the total crack growth rate $Y = da/dN$, which is due to these multiple factors, is essentially a multiplicative process with inputs from these factors. The methodology proposed here is a logical extension of the Paris crack growth rate law in which a new multiplicative law of the following form is hereby proposed:

$$Y = \frac{da}{dN} = \overline{\alpha}_0 \prod_{i=1}^{k} \left(\frac{X_i}{X_{io}}\right)^{\alpha_i} = \alpha_0 \prod_{i=1}^{k} X_i^{\alpha_i} \tag{2}$$

where $\alpha_0 = \overline{\alpha}_0 \{\prod_{i=1}^{k} X_{io}^{\alpha_i}\}^{-1}$, $Y_0 = \alpha_0 =$ is a constant, which has the units of da/dN and also corresponds to the initial value Y_0 of the crack growth rate; α_i is the exponent of each corresponding variable X_i for $i = 1, 2, \ldots, k$. X_{io} is the reference constant which corresponds to X_i and has the same physical units of X_i. Therefore, (X_i/X_{io}) for $i = 1, 2, \ldots, k$ is dimensionless. Alternatively, in this formulation of a theoretical model, X_{io} can be taken as a constant with the value of unity, which has the same dimension as X_i.

Figure 1 shows a schematic representation of the combinations of chemical, physical, and environmental factors, X_i for $i = 1, 2, \ldots, k$; with the states of the fatigue crack growth rates from the initial value $Y_0 = \alpha_0$, through the step-by-step stages, to Y_1, Y_2, . . . and eventually to Y_K, the final state of the crack growth rate, Y. At each stage of the multiplicative process, see Fig. 1, a transfer function that is mathematically a function of the relevant factor X_i of interest, $F_i(X_i)$, comes into play as

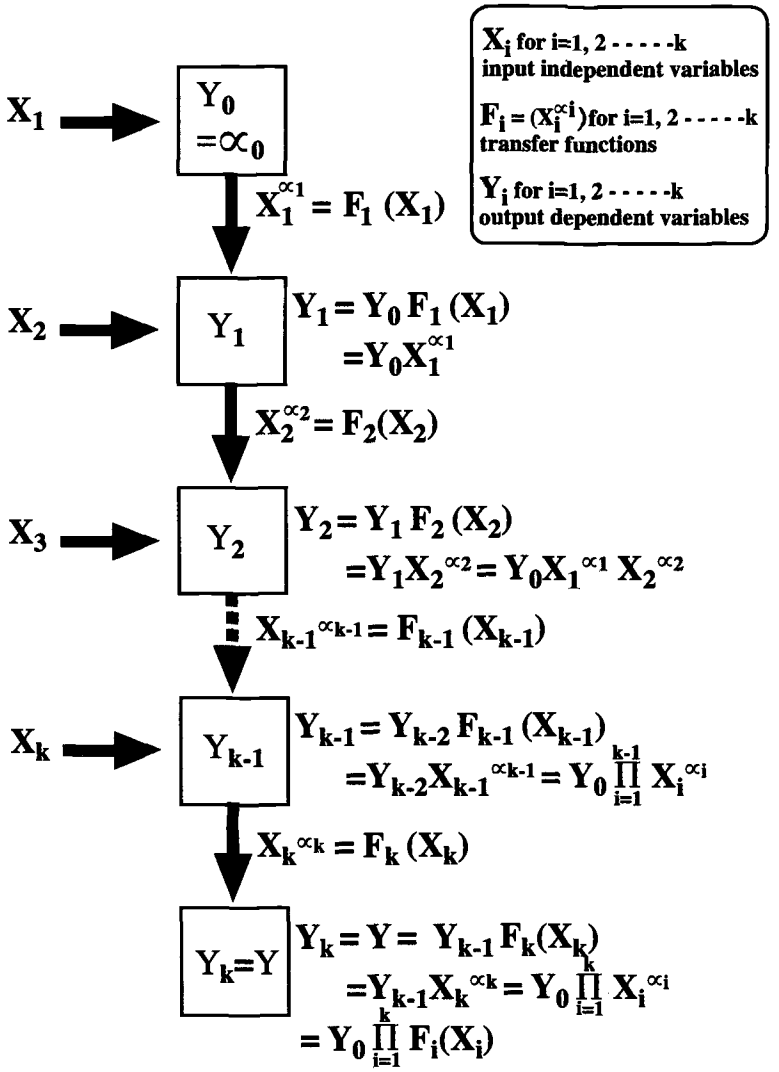

FIG. 1—*Diagramatic representation of the multiparameter model.*

follows:

$$\frac{Y_i}{Y_{i-1}} = F_i(X_i), \text{ for } i = 1, 2, \ldots, k \tag{3}$$

Equation 3 is important because it shows that the state of the rate Y_i depends only on the state of the rate Y_{i-1}, when the inputs of the $(i - 1)$ random variables, $X_i, \ldots, X_{(i-1)}$ have occurred. Y_i also depends on the value of the function $F_i(X_i)$, as shown in Eq 3, which is due to the effect of the random variable X_i. The effect of X_i can be expressed as $F_i(X_i)$, a function of X_i. Considering the inputs

of the k random variables $X_1, X_2, \ldots, X_k$ in sequence, it can be shown that (see Fig. 1):

$$\begin{aligned} Y_1 &= \alpha_0 F_1(X_1) \\ Y_2 &= Y_1 F_2(X_2) = \alpha_0 F_1(X_1) \cdot F_2(X_2) \\ &\vdots \\ Y = Y_K &= Y_{K-1} F_K(X_K) = \alpha_0 \prod_{i=1}^{k} F_i(X_i) \end{aligned} \tag{4}$$

In the general, in Eq 4 it is important to note that the function $F_i(X_i)$ needs to be carefully chosen in any fatigue crack growth problem, so that the mathematical form of this function represents, as closely as possible, the physical phenomenon of the fatigue crack growth rate process in any particular structural metallic material of interest.

For some factors X_i's that affect fatigue crack growth in structural metallic materials, $F_i(X_i)$ can be assumed to be a function of X_i, as follows: $F_i(X_i) = X_i^{\alpha_i}$, where the exponent α_i is a constant that can be derived from experimental data, as will be demonstrated later on in this paper. In view of the above, Eq 4 can be expressed as follows:

$$Y = \frac{da}{dN} = \alpha_0 \prod_{i=1}^{k} X_i^{\alpha_i} \tag{5}$$

For the use of Eq 5, care should be taken to ensure that appropriate form of the transfer function $F_i(X_i)$ is established for each of the random variables X_i's.

In order to satisfy this important condition, appropriate limits of the applicabilities of the variables X_i's can be determined from experimental data. The values of the $(k + 1)$ constants, $\alpha_0, \alpha_1, \alpha_2, \ldots, \alpha_K$ can be determined from a multivariate linear regression analysis of the experimental of the fatigue crack growth rate data.

By equating Eq 5 to Eq 1, it can be shown that the values of C, m, and ΔK in the Paris Eq 1 are related to the equivalent values in the multiparameter Eq 5 via:

$$C = \alpha_0 [X_1^{\alpha_1}]^{-1} \prod_{i=1}^{k} X_i^{\alpha_i} \tag{6}$$

where $m = \alpha_1$ and $\Delta K = X_1$.

Since $\alpha_0 = Y_0$, Eq 5 can be linearized to give Eq 7 as follows:

$$y = \ln Y = \ln \alpha_0 + \prod_{i=1}^{k} \alpha_i \ln X_i \tag{7}$$

(b) *Regression Analysis*

When adequate experimental data are available for Y and X_i, for $i, = 1, 2, \ldots, k$, multiple linear regression analysis can be used to determine the values of the $(k + 1)$ constants; α_0, and α_i for $i = 1, 2, \ldots, k$. Furthermore, correlation coefficients can be used to determine the statistical correlations between the dependent variable, Y, and the independent variables, X_i, for $i = 1, 2, \ldots, k$.

A detailed description of the multiple linear regression model is presented in Refs *7* and *8*. How-

ever, for clarity, a brief overview of the multiple linear regression analysis procedure will be presented in this section. First we note that Eq 7 can be expressed as:

$$y = \bar{\alpha}_0 + \sum_{i=1}^{k} \alpha_i x_i \tag{8}$$

where $y = \ln Y$, $\bar{\alpha}_0 = \ln \alpha_0$ or $e^{\bar{\alpha}_0} = \alpha_0$, $x_i = \ln X_i$, and $x_0 = 1$. The significance of Eq 8, which comes from Eq 7, is that when $k = 1$, we have the same result of the basic Paris law, as shown in Eq 1, where $\alpha_0 = C$, $X_1 = \Delta K$, and $\alpha_1 = m$. When $k > 1$, Eq 8 shows the contributions of only the effect of $X_1 = \Delta K$, the stress intensity factor range, expressed as $\ln(X_1)$, but also the effects of other additional factors, $X_2, X_3, \ldots, X_k$, expressed as $\ln X_2, \ln X_3, \ldots, \ln X_k$, respectively. Equation 8 can now be used to determine the values of the $(k + 1)$ constants $\bar{\alpha}_0, \alpha_1, \alpha_2, \ldots, \alpha_k$ from known experimental data of size n. In order to achieve this, it is necessary to find a mathematical expression for Q of the total sum of squares of the errors of prediction. Q is given by:

$$Q = \sum_{p=1}^{n} \left(y_i - \sum_{i=1}^{k} \alpha_p x_{pi} \right)^2 \tag{9}$$

The desirable results α_p for the estimated value of α are those that give the least value for Q in Eq 9. These can be obtained from the following equation:

$$\frac{\partial Q}{\partial \alpha} = 0 \quad \text{for} \quad p = 0, 1, 2, \ldots, k \tag{10}$$

These give $(k + 1)$ normal equations of the form:

$$\sum_{i=1}^{n} x_{qi} \left(y_i - \sum_{p=0}^{k} \hat{\alpha}_p x_{pi} \right) = 0 \tag{11}$$

In Eq 11, $x_0 = 1$ also as stated earlier. Now let

$$a_{pq} = \sum_i x_{pi} x_{qi} \quad \text{and} \quad Z_p = \sum_i y_i x_{qi} \tag{12a}$$

Then the normal equations can be represented by:

$$\sum_{p=0}^{k} a_{pq} \hat{\alpha}_p = Z_q \tag{12b}$$

Inverting the matrix a_{pq}, we get a^{pq}; hence, we have:

$$\hat{\alpha}_p = \sum_q a^{pq} \cdot Z_q \tag{12c}$$

Standard computer programs have been developed to estimate the above material constants via the analysis of actual experimental data. The standard error of the estimate, which can be derived from

Eq 9, measure the closeness with which the estimated values agree with the actual experimental data. Using the values of the $\hat{\alpha}_p$'s, the estimated value of $\hat{y}$ can be expressed as the mean value of y. This is given by:

$$\hat{y} = \sum_{p=0}^{k} \hat{\alpha}_p x_{pi} \tag{13}$$

where $x_0 = 1$.

The maximum likelihood estimate of the variance of the variable y is:

$$\hat{\sigma}^2 = \frac{1}{n} \sum_{i=1}^{n} \left(y_i - \sum_{p=0}^{k} \hat{\alpha}_p x_{pi} \right)^2 \tag{14}$$

The probability density function (p.d.f.) for the variable y is obtained by assuming that the variable y is normally distributed. This should be so for large values of n, the size of the experimental data set used in accordance with the central limit theorem [*12*]. Hence, the p.d.f. is given by

$$f(y) = \frac{1}{\hat{\sigma}\sqrt{2\pi}} \exp\left\{ -\frac{1}{2} \left(\frac{y - \hat{y}}{\hat{\sigma}} \right)^2 \right\}, \quad \text{for} \quad y \geq 0 \tag{15}$$

Since $y = \ln Y$, Eq 15 is good only for $y \geq 0$ and is zero for $y < 0$. This is so because the fatigue crack growth rate can only be real and positive. The mean value $\hat{y}$ and the standard deviation, $\hat{\sigma}$, are as given by Eqs 13 and 14. The coefficient of multiple correlation may also be estimated from the above analysis. This is a measure of the correlation between the experimental data and predictions based on the multiparameter equations (Eqs 4 and 7). A value of 1 indicates perfect correlation, and a value of 0 indicates no correlation. Furthermore, partial correlation coefficients measure the correlation between a dependent variable and each of the several independent variables.

(c) *Probability Density Functions*

The probability density function of the dependent variable, Y, which represents the fatigue crack growth rate, has a lognormal probability distribution function. This can be expressed as:

$$f(Y) = \frac{1}{Y\xi\sqrt{2\pi}} \exp\left[-\frac{1}{2} \left(\frac{\ln Y - \lambda}{\xi} \right)^2 \right]; \quad \text{for} \quad Y > 0 \tag{16}$$

where $\lambda = E(\ln Y)$ and

$$\xi = \sqrt{\text{Var}(\ln Y)}$$

are the mean and the standard deviation of $\ln Y$, respectively; and they are the parameters of the lognormal probability density function, $f(Y)$, for $Y > 0$.

These parameters can also be shown to be given by [*12,25*]:

$$\lambda = \ln \mu_Y - \frac{1}{2} \xi^2 \tag{17}$$

$$\xi = \left[\ln \left(\frac{1 + \sigma_Y^2}{\mu_Y^2} \right) \right]^{1/2} \tag{17a}$$

where μ_Y and σ_Y are the expected value of Y, and the standard deviation of Y, respectively. Y is the fatigue crack growth rate given by Eq 5. If (σ_Y/μ_Y) is not large, say ($\leq 0, 3$), then in Eq 18, we have $\ln [1 + \sigma_Y/\mu_Y] \simeq (\sigma_Y/\mu_Y)^2$. For such cases, Eqs 17 and 17a become, respectively,

$$\lambda \simeq \ln \mu_Y - \frac{1}{2}\left(\frac{\sigma_Y}{\mu_Y}\right)^2 \tag{18}$$

$$\xi \simeq \frac{\sigma_Y}{\mu_Y} \tag{18a}$$

(d) *Error Analysis*

It is often useful to develop the relationship between the variation ΔY in Y, as a function of the variation ΔX_i in X_i in Eq 5.

This has been done in this paper. The variations ΔY can be evaluated from the following equation, which has been derived:

$$\left(\frac{\Delta Y}{Y}\right)^2 = \sum_{i=1}^{k}\left(\alpha_i \frac{\Delta X_i}{X_i}\right)^2 + 2\sum_{i=1}^{k}\sum_{j=i+1}^{k}\left(\alpha_i \frac{\Delta X_i}{X_i}\right)\left(\alpha_j \frac{\Delta X_j}{X_j}\right) r_{ij} + \ldots \tag{19}$$

where r_{ij} is the simple correlation coefficient between the variations ΔX_i and ΔX_j associated with the variables X_i and X_j. The conditions for $r_{ij} = 0$ can occur when there are no correlations. Equation 19 then becomes:

$$\left(\frac{\Delta Y}{Y}\right)^2 = \sum_{i=1}^{k}\left(\alpha_i \frac{\Delta X_i}{X_i}\right)^2 + \ldots \tag{20}$$

The terms ΔY and Y can be used to represent the estimates of the standard deviation and the mean of the fatigue crack growth rate, Y, while ΔX_i and X_i can also be used to represent the corresponding estimates of the standard deviation and the mean of the random variables that can affect the fatigue crack growth rate.

(e) *Prediction of Fatigue Crack Growth*

The multiparameter model can be used directly to predict crack growth as a single function of multiple variables. Separating variables in Eq 5 and integrating between the appropriate limits gives:

$$Y = \frac{da}{dN} = \alpha_0 \prod_{i=1}^{k} X_i^{\alpha_i} \tag{21}$$

$$\int_{a_0}^{a'} da = \alpha_0 \int_0^{N'} \prod_{i=1}^{k} X_i^{\alpha_i}\, dN \tag{22}$$

or $a' = \sum \Delta a = \sum Y(\Delta N)$ where $N' = \sum(\Delta N)$. Equation 22 is, therefore, the integration of Eq 20 from an assumed initial crack size a_0 at $N = 0$, up to the value of crack size $a = a'$ when the number of cycles to failure is $N = N'$. The determination of the total crack size, $a = a'$, therefore, reduces to a simple step-by-step numerical integration process. Hence, as indicated above, Eq 22 may be used to predict the magnitude of the combined effects of the k major variables, X_i, for $i = 1, 2, \ldots, k$, that can affect fatigue crack growth. However, the required $k + 1$ model constants $\alpha_0, \alpha_1, \ldots, \alpha_k$ must be determined from experimental data using multiple linear regression methods described earlier in this paper.

TABLE 1—*Mechanical properties of mill-annealed Ti-6 Al-4V.*

Orientation	0.2% Offset Yield Stress, MPa (ksi)	Ultimate Tensile Stress, MPa (ksi)	Plastic Elongation to Failure, %
Longitudinal (LT)	881 (128)	887 (129)	7.5
Transverse (TL)	825 (120)	885 (128)	7.1

Validation of Multiparameter Fatigue Crack Growth Model

(a) *Introduction*

In order to confirm the validity of the multiparameter model, some of our previously reported fatigue crack growth data [*16–23*] were assessed within the same modeling framework presented above. Details of the experimental procedures and results are presented in Refs *16–23*. The current paper will, therefore, focus primarily on the synthesis of some of the experimental data within a multiparameter framework. The fatigue crack growth rate data were analyzed to determine the material constants in Eq 5. Data obtained from previous tests on Ti-6Al-4V [*16,18,24*], HY80 steel [*16,19,20*], and Inconel 718 [*21,22*] were used in the analysis. These were used to obtain multiparameter constants, error terms, and probability density functions within the same statistical framework. The multiparameter constants for Ti-6Al-4V, HY 80, and Inconel 718 will be presented in Sections (b) and (e). Correlation coefficients and probability density functions will also be presented for Ti-6Al-4V in Sections (c) and (d), respectively, before discussing the general applicability of the multiparameter approach in Section (e).

(b) *Experimental Fracture Mechanics Methods and Multivariate Analysis of Results*

A mill-annealed Ti-6Al-4V alloy, whose mechanical properties are shown in Table 1, was used for the fatigue crack growth experiments.

The fatigue crack growth experiments were carried out on standard compact tension specimens, as shown in Fig. 2 [*24*]. The specimens used in this study had nominal thickness of 12.7, 6.35, 3.18, and

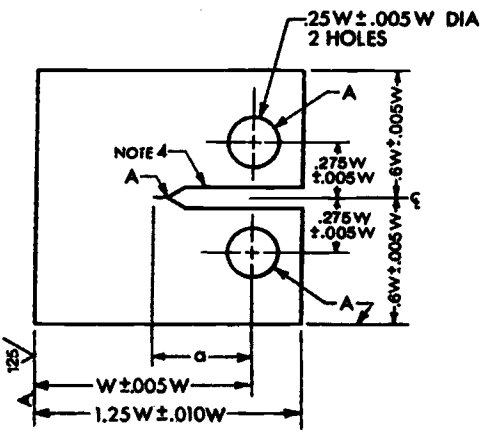

FIG. 2—*Standard compact tension specimen geometry (ASTM E 399).*

1.59 mm (½, ¼, ⅛, and 1/16 in.). The fatigue tests were conducted under computer control using a software/hardware system supplied by Fracture Technology Associates, Pleasant Valley, PA.

The stress intensity factor for compact tension specimens is expressed as [*24*]:

$$K = \frac{P}{BW^{1/2}} f\left(\frac{a}{W}\right) \tag{23}$$

where

$$f\left(\frac{a}{W}\right) = \frac{\left(2 + \frac{a}{W}\right)\left[0.886 + 4.64\left(\frac{a}{W}\right) - 13.32\left(\frac{a}{W}\right)^2 + 14.32\left(\frac{a}{W}\right)^3 - 5.6\left(\frac{a}{W}\right)^4\right]}{\left(1 - \frac{a}{W}\right)^{3/2}}$$

and B is the specimen thickness, P is the applied load, and a and W are the crack length and specimen width, respectively, as shown in Fig. 2.

The fatigue crack growth tests were carried out at stress ratios, $R = K_{min}/K_{max}$ of 0.1, 0.25, 0.5, and 0.8. Crack growth was monitored using compliance techniques [*24*] that involved the use of crack mouth opening displacements. The crack mouth clip gage was also used to measure crack closure throughout the fatigue test. Using the crack mouth clip gage, the crack mouth opening displacement, δ, was monitored and used to calculate the compliance of the specimen. This compliance, S, is defined as:

$$S = \frac{E\delta B}{P} \tag{24}$$

where E is the modulus of elasticity, and P and B are the same as defined above. The ratio, a/W, is then calculated as a function of this specimen compliance using the formula:

$$\frac{a}{W} = 1.00098 - 4.66951(u) + 18.4601(u)^2 - 236.825(u^3 + 1214.88(u)^4 - 2143.57(u)^5$$

where

$$u = \frac{1}{\sqrt{\frac{E\delta B}{P}} + 1} \tag{25}$$

Using this a/W, and the applied load P, the computer is able to calculate the applied stress intensity factor K.

The fatigue crack growth tests performed in this study were conducted using a K-decreasing, or K-shedding, procedure. The maximum stress intensity factor, K_{max}, was decreased in such a way as to minimize the effects of retardation due to the plastic zone ahead of the crack tip. This was accomplished by making fractional changes in the plastic zone size constant with increasing crack length, a, in accordance with the ASTM Test Method for Measurement of Fatigue Crack Growth Rates (E 647) code. The following load-shedding condition was used:

$$K_{max} = K_{max_0} e^{[C(a-a_0)]} \tag{26}$$

where K_{max_0} is the initial maximum stress intensity factor corresponding to the initial crack length,

a_0, a is the current crack length, and C is a constant called the K-shedding exponent. C is equal to $1/K \cdot (dK/da)$ and has the units of length^{-1}; for the present study, a value of $C = -0.08$ mm^{-1} (-2.0 in.$^{-1}$) was used in compliance with ASTM E 647 conditions.

In the calculation of K_{cl}, the stress intensity factor at which crack closure is detected, a 1% offset procedure was used in the determination of the crack closure loads. This procedure was used to collapse the "closure-corrected" data from low-stress ratio tests onto data obtained at high-stress ratios, which is considered "closure-free."

(b) *Multivariate Analysis*

A multivariate analysis of Ti-6Al-4V fatigue crack growth rate data yielded the following results from the $n = 530$ data points of *da/dN* [*24*] from 13 experimental tests. A single multiparameter relationship was obtained between *da/dN* and the stress intensity factor range, ΔK, stress ratio, R, specimen thickness, t, maximum stress intensity factor, K_{max}, and closure stress intensity factor, K_{cl}. This relationship is:

$$\frac{da}{dN} = 2.81 \times 10^{-11} (\Delta K)^{3.01} (R)^{0.44} (t)^{-0.002} (K_{max})^{3.82} (K_{cl})^{-2.32}, \text{(mm/cycle)} \qquad (27)$$

where $r^2 = 0.9433$ (see Fig. 3). In this analysis, the data of ln(*da/dN*) or the natural logarithm of *da/dN* were used. This relatively high value of the multiple correlation coefficient is an indication of the close agreement between the experimental data and the predictions of fatigue crack growth rates. It is important to note that when the experimental *da/dN* data were used for the $n = 530$ experimental data points, the measured and predicted results showed a correlation coefficient of $r^2 = 0.8886$ (see Fig. 4). Since the r^2 value of 0.8886 obtained for the *da/dN* data is less than the r^2 value of 0.9433 obtained for the ln (*da/dN*) data, the lognormal distribution should give a better prediction of errors (in the fatigue crack growth data) than the normal distribution.

Equation 27 can only be used within the parametric field of input variables ($X_1 = \Delta K$, $X_2 = R$, $X_3 = t$, $X_4 = K_{max}$, and $X_5 = K_{cl}$) in the fatigue experiments. The variables, which are indicated in Eq 27, have the following ranges of validities, which are shown in Table 2.

Figure 5 shows the graph of fatigue crack growth rate $Y = da/dN$, against stress intensity factor

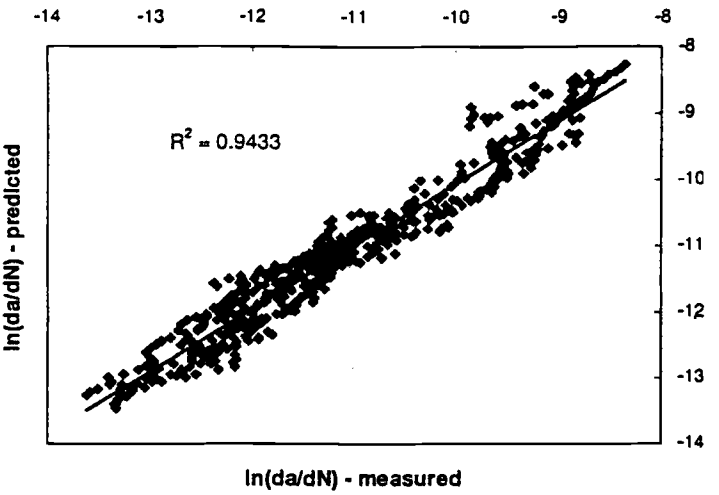

FIG. 3—*Goodness of fit between ln*(da/dN) *measured and ln*(da/dN) *predicted using the multivariate method.*

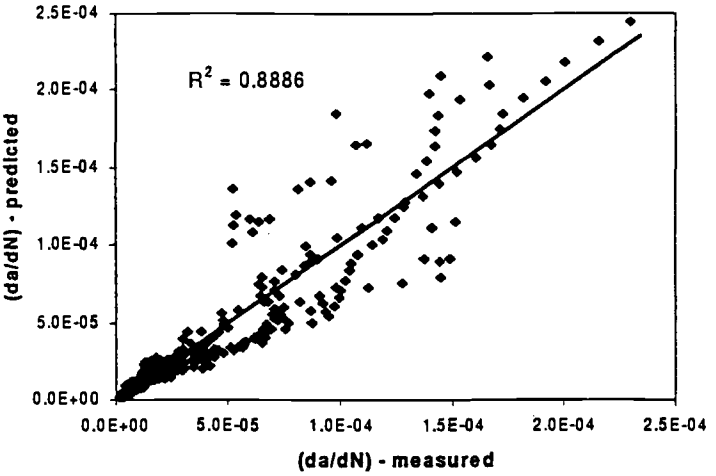

FIG. 4—*Goodness of fit between* (da/dN) *measured and* (da/dN) *predicted using the multivariate model.*

TABLE 2—*Multiparameter model variables and their ranges of validities.*

Variable	Range of Validity
$Y = da/dN$, mm/cycle	$1.21E-06 < da/dN < 2.35E-04$
$X_1 = \Delta K$, MPa$\sqrt{m}$	$5.90 < \Delta K < 26.700$
$X_2 = R$	$0.02 < R < 0.80$
$X_3 = t$, mm	$1.590 < t < 12.700$
$X_4 = K_{max}$, MPa$\sqrt{m}$	$10.60 < K_{max} < 54.60$
$X_5 = K_{cl}$, MPa$\sqrt{m}$	$3.30 < K_{cl} < 43.70$

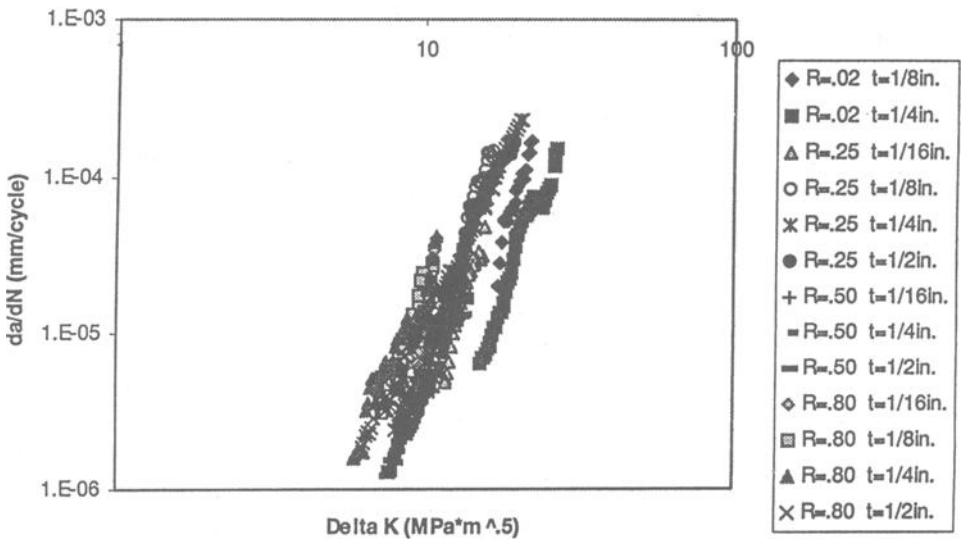

FIG. 5—*Fatigue crack growth rate versus stress intensity factor range,* ΔK, *for all tests performed.*

range $X_1 = \Delta K$, for all the experimental data generated in this study. Each experiment generated relevant data points for the five input variables, X_1, X_2, X_3, X_4, and X_5, and the output variable Y. Furthermore, each experiment was performed for fixed values of stress ratio, R, and specimen thickness, t. The fatigue crack growth rate data obtained in this study are summarized in Fig. 5 for the complete range of R and t.

It is also apparent from Eq 22 that the most important factor contributing to fatigue crack growth in Ti-6Al-4V is K_{max}, which has a positive exponent of 3.82. The second most important variable is the stress intensity factor range, ΔK, which has a positive exponent of 3.01. This is followed by the stress ratio, R, with the smallest positive exponent of 0.44. The factor of closure, K_{cl}, is also significant since it has a relatively high negative exponent (−2.32). The specimen thickness, t, has the smallest effect on the fatigue crack growth rate in Ti-6Al-4V, with a negative exponent of (−0.002).

(c) *Correlation Coefficients*

Since the above variables, X_i, are not necessarily independent, correlation coefficients between these variables were calculated. These were used to determine any pair of cross-correlations between variables. The correlation coefficient ρ_{ij} between any pair of variables X_i and X_j is given by [*25,26*]:

$$\rho_{ij} = \frac{\text{Cov}\,(X_i X_j)}{\sigma_{Xi}\,\sigma_{X_j}} \tag{28}$$

where X_i and X_j, for $i \neq j$, are any two of the five variables defined by $\ln(\Delta K)$, $\ln(R)$, $\ln(t)$, $\ln(K_{max})$, and $\ln(K_{cl})$, and where $\text{Cov}(X_i X_j)$ is the covariance of X_i and X_j, $i \neq j$; while σ_{x_i} and σ_{x_j} are the standard deviations of X_i and X_j, respectively.

The correlation coefficients between the different variables may be used to assess the extent to which the variables are linearly related. Table 3 presents correlation coefficients that were obtained for Ti-6Al-4V. Note that large positive correlation coefficients suggest that when large values of one variable are observed, large values of the other variable will be observed. On the other hand, a large negative correlation coefficient suggests that when large values of one variable are observed, small values of the other variable will occur.

The correlation coefficients in Table 3 provide some important new insights. For example, the correlation coefficients between $\ln(t)$ and the other variables are very small. This implies that thickness is linearly independent from the other variables. Also, the correlation coefficient between $\ln(K_{max})$ and $\ln(K_{cl})$ is very large. This implies that there is quite a strong linear relationship between K_{max} and K_{cl}. For the most part, all of the variables, except for thickness, are linearly correlated to some degree.

(d) *Probability Distribution Functions*

Another objective of the statistical analysis was to characterize the experimental distribution of crack growth rate, *da/dN*, as well as the distributions of the independent variables that were explored in this study.

TABLE 3—*Summary of correlation coefficients between variables used in multivariate modules.*

	$\ln(\Delta K)$	$\ln(R)$	$\ln(t)$	$\ln(K_{max})$	$\ln(K_{cl})$
$\ln(\Delta K)$	1	−0.781	−0.102	−0.263	−0.545
$\ln(R)$	−0.781	1	0.023	0.470	0.641
$\ln(t)$	−0.102	0.023	1	−0.112	−0.058
$\ln(K_{max})$	0.263	0.470	−0.112	1	0.926
$\ln(K_{cl})$	0.545	0.641	−0.058	0.926	1

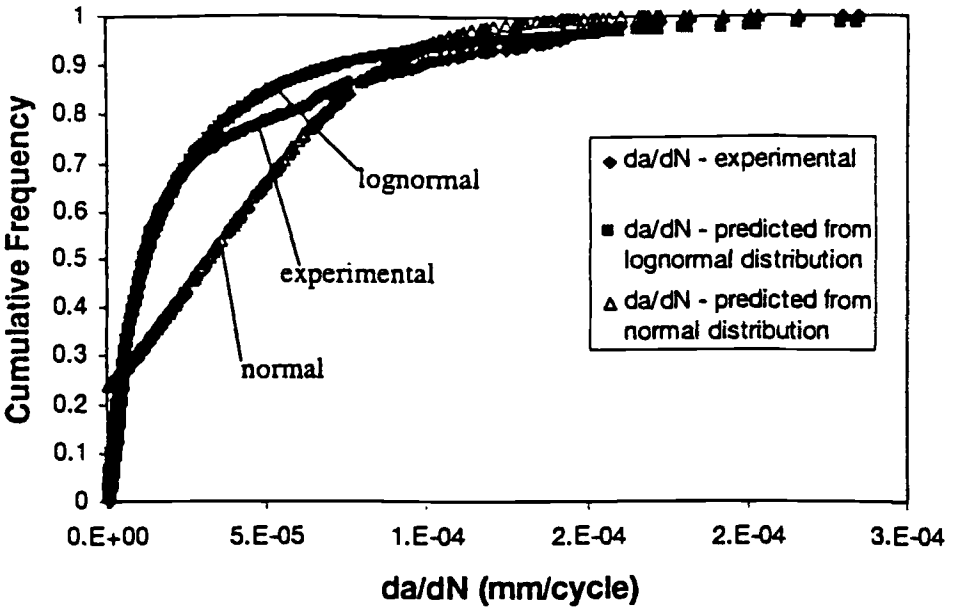

FIG. 6—*Comparison of cumulative frequency diagrams for the experimental* da/dN *and the predictions from the theoretical normal and lognormal distributions.*

From the central limit theorem of mathematical statistics [*12,25,26*], it can be shown that the distribution of a quantity will tend toward a lognormal distribution for a large number of observations if that quantity is equal to the product of a number of factors [*27*]. In the above discussions, we have modeled the crack growth rate, *da/dN*, using a multi-variate expression that is multiplicative in nature. Such a model is only appropriate if *da/dN* has a lognormal distribution.

Figure 6 shows the cumulative frequency diagram for crack growth rate, *da/dN*, as well as the theoretical cumulative frequency diagrams for the normal and lognormal distributions. The theoretical cumulative frequencies for the normal distribution were calculated using the mean and standard deviation of *da/dN*, while the theoretical values for the lognormal distribution were obtained using the mean and standard deviation of the 530 ln(*da/dN*) data points. It is clear from Fig. 6 that the distribution for the crack growth rate is very close to the theoretical lognormal distribution. If the crack growth rate was lognormally distributed, then ln(*da/dN*) would have to be normally distributed. Figure 7 compares the cumulative frequency diagram for the natural logarithm of the crack growth rate, ln(*da/dN*), with the theoretical cumulative frequency diagram for a normal distribution. The distribution of ln(*da/dN*) is observed to fit the normal distribution very well.

The Kolmogorov-Smirnov goodness-of-fit test [*12*] was also used to determine how closely the experimental distribution of *da/dN* fits a lognormal distribution. However, the Kolmogorov-Smirnov test is a normality test, which means that it compares an experimental distribution to a normal distribution, then determines how closely the experimental data fits the normal distribution. Since ln(*da/dN*)was assumed to be distributed normally, the Kolmogorov-Smirnov test was used to compare ln(*da/dN*) to a theoretical normal distribution.

Figure 8 shows the results from the Minitab statistics program for the Kolmogorov-Smirnov normality test [*12,25*] for ln(*da/dN*). The test produced a value for the greatest discrepancy between the two distributions of $D_n = 0.067$. For a significance level of $\alpha = 0.01$ and $n = 530$ (there were a to-

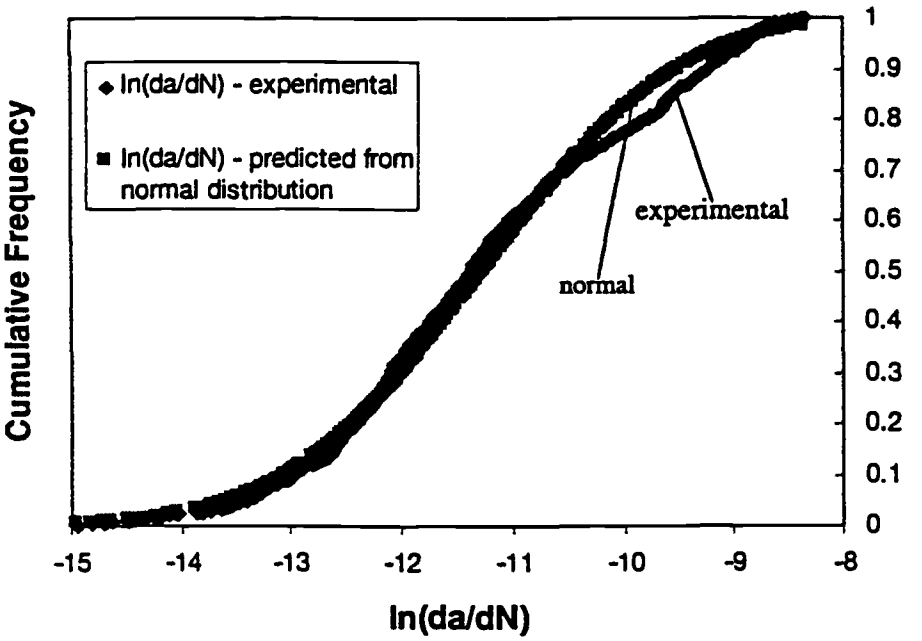

FIG. 7—*Comparison of cumulative frequency diagrams for the experimental ln*(da/dN) *and the prediction from the theoretical normal distribution.*

tal of 530 data points from the 13 fatigue experiments), the critical value D_n^{α} was calculated to be 0.071. At the significance level of $\alpha = 0.01$, the experimental distribution of ln(*da/dN*) was normally distributed since $D_n < D_n^{\alpha}$ (see Fig. 6). This implies that, to the same significance level, the crack growth rate, *da/dN*, was log-normally distributed. Therefore, the use of a multiplicative multivariate statistical model for the prediction of *da/dN* is clearly justified [*12,25,26*].

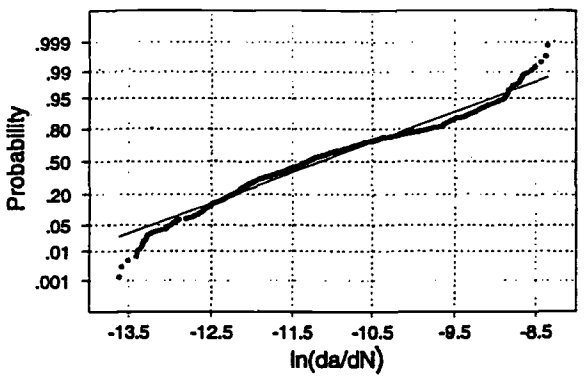

FIG. 8—*Use of the Kolmogorov-Smirnov normality test for the distribution of ln*(da/dN).

TABLE 4—*Summary of multiparameter coefficients, exponents, and multiple correlation coefficients for some structural metallic materials.*

Material	Multiparameter Coefficient Multiple, α_0	Multiparameter Exponents					Multiple Correlation Coefficient, r^2	References in this Paper
		α_1	α_2	α_3	α_4	α_5		
HY 80 Steel (Independent Variables)	2.9×10^{-9}	3.24 (ΔK)	0.357 (R)	...	...	...	0.92	[*19,23*]
HY 80 Steel (Independent Variables)	3.0×10^{-9}	3.33 (ΔK)	0.468 (R)	−0.124 (K_{cl})	...	...	0.94	[*19,23*]
Inconel 718 (Independent Variables)	3.39×10^{-10}	3.63 (ΔK)	0.52 (R)	...	...	...	0.98	[*21,22*]
Ti-6Al-4V (Independent Variables)	2.81×10^{-11}	3.01 (ΔK)	0.44 (R)	−09.002 (t)	3.82 (K_{max})	−2.32 (K_{cl})	0.94	[*24*]

(e) *General Applicability*

The above discussion has focused largely on the analysis of extensive data obtained from a detailed experimental program on Ti-6Al-4V [*24*]. However, the general applicability of the multiparameter law has also been demonstrated for fatigue crack growth in HY80 steel [*16,19,20*] and Inconel 718 [*21,22*]. The results are summarized in Table 4 along with the Ti-6Al-4V constants presented above. These include: the multiparameter coefficient, α_0, the multiparameter exponents, α_i's, and the multiple correlation coefficients, r^2. The appropriate references are also listed in the right-hand column in Table 4. It is important to note here that, prior to normalization, the variables in Table 2 have the following units: ΔK, stress intensity factor range (MPa$\sqrt{\text{m}}$); R, stress ratio; K_{max}, maximum stress intensity factor (MPa$\sqrt{\text{m}}$); K_{min}, minimum stress intensity factor (MPa$\sqrt{\text{m}}$); K_{cl}, stress intensity factor at closure (MPa$\sqrt{\text{m}}$); t, specimen thickness (*mm*); and *da/dN*, fatigue crack growth rate (mm/cycle). Furthermore, the following letters represent the following variables, mentioned above in Table 4. $X_1 = \Delta K$, $X_2 = R$, $X_3 = t$, $X_4 = K_{max}$, and $X_5 = K_{cl}$.

Two sets of results were reported for HY80 steel: in Table 4 the differences in the values of the multiparameter coefficient α_0 and the multiparameter exponents arose because one set of data gave results for the effects of the independent variables ΔK and R, while the second set of data gave results for the effects of the independent variables ΔK, R, and K_{cl}.

Also, the data presented in this paper have been obtained primarily in the Paris (mid-ΔK) regime for long fatigue cracks. The data presented in this paper, therefore, suggest that the multiparameter framework may be used as a generalized method for the prediction of long fatigue crack growth in the Paris regime. Furthermore, it is interesting to note that the multiparameter law (Eq 5) reduces to the Paris law when one variable, X_1, is considered within the multiparameter framework. This indicates that the constant, C, in the Paris law is as given in Eq 6. The multiparameter framework presented in this paper is, therefore, a logical extension of the Paris law.

It is also important to note that both the single parameter Paris formulation and the multiparameter approach proposed in this paper may be extended easily into a probabilistic fracture mechanics framework for the assessment of material reliability due to fatigue crack growth. Such an extension would require the integration of probability density functions within a multiparameter framework. Such integrations are beyond the scope of the current paper. However, it is clear from the statistical

analysis performed in this study that the variabilities in the fatigue crack growth data are best represented by lognormal distributions. Future efforts to develop material reliability functions may, therefore, assume lognormal distributions in the predictions of failure/survival probability as functions of multiple variables.

Conclusions

1. A multiparameter model has been presented for the characterization of fatigue crack growth. The model is essentially an extension of the single parameter Paris law for the mid-ΔK regime. It has been validated using long fatigue crack growth rate data obtained from mill-annealed Ti-6Al-4V, Inconel 718, and HY80 pressure vessel steel. Good agreement was demonstrated between the experimental data and predictions of the fatigue crack growth rate based on the multiparameter fatigue crack growth law.
2. The relative contributions of each variable, X_i, can be assessed by comparing the relative magnitudes of the exponents, α_i, in the multiparameter crack growth law. Such comparisons may provide useful insights into the susceptibility of materials and structures to fatigue.
3. The Kolmogorov-Smironov goodness of fit test shows quite clearly that the lognormal distribution of ln (da/dN) gives a better probabilistic distribution than the normal distribution of da/dN for fatigue crack growth rate in Ti-6Al-4V in the near-threshold and Paris regimes.
4. The multiparameter model can be applied readily to the prediction of fatigue crack growth under the influence of multiple variables. It may also serve as a deterministic framework for the estimation of material reliability within a probabilistic fracture mechanics framework.

Acknowledgments

The authors are grateful to the Division of Materials Research of the National Science Foundation for financial support. Appreciation is also extended to The Ohio State University for the provision of research facilities and financial support. The authors are grateful to Professors G. Gregorek and Robert Gustafsou, for their encouragement and support, and to Ms. Terry England for assistance with the preparation of the manuscript. Finally, the authors are grateful to the reviewers of this paper for their excellent critical reviews and helpful suggestions.

References

[1] Paris, P. C. Gomez, M., and Anderson, W. E., "A Rational Analytic Theory of Fatigue," *The Trend in Engineering,* Vol. 13, 1961, pp. 9–14.
[2] Paris, P. C. and Erdogan, F., "A Critical Analysis of Crack Propagation Laws," *Journal of Basic Engineering,* Vol. 85, 1963, pp. 528–534.
[3] Forman, R. G., Kearney, V. E., and Engle, R. M., "Numerical Analysis of Crack Propagation in Cyclic-Loaded Structures," *Journal of Basic Engineering,* Vol. 89, 1967, pp. 459–464.
[4] Walker, K., "The Effect of Stress Ratio During Crack Propagation and Fatigue for 2024-T3 and 7075-T6 Aluminum," *Effects of Environment and Complex Load History on Fatigue Life, ASTM STP 462,* American Society for Testing and Materials, Philadelphia, 1970, pp. 1–15.
[5] Suresh, S., "Fatigue of Materials," Cambridge University Press, 1991.
[6] Bannantine, J. A., Comer, J. J., and Handrock, J. L., *Fundamentals of Metal Fatigue Analysis,* Prentice Hall, Englewood Cliffs, NJ, 1990.
[7] Bruckner, A., "Numerical Methods in Probabilistic Fracture Mechanics," *Probabilistic Fracture Mechanics and Reliability,* J. N. Provan, Ed., Martinus Nijhoff, Dodrecht, The Netherlands, 1987, pp. 351–370.
[8] Soboyejo, A. B. O., "Plastic Flow in Reinforced Concrete," Technical Report No. 52, Department of Civil Engineering, Stanford University, Stanford, CA, 1965.
[9] Soboyejo, W. O., "On the Prediction of the Fatigue Propagation of Semi-Elliptical Defects," *Advances in Fatigue Lifetime Predictive Techniques, ASTM STP 1122,* American Society for Testing and Materials, West Conshohocken, PA, 1992, pp. 435–450.

[10] Soboyejo, W. O., Kishimoto, K., Smith, R. A. and Knott, J. F., "A Study of the Interaction and Coallescence of Two Coplanar Fatigue Cracks in Bending," *Fatigue and Fracture of Engineering Materials and Structures,* Vol. 12, 1988, pp. 167–174.

[11] Soboyejo, W. O., Knott, J. F., Walsh, M. J., and Cropper, K. R., "Fatigue Crack Propagation of Semi-Elliptical Cracks in Pure Bending," *Engineering Fracture Mechanics,* Vol. 37, 1990, pp. 323–340.

[12] Ang, A. H.-S. and Tang, W. H., *Probability Concepts in Engineering Planning and Design, Vol. I, Basic Principles,* John Wiley & Sons, New York, 1975.

[13] Soboyejo, A. B. O., "Evaluation of Structural Creep Reliability Using Entropy Principles," *Journal of Materials Science and Engineering,* Vol. 12, 1973, pp. 101–109.

[14] Ang, A. H.-S. and Tang, W. H., *Probability Concepts in Engineering Planning and Design, Vol. II,* John Wiley & Sons, New York, NY, 1984.

[15] Soboyejo, A. B. O., Ozkan, H. E., Soboyejo, W. O., et al., "Multiparameter Model for Nozzle Wear Rates and Applications in Engineering Design," *American Society of Agricultural Engineers (ASAE),* Paper No. 983166, ASAE Annual International Conference, Orlando, FL, July 1998, submitted to *Transactions of the ASAE,* 1998.

[16] Soboyejo, A. B. O. and Soboyejo, W. O., "Paris Law Extension for Low ΔK and High ΔK Regimes and Applications in Reliability-Based Engineering Design Against Fatigue," *High Cycle Fatigue of Structural Materials,* Proceedings of an International Symposium in Honor of Professor Paul C. Paris, at Indianapolis, Indiana, W. O. Soboyejo and T. S. Srivatsan, Eds., The Minerals, Metals and Materials Society and ASM International, Warrendale, PA, 1997.

[17] Dubey, S., Soboyejo, A. B. O., and Soboyejo, W. O., "An Investigation of the Effects of Stress Ratio and Crack Closure on the Micromechanisms of Fatigue Crack Growth in Ti-6Al-4V," *Acta Materialia,* Vol. 45, 1996, pp. 2777–2787.

[18] Foster, M., Soboyejo, A. B. O., Katsube, N., Dubey S., and Soboyejo, W. O., "An Investigation of the Effects of Multiple Parameters on the Fatigue Crack Growth Behavior of Ti-6Al-4V," *Transactions of the ASME Journal of Engineering Materials and Technology,* submitted, 1997.

[19] Soboyejo, W. O. and Knott, J. F., "Effects of Stress Ratio on Fatigue Crack Propagation in QIN(HY80) Pressure Vessel Steel," *International Journal of Fatigue,* Vol. 12, 1990, pp. 403–407.

[20] Soboyejo, W. O. and Knott, J. F., "An Investigation of Crack Closure and the Propagation of Semi-Elliptical Fatigue Cracks in QIN Pressure Vessel Steel," *International Journal of Fatigue,* Vol. 17, 1995, pp. 577–581.

[21] Mercer, C., Soboyejo, A. B. O., and Soboyejo, W. O., "An Investigation of Fatigue Crack Growth in Inconel 718," *High Cycle Fatigue of Structural Materials,* in honor of Professor Paul C. Paris, at Indianapolis, IN, W. O. Soboyejo and T. S. Srivatsan, Eds., The Mineral, Metals and Materials Society and ASM International, 1997, pp. 269–285.

[22] Soboyejo, A. B. O., Mercer, C., and Soboyejo, W. O. "Probabilistic Mechanics Model of Fatigue Crack Growth in a Nickel-Based Super Alloy," *Transaction of the ASME Journal of Engineering Materials and Technology,* submitted, 1997.

[23] Soboyejo, W. O., Soboyejo, A. B. O., Ni, Y., Li, Y., and Knott, J. F., "A New Multiparameter Approach to the Prediction of Fatigue Crack Growth," *International Journal of Fatigue and Fracture of Engineering Materials and Structures,* Vol. 21, 1998, pp. 541–555.

[24] Foster, M. A., "An Investigation of the Fatigue Crack Growth and Fracture Behavior of Ti-6Al-4V," M.S. thesis, Department of Aerospace Engineering, Applied Mechanics and Aviation, The Ohio State University, Columbus, OH, 1998.

[25] Soboyejo, A. B. O., "Probabilistic Methods in Engineering Design," Lecture Notes: Department of Food, Agricultural and Biological Engineering, The Ohio State University, Columbus, OH, 1996.

[26] Benjamin, J. R. and Cornell, A. C., *Probability, Statistics and Decision for Civil Engineers,* McGraw Hill, Inc., New York, 1970.

[27] Chow, V. T., "The Log-Probability Law and Its Engineering Applications," *Proceedings, ASCE,* Vol. 80, No. 536, September 1954.

Session V

Hans P. Rossmanith[1]

Fracture Mechanics: Forgotten German and Austrian Pioneers of the Turn of the 20th Century

REFERENCE: Rossmanith, H. P., **"Fracture Mechanics: Forgotten German and Austrian Pioneers of the Turn of the 20th Century,"** *Fatigue and Fracture Mechanics: 30th Volume, ASTM STP 1360,* P. C. Paris and K. L. Jerina, Eds., American Society for Testing and Materials, West Conshohocken, PA, 2000, pp. 347–356.

ABSTRACT: This contribution gives an overview of the early history of fracture mechanics and highlights the contributions of Karl Wieghardt and Alfons Leon to the development of the basic analytical equations of fracture mechanics. It is shown that the work of these pioneers anticipated many of the later developments by several decades. It will also be shown that particularly the work by Wieghardt was in fact directly related to a practical failure case and the neglect of his fundamental paper is unjustified.

KEYWORDS: history, fracture mechanics, crack tip stress field, crack initiation, damage, notch stresses

In the western countries the first historically recorded study of fracture strength is due to Leonardo da Vinci [*1,2*], who studied the strength of iron wires of different lengths. The testing apparatus depicted in da Vinci's notebook in the *Codex Atlanticus* is explained, and the results are discussed in the paper by Irwin and Wells [*3*]. On the contrary, Galileo Galilei [*4*] studied the strength of wires of constant length and various thicknesses and, in addition, also studied the fracture of marble columns. Around 1650, E. Mariotte, the court engineer of Louis XIV of France, was entrusted with the construction of a magnificent fountain to be built in the gardens of Versailles. This task required the containment of substantial amounts of pressurized water, and Mariotte designed and conducted tests by measuring the deformation and burst pressure of cylindrical pressure vessels and observed a direct proportionality between pressure and circumferential stretch [*5*]. He noted that the vessels would burst if the circumferential elongation increased by a certain fraction.

The great demand for iron and steel that developed in the course of the industrialization of the 19th Century as well as the accelerated expansion of the engineering world was accompanied by a rather large rate of failure of engineering structures. This situation led to an increased public concern and awareness about safety of railway transport and bridges. As a result, the designers were forced to become more concerned with suitable steel for particular applications and required accurate determination of relevant fracture-related material properties [*6,7*]. A large number of material-testing laboratories were established in Europe. During the early history of fracture, the conditions of failure were only poorly understood. The viewpoints on strength of materials at the start of the 20th century are presented well by Love in his *Treatise on the Mathematical Theory of Elasticity* [*8*]; however, the sections dealing with applicability of linear-elastic concepts show no influence of fracture studies in the period 1900–1926. With regard to fracture, Love, as late as in the fourth edition of his book in 1926 concludes "that the properties of rupture are but vaguely understood."

[1] Professor, Institute of Mechanics, Vienna University of Technology, Vienna, Wiedner Hauptstr. 8-10/325, A-1040, Austria.

Wieghardt—The Early Pioneer

The first analytical investigation in fracture mechanics and application to a practical engineering problem (mixed-mode fracture of a roller-bearing case) seems to be due to K. Wieghardt [*9*] (Fig. 1).

In 1907, while working at the Herzogliche Technische Hochschule in Braunschweig, Wieghardt published an elaborate study of the stress field in the vicinity of the tip of a wedge [*9,10*]. The paper consists of an introduction, two sections, and an appendix on the uniqueness of the solution.

The theoretical development rests on a special stress function (in German also "Ansatz") by Sommerfeld for the solution of the Boussinesq problem for a point load P acting normally on the surface of a half space. Sommerfeld's idea is to transform the boundary value problem of the biharmonic equation $\Delta\Delta F = 0$ into a simpler boundary value problem for the function $\Delta\phi$, where F is the Airy function and Δ denotes the Laplace operator. Sommerfeld's special ansatz is given by

$$\phi = \Delta F = -P/(i\pi)\,\{1/(\zeta - a) - 1/(\eta - a)\} \tag{1}$$

where $\zeta = \rho\exp(i\psi)$, $\eta = \rho\exp(-i\psi)$, and ρ and ψ are polar coordinates from the apex of the wedge. The quantity "a" is the distance of the load application point from the origin of the coordinate system (see Fig. 2). For the arbitrary wedge domain, Wieghardt generalizes this ansatz in the form:

$$\phi = \Delta F = -\alpha P/(i\pi)\,\{\zeta^{\alpha-1}/(\zeta^{\alpha} - a^{\alpha}) - \eta^{\alpha-1}/(\eta^{\alpha} - a^{\alpha})\} \tag{2}$$

FIG. 1—*K. Wieghardt (born 21 June 1874, Bergeborbeck, Germany; died 10 June 1924, Dresden, Germany) published his early paper on fracture mechanics in 1907 entitled "On Splitting and Cracking of Elastic Bodies"; Professor of Mechanics in Vienna at the Technische Hochschule 1911–1920.*

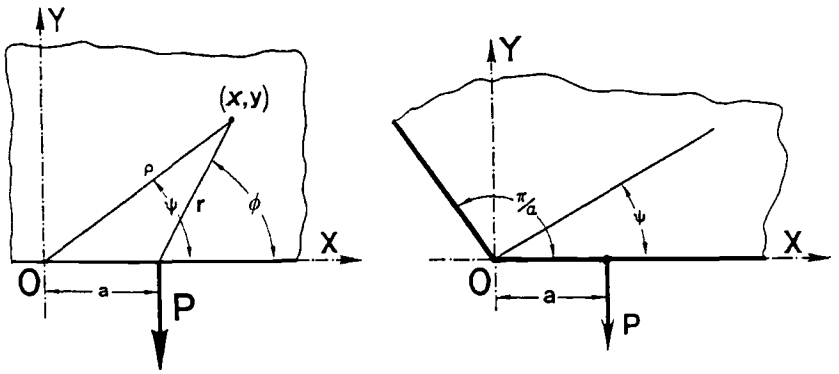

FIG. 2—*The wedge problem (coordinate system) (Ref 9).*

where π/α defines the opening angle of the wedge domain and shows that this function satisfies the appropriate boundary conditions and solves the stress problem for those wedge regions with opening angles of 0 and π.

After a discussion about the appearance of infinite stresses at the tip of the crack, Wieghardt derives the complete stress field in polar coordinates around a static crack subjected to a pair of splitting forces P, thereby noting the important $\sqrt{\rho}$-singularity

$$\begin{aligned}
\sigma_\rho + \sigma_\psi &= -P/\pi\, 1/\sqrt{(a\rho)}\, \sin(\psi/2) \\
\sigma_\rho - \sigma_\psi &= -P/\pi\, 1/\sqrt{(a\rho)}^{1/2}\, \sin\psi \cos(\psi/2) \\
\tau_{\rho\psi} &= P/\pi\, 1/\sqrt{(a\rho)}^{1/4}\, \sin\psi \sin(\psi/2)
\end{aligned} \tag{3}$$

Wieghardt now suggests to use these equations to provide answers to questions on the strength of the crack against the action of the force P. Wieghardt asks: "Given the strength parameters of our elastic material, what is the magnitude of the force P necessary for material fracture? And furthermore, at which place and in which direction will the fracture initiate?"

Regarding the first question, Wieghardt admits that he—and at that time everybody else, too—was at a loss for an answer because of the unbounded stresses that appear at the crack tip for any arbitrarily small load P. He puts the blame on the classical hypotheses of strength but concludes that fracture, if it occurs at all, will initiate at the crack tip. He then proposes to disregard the $1/\sqrt{\rho}$-infinite factor and suggests that the direction of crack initiation will occur on the basis of customary hypotheses of strength. According to Mohr, there are essentially two hypotheses on the direction of fracture initiation in an elastic material: the *shear stress hypothesis* and the *tensile stress hypothesis.* Wieghardt details that the behavior of ductile materials such as wrought iron seem to be better described by the shear stress hypothesis, whereas the brittle behavior of cast iron is in better correspondence with the tensile stress hypothesis.

Wieghardt then uses the expressions for the maximum shear and maximum tensile stress to derive the possible directions for crack initiation and, after some lengthy calculations, arrives at the conclusion that

"Assuming the validity of the shear stress hypothesis for our cracked material, knowledge of the theoretical stress distribution does not allow the direction of crack initiation upon exceeding

loading to be evaluated with certainty, and it is not at all possible to determine the path of further cracking." And he continues to tell the reader: "If we assume the tensile stress criterion to be valid, the results turn out to be more enjoyable."

In fact, he recognizes that the tensile stress criterion renders one single possible direction for crack initiation: ". . . . . upon over-stressing the material, the crack will initiate in the direction parallel to the crack line and, furthermore, should the crack continue to propagate further, cracking occurs along the direction given by the crack because the same conditions prevail after cracking."

At the end of this section, Wieghardt mentions that the stress function

$$Q/(8\pi)\{\zeta^{1/2}/(\zeta^{1/2} - a^{1/2}) + \eta^{-1/2}/(\eta^{1/2} - a^{1/2})\} \tag{4}$$

corresponds to the stress distribution for a crack problem with a force Q acting tangential to the boundary in place of P.

In the second part of his paper, Wieghardt applies his new theory to a problem of fracture of roller-bearing cases. It was known from an earlier test series conducted by Bach [*11*] that in roller-bearing cases fracture occurred in the corners 'a' and 'a'' (see Fig. 3*a*) upon sufficient over-stressing. Wieghardt argues that Bach's original ("customary") method of calculating the critical load for fracture as well as the direction of fracture initiation "was in bad agreement with reality."

Wieghardt treats the essentially three-dimensional problem as a plane problem and focuses on the re-entrant corner problem shown in Fig. 3*b*. The stress system in the roller-bearing problem is also simplified by considering single forces at first.

One highlight of the paper is the development of an alternating method for a nonsymmetrically loaded wedge domain loaded by a single normal force P. This method was later applied by various researchers for the derivation of the stress intensity factors for finite size cracked specimens including the famous edge crack and the cracked strips. The alternating technique, fortunately, converges very rapidly: a decisive computational advantage considering the tedious "bone" work required to arrive at solutions to problems of this sort at the turn of the last century with no computers whatsoever—not even slide rules were available.

Several pages of lengthy calculations follow in Wieghardt's original paper until he arrives at still another highlight in fracture mechanics.

In the chapter "On the Behavior of the Stresses in the Vicinity of the Apex," Wieghardt remarks that "it is awkward that the alternating method fails precisely where it is needed the most."

He continues: "In all probability and at least for the wedge domains $\alpha < 1$, the stresses in the vicinity of the corner may be factorized into a product of two functions, one of the angular coordinate ψ and the other of powers of the radial vector ρ."

FIG. 3—*Bach's roller-bearing problem:* (a) *mechanical model,* (b) *re-entrant corner.*

$$F(\rho, \psi) = \rho^n \text{ Function of } \psi \tag{5}$$

$$F(\rho, \psi) = \rho^n [A_1 \cos(n\psi) + A_2 \cos((n-2)\psi) + B_1 \sin(n\psi) + B_2 \sin((n-2)\psi)] \tag{6}$$

He adds, "At present, the author is lacking an exact proof of this decomposition . . . ."

Wieghardt then uses Eqs 5 and 6 for P as well as the analogue for the shear force Q and arrives at the following result:

> "In general, in the vicinity of a corner, the stresses generated by the action of a concentrated normal force differ in their order of unboundedness from those stresses produced by the action of tangentially acting concentrated forces; the normal force is associated with the smaller value of the two roots. Thus, when compared with tangential forces, the normal forces are associated with a higher order singularity of the stresses at the apex. The situation becomes more pronounced for wedge domains between the half-plane and the formation characterized by the condition $\tan(\pi/\alpha) = \pi/\alpha$, where only those stresses generated by normal concentrated forces but not those due to tangential forces become infinitely large. In the case of a crack both stress systems become unbounded at the crack tip."

In the section on the practical use of the alternating method, Wieghardt informs the reader that "for the case of the re-entrant corner the author has actually performed the calculations involved in the alternating method. A combined analytical and graphical approach proved to be most effective." The graphical part was concerned with integration. Wieghardt's calculations showed that in the case of the re-entrant corner subjected to a normal load P, the stress in the corner should tend to infinity in the order of $\rho^{-0.45}$. He also discloses to the reader that exactly these calculations have led him to suggest the validity of Eq 5!

Wieghardt closes this chapter with the question on crack initiation in the case of Bach's roller bearing problem, i.e., for the re-entrant corner. Similarly, as before, he employs the maximum shear stress hypothesis and the maximum tensile stress hypothesis and concludes his computations with the statement: "In any case, the results, which are valid for fracture initiation and based on the tensile stress hypothesis, are in agreement with the results of the tests by Bach [*11*]."

The paper finishes with an appendix on the uniqueness of the solutions found and clarifies the conditions and requirements for the forces to decay appropriately at infinity.

After Wieghardt's 1907 Paper

The publication of Wieghardt's work on the splitting and fracturing of elastic bodies in 1907 was well appreciated at the time among the German-speaking scientists and engineers. However, it has not been adequately recognized by the fracture mechanics community. There seem to be several reasons for this:

- The journal the paper was published in ceased publication in 1922, and this was certainly not favorable for the dissemination of his work. In contrast, the appearance of A. A. Griffith's paper in the famous *Proceedings of the Royal Society of London* has a tremendous advantage over Wieghardt's publication.
- At the time Wieghardt's paper was published, German was a leading language in physics and mathematics, and therefore Wieghardt published his paper in German. Nevertheless, Wieghardt's paper is written in a German rather difficult to read for any non-German scientist or engineer, and this did and still does not contribute to its dissemination.
- In addition, the fact that Wieghardt, a student of A. Sommerfeld and at times a coworker of Felix Klein, did not consider himself a practical engineer challenged by industrial consulting projects did not earn him a reputation as a practitioner.

- Although there were numerous failures by fatigue and fracture around 1907, the decisive missing item was the lack of accumulation of large-scale fracture failures in industry, which would have resulted in creating a driving force to develop the mechanics of fracture for solving such fracture problems. This happened only some 40 or 50 years afterwards when G. R. Irwin entered the stage of engineering characterized by "right" environment, which eventually promoted the development of fracture mechanics as an engineering discipline.

An English translation of the Wieghardt paper was provided by H. P. Rossmanith and published in the journal *FFEMS* [*10*].

It is, however, interesting to note that Griffith's paper of 1920 very quickly became well known and several researchers in Vienna and elsewhere rapidly responded to its publication. On the other hand, German papers were being read by British researchers: Prandtl's paper [*12*] on the soap film membrane analogy was known and acknowledged by Taylor and Griffith [*13*].

Wieghardt's pioneering paper of 1907 does not seem to have played any important role in the overall development of fracture mechanics as an engineering discipline. Wieghardt did not publish further papers on fracture problems. One can only speculate what might have happened if the First International Congress on Mechanics had taken place earlier, i.e., shortly after Wieghardt had finished his paper and if he had been able to present his paper to an international audience. Although his ground-breaking paper did not ignite the torch that led to the foundation of fracture mechanics, nevertheless Wieghardt's paper, and even more so his professorship in Vienna at the Technische Hochschule, was of importance to a string of Austrian professors including A. Leon, P. Ludwik, and K. Wolf, who worked in the field of materials testing and mechanics at the time.

Alfons Vincenz Leon

A. V. Leon (Fig. 4) occupied various academic professional positions in the Habsburg Empire and in Austria. His first paper addressing the issue of fracture was devoted to thickness shapes of rotating disks leading to equal fracture danger. Leon calculates the stress field for the rotating full disk and sphere as well as for a disk with a central hole and a sphere with a central cavity [*14*]. The paper discussed several fracture hypotheses including those based on a critical stress, strain, and work. A work-based fracture hypothesis is due to L. von Tetmajer, founder, in 1901, of the Laboratory for Materials Testing and Research associated with the Technische Hochschule Wien. Tetmajer suggested the use of *work capacity* of the various materials as a measure of fracture resistance quality: the larger the work capacity of a material, the more work has to be supplied by the external forces to rupture the material. He further explains: "The absolute value of the work capacity is directly related to the toughness of the material; it is smallest for brittle materials and largest for tough materials" [*14*].

Leon's contribution to the theory of notch stresses addressed at the time one of the most important questions in the theory of elasticity and strength of materials was of a lasting nature. It was known that abrupt changes of cross section and geometrical as well as material inhomogeneities in components would induce very large local stress elevations. These stress concentrations were regarded as responsible for fracture failures, particularly in connection with cyclic loading in ductile materials as well as in brittle materials subjected to static load levels far below the fracture stress. Design formulas frequently used in practice did not take into account these stress concentrations. It is Leon's merit not only to have stressed the importance of these stresses but to have worked out solutions to a number of important notch problems, either in closed form or in an approximate fashion. Leon solved the problem of the stress concentration in the vicinity of a spherical cavity [*15,16*] and in tensile bars weakened by holes [*17,18*].

A. V. Leon was a busy traveler. While working on problems associated with railways during the period 1906–08, Leon became confronted with the difficulties faced by the Swiss tunneling engineers in connection with primarily the Simplon tunnel. Based on his work on notch stresses in bodies with holes,

FIG. 4—*A. V. Leon (born 9 September 1881 in Ragusa, Austria-Hungary; died 30 May 1951 in Vienna, Austria) worked on problems of the theory of elasticity and developed a criterion for combined tension-shear fracture; Professor of Materials Testing in Vienna and Graz.*

Leon studied the deformation and damage around a circular tunnel subjected to overburden pressure and lateral confinement stresses. Leon's early publications on the stresses induced by circular holes and spherical cavities [*19–21*] became internationally known and was very well accepted, and Leon become heavily engaged with tunneling and its problems. The construction of the twin tunnel at the Simplon posed unexpectedly serious difficulties with regard to stress stability in the region between the two tunnels. In 1913, Leon carefully studied this problem theoretically and performed numerous accompanying experiments (Fig. 5). His publication of the damage formation in the region of twin tunnels [*22–24*] had a decisive influence on tunneling. It turned out that the decisive parameter is the relative distance between the two axes of the tunnels, and this parameter entirely controls the appearance of excessive compressive stresses in the wall between the tunnels and the sequence of damage inflicted.

In his later work, Leon contributed to the clarification of the hypothesis of strength for concrete [*25*] by proposing a parabolic form of the enveloping limit state. This enabled Leon to combine the fact that brittle materials such as concrete fracture in tension when pulled and in shear when compressed. Leon's enveloping parabola agreed very well with practical data of his own experiments as well as from other researchers. This work was presented by Leon at the 4th International Congress for Technical Mechanics in Cambridge in 1934. Leon's work was highly appreciated and included in the book by Nadai [*26*].

Old Ideas Reinvented

As the concept of toughness is associated with the breaking of materials—the tougher a material, the harder it is to break—the original measure of toughness was the amount of work done in break-

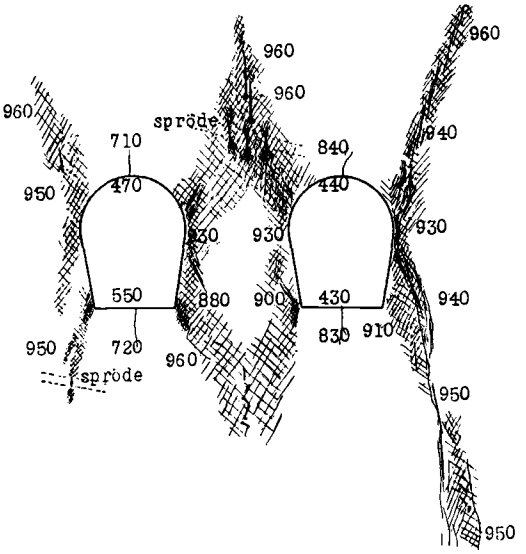

FIG. 5—*Regimes of severe fracturing around a twin tunnel (Refs 22–23): Brittle regimes are indicated by "spröde"; the numbers refer to compressive stresses with unknown reference level.*

ing a bar (the Tetmajer hypothesis), and, in 1975, toughness was still defined by ASTM as the ability of a metal to absorb energy and deform plastically before breaking. It is usually taken to be the measured energy loss in a notched-bar impact test and corresponds to the area under the stress strain curve in tension testing. Consequently, a brittle-behaving material is one that absorbs little energy, while tough-behaving materials would require a large expenditure of energy in the fracture process.

After WWI, engineers on both sides of the Atlantic Ocean developed renewed interest in notch effects as they very soon realized that fracture and fatigue are greatly influenced by notches. One can tacitly say that the story of failure is a tale of notches, nicks, key-ways, oil holes, screw threads, scratches, rough surfaces, quenching cracks, grinding cracks, sharp changes in section, thin outstanding fins, poor fillets, tool marks, inclusions in the metal, corrosion pits, and the like, i.e., some localized nucleus from which failure started. The fact that only a tiny spot needs to be stressed above the critical limit in order for the entire piece to fail by a crack developing from that spot deserves emphasis.

At that time, it was well known that the safety factors customarily used in design depended considerably upon judgment estimates of the possibilities of fracture; however, no attempts were made to replace the notch by a natural crack and measure the sensitivity of the steels to the presence of crack-like defects. In fact, at that time, in the 1940s, there was still inadequate recognition that cracks or crack-like defects were significant factors in reducing the load-carrying capacity of structures made from high-strength steels. The early work on notch sensitivity was rarely criticized because the notches were not sharp enough (Leon's work was on semi-circular notches!). If they resembled cracks, they were rather thought to be too sharp to represent any practical situation of high-stress concentration that might be encountered in service.

Following 1900, with the advent of automobiles followed by airplanes, the provision of adequate safety factors became increasingly more difficult and the need for better understanding of "rupture" more apparent. However, the response was directed mainly toward better materials, improved fabrication, and inspection. With these aids, the practice of fracture control consisting mainly of failure

experience, safety factors, and proof testing endured through the 1900–1950 period. As a guard against costs of (large) fracture failures, insurance was an available option. However, during this period several fracture investigations occurred that assisted the introduction of fracture mechanics.

Conclusions

This contribution highlights the development in mechanics and materials testing at the turn of the last century performed in Europe, particularly in the German-speaking countries. Particular emphasis is given to the "first" paper on fracture mechanics by K. Wieghardt. Wieghardt's appointment to professor of mechanics at the Technische Hochschule in Vienna started intensive research work in the field of notch effects and stress distributions around circular, elliptical, and crack-like openings and discontinuities.

The pioneering work by Wieghardt and the impressive work by Leon anticipate many of the results in fracture mechanics that were derived decades later, e.g., the stress distribution at the apex of a wedge-type opening, a mixed-mode fracture criterion, and the direction of crack initiation under combined loading [*27–28*]. The fact that most of these contributions have been published in German in journals comparatively little known outside Germany, Austria-Hungary, etc., may partly be responsible for their having fallen into oblivion. Renewed interest in the historical development of the discipline and a more subjective viewpoint might unveil the names of the other forgotten pioneers in fracture research and bring to light an appreciation of their early work.

It should be pointed out that Wieghardt's publication appeared 13 years before Griffith's famous paper [*29*]. The interested reader is referred to the publications [*30–31*] for further information about the contributions of these early pioneers and the history of fracture mechanics [*32*] in general.

Acknowledgments

The author would like to thank the Austrian Science Foundation for financially supporting this work under Contract No. P 10326 GEO. He would also like to express his deep appreciation to Professors Dr. G. R. Irwin and Dr. Paul C. Paris for the numerous stimulating technical discussions and their kind hospitality and cooperation in the course of this work. The author would also acknowledge the help of E. Jiresch, Head of the Archive of the Vienna University of Technology.

References

[*1*] da Vinci, L., date unknown, *Codice Atlantico,* folio 82 recto-b.
[*2*] Uccelli, A., *Leonardo da Vinci,* Reynal & Co., New York, 1956.
[*3*] Irwin, G. R. and Wells, A. A., "A Continuous Mechanics View of Crack Propagation," *Metallurgical Review,* Vol. 10, No. 38, 1965, pp. 223–270.
[*4*] Galilei, G., *Discorsi e Dimostrazioni Matematiche Sopra due Nuove Scienze,* Elsevini, Leiden, Netherlands, 1638.
[*5*] Mariotte, E., *Traite de Mouvement des Eaux,* Paris, 1686.
[*6*] Todhunter, I. and Pearson, K., *History of the Theory of Elasticity and of the Strength of Materials,* Cambridge University Press, UK, 1886.
[*7*] Timoshenko, S. P., *History of Strength of Materials,* McGraw-Hill Inc., New York, 1953.
[*8*] Love, A. E. H., *A Treatise on the Mathematical Theory of Elasticity,* Dover Publications, New York, 1926.
[*9*] Wieghardt, K., "Über das Spalten und Zerreissen elastischer Körper," *Z. Mathematik und Physik,* Vol. 55, Nos. 1–2, 1907, pp. 60–103.
[*10*] Rossmanith, H. P., English translation of [*9*]: Wieghardt, K., "On Splitting and Cracking of Elastic Bodies," *Fatigue and Fract. Eng. Mater. Struct.,* Vol. 12, No. 12, 1997, pp. 1371–1405.
[*11*] Bach, C., "Eine Stelle an manchen Maschinenteilen, deren Beanspruchung auf Grund der üblichen Berechnung stark unterschätzt wird" ("On a Particular Location in Machine Parts Where on the Basis of Conventional Theories the Stresses Will Be Highly Underestimated"), *Mitteilungen über Forschungen, VDI,* Issue 4, 1902.
[*12*] Prandtl, L. in *Zeitschrift für Physik,* Vol. 4, 1903.
[*13*] Griffith, A. A. and Taylor, G. I., "The Use of Soap Films in Solving Torsion Problems," *Proceedings of the Institute of Mechanical Engineers,* 1913, pp. 755–809.

[14] Leon, A. V., "Über Formen gleicher Bruchgefahr mit besonderer Berücksichtigung rotierender Scheiben" ("On the Shapes of Equal Fracture Danger with Special Regard of Rotating Disks"), *Österr. Ing.-u. Architekten-Verein,* Nos. 18 and 19, 1907.

[15] Leon, A. V., "Über die Störungen der Spannungsverteilung die in elastischen Körpern durch Bohrungen und Bläschen entstehen" ("On the Disturbances in the Stress Distribution in Elastic Bodies Due to Boreholes and Cavities"), *Österr. Wochenschrift für den öffentlichen Baudienst,* Vol. 4, 1908, pp. 163–168.

[16] Leon, A. V. and Willheim, F., "Über die Spannungsstörungen die in elastischen Körpern durch Höhlungen, Inhomogenitäten und eingeschlossenen Flüssigkeiten bewirkt werden" ("On Stress Disturbances in Elastic Bodies Caused by Cavities, Inhomogeneities and Fluid Inclusions"), *Zeitschrift für Architektur und Ingenieur-wesen, Hannover,* 1915, pp. 45–62.

[17] Leon, A. V. and Willheim, F., "Über die Spannungsverteilung im gelochten und gekerbten Zugstab" ("On the Stress Distribution in a Punched and Notched Tension Bar"), *Mitteilungen des Technischen Versuchsamtes Wien,* Vol. 3, No. 1, pp. 33–50, and Vol. 3, No. 2, 1914, pp. 37–52.

[18] Leon, A. V. and Willheim, F., "Über die durch eine Reihe von kreisförmigen Löchern in einem elastisch festen Körper auftretenden Spannungs- und Verzerrungsstörungen" ("On the Stress and Strain Disturbances in an Elastic Solid Caused by a Row of Circular Holes"), *Zeitschrift des Österr. Ing.-u. Architekten-Verein,* Vol. 66, 1914, pp. 424–428.

[19] Leon, A. V., "Über die Spannungsstörungen durch Kerben und Tellen und über die Spannungsverteilung in Verbundkörpern" ("On the Stress Disturbances Due to Notches and Dents and on the Stress Distribution in Composite Bodies"), *Österr. Wochenschrift für den öffentlichen Baudienst,* Vol. 14, 1908, pp. 770–776 and 783–787.

[20] Leon, A. V. and Willheim, F., "Über die Zerstörungen in tunnelartig gelochten Gesteinen—Teil I" ("On Damage in Rock Mass Weakened by a Tunnel—Part I"), *Österr. Wochenzeitschrift für den öffentlichen Baudienst,* Vol. 16, 1910, pp. 641–648.

[21] Leon, A. V. and Willheim, F., "Über die Zerstörungen in tunnelartig gelochten Gesteinen—Teil II" ("On Damage in Rock Mass Weakened by a Tunnel—Part II"), *Österr. Wochenzeitschrift für den öffentlichen Baudienst,* Vol. 18, 1912, pp. 281–285.

[22] Leon, A. V. and Willheim, F., "Über den Einfluß der Achsenentfernung auf die Zerstörungserscheinungen in einem Doppeltunnel" ("On the Effect of the Distance of the Tunnel Axes on Damage Formation in a Twin Tunnel"), *Österr. Wochenzeitschrift für den öffentlichen Baudienst,* Vol. 19, 1913, pp. 18–21.

[23] Leon, A. V. and Willheim, F., "Zur Frage über die durch einen Doppeltunnel bewirkten Spannungsstörungen im Gebirge und deren Beeinflussung durch die Achsenentfernung" ("On the Stress Disturbances Caused by a Twin Tunnel in a Rock Mass and the Effect of the Distance of the Tunnel Axes"), *Rundschau für Technik und Wirtschaft, Prag,* Vol. 6, Nos. 1–3, 1913.

[24] Leon, A. V. and Willheim, F., "Die Verteilung des Gebirgsdruckes und dessen Störungen durch den Bau tiefliegender Tunnel" ("The Distribution of the Overburden Pressure and its Disturbances Due to the Construction of Deep Level Tunnels"), *Zeitschrift für Architektur und Ingenieurwesen, Hannover,* 1914, pp. 191–199.

[25] Leon, A. V., "Über das Maß der Anstrengung bei Beton" ("On the Extent of Strength of Concrete"), *Ingenieur-Archiv,* Vol. 4, 1933, pp. 421–431.

[26] Nadai, A., *Theory of Flow and Fracture of Solids,* McGraw-Hill Co., New York, 1950.

[27] Westergaard, H. M., "Bearing Pressures and Cracks," *Applied Mechanics Transactions, ASME,* Vol. 6, 1939, pp. A49-A53.

[28] Williams, M. L., "Stress Singularities Resulting from Various Boundary Conditions in Angular Corners of Plates in Extension," *Journal of Applied Mechanics,* Vol. 74, 1952, pp. 526–528.

[29] Griffith, A. A., "The Phenomena of Rupture and Flow in Solids," *Philosophical Transactions of the Royal Society of London A,* Vol. 221, 1920, pp. 163–198.

[30] Rossmanith, H. P., an introduction to K. Wieghardt's historical paper, "On Splitting and Cracking of Elastic Bodies," *Fatigue and Fract. Engng. Mater. Struct.,* Vol. 12, No. 12, 1995, pp. 1367–1369.

[31] Rossmanith, H. P., "Die österreichischen Wegbereiter der Bruchmechanik und der Materialprüfung" ("Austrian Pioneers in Fracture Mechanics and Materials Testing"), *ÖIAZ,* Vol. 135, No. 10, 1990, pp. 526–537.

[32] Rossmanith, H. P., Ed., *Fracture Research in Retrospect,* G. R. Irwin 90th Birthday Anniversary Volume, Balkema, Rotterdam, 1997.

James A. Joyce[1] *and Robert L. Tregoning*[2]

Development of Consistent Size Criteria for ASTM Combined Fracture Mechanics Standards

REFERENCE: Joyce, J. A. and Tregoning, R. L., **"Development of Consistent Size Criteria for ASTM Combined Fracture Mechanics Standards,"** *Fatigue and Fracture Mechanics: 30th Volume, ASTM STP 1360,* American Society for Testing and Materials, West Conshohocken, PA, 2000, pp. 357–376.

ABSTRACT: Recent ASTM Subcommittee E08.08 on Elastic-Plastic Fracture Technology activities have concentrated on the development of a common fracture test standard that allows the evaluation of elastic and elastic-plastic fracture toughness properties from tests on a single specimen. Many technical changes have been made to allow this process to go forward, but one area in which progress has not been made is in clarifying the various specimen size requirements that were part of the earlier standards. Instead, the size requirements in the new toughness testing standard E1820 have been extracted from the earlier standards, like ASTM E399 and ASTM E813 and extended to the new standard without change, in spite of their clear inconsistency.

A review of the development of the E399 size criteria [*1*] seems to make it clear that the E399 size criterion was meant by its originators to represent only a requirement that allowed the 0.95 secant offset method to adequately evaluate a consistent measure of crack initiation. The later *J*-integral-based size criteria of E813, E1152, E1737, E1820, and the recent T_o Reference Temperature standard E1921 are based on finite element analysis [2], which ensures that a minimal deviation from small-scale yielding (SSY) occurs. This is intended to generate consistent crack tip constraint as the specimen size decreases or the crack length increases.

In this work, specimens from three materials, a 6061-T651 aluminum, a 6Al-4V titanium alloy, and a 4340 steel alloy, were tested to investigate what the proper size criteria should be for a combined fracture mechanics test standard. Larger specimens from each material were tested to obtain K_{Ic} values meeting the stringent size criteria of ASTM E399. Smaller specimens of each material were tested that intentionally failed the E399 size criteria, but satisfied the less stringent criteria of ASTM E813 and E1820. The unloading compliance method has been used in the testing of the smaller specimens so that an estimate of the true crack initiation point on the specimen load displacement record can be measured.

The fracture toughness at the onset of ductile crack extension is measured in terms of the *J* integral and converted to an equivalent stress intensity K_J value using the standard relationship. The fracture toughness at this crack initiation point can then be compared with the K_Q obtained using the 0.95 secant offset initiation point specified by the E399 K_{Ic} procedure, and the validity of the various measures of initiation toughness can be determined with respect to the different size criteria.

KEYWORDS: linear elastic fracture mechanics, elastic-plastic fracture mechanics, stress intensity, *J* integral, unloading compliance, constraint, size effects

Recent ASTM E08.08 Subcommittee activities have concentrated on the development of fracture test standards that allow the evaluation of K_{Ic}, J_{Ic}, δ_i, and a resistance curve like the *J-R* curve from fracture toughness tests from a single specimen. A parallel effort has been undertaken on the international stage under the auspices of the ISO. Many technical changes have been made to allow this process to go forward, but one area in which progress has not been made is in clarifying the various

[1] Professor of Mechanical Engineering, U.S. Naval Academy, Annapolis, MD.
[2] Mechanical engineer, Naval Surface Warfare Center, West Bethesda, MD.

specimen size requirements that were part of the earlier standards. Instead, the size requirements in the new toughness testing standard E1820[3] have been extracted from the earlier standards, like ASTM E399[4] and ASTM E813[5] and extended to the new standard, ASTM E1820, without change, in spite of their clear inconsistency.

A review of the development of the E399 size criteria [*1*] makes it clear that it was meant by its originators to represent only a requirement that allowed the 0.95 secant offset method to adequately evaluate a consistent measure of crack initiation. This criteria was developed based solely on experiments that used the 0.95 secant method to match the crack initiation location on the load displacement record and hence corresponding to K_Q. Therefore, variation of the resulting K_Q in small specimens from the value measured in larger specimens could be due to a failure of the secant method to correctly locate the crack initiation point. Only later, for example in the very influential textbooks of Refs *3* and *4*, was this experimental size requirement taken as a necessary condition for K_{Ic} to be transferrable from the laboratory tests to the structural applications, that is, it became an accepted requirement for the transferability of the experimentally measured K_{Ic} to the structure and flaw geometry of interest. No real justification appears to exist in the literature for this philosophy except that it is a conservative requirement that has led to safe engineering practice.

The more recent J integral-based size criteria of E813, E1152,[6] E1737,[7] E1820, and the recent T_o Reference Temperature standard E1921[8] are based on finite element analysis [*2*], which ensures that a minimal deviation from small-scale yielding (SSY) occurs. This generates consistent crack tip constraint as the specimen size decreases or the crack length increases.

In this work, specimens have been machined from a 6061-T651 aluminum, 6Al-4V titanium alloy, and 4340 steel to determine the proper size criteria for a combined fracture mechanics test standard. Larger specimens have been machined for each material that meet the stringent size criteria of ASTM E399. These specimens were tested according to current E399 practices without sidegrooves and without elastic unloadings. Smaller specimens of each material were machined as well, but these specimens were tested using standard J integral procedures with unloading compliance to developed single specimen J-R curves where possible. Most of these smaller specimens fail the E399 criteria, but satisfy the less stringent criteria of ASTM E813/E1820. The fracture toughness at the onset of ductile crack extension is measured in terms of the J integral and converted to an equivalent stress intensity K_J value using the standard relationship. The fracture toughness at this crack initiation point is then compared with the K_Q obtained using the 0.95 secant offset initiation point specified by the E399 procedure.

Analysis

The size requirement of ASTM E399 on in-plane specimen dimensions requires:

$$a, b \geq 2.5\left(\frac{K_Q}{\sigma_{ys}}\right)^2 \tag{1}$$

where

a = the crack length,
b = the remaining ligament,

[3] Test Method for Measurement of Fracture Toughness (E 1820).
[4] Test Method for Plane-Strain Fracture Toughness of Metallic Materials (E 399).
[5] Test Method for J_{Ic}, a Measure of Fracture Toughness (E 813).
[6] Test Method for Determining J-R Curves (E 1152).
[7] Test Method for J-Integral Characterization of Fracture Toughness (E 1737).
[8] Test Method for Determination of Reference Temperature TO for Ferritic Steels in the Transition Range (E 1921).

σ_{ys} = the material yield stress,
K_Q = the stress intensity factor at the intersection of the load crack opening displacement record and the 0.95 secant line.

The 2.5 factor was chosen, largely based on data sets presented in ASTM STP 463 [*5–7*], including the data sets shown in Figs. 1 and 2. For data sets like that of Fig. 1 [*6*], the K_Q became elevated as the specimen thickness B was reduced, corresponding to a transition from plane strain conditions to plane stress conditions. This transition can be controlled through the use of side grooves, and this issue is not part of this study.

The observation that K_Q falls off in the Fig. 2 data set [*7*] as the crack length, a, is reduced implies that the crack initiation measurement point is no longer accurately inferred in these specimens. The loss of crack tip strain field constraint would elevate the apparent K_Q initiation toughness as the crack size was reduced. The result shown in Fig. 2 indicates that the material becomes less tough as the crack tip constraint is reduced, which is contrary to current understanding of fracture and plasticity.

Elastic-plastic fracture test standards like E813, E1152, and E1820 have used a size requirement of the type:

$$a, b \geq M\,\delta_i \cong M\left(\frac{J_i}{\sigma_{ys}}\right) \tag{2}$$

where

δ_i = the critical crack tip opening displacement,
J_i = the critical J integral value, and
M = the size requirement factor.

Since high-constraint conditions would dictate that the specimen in-plane dimensions should be much larger than the crack tip opening displacement at fracture or ductile initiation, it seems reason-

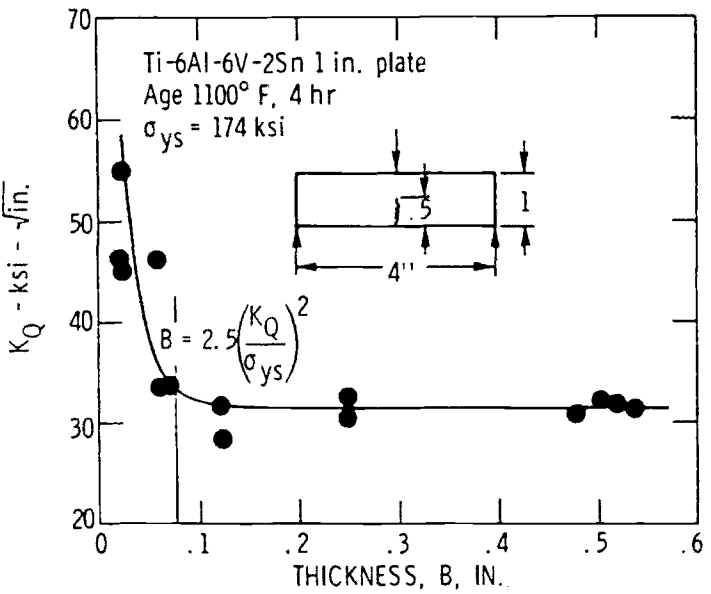

FIG. 1—*Early* K_Q *data showing effect of specimen thickness from Jones and Brown [5].*

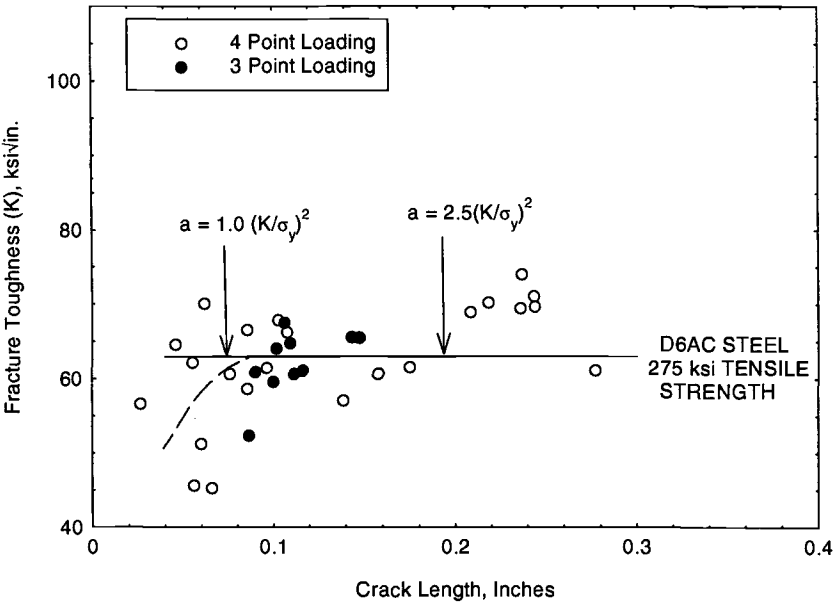

FIG. 2—*Early* K_Q *data showing effect of crack length from Jones and Brown [6].*

able that M be 10 or greater [*8*]. In fact, the following values of M are presently found in ASTM standards: $M = 25$ in E813/E1820 for J_{Ic} at ductile initiation; $M = 20$ in E1152/E1820 for the $J_{allowed}$ limit for the *J-R* curve; $M = 200$ for the onset of instability during ductile crack growth in E1820; and $M = 30$ for J_c in the new T_o standard ASTM E1921-98. The instability requirement of E1820, which is generally cleavage in ferritic steels, was chosen based on two-dimensional finite element analysis of Dodds et al. [*9*]. More recent three-dimensional analysis by Dodds and Nevalainen [*2*] supports the use of M between 50 and 100 instead of the present $M = 200$ requirement. The stress-dependent nature of cleavage requires that small-scale yielding (SSY) conditions be present in the vicinity of the crack tip, and maintenance of such conditions is the basis of the Dodds et al. analysis. This requirement is not essential for the ductile initiation or *J-R* curve standards, and the $M = 20$ and 25 requirements are based largely on experimental verification.

The requirements of Eq 1 and Eq 2 can be compared using the small-scale yielding relationship between J and K that:

$$K = \sqrt{E'J} \tag{3}$$

where $E' = E/(1 - \nu^2)$ is the material plane strain elastic modulus. Substituting this into Eq 1 provides an equivalent J integral E399 size requirement as:

$$b, a \geq 2.5 \left(\frac{E'}{\sigma_{ys}}\right)\left(\frac{J}{\sigma_{ys}}\right) \tag{4}$$

For typical metals $100 < E'/\sigma_{ys} < 1000$, and hence the E399 size requirement translates to:

$$b, a > 250 \rightarrow 2500 \left(\frac{J}{\sigma_{ys}}\right) \tag{5}$$

This requirement is thus from 10 to 100 times more stringent than the equivalent J integral crack initiation requirements, depending on whether the initiation occurs by cleavage or by ductile crack extension.

Description of the Experiments

Specimen Details

The experimental procedure involved tests on three structural materials, a 6061-T651 aluminum, a Ti-6Al-4V titanium alloy, and a 4340 steel. Initial tests were conducted on large specimens to obtain valid K_{Ic} results using ASTM E399. Tests were then conducted using J-integral, unloading compliance procedures using smaller-size specimens with a/W ratios from 0.5 to 0.82. These tests were performed according to the new ASTM E1820 standard. All specimens were precracked according to E1820, which is more stringent than E399, and thus all specimens met both the E1820 and E399 precracking requirements. Side grooves, cut with a standard Charpy cutter reducing the specimen thickness by 10% on each side, were machined after precracking in all cases in which they were used. All tests were conducted at room temperature in a displacement-controlled test machine using a displacement rate of 0.5 mm/min. Valid K_{Ic} measurements were made for each alloy using the 0.95 secant offset method of E399, which is now also a part of the combined standard E1820. All fracture mechanics tests were conducted in the TL orientation of E399.

The ambient temperature, quasi-static mechanical properties of the three materials tested obtained from standard round 0.505-in.-diameter tension specimens are presented in Table 1. All tension specimens were tested in the "T" orientation of E399.

Titanium Alloy

The titanium alloy was obtained as a 50-mm (2-in.)-thick plate and was tested in the mill-annealed condition. K_{Ic} was evaluated according to ASTM E399 using the five 1.5T C(T) and SE(B) specimens with $a/W = 0.5$, as summarized in Table 2. Six additional 1.5T C(T) and SE(B) specimens were tested with $a/W = 0.7$ using the E399 test procedure. While the $a/W = 0.7$ results were not strictly valid according to E399, the K_Q measurements obtained were clearly consistent with the valid results from the $a/W = 0.5$ specimens. Four 1T and fifteen ½T C(T) specimens of the E1152/E1820 J-integral geometry were also prepared from this material. These specimens were prepared with a range of a/W ratios from 0.5 to 0.82, side grooved using a standard Charpy notch cutter to a total thickness reduction of 20%, and tested using the unloading compliance technique according to E1152/E1820 to obtain a J-R curve when stable ductile crack extension existed. All of these specimens had notches oriented in the T-L plane, as specified by E399, and they were all tested at approximately 18°C.

TABLE 1—*Tensile mechanical properties of the materials investigated.*

	Ti-6Al-4V	6061-T651	4340 Steel
Yield stress, MPa (ksi)	890.0 (130.0)	299.0 (43.7)	945.0 (138.0)
Ultimate stress, MPa (ksi)	952.0 (139.0)	307.0 (44.8)	1000.0 (146.0)
% Elongation	11.0 (50 mm)	14.0 (50 mm)	10.0 (50 mm)
% Reduction in area	19.0	38.0	30

TABLE 2—*Ti-6Al-4V titanium specimen test matrix—nominal dimensions. All specimens except* J*-type C(T) specimens are ASTM E399 configurations.*

Specimen Type	Width, W (mm)	a/W Ratio	Thickness, B (mm)	Ligament, b (mm)	Number of Tests
ASTM C(T)	76.2	0.5	38.1	38.1	2
ASTM C(T)	76.2	0.7	38.1	22.9	3
ASTM C(T) *J* Type	50.8	0.55 to 0.69	25.4	22.8	4
ASTM C(T) *J* Type	25.4	0.5 to 0.82	12.7	15.7	15
ASTM SE(B)	76.2	0.5	38.1	38.1	3
ASTM SE(B)	76.2	0.7	38.1	22.9	3

Aluminum Alloy

The 6061-T651 aluminum alloy specimen blanks were machined from 38-mm (1.5-in.)-thick plate. Large specimens for the evaluation of K_{Ic} were prepared according to the dimensions shown in Table 3. Larger in-plane dimensions were used for the $a/W = 0.7$ specimens to maintain the E399 size requirements, based on K_{Ic} estimates available for the plate. While the $a/W = 0.7$ specimens are not strictly valid according to E399, the results from all of these larger C(T) and SE(B) specimens were consistent. All cracks were oriented in the T-L plane as specified by E399. Four 1T C(T) specimens were also prepared with side grooves as per the E1152/E1820 *J*-type specimen drawing and tested according to E399 without elastic unloadings. While these specimens failed several E399 criteria, they still gave K_Q results that corresponded to the valid results of the larger E399 C(T) and SE(B) specimens.

Four 1T and 16 ½T C(T) *J*-integral-type specimens were also machined from the center plane of the 6061-T651 plate according to E1820 and including side grooves cut to a total thickness reduction of 20% using a standard Charpy notch cutter. These two specimen types were tested using standard E1820 procedures with the unloading compliance technique, up to the point of tearing instability. All cracks were oriented in the T-L plane as specified by E399.

4340 Steel

The 4340 steel specimens were machined from a 25 by 125-mm bar. All specimens were *J*-type 1T and ½T C(T) specimens according to E1152/E1820. All specimens were machined with notches in

TABLE 3—*6061-T651 aluminum specimen test matrix—nominal dimensions. All specimens except* J*-type specimens are ASTM E399 configurations.*

Specimen Type	Width W (mm)	a/W Ratio	Thickness, B (mm)	Ligament, b (mm)	Number of Tests
C(T)	63.5	0.45 to 0.5	31.7	28.0 to 32.0	3
C(T)	84.5	0.68	31.7	27.0	3
C(T) *J* Type	50.8	0.60	25.4	20.3	4
C(T) *J* Type	25.4	0.52 to 0.82	12.7	6.0 to 12.0	16
SE(B)	62.9	0.45	31.7	34.6	3
SE(B)	84.7	0.70	31.7	31.7	3

TABLE 4—*Experimental results—Ti-6Al-4V Titanium alloy C(T) specimens.*

Specimen ID	W, mm	a/W	b, mm	K_Q, MPa$\sqrt{\text{m}}$	J_{Ic}, kJ/m^2	K_{JIc}, MPa$\sqrt{\text{m}}$	2.5, $(K_Q/\sigma_{ys})^2$, mm
HCC-10	76.2	0.70	22.7	81.6	...	...	21.0
HCC-11	76.2	0.70	21.3	75.7	...	...	18.0
HCC-14	76.2	0.73	20.9	80.0	...	...	20.2
HCC-16	76.2	0.52	36.8	84.4	...	...	22.5
HCC-12	76.2	0.50	38.1	79.4	...	...	19.9
HCC-31	50.4	0.56	22.4	81.6	59.5	86.2	21.0
HCC-61	50.4	0.55	22.9	87.2	70.0	93.4	24.0
HCC-62	50.4	0.69	15.7	75.8	59.5	86.2	18.0
HCC-32	50.4	0.69	15.7	81.1	64.8	89.9	20.8
HCC-XX11	25.4	0.82	4.5	53.1	56.9	84.3	8.9
HCC-XX12	25.4	0.54	11.8	78.2	70.0	93.5	19.3
HCC-XX13	25.4	0.61	9.9	67.5	55.2	82.9	14.4
HCC-XX14	25.4	0.79	5.4	50.5	49.0	78.2	8.0
HCC-XX15	25.4	0.61	9.9	68.1	47.3	76.8	14.6
HCC-XX16	25.4	0.53	11.9	76.6	63.0	88.7	18.5
HCC-XX17	25.4	0.68	8.1	61.4	49.0	78.2	11.9
HCC-XX18	25.4	0.69	7.9	63.3	61.3	87.4	12.6

the T-L orientation and had side grooves machined with a standard Charpy notch cutter to a total thickness reduction of 20%. The specimens were heat treated after machining but before precracking and sidegrooving by austenitizing at 816°C for 25 min, oil quenching to 20°C, quenching in liquid nitrogen (−195°C) for 20 min to assure a full transition to martensite, tempering at 593°C for 1 h, and finally air cooling to ambient temperature. All tests were conducted at an ambient temperature of approximately 18°C. The 1T specimens were tested in monotonic loading as specified by E399 so that a P_Q and K_Q could be located clearly without interference from the superimposed elastic unloadings. All ½T specimens were tested using unloading compliance according to E1152/E1820. The fracture mode in all tests was ductile hole growth, not cleavage.

Discussion of the Results

K_Q *Evaluation*

The 0.95 secant procedure of E399 was applied to all specimens. The results are tabulated in Tables 4 to 8. The larger specimens of each material, at the standard a/W ratio of approximately 0.5, be-

TABLE 5—*Experimental results—Ti-6Al-4V Titanium alloy SE(B) specimens.*

Specimen ID	W, mm	a/W	b, mm	K_Q, MPa$\sqrt{\text{m}}$	J_{Ic}, kJ/m^2	K_{JIc}, MPa$\sqrt{\text{m}}$	2.5, $(K_Q/\sigma_{ys})^2$, mm
HCC-2	76.2	0.49	38.7	81.2	...	...	20.8
HCC-4	76.2	0.48	39.8	81.3	...	...	20.8
HCC-7	76.2	0.49	38.9	80.2	...	...	20.3
HCC-1	76.2	0.72	21.7	76.4	...	...	18.4
HCC-3	76.2	0.72	21.6	79.1	...	...	19.7
HCC-8	76.2	0.71	22.4	76.1	...	...	18.3
HCC-6	76.2	0.84	12.5	64.1	...	...	13.0
HCC-5	76.2	0.77	17.5	65.8	...	...	13.7

TABLE 6—*Experimental results—6061-T651 Aluminum alloy C(T) specimens.*

Specimen ID	W, mm	a/W	b, mm	K_Q, MPa$\sqrt{\text{m}}$	J_{Ic}, kJ/m^2	K_{JIc}, MPa$\sqrt{\text{m}}$	2.5 $(K_Q/\sigma_{ys})^2$, mm
JC4-1	63.5	0.44	35.6	37.7	...	...	39.7
JC4-2	63.5	0.41	37.5	31.9	...	...	28.5
JC4-3	63.5	0.44	35.6	35.1	...	...	29.3
JC7-1	63.5	0.68	20.3	35.3	...	...	34.8
JC7-2	63.5	0.68	20.3	32.0	...	...	28.6
JC7-3	63.5	0.68	20.3	31.2	...	...	27.2
JJ71-1	50.8	0.49	25.9	32.3	...	...	29.2
JJ71-3	50.8	0.50	25.4	32.0	...	...	28.6
JJ71-C1	50.8	0.61	20.1	30.6	...	...	26.2
JJ71-C2	50.8	0.60	20.3	30.3	...	...	25.7
JB7-2a	50.8	0.68	16.4	34.6	21.9	40.4	33.5
JB7-2b	50.8	0.70	15.3	30.7	26.2	44.3	26.4
JB7-3a	50.8	0.68	16.1	31.5	17.5	36.1	27.7
JB7-3b	50.8	0.68	15.8	36.0	30.6	47.9	36.2
JB7-XC	25.4	0.70	7.65	27.7	19.3	37.9	21.5
JB7-XD	25.4	0.81	4.95	20.9	14.0	32.3	12.2
JB7-XE	25.4	0.61	9.91	28.4	16.6	35.2	22.6
JB7-XF	25.4	0.59	10.4	31.5	21.9	40.4	27.7
JB7-XG	25.4	0.60	9.91	26.5	15.4	33.9	19.6
JB7-XH	25.4	0.72	7.16	20.9	25.4	43.5	12.2
JB7-XI	25.4	0.57	10.9	27.4	14.0	32.3	21.0
JB7-XJ	25.4	0.81	4.93	17.4	14.9	33.3	8.5
JB7-YC	25.4	0.70	7.52	24.7	15.8	34.3	17.1
JB7-YD	25.4	0.58	10.7	29.4	14.0	32.3	24.2
JB7-YE	25.4	0.61	9.86	28.6	15.8	34.3	22.9
JB7-YF	25.4	0.60	10.1	33.0	24.5	42.7	30.5
JB7-YG	25.4	0.72	7.19	25.4	39.4	54.2	18.0
JB7-YH	25.4	0.80	5.03	16.3	18.0	36.7	7.4
JB7-YI	25.4	0.61	9.91	25.0	17.5	36.2	17.5
JB7-YJ	25.4	0.70	7.70	23.8	15.8	34.3	15.8

haved in a similar manner as illustrated in Fig. 3 for the 6061-T651 alloy. For the materials investigated here, P_Q corresponded to the 0.95 secant intersection P_5 in every case, with the specimen remaining stable until the load displacement record was beyond the 0.95 secant offset intersection. The large specimens with the deeper crack length ratios showed greater plasticity, but still P_Q corresponded to P_5, and the secant intersection point defined the K_Q calculation. For all three materials, the larger geometry met the E399 size criteria, as shown in the tabulated results presented in Tables 4 to 8. In many cases, large $a/W = 0.5$ SE(B) specimens would violate the E399 requirement that $P_{max}/P_Q < 1.1$ after the measured COD value reached a large value of approximately 2 mm. This cor-

TABLE 7—*Experimental results—6061-T651 Aluminum alloy SE(B) specimens.*

Specimen ID	W, mm	a/W	b, mm	K_Q, MPa$\sqrt{\text{m}}$	J_{Ic}, kJ/m^2	K_{JIc}, MPa$\sqrt{\text{m}}$	2.5 $(K_Q/\sigma_{ys})^2$, mm
JB4–1	63.5	0.39	38.7	29.0	...	...	23.5
JB4–2	63.5	0.46	34.3	32.3	...	...	29.2
JB4–3	63.5	0.46	34.3	32.3	...	...	29.2
JB7–1	84.6	0.71	24.5	32.5	...	...	29.5
JB7–2	84.6	0.70	25.4	38.2	...	...	40.8
JB7–3	84.6	0.69	26.2	27.5	...	...	21.1

TABLE 8—*Experimental results—4340 steel alloy specimens.*

Specimen ID	W, mm	a/W	b, mm	K_Q, MPa$\sqrt{m}$	J_{Ic}, kJ/m^2	K_{JIc}, MPa$\sqrt{m}$	2.5 $(K_Q/\sigma_{ys})^2$, mm
J43-a	50.8	0.52	24.6	68.9	23.6	68.2	13.3
J43-b	50.8	0.48	26.3	73.0	31.5	78.7	14.9
J43-c	50.8	0.70	15.1	70.6	28.9	75.4	14.0
J43-d	50.8	0.51	24.9	49.1	19.3	61.6	6.7
J43-e	50.8	0.70	15.2	73.4	27.1	73.1	15.1
J43-S1	25.4	0.71	7.47	62.5	39.4	88.1	10.9
J43-S3	25.4	0.52	12.2	72.4	30.6	77.7	14.7
J43-S4	25.4	0.52	12.3	73.2	36.8	85.1	15.0
J43-S6	25.4	0.74	6.50	62.3	28.0	74.2	10.9
J43-S7	25.4	0.79	5.28	43.7	27.1	73.1	5.3
J43-S8	25.4	0.59	10.3	57.0	30.6	77.6	9.1
J43-S9	25.4	0.70	7.72	62.3	36.8	85.1	10.9
J43-S10	25.4	0.76	6.22	61.5	28.0	74.2	10.6
J43-S11	25.4	0.52	12.1	72.6	35.9	84.0	14.8
J43-S12	25.4	0.59	10.4	63.3	36.8	85.1	11.2

responded to the presence of tunneled crack extension and the development of large shear lip regions that carried increasingly more of the applied load. In most cases a small elastic unloading was taken beyond the first load drop, as shown in Fig. 3, and the compliance change that was measured was used to assure that ductile crack growth was present at this time, and that the E399 requirement that $P_{max}/P_Q < 1.1$ could be ignored. For the specimen shown in Fig. 3, the compliance change measured at the unloading shown corresponded to an average crack extension of more than 2 mm, and the subsequent load rise to a P_{max} value is of no consequence to the test.

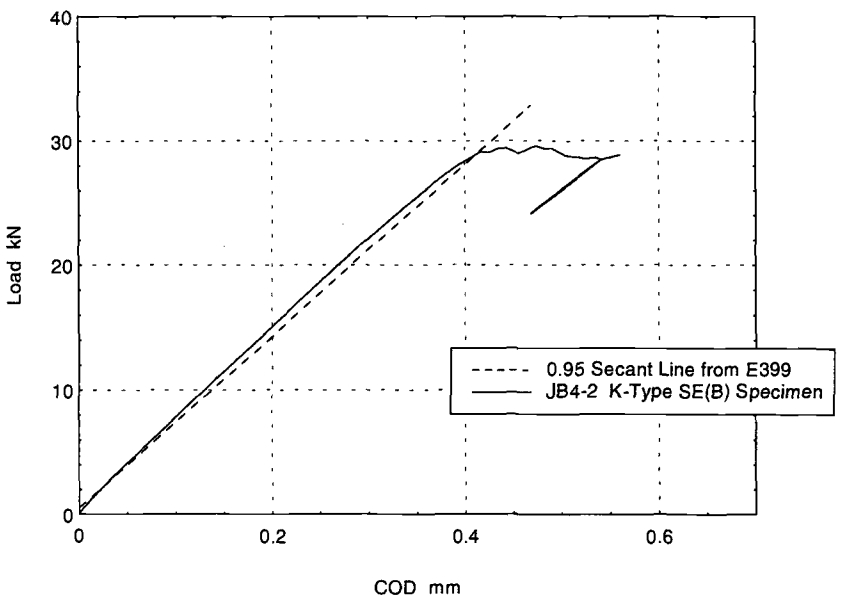

FIG. 3—*Typical evaluation of* K_Q *for a large K-type SE(B) specimen of the 6061-T651 aluminum alloy.*

The toughnesses measured for the largest-size specimens of the titanium and aluminum alloys tested here correspond well with measurements for these alloys found in the classic Air Force Materials Laboratory Damage Tolerant Design Handbook [*10*]. The 4340 steel alloy was heat treated specifically for this study to give toughnesses that were valid by E399 for the 1T specimen size and invalid for the smaller ½T C(T) test geometry.

For all of the ½T C(T) specimens, the P_Q corresponded to the P_5 intersection point as shown in the example in Fig. 4, except that for the majority of these specimens the maximum load was often well in excess of $1.1P_Q$. Since these specimens were all tested using unloading compliance, the true crack initiation point could be estimated for these specimens from the measured compliance changes. Figure 5 shows an example of an $a/W = 0.54$ ½T C(T) specimen of the Ti-6Al-4V alloy for which the E399 secant offset "crack initiation" prediction and the unloading compliance crack initiation prediction agree quite well.

As the ½T C(T) specimen's remaining ligament, b, was further reduced, the maximum load point was found to move further beyond the $P_5 = P_Q$ measurement point, giving smaller and smaller K_Q measurements. At the same time in these specimens, the P_5 point moved dramatically away from the correct crack initiation location as defined by the unloading compliance technique. This is shown in Figs. 6 for an $a/W = 0.82$ ½T C(T) specimen of the titanium alloy. The resulting measurement of $K_Q = 53.1$ MPa$\sqrt{\text{m}}$ is considerably less than the correct value of approximately 80 MPa$\sqrt{\text{m}}$ for this alloy, and hence the E399 measurement is conservative, but the 34% error is unacceptable if the test method can be updated by the use of the unloading compliance/K_{JIc} method.

Figures 7 to 9 show plots of K_Q versus b for the three materials. These figures are very similar to the results of Steigerwald [*6*] shown previously in Fig. 2, even though the Steigerwald plot has crack length, a, rather than remaining ligament b on the absissca. The existing E399 requirement of Eq 1 is plotted on these figures and clearly defines a conservative limit for specimen size for the use of the 0.95 secant offset method on these materials and specimens. The K_Q quantity falls as b is reduced (or

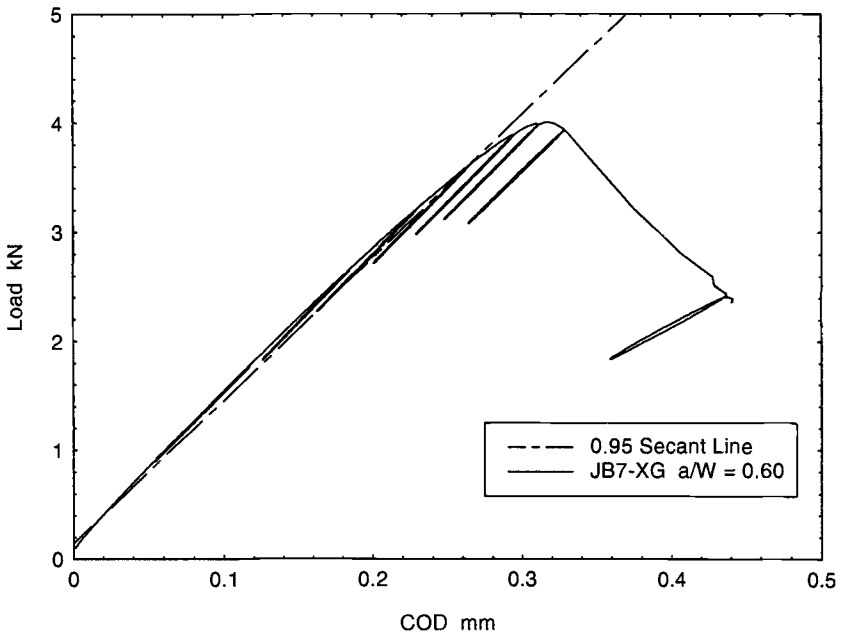

FIG. 4—*Evaluation of a 0.95 secant* K_Q *for a small* J*-type C(T) specimen that had been tested using unloading compliance.*

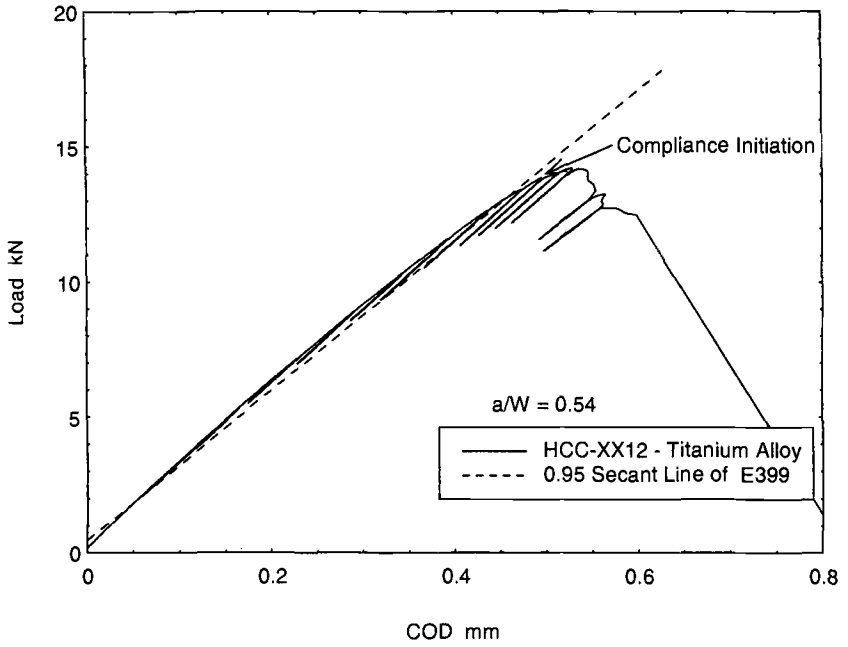

FIG. 5—*Titanium alloy C(T) specimen with* a/W = *0.54 showing close agreement between the E399 secant intersection and the unloading compliance predicted crack initiation location on the load COD record.*

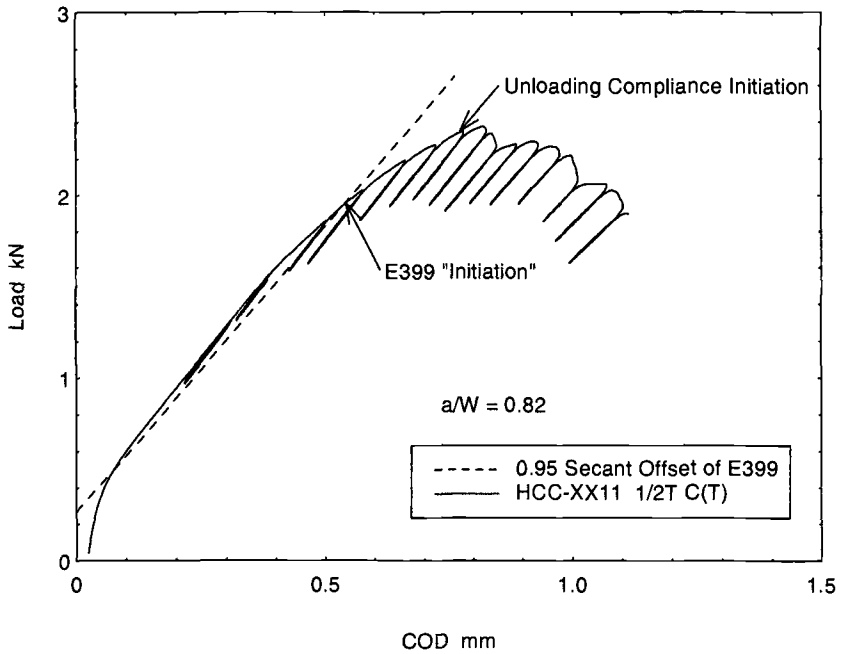

FIG. 6—*Divergence of initiation sites is demonstrated for an* a/W = *0.82 C(T) specimen of the titanium alloy.*

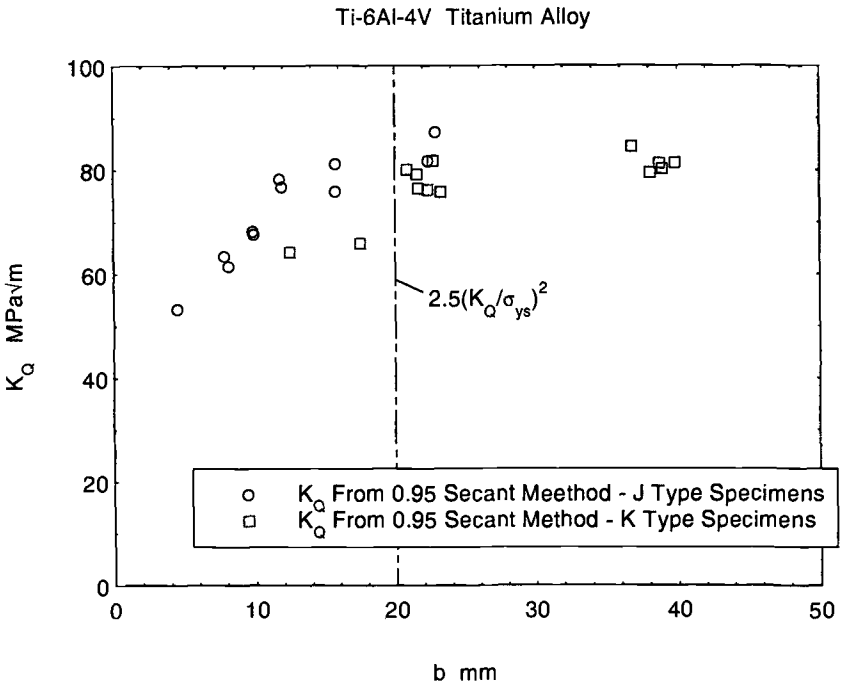

FIG. 7—*Comparison of* K_Q *versus the remaining ligament* b *for the* K*-type and* J*-type specimens of the titanium alloy.*

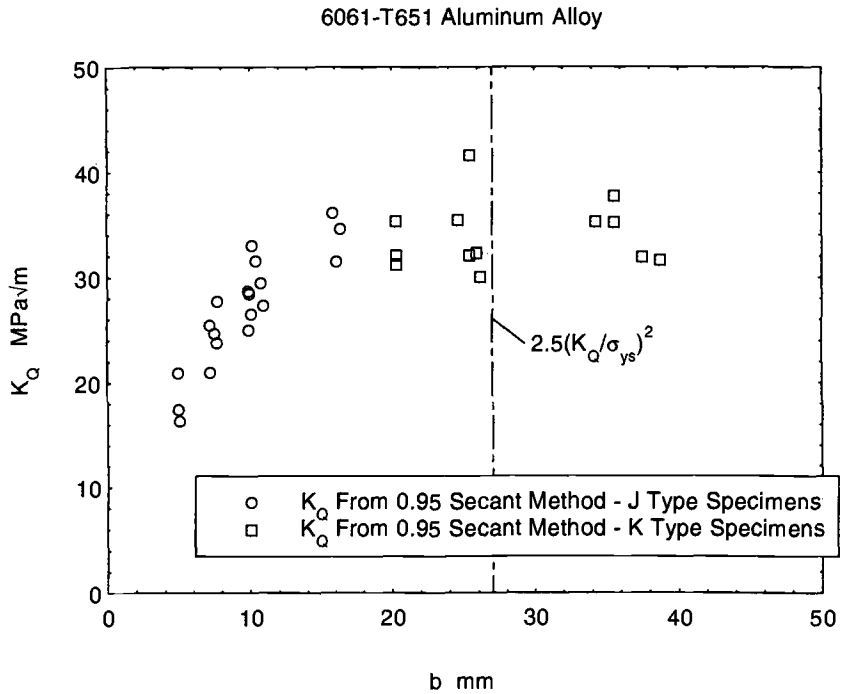

FIG. 8—*Comparison of* K_Q *versus the remaining ligament* b *for the* K*-type and* J*-type specimens of the aluminum alloy.*

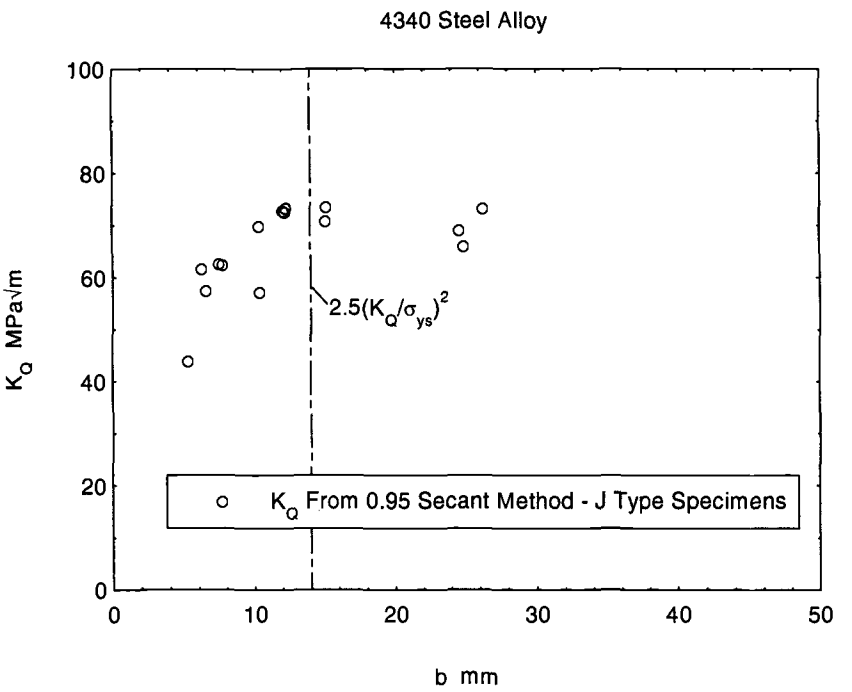

FIG. 9—K_Q *versus the remaining ligament* b *for the* J*-type specimens of the steel alloy.*

a for that matter), not because the intensity of the driving force is falling, but simply because the measurement point is being determined erroneously as the shape of the load versus COD curve changes with specimen geometry.

Defining a K_{Ic} *Size Criterion*

The above results show that the E399 size requirement is correct in that, if it is met or exceeded, consistent measurements of K_Q results from the application of the 0.95 secant method to load versus COD records obtained from standard E399 SE(B) and C(T) specimens. The results also show that the E399 size criterion is not necessarily a necessary condition for the transferability of the measured toughness result to a structural application. Taking *J* to be separable into elastic and plastic components as is done in the E813 and E1820 standards, it stands to reason that a linear elastic evaluation of K_Q would only be accurate for a specimen or a structure if the plastic component of *J*, J_{pl}, is negligible in comparison with the total *J*. In general, the relative size of the plastic and elastic components of the *J* integral depends on the flaw size, the test or structural configuration, and on the mode of loading.

The *J* type 1T and ½T C(T) specimens tested here were tested using an elastic unloading compliance procedure, and for these specimens a limited *J-R* curve was generated using the methods of E1152/E1820. Example *J-R* curves for three aluminum ½T C(T) specimens are shown in Fig. 10. Some specimens demonstrated very little stable tearing, while other specimens demonstrated extensive stable ductile crack extension, and this is the case, of course, because the percentage of the total *J*-integral that is contributed by the plastic *J* component varies markedly in these specimens.

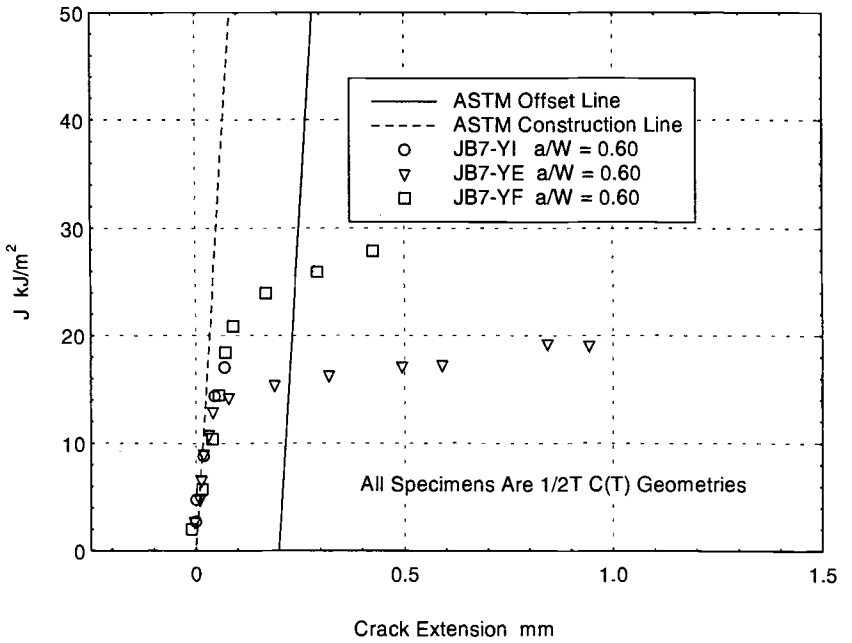

FIG. 10—*Typical* J-R *curves for similar* ½*T C(T) aluminum alloy* J*-type specimens.*

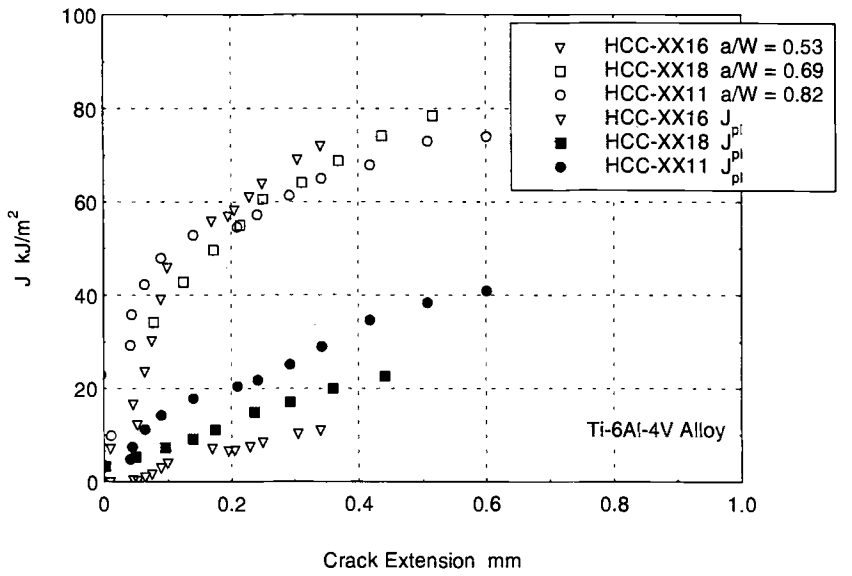

FIG. 11—*Separation of elastic and plastic* J *components to show the relative sizes of these components for a variety of* a/W *ratios.*

These *J-R* curves can be used to define a more correct size requirement for evaluation of K_Q and hence K_{Ic}, at least for the C(T) and SE(B) test geometries used here. *J-R* curves are shown in Fig. 11 for three ½T C(T) specimens of the titanium alloy with a wide range of *a/W* ratios. Also shown on this figure are three curves showing the plastic components of the *J* integral for these same three specimens calculated using the equations of E1820. As is typical of *J-R* curves of deeply cracked bend specimens, the total *J-R* curves are consistent, even though the magnitudes of the elastic and plastic *J* components vary as the specimen remaining ligament is reduced, with the plastic component of *J* varying from 1 or 2% to more than 50% of the total *J*. J_{Ic} values were calculated for all unloading compliance *J*-type specimens according to E813/E1820 using the offset blunting method, as shown in Fig. 10. The plastic component of J_{Ic} was then evaluated using the unloading compliance equations of E1820.

If one wishes to obtain K_Q from the load and crack length alone, the plastic component of the applied *J* at the onset of ductile crack growth must be small. The criterion adopted here is that no more than a 10% error is acceptable in the K_Q calculation, which is equivalent to a plastic *J* component of 20% at crack initiation. With this in mind, the percentage of the total J_{Ic} that was obtained from J_{pl} was calculated for each specimen, and the results are plotted versus $M = b\sigma_{ys}/J_{Ic}$ in Fig. 12. In this plot the J_{Ic} used to calculate *M* was an average value obtained from the largest specimens of each material, not the result obtained from each individual specimen. As shown on Fig. 12 a requirement that *M* be greater than 330 seems consistent here with dominant elastic conditions for the aluminum and 4340 steel C(T) and SE(B) specimens. This is much less stringent than the E399 criteria of Eq 1 above, which would require that *M* be greater than 1350 and 1500 for these two materials, respectively. Figure 12 shows that for the titanium alloy *M* would need to be greater than 120, which is also less stringent than the E399 requirement that *M* be greater than 400 for this material. While in this case these calculations are being done on specimen geometries rather than structural geometries, the important point is that this transferability requirement is based directly on limiting the error involved in calculating the driving force *K* in these geometries when using only the linear-elastic, load-based, fracture mechanics quantity *K*.

Even in this restricted case, a single criterion based solely on *M* rather than a J_{pl} calculation, and hence on a ratio of yield strength to toughness, does not work well for these three materials. Such a

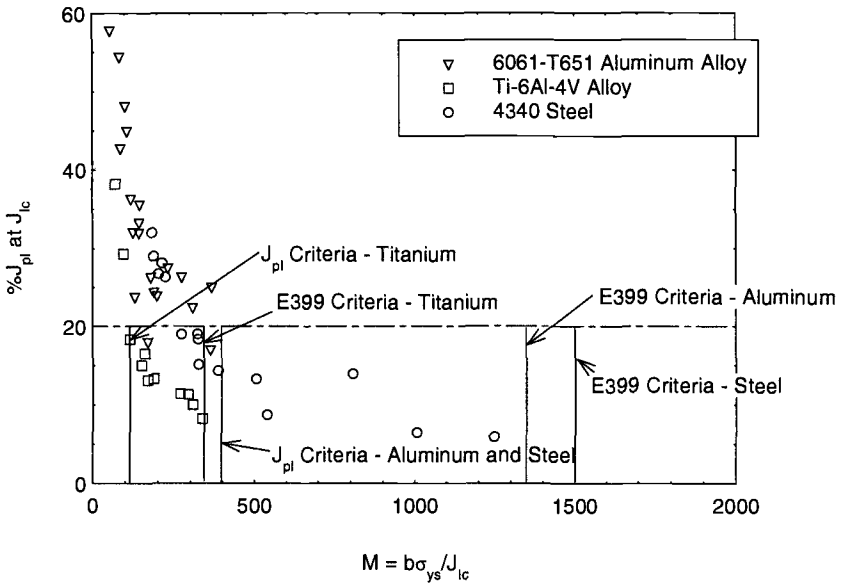

FIG. 12—J-*integral-based size requirement defined for the three materials investigated here.*

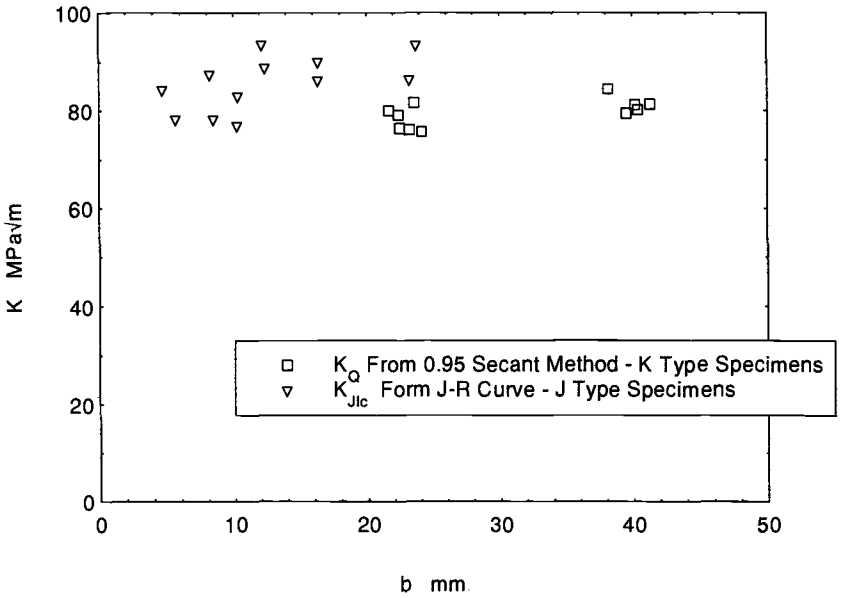

FIG. 13—K_{JIc} *and* K_Q *versus* b *showing no apparent size effect for the titanium alloy.*

criteria is also not likely to be useful as a size criterion for structural applications since the cracks would then be shallow and the loading predominantly tensile. For structures, a criterion based on the crack tip stress fields remaining predominantly elastic probably needs to developed on a case by case basis using elastic-plastic finite element or other appropriate analysis.

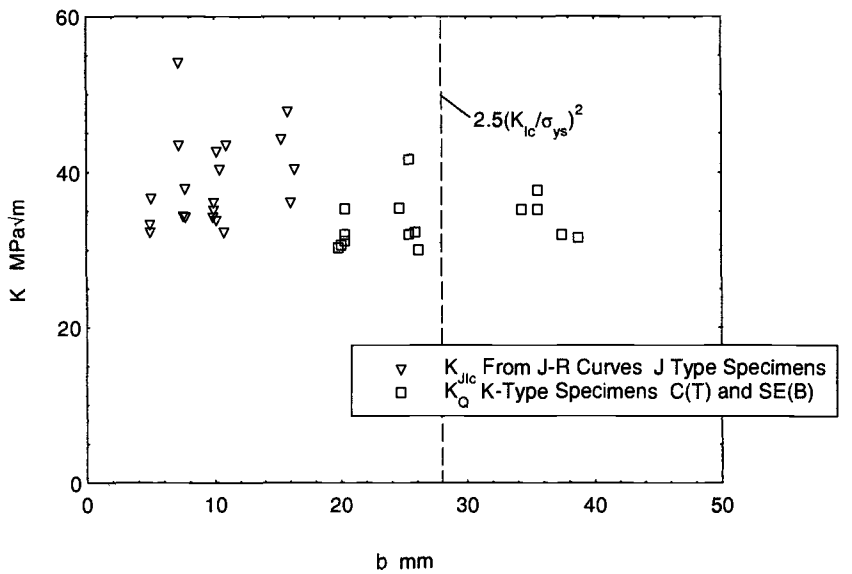

FIG. 14—*Comparison of* K_{JIc} *and* K_Q *showing no size effect for the 6061-T651 aluminum alloy.*

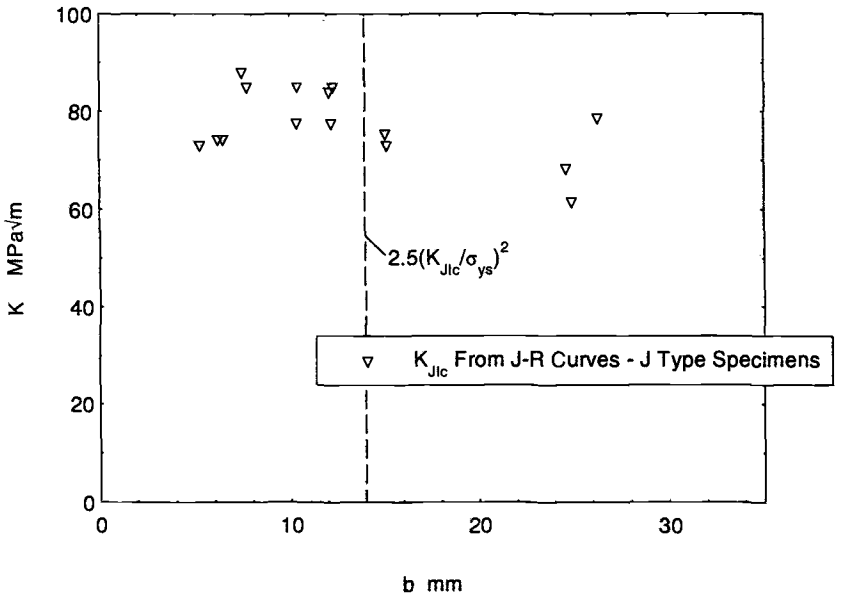

FIG. 15—K_{JIc} *versus remaining ligament* b *showing no size effect for the 4340 steel.*

Size Requirements for K_{JIc}

K_{JIc} is plotted versus b in Figs. 13 to 15. Also shown on these figures are the K_{Ic} results obtained from the large K-type specimens from each material. While these results correspond to slightly different criteria of ductile crack initiation, they should provide similar initiation toughness measure-

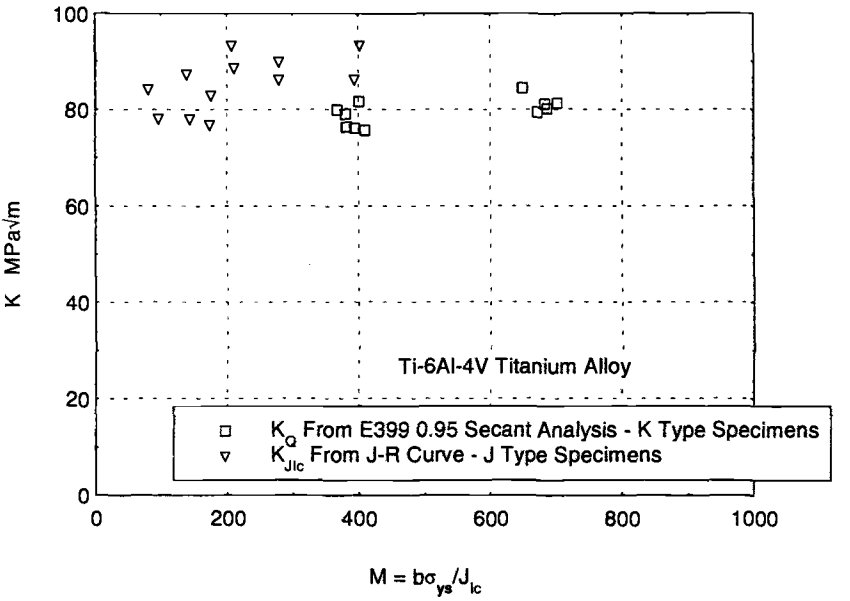

FIG. 16—*Comparison of* K_{JIc} *and* K_Q *versus* M *showing no size effect for the titanium alloy.*

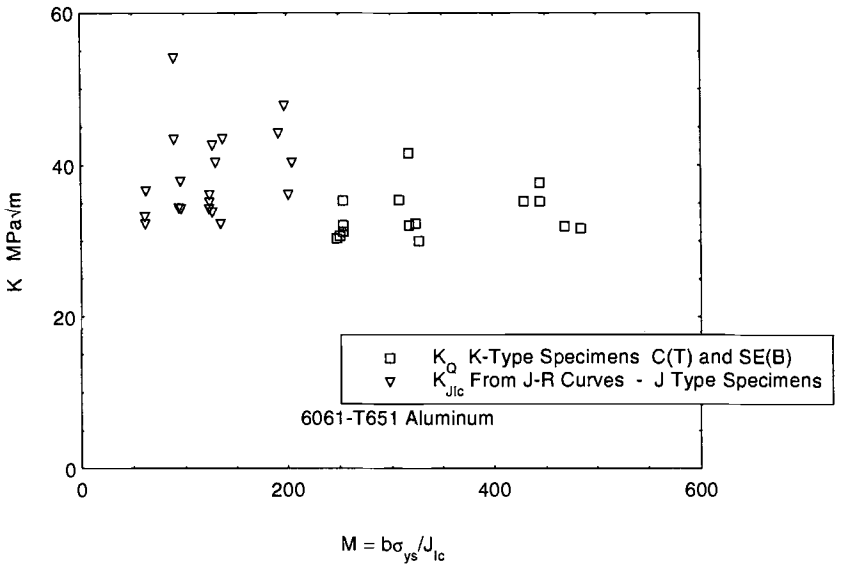

FIG. 17—*Comparison of* K_{JIc} *and* K_Q *versus* M *showing no size effect for the 6061-T651 aluminum alloy.*

ments if SSY conditions are present in all tests. These plots exhibit a slight elevation of K_{JIc} in comparison with K_{Ic}, but no dependence of the overall magnitude on specimen size, at least as measured by *b*. These data are replotted in Figs. 16 to 18 as a function of *M*, where *M* is calculated from the average J_{Ic} and yield stress of each material. For these relatively low-toughness materials, the smallest

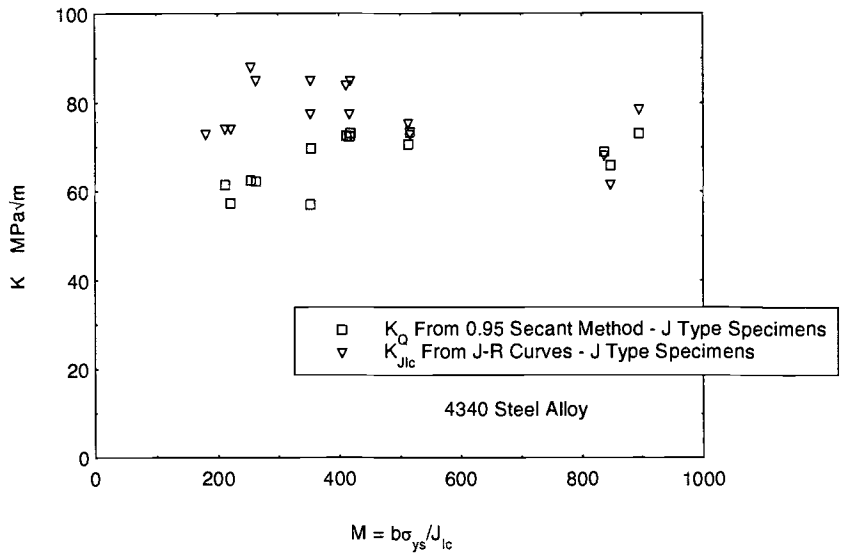

FIG. 18—*Comparison of* K_{JIc} *and* K_Q *versus* M *showing no size effect for the 4340 steel.*

M values reached are about 80, but over the range of M investigated, namely $80 > M > 1200$, no systematic variation in the measured K_{JIc} is demonstrated for these geometries and materials. It seems clear from these results that it is reasonable to evaluate J_{Ic} using the unloading compliance method of E813/E1820, convert the result to K_{JIc}, and then use the result as one would use K_{Ic} for structural applications where the conditions near the postulated crack tip were predominantly elastic. However, care must be taken to assure that cracks expected in the structural application would remain within predominantly elastic stress fields and also that ductile crack growth is the mode of fracture, as demonstrated by the specimens.

Conclusions

The principal conclusions of this study are:

1. The current size criteria of E399 is required if the 0.95 secant method is used to evaluate a size-independent K_Q. This criteria should not be interpreted as a requirement for the transferability of the resulting K_{Ic} measurement to a structural application.
2. Application of the current E399 size requirement to applications would lead to a very conservative and safe result. The results shown here demonstrate that in many cases linear elastic fracture mechanics would be applicable to cases with much more extensive plasticity than would be allowed by application of the E399 size criteria as a transferability requirement for structural applications.
3. The relative contributions of the elastic and plastic J-integral components is a better measure of the elastic dominance in a specimen or in a structural application. Evaluating the relative sizes of the J-integral components in a structural application, however, probably requires an elastic-plastic analysis, and if this is available, the engineer can use the J integral directly and not need to transfer to a LEFM analysis using K_{JIc} as the criteria of ductile crack initiation.
4. For the materials and specimens investigated here, it appears reasonable to evaluate J_Q using the unloading compliance method of E813/E1820, and then, if this meets the size requirements of E813/E1820 ($M > 25$), convert the result to J_{Ic} and then to K_{JIc}, and then use K_{JIc} as one would use K_{Ic} for structural applications where the conditions were predominantly elastic. However, care must be taken to assure that cracks expected in the structural application would remain within predominantly elastic stress fields and also that ductile crack growth is the mode of fracture, as demonstrated by the specimens.

References

[1] Brown, W. F., Jr., Ed., *Review of Developments in Plane Strain Fracture Toughness Testing, ASTM STP 463,* American Society for Testing and Materials, 1970.

[2] Nevalainen, Markku, and Dodds, R. H., "Numerical Investigation of 3-D Constraint Effects on Brittle Fracture in SE(B) and C(T) Specimens," *International Journal of Fracture,* Vol. 74, 1995, pp. 131–161.

[3] Kanninen, M. F. and Popelar, C. H., *Advanced Fracture Mechanics,* Oxford University Press, New York, 1985.

[4] Rolfe, S. T. and Barsom, J. M., *Fracture and Fatigue Control in Structures,* Prentice Hall, Englewood Cliffs, New Jersey, 1977.

[5] May, M. J., "British Experience with Plane Strain Fracture Toughness (K_{Ic}) Testing," *Review of Developments in Plane Strain Fracture Toughness Testing, ASTM STP 463,* W. F. Brown, Jr., Ed., American Society for Testing and Materials, 1970, pp. 63–101.

[6] Jones, M. H. and Brown, W. F., Jr., "The Influence of Crack Length and Thickness in Plane-Strain Fracture Toughness Tests," *Review of Developments in Plane Strain Fracture Toughness Testing, ASTM STP 463,* W. F. Brown, Jr., Ed., American Society for Testing and Materials, 1970, pp. 63–101.

[7] Steigerwald, E. A., "Crack Toughness Measurements of High Strength Steels," *Review of Developments in Plane Strain Fracture Toughness Testing, ASTM STP 463,* W. F. Brown, Jr., Ed., American Society for Testing and Materials, 1970, pp. 102–123.

[8] Paris, P. C., "Discussion to J. A. Begley and J. D. Landes," *Fracture Mechanics, ASTM STP 514*, American Society for Testing and Materials, 1972, pp. 21–22.

[9] Anderson, T. L. and Dodds, R. H., "Specimen Size Requirements for Fracture Toughness Testing in the Ductile-Brittle Transition Region," *Journal of Testing and Evaluation*, Vol. 19, 1991, pp. 123–134.

[10] "Damage Tolerant Design Handbook," MCIC-HB-01, Air Force Materials Laboratory, Wright Patterson Air Force Base, Ohio, 1973.

Gregory N. Vigilante,[1] *John H. Underwood,*[2] *and Dan Crayon*[3]

Use of the Instrumented Bolt and Constant Displacement Bold-Loaded Specimen to Measure In-Situ Hydrogen Crack Growth in High-Strength Steels

REFERENCE: Vigilante, G. N., Underwood, J. H., and Crayon, D., **"Use of the Instrumented Bolt and Constant Displacement Bold-Loaded Specimen to Measure In-Situ Hydrogen Crack Growth in High-Strength Steels,"** *Fatigue and Fracture Mechanics: 30th Volume, ASTM STP 1360,* P. C. Paris and K. L. Jerina, Eds., American Society for Testing and Materials, West Conshohocken, PA, 2000, pp. 377–387.

ABSTRACT: The aggressive environments experienced by large-caliber gun tubes during processing and firing have led to much investigation of the hydrogen-induced cracking susceptibility of high-strength steels. Constant displacement bolt-loaded specimens were used to determine the hydrogen crack growth rates and threshold stress intensities of AF1410, both conventionally and isothermally heat treated, and AerMet 100. The severe susceptibility of high-strength steels necessitated the application and modification of a low-cost, highly reliable in-situ crack measurement method, the instrumented bolt. The instrumented bolt consisted of a full bridge, strain-gaged stainless steel bolt coupled to an automatic data acquisition system. New expressions were developed for use with the instrumented bolt and bolt-loaded specimen to relate load to crack growth. Stage II crack growth rates for the AF1410 were 1.1×10^{-2} and 2.3×10^{-2} mm/s for conventional and isothermal AF1410, respectively. Threshold stress intensity levels for AF1410 were 16.0 and 13.7 MPa $\cdot$ $m^{1/2}$, respectively. Stage II crack growth rates for AerMet 100 were 2.4×10^{-2} mm/s, while the threshold stress intensity was 14.1 MPa $\cdot$ $m^{1/2}$.

KEYWORDS: hydrogen-induced cracking, hydrogen embrittlement, environmental cracking, environmental fracture, instrumented bolt, bolt-loaded specimen, high-strength steels, A723, AF1410, AerMet 100

Hydrogen-induced cracking has been a particular problem in armament applications because of the use of aggressive manufacturing environments [*1*] and developmental propellants [*2,3*]. Furthermore, to meet the battlefield demands of increased range and muzzle velocity, higher-yield-strength gun tube materials are being developed. This ultimately will result in a greater susceptibility of these materials to hydrogen-induced cracking. Of course, hydrogen-induced cracking is not a problem isolated to armament applications, but is also a persistent problem in a variety of other industries including the welding, chemical, paper processing, oil and gas, and aerospace industries.

Previous hydrogen-cracking studies were conducted on ASTM A723 steel using the constant displacement bolt-loaded compact specimen [*4*]. Stage II crack growth rates (*da/dt*) increased by approximately an order of magnitude from 10^{-5} to 10^{-4} mm/s upon increasing the yield strength from 1130 to 1275 MPa. This work was recently investigated further to determine the hydrogen-cracking susceptibility of A723 steel at yield strengths up to 1380 MPa. Under identical test conditions, results

[1] Mechanical engineer, U.S. Army Armament Research Development and Engineering Center, Watervliet, NY 12189-4050.

[2] Materials research engineer, U.S. Army Armament Research Development and Engineering Center, Watervliet, NY 12189-4050.

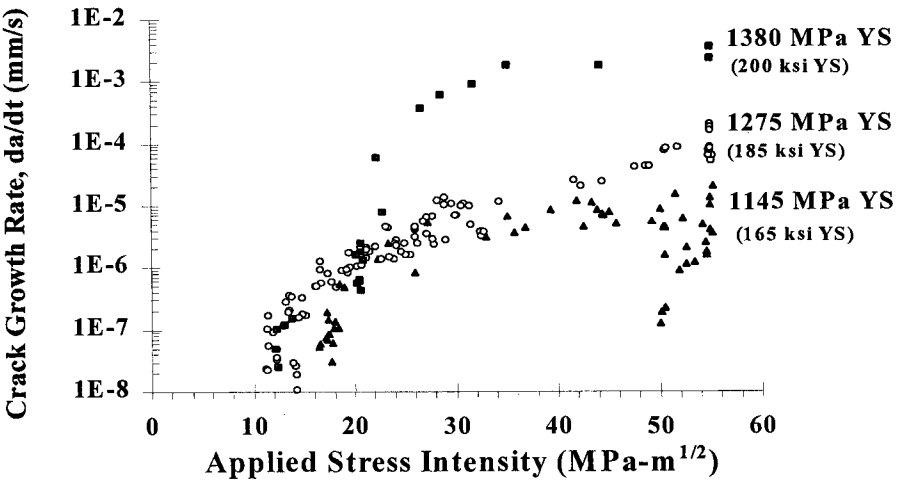

FIG. 1—*Effect of increasing yield strength on crack growth rates in ASTM A723 steel.*

again demonstrated a dramatic correlation between yield strength and crack growth rates. In fact, for only a 22% increase in yield strength from 1130 to 1380 MPa, Stage II *da/dt* increased by approximately 300 fold (Fig. 1).

The rapid crack growth rates observed with A723 steel necessitated development of an in-situ crack growth technique, since even higher-strength materials (i.e., AF1410, AerMet 100) were to be tested. Before the in-situ crack measurement technique was developed, crack measurements were laboriously measured using an optical microscope.

Initially, both the direct current potential drop (DCPD) and instrumented bolt techniques were pursued. However, with the DCPD method, significant underestimation of crack length occurred. This was attributed to electrical shorting between the pin and the bolt and/or shorting between the crack surfaces [*5*]. Consequently, instrumented bolts were investigated because of their low cost and relative ease of use.

A comprehensive literature review was performed to determine previous environmental cracking investigations using the bolt-loaded specimen and instrumented bolt. Surprisingly, the only published investigations found on environmental cracking using the bolt-loaded specimen and instrumented bolt were by Chung et al. [*6,7*], who conducted stress corrosion cracking studies on sensitized 304 stainless steel at elevated temperatures.

Materials, Heat Treatments, and Test Environment

AF1410 and AerMet 100 steels were tested in this investigation to demonstrate the instrumented bolt technique. AF1410 is an Air Force developed Fe-Co-Ni alloy used for its high strength and high

TABLE 1—*Material chemistry for AF1410 and AerMet 100 (wt%).*

	C	Co	Ni	Cr	Mo	Mn	S	P	Ti	Fe
AF1410	0.13–0.17	13.5–14.5	9.5–10.5	1.8–2.2	0.90–1.10	0.10 max	0.005 max	0.008 max	0.015 max	Bal
AerMet 100	0.21–0.25	13.0–14.0	11.0–12.0	2.9–3.3	1.1–1.3	0.10 max	0.005 max	0.008 max	0.015 max	Bal

TABLE 2—*Pertinent physical and mechanical properties.*

	Young's Modulus, E (GPa)	0.2% Yield Strength, MPa	Fracture Toughness, K_{max} (MPa · $m^{1/2}$)
AF1410 Conventional	203	1551	172
AF1410 Isothermal	203	1530	187
AerMet 100	193	1725	127

toughness. AF1410 is strengthened by the martensite transformation as well as formation of coherent chromium and molybdenum carbides [*8*]. AF1410 was tested in the conventional heat-treated condition as well as the isothermally processed condition. The ASTM grain size number of conventionally heat-treated AF1410 was approximately 10.8. Previous work conducted by Vigilante et al. [*9*] demonstrated that the producibility of AF1410 could be greatly improved through molten salt isothermal processing. In this process, a mixture of bainite and martensite is formed. Initial tests determined no significant changes in the mechanical properties of AF1410 containing this microstructure. The ASTM grain size number of the isothermally processed AF1410 was approximately 10.7. AerMet 100 is a derivative of AF1410, which has even higher strength due to an increase in the carbon, chromium, and molybdenum content for additional precipitation hardening. AerMet 100 is used in critical applications where ultrahigh strength and high toughness are essential, such as in military aircraft landing gear. The ASTM grain size number of the AerMet 100 tested was approximately 11.1. Material chemistry and pertinent physical and mechanical property data can be found in Tables 1 and 2, and heat treatment information can be found in Table 3.

A concentrated 50% H_2SO_4–50% H_3PO_4 solution by volume (pH ~ 1) was used to generate hydrogen in all of the tests conducted. This solution has been used in prior work to promote rapid hydrogen cracking in high-strength steels and nickel-iron superalloys [*4*].

Test Procedure

Constant Displacement Bolt-Loaded Compact Specimen

The 0.486 H/W constant displacement bolt-loaded compact specimen was used for all tests (Fig. 2). Two bolt-loaded specimens were tested for each material/heat treatment investigated. The W dimension was 50.8 mm for these specimens. The thickness of the specimens was 0.375W rather than 0.50W in order to increase the applied stress intensity while remaining within the maximum load capacity of the instrumented bolt. Since these materials are highly susceptible to hydrogen-induced cracking and have low-hydrogen-induced cracking stress intensity thresholds (K_{IHIC}), a small reduc-

TABLE 3—*Heat treatments employed.*

Materials	Heat Treatment
AF1410 Conventional	900°C, 1 h, air cool, 840°C, 1 h, air cool, age 510°C, 5 h, air cool
AF1410 Isothermal	900°C, 1 h, air cool, 840°C, 1 h, air cool to 300°C, isothermal hold for 1 h, air cool, age 510°C, 5 h, air cool
AerMet 100	885°C, 1 h, oil quench, refrigerate @ −73°C, 1 h, air warm, age 482°C, 5 h, air cool

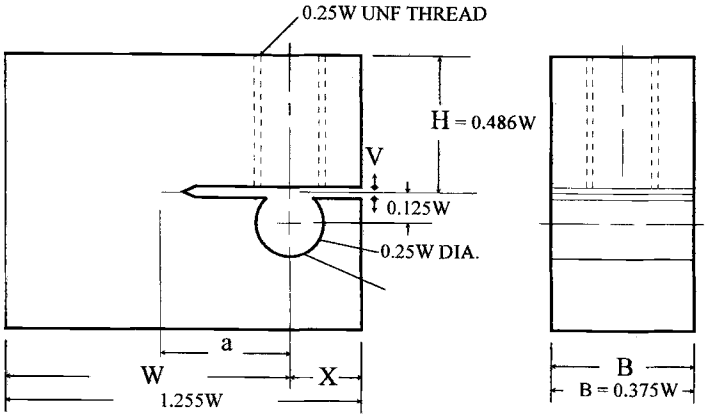

FIG. 2—*0.486 H/W bolt-loaded specimen.*

tion in the thickness will not affect the validity of the test to meet plane strain requirements. All bolt-loaded specimens were fatigue precracked at stress intensity levels less than 75% of the initial applied stress intensity during hydrogen cracking testing. All specimens were tested at either initial applied stress intensity levels of 55 or 82 MPa · $m^{1/2}$ and were tested with an initial a/W of approximately 0.5 in order to reduce the applied load. Test durations using the instrumented bolt were typically 1 to 2 h. As will be discussed later, this was more than enough time to achieve significant cracking and to reach K_{IHIC}. However, for more accurate threshold measurements, additional specimens were tested with standard bolts for longer durations, typically 1000 h. After test termination, each specimen was manually overloaded to expose the fracture surfaces. The remaining ligament was measured using a machinist's microscope to determine K_{IHIC}. The fracture surfaces were examined using the scanning electron microscope to characterize the fracture morphology.

Instrumented Bolt

Instrumented bolts are commonly used to measure tensile loads for a variety of different applications. However, with the constant displacement bolt-loaded specimens, the bolts undergo compressive loading. Several ½-20 UNF instrumented bolts were fabricated out of 17-4 PH martensitic stainless steel (H1025 condition) for these tests. The bolts were instrumented with a full bridge strain gage 9.525 mm (⅜ in.) from the end of the bolt and had a load-bearing capacity of 44.5 kN (10 000 lb). A drawing of the instrumented bolt can be found in Fig. 3. The cost of each bolt was less than five hundred dollars and thus provided a cost-effective technique to measure in-situ crack growth.

The instrumented bolt was mounted in a servo-hydraulic mechanical test machine to determine the accuracy of the bolt. The load output (mv) from the instrumented bolt was compared to the load cell output from the mechanical test machine at 4.5-kN (1000-lb.) intervals from 4.5 to 40 kN (9000 lb). The load from the instrumented bolt was accurate to ±155 N (35 lb) and was repeatable to ±45 N (10 lb) over the full range of load tested. The load output from the instrumented bolt was also compared to the theoretical v/P expressions for the 0.486 H/W bolt-loaded specimen at a/W of 0.3 to 0.9. Care was taken to ensure that both the pin hole and the bolt hole were parallel and perpendicular within 0.0254 mm of reference surfaces. A hardened hemispherical ball bearing was used between the pin and the instrumented bolt to facilitate point contact and alignment. At all a/W, the load from the instrumented bolt underestimated the theoretical load for the bolt-loaded specimen by approximately 20%. This error was overcome by uniformly adjusting the load output from the instrumented bolt after test termination. The reasons for this error will be discussed later.

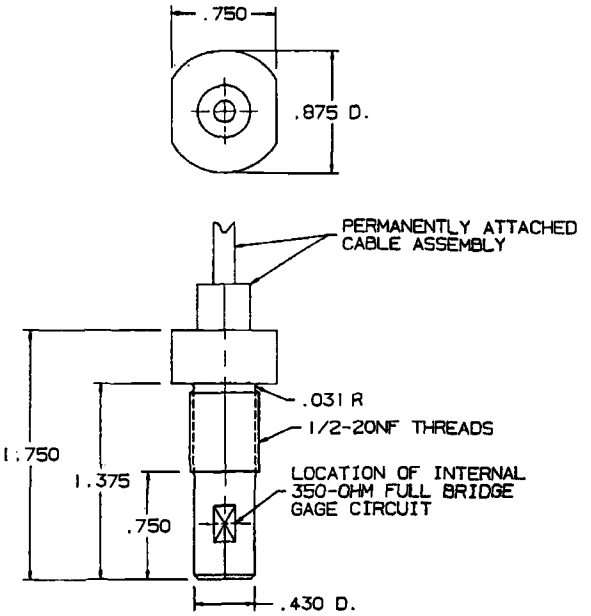

FIG. 3—*17-4 PH stainless steel instrumented bolt (Note: English units). Printed with permission from Strainsert Company, West Conshohocken, PA.*

The instrumented bolt was attached to an automatic data acquisition system to measure and record the drop in load with time as the crack advanced. A 12-bit resolution analog/digital (A/D) plug-in card was used to monitor the instrumented bolt output. The gain on the acquisition software was maximized to improve sensitivity. The floating error with the data acquisition system was ±135 N (30 lb).

v/P, K/P *and* a/W *Expressions*

The wide range expression for K/v versus a/W used with the bolt-loaded specimens tests here was recently published by Underwood et al. [*1*]. This is also the expression used for the on-going incorporation of the bolt-load specimen in ASTM Method 1681 for environment-assisted cracking tests on metallic materials. The expression is:

$$KW^{1/2}/Ev(1 - a/W)^{1/2} = 0.654 - 1.88(a/W) + 2.66(a/W)^2 - 1.233(a/W)^3$$
$$\text{for } X/W = 0.255,\ H/W = 0.486,\ 0.3 < a/W < 1.0 \tag{1}$$

However, for instrumented bolt tests, additional expressions for K/P and v/P versus a/W are necessary to determine stress intensity and crack growth from the load output of the instrumented bolt. Figure 4 summarizes some available K/P versus a/W results for the bolt-load specimen as well as a new K/P expression developed here. Newman's numerical data used by Lisagor are shown along with the plot of Lisagor's expression fitted to the Newman data [*10*]. Using the deep crack bending limit K solution [*11*], it can be shown that the limit of the K/P expression in the form here is:

$$\lim_{a/W \to 1} [(KBW^{1/2}/P)(1 - a/W)^{3/2}/(2 + a/W)] = 1.325 \tag{2}$$

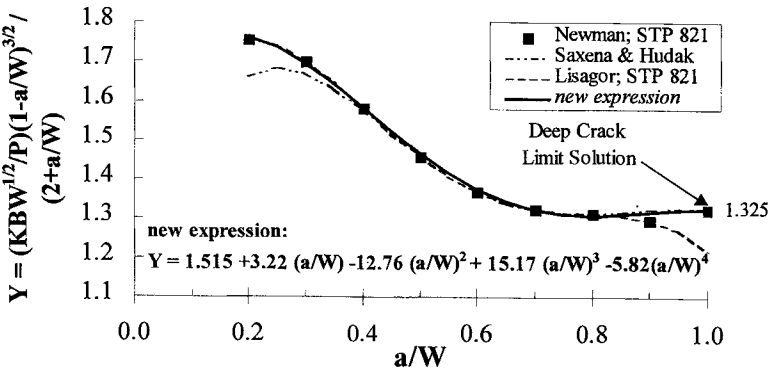

FIG. 4—*New* K/P *versus* a/W *expression for the 0.486* H/W *bolt-loaded specimen.*

Note that the Lisagor expression does not approach the deep crack limit. The expression of Saxena and Hudak [*12*] properly approaches the deep crack limit, but it deviates from the Newman data at small *a/W,* because apparently it was fitted to earlier Newman data that did not represent the bolt and pin configuration as well as the later data used here. The *K/P* expression developed here is:

$$(KBW^{1/2}/P)(1 - a/W)^{3/2}/(2 + a/W) = 1.515 + 3.22(a/W) - 12.76(a/W)^2 + 15.17(a/W)^3 - 5.82(a/W)^4 \quad (3)$$

$$\text{for } X/W = 0.255,\ H/W = 0.486,\ 0.2 \leq a/W \leq 1.0$$

This expression fits the Newman data within 0.6%, except for $a/W = 0.9$, where the fit is within 1.5%. However, the 1.5% difference at $a/W = 0.9$ can be disregarded, considering that the expression fits the deep crack limit within 0.1% and that numerical methods at high *a/W* can be in error.

An *a/W* versus *v/P* expression is useful with instrumented bolt specimens to calculate crack length and crack growth rates from load values as the test proceeds. Using the deep crack bending limit angular displacement solution [*12*],

$$\theta = 15.80\, M/EB\, (W - a)^2 \quad (4)$$

and the relationships $M = PW$ and $\theta = v/(W + X)$, which hold at the deep crack limit, gives

$$(vEB/P)\,(1 - a/W)^2 = 15.80\,(1 + X/W) \quad (5)$$

Equation 5 shows that an expression in the form $a/W = function\ [1/(vEB/P)^{1/2}]$ would be expected to provide a good fit of the data. The expression developed using this form is shown in Fig. 5 and is given as:

$$a/W = 1 - 3.91\,Z - 4.77\,Z^2 + 32.03\,Z^3 \quad (6)$$

where

$$Z = 1/(vEB/P)^{1/2},\ H/W = 0.486, X/W = 0.255, 0.3 \leq a/W \leq 1.0$$

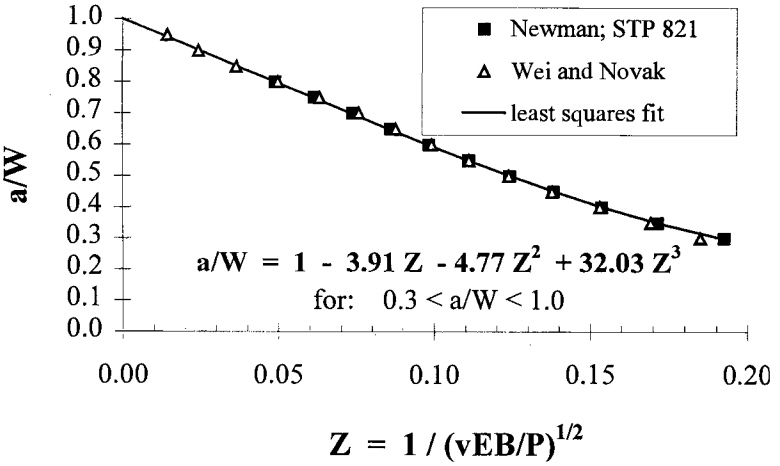

FIG. 5—*New* a/W *versus v/*P *expression for the 0.486* H/W *bolt-loaded specimen.*

Using Eq 6 with (*vEB/P*) from the Newman numerical data, the calculated *a/W* is within 0.003 of the actual values of *a/W*.

The expressions of Eqs 1, 3, and 6 were used to calculate crack mouth displacement, load, and crack length for the bolt-load compact specimen tests described here. The new expressions, Eqs 3 and 6, are particularly useful for determining crack growth rate, *da/dt,* using an instrumented bolt, as described here.

Results and Discussion

Crack Growth Rates, da/dt, *and Threshold Stress Intensities,* K_{IHIC}

As mentioned earlier, test durations of only a few hours were sufficient to achieve deep cracking and K_{IHIC} limits. $K_{applied}$ versus time for A723 (1380 MPa YS), AF1410, and AerMet 100 tests can be found in Fig. 6. This figure dramatically illustrates the rapid hydrogen crack advance in these materials as well as the need for in-situ crack measurement techniques such as the instrumented bolt.

Stage II *da/dt* values for conventionally processed AF1410 were approximately 1.1×10^{-2} mm/s compared to 2.3×10^{-2} mm/s for the isothermally processed AF1410 (Fig. 7). Threshold stress intensity values for the conventionally processed AF1410 were approximately 16.0 MPa-$m^{1/2}$ compared to approximately 13.7 MPa · $m^{1/2}$ for the isothermally processed AF1410. The increase in susceptibility of the isothermally processed AF1410 could be attributed to pockets of metastable retained austenite ahead of the crack tip, which transforms into a highly susceptible martensitic microstructure; however, this was not confirmed.

The Stage II *da/dt* values for the AerMet 100 specimens were approximately 2.4×10^{-2} mm/s (Fig. 7). This is much higher than the Stage II *da/dt* of 2.0×10^{-5} mm/s measured by Atrens and reported by Graves [*13*] in 3.5% NaCl. The hydrogen crack growth rates are believed to be higher simply because the acid environment used for these tests is a much more aggressive environment. The threshold stress intensity of the AerMet 100 specimens tested was approximately 14.1 MPa · $m^{1/2}$.

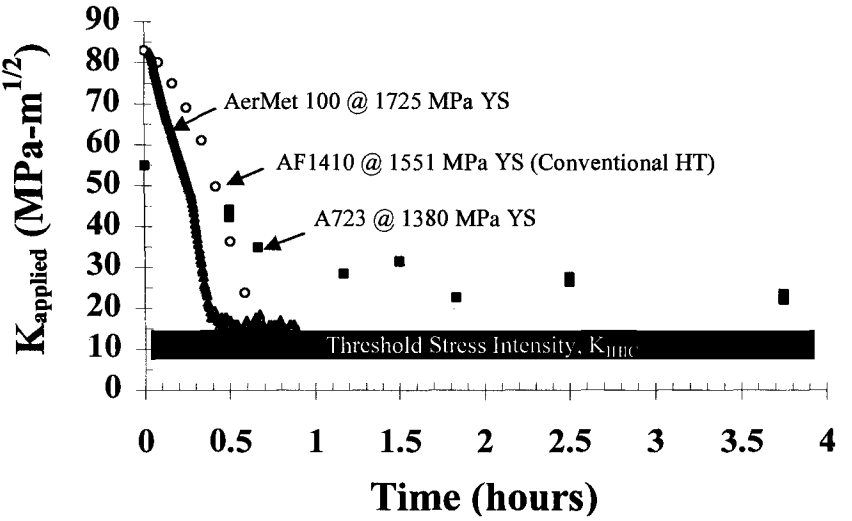

FIG. 6—*Representative $K_{applied}$ versus time data for A723, AF1410, and AerMet 100; bolt-loaded specimen testing in H_2SO_4-H_3PO_4 acid.*

The hydrogen-cracked fracture morphology of the AF1410 specimens, both conventional and isothermal, was predominantly intergranular while the remaining ligament was ductile (microvoid coalescence). The hydrogen-cracked fracture morphology of the AerMet 100 specimens tested was both transgranular and intergranular. The remaining ligament, however, was entirely microvoid coalescence. The fractographs of an AF1410 and AerMet 100 specimen can be found in Fig. 8 and Fig. 9.

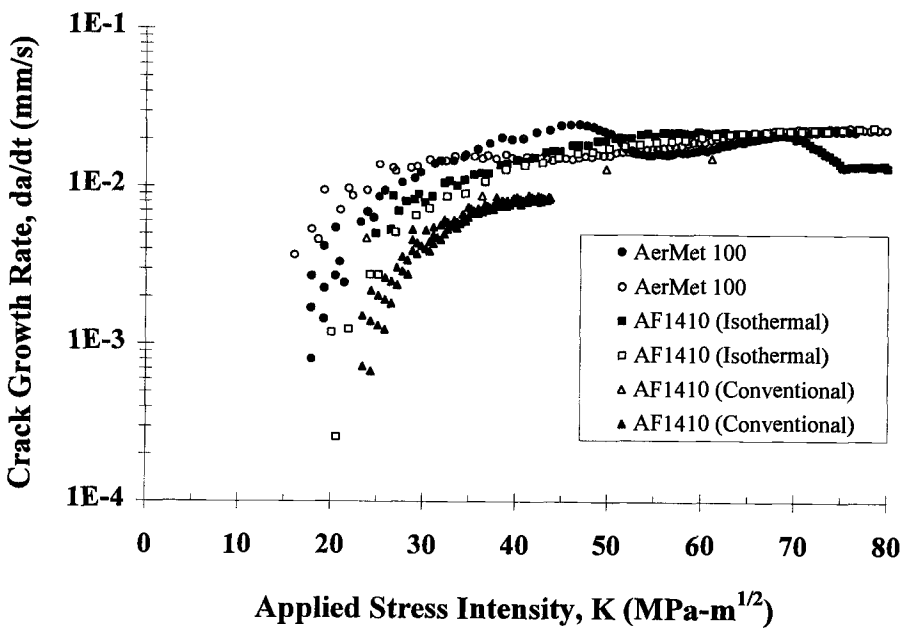

FIG. 7—da/dt *data on AF1410 and AerMet 100 using the instrumented bolt.*

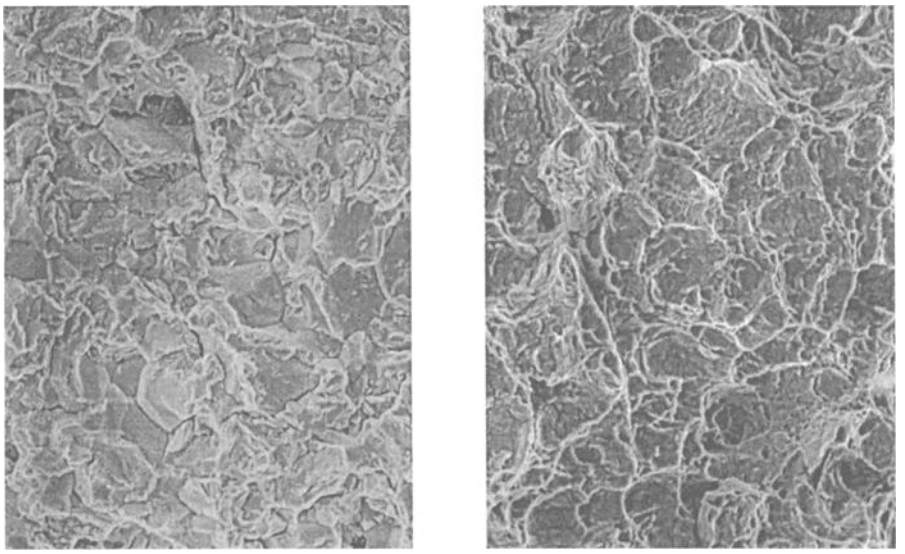

FIG. 8—*The morphology of the hydrogen cracked portion of AF1410, both conventional and isothermal, was predominantly intergranular (left) while the remaining ligament was entirely ductile (right). Magnified at ×500.*

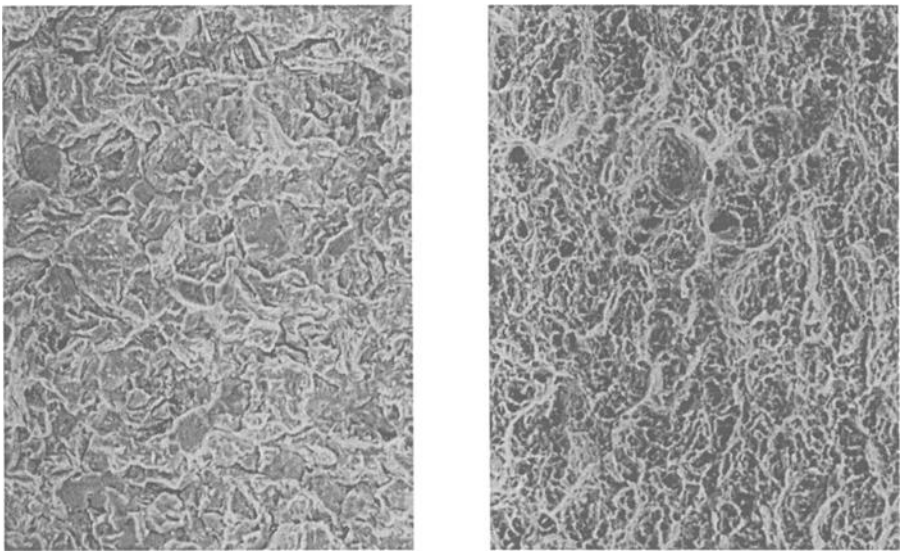

FIG. 9—*The hydrogen cracked region of AerMet 100 was both intergranular and transgranular (left) compared to the remaining ligament which was ductile (right). Magnified at ×500.*

Instrumented Bolt

A/D conversion errors affected post-test analysis in the Stage I portion of cracking. The slow crack advance in these regions coupled with a relatively high sampling rate resulted in fluctuations in the load measurement; for example, see the AF1410 (conventional) data in Fig. 7. This caused initial errors in da/dt analysis. These errors were mitigated through the use of a ten-point (or less) moving average of the data and also by decreasing the sampling rate.

The inherent errors in the instrumented bolt and in the 12-bit A/D converter card had a minimal effect on the crack length measurement. For example, under the test conditions used in this work, at the initial $K_{applied}$ ($a/W = 0.5$), a 155-N error results in only a 0.05-mm error in crack length. However, at deep cracks, e.g., a/W of 0.9, a 155-N error results in an 0.3-mm error in crack length. These errors can be further reduced from ± 155 to ± 8 N by using a 16-bit card rather than a 12-bit card in the data acquisition electronics.

The discrepancy between the load from the instrumented bolt and the predicted load from the bolt-loaded specimen expressions is believed to be a fundamental problem with the use of an instrumented bolt with the bolt-loaded specimen. This is a logical conclusion since: (1) the load from the instrumented bolt was known to be accurate when compared to a mechanical tester in near perfect alignment, (2) the pin and bolt holes in the bolt-loaded specimen were precisely machined, and (3) a point contact was made between the instrumented bolt and the pin in the bolt-loaded specimen. The source of error is believed to be caused by two aspects of the instrumented bolt and bolt-loaded specimen configurations. First, the bolt-loaded specimen is asymmetric and the loading arms bend during application of the load. This results in misalignment between the axis of the instrumented bolt and the axis of the load applied to the end of the bolt. Second, because of the close proximity of the strain gage to the end of the bolt, the strain gage output is affected by the misalignment between the bolt and load axes. The result is an underestimation of the load in the bolt-loaded specimen by approximately 20%.

Summary and Conclusions

1. Rapid Stage II hydrogen crack growth rates in high-strength steels necessitated the development of a low-cost, reliable in-situ crack measurement technique, the instrumented bolt.
2. A ½-20 UNF bolt instrumented with a full bridge strain gage was coupled to an automatic data acquisition system to measure and record in-situ hydrogen crack growth.
3. In order to fully utilize the capabilities of the instrumented bolt and bolt-loaded specimen, new expressions were developed for K/P versus a/W and a/W versus v/P.
4. The load measured from the instrumented bolt was approximately 20% less than the predicted load from expressions for the bolt-loaded specimen. This was overcome by calibrating the load data accordingly after test termination. This discrepancy in load is a fundamental problem with the configuration of the bolt-loaded specimen due to bending in the loading arms of the bolt-loaded specimen coupled with the proximity of the strain gage to the end of the instrumented bolt.
5. AF1410 and AerMet 100, two ultrahigh-strength steels, were used to demonstrate the capabilities of the instrumented bolt. In addition, a new isothermal heat treatment of AF1410 was tested to characterize the material's hydrogen embrittlement susceptibility.
6. The Stage II crack growth rates of isothermal and conventional AF1410 were 1.1×10^{-2} and 2.3×10^{-2} mm/s, respectively. The threshold stress intensity levels of the two heat treatments of AF1410 were 16.0 and 13.7 MPa $\cdot$ m$^{1/2}$, respectively. The Stage II crack growth rates of the AerMet 100 material were 2.4×10^{-2} mm/s, and the threshold stress intensity was 14.1 MPa $\cdot$ m$^{1/2}$.

Acknowledgments

The authors would like to thank Mr. C. Mossey for specimen preparation and Mr. A. Kapusta for fractography of the bolt-loaded specimens.

References

[1] Underwood, J. H., Olmstead, V. J., Askew, J. C., Kapusta, A. A., and Young, G. A., "Environmentally Controlled Fracture of an Overstrained A723 Steel Thick-Wall Cylinder," *Fracture Mechanics: Twenty-Third Symposium, ASTM STP 1189,* R. Chona, Ed., American Society for Testing and Materials, 1993, pp. 443–460.

[2] Troiano, E., Underwood, J. H., O'Hara, G. P., and Crayon, D., "Fatigue Analysis of a Pressure Vessel Experiencing Pressure Oscillations," *Fatigue and Fracture Mechanics: 28th Volume, ASTM STP 1321,* J. H. Underwood, B. D. Macdonald, and M. R. Mitchell, Eds., American Society for Testing and Materials, 1997.

[3] Underwood, J. H., Parker, A. P., Cote, P. J., and Sopok, S., "Compressive Thermal Yielding Leading to Hydrogen Cracking in a Fired Cannon," ASME Pressure Vessel and Piping Conference Proceedings, San Diego, CA, 26–30 July 1998, ASME, New York.

[4] Vigilante, G. N., Underwood, J. H., Crayon, D., Tauscher, S., Sage, T., and Troiano, E., "Hydrogen Induced Cracking Tests of High Strength Steels and Nickel-Iron Base Alloys Using the Bolt-Loaded Specimen," *Fatigue and Fracture Mechanics: 28th Volume, ASTM STP 1321,* J. H. Underwood, B. D. Macdonald, and M. R. Mitchell, Eds., American Society for Testing and Materials, 1997.

[5] Landes, J. D. and Wei, R. P., "The Kinetics of Subcritical Crack Growth Under Sustained Loading," *International Journal of Fracture,* Vol. 9, No. 3, September 1973, pp. 277–293.

[6] Chung, P., Yoshitake, A., Cragnolino, G., and MacDonald, D. D., "Environmentally Controlled Crack Growth Rate of Type 304 Stainless Steel in High Temperature Sulfate Solutions," *Proceedings, Corrosion '84,* New Orleans, LA, Paper No. 166, 1984.

[7] Chung, P. C., Cragnolino, G., and MacDonald D. D., "Instrumented Loading Devices for Monitoring Environmentally Assisted Crack Growth in High Temperature Aqueous Systems," *Corrosion—NACE,* Vol. 41, No. 3, March 1985.

[8] Unimach AF-1410 High Strength Steel Technical Data Sheet, Universal-Cyclops Specialty Steel Division, Pittsburgh, PA, 1978.

[9] Vigilante, G. N., Cote, P. J., Hickey, T., and Pan, S. K., "Isothermal Bainite in AF1410," ARDEC Technical Report, ARCCB-TR-96012, Benet Laboratories, Watervliet, NY, April 1996.

[10] Lisagor, W. B., "Influence of Precracked Specimen Configuration and Starting Stress Intensity on the Stress Corrosion Cracking of 4340 Steel," *Environment-Sensitive Fracture: Evaluation and Comparison of Test Methods, ASTM STP 821,* American Society for Testing and Materials, 1984, pp. 80–97.

[11] Tada, H., Paris, P. C., and Irwin, G. R., *The Stress Analysis of Cracks Handbook,* Paris Productions, Inc., St. Louis, MO, 1985, p. 91.

[12] Saxena, A. and Hudak, S. J., Jr., "Review and Extension of Compliance Information for Common Crack Growth Specimens," *International Journal of Fracture,* Vol. 14, No. 5, 1978, pp. 543–468.

[13] Graves, J. H., "Effect of Heat Treatment on the Microstructure and Properties of AerMet 100 Steel," Army Research Laboratory Technical Report ARL-TR-507, Watertown, MA, August 1994.

John R. Brockenbrough[1] *and Gary H. Bray*[1]

Prediction of S-N Fatigue Curves Using Various Long-Crack-Derived ΔK_{eff} Fatigue Crack Growth Curves and a Small Crack Life Prediction Model

REFERENCE: Brockenbrough, J. R. and Bray, G. H., **"Prediction of S-N Fatigue Curves Using Various Long-Crack-Derived ΔK_{eff} Fatigue Crack Growth Curves and a Small Crack Life Prediction Model,"** *Fatigue and Fracture Mechanics: 30th Volume, ASTM STP 1360,* P. C. Paris and K. L. Jerina, Eds., American Society for Testing and Materials, West Conshohocken, PA, 2000, pp. 388–402.

ABSTRACT: In this study, stress-life (S-N) fatigue curves are predicted for high-strength aluminum alloy 7055 for open-hole specimens at two stress ratios, $R = 0.1$ and 0.5, and smooth specimens at $R = 0.1$ using the small-crack growth model of Brockenbrough et al. [*1,2*] and closure-free FCG curves obtained from long-crack tests by the following methods: (1) high R testing at $R = 0.7$; (2) constant K_{max} testing at K_{max} of 11 and 24.7 MPa$\sqrt{m}$; (3) a ΔK_{eff} curve obtained at the appropriate stress ratio ($R = 0.1$ or 0.5) by the ASTM method; and (4) a ΔK_{eff} curve obtained at the appropriate stress ratio by the adjusted compliance ratio (ACR) method. The predictions were compared to experimental S-N fatigue data. The objective of the study was to determine which method of obtaining closure-free FCG curves from long-crack tests provided the best estimates of fatigue life for the three combinations of specimen type and stress ratio in conjunction with the small-crack growth model employed. The ΔK_{eff} curves obtained by the ACR method yielded the closest and most consistent fatigue predictions for all three conditions. This was attributed to this method being able to account for K_{max} sensitivity of fatigue crack growth rates in aluminum alloys that could not be accounted for by the other methods.

KEYWORDS: fatigue, fatigue crack growth, effective stress intensity, crack closure, life prediction, modeling, aluminum alloys

Life predictions for small cracks emanating from small flaws are becoming increasingly important for multiple reasons, including: (1) concerns over widespread fatigue damage (WFD) in aging aircraft; (2) a desire in new aircraft designs to replace traditional built-up structure with integral structure, and (3) a shift in philosophy for fatigue initiation design from the stress-life (S-N) approach to the equivalent initial flaw size (EIFS) approach [*1,2,18*]. The existence of WFD in an aging aircraft structure can impact its airworthiness, which in some cases may have been certified considering only large cracks in an otherwise undamaged structure. Similarly, integral structure removes some of the redundancies associated with built-up structure requiring greater attention to small crack growth.

Three components are needed to obtain a reliable life prediction for small cracks emanating from small flaws: (1) an accurate representation of the distribution of flaw sizes resulting from manufacturing damage, pre-existing fatigue cracks, corrosion damage such as pits, material microstructural features, or other sources; (2) a fatigue crack growth (FCG) curve that accurately reflects small-crack

[1] Engineering associate and technical specialist, respectively, Alcoa Technical Center, Aluminum Company of America, 100 Technical Dr., Alcoa Center, PA 15069.

behavior; and (3) and a crack growth model with the ability to incorporate defect size, shape, and location in the model prediction.

FCG curves for small-crack life prediction have typically been obtained in one of three ways: (1) measuring the fatigue crack growth rates of small cracks (e.g., ASTM Test Method for Measurement of Fatigue Crack Growth Rates (E 647) Appendix X3, Guidelines for Measuring the Growth Rates of Small Cracks); (2) performing long-crack tests at high stress ratio R or at constant K_{max} (variable R) at a sufficiently high K_{max} [*3*] to eliminate crack closure that is absent or minimal in small cracks; or (3) performing long-crack, constant R tests at the relevant stress ratio and measuring crack closure levels (K_{op}) in accordance with ASTM E 647 Appendix X2, Recommended Practice for Determination of Fatigue Crack Opening Load from Compliance, in order to obtain an FCG curve versus effective stress intensity factor range ΔK_{eff} ($K_{max} - K_{op}$) [*4*].

Each of the above methods has disadvantages as currently practiced. The disadvantage of small crack testing is that it requires much more sophisticated test instrumentation and techniques than long-crack testing, making it prohibitively expensive to perform on a routine basis. Small crack tests also sample only a small volume of material and typically exhibit large scatter, so multiple tests must be performed in order to determine the typical or average behavior of the material. Long-crack tests are preferable with respect to these shortcomings, but they also have their disadvantages as currently practiced. A disadvantage of the high R and constant K_{max} approach is that they assume that crack growth rates are independent of K_{max}. It has long been recognized that K_{max} affects fatigue crack growth rates at high ΔK as it approaches the fracture toughness of the material. Multiple studies [*5–8*] indicate that K_{max} effects fatigue crack growth rates even at low ΔK in the near-threshold region, which is usually most relevant to small crack growth. When K_{max} effects are present, the closure-free FCG curve will depend on the high R or K_{max} selected for the test.

The possibility of K_{max} effects suggests that performing the fatigue crack growth tests at the relevant stress ratio and subtracting out crack closure effects to obtain the FCG curve versus ΔK_{eff} might be preferable. However, this approach as currently practiced has its difficulties, particularly in the near-threshold region. Several experimental studies suggest the estimate of ΔK_{eff} determined in accordance with ASTM E 647 Appendix X2 has often been observed to be unrealistically low [*8–11*]. This implies that a portion of the load cycle below K_{op} is contributing to the driving force for crack propagation. Experimental results of Chen et al. [*12*] indicate that this is the case and that the additional crack-driving force below K_{op} must be taken into account to obtain a reliable estimate of ΔK_{eff}. Donald [*10*] recently introduced a new method for estimating ΔK_{eff} designed to account for this additional driving force called the adjusted compliance ratio (ACR) technique. Several follow-on evaluations of the ACR method by Donald and coworkers [*8,13,14*] indicate that the ACR method provides a better estimate of ΔK_{eff} than the ASTM method in the near-threshold region.

An implicit assumption in all long-crack approaches for deriving FCG curves for small crack life prediction is that the crack closure is entirely responsible for the short crack effect. Other factors believed to contribute to the small-crack effect include breakdown of LEFM and continuum mechanics as the physical crack length approaches that of the plastic zone and scale of the microstructure, and different chemical environments at the crack tip of short and long cracks. These potential influences are not accounted for in any of the above-described long-crack approaches.

In this study, stress-life (S-N) fatigue curves are predicted for high-strength aluminum alloy 7055 at two stress ratios ($R = 0.1$ and 0.5) using the small-crack growth model of Brockenbrough et al. [*1,2*] and closure-free FCG curves obtained from long-crack tests by the following methods: (1) high R testing; (2) constant K_{max} testing; (3) ΔK_{eff} curve obtained at the appropriate stress ratio ($R = 0.1$ or 0.5) by the ASTM method; and (4) ΔK_{eff} curve obtained at the appropriate stress ratio by the ACR method. The predictions were compared to experimental S-N fatigue data. The objective of the study was to determine which method of obtaining closure-free FCG curves from long-crack tests provided the best estimates of fatigue life in conjunction with the small-growth model employed.

Background

The adjusted compliance ratio (ACR) method and the small-crack life prediction model are discussed briefly in this section. For more detail, see Refs *8, 10, 13,* and *14* for the ACR method and Refs *1* and *2* for the small crack life prediction model.

Adjusted Compliance Ratio Technique

The experimental setup, instrumentation, and data collection for the ACR method are the same as that for the ASTM method. The primary difference between the two methods is in the analysis of the load versus displacement curve (Fig. 1). In the ASTM method, the point at which the compliance is 2% less than the compliance of the fully open crack is designated K_{op}, and ΔK_{eff} is estimated to be $K_{max} - K_{op}$. In the ACR method, the estimate of ΔK_{eff} is related to the ratio of the actual displacement (δ_{cl}) to the displacement range that would have occurred in the absence of closure (δ_{nc}). This ratio is equivalent to the secant compliance between the minimum and maximum load-COD points (C_s) and the compliance of the specimen above the opening load (C_o). To minimize sensitivity to crack length and measurement location, the compliance prior to the initiation of the crack (C_i) is subtracted from the secant compliance (C_s) and the compliance above the opening load (C_o) as follows:

$$\text{ACR} = \frac{C_s - C_i}{C_o - C_i} \tag{1}$$

This yields the adjusted compliance ratio (ACR). The effective stress intensity factor is then obtained

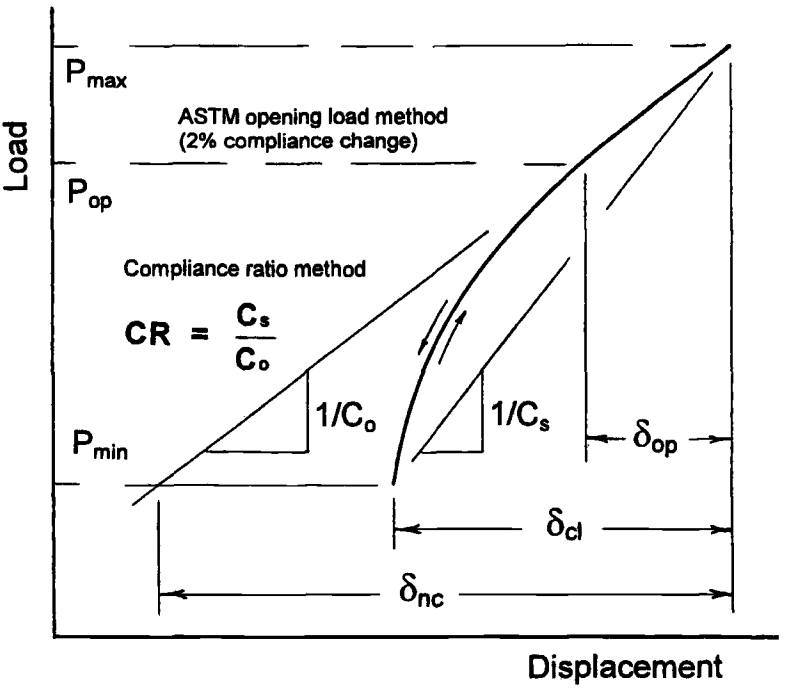

FIG. 1—*Schematic comparing analysis of Load-COD curve by ASTM and ACR methods.*

by multiplying the applied stress intensity by ACR as follows:

$$\Delta K_{\text{eff}} = \text{ACR} \cdot \Delta K_{\text{app}} \tag{2}$$

Both the ASTM and ACR methods should be considered as means to estimate the "true" ΔK_{eff} or "driving force" for crack propagation. The fundamental cause or "driving force" for crack propagation is widely believed to be the accumulation of microstructural damage resulting from the cyclic plastic strain ahead of the crack tip. The ASTM method is reasonable from a continuum mechanics viewpoint since the crack tip singularity and concomitant stress intensification responsible for plastic strain disappear once the crack tip has closed. This concept may be accurate at higher ΔK, where plasticity-induced closure is the primary closure mechanism. In this case, the closure mechanism is "stiff" or non-compliant, and the magnitude of additional plastic strain below K_{op} is expected to be small. However, this may breakdown in the near threshold region, where the crack tip displacements are small and the contact area of the crack faces may be small due to the presence of surface asperities. In this case, the closure mechanism is "soft" or compliant, and additional plastic strain below K_{op} may be a significant portion of the total strain. The ACR method is designed to account for this additional plastic strain. Thus, it is quite likely that the ASTM method provides the best estimate of ΔK_{eff} at higher applied ΔK and other situations such as overloads, where plasticity is the dominant closure mechanism and the ACR method provides the best estimate in the near threshold region.

More recently, Donald, Connelly, Paris, and Tada [*15*] have sought to put the ACR method on a firmer theoretical basis. In their investigation, finite element (FEM) analysis and theory of elasticity were compared to the experimental compliance measurements of a large center crack panel with multiple displacement and strain gage measurement locations. A milled slot replaced the traditional crack to allow crack closure or crack wake interference to be simulated by locating precision steel blocks of varying heights, lengths, and positions in the wake of the crack (slot). Using previously known closed-form solutions for stress intensity and remote centerline displacements as a function of stress and concentrated force on the crack surface, they derived a non-dimensional relationship between a remote load-displacement curve and the crack tip stress intensity factor that they designated the influence ratio (IFR). Their experimental and FEM calculations were in excellent agreement with the solutions obtained from the IFR relationship. The ACR method was shown mathematically to be equivalent to the IFR relationship for a uniformly distributed force on the crack surfaces. While this may be only a rough approximation of the actual stress distribution in the crack wake, the experimental work of Bray and Donald [*8*] demonstrates that the ACR method provides a much better estimate of ΔK_{eff} for constant amplitude loading in the near-threshold region than does the ASTM method. Other advantages of the ACR method are less sensitivity in the measurement of ΔK_{eff} to measurement location and crack length [*13*] and reduced measurement variability [*14*].

Small-Crack Life Prediction Model

The small-crack life prediction model used in this study is discussed briefly in this section. The model of Brockenbrough et al. [*1,2*] is based on the assumption that fatigue life is entirely composed of crack growth from an initial microstructural inhomogeneity. Specifically, fatigue crack growth is considered to start from a near-surface micropore, cracked particle, or debonded particle. The model accounts for the local stress conditions near a microstructural crack-initiating feature to describe an initial crack driving force as well as stress gradients resulting from a stress concentrator such as a hole.

It is assumed that either type of inhomogeneity contains an initial equatorial crack of length b. The particle or void size is $2R$ (Fig. 2). The remote stress σ is applied in the z direction perpendicular to

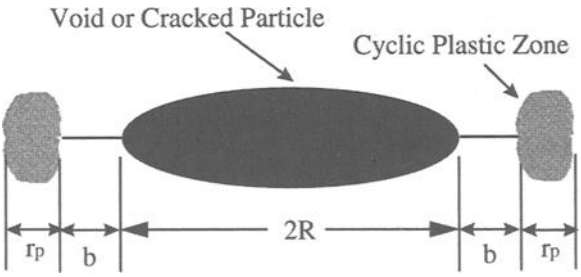

FIG. 2—*Model for the initial crack size starting from an ellipsoidal inhomogeneity.*

the plane of crack growth. The physical crack length b can be thought of as an initiation parameter; it is assumed that for a given far-field cyclic stress, $\Delta\sigma$, a crack of length b, forms in the first few cycles. An assumption is that the physical crack length b equals the size of the cyclic plastic zone associated with the inhomogeneity and surrounding crack.

To make these ideas more precise, consider the Trantina-Barishpolsky effective stress intensity factor [*16*] for the flaw geometry shown in Fig. 2. The stress intensity factor associated with the crack surrounding the inhomogeneity can be expressed as

$$K_{T-B} = \beta\sigma\sqrt{\pi b} \tag{3}$$

where the dimensionless term β is given by

$$\beta = \frac{2}{\pi} + B\left(1.12k_t - \frac{2}{\pi} - 1\right)\left(\frac{R}{b+R}\right)^{10} + \left(\frac{R}{b+R}\right)^{1.8} \tag{4}$$

Here B is a constant that is 1 for a void, 2 for a bonded cracked inclusion, and 0.3 for an unbonded inclusion. The parameter k_t is the local elastic stress concentration factor for the ellipsoidal void or inclusion without the crack. Note that β depends on the geometry through the ratio $R/(b + R)$, so that for $b \gg R$, Eqs 3 and 4 reduce to the stress intensity factor solution for an embedded elliptical crack, where the void or inclusion has no influence on stress intensity factor. At the other extreme, for $b = 0$, the stress intensity factor is zero from Eq 5. Assuming no crack closure, under the imposition of a far-field cyclic stress range $\Delta\sigma$, the cyclic stress intensity factor is

$$\Delta K_{T-B} = \beta\Delta\sigma\sqrt{\pi b} \tag{5}$$

A measure of the cyclic plastic zone size associated with ΔK_{T-B} is

$$r^* = \frac{1}{\pi}\left(\frac{\Delta K_{T-B}}{2\sigma_y}\right)^2 \tag{6}$$

where σ_y is the yield stress of the material. The procedure used to calculate the initiation parameter, b, is to equate it to this measure of plastic zone size. That is,

$$\text{Find } b \text{ such that} \qquad b = \frac{1}{\pi}\left(\frac{\Delta K_{T-B}}{2\sigma_y}\right)^2 \tag{7}$$

This procedure amounts to finding the ratio $R/(b + R)$ which satisfies

$$\frac{\beta\Delta\sigma}{2\sigma_y} = 1 \tag{8}$$

The basis for this is the assumption that crack initiation occurs as a low-cycle fatigue process through the cyclic plastic zone. Subsequent crack growth is then to assumed to follow the fatigue crack growth curve to final failure. A consequence of Eq 8 is that it can be used to estimate a limiting stress for fatigue crack growth, $\Delta\sigma_\infty$. For long life, $\beta = 0$, and solving for $\Delta\sigma$ gives

$$\Delta\sigma_\infty = \frac{2\sigma_y}{\frac{2}{\pi} + B\left(1.12k_t - \frac{2}{\pi} - 1\right) + 1} \tag{9}$$

Although the number of cycles to failure is sensitive to the initial void or particle size, Eq 9 suggests that if fatigue lifetime is controlled by the growth of a crack from a inhomogeneity, the long lifetime stress is independent of void or particle size. It is proportional to yield stress and shows a strong dependence on the local stress concentration factor k_t and the type of inhomogeneity through B.

To apply this model to a crack that initiates at the surface, the following effective stress intensity factor is defined [*17*]

$$K = \frac{K_{T-B}}{K_{penny}} K_{N-R} \tag{10}$$

Here K_{T-B} is the Trantina-Barishpolsky stress intensity factor from Eq 3, K_{penny} is the stress intensity factor for a circular penny-shaped crack in an infinite body, and K_{N-R} is the Newman and Raju [*18*] stress intensity factor solution for a surface of corner crack along the bore of the hole. The crack is assumed to have an initial semi-circular profile at the surface.

Experimental Method and Results

Material Testing and Characterization

Material—The material used in this study was 44.4-mm-thick 7055-T7751 plate. Alloy 7055 is a commercially available aluminum-zinc-magnesium-copper alloy primarily used for aircraft applications requiring very high strength with good fracture toughness and corrosion resistance. The combination of high strength and good corrosion resistance are achieved in this alloy by artificial aging using the Alcoa-proprietary-T77 temper. The predominant strengthening precipitates in the alloy are precursors to the M-phase ($Mg(Zn,Al,Cu)_2$). The grain structure of the alloy is predominantly unrecrystallized. The particular lot used in this study had a longitudinal tensile yield strength (2% offset) of 610 MPa, ultimate tensile strength of 635 MPa, and elongation (4D) of 9.4%.

Fatigue Crack Growth Curves—Closure-free fatigue crack growth curves for the L-T orientation had been obtained in an earlier study from this same plate by the four methods described previously. The specimens had a thickness of 6.35 mm and were located at the mid-plane ($t/2$) of the parent plate. The details of the testing can be found in Ref *8*. No closure was detected in either the high R test ($R = 0.7$) or the constant $K_{\max}$ tests ($K_{\max} = 11.0$ and 24.7 MPa$\sqrt{\text{m}}$) by either the ASTM or ACR method, so the resulting curves (Fig. 3) are presumed to be free of closure.

Crack closure was detected in the constant R tests at $R = 0.1$ and 0.5 and was measured and re-

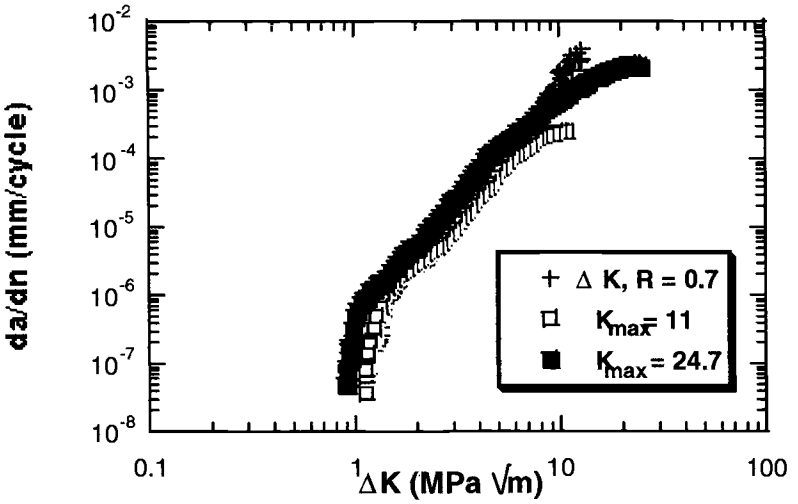

FIG. 3—*Fatigue crack growth curves from constant* K_{max} *and high R tests.*

moved by the ASTM and ACR method to obtain closure-free ΔK_{eff} FCG curves for these stress ratios (Figs. 4 and 5). The estimates of ΔK_{eff} obtained from the ASTM method were much lower than those obtained by the ACR method in the near-threshold region, resulting in the FCG curves of the ASTM method lying much further to the left. The ΔK_{eff} FCG curves from the ASTM method also exhibited a negative K_{max} dependence, while those from the ACR method exhibited a positive K_{max} dependence (i.e., for negative dependence, the ΔK_{eff} curve for $R = 0.5$ lies to the right of the ΔK_{eff} curve for $R = 0.1$ curve and vice versa for positive dependence). The ΔK_{eff} FCG curves from the ASTM method also lie to the left of the high R and constant K_{max} FCG curves (compare Figs. 3 and 4), while

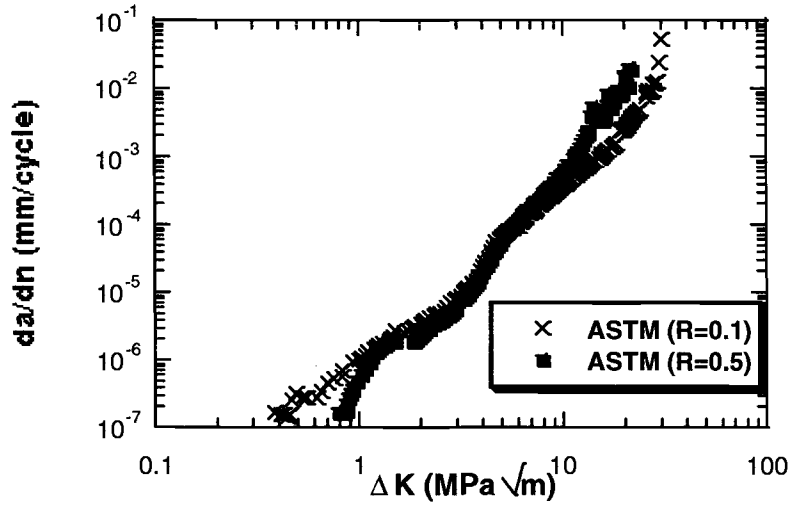

FIG. 4—*Fatigue crack growth curves versus* ΔK_{eff} *at* R *= 0.1 and 0.5 obtained by ASTM method.*

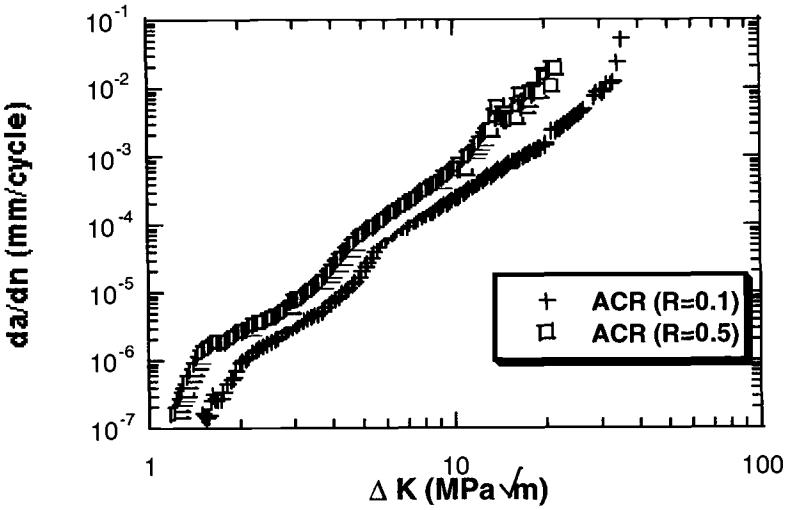

FIG. 5—*Fatigue crack growth curves versus* ΔK_{eff} *at* R = *0.1 and 0.5 obtained by ACR method.*

the ΔK_{eff} FCG curves from the ACR method lie to the left (compare Figs. 5 and 6) consistent with the positive K_{max} dependence observed in the constant K_{max} tests. The ΔK_{eff} curves from $R = 0.1$ and 0.5 in Fig. 5 do not collapse onto a single curve because of this positive K_{max} dependence.

S-N Fatigue Testing—Twenty-six double-open-hole fatigue specimens were machined from the 7055 plate with their length (or axial load) dimension parallel to the rolling direction (L) of the parent plate. The specimens had a thickness of 3.17 mm and a width of 25.4 mm. Two 4.75-mm holes were located 25.4 mm apart at mid-length of the specimen. The hole were drilled, reamed, and deburred. The

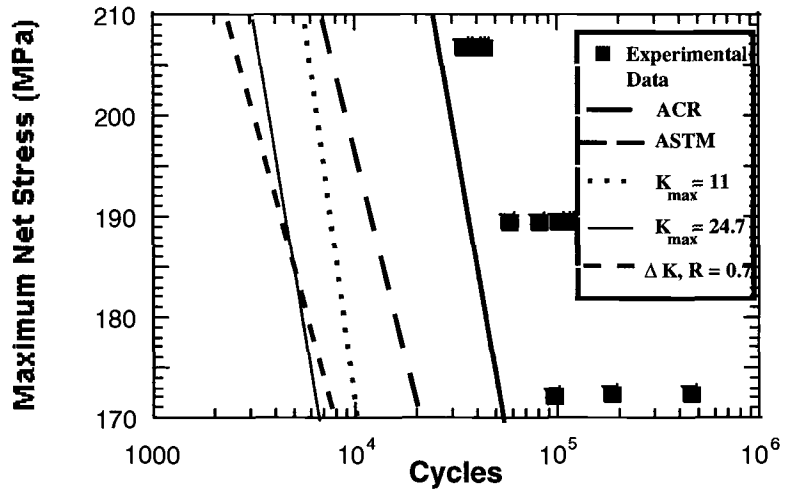

FIG. 6—*Model S-N lifetime prediction using 30-μm particle size in open hole fatigue specimen, compared to experimental data at stress ratio of* R = *0.1.*

stress concentration factor (k_t) of this specimen based on net stress is 2.54. Thirteen specimens each were tested in laboratory air at stress ratios of $R = 0.1$ and 0.5 at multiple stress levels in order to define stress-life (S-N) fatigue curves. A limited number (five) of smooth specimens ($k_t = 1.0$) were machined and tested at $R = 0.1$. These specimens had a diameter of 7.62 mm and a uniform gage length of 34 mm.

SEM Fractography—Fractography was performed on the failed open hole specimens only. The purpose was to identify the controlling microstructural feature that limits the lifetime and to quantify the controlling size feature distribution and location for use as input into the fatigue life prediction model. In the large majority of specimens, the primary fatigue crack initiated at a single origin at one of the two holes. In a few specimens, the primary fatigue crack initiated at two origins. Approximately 30% of the origin areas were at the hole corners, and the remaining 70% were located randomly along the hole bore. In almost all cases, the initiating feature was a constituent particle or cluster of particles ranging in size from 10 to 30 μm. Analysis by EDX indicated that these particles were primarily composed of magnesium and silicon or aluminum, copper, and iron. The depth of the particles from the bore ranged from 0 to 24 μm with most particles intersecting the bore surface and the large majority within 10 μm of the surface. Constituent particles are known to be detrimental to fatigue and fracture toughness of high-strength aluminum alloys. The volume fraction of constituent particles in 7055 is minimized by alloy composition and special thermo-mechanical processing, but they cannot be entirely avoided in 7055 or any other commercial aluminum alloy. Secondary fatigue cracks were typically located on the opposite side of the hole bore. Secondary cracks were distinguished from primary cracks by their shorter crack length at failure.

Model Calculations of Fatigue Data

The stress intensity factors of Newman and Raju [*18*] were used in the model for a crack emanating from a hole in a finite width plate under far-field tension. The crack was assumed to start from either the corner or the center of the bore. The crack started as a semi-ellipse with an aspect ratio equal to that of the particle, which was approximately 2:1. The shape of the crack was updated by evaluating the stress intensity factors at both the surface (s) and the point of deepest penetration (a) and then updating the profile based on the relative growth rates at these locations. The crack first grew through the thickness of the plate; then the through-crack grew outwards from the hole. The number of cycles to grow a through crack was calculated as:

$$N_1 = \int_{s_i}^{sf} \frac{da}{A\Delta K^m} \tag{11}$$

where s_f is defined as a break-through condition where the stress intensity factor at the surface is greater than K_{Ic}. The expression for ΔK is computed from Eq 10. At breakthrough, the crack depth through the thickness is the associated a_f. The through-thickness crack is then grown until it reaches a size, a_c such that the stress-intensity factor is greater than K_{Ic}.

$$N_2 = \int_{a_f}^{a_c} \frac{da}{A\Delta K^m} \tag{12}$$

Here ΔK is the stress intensity for a through crack for a plate containing a hole [*19*]. The total life is the sum:

$$N_{total} = N_1 + N_2 \tag{13}$$

Most of the lifetime was spent in the through-thickness growth of the crack. Model calculations of S-N fatigue curves were made for the three combinations of specimen type and stress ratio using five

different fatigue crack growth curves: high R and constant K_{max} curves (Fig. 3) and ΔK_{eff} curves from the ASTM and ACR method at the appropriate stress ratio, $R = 0.1$ or 0.5 (Figs. 4 and 5). Each of the curves was used in their entirety in the model without any curve fitting.

The results for the open hole specimen at a stress ratio of $R = 0.1$ is shown in Fig. 6. The five calculated S-N curves are labeled ACR, ASTM, $K_{max} = 11$ MPa$\sqrt{m}$, $K_{max} = 24.7$ MPa$\sqrt{m}$, and $R = 0.7$, corresponding to each fatigue crack growth curve used. The results are for a particle size of 30 μm, which was the largest particle observed in the fractography. Since increasing particle size decreases lifetime at any stress level, these results represent a lower bound on lifetime from the model. Also, for determination of the lower bound, the crack was assumed to start at the center of the bore since lifetime for this origin location was shorter than for the hole corner, although the difference between the two locations was not large. For stress levels above the run-out stress (Eq 7), there is about a factor of 4 difference in lifetime between the five different FCG curves used. The ordering from longest to shortest life is: (1) ΔK_{eff} from ACR method ($R = 0.1$); (2) ΔK_{eff} from ASTM method ($R = 0.1$); (3) constant K_{max} at 11 MPa$\sqrt{m}$; (4) constant K_{max} at 24.7 MPa$\sqrt{m}$; and (5) $R = 0.7$ curve. All five FCG curves underpredicted the experimental lifetimes. The ΔK_{eff} curve from the ACR method gave the closest results with a ratio of the predicted to experimental lower bound lifetime of 0.6 to 0.8 depending on stress level. Fatigue life predictions are generally deemed acceptable when they are within a factor of 2 of the experimental fatigue lives. The next best result was obtained using the ΔK_{eff} curve from the ASTM method. This method yielded a ratio of predicted to experimental lower bound lifetime of approximately 0.2.

Model calculations for the open hole specimen were also made for a stress ratio of $R = 0.5$ (Fig. 7). These results are for a 30-μm particle as the fatigue crack initiator located at the center of the bore. Again, each of the fatigue crack growth curves were used in the model to predict the S-N fatigue lifetime, except that now the ΔK_{eff} curves from the ASTM and ACR method were from the constant R test at $R = 0.5$. In this case, the predictions obtained using the ΔK_{eff} curves from the ACR and ASTM methods, the constant K_{max} curve at 11 MPa$\sqrt{m}$, and the $R = 0.7$ curve all yielded similar predictions of the lower bound. The ratio of the predicted to experimental lower bound lifetimes for these FCG curves was about 0.7. The predicted lifetimes from the constant K_{max} curve at 24.7 MPa$\sqrt{m}$ were significantly shorter.

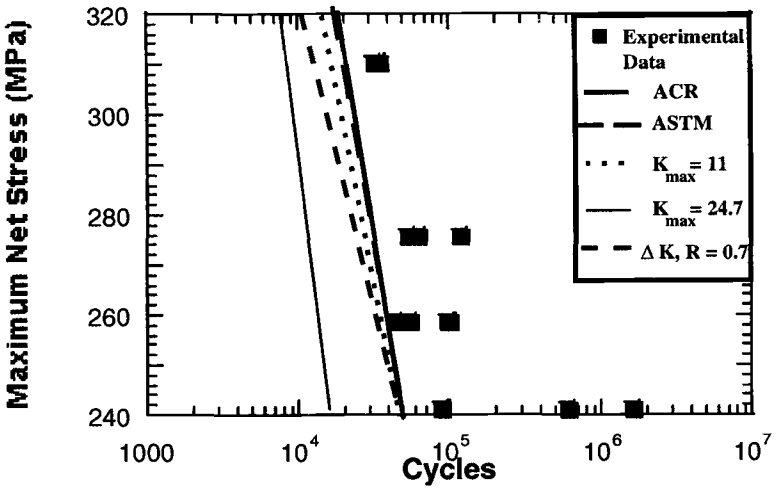

FIG. 7—*Model S-N lifetime prediction using 30-μm particle size in open hole fatigue specimen, compared to experimental data at stress ratio of* R = *0.5.*

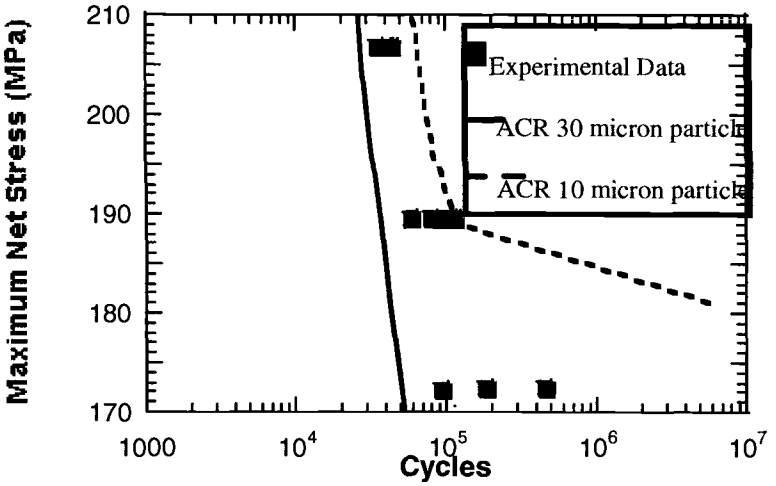

FIG. 8—*Variation in predicted life with particle size at* R = *0.1 for the open hole specimen using ACR fatigue crack growth curve.*

Variability in lifetime at fixed stress level in the model is dependent only on variability in the initiating particle size and starting location of the crack along the bore. Calculations showed that starting location was not a significant source of variability in life at the applied stress levels of interest. The maximum variability in life came from varying the fatigue crack initiating particle size. The range of particle sizes measured in fractography was 10 to 30 μm. The influence of the variance of particle size on predicted S-N lifetime curve was determined for the open hole fatigue specimen at a stress ratio of $R = 0.1$ (Fig. 8) and $R = 0.5$ (Fig. 9). Only the ΔK_{eff} curves from the ACR method at the corresponding stress ratio ($R = 0.1$ or 0.5) was used since these curves provided the best predic-

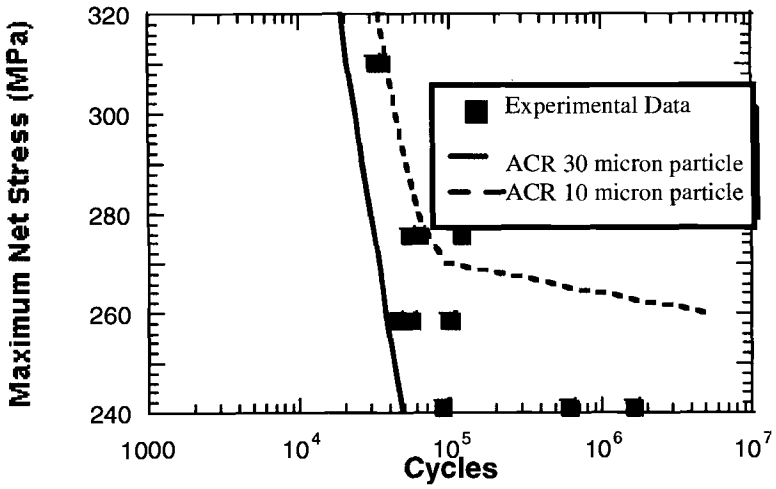

FIG. 9—*Variation in predicted life with particle size at* R = *0.5 for the open hole specimen using ACR fatigue crack growth curve.*

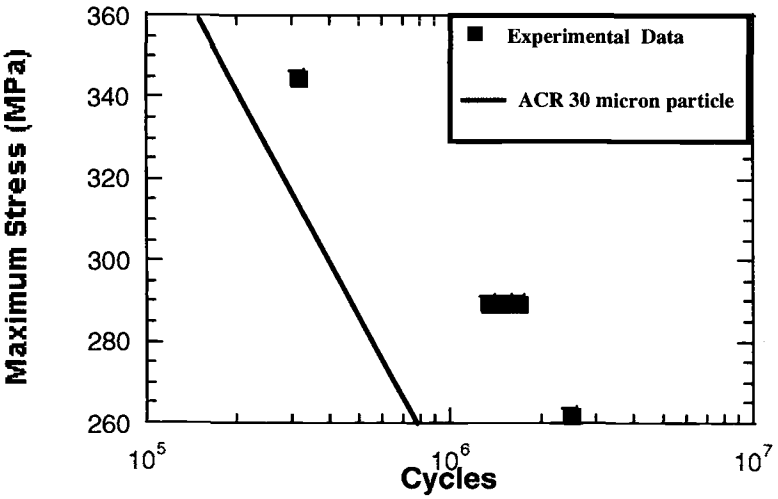

FIG. 10—*Model S-N lifetime prediction using 30-μm particle size in smooth specimen, compared to limited experimental data at stress ratio of* R = *0.1.*

tions. In both cases, the variability in particle size accounted for the observed scatter in experimental fatigue life data.

In order to evaluate the robustness of the fatigue crack growth model, predictions were made for the smooth specimen at $R = 0.1$ using only the ΔK_{eff} curve ($R = 0.1$) from the ACR method (Fig. 10). Only a limited number (five) experimental results were available for comparison. The smooth specimen differs significantly than the open hole specimen with respect to stress concentration factor and local stress gradient. A single particle size of 30 μm was used in the calculation, since there is a much greater volume of material under maximum stress in the smooth axial specimen compared to the open hole specimen. Thus, the likelihood of encountering a large particle in the sample is much greater. No fractography results were available for the smooth axial specimens to confirm the size of the fatigue crack initiator. For the smooth specimen, the ratio of the predicted to the experimental lower bound lifetime was approximately 0.25 to 0.6 depending on stress level. With additional tests, it is likely that the experimental lower bound would have shifted to shorter lifetimes and given better agreement. Predictions made using the other FCG curves would have yielded significantly shorter lifetimes as they did in the open hole specimen based on their relative positions.

Discussion

The results of this study indicate that K_{max} effects are an important consideration in small-crack life prediction in materials and environments where fatigue crack growth rates exhibit a K_{max} sensitivity. A sensitivity to K_{max} may result from crack-tip mean strain effects, contribution of static fracture mechanisms as the fracture toughness is approached, environmental contributions to crack growth, or a creep contribution to crack growth at elevated temperatures or a combination of these factors. The K_{max} sensitivity of the 7055 alloy in the present investigation is most likely a combination of environment (i.e., moist air is known to be an aggressive environment for aluminum alloys [*20*]), mean strain, and fracture toughness effects.

Only the ΔK_{eff} curves from the ACR method (at the appropriate stress ratio) provided consistent predicted lifetimes for the two stress ratios, $R = 0.1$ and 0.5. That is, the ratio of predicted lifetime to experimental lifetime at both stress ratios was approximately 0.6. For the constant K_{max} curves at

K_{max} = 11 MPa$\sqrt{m}$ and 24.7 MPa$\sqrt{m}$ and the high R curves at R = 0.7, the predicted lifetimes were significantly shorter than experimental lifetimes at R = 0.1, while at R = 0.5 reasonable predictions were obtained from all except the constant K_{max} curve at 24.7 MPa$\sqrt{m}$. The inability of these approaches to predict the R = 0.1 data while providing reasonable predictions at R = 0.5 can be attributed to K_{max} effects in fatigue crack growth rates being ignored in these predictions. The fatigue life is significantly underpredicted at R = 0.1, while reasonable predictions are obtained at R = 0.5 because K_{max} at R = 0.1 is further from the K_{max} reflected in the fatigue crack growth curves than K_{max} at R = 0.5. A further weakness in the constant K_{max} and high R predictions for K_{max} sensitive materials is that the predicted lifetimes depend on the K_{max} or stress ratio selected for the fatigue crack growth tests. This is illustrated by comparing the predictions from the constant K_{max} FCG curves at 11 and 24.7 MPa$\sqrt{m}$, the latter giving significantly lower predicted lifetimes. The same problem would have occurred if another fatigue crack growth curve at a second stress ratio, R = 0.9 for example, would have been used to make predictions. The ACR method for obtaining ΔK_{eff} fatigue crack growth curves is superior in this regard since the ΔK_{eff} curve is obtained at the stress ratio of interest. This is also the case for ΔK_{eff} fatigue crack growth curves obtained by the ASTM method. However, the curves obtained by this method (see Fig. 4) exhibited a negative K_{max} dependence that cannot be rationalized on the basis of any mechanism known to the authors and is inconsistent with the constant K_{max} FCG curves. Thus, it is presumed to be an artifact of the ASTM closure measurement method and not an accurate representation of the K_{max} sensitivity.

Several factors may have contributed to the model slightly underpredicting the experimental fatigue lifetimes using ΔK_{eff} curves obtained by the ACR method. First, the assumptions made in the model itself may lead to underprediction. In particular, the model assumes that a semi-elliptical surface initiates immediately from the cracked particle. This assumption could cause lifetimes to be underpredicted. Second, the FCG curves used in the predictions are closure-free. The assumption in using these curves is that crack closure would be absent or minimal. This is almost certainly true initially, but crack closure is expected to build up in the crack wake as the crack extends. The extent to which this closure would effect the predicted lifetimes if included depends on the rate and distance over which crack closure builds up relative to the proportion of the total lifetime at that point. Crack closure effects are not accounted for in the model. Finally, the fatigue crack growth specimens were tested in high-humidity air (RH > 90%), while the open hole and smooth fatigue specimens were tested in lab air, with relative humidity ranging possibly ranging anywhere from 15 to 75%. The fatigue crack growth rates are expected to be faster in the high-humidity environment than at lower humidity due to environmental effects, thereby contributing to the underprediction.

With respect to variability in lifetime, the model was able to capture the range of variability in the experimental data by considering only the range of initiating particle sizes. This is somewhat surprising considering the other factors that could have contributed to variability not accounted for in the model or in the long-crack-derived crack growth data. Changes in humidity during testing may also have played a role in the variability in the experimental data. Also, FCG curves from long-crack tests yield a typical or average behavior of the material over many grains. Small cracks sample only a small volume of material, possibly only a few grains that resists slip to varying degrees depending on orientation and proximity of grain boundaries. As a result, fatigue crack growth rates of short cracks exhibit much more scatter than is typically observed in long cracks. The greater scatter in short cracks is not considered in the model.

Summary

The objective of the study was to determine which method of obtaining closure-free FCG curves from long-crack tests provided the best estimates of fatigue life for the three combinations of specimen type and stress ratio in conjunction with the small-crack growth model of Brockenbrough et al. [*1,2*]. The ΔK_{eff} FCG curves obtained by the ACR method of Donald [*10*] at the same stress ratio as

the fatigue tests yielded the best and most consistent predictions for all three conditions. The more consistent predictions obtained from this type of closure-free FCG curve are attributed to a K_{max} effect on fatigue crack growth rates in aluminum alloys. Since the ΔK_{eff} FCG curve obtained by the ACR method is at the same stress ratio as fatigue tests being predicted, K_{max} for a given ΔK_{eff} is the same in both cases. In comparison, K_{max} corresponding to a given ΔK in the constant K_{max} and high R FCG curves is much higher than in the fatigue tests. This situation is most severe for predictions at low stress ratios, resulting in a larger difference between prediction and experiment at $R = 0.1$ than at $R = 0.5$. The ΔK_{eff} curves from the ASTM method were also at the same stress ratio as the fatigue tests being predicted but did not provide consistent predictions at the two stress ratios. The reason was that the curves obtained by this method exhibited an unexplainable negative K_{max} dependence considered an artifact of the method. The results of this study indicate that K_{max} effects need to be considered in fatigue life prediction.

References

[1] Brockenbrough, J. R., Hinkle, A. J., Magnusen, P. E., and Bucci, R. J., "Microstructurally Based Model of Fatigue Initiation and Growth," *Proceedings, FAA/NASA International Symposium on Advanced Structural Integrity Methods for Airframe Durability and Damage Tolerance,* C. E. Harris, Ed., NASA Conference Publication 3274, Part I, September 1994, pp. 71–84.

[2] Magnusen, P. E., Bucci, R. J., Hinkle, A. J., Brockenbrough, J. R., and Konish, H. J., "Analysis and Prediction of Microstructural Effects on Long-Term Fatigue Performance of an Aluminum Aerospace Alloy," *International Journal of Fatigue,* Vol. 19, Supplement No. 1, 1997, pp. 275–283.

[3] Hertzberg, R., Herman, W. A., Clark, T., and Jaccard, R., "Simulation of Short Crack and Other Low Closure Loading Conditions Utilizing Constant K_{max} ΔK-Decreasing Fatigue Crack Growth Procedures," *Small-Crack Test Methods, ASTM STP 1149,* J. M. Larsen and J. E. Allison, Eds., American Society for Testing and Materials, 1992, pp. 197–200.

[4] Donald, J. K., "A Procedure for Standardizing Crack Closure Levels," *Mechanics of Fatigue Crack Closure, ASTM STP 982,* J. C. Newman, Jr. and W. Elber, Eds., American Society for Testing and Materials, 1988, pp. 222–229.

[5] Döker, H. and Peters, M., "Fatigue Threshold Dependence on Material, Environment and Microstructure," *Proceedings, Fatigue 84,* Vol. 1, C. J. Beevers, Ed., Engineering Materials Advisory Services, United Kingdom, 1884, pp. 275–285.

[6] Sadananda, K. and Vasudevan, A. K., "Analysis of Fatigue Crack Closure and Thresholds," *Fracture Mechanics: 25th Volume, ASTM STP 1220,* Erdogan and Hartranft, Eds., American Society for Testing and Materials, 1995.

[7] Sadananda, K. and Vasudevan, A. K., "Short Crack Growth Behavior," *Fatigue and Fracture Mechanics: 27th Volume, ASTM STP 1296,* R. Piascik, N. Dowling, and J. Newman, Eds., American Society for Testing and Materials, 1997.

[8] Bray, G. H. and Donald, J. K. "Separating the Influence of K_{max} from Closure-Related Stress Ratio Effects Using the Adjusted Compliance Ratio Technique," *Advances in Fatigue Crack Closure Measurement and Analysis: Second Volume, ASTM STP 1343,* R. C. McClung and J. C. Newman, Jr., Eds., American Society for Testing and Materials, 1997.

[9] Hertzberg, R. W., Newton, C. H., and Jaccard, R., "Crack Closure: Correlation and Confusion," *Mechanics of Fatigue Crack Closure, ASTM STP 982,* American Society for Testing and Materials, 1988, pp. 139–148.

[10] Donald, J. K., "Introducing the Compliance Ratio Concept for Determining Effective Stress Intensity," *International Journal of Fatigue,* Vol. 19, Supplement No. 1, 1997, pp. 191–195.

[11] Allison, J. E. and You, C. P., "Problems Associated with the Quantification of Fatigue Crack Closure," *Proceedings, Fatigue '90,* H. Kitigawa and T. Tanaka, Eds., Materials and Components Engineering Publications, Ltd., United Kingdom, 1990, pp. 1249–1255.

[12] Chen, D. L., Weiss, B., and Stickler, R., "Contribution of the Cyclic Loading Portion Below the Opening Load to Fatigue Crack Growth," *Materials Science and Engineering,* Vol. A208, 1996, pp. 181–187.

[13] Donald, J. K., Bray, G. H., and Bush, R. W., "An Evaluation of the Adjusted Compliance Ratio Technique for Determining the Effective Stress Intensity Factor," *Proceedings, 29th National Symposium on Fatigue and Fracture Mechanics, ASTM STP 1332,* T. L. Panontin and S. D. Sheppard, Eds., American Society for Testing and Materials, 1997.

[14] Donald, J. K. and Phillips, E. P., "Analysis of the Second ASTM Round Robin Program on Opening-Load Measurement Using the Adjusted Compliance Ratio Technique," *Advances in Fatigue Crack Closure Mea-*

surement and Analysis: Second Volume, ASTM STP 1343, R. C. McClung and J. C. Newman, Jr., Eds., American Society for Testing and Materials, 1997.

[*15*] Donald, J. K., Connelly, G. M., Paris, P. C., and Tada, H., "Crack Wake Influence Theory and Crack Closure Measurement," *National Symposium on Fatigue and Fracture Mechanics: 30th Volume, ASTM STP 1360,* P. C. Paris and K. L. Jerina, Eds., American Society for Testing and Materials, 1999, pp. 185–200.

[*16*] Trantina, G. G. and Barishpolsky, M., "Elastic-Plastic Analysis of Small Defect-Voids and Inclusions," *Engineering Fracture Mechanics,* Vol. 20, No. 1, 1984, pp. 1–10.

[*17*] Grandt, A. F. et al., "Modeling the Influence of Initial Material Inhomogeneities on the Fatigue Life of Notched Components," *Fatigue Fract. Engng Mater. Struct.,* Vol. 16, No. 2, 1993, pp. 199–213.

[*18*] Raju, I. S. and Newman, J. C., Jr., "Stress Intensity Factor for a Wide Range of Semi-Elliptical Surface Cracks in Finite-Thickness Plates," *Engineering Fracture Mechanics,* Vol. 11, No. 4, 1979, pp. 817–819.

[*19*] Tada, H., Paris, P. C., and Irwin, G. R., *The Stress Analysis of Cracks Handbook: Second Edition,* Paris Productions Inc., 1985.

[*20*] Gangloff, R. P., Piascik, R. S., Dicus, D. L., and Newman, J. C., Jr., "Fatigue Crack Propagation in Aerospace Aluminum Alloys," Paper ICAS-90-4.5.1, *Proceedings of the 17th Congress of the International Council of the Aeronautical Sciences,* Stockholm, Sweden, 1990, pp. 894–908.

J. C. Newman, Jr.,[1] *W. G. Reuter,*[2] *and C. R. Aveline, Jr.*[3]

Stress and Fracture Analyses of Semi-Elliptical Surface Cracks

REFERENCE: Newman, J. C., Jr., Reuter, W. G., and Aveline, C. R., Jr., **"Stress and Fracture Analyses of Semi-Elliptical Surface Cracks,"** *Fatigue and Fracture Mechanics: 30th Volume, ASTM STP 1360,* P. C. Paris and K. L. Jerina, Eds., American Society for Testing and Materials, West Conshohocken, PA, 2000, pp. 403–423.

ABSTRACT: The present paper concentrates on both elastic and elastic-plastic finite-element stress analyses of the surface crack in a plate subjected to tension and bending loads. Stress-intensity factor (K) equations that cover a wider range of crack-length-to-width ratios, than those previously developed by Newman and Raju, for various crack-depth-to-crack-length ratios and crack-depth-to-plate-thickness ratios have been developed and are presented. These equations are used in the subsequent fracture analyses of surface crack specimens subjected to tension and bending loads. From elastic-plastic finite-element analyses, the variations of a hyper-local constraint parameter (α_h) along the surface-crack front were studied to identify the region of maximum constraint and the critical fracture location. (The hyper-local constraint parameter is based on the average normal stresses acting over the plastic-zone region on a line in the crack plane perpendicular to the crack front.) The application of linear-elastic fracture mechanics to fracture of surface-crack specimens made of a high-strength D6AC steel are presented for both tension and bending loads. Two methods were used to characterize fracture: the K^2-integral around the crack front and K at a critical fracture location (ϕ_c). The critical fracture location was the location of the maximum of the product of K times α_h. These two methods were used to evaluate the fracture toughness for both the crack-initiation loads and at the maximum failure load conditions. For tension and bending loads, the K^2-integral method correlated 90% of the fracture data within ±25% in terms of load, whereas K at the critical fracture location correlated the data within ±20%.

KEYWORDS: surface cracks, fracture, stress-intensity factor, finite-element analysis, constraint, elasticity, plasticity, steel

Nomenclature

A_n	Projected area of yielded element, n, on x-z plane, mm^2
A_r	Total projected area along a ray perpendicular to crack front, mm^2
a	Surface-crack depth, mm
c	Half-length of surface crack, mm
d	Smallest finite-element size along surface-crack front, mm
E	Modulus of elasticity
F_b	Boundary-correction factor for surface crack under bending
F_s	Stress-intensity boundary-correction factor for surface crack
F_t	Boundary-correction factor for surface crack under tension
h	Half-height of specimen
K	Mode I stress-intensity factor, MPa · m$^{1/2}$
K_{Ic}	Plane-strain fracture toughness, MPa · m$^{1/2}$

[1] Senior scientist, NASA Langley Research Center, MS 188E, Hampton, VA 23681.
[2] Scientific fellow, Idaho National Engineering Laboratory, Lockheed Martin Idaho Technologies Company, Idaho Falls, ID 83415-2218.
[3] Graduate student, Mississippi State University, Mississippi State, MS 39762.

K^* Average stress-intensity factor around surface-crack front, MPa · $m^{1/2}$
K_c^* Critical value of average stress-intensity factor at maximum load, MPa · $m^{1/2}$
K_{Ic}^* Critical value of average stress-intensity factor at crack initiation, MPa · $m^{1/2}$
K_ϕ Stress-intensity factor at location ϕ, MPa · $m^{1/2}$
$(K_\phi)_c$ Critical stress-intensity factor at location ϕ_c at maximum load, MPa · $m^{1/2}$
$(K_\phi)_{Ic}$ Critical stress-intensity factor at location ϕ_c at crack initiation load, MPa · $m^{1/2}$
M Applied moment, Nm
S Applied remote stress, MPa
S_t Remote tensile stress, MPa
S_b Remote outer-fiber bending stress, MPa
t Thickness of specimen, mm
W Width of specimen, mm
w Half-width of specimen, mm
x,y,z Cartesian coordinates
α_h Hyper-local normal-stress constraint factor
ν Poisson's ratio
σ_{ij} Stress tensor, MPa
σ_o Flow stress (average of yield and ultimate strength), MPa
σ_u Ultimate strength, MPa
σ_{ys} Yield stress (0.2% offset), MPa
ϕ Parametric angle for semi-elliptical crack, degree
ϕ_c Critical parametric angle for semi-elliptical surface crack, degree
χ_h Hyper-local hydrostatic-stress constraint factor

The surface crack (Fig. 1) is one of the most important crack configurations in both the nuclear and aerospace industries because these types of cracks initiate at material and manufacturing defects and may exist for a large portion of the life of a structural component. This crack configuration will continue to exist in a structure until it grows to a critical size, resulting in unstable crack growth or the crack penetrates the wall thickness and causes either a leak or unstable crack growth. For fatigue crack growth, the elastic stress-intensity factors have proven to be very useful in predicting the crack growth shapes and the rate of growth under constant-amplitude cyclic loading. But under variable-amplitude cyclic loading, the effects of constraint on the crack-closure behavior and the growth of surface cracks have yet to be studied. Also, the prediction of fracture of surface cracks even under brittle (K_{Ic}) conditions and especially under elastic-plastic conditions is still not well established.

A common approach is to use the stress-intensity factors, such as those developed by Raju and Newman [*1,2*], to calculate the applied stress-intensity factor (K) as a function of the location around the perimeter of the surface crack. The K values can be used to calculate fatigue crack growth rates for cyclic loading, if applicable data (da/dN against K) are available or to identify "failure" when $K = K_{Ic}$ (plane-strain fracture toughness). The use of K to predict fatigue-crack growth under cyclic loading conditions has been found to be quite accurate [*3*]. But for monotonic loading to failure, Reuter et al. [*4,5*] observed that the use of the maximum value of $K = K_{Ic}$ as a failure criterion was very conservative, especially for brittle materials tested under bending. For the Ti-15-3 titanium alloy [*4*], the ratio of the maximum value of K at crack initiation to K_{Ic} ranged from 1 to 2; for a high-strength D6AC steel [*5*], the K_{max}/K_{Ic} ratio ranged from 0.9 to 1.8.

For elastic-plastic conditions, Hancock et al. [*6*], Reuter et al. [*7*], Sommer and Aurich [*8*], and Brocks and Künecke [*9*] showed the need to incorporate a constraint term in addition to the crack-driving force, J-integral, or crack-tip opening displacement (CTOD) when using test data generated with compact tension or single-edge-notch bend specimens to predict initiation of crack growth in surface-crack specimens. Either the T-stress [*6*] or the local hydrostatic stress [*7–9*] along the crack front was used to characterize fracture using the particular crack-driving-force parameter. Faleskog

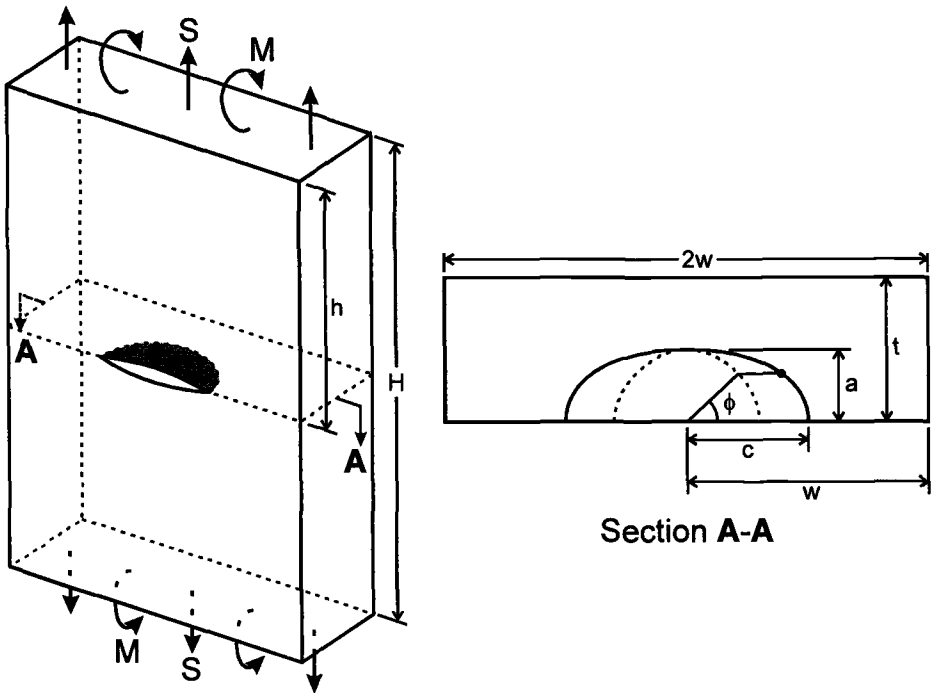

FIG. 1—*Surface crack configuration tested and analyzed.*

[*10*] has used the three-dimensional finite-element method to study the effects of local constraint variations on surface cracks using the *J-Q* theory for cleavage fracture of a pressure vessel steel. For cleavage fracture, the local constraint parameters, such as the *T*-stress, *Q*-stress, or the local hydrostatic stress, are currently used to characterize fracture. However, for surface cracks in materials that exhibit ductile tearing, the cell model [*11*] is currently being used to predict initiation and stable crack growth behavior [*12*]. This approach has been able to predict the critical location of crack-growth initiation. Three-dimensional finite-element analyses are also being used to study a global constraint parameter [*13,14*], based on the average normal stress in the plastic-yield region, to characterize crack-front deformations and fracture for through cracks in ductile materials. This approach has been able to explain why the critical CTOD [or crack-tip-opening angles (CTOA)] values, measured and predicted, for tension and bend specimens agree quite well (same global constraint factor [*14*]).

The present paper concentrates on both elastic and elastic-plastic finite-element stress analyses of the surface crack in a plate subjected to tension and bending loads. Stress-intensity factor (K) equations that cover a wider range of crack-length-to-width (c/w) ratios, than those previously developed by Newman and Raju [*15*], for various crack-depth-to-crack-length ratios and crack-depth-to-plate-thickness ratios have been developed herein. These equations were developed from stress-intensity factor calculations made by Raju and Newman [*1,2*] using elastic finite-element analyses but the results were not used in developing the previous equations. (These improved equations are being proposed for incorporation into a revised version of the ASTM Standard Practice for Fracture Testing with Surface-Crack Tension Specimens, ASTM E 740.) These equations were used in the subsequent fracture analyses of surface-crack specimens subjected to tension and bending loads. From elastic-plastic finite-element analyses, the variations of a hyper-local constraint parameter (α_h) along the surface-crack front was studied to identify the region of maximum constraint and the critical fracture locations.

The hyper-local constraint parameter is based on the average normal stresses acting over the plastic-zone region on a line in the crack plane perpendicular to the crack front. The application of linear-elastic fracture mechanics to fracture of surface-crack specimens made of a high-strength D6AC steel are presented for both tension and bending loads. Two methods to characterize fracture: the K^2-integral around the crack front and K at a critical fracture location (ϕ_c) were used to analyze the D6AC steel test data. The critical fracture location was the location of the maximum of the product of K times α_h. These two methods were used to evaluate the fracture toughness for both crack-initiation loads and at the maximum failure loads. An assessment was made of how well these improved stress-intensity factor equations and the two fracture-analysis methods (K^2-integral and the critical fracture location based on the hyper-local constraint factor) can correlate the fracture data on the D6AC steel specimens.

Experimental Results on D6AC Steel

An International Cooperative Test Program on Surface-Crack Specimens [*5*] was conducted in the mid-1990s to investigate a wide range of surface-crack configurations made of a brittle material, D6AC steel, tested under remote tension and bending. The test program involved six laboratories. The nominal range of crack-configuration parameters tested were: a/t = 0.25, 0.45, 0.65, and 0.85, and a/c = 0.2, 0.4, and 1.0 with W = 50.8 or 101.6 mm and a thickness (t) of 6.35 mm. Some tests were also conducted with a width (W) of 76 mm and thicknesses of 3.15 and 10 mm.

The test specimens in the cooperative program were machined from three different heat-treatment batches. Because D6AC steel is sensitive to the heat-treatment process, tests have been identified with the Heat Treat Batch Number. However, only the results from Batch No. 2 were analyzed herein, except for the tests conducted by the Idaho National Engineering Laboratory (INEL) which came from Batch No. 3. Specimens from Batch No. 2 were tested by Engineering Material Research (EMR), Martin-Marietta (MM), NASA-Ames Research Center (ARC), NASA-Langley Research Center (LARC), and the University of Karlsruhe (UK). For Batch No. 2 and 3 [*5*], the yield stress was 1700 and 1540 MPa, the ultimate tensile strength was 2180 and 2010 MPa, respectively, and the plane-strain fracture toughness [ASTM Standard Test Method for Plane-Strain Fracture Toughness of Metallic Materials (E 399-90)], from single-edge-bend specimens, was 53 MPa $\cdot$ $m^{1/2}$ for both batches.

Triangular-shaped electrical-discharge-machine (EDM) notches of various shape were cut into each specimen and fatigue pre-cracked either under remote tension, remote bending, or both to help produce the desired final surface-crack shapes and sizes. In a few cases, the fatigue pre-crack did not extend completely around the EDM notch or the surface-crack shape did not fit the semi-elliptical shape but was triangular in shape. Herein, all specimens will be analyzed using the measured maximum crack depth, a, and maximum crack length, $2c$, and assuming a semi-elliptical shape. The exceptional cases will be pointed out as needed.

Two types of fracture tests were conducted on the surface-cracked specimens. First, two participants (ARC and INEL) used a d-c potential drop technique to detect the load at which crack-growth initiation occurred [*5*]. These results are given in Tables 7 and 8 in Ref *5*. During some of these tests, the specimen was loaded until the d-c potential drop technique indicated crack initiation (5% potential change) and the test was stopped. The load was then reduced and the specimen was fatigue cycled to mark the outline of the stable crack growth region. After some fatigue crack growth the specimen was then loaded to failure. These results indicated the crack-initiation region in terms of the parametric angle, ϕ. In the second type of fracture tests, four participants (EMR, MM, LARC, and UK) loaded the specimens to failure and recorded the maximum load. These results are given in Tables 5 and 6 in Ref *5*. These two types of test results, fracture at crack initiation and at maximum load, will be analyzed herein.

Stress Analyses

Elastic and elastic-plastic stress analyses of the surface crack configuration were used to obtain stress-intensity factors and hyper-local constraint factors from a wide range of crack shapes and sizes

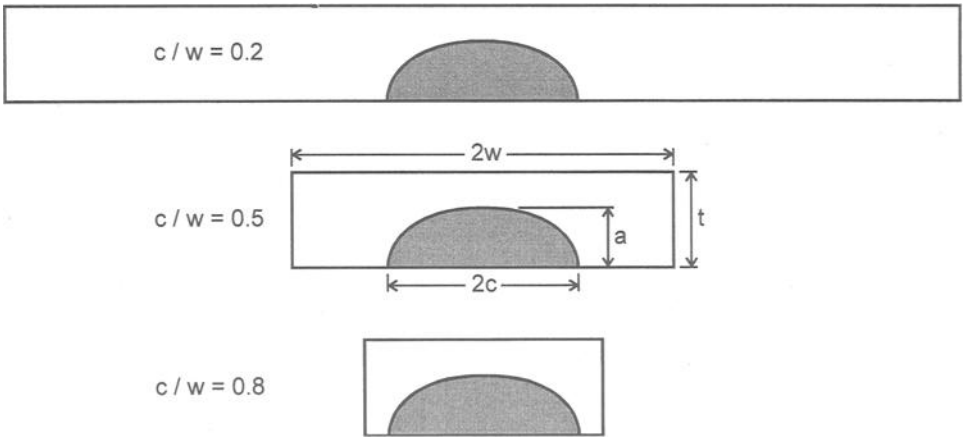

FIG. 2—*Relative surface crack shape and plate sizes analyzed.*

for tension and bending loads. The stress-intensity factors for the surface crack were obtained from the finite-element results of Raju and Newman [*1,2*]. The range of crack-configuration parameters analyzed were: $0.2 \leq a/t \leq 0.8$, $0.2 \leq a/c \leq 1$, and $0.2 \leq c/w \leq 0.8$. Figure 2 shows the relative surface-crack and plate sizes analyzed for a typical surface crack. Elastic-plastic finite-element analyses were made with ANSYS Version 5.4 [*16*]. The surface crack and plate sizes analyzed with ANSYS were selected to match most of the specimens in the International Cooperative Test Program on Surface Crack Specimens [*5*].

Elastic Stress-Intensity Factor Equations

The stress-intensity factor, K, at any point along a surface crack of depth, a, and half-length, c, in a finite plate, such as that shown in Fig. 1, is expressed as

$$K = (S_t + H_s S_b)\,(\pi a/Q)^{1/2}\,F_s = (S_t + S_b)\,(\pi c)^{1/2}\,F \tag{1}$$

where S_t is remote tensile stress, S_b is the remote outer-fiber bending stress, Q is the shape factor for an ellipse, H_s is a correction factor for bending, and F_s is the boundary-correction factor. (Note that the second form of the K-equation is used to correlate fracture data on surface-crack specimens with the length quality, cF^2 [*17*]. This form will be used later on the fracture analysis of the D6AC steel specimens. For bending, $F = F_b$ and for tension $F = F_t$.) The shape factor, Q, is given by the square of the complete elliptic integral of the second kind [*18*]. The boundary-correction factor, F_s, accounts for the influence of various boundaries and is a function of crack depth, crack length, plate thickness, plate width, and the parametric angle of the semi-elliptical crack. The boundary-correction factor is given as

$$F_s = M(a/c, a/t)\; g(a/c, a/t, \phi)\, f_\phi(a/c, \phi)\, f_w(c/w, a/t) \tag{2}$$

where M and g are functions that account for the influence of the front and back face on stress-intensity factors, f_ϕ is an angular function derived from the solution for an elliptical crack in an infinite solid [*19*], and f_w is a finite-width correction factor. Expressions for the functions in Eqs 1 and 2 are given in Ref *2*. In Ref *2*, the f_w function was restricted to c/w ratios less than 0.5. Herein, an improved finite-width correction was developed for c/w ratios, as large as 0.8, for remote tension. It was found

that angular functions, in terms of ϕ, were needed in the f_w function for large cracks. For remote bending, it was found that the original f_w function was adequate for $c/w \leq 0.8$. The improved finite-width corrections are presented and discussed in Appendix 1.

Elastic-Plastic Finite-Element Analyses

ANSYS Version 5.4 [*16*] was used to conduct the elastic-plastic finite-element analyses of various surface crack shapes and sizes to determine the plastic zone region and the hyper-local constraint parameters. The crack configurations analyzed were selected to match most of the test specimens previously discussed.

Finite-Element Meshes—The finite-element meshes were generated with a code, mesh3d_scpcell, from Faleskog (Royal Institute of Technology, Stockholm, Sweden). This program assumes two planes of symmetry exist in terms of both configuration and loading; therefore, only one quarter of each cracked plate was modeled. The size of these models ranged from about 33 500 to 51 500 nodes and 30 000 to 46 400 eight-noded hexahedral elements. The cell-model generator code produced a region of uniform elements (40) normal to the crack front and along the crack plane. The smallest element size (d) of these uniform elements was about 0.002 times the plate thickness (t). A typical model is shown in Fig. 3.

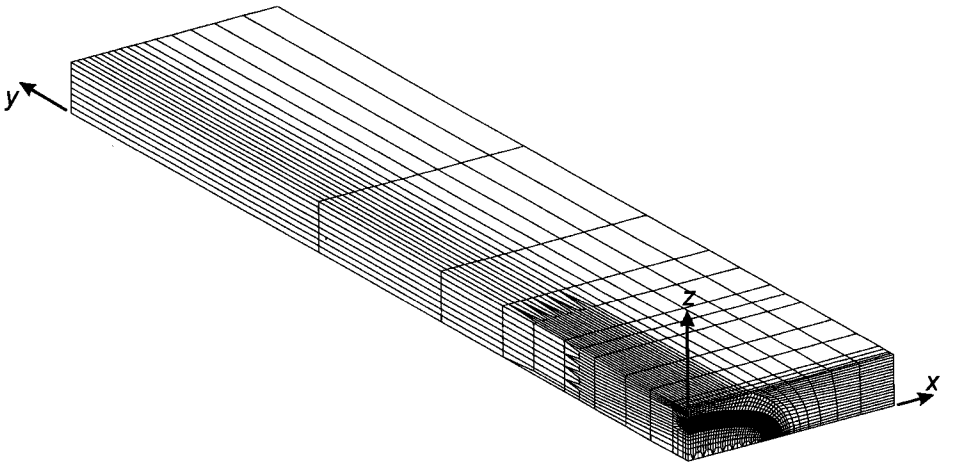

(a) Model of surface-crack specimen

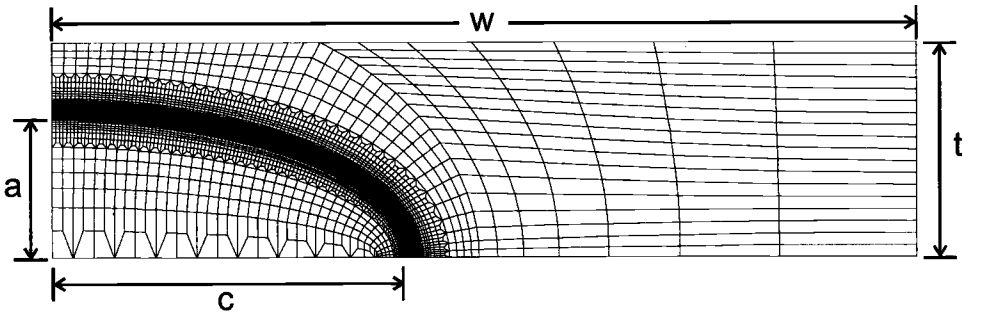

FIG. 3—*Typical finite-element model of surface-crack configuration (nodes = 47 700; elements = 43 000; smallest element size ratio (*d/t*) = 0.002).*

The plate size (see Fig. 1) in all of the surface-crack models analyzed were constant with thickness, $t = 6.35$ mm, and half-width, $w = 25.4$ mm, to be consistent with the specimens. Model half-height, h, was arbitrarily chosen to be sufficiently large enough ($h = 2.5w$) so as not to affect the stress distribution near the crack. The crack configurations had crack-depth-to-plate-thickness ratios (a/t) of 0.45, 0.65, and 0.85 with crack-depth-to-crack-half-length ratios (a/c) of 0.4 or 1.0. (Further study is needed of a/t ratios less than 0.45.) The D6AC steel was modeled as elastic-perfectly plastic with a flow stress, σ_o, of 1930 MPa, modulus of elasticity, E, of 21 GPa, and Poisson's ratio, ν, of 0.3.

Finite-Element Solution—The solution of each analysis was generated with ANSYS using the iterative Jacobi Conjugate Gradient solver on a 400-MHz processor PC with 256-MB RAM. This solver served well in reducing the solution times of these relatively large models to about 12 to 16 h each. The von Mises yield criterion, elastic-perfectly-plastic stress-strain behavior, small-deformation theory, and the associated flow rule were used in the nonlinear analyses.

Displacement of nodes lying on the $x = 0$ (see Fig. 3*a*) symmetry plane were fixed in the x-direction. Nodes lying on the crack plane, $y = 0$, and outside of the quarter-ellipse defined by the crack parameters, $(x/c)^2 + (z/a)^2 = 1$, were fixed in the y-direction. In order to prevent model translation, the node located at $\{x = w, y = 0, z = 0\}$ was fixed in the z-direction.

The models were loaded monotonically in either tension or pure bending by applied pressure on the $y = h$ plane. Tension was applied as a constant pressure, S, and bending was applied as a moment, M, simulated as a linearly varying pressure in the z-direction. The maximum applied stresses applied to the models were chosen from the failure stresses on the specimens.

Constraint Definition—The hyper-local normal-stress constraint factor, α_h, was developed in the present study for use with 3D surface-crack models, such as the Dugdale-type strip-yield model [*20*]. This constraint factor is similar to the global-constraint factor, α_g, developed by Newman et al. [*13,14*] for straight, through-crack configurations. Crack-surface deformations in the neighborhood of a crack front appear to be controlled more by the global (or average) constraint factor than by the local constraint at the crack front [*14*]. Whereas the global constraint factor was averaged over the complete plastic region for through-the-thickness cracks, it is expected that the local average in the "neighborhood" of a surface-crack front would characterize the crack-surface deformations and crack-front strains for a surface crack. The hyper-local constraint factor is the average of the normal opening mode stress, σ_{yy}, acting along a "ray" perpendicular to the crack front of the yielded elements. The constraint factor is defined as

$$\alpha_h(\phi) = \frac{1}{A_r(\phi)} \sum_{n=1}^{N(\phi)} (\sigma_{yy}/\sigma_o)_n A_n \tag{3}$$

where A_n is the projected area of the yielded element n on the crack plane, $(\sigma_{yy}/\sigma_o)_n$ is the normalized centroidal stress perpendicular to the crack plane for element n, and $A_r(\phi)$ is the total projected area for all yielded elements along a given ray, $N(\phi)$. Yielded elements are defined by a non-zero equivalent plastic strain. Each ray of elements were defined by the parametric angle, ϕ, along the crack front. This angle was calculated at the midpoint of the two nodes of each element immediately adjacent to the crack front.

For comparison, a hyper-local hydrostatic constraint factor was also defined herein and was given by

$$\chi_h(\phi) = \frac{1}{A_r(\phi)} \sum_{n=1}^{N(\phi)} \left[\frac{1/3(\sigma_{xx} + \sigma_{yy} + \sigma_{zz})}{\sigma_o} \right]_n A_n \tag{4}$$

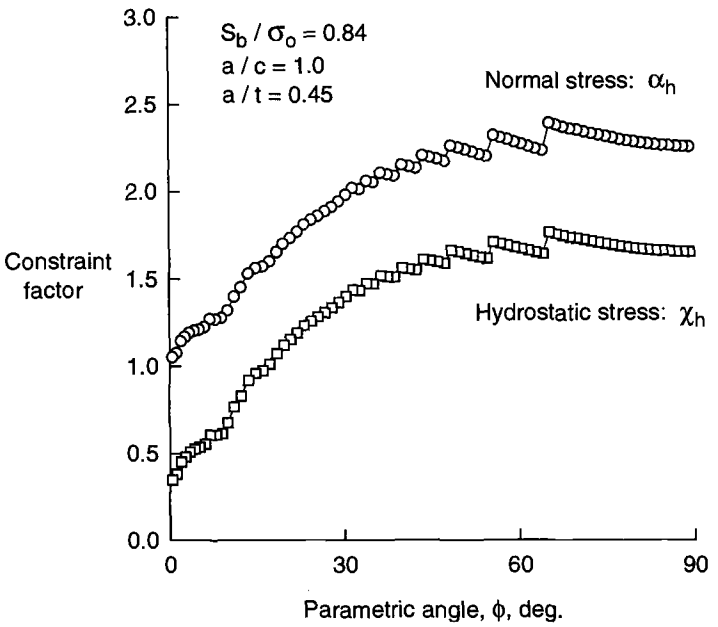

FIG. 4—*Comparison of hyper-local normal-stress and hydrostatic-stress constraint factors.*

Again, the stress components, σ_{ii}, are evaluated at the centroid of each yielded element, *n*. A comparison of the hyper-local normal-stress and hydrostatic-stress constraint factor variation along the crack front is shown in Fig. 4 for a surface crack subject to remote bending. The α_h factor is near unity (plane stress) at the free surface, as expected, but rises to about 2.3 at the maximum depth location (ϕ = 90°). The sharp steps in the results are due to the number of elements that have yielded and the method of treating a yielded element in the constraint calculation. Near the maximum depth location, only two to three elements have yielded. Thus, the accuracy in the constraint calculation is suspect when fewer than four elements have yielded [*13*]. Also, the total projected area of a yielded element is used in the calculation. In retrospect, the projected area should be prorated on the basis of the number of yielded Gauss points for each element. The relative magnitude of these steps decreases as more elements yield for $\phi < 60°$. Near the free surface (ϕ = 0), more than 50 elements have yielded. But here, the current constraint calculations give more weight to the larger yielded elements away from the crack front than those in the uniform mesh region (40 elements). This gives rise to the sporadic changes in the constraint factor near the free surface.

For comparison, the global constraint factor for a through-the-thickness crack under pure plane-strain bending was about 2.7 [*14*], somewhat higher than the results shown in Fig. 4. The hyper-local hydrostatic-stress constraint factor also shows the same trends as the normal-stress constraint factor but at lower magnitudes. Thus, either the normal-stress or hydrostatic-stress constraint factors could be used to characterize the surface-crack constraint behavior.

Constraint Evaluations—Figures 5 and 6 show some typical constraint variaions in α_h along the crack front (ϕ) for different crack configurations subjected to remote bending and tension, respectively. The highest applied stress level in these figures are close to the actual experimental failure stresses on the D6AC steel specimens for these particular surface-crack shapes and sizes. For the highest stress level and at the maximum depth location, four and eight elements have yielded for re-

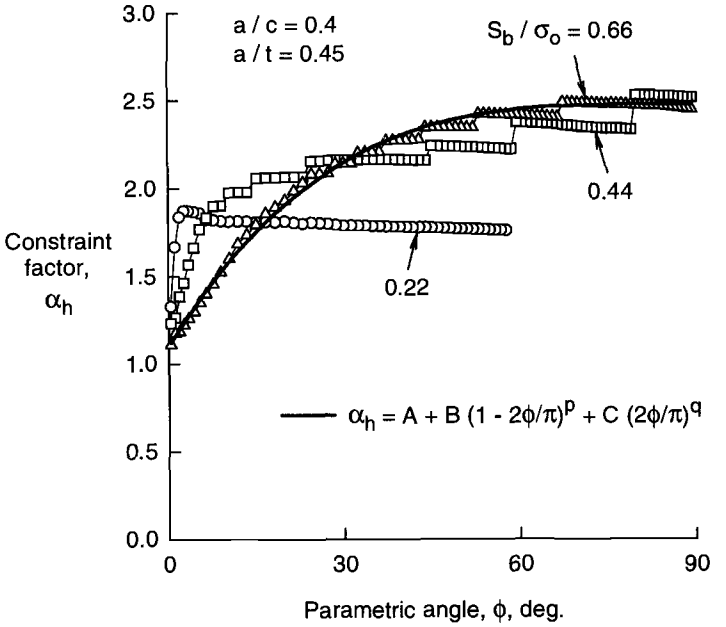

FIG. 5—*Normal stress constraint factor for surface crack under remote bending.*

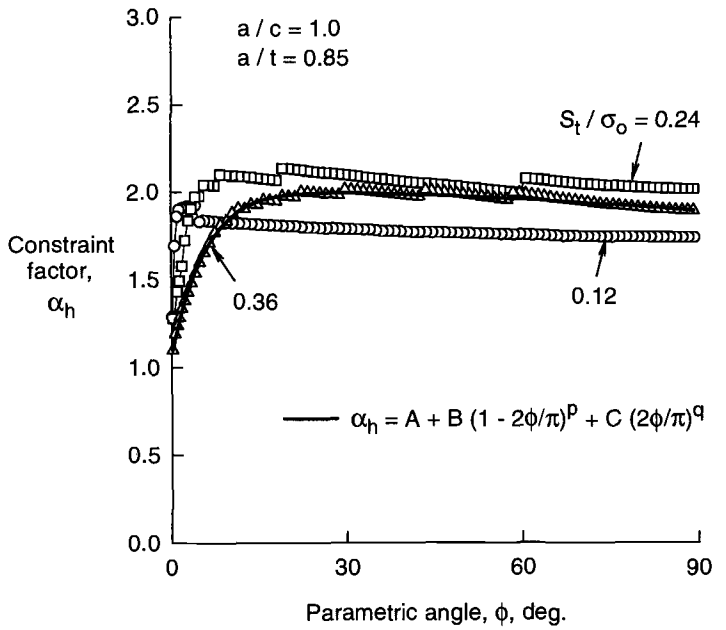

FIG. 6—*Normal stress constraint factor for surface crack under remote tension.*

mote bending and tension, respectively. Near the free surface, 30 to 40 elements have yielded for both load cases at the highest applied stress level. From previous constraint studies, at least four yielded elements are necessary to achieve reasonable constraint factors [*13*]. At the lowest applied stress level, the constraint variations are highly suspect because only one to two elements have yielded. However, these preliminary results at the low stress level indicate that the peak constraint occurs near the free surface, similar to the critical fracture location ($\phi_c = 2°$) presented by Chao and Reuter [*21*] using the *K-T* theory for brittle fracture behavior. Even though the yield region is small for the D6AC steel, it is sufficient to shift the peak constraint to the interior region of the surface crack.

The solid curve in Fig. 5 and 6 is an equation that was chosen to fit these results. For each crack configuration and at the average applied stress at fracture (from the D6AC fracture tests), the hyper-local normal-stress constraint factor along the crack front was fitted to an equation of the form:

$$\alpha_h(\phi) = A + B(1 - 2\phi/\pi)^p + C(2\phi/\pi)^q \tag{5}$$

The second term accounts for the constraint loss near the free surface ($\phi = 0$), and the third term accounts for constraint loss at the maximum depth location for deep cracks (large *a/t*). The five parameters (*A, B, C, p,* and *q*) are dependent upon the crack-configuration parameters (*a/t, a/c*) and loading type (tension or bending). These five parameters are also a function of the applied stress level, but the current equations were evaluated at the maximum failure load. Thus, in principle, they should only be applied at the fracture condition. Note that stable tearing was not considered. The maximum failure load is applied to the initial crack configuration. These equations were used to predict the constraint variation for any surface-crack shape and size at both the crack-initiation load and the maximum failure load. The parameters in Eq 5 are given and discussed in Appendix 2.

Figure 7 compares the constraint variations for tension and bending loads for the same surface-crack shape and size using Eq 5. At the maximum depth location, the surface crack under bending has

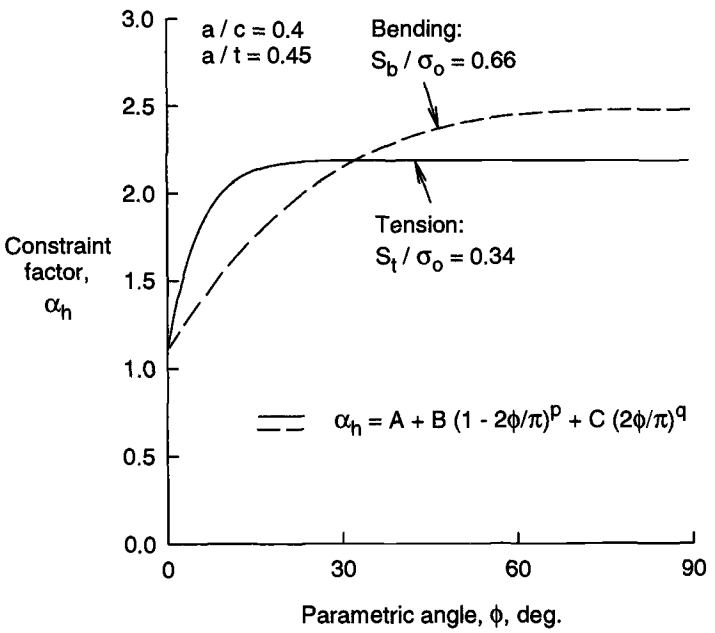

FIG. 7—*Comparison of normal-stress constraint factor for same surface-crack shape and size.*

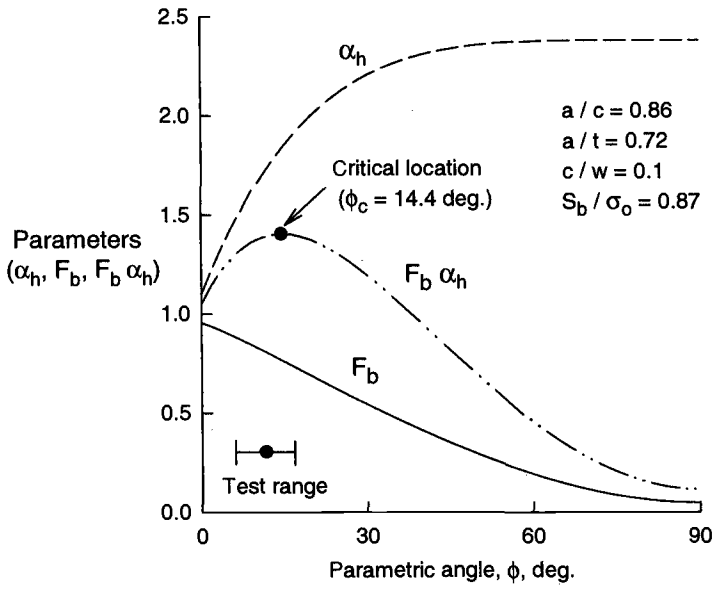

FIG. 8—*Determination of critical fracture location for surface crack under remote bending.*

a higher constraint than the surface crack under remote tension. However, the bending case exhibited a more rapid constraint loss near the free surface than the tension case due to the higher outer-fiber stresses and more yielding in the surface layer. All analyses showed that the constraint factor at the free surface ($\phi = 0$) was about 1.1 for both tension and bending loads.

Critical Fracture Location Evaluations

For the present study, a combination of the hyper-local normal-stress constraint factor, $\alpha_h(\phi)$, and the stress-intensity factor, $K(\phi)$, was used to determine the critical fracture location. The objective was to develop a rationale to predict the critical location ϕ_c. The stress-intensity boundary-correction factor, F_b, and the constraint factor, α_h, variation as a function of ϕ for a surface crack under remote bending is shown in Fig. 8. The maximum F_b (or K) occurs at the free surface, but here the constraint factor is low (nearly plane stress). In contrast, at the maximum depth location where the constraint factor is high (nearly plane strain), the F_b (or K) value is very low. Thus, fracture should initiate in the interior but not at the maximum depth location and, probably, not at the free surface. From the fracture test, the crack-initiation region was measured from 6 to 17° [*5,21*], as denoted by the "test range." Using a simple product of $F_b\alpha_h$ (or $K\alpha_h$), as shown by the dash-dot curve, the peak value occurred at 14.4°. This value fell within the experimental test range. The rationale is that the region where the "stress-intensity factor and constraint" maximizes would be the most likely location for fracture to initiate.

For the case of remote tension, Fig. 9 shows that the highest constraint occurred at $\phi = 25°$ but the constraint factor was nearly constant over a very wide range ($\phi = 20$ to 90°). The highest value of stress intensity occurred at the maximum depth location. The product of $F_t\alpha_h$ (or $K\alpha_h$) gave the critical fracture location (ϕ_c) as 81°. The test indicated 85 to 90° as the critical fracture location [*5*]. But, the peak value of $F_t\alpha_h$ was almost the same over a rather large region (70 to 90°), so any location within this range would be a likely location for fracture initiation.

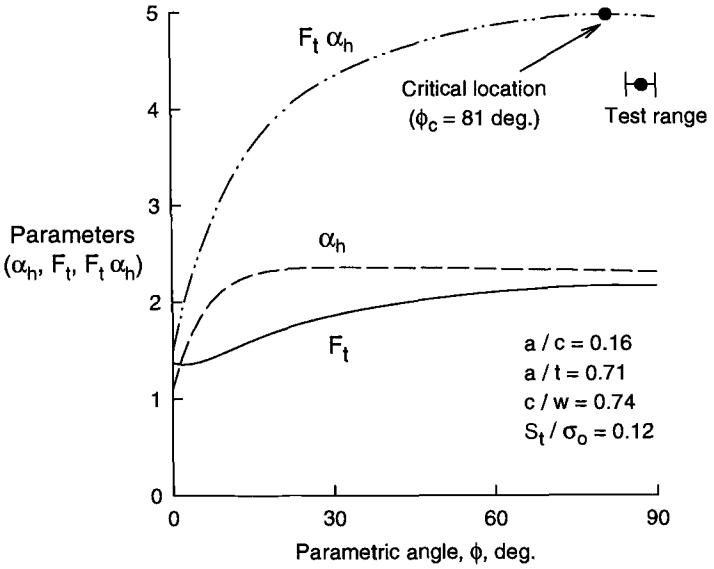

FIG. 9—*Determination of critical fracture location for surface crack under remote tension.*

Fracture Analyses

Two types of fracture tests were conducted on the D6AC steel surface-crack specimens: crack initiation load and maximum failure load. Also, two methods to characterize fracture: the K^2-integral method around the crack front and K at a critical fracture location (ϕ_c) were used to analyze the D6AC steel data.

Average (K^2 Integral) Fracture Toughness Evaluations

The method to calculate the K^2-integral around the surface-crack front is similar to a method developed by Cruse and Besuner [*22*]. They calculated "local average" values at two locations (major and minor axes) for surface cracks. Their calculations weighted the local average more at either the major or minor axes than elsewhere. Herein, the average stress-intensity factor (denoted as K^*) gives equal weight to all locations around the crack front and is given by

$$K^* = \sqrt{\frac{1}{\pi}\int_0^{\pi} K^2 d\phi} \tag{6}$$

Basically, K^* represents the root-mean-square of $K(\phi)$ along the crack front. This fracture parameter is very much like a single value of G ($= K^2/E$) to characterize fracture for surface cracks.

Crack Initiation Load—ARC and INEL conducted fracture tests on surface-crack specimens using the d-c potential technique to measure the crack-initiation loads (defined as a 5% change in potential). The *a/c* ratios ranged from 0.16 to 1, and the *a/t* ratios ranged from 0.1 to 0.9. The K^* values from these tests are shown in Fig. 10 for specimens subjected to tension and bending loads. The average of the bend tests was slightly lower (about 10%) than the average from the tension tests, but 88% of all of the data fell within ±20%. The average value from all tests K^*_{Ic} = 53.2 MPa · $m^{1/2}$ agreed quite well with the plane-strain fracture toughness (K_{Ic}) of 53 MPa · $m^{1/2}$.

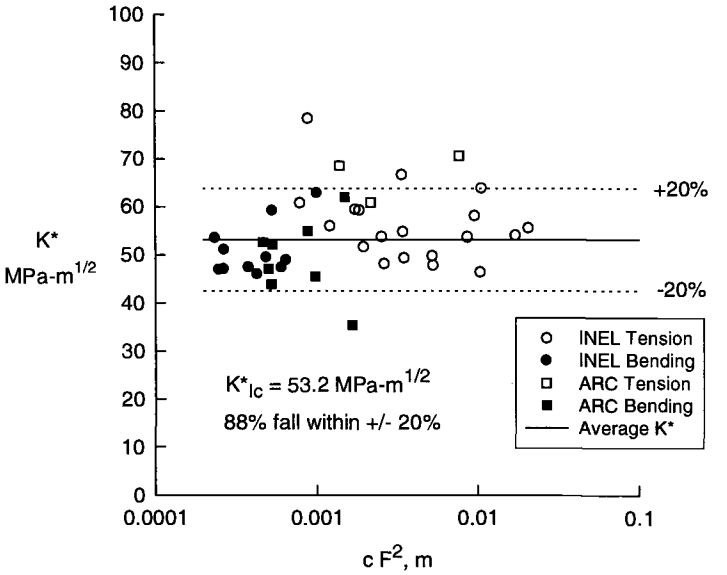

FIG. 10—*Average critical stress-intensity factor for D6AC steel at crack initiation.*

Maximum Failure Load—Four laboratories conducted fracture tests on surface-crack specimens to measure the maximum failure loads. The *a/c* ratios ranged from 0.16 to 1.2; and the *a/t* ratios ranged from 0.24 to 0.9. These results are shown in Fig. 11. The average K^* from the bend tests was extremely close to the average K^* value from the tension tests. Here the average K_c^* was 63.2 MPa · $m^{1/2}$ with 86% of the data falling within ±20%.

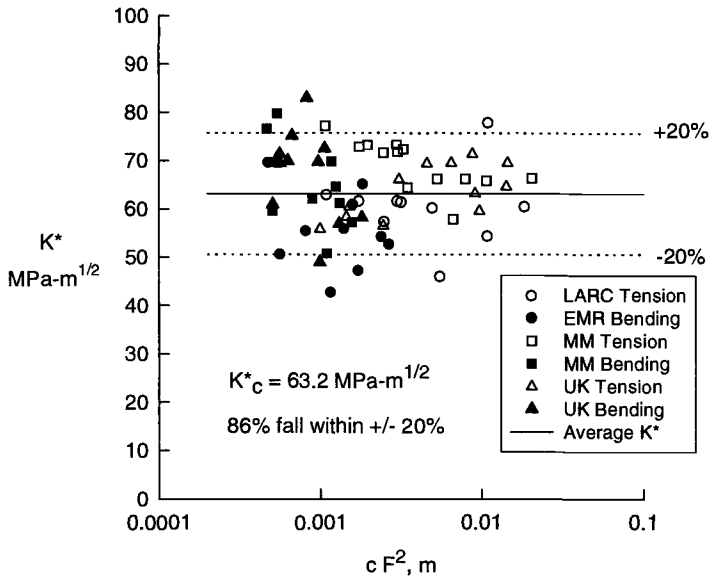

FIG. 11—*Average critical stress-intensity factor for D6AC steel at maximum load.*

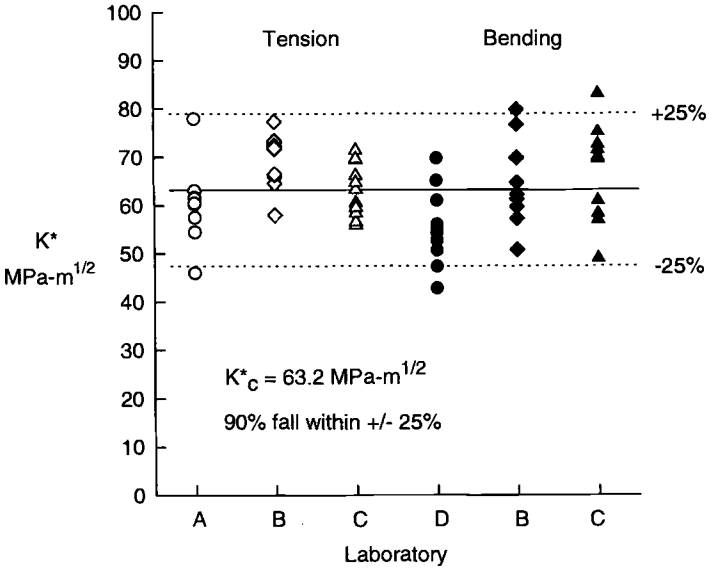

FIG. 12—*Comparison of average critical stress-intensity factor at maximum load from various laboratories under remote tension and remote bending.*

A close examination of the particular K^* values from each laboratory indicated some trends in laboratory variability. These results are shown in Fig. 12 for Laboratories A to D. Laboratories B and C prepared their own specimens and conducted their own tests under both tension and bending loads. Specimens for Lab A and D were prepared at one laboratory and tested at separate labs. All laboratories were trying to develop the same surface-crack shapes and sizes in their specimens. Laboratories A and D fatigue pre-cracked under tension or bending and tested under the same condition, whereas some tests from Laboratories B and C were fatigue pre-cracked under tension or bending and tested under the opposite (bending or tension) condition. All laboratories had some specimens where the fatigue pre-crack did not extend beyond the EDM notch. The scatter from the tension specimens appeared to be less than similar tests under bending. For tension loading, the average K^* from Laboratory B was higher than either Laboratories A or C. Whereas, for the bending tests, the K^* average for Laboratory D was lower than Laboratories B and C. One interesting observation was that the average for tension and bending load tests from a particular laboratory agreed better than from lab to lab. The average K^* for tension from Lab A and bending from Lab D also agreed well. Whether the trends were due to specimen preparation or testing could not be established. But 90% of the K^* values from all labs correlated within ±25%.

K_ϕ *Fracture Toughness Evaluations*

The stress-intensity and constraint factor equations (Eqs 1 and 5) were used to determine the critical fracture location ϕ_c and the critical stress-intensity factor at that location. This approach was applied to the two types of fracture tests conducted on the D6AC steel specimens.

Crack Initiation Load—Analyzing the ARC and INEL fracture tests at the crack-initiation loads using K_ϕ at the critical location (ϕ_c) produced the correlation shown in Fig. 13. Here the average of the bending specimens was extremely close to the average of the tension tests. The average value from all tests was $(K_\phi)_{Ic} = 61.5$ MPa · $m^{1/2}$ with 93% of the data falling within ±20%.

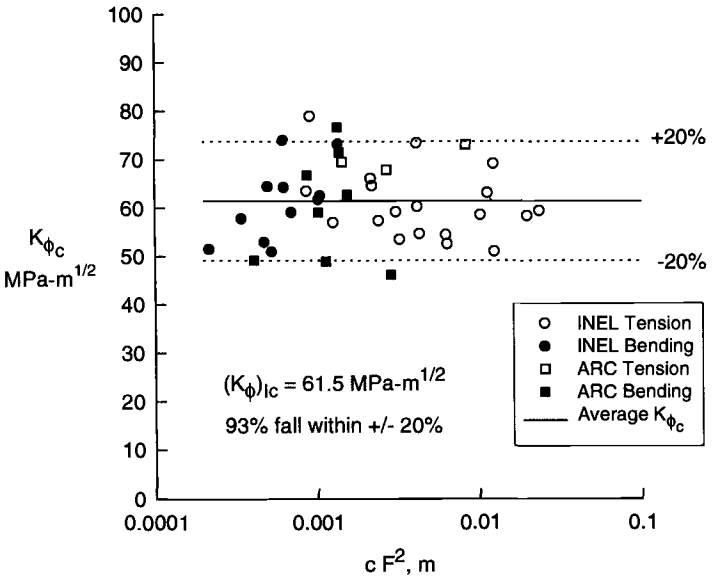

FIG. 13—*Stress-intensity factor at critical location for D6AC steel at crack initiation.*

Maximum Failure Load—Figure 14 shows the K_ϕ results on the fracture tests conducted by EMR, LARC, MM, and UK on surface-crack specimens using the maximum failure loads and the initial crack dimensions. Here 90% of the critical K_ϕ values fell within ±20% of $(K_\phi)_c$ = 70.3 MPa · m$^{1/2}$. But three tests produced extremely large values of toughness near 100 MPa · m$^{1/2}$. On examination of these particular specimens, all three had fatigue pre-cracks that did not extend beyond the EDM notch

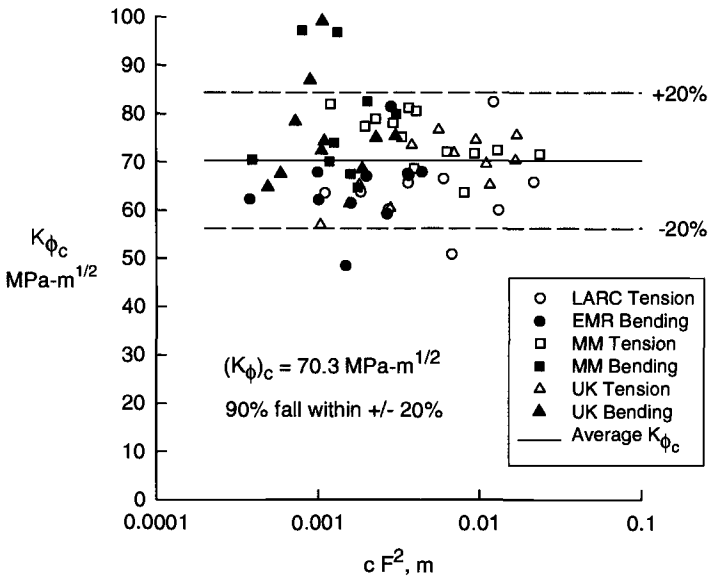

FIG. 14—*Stress-intensity factor at critical location for D6AC steel at maximum load.*

or they had a crack shape that was more like a "triangular" shaped surface crack than a semi-ellipse. Thus these specimens should be removed from the correlation. Removing these specimens from the previous fracture analyses would also improve the correlations.

Conclusions

Stress and fracture analyses of surface-crack specimens made of D6AC steel subjected to remote tension and bending support the following:

1. Stress-intensity factor equations developed for very wide range in surface-crack configuration parameters, especially crack-length-to-width (c/w) ratios, were within ±5% of the values calculated from elastic finite-element analyses.
2. Hyper-local normal-stress constraint factors show higher values for remote bending than tension loads in the interior of a surface crack but showed a more rapid loss of constraint near the free surface for the same surface-crack shape and size at the failure load condition.
3. Fracture toughness for D6AC steel tension and bending loaded specimens correlated within ±25% using the K^2-integral method and within ±20% using K at the critical fracture location (maximum of stress-intensity factor times hyper-local constraint factor).

Acknowledgments

The author (WGR) expresses his appreciation to the U.S. Department of Energy, Office of Energy Research, Office of Basic Energy Sciences under DOE Idaho Field Office Contract DE-AC07-98ID13223 for supporting part of this work. The authors thank Professor Robert Dodds, University of Illinois, for providing the Faleskog mesh-generator code and Professor Steve Daniewicz, Mississippi State University, for providing support for the author (CRA) to spend the Summer at the NASA Langley Research Center.

APPENDIX 1

Stress-Intensity Factor Equations for Surface Cracks

The stress-intensity factor, K, at any point along a surface-crack in a finite plate subjected to remote tension and bending loads is expressed as

$$K = (S_t + H_s S_b)\,(\pi a/Q)^{1/2}\,F_s \tag{7}$$

The effects of plate thickness and width on the stress-intensity factor is accounted for in the boundary-correction factor F_s and is given by

$$F_s = M(a/c,\ a/t)\ g(a/c,\ a/t,\ \phi)\, f_\phi\,(a/c,\ \phi)\, f_w(c/w,\ a/t,\ \phi) \tag{8}$$

In Ref 2, the original f_w function was independent of ϕ and was restricted to c/w ratios less than 0.5. The original f_w function was

$$f_w = \{\sec[(\pi c/(2w))\ (a/t)^{1/2}]\}^{1/2} \tag{9}$$

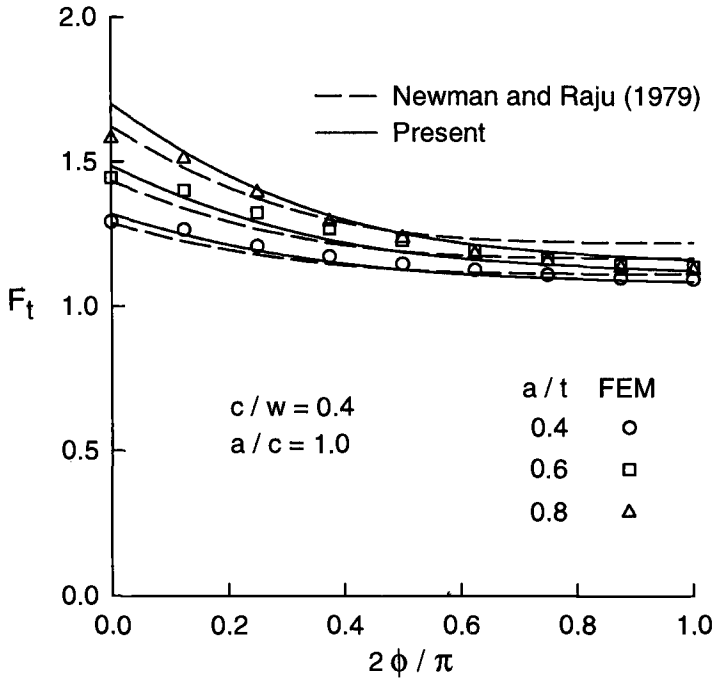

FIG. 15—*Comparison of stress-intensity factor equations with finite-element results for semi-circular surface crack under remote tension.*

For remote tension, an improved finite-width correction was developed for larger c/w ratios than the original equation. It was found that an angular function, in terms of ϕ, was needed in the f_w function for the large cracks. Using the stress-intensity factors calculated from 3D finite-element analyses for large c/w ratio analyses [2], the improved f_w function was

$$f_w = f_b \{\sec[(\pi c/(2w))\,((a/t)\,(1 - 0.6 \sin \phi))^{1/2}]\}^{1/2} \tag{10}$$

where $f_b = 1 + 0.38\,(a/c)\,(a/t)\,(c/w)^2 \cos \phi$. The f_b term accounts for the induced bending effects due to the unsymmetrical surface-crack configuration. A comparison of the original and improved boundary-correction factors for a semi-circular surface crack with $c/w = 0.4$ for various a/t ratios is shown in Fig. 15. The improved equation (solid curve) gives better comparison at both the maximum depth location and near the free surface with the finite-element method (FEM) results (symbols). The FEM results at the free surface are, of course, suspect due to the boundary-layer effect and the loss of the square-root singularity [23]. The original equation results are shown by the dashed curves. Figure 16 shows a comparison of a very deep semi-circular and semi-elliptical surface crack with $c/w = 0.8$. The symbols show the FEM results [2], and the curves show the original (dashed) and improved (solid) equations. Of course, the original equation was not fitted to such a large crack, and the results severely overpredict the stress-intensity factors. Equation 10 fits the FEM results quite well.

For remote bending, it was found that the original f_w function (Eq 9), was adequate for $c/w \leq 0.8$. Figure 17 shows a comparison of the original boundary-correction factors for a semi-circular surface crack with $c/w = 0.4$ for various a/t ratios subjected to remote bending. The original equation (solid curve) fit the FEM results (symbols) quite well. A comparison of the original equations for a very

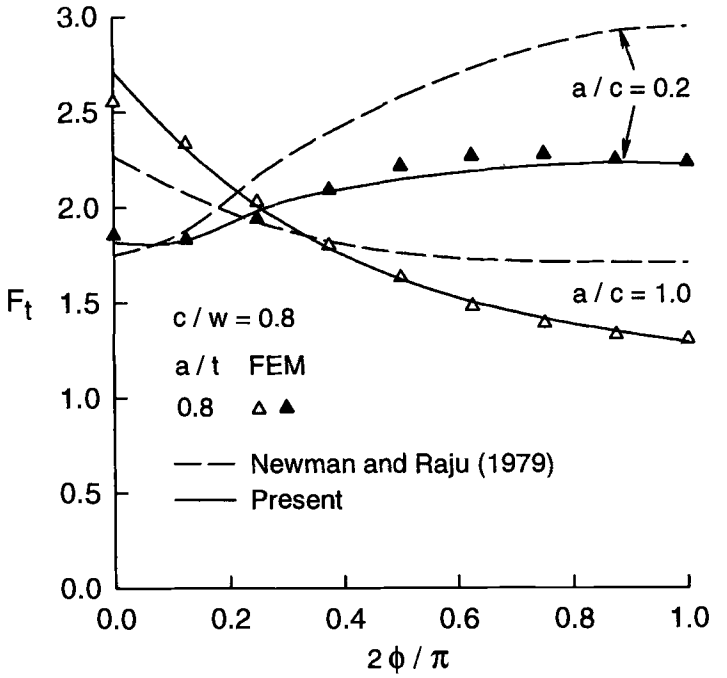

FIG. 16—*Comparison of stress-intensity factor equations with finite-element results for very large crack-length-to-width ratio surface cracks under remote tension.*

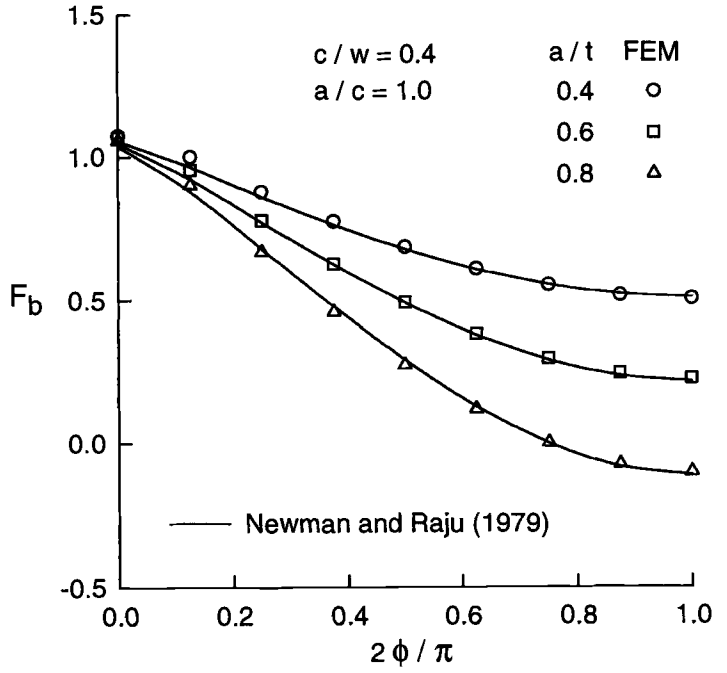

FIG. 17—*Comparison of stress-intensity factor equations with finite-element results for semi-circular surface crack under remote bending.*

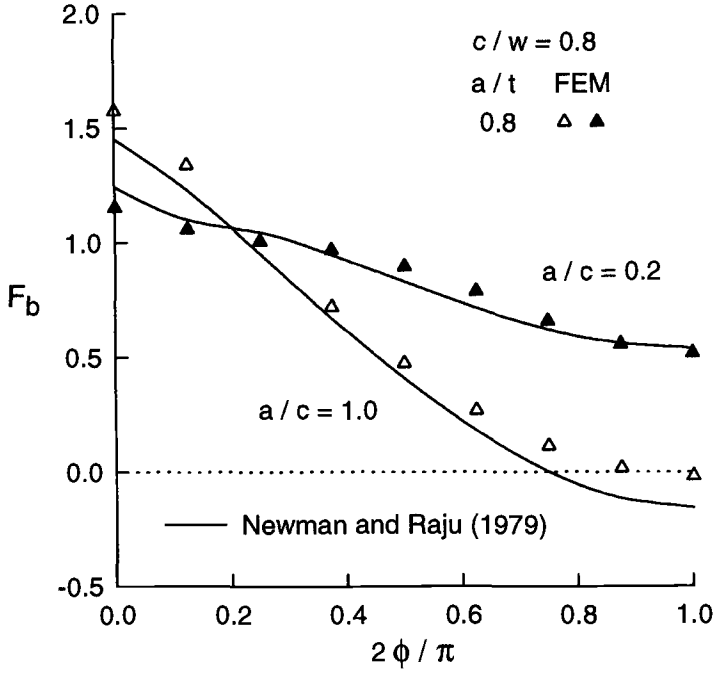

FIG. 18—*Comparison of stress-intensity factor equations with finite-element results for very large crack-length-to-width ratio surface cracks under remote bending.*

deep semi-circular and semi-elliptical surface crack with $c/w = 0.8$ is shown in Fig. 18. The results for the semi-elliptical crack compared very well, but the equations under predict the boundary-correction factors for the semi-circular crack, especially at the maximum depth location. The maximum difference was about 5% based on the peak value.

APPENDIX 2

Hyper-Local Normal-Stress Constraint Factor Equations

The hyper-local normal-stress constraint factors along the surface crack front, calculated from the elastic-plastic finite-element stress analyses, were fitted to an equation of the form:

$$\alpha_h(\phi) = A + B(1 - 2\phi/\pi)^p + C(2\phi/\pi)^q \tag{11}$$

In the finite-element analyses, the plate size (see Fig. 1) in all of the surface-crack models analyzed were constant with thickness $t = 6.35$ mm and half-width $w = 25.4$ mm to be consistent with the specimens. The surface-crack configurations analyzed had crack-depth-to-plate-thickness ratios (a/t) of 0.45, 0.65, and 0.85 with crack-depth-to-crack-half-length ratios (a/c) of 0.4 or 1.0. An estimate of

the applied failure stress for each of these crack shapes and sizes were estimated from the tests conducted on the D6AC steel specimens under tension and bending loads. Thus, Eq 11 will give the constraint variations at the failure load condition with the initial surface-crack configuration. Further study is needed on constraint variations for a/t ratios less than 0.45.

For remote tension: $A = 2.7 - 0.7\,(a/c)^{0.4}$; $B = 1.1 - A$; $p = 15$; $C = -0.15\,(a/t)^3$; and $q = 2$ for $a/c \leq 1$. The coefficient 2.7 is an estimate for the maximum value of constraint for plane-strain bending [*14*]. The second term in Eq 11 models the constraint-loss near the free surface ($\phi = 0$), and the limiting value of constraint at the free surface was selected as 1.1. The third term models the constraint loss at the maximum depth location. For the D6AC steel, constraint loss at the maximum depth location was small, and the contributions of the third term are weak.

For remote bending: $A = 2.7 - 0.35\,(a/c)^{0.6}$; $B = 1.1 - A$; $p = 2 + (6 - 1.5\,a/c)(a/t)^{1.5}$; and $C = 0$ for $a/c \leq 1$. The third term was not a factor in the bending results on the D6AC steel. Because models were not constructed for a/t ratios less than 0.45, further study is needed for shallow cracks to verify the accuracy of the constraint equations.

References

[*1*] Raju, I. S. and Newman, J. C., Jr., "Stress-Intensity Factors for a Wide Range of Semi-Elliptical Surface Cracks in Finite-Thickness Plates," *Engineering Fracture Mechanics,* Vol. 11, No. 4, 1979, pp. 817–829.

[*2*] Newman, J. C., Jr. and Raju, I. S., "Analysis of Surface Cracks in Finite Plates Under Tension and Bending Loads," NASA Technical Paper 1578, National Aeronautics and Space Administration, Washington, DC, December 1979.

[*3*] Newman, J. C., Jr. and Raju, I. S., "Prediction of Fatigue Crack-Growth Patterns and Lives in Three-Dimensional Cracked Bodies," *Advances in Fracture Research,* S. R. Valluri, D. Taplin, P. Rao, J. Knott, and R. Dudey, Eds., Pergamon Press, Oxford, 1984, pp. 1597–1608.

[*4*] Reuter, W. G., Newman, J. C., Jr., Macdonald, B. D., and Powell, S. R., "Fracture Criteria for Surface Cracks in Brittle Materials," *Fracture Mechanics: 24th Volume, ASTM STP 1207,* J. D. Landes, D. E. McCabe, and J. A. M. Boulet, Eds., American Society for Testing and Materials, 1994, pp. 617–635.

[*5*] Reuter, W. G., Elfer, N., Hull, D. A., Newman, J. C., Jr., Munz, D., and Panontin, T. L., "Fracture Toughness Results and Preliminary Analysis for International Cooperative Test Program on Specimens Containing Surface Cracks," *Fatigue and Fracture Mechanics: 28th Volume, ASTM STP 1321,* J. H. Underwood, B. D. Macdonald, and M. R. Mitchell, Eds., American Society for Testing and Materials, 1997, pp. 146–166.

[*6*] Hancock, J. W., Reuter, W. G., and Parks, D. M., "Constraint and Toughness Parameterised by T," *Constraint Effects in Fracture, ASTM STP 1171,* E. Hackett, K.-H. Schwalbe, and R. Dodds, Eds., American Society for Testing and Materials, 1993, pp. 21–40.

[*7*] Reuter, W. G., Graham, S. M., Lloyd, W. R., and Williamson, R. L., "Ability of Using Experimental Measurements of δ to Predict Crack Initiation for Structural Components," *Defect Assessment in Components—Fundamentals and Applications, ESIS/EGF9,* J. G. Blanel and K.-H. Schwalbe, Eds., Mechanical Engineering Publication Limited, London, 1991, pp. 175–188.

[*8*] Sommer, E. and Aurich, D., "On the Effect of Constraint on Ductile Fracture," *Defect Assessment in Components—Fundamentals and Applications, ESIS/EGF9,* J. G. Blanel and K.-H. Schwalbe, Eds., Mechanical Engineering Publication Limited, London, 1991, pp. 141–174.

[*9*] Brocks, W. and Künecke, G., "On the Influence of Triaxiality of the Stress State on Ductile Tearing Resistance," *Defect Assessment in Components—Fundamentals and Applications, ESIS/EGF9,* J. G. Blanel and K.-H. Schwalbe, Eds., Mechanical Engineering Publication Limited, London, 1991, pp. 189–201.

[*10*] Faleskog, J., "Effects of Local Constraint Along Three-Dimensional Crack Fronts—A Numerical and Experimental Investigation," *Journal of the Mechanics and Physics of Solids,* Vol. 43, No. 3, 1995, pp. 447–493.

[*11*] Xia, L. and Shih, C. F., "Ductile Crack Growth—I. A Numerical Study Using Computational Cells with Microstructurally-Based Length Scales," *Journal of the Mechanics and Physics of Solids,* Vol. 43, 1995, pp. 233–259.

[*12*] Gao, X., Faleskog, J., Shih, C. F., and Dodds, R. H., "Ductile Tearing in Part-Through Cracks: Experiments and Cell-Model Predictions," *Engineering Fracture Mechanics,* Vol. 59, No. 6, 1998, pp. 761–777.

[*13*] Newman, J. C., Jr., Bigelow, C. A., and Shivakumar, K. N., "Three-Dimensional Elastic-Plastic Finite-Element Analyses of Constraint Variation in Cracked Bodies," *Engineering Fracture Mechanics,* Vol. 46, No. 1, 1993, pp. 1–13.

[14] Newman, J. C., Jr., Crews, J. H., Jr., Bigelow, C. A., and Dawicke, D. S., "Variations of a Global Constraint Factor in Cracked Bodies Under Tension and Bending Loads," *Constraint Effects in Fracture Theory and Applications: Second Volume, ASTM STP 1244,* M. Kirk and A. Bakker, Eds., American Society for Testing and Materials, 1995, pp. 21–42.

[15] Newman, J. C., Jr. and Raju, I. S., "An Empirical Stress-Intensity Factor Equation for the Surface Crack," *Engineering Fracture Mechanics,* Vol. 15, No. 1, 1981, pp. 185–192.

[16] *ANSYS User's Manuals,* Revision 5.4, Swanson Analysis Systems, Inc., 1998.

[17] Newman, J. C., Jr., "Fracture Analysis of Surface- and Through-Cracked Sheets and Plates," *Engineering Fracture Mechanics,* Vol. 5, 1973, pp. 667–689.

[18] Green, A. E. and Sneddon, I. N., "The Distribution of Stress in the Neighborhood of a Flat Elliptical Crack in an Elastic Solid," *Proceedings, Cambridge Philosophy Society,* Vol. 47, 1950, pp. 159–164.

[19] Irwin, G. R., "The Crack Extension Force for a Part-Through Crack in a Plate," *ASME Journal of Applied Mechanics,* Vol. 29, 1962, pp. 651–654.

[20] Daniewicz, S. R., "Prediction of Plasticity-Induced Closure in Surface Flaws Using a Modified Strip-Yield Model," *Fatigue and Fracture Mechanics: 29th Volume, ASTM STP 1321,* T. L. Panontin and S. D. Sheppard, Eds., American Society for Testing and Materials, 1998.

[21] Chao, Y. J. and Reuter, W. G., "Fracture of Surface Cracks Loaded in Bending," *Fatigue and Fracture Mechanics: 28th Volume, ASTM STP 1321,* J. H. Underwood, B. D. Macdonald, and M. R. Mitchell, Eds., American Society for Testing and Materials, 1997, pp. 214–242.

[22] Cruse, T. A. and Besuner, P. M., "Residual Life Prediction for Surface Cracks in Complex Structural Details," *Journal of Aircraft,* Vol. 12, No. 4, 1975, pp. 369–375.

[23] Hartranft, R. J. and Sih, G. C., "An Approximate Three-Dimensional Theory of Plates with Application to Crack Problems," *International Journal of Engineering Science,* Vol. 8, No. 8, 1970, pp. 711–729.

Session VI

Volker Weiss,[1] *Neil Goldfine,*[2] *and MarjorieAnn Natishan*[3]

Early Stage Fatigue Damage Characterization in Aluminum Alloys and Stainless Steels with Meandering Winding Magnetometer Technology

REFERENCE: Weiss, V., Goldfine, N., and Natishan, M., **"Early Stage Damage Characterization in Aluminum Alloys and Stainless Steels with Meandering Winding Magnetometer Technology,"** *Fatigue and Fracture Mechanics: 30th Volume, ASTM STP 1360,* P. C. Paris and K. L. Jerina, Eds., American Society for Testing and Materials, West Conshohocken, PA, 2000, pp. 427–438.

ABSTRACT: It is shown that pre-crack and early stage fatigue damage can be characterized by a new sensor technology, the Meandering Winding Magnetometer (MWM™). This new technology consists of a conformable sensor, the MWM, and associated measurement grids that are model based.

Measurements on type 304 stainless steel indicated that damage is readily detectable at 20% of life ($N/N_F = 0.2$) and causes a 1.5% conductivity loss. Near failure the conductivity loss in the crack-free region was approximately 4%. In 2024 aluminum the onset of detectable fatigue damage was observed at approximately 50% of total life. For the probe geometry employed, the conductivity loss in the microcrack region just prior to failure was 7%; in the macrocrack region it reached 13%.

KEYWORDS: Fatigue, aluminum alloys, magnetometers

Reliable detection of early fatigue damage, in the pre-crack and early small-crack regime, is of considerable technological importance. Fatigue-critical applications include aerospace structures, sea- and land-based transportation structures, fossil fuel and nuclear power plants, medical implants and devices, and many other critical components subjected to fluctuating loads. This translates into a requirement for a rapid, low cost, and easily portable nondestructive inspection system to map early-stage fatigue damage, fatigue cracks, and other age-related degradation in such systems. Also, it is desirable that inspections be performed without paint or applique removal. The inspection system must provide quantitative data that are reproducible (i.e., independent of operator and repeatable day after day on the same part without significant variation) and which is robust (substantially independent of operating conditions, paint thickness, and other uncontrolled variables).

The use of X-ray diffraction methods to measure fatigue damage was pioneered in the 1930s by Regler [*1,2*] and later perfected in Japan by Taira and Hayashi [*3*] and again by Cohen [*4*], Kramer [*5*], and Weiss et al. [*6*]. All these studies relate diffraction line broadening, due to increasing microstrain (or dislocation density), to fatigue damage. The Syracuse studies [*6*] on aluminum alloys and steels have shown that for reliable and reproducible results diffraction line broadening needs to be measured at two depths, ~10 μm and ~150 μm. Fatigue damage, as expressed by life fraction, can then be related to the ratio of dislocation density at ~150 μm below the surface to dislocation density near (~10 μm) the surface, Fig. 1. These data indicate that fatigue cycling disrupts the surface and

[1] Syracuse University.
[2] JENTEK Sensors, Inc.
[3] University of Maryland.

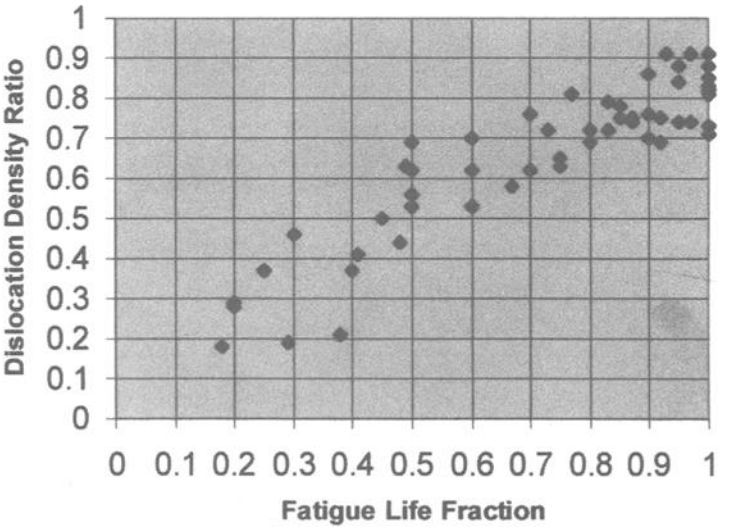

FIG. 1—*Summary plot of X-ray diffraction data [6]. The fatigue life fraction is plotted against the ratio of dislocation density 150 μm below the surface to that near the surface, ~10 μm deep. The surface density in the as-received state is generally higher due to the lattice distortions caused by the oxide layer.*

near-surface microstructure prior to the formation of micro- and macro-cracks. While these disruptions can be detected by careful X-ray diffraction line shape analysis, they should also affect other properties of the material, notably local, near surface, electrical resistivity. This then suggested exploring methods using precise measurements of local near-surface electrical conductivity for fatigue damage characterization.

The present paper describes the application of a new nondestructive detection system for early detection of fatigue damage based on precision surface and near surface conductivity measurements, the meandering winding magnetometer technology. First the MWM and grid measurement technology is described. Then the application of this new technology to early stage fatigue damage detection is demonstrated. Finally, examples of further possible applications for aerospace components are presented.

Background on MWM and Grid Measurement Methods for Absolute Conductivity Mapping

The MWM Sensor

The MWM, shown schematically in Fig. 2, and the MWM-array are thin and conformable sensors, designed to measure absolute magnetic and conducting properties of ferrous and nonferrous metals on flat and curved surfaces [7]. The MWM or MWM-array can be surface mounted, like a strain gage, in difficult-to-access locations that currently require disassembly for inspection.

Instead of designing the windings first and then trying to model them, the MWM was designed to match the Cartesian coordinate (x,y,z) model formulation for the magnetic diffusion equation. This results in accurate response prediction, permits model-based simulations to be performed for sensor optimization, and provides real time property measurements with minimal calibration requirements [8,9]. This is also what makes absolute conductivity measurements possible without using reference parts for calibration.

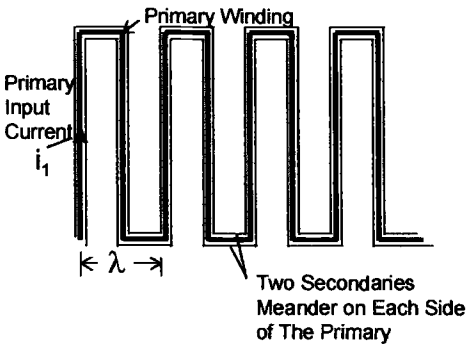

FIG. 2—*Schematic of MWM sensor.*

Measurement grids are generated, off-line, for different MWM sensor geometries and operating frequencies. This is accomplished using a continuum electromagnetic model of the MWM interactions with multiple-layered materials, such as aircraft skins with Alclad coatings. These grids are then used to provide real-time quantitative estimates of the material properties of interest [*8–15*].

The MWM has a primary winding fabricated in a square wave pattern, as shown in Fig. 2. The MWM winding spatial wavelength is indicated by λ. A current, i_1, is applied to the primary winding, and a voltage is measured at the terminals of the secondary windings. Two secondary windings meander on opposite sides of the primary to maintain symmetry. The magnetic vector potential produced by the current in the primary can be accurately modeled as a Fourier series summation of spatial sinusoids, with the dominant mode having the spatial wavelength λ. In the magneto-quasistatic regime, the MWM primary winding produces a dominant mode with a sinusoidal "standing wave" magnetic vector potential. The spatial wavelength of this dominant mode standing wave is determined by the MWM primary winding geometry and is independent of the input current "temporal" frequency. The fundamental Fourier mode wavelength is equal to the physical, "spatial" wavelength of the MWM primary winding.

A photograph of the GridStation™ measurement system is shown in Fig. 3. The system is comprised of a portable computer, an MWM probe, and a multiple frequency impedance instrument board.

The Grid Measurement Methods

Figure 4 shows a schematic diagram that describes the use of the model-based grid methods, as compared to more conventional eddy-current lift-off compensation methods. The problem with con-

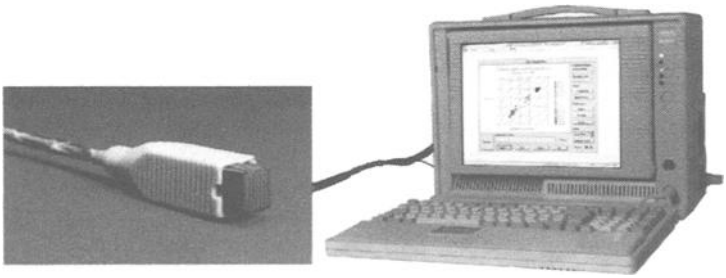

FIG. 3—*Photograph of JENTEK GridStation system with new MWM probe.*

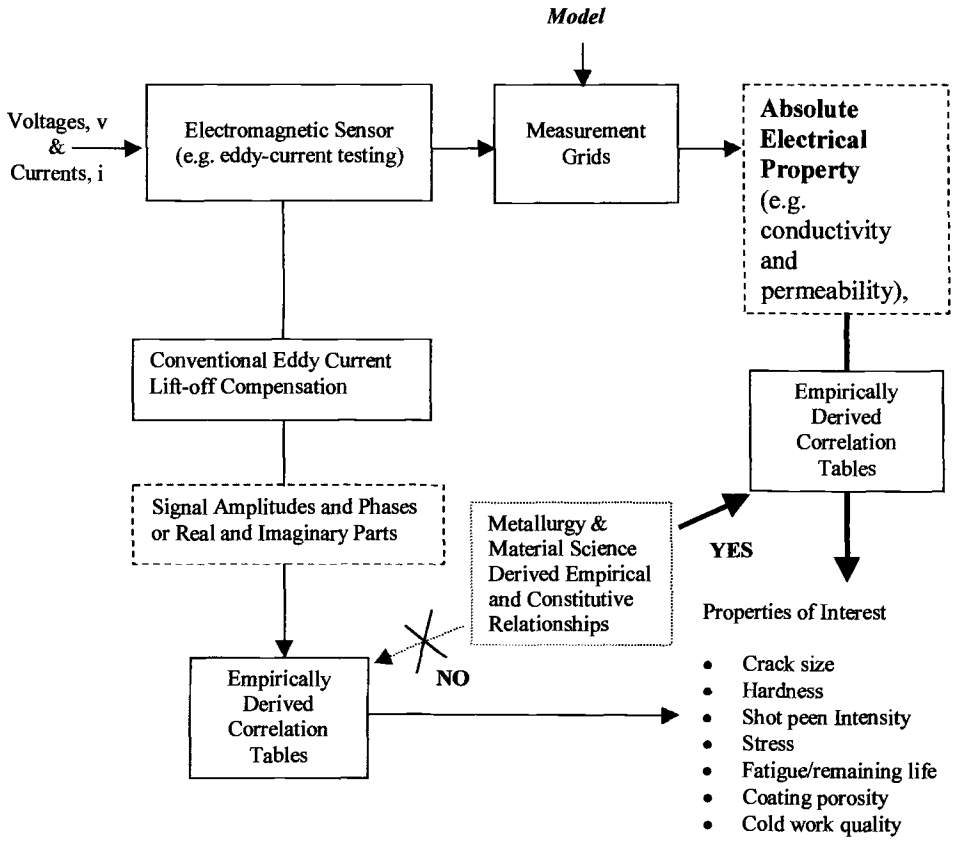

FIG. 4—*The grid methods permit direct, model-based determination of absolute properties.*

ventional eddy-current methods is that empirical correlation tables that relate the amplitude and phase of a lift-off compensated signal to properties of interest such as crack size or hardness will be inherently limited. With conventional methods, only signal amplitudes are typically provided, not absolute conductivities. By providing absolute conductivities, the MWM and grid measurement method permits the application engineer to tap into decades of scientific research that relates electrical properties to "dependent" properties such as hardness and stress.

Also, measurement grids permit independent measurement of lift-off and conductivity. Lift-off is the distance between the MWM winding plane and the first conducting surface (e.g., the outside surface of the aluminum or Alclad coating on an aircraft skin). Using an air calibration only, lift-off can be measured to a fraction of a micron. For the rapid scanning of lap joints, this lift-off measurement and resulting compensation is necessary to avoid contamination of absolute conductivity measurements by uncontrolled variations in liftoff, especially for fatigue damage and crack mapping without paint removal.

Figure 5 shows a conductivity/lift-off grid. A conductivity/lift-off grid is used to convert measurements of the MWM transinductance into absolute values of conductivity and lift-off. Many other measurement grids have been constructed for other pairs of unknowns, such as Alclad layer thickness and lift-off or magnetic permeability and conductivity. As shown in the flow diagram in Fig. 6, each grid point is generated using a forward model of the MWM magnetic field interactions

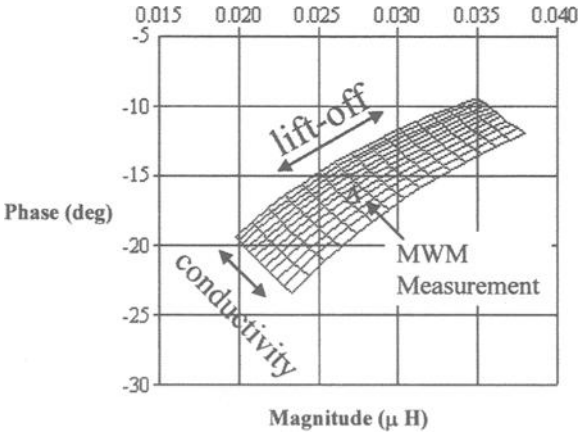

FIG. 5—*Conductivity/lift-off grid used for absolute conductivity measurement and real-time impedance data.*

with a multiple-layered media. These grids are generated off-line and do not need to be regenerated. The GridStation software converts the MWM impedance measurements, using a look-up table (represented by the measurement grid) and interpolation algorithm, into estimates of lift-off and conductivity. Also, multiple grids can be used to solve problems with more than two unknowns (e.g., four unknowns: coating thickness, coating conductivity, substrate conductivity, and liftoff for Alclad aircraft skins).

One grid is generated for each probe at each frequency for the property range of interest. For example, the grid in Fig. 5 is valid for structural aluminum alloys like Al-2024, Al-7075, Al-7050, Al-6061, etc.), for the standard 0.5 by 0.5-in. (12.7 by 12.7-mm) MWM probe, at a 5-MHz input current frequency. The air calibration point represents infinite liftoff. All lines of constant conductivity converge to this air calibration point. This is the only reference point required to "anchor" the grid and account for instrument drift. Standard cable compensation methods are used to account for cable variations. Thus, accurate liftoff and conductivity measurements are provided without the need for lift-off or conductivity standards.

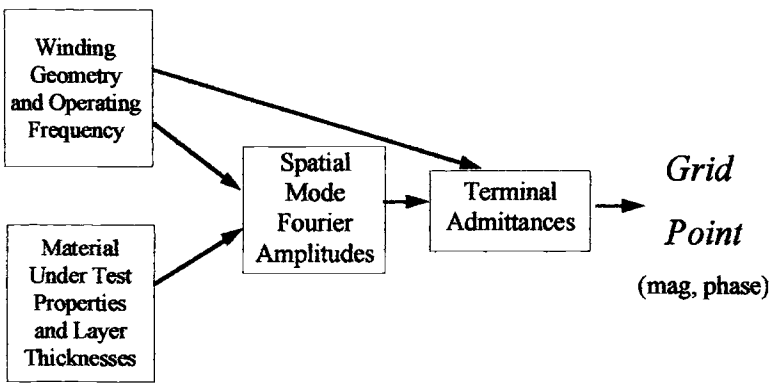

FIG. 6—*Flow diagram of MWM continuum electromagnetic forward model for grid generation.*

Application of MWM and Grid Methods to Fatigue Damage Characterization

MWM conductivity/lift-off grids for both stainless steel and aluminum alloys were used to demonstrate the correlation of MWM conductivity measurements with accumulated fatigue damage. Fatigue cycling was conducted in fully reversed bending ($R = -1$). Hourglass and "dog-bone" shaped specimens were exposed to varying fractions of their fatigue life at a known alternating stress level. MWM electrical conductivity measurements for some of the dog-bone specimens are shown in Fig. 7 as a function of fatigue life fraction. As illustrated in the figure, significant changes in conductivity were observed. Similar plots will be developed in future work for titanium and nickel alloys for engine blade fatigue studies. Figures 7 through 10 provide MWM scans for coupons exposed to fully reversed bending. For Al-2024, the MWM begins to detect significant reductions in conductivity at about 60% of fatigue life. Photomicrographs have shown that clusters of microcracks, 0.001 to 0.003 in. deep, begin to form at this stage. Although detectable with the MWM, these microcrack clusters were not detectable with liquid penetrant testing except at the very edge of the 90% specimen. This same behavior has been observed for MWM measurements on military aircraft structural members.

To evaluate the ability of the MWM to detect the spatial distribution of fatigue damage, the sensor was scanned along the length of the specimens. These measurements reveal a pattern of fatigue damage focused near the dog-bone specimen transition region for both the 70 and the 90% specimens (see Fig. 8). The minimum conductivity at the 3-cm point on the specimen that reached 90% of its fa-

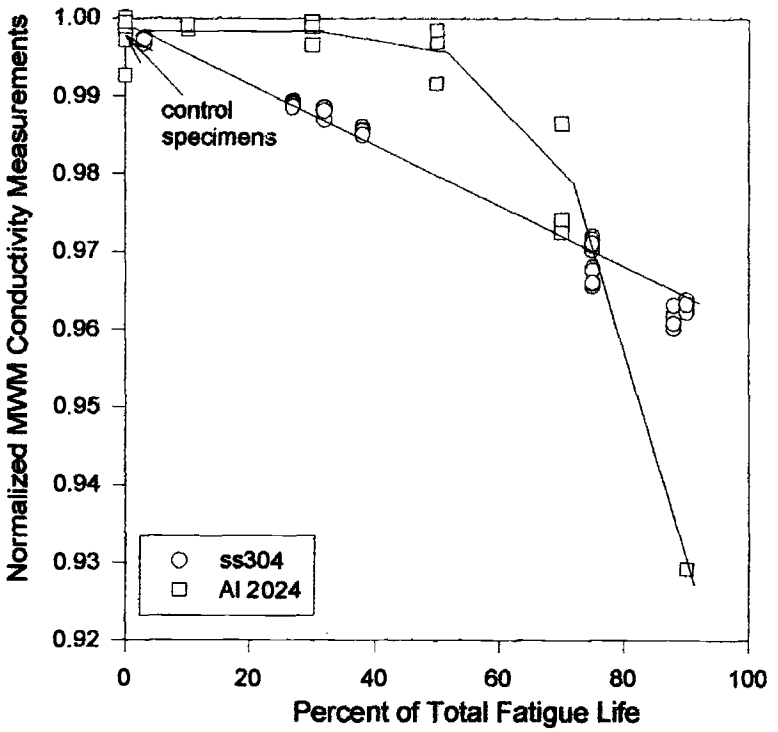

FIG. 7—*MWM conductivity measurements as a function of percent fatigue life of 304 stainless steel and 2024 aluminum.*

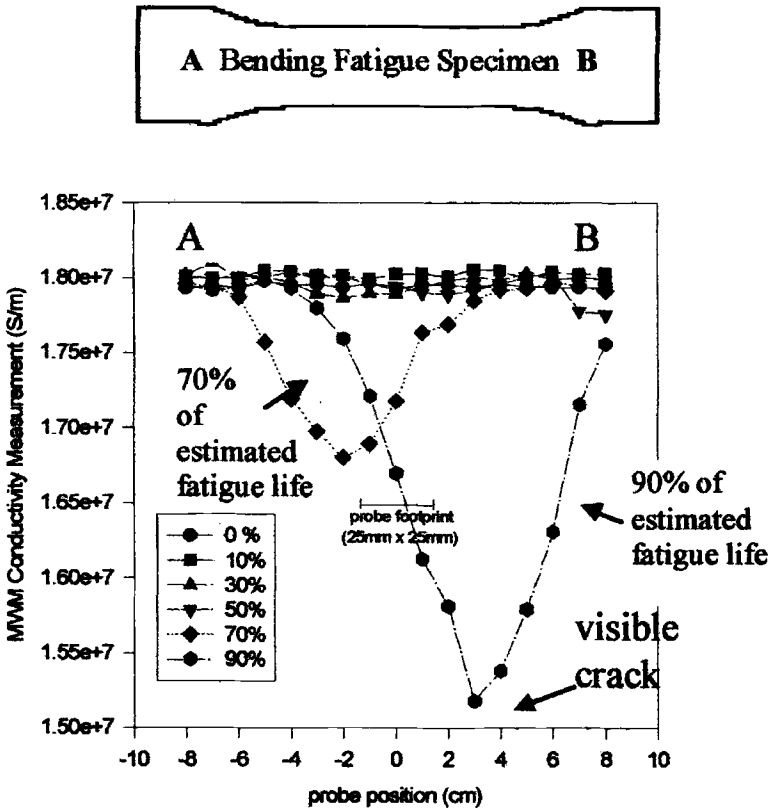

FIG. 8—*Plots of MWM absolute conductivity scans across 2024 aluminum hour-glass specimens fatigued to 0, 10, 30, 50, 70, and 90% of fatigue life.*

tigue life corresponds precisely with the location of a visible crack. The presence of a damaged region in the vicinity of the crack is indicated by the depressed conductivity on either side of the crack, *even when the crack is not under the footprint of the sensor* (see Fig. 9). In other words, bending fatigue in aluminum produces an area damaged by microcracks prior to the formation of a dominant macrocrack, and that damaged area is detectable as a significant reduction in the MWM-measured conductivity.

The data in the previous plots were taken after a reference part calibration that assumed a 1.74E7 S/m absolute conductivity for the 2024 coupons before exposure to loading. These measurements have since been repeated with our recently improved air calibration methods. The actual absolute conductivity was determined to be approximately 1.77E7 S/m, using the air calibration. Two-dimensional MWM absolute conductivity scans were made on the specimens and are shown in Figs. 10*a* and 10*b*.

Note that the density and size increases are indicated by an increased reduction in the MWM absolute conductivity measurements. Thus, as expected, the microcrack size and density increase near the coupon edges and are lower at the center. This indication, when the longer winding segments of the MWM are parallel to the bending moment axis, is caused by segments of the macrocrack that deviate from the bending moment axis direction. Thus, they produce only reduced conductivity indications when the macrocrack is in the sensor footprint.

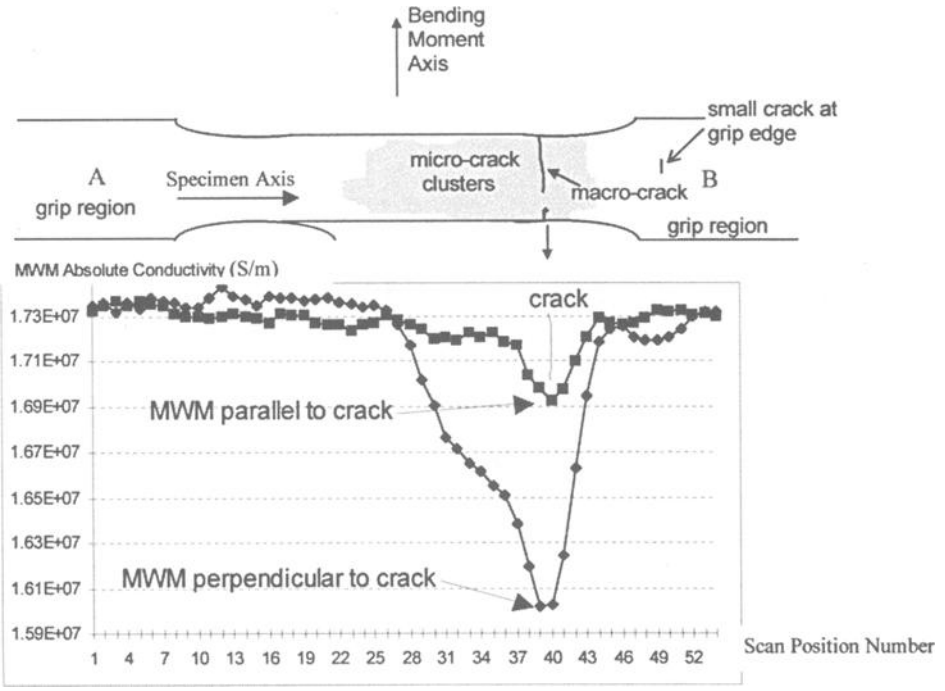

FIG. 9—*MWM measurements of fatigue damage in bending fatigue coupon cycled to 90% of estimated fatigue life, with the longer MWM winding segments oriented both parallel and perpendicular to the crack at MWM scan position 39. A four-point moving average was applied to these data. Without the moving average, the fretting crack shows up as a flat bottom signature. New MWM sensors are being equipped with rolling encoders to support spatial image building.*

Further Applications of MWM and Grid Methods to Fatigue Damage Characterization

During the last four years, investigations into the mapping of early stage fatigue damage and fatigue cracks using the MWM and grid methods have included:

1. Correlation of MWM measurements with loading history, optical microscopy, and X-ray diffraction for aluminum alloy bending fatigue coupons.
2. MWM measurements on full-scale bulkhead fatigue specimens.
3. MWM measurements on the passenger window lap joints and the skin panels under the pilot window post of a service-exposed Boeing 737 at the FAA/AANC.
4. MWM measurements on other fatigue-tested and service-exposed commercial and military aircraft components.

An example of the capability of the method is presented in Fig. 11. MWM measurements were made at the FAA/AANC on the lap joint of the Boeing 737 (test bed at Sandia National Laboratories) near the passenger windows and on the skin panels under the pilot window post [*16*]. The Alclad layer thickness on the 0.040-in. (1.02-mm) thick Boeing 737 fuselage skin was approximately 0.002 in. (0.051 mm). The skin depth at the highest frequency was selected to be slightly greater than the Alclad thickness, while the skin depth at the lowest frequency was selected to be less than 25% of the total 0.040-in. (1.02-mm) outer skin thickness.

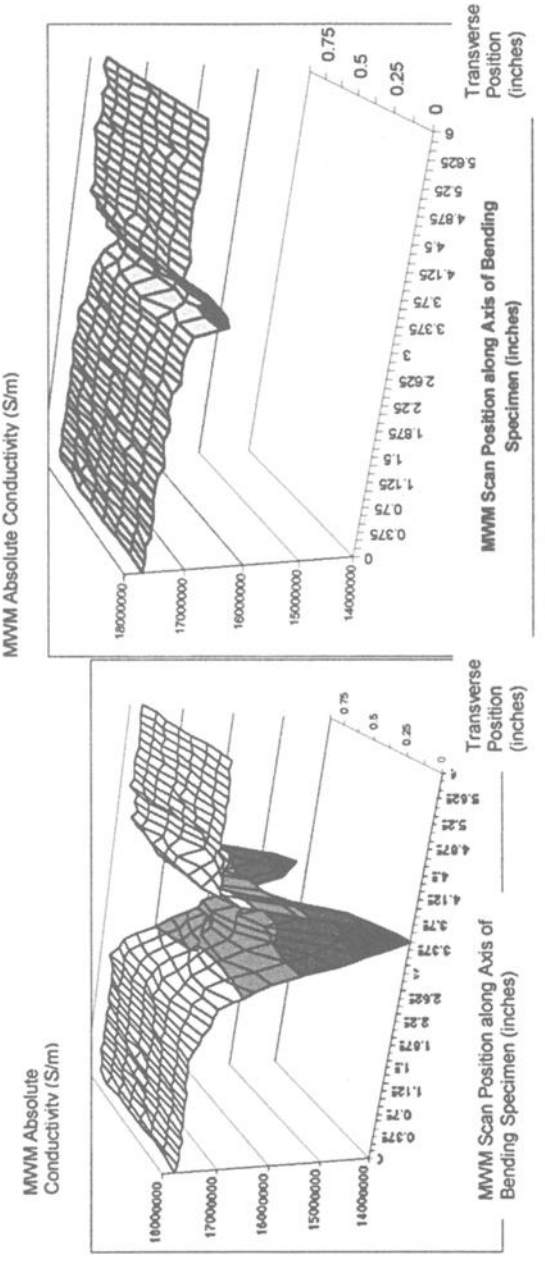

FIG. 10—*Two-dimensional MWM absolute conductivity (S/m) scans with windings* (a) *perpendicular to macro-crack orientation (i.e., perpendicular to bending moment axis), and* (b) *parallel to macro-crack orientation for cracking in the aluminum bending coupon shown in Fig. 12.*

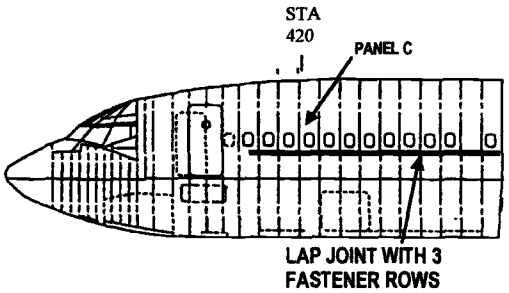

FIG. 11—*Locations of 737 panels tested during visits to the FAA /AANC.*

Panel C (shown in Fig. 11), containing the passenger windows above the lap joint near the center of the aircraft, exhibited substantial MWM-measured conductivity variations. MWM horizontal and vertical scans identified regions near and *away* from fasteners that exhibited fatigue-like features associated with micro-cracking and thus represented the most likely locations in the lap joint for macro-crack formation. MWM fatigue coupon studies on 2024 aluminum alloy, described earlier, demonstrated detection of micro-crack clusters after 50% of fatigue life. Figure 12*a* shows a horizontal scan *several inches above* the top fastener row. For this scan, the MWM-measured conductivity has minimums that correspond consistently with the vertical window edge locations. Thus, several inches above the lap joint fastener rows, substantial bending fatigue-like damage was detected by the MWM. The bending fatigue coupon data suggests that this region is beyond 60% of its fatigue life, although it probably does not contain macro-cracks, which would be detectable with conventional differential eddy-current methods. Vertical scans showed that damage begins near the bottom of the windows and increases steadily, with the maximum damage occurring at the fasteners, as expected. The vertical scan data are shown in Fig. 12*b*. The key is that this damage is detectable more than 6 in. away from the fasteners. Thus, when scanning a lap joint it may be desirable also to scan the regions above and below the lap joint.

For this particular 737 aircraft, five cracks have been documented on the lap joints immediately above and below the passenger windows on the port side of the aircraft. Each of these cracks occurred within one fastener of the edge of the window. Two of these cracks have not been repaired and are detectable with conventional eddy-current methods. Three of the cracks had been repaired by addition of patches at these locations. This provides a partial validation of the MWM capability to detect wide spread fatigue damage (WFD) onset.

One additional observation based on the MWM data is that the edges of a patch should be away from the minimums in the MWM conductivity (e.g., a location of maximum fatigue damage). Additional scans on other commercial aircraft components have shown similar promising results. Information such as this can improve selection of patch location and size, potentially reducing follow-on maintenance costs. Ultimately, the MWM information might be used to identify specific regions that require fastener inspections, as well as to support inspection, maintenance scheduling, and redesign efforts.

Conclusions

The capability to measure absolute electrical conductivity for flat samples as well as complex aircraft surfaces has been demonstrated without the use of conductivity standards. This capability, achieved with MWM technology, represents a major advance in the characterization of early fatigue damage. Ongoing efforts are focused on implementations for specific fatigue monitoring applications. The U.S. Navy, Air Force, and the FAA have provided ongoing funding for aircraft applications.

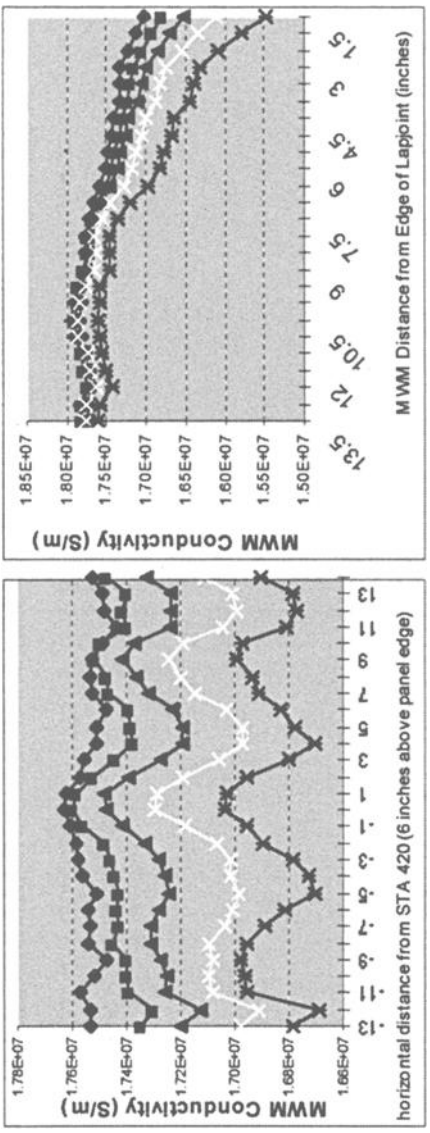

FIG. 12—*MWM multiple frequency scans on Boeing 737 at FAA/AANC* (a) *horizontal, and* (b) *vertical scan data on panel C. Lower conductivity, measured at higher frequency, indicates that greater damage is present nearer to the surface of the tested material.*

References

[1] Regler, F., *Zeitschrift für Elektrochemie,* Vol. 43, 1937, p. 546.

[2] Regler, F., *Verformung und Ermüdung metallischer Werkstoffe,* 1939.

[3] Taira, S. and Hayashi, K., *Proceedings,* 9th Japanese Congress of Testing Materials, 1966.

[4] Cohen, J. B., *Local Atomic Arrangements Studied by X-Ray Diffraction,* Gordon and Breach, NY, 1965.

[5] Kramer, I. R., *Metallurgical Transactions,* Vol. 5, 1974 p. 1735.

[6] Weiss, V. and Oshida, Y., "Fatigue Damage Characterization Using X-Ray Diffraction Line Analysis," *Fatigue 84,* Butterworth, 1984, p. 1151.

[7] Goldfine, N. J., Clark, D., and Eckhardt, H., "Apparatus and Methods for Measuring Bulk Materials and Surface Condition for Flat and Curved Parts," Serial Number 60/002,804 U.S. Patent Pending.

[8] Goldfine, N. J. and Melcher, J. R., "Magnetometer Having Periodic Winding Structure and Material Property Estimator," U.S. Patent Number 5,453,689, 26 Sept. 1995.

[9] Melcher, J. R., "Apparatus and Methods for Measuring Permeability and Conductivity in Materials Using Multiple Wavelength Interrogations," U.S. Patent Number 5,015,951, 14 May 1991.

[10] Goldfine, N. J., "Early Stage Fatigue Detection with Application to Widespread Fatigue Damage Assessment in Military and Commercial Aircraft," *Proceedings,* 1st DOD/FAA/NASA Conference on Aging Aircraft, July 1997.

[11] Goldfine, N. J. and Clark, D., "Age Degradation Monitoring by Correlation with Surface and Bulk Electrical Property Variations," *Aeromat Exposition, Advanced Aerospace Materials and Processes,* 1996.

[12] Goldfine, N. J., Washabaugh, A., Yates, A., and Welch, J., "Meandering Winding Magnetometers Suitable for In-Situ Electrical Conductivity and Complex Permeability Profiling," TMS Conference Presentation, 1993.

[13] Goldfine, N. J., "Conformable Meandering Winding Magnetometer (MWM) for Flaw and Materials Characterization in Ferrous and Nonferrous Materials," *ASME Pressure Vessels and Piping Conference,* 1997.

[14] Goldfine, N. J., "On-Line Fatigue Monitoring for Structural Components, Using New Surface Mountable Eddy-Current Sensors," 46th Defense Working Group (DWG) on Nondestructive Testing, 1997.

[15] Goldfine, N. J. and Lovett, T., "Materials Characterization Using Model Based Meandering Winding Eddy Current Testing (MW-ET)," EPRI Topical Workshop: Electromagnetic NDE Applications in the Electric Power Industry, 1995.

[16] Goldfine, N. J. and Roach, D., "Early Stage and Widespread Fatigue Damage Assessment for Aircraft Structures and Engines, Using a New Conformable Multiple-Frequency Eddy Current Sensor," *Proceeding,* 41st Annual ATA NDT Forum, 1997.

Wei-Ming Chi,[1] *Gregory G. Deierlein,*[1] *and Anthony R. Ingraffea*[2]

Finite-Element Fracture Analyses of Welded Beam-Column Connections

REFERENCE: Chi, W.-M., Deierlein, G. G., and Ingraffea, A. R., **"Finite-Element Fracture Analyses of Welded Beam-Column Connections,"** *Fatigue and Fracture Mechanics: 30th Volume, ASTM STP 1360,* P. C. Paris and K. L. Jerina, Eds., American Society for Testing and Materials, West Conshohocken, PA, 2000, pp. 439–455.

ABSTRACT: Unexpected brittle cracking of welded beam-column connections during the 1994 Northridge earthquake has raised serious concerns about standards and practice for the seismic design and construction of steel moment resisting frames. As part of a nationally coordinated program to investigate the connection damage, finite-element fracture analyses are used to quantify fracture toughness demands in welded beam-column connections as influenced by various detailing parameters. Toughness demands at weld root defects in the beam flange groove welds are quantified in terms of K_I, CTOD, and CTOA. Summarized are insights concerning the role of finite-element fracture analyses to investigate fracture behavior and the influence of factors such as flaw sizes, weld strengths, inelastic crack growth, and other parameters affecting fracture toughness demands.

KEYWORDS: fracture toughness, finite-element analysis, welded connections, steel, frames, ductility, seismic design, earthquake engineering

Structural design criteria for seismically designed moment-resisting frames are predicated on the assumption that beam-column connections will have sufficient strength and ductility to dissipate energy through large inelastic deformations. Design specifications, such as the AISC Provisions for the Seismic Design of Steel Structures [*1*], include criteria to detail beam-column connections and members so as to insure stable inelastic response under large earthquakes. Standards for design and construction were brought into question, however, when inspections following the 1994 Northridge earthquake revealed widespread cracking of welded beam-column connections. Damage has been reported in over 100 buildings, many of which were built after 1980 and a few of which were under construction during the earthquake [*2*]. In many cases the fractures occurred with little or no evidence of beam yielding, indicating that the connections are much more prone to brittle fracture than generally assumed. Although none of the affected buildings collapsed, the fractures raised serious concerns about the reliability of frames designed and detailed according to standard practice.

In response to concerns raised, the Federal Emergency Management Agency (FEMA) funded a national study through the SAC Joint Venture[3] to identify causes of the damage, propose solutions for new construction, and quantify the hazards posed by existing welded moment frame buildings. Investigations conducted to date have established that the fractures resulted from a combination of factors including: (1) mechanical and metallurgical defects created by poor quality field welding and inspection procedures, (2) use of low-toughness weld metal, (3) use of heavy members with

[1] Graduate research assistant and associate professor, respectively, Department of Civil and Environmental Engineering, Terman Engineering Center, Stanford, CA 94305-4020.

[2] Professor, School of Civil and Environmental Engineering, Hollister Hall, Cornell University, Ithaca, NY 14853-3501.

[3] The SAC Joint Venture is a partnership of the Structural Engineers Association of California, the Applied Technology Council, and the California Universities for Research in Earthquake Engineering.

thick highly stressed welds, and (4) weld details with large built-in stress risers. A number of solutions have since been proposed to rectify these conditions, however, there is still a lack of reliable data on the fracture behavior itself. Summarized herein are results from the initial phase of an ongoing investigation to determine fracture toughness demands in welded beam-column moment connections.

Beam-Column Connection Details and Behavior

Shown in Fig. 1 is a beam-column connection detail typical of those that suffered damage during the Northridge earthquake. The connection consists of a bolted beam web shear tab and full penetration groove welds joining the beam flanges to the column. Per code requirements in effect at the time, supplemental fillet welds connecting the shear tab to the beam are provided to help mobilize the beam web in resisting bending. Framing members are usually specified as A36 or A572 (Grade 50) steel with E70XX weld metal. Prior to the Northridge earthquake, it was common practice in California to use a flux core arc welding (FCAW) process with E70T-4 electrodes, which in accordance with building code provisions did not have any minimum specified notch toughness requirements.

With the standard practice of leaving the weld backing bars in place, a built-in notch exists at the bottom side of the beam flange weld, formed by the gap between the backing bar and column face that adjoins any weld-root defects that are present. As shown in Fig. 2, depths of the weld-root defects tend to vary across the beam width and are likely to be largest in the center of the bottom flange as a result of restricted access for field welding and inspection around the weld access hole in the beam web. Post-fracture inspections [*4*] have revealed weld discontinuities (lack of fusion, slag inclusions, etc.) with depths up to about a_o = 0.4 in. (10 mm), even in joints that were inspected and supposedly met the requirements of ANSI/AWS D1.1 Structural Welding Code.

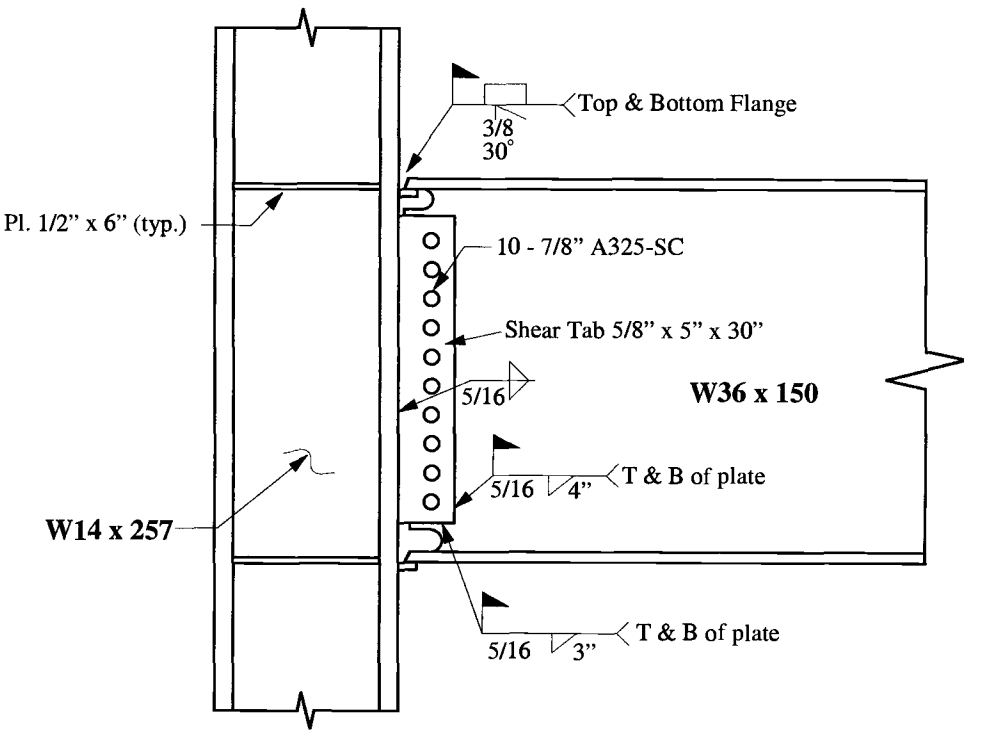

FIG. 1—*Typical welded-flange bolted-web moment connection.*

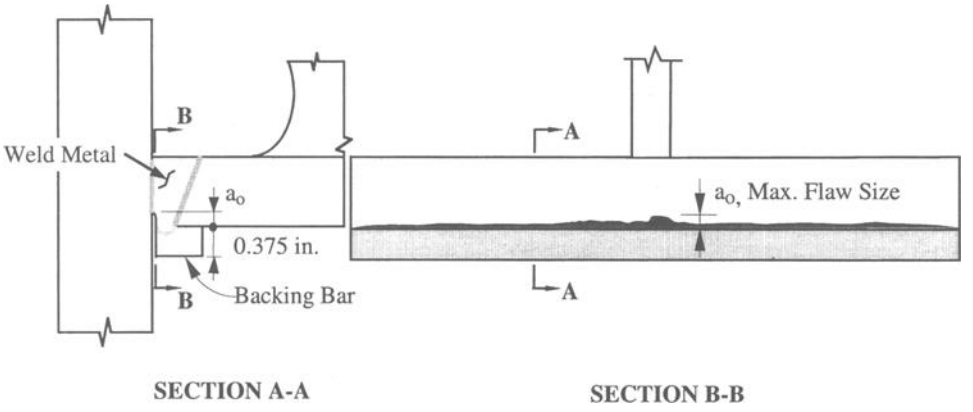

FIG. 2—*Detail of backing bar gap and weld root imperfections.*

As part of the SAC Joint Venture, full-scale tests of six nominally identical connections were conducted at the Universities of California and Texas [*5,6*] to establish benchmark data on connection performance. We have used these tests as prototypes for the fracture analyses reported herein. The connection detail is the same as described previously in Fig. 1, and the overall specimen configuration, member sizes, and steel strengths are shown in Fig. 3. Note that one important difference between the specimens is that two of the six had high-yield-strength (A572-Grade 50) beams while the

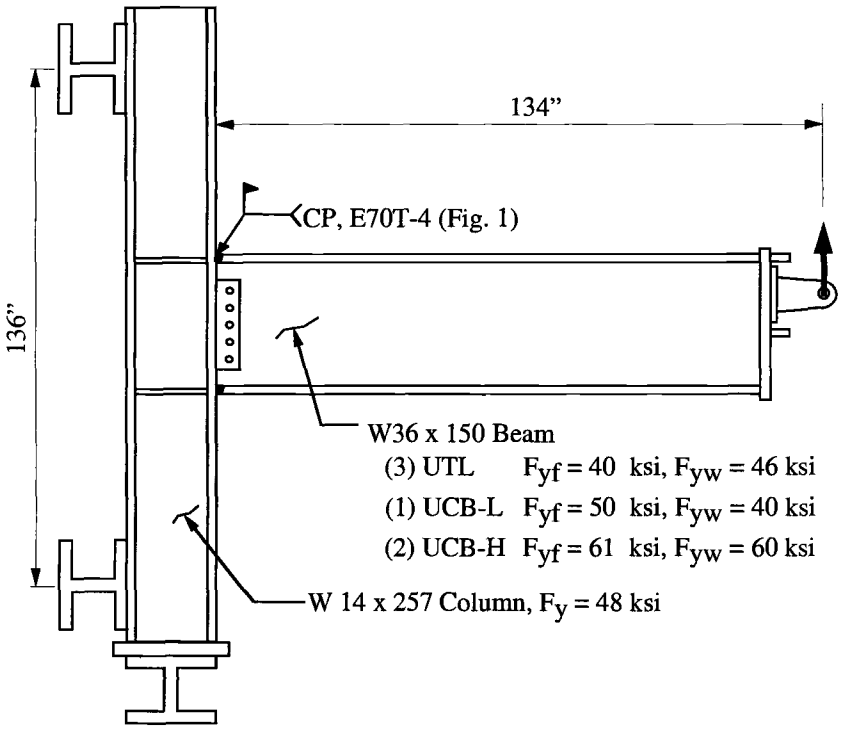

FIG. 3—*Full-scale connection specimen.*

other four had lower-strength A36 beams. Commercial steel fabricators prepared the specimens using approved procedures representative of typical field conditions.

Shown in Fig. 4*a* is a load versus deformation plot that is fairly representative of the behavior that resulted from fairly brittle weld fractures in all six connection tests. As summarized in Ref *3*, the maximum moments only reached 0.7 to 1.1 times the plastic moment strength of the beam, often failing prior to any significant yielding. Shown in Fig. 4*b* are the two observed modes of failure. In the four connections with A36 beams, fractures initiated at the weld root and propagated nearly vertically through the weld or slightly into the column flange, followed by subsequent tearing of the web shear tab and/or shear failure of the web bolts. In the two connections with A572 (Grade 50) beams, fractures initiated in the weld but then propagated through the column flange and into the column web.

Finite-Element Fracture Analyses

With the preceding discussion as background, objectives of the present study are to: (1) demonstrate the effectiveness of finite-element fracture analyses to understand fracture behavior in the connections, (2) quantify the influence of various connection detailing parameters on fracture toughness requirements, and (3) lay the groundwork for developing a fracture-mechanics-based methodology to evaluate and design fracture behavior in welded connections. Included are two- and three-dimensional elastic and inelastic analyses for fracture initiation and propagation of cracks originating at the root of the lower beam flange weld.

Finite-element models of the full-scale connection specimens are shown in Figs. 5*a* and 5*b*. The two-dimensional model (Fig. 5*a*) consists of eight-node quadrilateral elements and six-node triangular elements created and analyzed using the program FRANC2D[4]. All elements are plane stress except for those in a small region around the crack tip where plane strain elements are used to represent the local out-of-plane constraint. Crack tip elements for the elastic analyses are singular quarter-point elements from which K_I is determined using the J-integral and displacement correlation methods. For the inelastic analyses, collapsed quadrilateral elements are used to simulate crack tip blunting and permit explicit measurement of CTOD and CTOA from the deformed mesh.

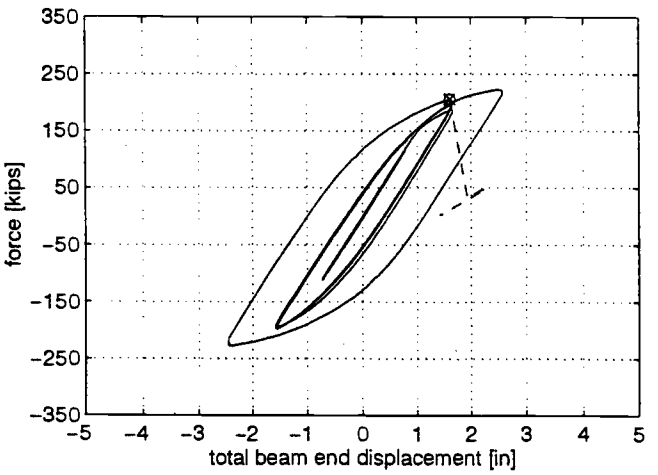

FIG. 4—*Representative specimen behavior:* (a) *load versus deformation response,* (b) *failure modes.*

[4] FRANC2D is a finite element with specialized fracture analysis features developed by A. R. Ingraffea and his research group at Cornell University. For further information see http://www.cfg.cornell.edu.

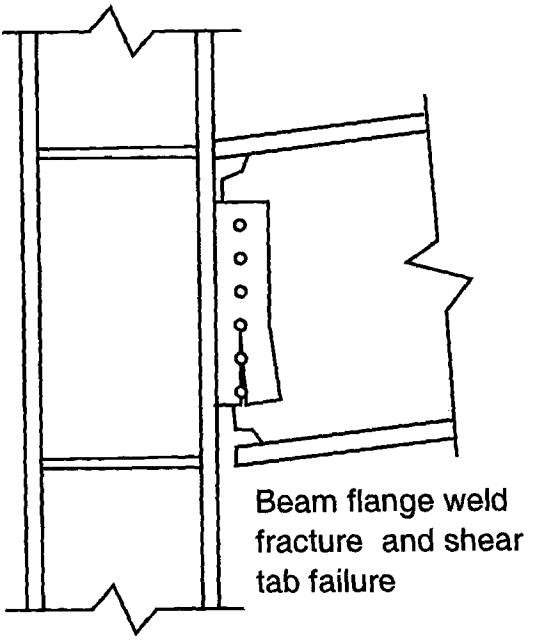

UTL, UCB-L

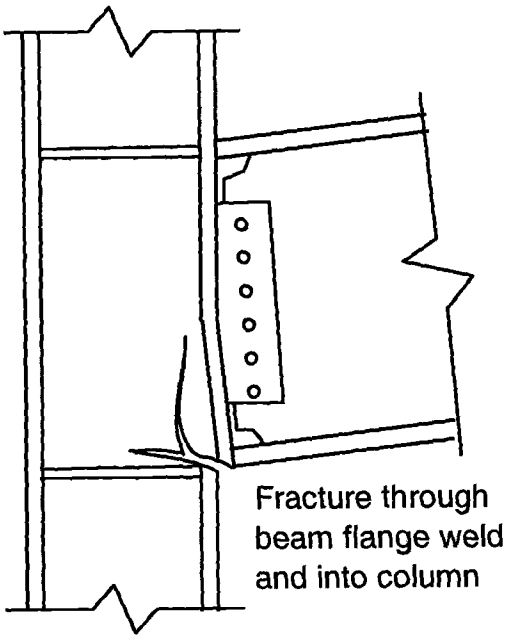

B **UCB-H**

FIG. 4—*(Continued)*

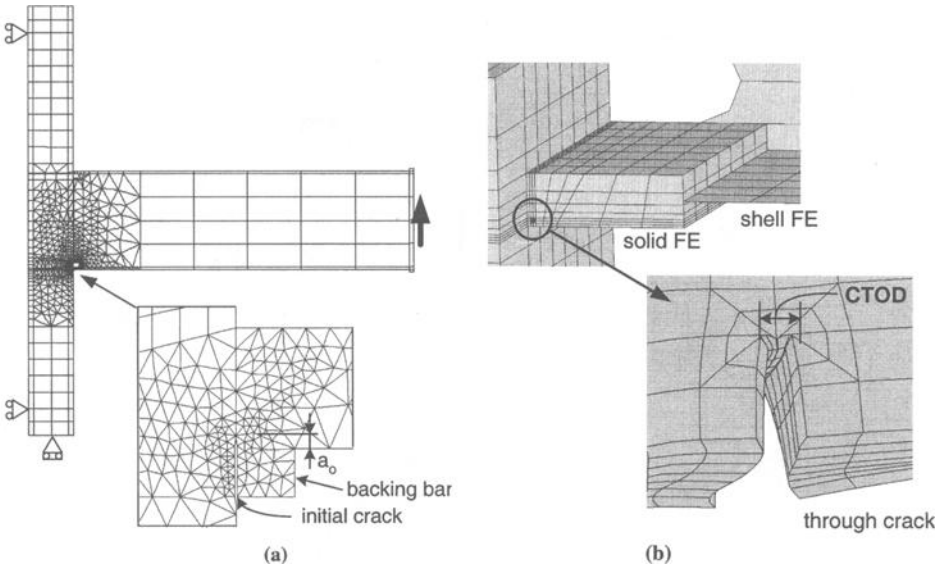

FIG. 5—*Finite-element models:* (a) *two-dimensional,* (b) *three-dimensional.*

The three-dimensional models, consisting of eight-node shell and twenty-node brick elements, were run using ABAQUS (Version 5.1). As shown in Fig. 5*b,* solid elements in the vicinity of the lower beam flange weld are linked to shell elements through kinematic constraints. Crack tip elements consist of collapsed twenty-node brick elements. For elastic analyses mid-side nodes of the brick elements were moved to quarter-point locations, and for the inelastic analyses the collapsed brick elements were free to expand to model crack tip blunting. As in the two-dimensional analyses, K_I was calculated from the elastic models using *J*-integrals. For inelastic analyses CTOD was measured both directly from the blunted crack tip mesh and indirectly by converting from *J* to CTOD. In general, *J* and CTOD were nearly linearly related to one another.

Material Properties and Flaw Size Data

For all analyses an elastic modulus of $E = 29\,000$ ksi (200 000 MPa) and Poisson's ratio of $v = 0.25$ were assumed. For inelastic analyses, yield strengths of the rolled shapes were based on tension coupon tests whose values are reported in Fig. 3, and a nominal yield strength of $Fy = 60$ ksi (413 MPa) was assumed for the E70 weld metal. A von Mises yield criterion with 1% strain hardening was assumed for both the weld and base materials.

Only limited material toughness and flaw size data for the in situ welds and heat affected zones (HAZ) of the beam-column joints are available, and so it was not possible to quantify these in a statistically meaningful way. We modeled flaws to be consistent with the backing bar configuration (see Fig. 2) and the maximum weld root defects of $a_o = 0$ to 0.4 in. (0 to 10 mm) as measured by Kaufmann and Fisher [*4*] in post-test inspections of the fractured connection specimens. We assumed the toughness of the in situ welds and HAZ as CVN = 5 to 10 ft-lb at 70°F (7 to 14 *J* at 21°C) based on material samples from damaged buildings [*4*]. From these CVN data, we then calculated weld region toughness of $K_{Ic} = 40$ to 60 ksi$\sqrt{\text{in.}}$ (44 to 66 MPa$\sqrt{\text{m}}$) and $\text{CTOD}_c = 0.8$ to 1.7×10^{-3} in. (0.02 to 0.04 mm) using empirical correlation equations by Barsom and Rolfe [*7*], including a temperature shift to account for loading rate differences in the lower transition region. For mild steel base metal,

the following upper-transition region toughness values are assumed: CVN = 80 ft-lb at 70°F (108 *J* at 21°C), K_{Ic} = 140 ksi$\sqrt{in.}$ (154 MPa$\sqrt{m}$), and $CTOD_c = 7 \times 10^{-3}$ in. (0.18 mm). These base metal values are also considered as representative of welds made with high-toughness electrodes that meet the recently revised AISC Seismic Provisions [*1*], which now require specified filler metal toughness of CVN = 20 ft-lb at −20°F (27 *J* at −29°C).

Two-Dimensional Crack Initiation Analyses

Elastic K_I *Analyses*

Shown in Fig. 6 are K_I values for elastic analyses with various size weld root flaws in the beam flange weld. The total length of the initial crack is equal to the backing bar gap length *W* (equal to the backing bar thickness) plus the initial weld root flaw length a_o. Note that the initial weld root flaw length (a_o), and *not* the total length ($W + a_o$), is plotted along the horizontal axis in Fig. 6. On the vertical axis, K_I is normalized by the nominal flange bending stress $\sigma = M/S$ where *M* is the beam moment at the column face and *S* is the elastic section modulus of the beam. In comparing the four FEM analysis curves in Fig. 6, one can see that the backing bar thickness (*W*) does not influence the stress intensity value. Rather, comparing the analysis for $W = 0$ to the other three cases indicates that the presence of a backing bar of any thickness causes about the same stress intensity value as a small initial flaw on the order of a_o = 0.01 to 0.05 in. (0.3 to 1.3 mm). Other analyses, not shown here, further confirm that the K_I demands are not sensitive to the length of the fusion region between the backing bar and weld.

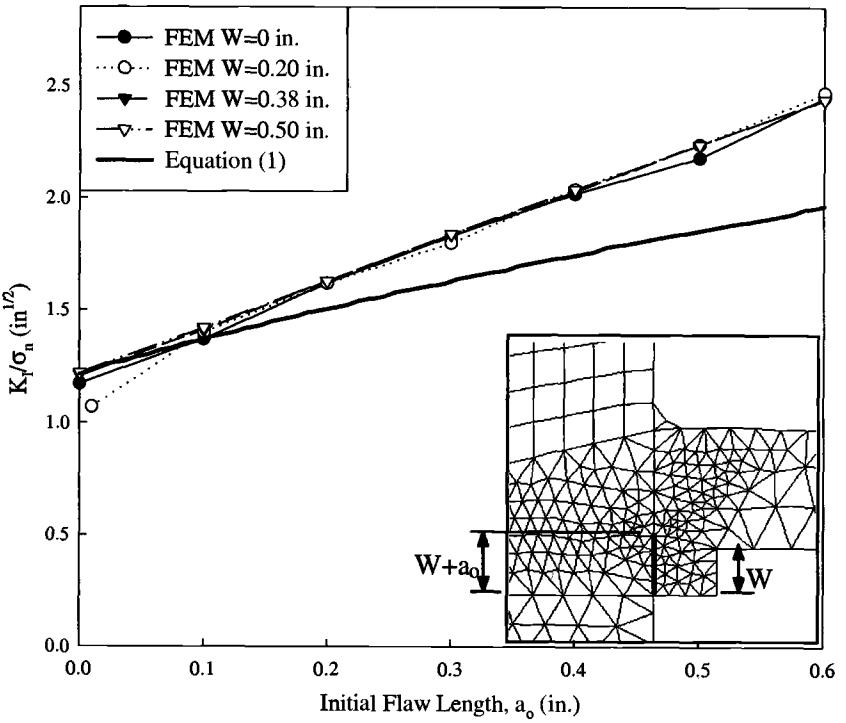

FIG. 6—*Normalized stress intensity factor at weld root in beam-column connection.*

In addition to the FEM analysis results, values for K_I are plotted in Fig. 6 using the following equation for an edge crack in a semi-infinite uniformly stressed bar:

$$\frac{K_I}{\sigma} = 1.12\sqrt{\pi a} \tag{1}$$

where $a = C + a_o$, a_o is the initial flaw length (plotted in Fig. 6), and C is a calibration coefficient that accounts for the nonuniform stress distribution and the presence of the backing bar notch. Plotted in Fig. 6 are values for Eq 1 with $C = 0.38$ in. (10 mm) that produces rather good agreement with the FEM results. Coincidentally, this value of C (0.38 in. or 10 mm) equals the actual backing bar thickness W in the specimens, but as demonstrated by the FEM results for varying bar thickness, the similarity of C and W is a coincidence and there is no theoretical justification for taking C equal to the backing bar gap. Further, considering that the relationship between K_I and a_o from the FEM analyses is fairly linear, a more straightforward equation for K_I might take the form:

$$\frac{K_I}{\sigma} = C_1 + C_2 a_o \tag{2}$$

where C_1 and C_2 are two calibration coefficients that carry units of $\sqrt{\text{length}}$ and $1/\sqrt{\text{length}}$, respectively. As part of an ongoing study, we are conducting parametric analyses to develop such an equation to estimate fracture demands for a variety of connection configurations.

To further examine the influence of backing bar thickness, we ran analyses of simpler configurations, the three uniformly stressed straight bars shown in Fig. 7*a*. Here, the backing bars are represented by "lugs" that act as unloaded attachments. For the plotted K_I results in Fig. 7*b*, positive values of flaw length correspond to cases where the crack extends into the bar, and the negative values correspond to flaws that do not extend out of the "lug" material in Bars II and III. So, for example, the initial flaw length of −0.38 in. (−10 mm) corresponds to analyses for Bars II and III with zero flaw sizes, and an initial flaw length of zero corresponds to analyses where the flaws in Bars II and III extend through the "lugs" to the parent bar material. Incidentally, although not plotted in Fig. 7, the FEM results for Bar I are nearly identical to those given by Eq 1 with $a = a_o$.

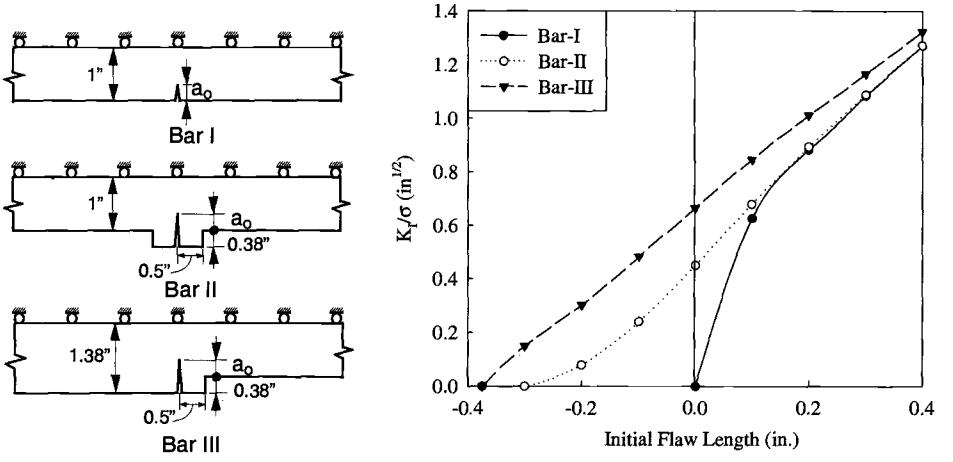

FIG. 7—*Uniformly stressed bar with edge crack:* (a) *finite-element models,* (b) *normalized stress intensity factors versus flaw size.*

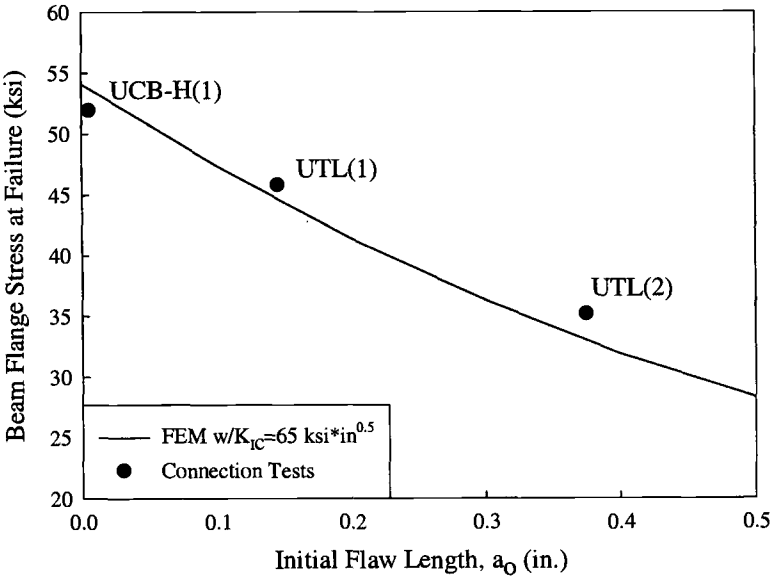

FIG. 8—*Back-calculation of material toughness from elastic fracture analyses.*

Comparing results for Bars I and II confirms observations made previously for the connections that the unloaded attachments create the effect of a small flaw in the bar. Once the flaw length a_o reaches a threshold size, the presence of the lug has essentially no effect. Thus, as in the connections, the thickness of the lug would not significantly affect the results. The difference in results between Bars II and III reflects the effect of the nonsymmetric stress field caused by nonsymmetry of the bars, where Bar III is a bit more representative of conditions in the beam-column flange weld. However, comparing Figs. 6 and 7*b*, the stress field and resulting K_I values in the connection are more severe than in the uniformly stressed bars.

In theory, the analysis results shown in Fig. 6 can be checked against the connection test data provided that the failure loads, initial flaw sizes, and the material toughness are all known. However, such complete information is not available. Toughness data of the weld metal/HAZ materials were not reported from any of the six connection tests, and initial flaw sizes are only known for three of the tests. Nevertheless, using data that are available, flaw sizes for three connection specimens obtained from post-test inspections by Kaufmann et al. [*4*] and the measured connection failure loads, the critical value of material toughness can be back-calculated. Shown in Fig. 8 is a plot of maximum nominal bending stress versus flaw size from these three tests and the FEM analyses. As indicated, assuming a constant value of material toughness, K_{Ic} = 65 ksi$\sqrt{\text{in.}}$ (71 MPa$\sqrt{\text{m}}$), the FEM results agree fairly well with the three tests. Given that K_{Ic} = 65 ksi$\sqrt{\text{in.}}$ (71 MPa$\sqrt{\text{m}}$) is in the range of expected toughness for E70T-4 weld metal, these results help confirm the accuracy of the analyses.

Inelastic CTOD Analyses

Results from inelastic analyses of connections with a flaw size a_o = 0.1 in. (2.5 mm) are summarized in Fig. 9. The three cases shown are for connections with varying beam yield strengths, F_{yb}, as noted in Fig. 3. With the assumed weld yield strength of F_{yw} = 60 ksi (413 MPa), the welds in Specimens UT-L and UCB-L are overmatched compared to the beam flange material (F_{yw}/F_{yb} = 1.2 to 1.5), while welds in specimen UCB-H are exactly equal in strength to the base metal (F_{yw}/F_{yb} = 1.0).

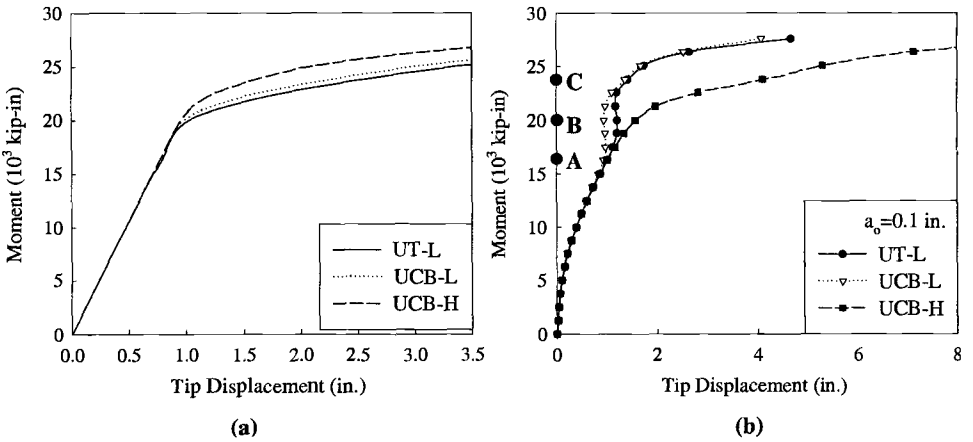

FIG. 9—*Inelastic analysis results:* (a) *moment versus deformation,* (b) *moment versus CTOD.*

In spite of the fact that the beam yield strength in UCB-H is significantly higher than in the other connections, as shown in Fig. 9*a* the overall inelastic strength is not much larger. This is due to the fact that significant inelastic deformations occur in the joint panel zone of the column, which limits the strength in all three connections. Referring to Fig. 9*b,* the data suggest that the beam strength—or more aptly the degree of weld overmatching—significantly affects the CTOD demand as a function of the applied moment. For example, whereas the CTOD demand for Specimen UCB-H begins to increase rapidly for beam moments of $M > 20\,000$ kip-in. (2260 kN-m), for the other specimens there is a region from about $M = 17\,500$ to 23 800 kip-in. (1990 to 2690 kN-m) during which CTOD does not increase. These differences in behavior can be explained by the progression of yielding in and around the weld region and the initial flaw.

Shown in Figs. 10*a* and 10*b* are stress contours for *yielded* finite elements in the weld region for connections UCB-L and UCB-H at the three load levels, A to C, corresponding to the circle markers in Fig. 9*b*. Recall that the weld metal in both cases has a strength of $F_{yw} = 60$ ksi (413 MPa), and the beam flange strengths are $F_{yf} = 40$ and 60 ksi (275 and 413 MPa), respectively, for UCB-L and UCB-H. For Specimen UCB-L, plastification around the crack tip and CTOD do not increase between Load Level A and B because the progressive spread of plastification through the flange thickness tends to shield the crack tip from increasing stresses and strains. This continues until Load Level C, at which point the flange is fully plastified and begins to strain harden, giving rise to higher CTOD demands. A key ingredient in this behavior is the overmatching weld metal that limits yielding in the weld. On the other hand, for connection UCB-H there is no overmatching and yielding concentrates in the weld causing higher CTOD at the root flaw.

Considering that the estimated in situ toughness of E70T-4 electrodes is $CTOD_c = 0.0005$ to 0.0012 in. (0.01 to 0.03 mm), the difference in behavior due to the degree of overmatching apparent in Fig. 9 may result in large differences in the fracture loads. Trends in the connection tests tend to support this theory, although more test data are needed to confirm the role of overmatching for improving the performance of these connections. The observation regarding overmatching is significant, however, given the common practice to specify E70 electrodes for both A36 and A572 steel without appreciating the resulting differences in overmatching, differences that can affect the interpretation of test data and the establishment of appropriate weld design criteria.

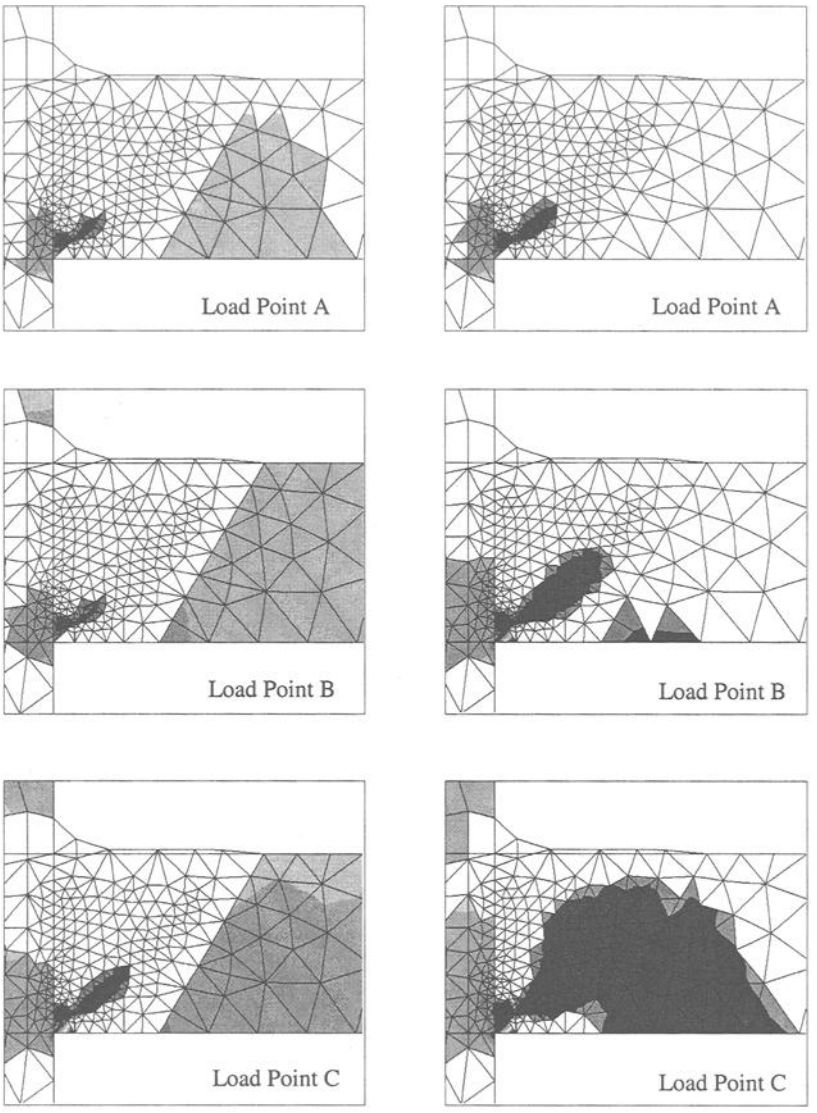

FIG. 10—*Progression of yielding in vicinity of initial flaw:* (a) *overmatching weld with* $F_{yw}/F_{yb} = 1.7$; (b) *matching weld with* $F_{yw}/F_{yb} = 1.0$.

Comparison of Elastic and Inelastic Analysis Results

Results for the elastic and inelastic analyses are superimposed in Fig. 11, where K_I and CTOD are correlated by the standard expression,

$$K_I = \sqrt{\lambda F_y E \text{CTOD}} \tag{3}$$

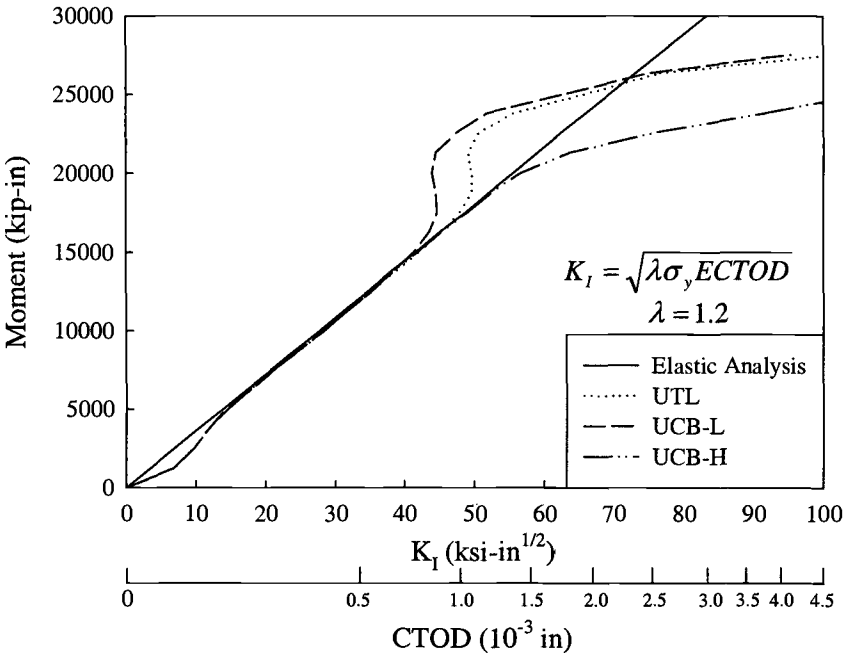

FIG. 11—*Comparison of fracture toughness demands from for elastic and inelastic analyses.*

in which F_y is the material yield stress, E is the elastic modulus, and the coefficient $\lambda = 1.2$ is determined to achieve agreement between K_I and CTOD at low stresses where the behavior is elastic. Coincidence of the curves in the initial region confirms that the elastic analyses are accurate for predicting fracture for calculated toughness up to about $K_I = 60$ ksi$\sqrt{\text{in.}}$ (66 MPa$\sqrt{\text{m}}$). For these connections, this coincides with applied nominal beam flange stresses of $\sigma = 40$ ksi (276 MPa)—roughly equal to yield in A36 steel and about ⅔ of yield in A572-Grade 50 steel. Beyond this point the elastic analyses do not capture important differences in behavior due to weld overmatching and other inelastic effects.

Summarized in Table 1 are critical values of material toughness back-calculated for the three connection tests where the initial flaw size is known. K_{Ic} values are the same as those plotted previously in Fig. 8 where on average $K_{Ic} \approx 65$ ksi$\sqrt{\text{in.}}$ (71 MPa$\sqrt{\text{m}}$). The average back-calculated $CTOD_c \approx 0.0023$ in. (0.06 mm) is larger than critical values of $CTOD_c = 0.0008$ to 0.0017 in. (0.01 to 0.03 mm) that we estimated from CVN data. There is also more variability in the $CTOD_c$ than K_{Ic} results.

TABLE 1—*Summary of weld metal toughness values back-calculated from elastic and inelastic fracture initiation analyses.*

	Test Data		Elastic	Inelastic	
Specimen	Flaw a_o, in. (mm)	$\sigma_{b,\max}$, ksi (MPa)	K_{Ic}, ksi$\sqrt{\text{in.}}$ (MPa$\sqrt{\text{m}}$)	$CTOD_c$, in. (mm)	$CTOA_c$, degrees
UCB-H	0.005 (0.1)	52 (358)	61.4 (67.4)	0.0024 (0.061)	5.2
UT-L(1)	0.380 (9.7)	35 (241)	70.5 (77.4)	0.0026 (0.066)	4.3
UT-L(2)	0.145 (3.7)	46 (317)	66.2 (72.7)	0.0018 (0.046)	3.6

Likely reasons for larger discrepancies in $CTOD_c$ are the inherent inaccuracies in the estimated critical toughness and approximations made in the analyses. As will be described below, the average values of CTOD obtained from the two-dimensional analyses can be significantly less than peak values calculated from three-dimensional analyses, particularly when the average flange stresses exceed about 2/3 σ_y. Therefore, $CTOD_c$ values back calculated from three-dimensional analyses would be smaller than those reported in Table 1. Finally, also reported in Table 1 are critical values of $CTOA_c$ that we back-calculated from the inelastic analyses in the same manner that we determined $CTOD_c$. The $CTOA_c$ values are used in the inelastic crack propagation analyses, described later, where we assume a constant value of $CTOA_c$ as the crack propagation criterion.

Crack Propagation Analyses

Two matters of interest beyond what can be resolved by crack initiation analyses are: (1) the degree to which stable crack growth or crack arrest might occur, and (2) the likely crack trajectories. The first is important to establish whether crack initiation is a reasonable measure of the connection strength limit state. The second is of interest to better understand the behavior and because the crack trajectory will affect the necessary post-earthquake repairs. As shown in Fig. 3, observed failure modes ranged from cases where the fractures propagated straight through the welds (sometimes pulling small "divots" of steel from the column) to ones where the cracks propagated into the column. Differences of this sort have obvious and significant implications on the feasibility and cost of repair.

Example results from two elastic crack propagation analyses are shown in Fig. 12 where the crack trajectories are established by comparing K_I and K_{II}, calculated at the updated crack tip location. It should be emphasized that the predicted trajectories in Fig. 12 are calculated from pure elastic stress analyses and, since they do not consider strain-rate and path-dependent effects, the analyses do not provide information on the extent of unstable crack growth. But, they do provide data on how the changing elastic stress field will affect the crack trajectory and the rate of dK_I/da. The crack trajectory shown in Fig. 12*a* corresponds to the basic connection geometry with input parameters for the connection tests described previously. This analysis suggests that weld root cracks will tend to prop-

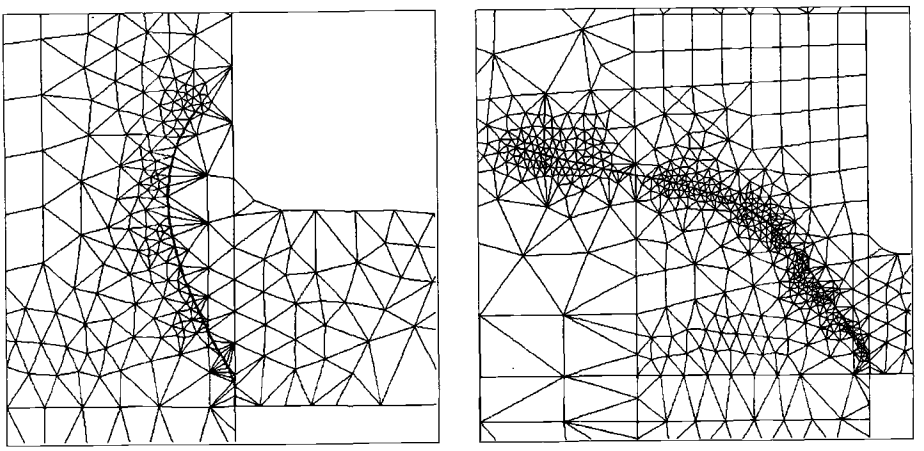

(a) (b)

FIG. 12—*Elastic crack trajectories:* (a) *basic case,* (b) *with axial tension in column.*

agate in a curvilinear path, suggestive of the "divot" type failure surfaces observed in many of the connection tests and damaged buildings. The trajectory shown in Fig. 12*b* is for the same connection, but with the superposition of an axial tension stress of 10 ksi (69 MPa) in the column. In this case, the change in stress field is enough to cause the crack to propagate into and across the column. Analyses of other factors reported by the authors [*3*] indicate that a number of parameters can influence the crack trajectories including (a) the connection geometry and details, (b) anisotropy in the materials, (c) the location and orientation of the initial flaw, and (d) the proportion of moment carried through the shear tab. These findings are significant since they help resolve debates in the earthquake engineering community as to whether crack propagations into the column, which had not been observed either in tests or actual buildings before the Northridge earthquake, were due to an anomaly in the earthquake ground motion (e.g., unusually large vertical accelerations) or other effects. Our conclusion is that there are several parameters that could create trajectories into the column, and while vertical ground accelerations could play a role, they were probably not the dominant factor in dictating the crack trajectories.

We also ran a limited number of inelastic crack propagation analyses to shed light on the whether there is significant stable inelastic crack growth in the connections prior to failure. In these analyses a pre-defined crack path was "unzipped" using a constant value of $CTOA_c$ as a criterion for crack extension. We recognize that there are a number of other approaches for predicting ductile tearing which may precede unstable crack growth, e.g., J_R, K_R, and T_R^*; however, given our objective to estimate the capacity for ductile tearing before crack instability, any of these methods can give a reasonable first-order estimate. The CTOAc approach has been shown to be as versatile and valid as some of these other approaches [*8*], and it was a method that was readily available to us through the FRANC2D analysis code.

The critical value of $CTOA_c = 5.2°$ was determined based on the value back-calculated value from the elastic crack initiation analysis for connection UCB-H. Shown in Fig. 13 are plots of overall connection response (moment versus tip displacement) and of moment versus crack growth for connection UCB-H with a small initial flaw. Subject to the assumed criterion of constant $CTOA_c$, data in Fig. 13*b* suggest that stable crack growth up to about 0.2 in. may have occurred, corresponding to an overall strength increase of about 5% between crack initiation and unstable growth. This suggests that, for connections with low toughness weld metal (e.g., $CTOA_c = 5.2°$), the additional strength and ductility associated with inelastic crack growth is fairly insignificant from the standpoint of practical design. However, this may not be true for improved connections made with higher toughness materials.

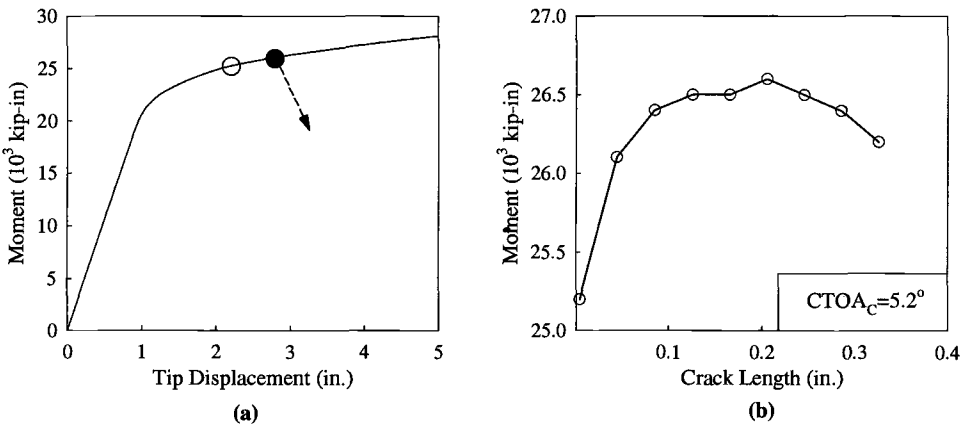

FIG. 13—*Inelastic crack propagation for constant* $CTOA_c = 5.5°$: (a) *moment versus deformation;* (b) *moment versus crack extension.*

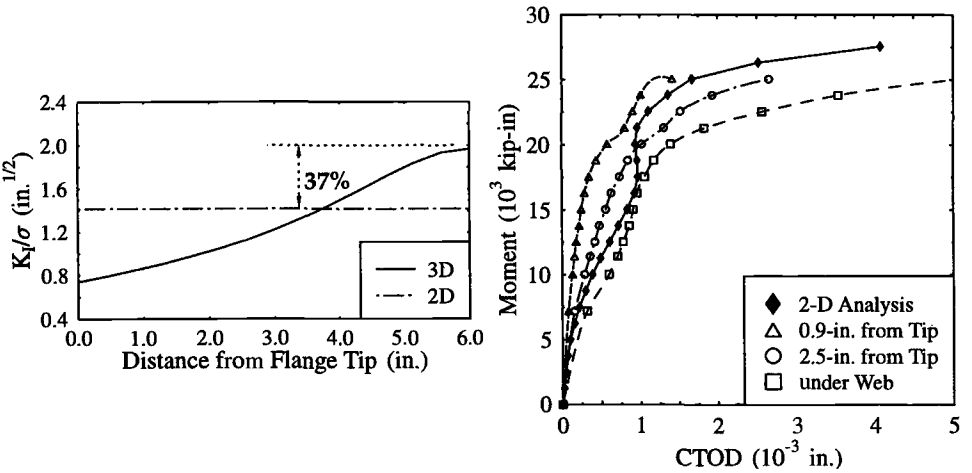

FIG. 14—*Two-versus three-dimensional analysis results:* (a) *elastic* K_I, (b) *inelastic CTOD.*

Three-Dimensional Behavior

All of the data presented thus far are from two-dimensional analyses that do not account for nonuniform stresses and strains across the flange width, differences between through cracks versus partial surface cracks (e.g., half-penny shaped cracks), and other three-dimensional effects. A limited number of three-dimensional analyses were run using the model in Fig. 5*b* to investigate three-dimensional behavior in a connection with a through crack. Shown in Fig. 14*a* is a comparison of K_I values from the two- and three-dimensional elastic analyses for an initial flaw size of a_o = 0.1 in. (3 mm). The horizontal axis in Fig. 14*a* corresponds to the locations across the beam flange where the left and right sides of the plot correspond to the flange tip and the beam center (directly under the web), respectively. As indicated, the maximum K_I that occurs under the web in the three-dimensional analyses is about 37% larger than the average value calculated in the two-dimensional analyses. More complete data reported elsewhere [*3*] show that this increase roughly parallels the elastic bending stress distribution across the flange width.

Differences between CTOD values from the inelastic analyses of connection UCB-L are shown in Fig. 14*b*. The two-dimensional results are the same as those previously shown in Fig. 9*b*, and values from the three-dimensional analyses are plotted for three locations across the beam flange. As with the elastic analyses, the largest CTOD values are at the center of the flange, and differences between the two- and three-dimensional results can become larger as the flange starts to yield. The three-dimensional effects tend to obscure the shielding behavior caused by weld overmatching; however, overmatching is still shown to significantly affect the maximum CTOD demand. Differences between the two- and three-dimensional analyses indicate the importance of three-dimensional effects on toughness demands in the connections.

Design Implications

To further summarize the results and demonstrate the potential role of fracture analyses in earthquake-resistant design of steel structures, data from the inelastic analyses are summarized in Fig. 15. Here, the fracture toughness demand for a connection with a_o = 0.1 in. (3 mm) is plotted versus deformation where the latter is described in terms of both beam tip displacement and inelastic connection rotation. The inelastic rotation is determined by separating the beam tip displacement into elas-

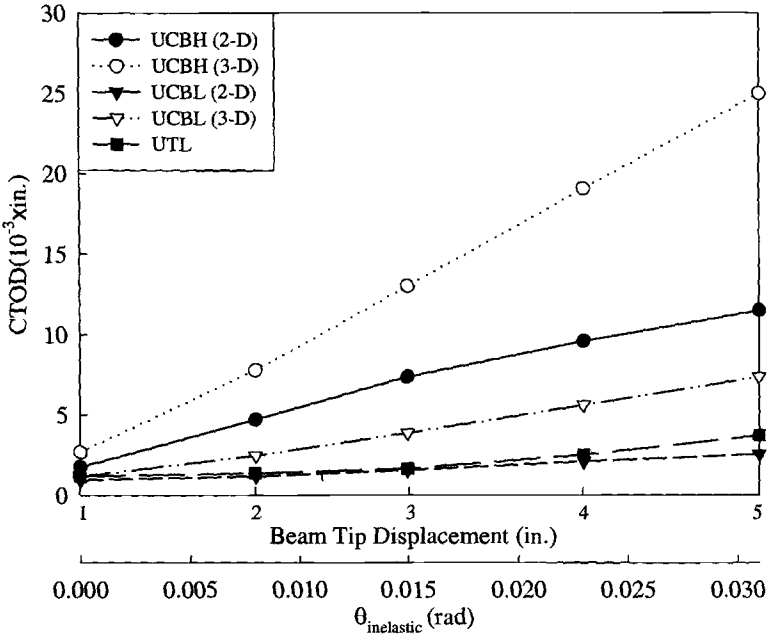

FIG. 15—*Fracture toughness versus inelastic connection deformations.*

tic and plastic components, and then assuming that the plastic deformations are concentrated in a plastic hinge located one half of the beam depth away from the column face.

When plotted in the way of Fig. 15, the CTOD demand is seen to increase nearly linearly with the inelastic deformation of the connection. This is important since ductility demand, more so than strength, is the governing design requirement for seismic design. For example, current seismic design standards [*1*] require a minimum connection rotation capacity of $\theta_{inelastic} = 0.03$ radians for ductile moment resisting frames. Comparisons between the two-dimensional analyses of connections with overmatching (UTL and UCB-L) and matching welds (UCB-H) in Fig. 15 clearly demonstrate the large potential benefit of overmatched welds. Of course, the reduction in toughness demand for overmatched welds needs to be weighed against unfavorable tradeoffs that may be encountered with overmatching, e.g., lower inherent toughness in higher-strength electrodes, higher residual stresses, concentration of shrinkage strains in the HAZ, etc. The three-dimensional results for UCB-L and UCB-H further indicate how the two-dimensional analyses significantly underestimate the peak toughness requirements by neglecting the variation in strains across the flange width.

Finally, given that the E70T-4 electrodes in common use for construction prior to the Northridge earthquake have low toughness, on the order of $CTOD_c \approx 0.001$ in. (0.03 mm), the data in Fig. 15 show that with an initial flaw size of $a_o = 0.1$ in (2.5 mm), it is impossible for any of the connections to reliably achieve the minimum ductility levels. Conversely, to reach the required plastic hinge rotation capacity of 0.03 radians, the three-dimensional analyses for connections UCB-L and UCB-H imply a required material toughness of $CTOD_c = 0.007$ to 0.017 in. (0.18 to 0.43 mm). Assuming a higher toughness electrode with an upper shelf $CTOD_c \approx 0.007$ in. (0.18 mm), connection UCB-L with overmatching electrodes may be acceptable, whereas Specimen UCB-H would not. However, further tests and analyses are needed to confirm that such connections would perform satisfactory under cyclic earthquake loading.

Final Remarks

This study demonstrates finite-element fracture analyses to be an important tool in understanding factors affecting toughness demands and the likelihood of cracking in beam-column connections with complicated geometries. Some of the issues raised in this paper, such as the relative influence of the backing bar gap and weld root defects, the potential benefits of using overmatching electrodes, etc., are subtle effects that are otherwise difficult to explain and quantify. The analyses described herein are a limited study looking at cracks initiating at a one of several possible internal flaws, and more work remains to determine appropriate toughness requirements, weld acceptance criteria, and related provisions to achieve fracture-resistant connections for seismic design. Beyond the connection design itself, there are many additional issues affecting the overall building system performance and safety beyond the scope of this paper, such as the effect of connection fractures on the stability of frames under dynamic loads. These and other questions raised by damage to steel frames during the Northridge earthquake are presently under study through the SAC Joint Venture [*9*].

Acknowledgments

This study was supported by the SAC Joint Venture through a contract from the Federal Emergency Management Agency. The authors are solely responsible for the results, statements, and interpretations contained in this paper.

SI Conversions

1 kip = 4.45 kN
1 in. = 25.4 mm
1 ksi = 6.89 MPa
1 ft-lb = 1.355 J

References

[*1*] American Institute of Steel Construction, "Seismic Provisions for Steel Buildings," AISC, Chicago, IL, 1997.

[*2*] SAC, "Interim Guidelines: Evaluation, Repair, Modification and Design of Steel Moment Frames," FEMA 267 (267a), Federal Emergency Management Agency, 1995 (updated 1997).

[*3*] Chi, W.-M., Deierlein, G. G., and Ingraffea, A. R., "Finite Element Fracture Mechanics Investigation of Welded Beam-Column Connections," SAC/BD-97/05, National Information Service for Earthquake Engineering, Berkeley, CA.

[*4*] Kaufmann, E. J. and Fisher, J. W., "Fracture Analysis of Failed Moment Frame Weld Joints Produced in Full-Scale Laboratory Tests and Buildings Damaged in the Northridge Earthquake," Technical Report: Experimental Investigations of Materials, Weldments and Nondestructive Examination Techniques, SAC 95-08, Part 2, 1996, pp. 1-1–1-21.

[*5*] Popov, E. P., Blondet, M., Stepanov, L., and Stojadinovic, B., "Full Scale Steel Beam-Column Connection Tests," Technical Report: Experimental Investigations of Beam-Column Subassemblies, SAC 96-01, Part 2, 1996, pp. 4-1–4-129.

[*6*] Shuey, B. D., Engelhardt, M. D., and Sabol, T. A., "Testing of Repair Concepts for Damaged Steel Moment Connections," Technical Report: Experimental Investigations of Beam-Column Subassemblies, SAC 96-01, Part 2, 1996, pp. 5-1–5-332.

[*7*] Barsom, J. M. and Rolfe, S. T., *Fracture and Fatigue Control in Structures—Applications of Fracture Mechanics,* Prentice Hall, Englewood Cliffs, NJ, 1987.

[*8*] Dawicke, D. S. and Newman, J. C., Jr., "Evaluation of Various Fracture Parameters for Predictions of Residual Strength in Sheets with Multi-Site Damage," *Proceedings,* 1st Joint DoD/FAA/NASA Conference on Aging Aircraft, Ogden, Utah, 8–10 July 1997, pp. 1307–1326.

[*9*] Mahin, S., Hamburger, R., and Malley, J., "National Program to Improve Seismic Performance of Steel Frame Buildings," ASCE, *Journal of Performance of Constructed Facilities,* Vol. 12, No. 4, 1998, pp. 172–179.

E. H. Glaessgen,[1] *I. S. Raju,*[2] *and C. C. Poe, Jr.*[2]

A Plate Element-Based Model for Mixed-Mode Debonding of Composite Stitched Stiffened Panels

REFERENCE: Glaessgen, E. H., Raju, I. S., and Poe, C. C., Jr., **"A Plate Element-Based Model for Mixed-Mode Debonding of Composite Stitched Stiffened Panels,"** *Fatigue and Fracture Mechanics: 30th Volume, ASTM STP 1360,* P. C. Paris and K. L. Jerina, Eds., American Society for Testing and Materials, West Conshohocken, PA, 2000, pp. 456–472.

ABSTRACT: An analysis based on plate finite elements and the virtual crack closure technique is used to study the effect of stitching on Mode I and Mode II strain energy release rates for a stitched warp-knit composite debond configuration. The stitches were modeled as discrete nonlinear fastener elements with a compliance determined by experiment. The axial and shear behavior of the stitches was considered with both the compliances and failure loads assumed to be independent. The effect of model slenderness ratio on the accuracy of the strain energy release rates determined with the plate element models for configurations without stitching was determined by comparison with similar plane strain models. The analysis showed that stitches are very effective in reducing Mode I strain energy release rate, G_{I}, by closing the debond faces near the debond front; however, they are less effective in reducing the Mode II strain energy release rate, G_{II}.

KEYWORDS: woven composites, stitching, stiffener debonding, plate finite elements, VCCT

Stitched warp-knit textile composite materials are currently being considered for use in primary aircraft structures [*1*]. In the NASA Advanced Subsonic Technology (AST) program, a stitched composite wing skin is being developed to demonstrate both the manufacturing and analytical technology needed to produce such structures. Structural panels, such as the one shown in Fig. 1, consist of the skin, stiffeners, and intercostals. These panels are typically made of between two and ten stacks of 1.40-mm-thick carbon warp-knit fabric that are layered and stitched with Kevlar yarns to form a skin. The stiffeners and intercostals are made of a similar number of stacks of layered and stitched fabric and are then stitched to the skin. Once the preform is assembled, the entire structure is infused with epoxy resin.

Stiffened panels are typically subjected to large in-plane and out-of-plane loads that produce considerable bending and shearing stresses at skin-stiffener interfaces [*2*]. Much of the research on skin-stiffener debonding has focused on the calculation of these skin-stiffener interface stresses [*3–5*]. The interface stresses may be large enough to cause a separation between the skin and stiffening elements, resulting in a delamination or debond.

Fracture-mechanics-based approaches have been applied to unstitched materials for the characterization of delaminations and debonds that may initiate as a result of large skin-stiffener interface stresses. Two-dimensional plane strain models have been used for analysis of skin-stiffener debond-

[1] National Research Council resident associate, MS 188E, NASA Langley Research Center, Hampton, VA 23681.

[2] Head and senior scientist, respectively, Mechanics of Materials Branch, MS 188E, NASA Langley Research Center, Hampton, VA 23681.

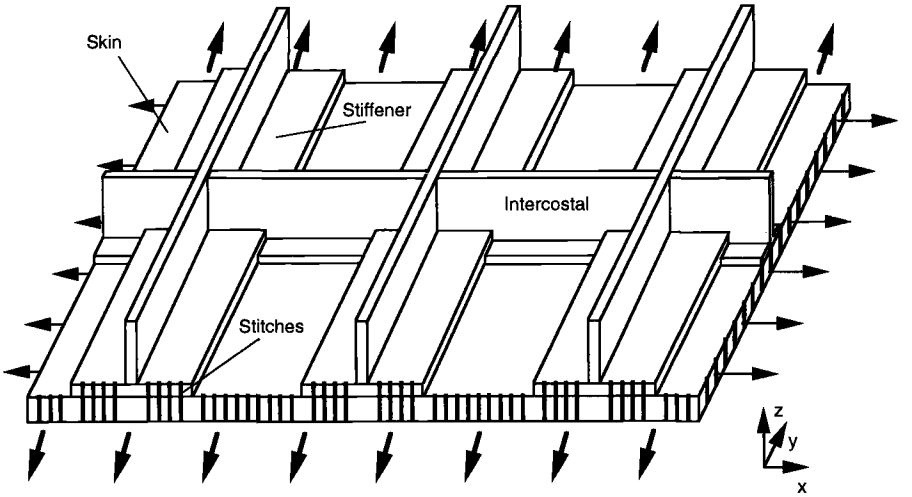

FIG. 1—*Stitched composite panel with stiffeners.*

ing [*6–8*], while models based on quasi-3D or 3D brick finite element models have been used for analysis of edge delamination and near-surface delamination of composites [*9–11*]. However, since many layers of brick elements are often required to model both the skin panel and the associated stiffeners, finite element models with large numbers of degrees-of-freedom may be required.

In an effort to develop computationally efficient models, Refs *12–15* proposed the use of plate elements to model skin-stiffener debond problems and calculate strain energy release rates using the virtual crack closure technique (VCCT). Conventional plate modeling inherently assumes that the reference surface of the plate coincides with the middle surface. Thus, the skin and stiffener are usually modeled by plate elements with nodes at their respective mid-planes. This conventional method is not convenient for modeling debonding because it entails complex constraints that account for both nodal translations and nodal rotations to tie the flange nodes to the corresponding skin nodes. The approach taken in Refs *12–17* and the present analysis is to offset the skin nodes and the stiffener nodes from their mid-planes by one half of the thickness of the skin and stiffener, respectively, such that the reference surface is positioned along the skin-stiffener interface. Plate element models using this technique can be used to evaluate accurate values of Mode I and Mode II strain energy release rates [*16*].

Stitching the skin to the stiffeners and intercostals may suppress growth of the debonds by effectively reducing the strain energy release rates at the debond front. The effects of stitching on delamination or debond growth in composites have been examined in simple configurations with some success [*18–25*]. In these works, the stitches are modeled as truss or beam elements connecting nodes through the thickness of the material. References *18–23* modeled laminates as two-dimensional plane strain structural components, while Refs *24–25* modeled the laminates as three-dimensional solids. An advantage of the three-dimensional modeling is to allow the stitches to be modeled discretely rather than as structural components with an "effective" stiffness.

In this paper, the method for computing strain energy release rates in stitched composite structures involves the use of plate elements to model the skin and stiffener (as in Refs *12–17*), nonlinear fastener elements to model the stitches, and multipoint constraints to model the contact problem. Since the nodes of the plate elements modeling the skin and stiffener are coincident, finite length spar or beam elements cannot be used to model the stitches as in Refs *18–25*. Rather, the stitches are mod-

eled as nonlinear fastener elements with axial and shear compliances determined by experiment. The fastener elements are composed of nonlinear spring elements offset with rigid links. This modeling technique allows an experimentally determined load versus deflection behavior to be considered for each stitch that includes the local effects of the stitch debonding from the laminate in addition to nonlinearity of the stitch material itself.

Consideration of the contact problem is required because the stitch forces may displace the skin and stiffener flange in the region of the debond such that their adjacent faces interpenetrate. Since this is a physically impossible situation, a means for preventing the penetration is included in the model.

The objective of this paper is to present the combined plate and nonlinear fastener element-based technique and to quantify the effect of stitches on the Mode I and Mode II strain energy release rates of a mixed mode, skin-stiffener debond configuration. The plate element modeling technique is used to analyze the debond configurations, and the virtual crack closure technique [*26,27*] is used to calculate strain energy release rates. In this paper, the effect of parameters such as stitch stiffness, applied load, and debond length on the strain energy release rates are studied.

Analysis

Figure 1 shows the configuration and loading of a typical skin-stiffened stitched composite panel. Three-dimensional modeling and analysis of this complex configuration may require a large finite element model with several thousand degrees of freedom. However, considerable insight into the behavior of complicated debond configurations can be gained by examining simple configurations such as the flange-skin configuration shown in Fig. 2*a* while reducing modeling complexity. The config-

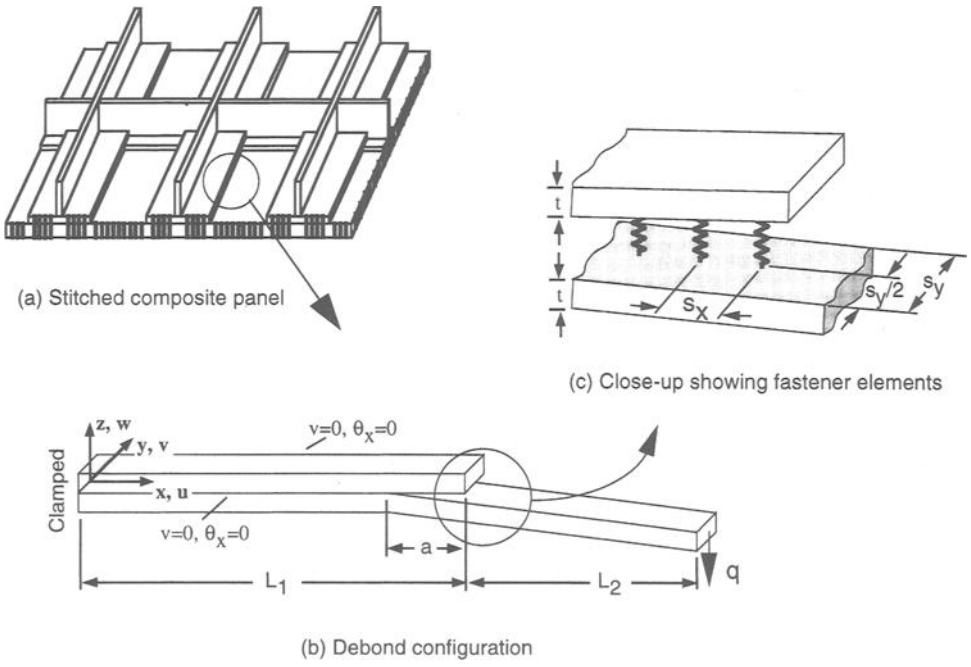

FIG. 2—*Stitched composite panel and debond configeration.*

uration was modeled using the STAGS finite element code [*28,29*] as an infinitely wide strip of length $L_1 = 63.5$ mm and $L_2 = 38.1$ mm and a width corresponding to the y-direction stitch spacing of $s_y = 3.18$ mm. The skin and stiffener flange have equal thickness, t, of 5.59 mm and are subjected to cylindrical bending repeating unit boundary conditions ($v = 0$, $\theta_x = 0$) on $y = \pm s_y/2$ in Fig. 2*c* at a model width corresponding to the stitch row spacing, s_y.

Material and skin thicknesses that are representative of the AS4/3501-6 warp-knit fabric stitched composite upper wing skin used in the NASA Advanced Subsonic Technology (AST) program are considered [*1*]. The same material is assumed for both the skin and the stiffener flange with each stack of material oriented with its primary axis in the x-direction and having a thickness of 1.40 mm. The equivalent laminate stacking sequence of each stack of material is $(45/-45/0/90/0/-45/45)_{ns}$ where $n = 4$ for both the flange and the skin. The overall density of the fabric expressed in areal weight is 1425 g/m^2 with 612, 640, and 173 g/m^2 for the 45, 0, and 90° fibers, respectively. In these analyses, the laminates are assumed to be homogeneous, with axial properties determined experimentally and all others estimated using the equivalent stacking sequence and classical lamination theory as

$$E_{11} = 63.8 \text{ GPa} \qquad \mu_{12} = 15.7 \text{ GPa} \qquad \upsilon_{12} = 0.40$$

$$E_{22} = 32.2 \text{ GPa} \qquad \mu_{13} = 11.1 \text{ GPa} \qquad \upsilon_{13} = 0.30$$

$$E_{33} = 11.2 \text{ GPa} \qquad \mu_{23} = 5.53 \text{ GPa} \qquad \upsilon_{23} = 0.30$$

where E_{ii}, μ_{ij}, υ_{ij} $(i,j = 1,2,3)$ are the Young's moduli, shear moduli, and Poisson's ratio, respectively, and Subscripts 1, 2, and 3 represent the fiber, transverse, and out-of-plane directions, respectively. The stitch spacings, s_x and s_y, were 3.18 mm in the x- and y-directions, respectively.

Strain Energy Release Rates

The virtual crack closure technique (VCCT) [*26,27*] can be used to calculate strain energy release rates, G, with plate elements using the techniques discussed in Refs *12–15*. The configuration was modeled with the STAGS (Structural Analysis of General Shells) finite element code using a 9-node quadratic shear deformable plate/shell element [*28,29*]. A comparison of strain energy release rates computed with the plate element-based models and similar plane strain element-based models for skin-stiffener configurations without stitching is offered in Appendix A. Additional considerations that arise from debond modeling with plate elements are discussed in Ref *16*.

A representation of the 9-noded plate elements near a debond front with rectangular grid type modeling is shown in Fig. 3 with element lengths of 0.13 and 0.80 mm in the x- and y-directions, respectively. Reference *16* suggests that allowing the elements ahead of the debond front to have free rotations ensures accurate modeling and evaluation of the strain energy release rates. If there are free rotations ahead of the debond front, then the G values can be calculated using the nodal forces (F_x, F_y, F_z) and displacements (u, v, w) near the debond front and the increment of new debond area created as (see Fig. 3) [*12*]:

Mode I components:

$$\begin{aligned}
(G_I)_i &= -\frac{1}{2\Delta b_i}\left[F_{z_i}(w_p - w_{p'}) + F_{z_e}(w_l - w_{l'})\right] \\
(G_I)_j &= -\frac{1}{2\Delta b_j}\left[F_{z_j}(w_q - w_{q'}) + F_{z_f}(w_m - w_{m'})\right] \\
(G_I)_k &= -\frac{1}{2\Delta b_k}\left[F_{z_k}(w_r - w_{r'}) + F_{z_g}(w_n - w_{n'})\right]
\end{aligned} \tag{1}$$

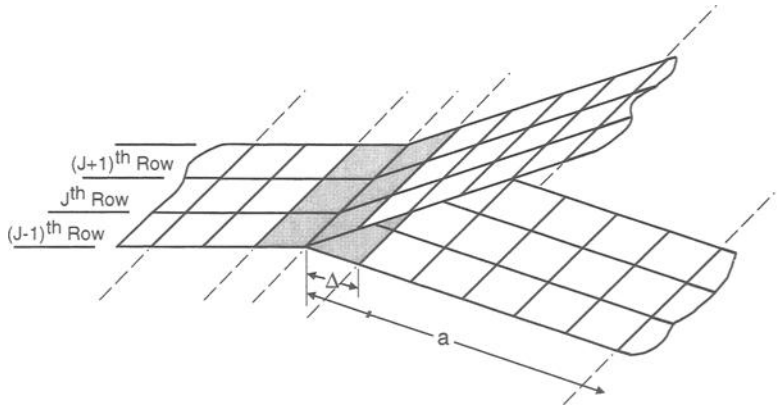

(a) Plate element modeling near the debond front

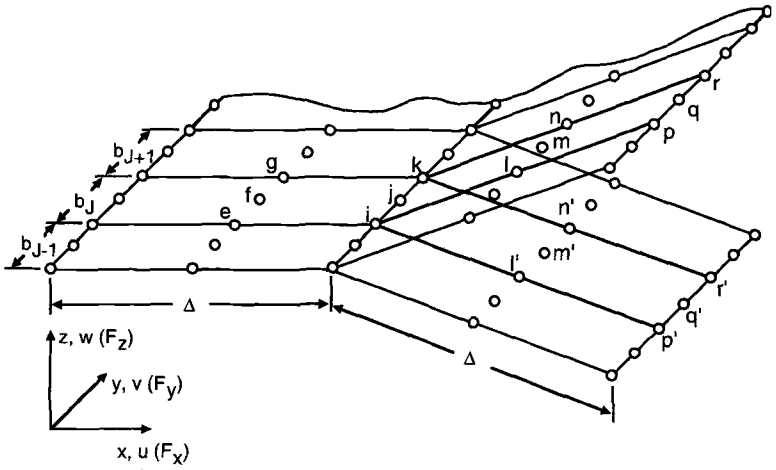

(b) Details of the model near the debond front

FIG. 3—*Debond configuration modeled using nine-node plate elements.*

Mode II components:

$$(G_{II})_i = -\frac{1}{2\Delta b_j}\left[F_{x_i}(u_p - u_{p'}) + F_{x_e}(u_l - u_{l'})\right]$$

$$(G_{II})_j = -\frac{1}{2\Delta b_j}\left[F_{x_j}(u_q - u_{q'}) + F_{x_f}(u_m - u_{m'})\right] \tag{2}$$

$$(G_{II})_k = -\frac{1}{2\Delta b_k}\left[F_{x_k}(u_r - u_{r'}) + F_{x_g}(u_n - u_{r'})\right]$$

Mode III components:

$$(G_{III})_i = -\frac{1}{2\Delta b_i}[F_{y_i}(v_p - v_{p'}) + F_{y_e}(v_l - v_{l'})]$$

$$(G_{III})_j = -\frac{1}{2\Delta b_j}[F_{y_j}(v_q - v_{q'}) + F_{y_f}(v_m - v_{m'})] \tag{3}$$

$$G_{III})_k = -\frac{1}{2\Delta b_k}[F_{y_k}(v_r - v_{r'}) + F_{y_s}(v_n - v_{n'})]$$

with

$$(G_{Total})_\gamma = (G_I + G_{II} + G_{III})|_\gamma, \text{ and} \tag{4}$$

$\gamma = i, j$, and k indicate nodes at the debond front as shown in Fig. 3*b*.

The elements are assumed to have the same length, Δ, ahead of and behind the debond front (as shown in Fig. 3). In Eqs 1–3, the equivalent widths apportioned to the two corner debond-front nodes are b_i and b_k, and to the midside debond front node is b_j. These are

$$b_i - \frac{1}{6}[b_{J-1} + b_J]$$

$$b_j = \frac{2}{3}b_J, \tag{5}$$

$$b_k = \frac{1}{6}[b_J + b_{J+1}]$$

where b_{J-1}, b_J, and b_{J+1} are the widths of element rows $J - 1$, J, and $J + 1$, respectively, as shown in Fig. 3*b*. Note that this modeling strategy, which assumes no rotational constraints ahead of the debond front, is termed "Technique-B" in Refs *14–15*. The strain energy release rates along the debond front of the mixed-mode skin-stiffener debond configurations are calculated using Eqs 1–5.

Modeling Stitches

Because of the implementation of the fastener elements, the configurations have been analyzed with a geometrically nonlinear finite element analysis within the STAGS finite element code. Unlike the two-dimensional plane strain and three-dimensional solid models considered in Refs *18–25*, the plate element-based modeling technique does not allow through-the-thickness modeling of details such as the stitches; nor does it allow nodal connections other than at the plate element reference surface. Thus, in the present technique, the stitches are not modeled as spar or beam elements, but rather as STAGS fastener elements.

The fastener elements are imposed as nonlinear springs offset by rigid links within the plate element model [*28,29*]. The fastener elements have both axial and shear stiffnesses, K_{axial} and K_{shear}, and are schematically shown as springs in Fig. 2. Only the fastener elements behind the debond front ($L_1 - a < x < L_1$ in Fig. 2) carry load since the upper and lower plate elements ahead of the debond front are coupled using constraint equations to have identical translational displacements. Stitches are considered in the model only along the debonded length of the skin and stiffener, so the number of fastener elements in the model representing the stitches in the structure is dependent on the debond length. The fastener elements are evenly spaced along the line $y = 0$ over the debonded length of the model ($L_1 - a < x < L_1$) in regular intervals of 3.18 mm corresponding to the stitch locations and coincide with plate element nodal locations.

Accurate compliance curves for both axial and shear behavior of the stitches were developed in Ref *31* using flatwise tension and double lap shear tests (see Fig. 4), respectively. These compliance

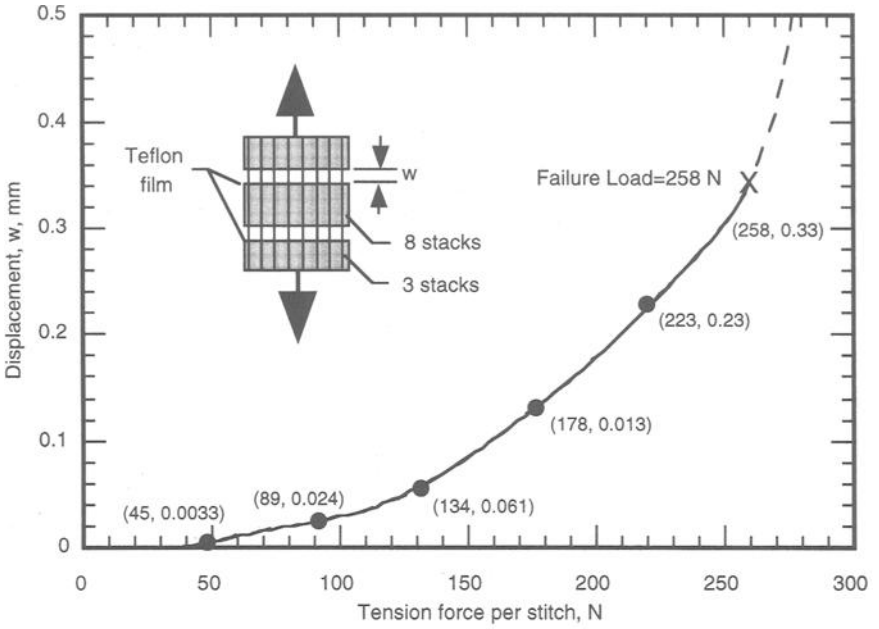

(a) Compliance of stitches in tension

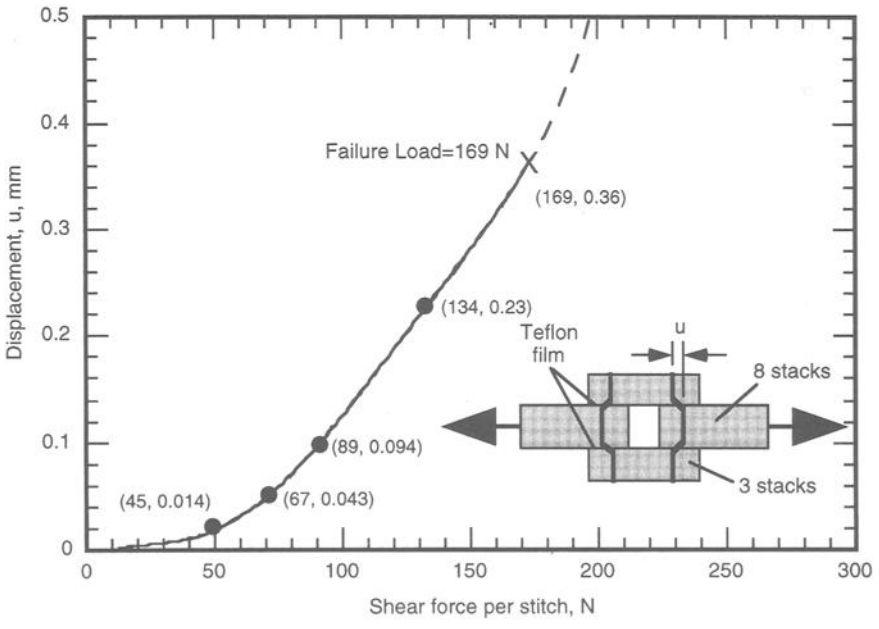

(b) Compliance of stitches in shear

FIG. 4—*Stitch compliance (experimental results taken from Ref* 31).

curves represent the net behavior of the stitch due to stitch material nonlinearity and stitch debonding. The contribution due to the compliance of the stacks of carbon/epoxy has been accounted for and does not contribute to the values shown in the curves of Fig. 4 [*31*].

A piecewise linear representation of these data is used in the finite element model. The points used in the linearization of the compliance curves are also shown in Fig. 4. Examination of the flatwise tension test data revealed that the axial compliance of the stitches increases from approximately 7.42 $\times 10^{-8}$ m/N (1.35×10^7 N/m stiffness) initially to 2.78×10^{-6} m/N (3.59×10^5 N/m stiffness) near failure. Similar examination of the double lap shear test data showed that the shear compliance of the stitches increases from approximately 3.14×10^{-7} m/N (3.19×10^6 N/m stiffness) initially to 3.57 $\times 10^{-6}$ m/N (2.80×10^5 N/m stiffness) near failure. Since the axial and shear responses of the stitches shown in Fig. 4 were determined independently using flatwise tension and double lap shear tests, their responses must be considered to be independent in the analysis as well. Also note that failure of the stitches occurs at a load of 258 N per stitch in tension and 169 N per stitch in shear. These stiffness and failure loads will be used for the characterizations in this paper.

Modeling the Contact Problem

Closure of the debond faces may occur once the debond is of sufficient length. In the finite element analysis, contact of the faces is allowed, while interpenetration of the faces is not. Interpenetration of the faces can be prevented either by adding gap elements (STAGS 810 PAD elements) to the model between the debond faces where interpenetration is likely to occur or by adding multipoint constraints along a known region of interpenetration to impose the requirement of identical z-direction (w) displacements among elements in contact. No constraint on the relative sliding displacements (u, v) is imposed using either technique. Because of issues concerning the tolerances on overclosure allowed with the gap elements and the resulting negative stitch forces that may be computed, the multipoint constraint-based procedure was used in the present analysis even though it requires that multiple analyses be executed to determine the actual contact length.

Results and Discussion

The mixed-mode skin-stiffener debond configuration exhibits both Mode I and Mode II deformations at the debond front and assumes self-similar debond growth between the skin and stiffener. Thus, no variation in G across the width of the model is assumed, and the values of G reported are those calculated along the lines of the stitching ($y = 0$ in Fig. 2). Examination of the distribution of G_{I} and G_{II} across the width for this debond configuration shown in Fig. 2 showed less than 2% percent difference between the location in line with the stitches ($y = 0$) and the location midway between the stitches ($y = \pm s_y/2$). Although a tendency for the debond to leave the skin-stiffener interface has been shown in some composite skin-stiffener structures [*6–8*], experimental evidence suggests that the self-similar assumptions are valid for this type of stitched woven composite [*30*].

Effect of Stitch Stiffness

To isolate the effects of stitch stiffness on G_{I}, G_{II}, and stitch force, a distributed load, q, of 17 500 N/m was applied to the configuration shown in Fig. 2*b* with a single load-bearing stitch. A fixed debond length, a, of 6.35 mm was chosen as it is the longest debond that may exist with only one load-bearing stitch at the stitch spacing (s_x, s_y) of 3.18 mm. The dependence of G and stitch force on stitch stiffness was determined for configurations with constant values of axial and shear stiffnesses of the stitches from 1.75×10^2 to 1.75×10^7 N/m increased in orders of magnitude and also at 3.50×10^7 and at 5.00×10^7 N/m. These stiffnesses bound the measured stitch stiffnesses shown in Fig. 4 that are used in the forthcoming sections of this paper. The analysis was conducted for a given applied force of $q = 17\,500$ N/m. Figure 5 presents the strain energy release rate, G, and the axial and

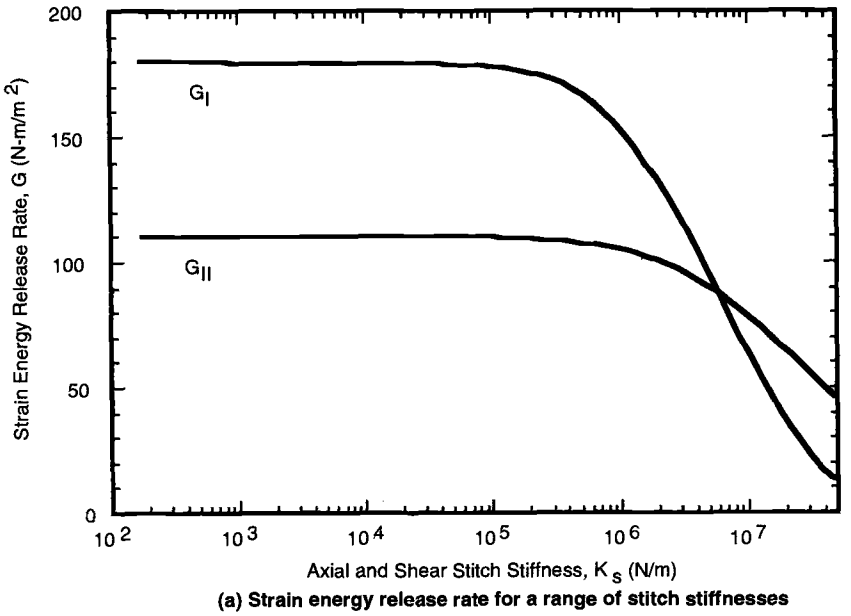

(a) Strain energy release rate for a range of stitch stiffnesses

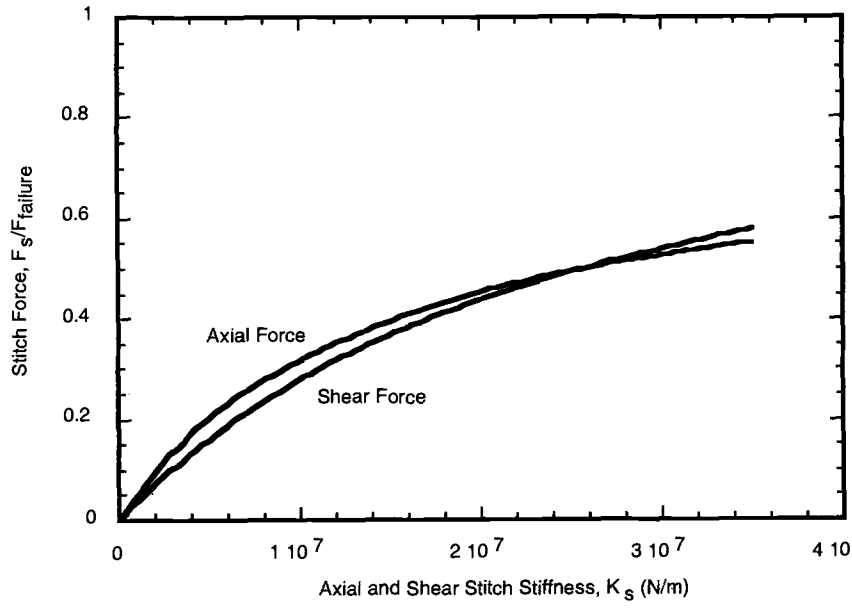

(b) Stitch force for a range of stitch stiffnesses

FIG. 5—*Effect of stitch stiffness on strain energy release rate and stitch force* (q = *17 500 N/m,* a = *6.35 mm,* s_x = *3.18 mm,* s_y = *3.18 mm).*

shear stitch forces normalized by their respective failure loads, $F_{axial}/F_{axial\ failure}$ and $F_{shear}/F_{shear\ failure}$, for the debond configuration. The computed values of G_I and G_{II} are nonlinear functions of the stitch stiffness. As stitch stiffness increases, the strain energy release rate decreases because much of the load is transferred from the skin to the flange by the stiff stitches. Comparison of the measured initial axial stitch stiffness of about 1.35×10^7 N/m from the flatwise tension test data and initial shear stitch stiffness of about 3.19×10^6 N/m from double lap shear test data with the curves of Fig. 5*a* suggests that in the presence of a single stitch, G_I may be decreased by nearly an order of magnitude, while G_{II} may be decreased by as much as a factor of two compared with the unstitched values.

The force carried by the single stitch increases with increasing stitch stiffness throughout the range of stiffnesses considered as shown in Fig. 5*b*. However, a decrease in the slope of the curves indicates that both the axial and shear force in the stitches will reach a maximum value at very large stitch stiffnesses. For this configuration, the values of the stitch force become asymptotic at very large stitch stiffnesses and reach approximately $F_{axial}/F_{axial\ failure} = 0.78$ and $F_{shear}/F_{shear\ failure} = 1.00$ at stitch stiffnesses near 1.0×10^{10} N/m at the applied load of 17 500 N/m.

Effect of Increasing Load

Finite element models utilizing the compliance curves shown in Fig. 4 were used to evaluate the response of the debond configuration to increasing load. As shown in Fig. 6*a*, both G_I and G_{II} increase with increasing applied load; however, G_I exhibits a larger sensitivity to the increase in load than does G_{II}. Figure 6*b* shows the increase in normalized axial and shear forces in the stitches with increasing applied load. From Fig. 4, stitch stiffness decreases as stitch load increases; thus, the slope of the stitch force versus applied load curves also decrease.

The maximum values of strain energy release rate shown in Fig. 6*a* are well beyond the value required to propagate the debond in an epoxy resin; G_{IC} for a brittle epoxy resin is approximately 175 J/m^2 [*32*]. These large values of G_I and G_{II} are a result of the large applied loads required to reach the nonlinear region of the stitch response for the single stitch configuration. As will be seen in the following section, large stitch forces are attained at much lower loads once the debond grows.

An applied load of 80 000 N/m results in an axial stitch load of approximately 129 N ($F_{axial}/F_{axial\ failure}$) = 0.50 in Fig. 6*b* in the stitches and corresponds to a stitch stiffness of 1.20×10^6 N/m in Fig. 4*a*. This represents a decrease in axial stitch stiffness by a factor of 12 compared with the initial value. Although the stitches significantly retard debond growth when carrying low loads, they have a decreased effect on strain energy release rate once they are heavily loaded.

Effect of Increasing Debond Length

The effect on increased debond length is studied next. The strain energy release rates and stitch forces were determined over a range of debond lengths for the debond configuration with a fixed applied load of 17 500 N/m. In Fig. 7, both the Mode I and Mode II strain energy release rates, G_I and G_{II}, for the unstitched configurations increase with increasing debond length over the range of debond lengths, a, presented. The increasing strain energy release rates suggest that a condition for unstable debond growth exists in the unstitched configurations.

Stitching has a significant effect on both G_I and G_{II}. The Mode I G-value initially increases with debond length and then begins to decrease after the debond advances past the first stitch (first vertical line in Fig. 7), decreasing as additional stitches begin to carry load, eventually reaching values of zero for long debonds ($a/t > 3.41$). These zero values for long debonds correspond to a region of contact immediately behind the debond front that increases with increasing debond length. In contrast, G_{II} is a weaker function of debond length since the shearing displacements are not reduced to zero as the stitches close the debond faces. Rather, the shearing force and displacement are gradually reduced as additional stitches transfer an increasing fraction of the load. Thus, even though the Mode

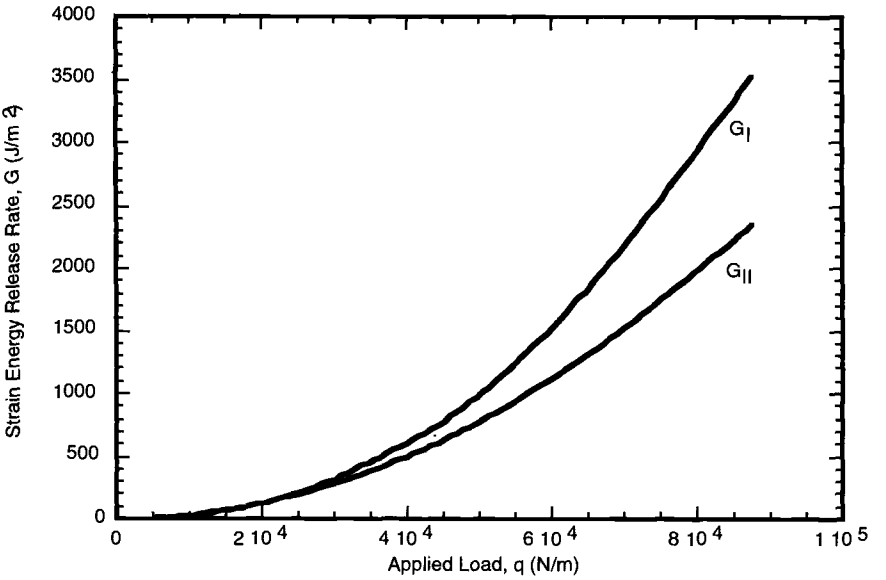

(a) Strain energy release rate as a function of applied load

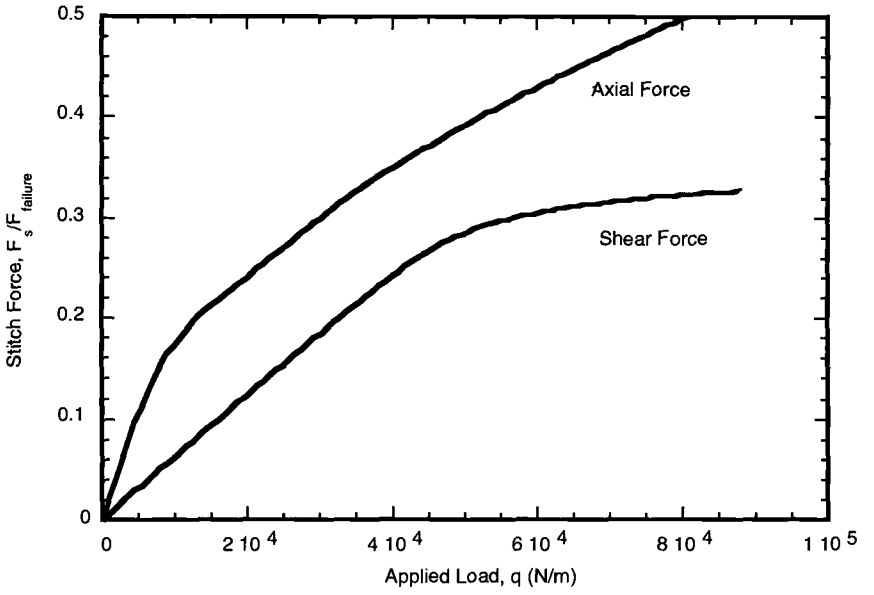

(b) Stitch force as a function of applied load

FIG. 6—*Effect of applied load on strain energy release rate and stitch force* (a = *6.35 mm*, s_x = *3.18 mm*, s_y = *3.18 mm*).

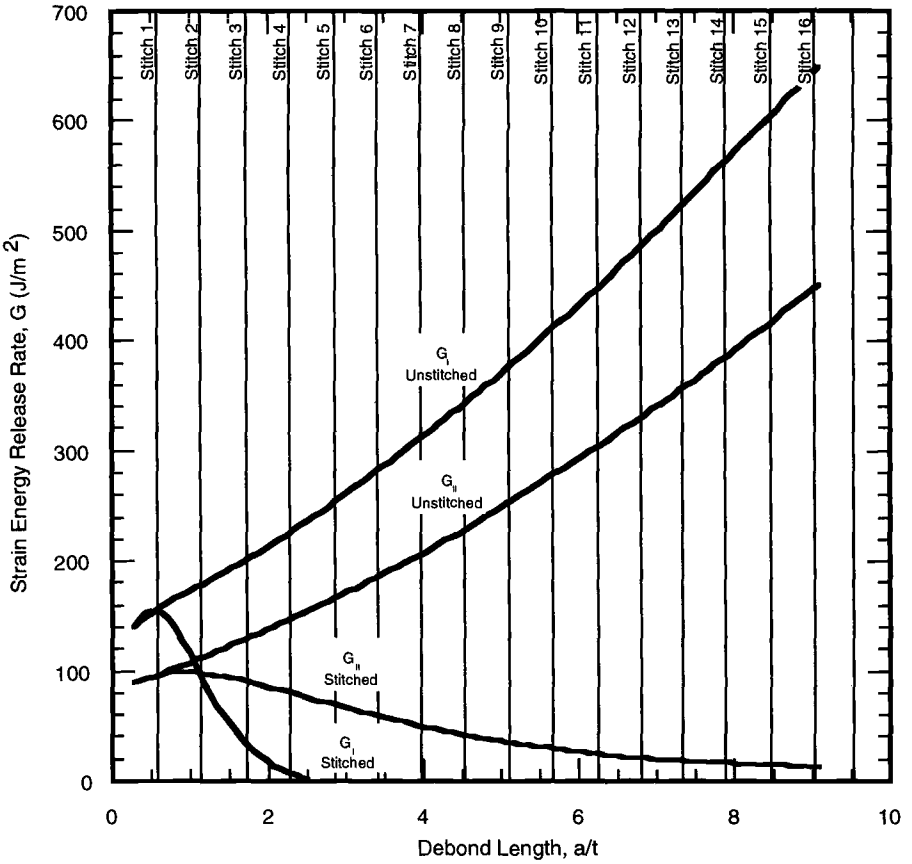

FIG. 7—*Effect of multiple stitches on* G_I *and* G_{II} (q = 17 500 N/m, s_x = 3.18, s_y 3.18 mm).

I contribution is driven to zero for $a/t > 3.41$, there may be sufficient energy due to Mode II present to drive the debond for much longer lengths.

Figures 8*a* and 8*b* show the normalized axial and shear force in the stitches. As seen in Fig. 8*a*, of the 15 active stitches in the model, only Stitches 1 through 3 have nonzero axial force (F_{axial}) over the range of debond lengths considered. The axial force reaches a near-constant value for debond lengths corresponding to the region of zero Mode I ($a/t > 3.41$). However, a shearing force (F_{shear}), shown in Fig. 8*b*, is also present in the stitches and is nonzero for all of the stitches (Stitches 1 through 15) along the debond. Results were evaluated from the finite element model with increments of debond growth of 6.35 mm ($a/t = 1.14$), so the force corresponding to the first 6.35 mm ($a/t = 1.14$) of debond growth beyond a given stitch location in the finite element model was not recovered in the analysis and is represented by the dashed lines in the figure. For long debonds considered in this analysis ($a/t > 3.41$), the normalized shear force ($F_{shear}/F_{shear\ failure}$) in the first stitch is larger than the corresponding normalized axial force ($F_{axial}/F_{axial\ failure}$).

There are two ways that the debond may continue to grow in this mixed-mode configuration. If the load in the stitches remains below the failure load, the debond may continue to grow by Mode II as shown in Fig. 7*a*. However, at higher loads, the stitches may fail and non-zero Mode I may be present that could contribute to the growth of the debond. The present analysis suggests that the former may be the preferred growth mode for this configuration with the 17 500 N/m load.

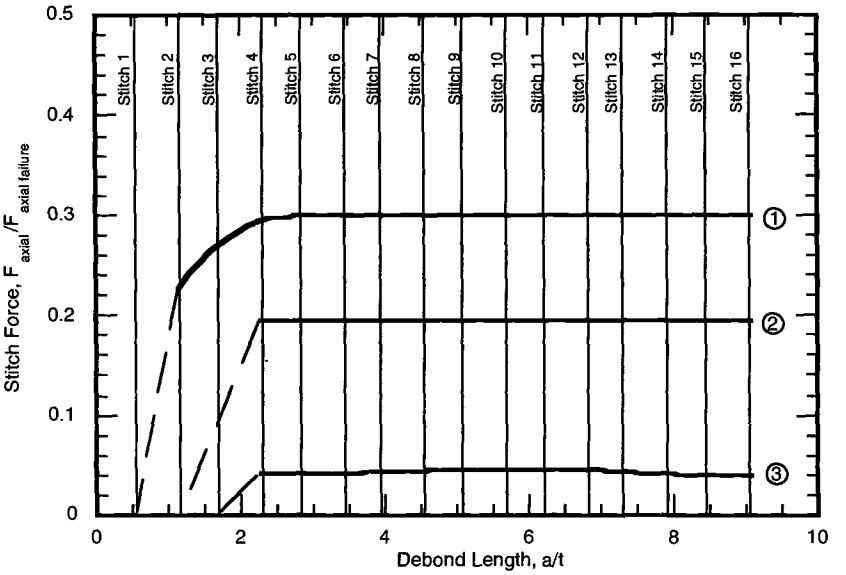

(a) Stitch axial force as a function of debond length

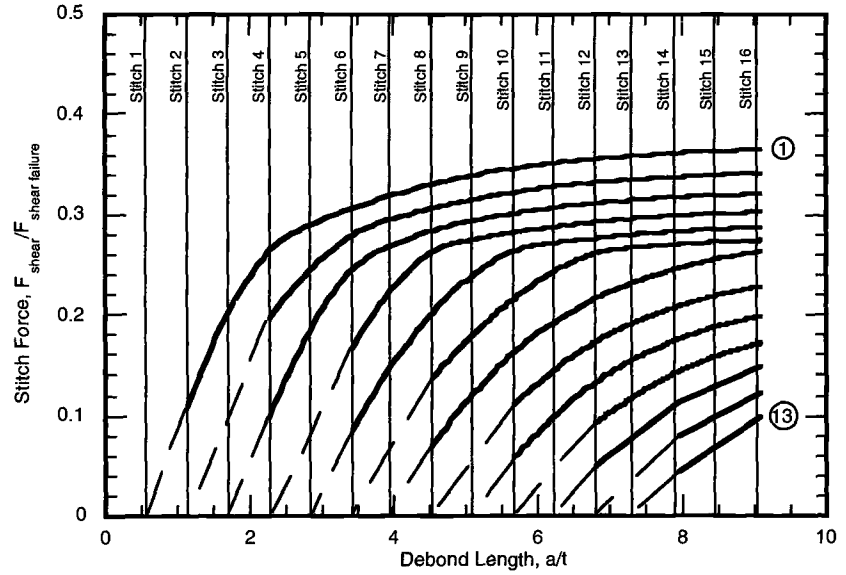

(b) Stitch shear force as a function of debond length

FIG. 8—*Effect of multiple stitches on stitch force* (q = *17 500 N/m,* s_x = *3.18 mm,* s_y = *3.18 mm). Circled numbers indicate the number of the stitch.*

Concluding Remarks

The effect of stitches on the Mode I and Mode II strain energy release rates of a mixed-mode skin-stiffener debond configuration with an initial debond was studied. A modeling technique was developed that uses the virtual crack closure technique (VCCT) to calculate the strain energy release rates, plate elements with an offset reference surface to model the skin and stiffener, nonlinear fastener elements to model the stitches, and multipoint constraints to model the contact problem. The effect of parameters such as stitch stiffness, applied load, and debond length on the strain energy release rates were studied.

The debond growth between the flange and the skin was assumed to be self-similar and continuous along the length of the flange-skin interface. The technique is well suited to configurations that would normally lend themselves to being modeled with plate elements, that is, configurations wherein shear deformable plate assumptions are valid. The stitches were modeled as discrete nonlinear fastener elements with their compliance determined by experiment. Both axial and shear behavior of the stitches were considered; however, the two compliances and failure loads were assumed to be independent. The contact problem was modeled using multi-point constraints rather than gap elements because the no-penetration condition could be imposed exactly with the multi-point constraints, whereas the gap elements enforce no penetration to a small but finite tolerance.

Stitches with stiffnesses in excess of 2×10^5 N/m in the 3.18 by 3.18-mm stitching pattern were required to noticeably affect the values of strain energy release rate for the configurations studied. For fixed debond lengths, an increase in applied load results in an increase in the load carried by the stitches; thus, stitch compliance increases and contributes to an increase in G_{I}. However, as the debond length increases at a fixed applied load, additional stitches begin to carry load resulting in a decrease in G_{I}. For long debonds, the stitches may produce enough compressive force at the debond front to close the debond and reduce G_{I} to zero. In contrast, the stitches have less effect on Mode II, and G_{II} remains nonzero throughout the range of debond lengths considered. Thus, there are two ways that the debond may continue to grow in this mixed-mode configuration. If the stitches do not fail, the debond may continue to grow by Mode II. However, if the stitches fail, non-zero Mode I may be present and may also contribute to the growth of the debond.

APPENDIX A

Verification of Plate Element Models

Although Refs *12–15* provide validation of the plate element-based analyses through comparison with corresponding plane strain analyses, comparison is provided here for the specific configuration of interest. Geometrically linear analyses with a unit bending load are considered.

Plane strain-based analyses that model the cross-sectional deformation of the skin and stiffener are inherently more accurate than plate element-based analyses that make the assumption that plane sections remain plane throughout the thickness. However, the plate assumptions become increasingly valid as the slenderness ratio (ratio of plate length, l, to thickness, $2t$) increases.

Figure A1*a* shows a comparison between the plate element and plane strain element-based techniques for an unstitched version of the configuration shown in Fig. 2. The configuration has a slenderness ratio of $l/2t = 9.09$. As seen in the figure, the plate element-based technique predicts values of G_{I} and G_{II} that are consistently less than the plane strain values. The differences between the two

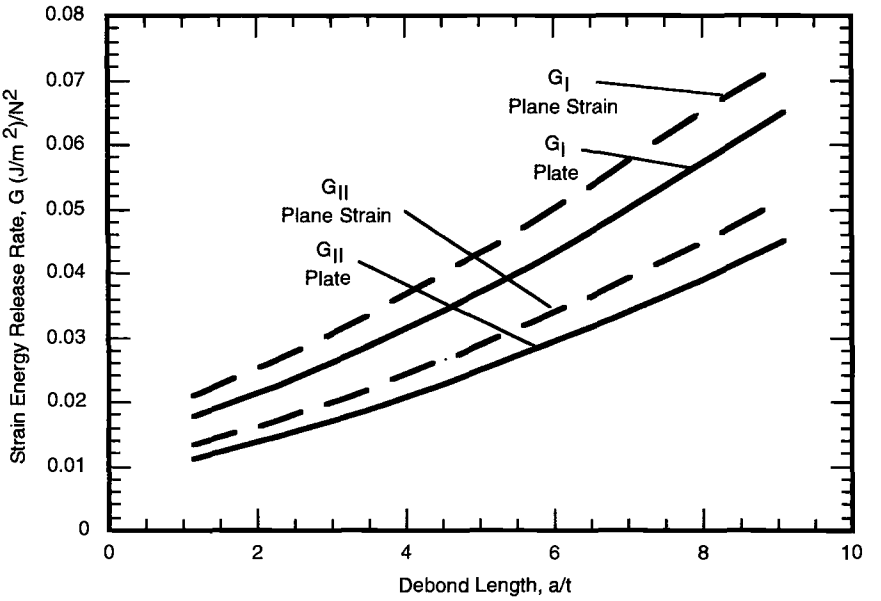

(a) Debond configurations with thickness, *l*/2*t*=9.09

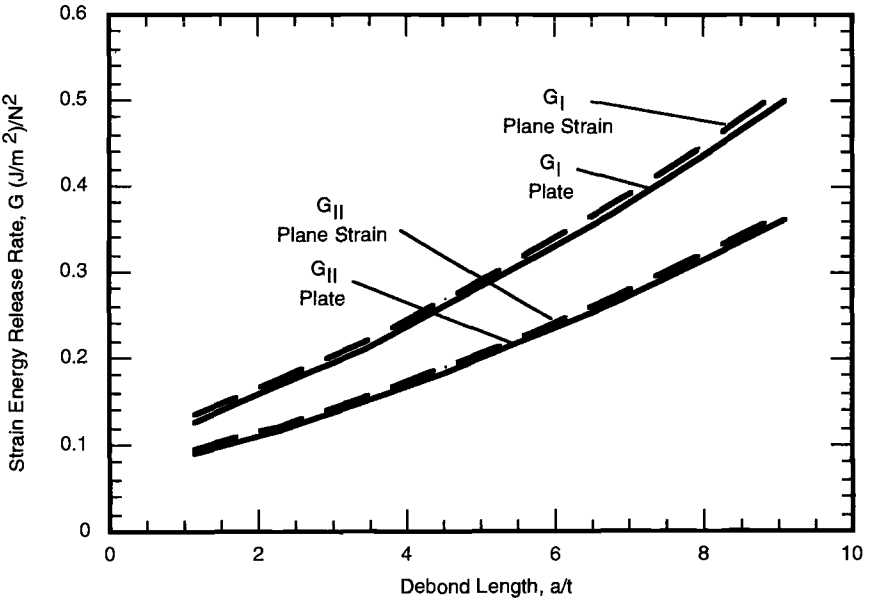

(b) Debond configurations with thickness, *l*/2*t*=18.2

FIG. A1—*Comparison of plate and plane strain analyses.*

analyses are a weak function of the debond length and are about 17 and 18% for G_I and G_{II}, respectively, at values of $a/t = 1.14$ and 12 and 14% for G_I and G_{II}, respectively, at values of $a/t = 9.09$.

Figure A1*b* shows a similar comparison between plate and plane strain values, but for a slenderness ratio of $l/2t = 18.2$. As seen in this figure, the plate element-based technique predicts values of G_I and G_{II} that are only slightly less than the plane strain values. The difference between the two analyses is again a weak function of the debond length and are about 7 and 4% for G_I and G_{II}, respectively, at values of $a/t = 1.14$ and 3 and 2% for G_I and G_{II}, respectively, at values of $a/t = 9.09$. Thus, a comparison of the results obtained for these two configurations indicates that the validity of the plate element-based analyses using the STAGS 480 elements improves with increasing slenderness ratio and that the accuracy is a weak function of debond length.

References

[1] Dow, M. B. and Dexter, H. B., "Development of Stitched, Braided and Woven Composite Structures in the ACT Program and at Langley Research Center," NASA TP-97-206234, November 1997.

[2] Wang, J. T., Jegley, D. C., Bush, H. G., and Hinrichs, S. C., "Correlation of Structural Analysis and Test Results for the McDonnell Douglas Stitched/RFI All-Composite Wing Stub Box," NASA TM-110267, 1996.

[3] Wang, J. T. S. and Biggers, S. B., "Skin/Stiffener Interface Stresses in Composite Stiffened Panels," NASA CR 172261, 1984.

[4] Hyer, M. W. and Cohen, D., "Calculation of Stresses and Forces Between the Skin and Stiffener in Composite Panels," *Proceedings, 28th AIAA/ASME/ASCE/AHS Structures, Structural Dynamics and Materials Conference,* AIAA Paper 87-0731-CP, 1987.

[5] Cohen, D. and Hyer, M. W., "Influence of Geometric Nonlinearities on Skin-Stiffener Interface Stresses," *Proceedings, 29th AIAA/ASME/ASCE/AHS Structures, Structural Dynamics and Materials Conference,* AIAA Paper 88-2217-CP, 1988.

[6] Minguet, P. J., "Analysis of the Strength of the Interface between Frame and Skin in a Bonded Composite Fuselage Panel," *Proceedings, 38th AIAA/ASME/ASCE/AHS Structures, Structural Dynamics and Materials Conference,* AIAA Paper 97-1342-CP, 1997, pp. 2783–2790.

[7] Minguet, P. J. and O'Brien, T. K., "Analysis of Composite Skin-Stringer Bond Failures Using a Strain Energy Release Rate Approach," *Proceedings, Tenth International Conference on Composite Materials,* Vol. I, Woodhead Publishing Ltd., 1995, pp. 245–252.

[8] Minguet, P. J. and O'Brien, T. K., "Analysis of Test Methods for Characterizing Skin/Stringer Debonding Failures in Reinforced Composite Panels," *Composite Materials: Testing and Design, Twelfth Volume, ASTM STP 1274,* August 1996, pp. 105–124.

[9] O'Brien, T. K., "Characterization of Delamination Onset and Growth in a Composite Laminate," *Damage in Composite Materials, ASTM STP 775,* 1982, pp. 140–167.

[10] Wang, A. S. D. and Crossman, F. W., "Initiation and Growth of Transverse Cracks and Edge Delamination in Composite Laminates, Part 1: An Energy Method," *Journal of Composite Materials,* Vol. 14, 1980, pp. 71–87.

[11] Whitcomb, J. D., "Instability-Related Delamination Growth of Embedded and Edge Delaminations," NASA TM 100655, 1988.

[12] Wang, J. T., Raju, I. S., and Sleight, D. W., "Composite Skin Stiffener Debond Analyses Using Fracture Mechanics Approach with Shell Elements," *Composites Engineering,* Vol. 5, No. 2, 1995, pp. 277–296.

[13] Raju, I. S., Sistla, R., and Krishnamurthy, T., "Fracture Mechanics Analyses for Skin-Stiffener Debonding," *Engineering Fracture Mechanics,* Vol. 54, No. 3, 1996, pp. 371–385.

[14] Wang, J. T., Raju, I. S., Davila, C. G., and Sleight, D. W., "Computation of Strain Energy Release Rates for Skin-Stiffener Debonds Modeled with Plate Elements," *Proceedings, 34th AIAA/ASME/ASCE/AHS Structures, Structural Dynamics and Materials Conference,* AIAA Paper 93-1501-CP, 1993, pp. 1680–1692.

[15] Wang, J. T. and Raju, I. S., "Strain Energy Release Rate Formulae for Skin-Stiffener Debond Modeled with Plate Elements," *Engineering Fracture Mechanics,* Vol. 54, No. 2, 1996, pp. 211–228.

[16] Glaessgen, E. H., Riddell, W. T., and Raju, I. S., "Effect of Shear Deformation and Continuity on Delamination Strain Energy Release Rate," *Proceedings, 39th AIAA/ASME/ASCE/AHS Structures, Structural Dynamics and Materials Conference,* AIAA Paper 98-2023-CP, 1998.

[17] Glaessgen, E. H., Raju, I. S., and Poe, Jr., C. C., "Fracture Mechanics Analysis of Stitched Stiffener-Skin Debonding," *Proceedings, 39th AIAA/ASME/ASCE/AHS Structures, Structural Dynamics and Materials Conference,* AIAA Paper 98-2022-CP, 1998.

[18] Mignery, L. A., Tan, T. M., and Sun, C. T., "The Use of Stitching to Suppress Delamination in Laminated Composites," *Delamination and Debonding of Materials, ASTM STP 876,* 1985, pp. 371–385.

[19] Chen, V. L., Wu, X. X., and Sun, C. T., "Effective Fracture Toughness in Stitched Laminates," *Proceedings of the Eight Technical Conference of the ASC,* 1994, pp. 453–462.

[20] Sharma, S. K. and Sankar, B. V., "Effects of Through-the-Thickness Stitching on Impact and Interlaminar Fracture Properties of Textile Graphite/Epoxy Laminates," NASA CR195042, 1995.

[21] Sankar, B. V. and Sonik, V., "Modeling End-Notched Flexure Tests of Stitched Laminates," *Proceedings of the American Society for Composites,* ASC, 1995, pp. 172–181.

[22] Byun, J.-H., Gillespie, Jr., J. W., and Chou, T.-W., "Mode I Delamination of a Three-Dimensional Fabric Composite," *Journal of Composite Materials,* Vol. 24, May 1990, pp. 497–518.

[23] Flanagan, G. and Furrow, K., "Parametric Studies of Stitching Effectiveness for Preventing Substructure Disbond," *Proceedings, Mechanics of Textile Composites Conference,* NASA CP 3311, October 1995, pp. 539–554.

[24] Tsai, G. C., "Global/Local Stress Analysis of Stitched Composite Laminates," *Proceedings, 23rd International SAMPE Technical Conference,* SAMPE, 1991, pp. 297–305.

[25] Lee, C. and Liu, D., "Tensile Strength of Stitching Joint in Woven Glass Fabrics," *Journal of Engineering Materials and Technology,* Vol. 112, April 1990, pp. 125–130.

[26] Rybicki, E. F. and Kanninen, M. F., "A Finite Element Calculation of Stress Intensity Factors by a Modified Crack Closure Integral," *Engineering Fracture Mechanics,* Vol. 9, 1977, pp. 931–938.

[27] Raju, I. S., "Calculation of Strain-Energy Release Rates with Higher Order and Singular Finite Elements," *Engineering Fracture Mechanics,* Vol. 28, No. 3, 1987, pp. 251–274.

[28] Brogan, F. A., Rankin, C. C., Cabiness, H. D., and Loden, W. A., *STAGS User Manual,* Lockheed Martin Missiles and Space Co., July 1996.

[29] Young, R. D., Rankin, C. C., Starnes, J., and Britt, V., *Introduction to STAGS,* Lecture Notes from a Workshop at NASA Langley Research Center, Hampton, VA, 8–9 March 1995.

[30] Davis, J. G., Shuart, M. J., and Bowles, D. E., Eds., *Proceedings, Fifth NASA /DoD Advanced Composites Technology Conference,* NASA CP 3294, May 1995.

[31] Adams, D. O., "Stitch Compliance in Delaminated Composites," *Proceedings, 29th SAMPE Technical Conference,* Orlando, FL, October 28–31 1997.

[32] Reinhart, T. J., *Engineered Materials Handbook, Vol. 1 Composites,* ASM International, 1987.

Author Index

A

Aveline, Jr., C. R., 403

B

Bray, Gary H., 388
Brockenbrough, John R., 388
Brocks, Wolfgang, 139

C

Chi, Wei-Ming, 439
Connelly, Guy M., 185
Crayon, Dan, 377

D

Dawicke, David S., 85
Deierlein, Gregory G., 439
Dodds, Jr., Robert H., 85
Donald, J. Keith, 185
Donoso, J. R., 34
Dougherty, John D., 227

E

Ernst, Hugo A., 115

F

Farkas, Diana, 278
Foster, M. A., 327

G

Gioielli, Paulo C., 61
Glaessgen, E. H., 456
Glinka, Gregory, 240
Goldfine, Neil, 427
Grandt, Jr., Alten F., 214
Gullerud, Arne S., 85

H

Hampton, Roy W., 85
Hauge, Mons, 102
Hertzberg, Richard W., 263
Howard, I. C., 152

I

Ingraffea, Anthony R., 169, 439

J

Jerina, Kenneth L., ix
Joyce, James A., 357

K

Kim, Young Jin, 313
Kirk, Mark T., 51

L

Lambert, Dennis M., 115
Landes, John D., 3, 34, 61, 69
Lang, Markus, 201
Larsen, James M., 201
Lee, Jin Ho, 313
Li, Z. H., 152
Loushin, Les, 61

M

McCabe, Donald F., 21
Mercer, Chris, 278, 327
Merkle, John G., 21

N

Natishan, MarjorieAnn E., 51, 427
Newman, J. C., 403

P

Padovan, J., 227
Papritan, J. C., 327
Paris, Paul C., ix, 61, 185
Poe, Jr., C. C., 456

R

Raju, I. S., 456
Ranestad, Øyvind, 102
Reuter, W. G., 403
Rossmanith, Hans P., 347

S

Sheikh, M. A., 152
Siegmund, Thomas, 139
SIRIUS, 152
Soboyejo, A. B. O., 327
Soboyejo, Winston O., 278, 327
Srivatsan, T. S., 227
Stephens, Ralph I., 240

T

Tada, Hiroshi, 61, 185
TerMaath, Stephanie C., 169
Thaulow, Christian, 102
Topper, T. H., 299
Tregoning, Robert L., 357

U

Underwood, John H., 377

V

Varvani-Farahani, A., 299
Vigilante, Gregory N., 377

W

Wallin, Kim, 21
Wang, Hsing-Ling, 214
Wawrzynek, Paul A., 169
Weiss, Volker, 427
Wilson, Christopher D., 69

Y

Ye, Fan, 278
Yoon, Kee Bong, 313

Z

Zhang, Hong-Yan, 240
Zhang, Zhiliang L., 102

Subject Index

A

Adjusted compliance ratio, 388
Aluminum
  ductile crack growth, 85
  early state fatigue damage, 427
  stress-life fatigue curves, 388
ASTM E 399, 357
ASTM E 813, 69, 357
ASTM E 1152, 69, 357
ASTM E 1737, 357
ASTM E 1820, 61, 357
ASTM E 1921, 21, 51, 357
Atomistic simulation, 278

B

Bending stresses, induction-hardened shafts, 240
Biaxial fatigue, 299
Bolt-loaded specimen, 377
Brittle cracks, welded beam-column connections, 439

C

Cell modeling, ductile-to-brittle transition, 152
Charpy impact energy, 61
Cohesive strength, ductile fracture modeling, 139
Cohesive zone models, 139
Common format equation, 34
Compliance ratio, 185
  adjusted, 388
Confocal scanning laser microscopy technique, 299
Constraint
  physical evidence, 115
  quantifying, 102
  semi-elliptical cracks, 403
Crack
  elliptical subsurface, 240
  environmental, 377
Crack closure, 201, 227, 388
  elastic, 185
  metal alloys, 263
  plasticity-induced, 227
Crack face displacements, 115
Crack growth
  ductile, 85
  hydrogen, 377
Crack initiation, 347
Crack propagation, 227
  stress intensity factor, 201
Crack tip opening angle, 85
Crack tip opening displacement, 115
Crack tip shielding, 227
Crack tip stress field, 347
Crack wake influence, 185
Creep deformation, accumulated, 313
Creep-fatigue crack growth rate, 313
Creep fracture parameter, effects of accumulated creep deformation, 313
CVN impact test, 61

D

Damage mechanics, 152
Damage tolerance, honeycomb core sandwich panels, 169
Debonding, stiffener, 456
Disbond, facesheet-from-core, 169
Discontinuities, 115
Dissipation rate, 139
Ductile fracture, modeling, 139
Ductile-to-brittle transition
  fracture toughness, 21
  modeling, 152
Ductility, welded beam-column connections, 439

E

Earthquake engineering, 439
Elasticity, semi-elliptical cracks, 403
Elastic-plastic fracture mechanics, 3, 357
Elastic region, common format equation, 34
Energy release rate, 169
Environmental cracking and fracture, 377

F

Facesheet-from-core disbond, honeycomb core sandwich panels, 169
Failure assessment, fusion line cracks, 102
Fatigue, stress-life curves, 388
Fatigue crack, subsurface initiation, 240
Fatigue crack growth
  biaxial strain ratio and, 299
  mechanism, 299
  multiparameter model, 327
  niobium aluminide intermetallics, 278
  stress-life curves, 388
Fatigue crack propagation, 201
  lap joint specimens, 214
  metal alloys, 263
  subsurface, 240
Fatigue life, effective, 299
Finite element analysis, 227
  creep fracture parameter, 313
  honeycomb core sandwich panels, 169
  semi-elliptical cracks, 403

size criteria, 357
3-D, 85
welded beam-column connections, 439
Finite radii notches, 69
Fracture
displacement-based characterization, 115
environmental, 377
niobium aluminide intermetallics, 278
semi-elliptical cracks, 403
Fracture mechanics
computational approach, 169
elastic-plastic, 3, 357
history, 347
linear elastic, 357
multiparameter model, 327
time dependent, 313
validity limits, 115
Fracture toughness
apparent, 69
evaluations in transition range, 21
niobium aluminide intermetallics, 278
predicting *J-R* curve, 61
testing, notched round bars, 69
transition behavior, 51
unifying principles for evaluating, 34
welded beam-column connections, 439
Fusion line cracks, failure assessment, 102

G

Geometry effects, 102, 139
Gurson model, 139

H

Hole expansion, 214
Honeycomb core sandwich panels, facesheet-from-core disbond, 169
Hoop strain, 299
Hydrogen embrittlement, 377
Hydrogen-induced cracking, 377

I

Impact energy, Charpy, 61
Induction hardening, 240
Instrumented bolt, 377

J

J-integral, 69, 357
as function of depth below surface, 115
J-Q-M approach, 102
J-R curve, predicting, 61

L

Lap joints, 214
Large-scale tests, ductile-to-brittle transition, 152
Leon, Alfons, 347
Life prediction
induction-hardened steel, 240
lap joint specimens, 214
stress-life fatigue curves, 388
structural metallic materials, 327
titanium, 201
Linear elastic fracture mechanics, 357
Load interaction, 201
Load transfer mechanism, 214

M

Magnetometers, 427
Master curve, 21, 201
micromechanical evaluation, 51
Material mismatch effects, 102
Meandering Winding Magnetometer, 427
Metal alloys, fatigue crack propagation, 263
Micromechanical models, 278
ductile fracture, 139
Modified crack closure method, 169
Multi-cell modeling, ductile-to-brittle transition, 152
Multiparameter model, 327
Multiple site damage, 214

N

Niobium aluminide intermetallics, forged damage-tolerant, 278
Notched round bar, 69
Notch stresses, 347

O

Out-of-plane bending, 85
Overload effects, 227
Overstrains, compressive, 299

P

Periodic compressive overstrain, 299
Planar fracture specimens, fracture toughness evaluation, 34
Plasticity, semi-elliptical cracks, 403
Plastic region, common format equation, 34
Plate finite element, 456
Pressure vessel steels
fracture toughness evaluations, 21
modeling ductile-to-brittle transition, 152
Probabilistic methods, 327

R

Reference temperature, 51
Residual stresses, 201
  induction-hardened shafts, 240
Rivets, 214

S

Seismic design, 439
Separation energy, ductile fracture modeling, 139
Size criteria, consistent, 357
Slenderness ratio, 456
Stainless steels, early state fatigue damage, 427
Steel
  biaxial fatigue tests, 299
  crack closure effects, 227
  high-strength, 377
  induction-hardened, 240
  semi-elliptical cracks, 403
  welded beam-column connections, 439
Stiffener debonding, 456
Stitching, 456
Strain
  mean, 227
  range, 227
Strain energy release, stitching effect, 456
Strain ratio, biaxial, 299
Stress, semi-elliptical cracks, 403
Stress intensity, 357
  effective, 185, 388
Stress-intensity factor
  crack propagation, 201
  semi-elliptical cracks, 403
Structural metallic materials,fatigue crack growth, 327
Substructuring, 227
Surface cracks, semi-elliptical, 403

T

Titanium, fatigue crack propagation, 201
Transition range, fracture toughness evaluation, 21

U

Unloading compliance, 357
Unstable fracture, 102

W

Weighardt, Karl, 347
Welded beam-column connections, finite element analysis, 439
Weldments, constraints, quantifying, 102
Woven composites, plate element-based model, 456

ISBN 0-8031-2617-4